Characterization of Flow-based Bobbin Friction Stir Welding Process

A thesis submitted for the Degree of
Doctor of Philosophy in
Mechanical Engineering
University of Canterbury

By Abbas Tamadon

Supervisors:
Dirk Pons (Senior Supervisor)
Don Clucas (Co-supervisor)
Kamil Sued (Associate Supervisor)

November 2019

Context

Friction stir welding (FSW) is a solid-state joining method whereby instead of melting of material, rotating tool ploughs through the interface of the two plates to be joined, and mixes the materials into a bonded structure by heat and stirring, generated from friction between the rotating tool and the workpiece. It offers an alternative to conventional fusion welding processes providing a potential to make welds in a single pass, while eliminating fume, reducing distortion, and eliminating solidification defects. BT-FSW: There is a class of FSW tools called bobbin tools, consisting of two shoulders, one on each side of the workpiece connected by the tool pin, which here runs through the material. Recent trials using this symmetrical process have highlighted some of the benefits, compared to conventional FSW. Along with the complete elimination of root flaws and the need for a backing bar, lower distortion and fully penetrated joints are produced due to lower heat input and a balanced weld profile. Process benefits are also realized through a simpler FSW machine, regarding the complex holding fixture and almost zero weld forging forces acting during the process. Nevertheless, bobbin-FSW is still a young process and most of the research has been focused on the empirical phase based on a trial and error approach. To promote the process as a standard technique applicable in the industry first should provide a theory for the process. The BFSW as a welding technique needs to guarantee the quality of the weld to produce a defect-free joint. Hence, the main approach in this research is focused on the study of the mechanism of the defect formation (induced on the flow-based stirring action) and finding the solution to control and eliminate the structural defects from the weld. In this regards, the physical trials, the study of the weld properties by a focus on microstructure observation, and proposing a physical model of the defect formation mechanism are the main ideas for the methodology of the research.

Abstract

In bobbin friction stir welding, achieving the defect-free joints needs a comprehensive control of the process parameters. Material flow transportation around the rotating tool and the mass deposition at the backside of the tool are critical characteristics of friction stir welding. To achieve an optimized weld structure, the history of the plastic deformation needs to be identified with a flow-based elucidation. In this study, an analogue model was developed to evaluate the formation of a banded structure using the bobbin tool, with a focus on the interaction between the tool-workpiece. The flow visualization in plasticine analogue was validated in comparison with the aluminium welds. The cross-section of the weld demonstrated the details of the formation of tunnel voids, caused by the failure of flow regimes. A physical model of the material flow was proposed to explain the formation mechanism of the tunnel void as a discontinuity during the mass refilling at the rear of the tool. The microscopic analysis was used to determine further microstructural evolution in BFSW aluminium welds. The metallurgic measurements of the weld texture showed the formation of low-angle and high-angle grain boundaries (LAGBs, HAGBs) in different regions of the weld microstructure, as a consequence of thermomechanical nature of the process. The stirring zone (SZ) underwent severe grain fragmentation and a uniform dynamic recrystallization (DRX). The transition regions of the weld experienced stored strain which changed the grain size and morphology via grain misorientation transformations. Other observations were of micro-cracks, the presence of oxidization, and the presence of strain hardening associated with precipitates. Flow arms in welds are caused by DRX processes including shearing deformation, which affects microstructural integrity of the internal plastic flow. The work evaluated the internal flow features of the aluminium butt-joints in bobbin friction stir welding, using the metallographic observations. A model of discontinuous flow within the weld was proposed the key findings are that the packets of material ('flow patches') being transported around the pin during the stirring action. The intermixing of the flow patches from both the advancing and retreating sides of the weld experience high localized shearing at the stirring zone, evidenced in the boundary layers of the deposited mass within the weld structure. The flow failure of the plasticized mass during the deposition and refilling of the material at the trailing edge of the tool causes a discontinuity within the weld seam, leading in formation of the flow-based defects, e.g. tunnel void.

ACKNOWLEDGEMENTS

This dissertation is the result of a full-time PhD research in the department of mechanical engineering, at the University of Canterbury.

I want to give my sincere appreciation and thanks to the mentioned individuals listed below whom without their help and support this inspirational journey would not have been possible.

- First of all, thanks to Dirk, my senior supervisor, for his endless support through project meetings, scientific discussions, and just always being there to help me with my study and publications. He has had plenty of patience to keep me going on the right track, and has encouraged me to pursue my academic goals.
- My co-supervisor, Don, who was always available for first reviewing of my journal papers and comments on my results. His ideas have helped me with promoting the quality of my work.
- My associate supervisor, Kamil, whom I would like to thank him for his generous support regarding providing me with weldments and technical discussion on the operation details of the welding process.
- The technicians at the University of Canterbury; always said I can, not I can't help you.
- Also, I would like to thank the college of engineering, for granting me a scholarship which helped me concentrate on my research with no financial concerns.
- Last but not least; my family members, back home in IRAN, also my family and friends here in NZ. Their amazing support throughout my PhD study has been vital.

Abbas Tamadon

Contents

CHAPTER 1: INTRODUCTION

Bobbin Friction Stir Welding (BFSW) is a new class of solid-phase joining techniques, whereby a symmetrical rotating system (consisting of two shoulders, one on each side of the workpiece connected by the tool pin) ploughs through the interface of the two plates, and mixes the materials into a fully penetrated bonding by heat and stirring.

Due to severe dynamic plastic deformation and failure of the material flows during the process, the existence of discontinuity defects line (e.g. tunnel defect) in the weld region is one of the challenges of the work. There is no solid theory about variables of process and method of control to achieve the optimum parameters. Therefore, a transition from trial and error to a science-based approach is extremely essential.

While the metallurgy of friction stir welding (related to the phase transformation phenomena) is known, the control of process parameters have received less attention, and this is where the current project focuses. This research aims to present a physical model for BFSW to optimize the variables of the process with specific tool features by consideration of their interaction on each other. This model should find a way for characterizing weld defects and also explain the microscopic alterations during the process and how the flow behaviour can promote the quality of the weld structure.

Experimental works were conducted on analogue modelling of BFSW process and microstructure elucidations to understanding the variables of the process. Characterization of the internal flow features provides a theory for predicting flow failure in emerging of the weld defects. The modelled weld structures by analogue methodology can elucidate the relationships between flow features and defects near to real circumstances of the BFSW welds. The entry zone of the weld line is interesting in research as the origin of spray defect and tunnel void. These defects can result in other defects in the weld region, caused by loss of material and discontinuity in the weld. Besides the tunnel void as an apparent macro-size defect, there are some other problems in micro-scale e.g. oxidation layers, micro-cracks, recrystallization difficulties and grain misorientation as the thermo-mechanical outcomes of the BFSW process which can affect the properties of the weld for achieving a defect-free structure. EBSD and electron microscopy can elucidate the microscopic details of the weld microstructure (e.g. grain refinement, dynamic recrystallization and precipitation).

After a better understanding of the weld parameters using the microstructural evolution of the weld texture, the research has more approached to the main objective of this research. The nature of the defects can be elucidates based on a physical model, to explain the nature of thermomechanical behaviour of the BFSW

processes and also the optimization suggesting for controlling of the defect formation in the welding stage.

Due to the complex nature of BFSW process and interaction of variables, up to now the study of BFSW process and tool development has been mostly empirical. On the other hand, there are some difficulties about control of process parameters for bobbin-tool FSW to avoid tool failure and weld defects occurrence. On the other hand, because of the plastic deformation basis of the process, the majority of the macro- and micro-defects of the BFSW weld have a flow-based origin. Physio-mechanical characterization of the BFSW weld structure and developing of a theory for the flow behaviour of the stirring action in the polycrystalline weld texture can result in a multi-scale physical model to understand the formation mechanism of the defects in the metallic structure of the BFSW weld. Understanding of the material flow regimes during the process have a significant potential to explain the thermo-mechanical behaviour of the BFSW process, observed in the dynamically recrystallized microstructure of the BFSW weld.

The understanding of the BFSW process initially was commenced by the previous PhD researcher of the current supervisory team. There were good results about manufacturing parameters of the BFSW welds. The current research, instead of empirical works is focused to present a theory about the variables of the process with an emphasis on the characterization of the flow regimes and relevant defect formation mechanisms. As it has been found that there is an intrinsic defect for the BFSW process, called tunnel void, the main aim is to study the internal flow details to characterize the origins of the defect formation within the weld structure. However FSW process is considered as a thermo-mechanical process, but the primary analogue models for the tunnel void imply on the main role for the failure of material flow regimes rather than thermal flow. On the other hand, the materials studies have shown a joining band without any significant metallurgical phase transformation during or after the process. Therefore to remove the tunnel void defect, studies will be focused on the characterization of the material flow regimes to develop a physical model predicting an optimized weld without any defect.

The first adopted method for the flow studies was Analogue modelling. To develop an analogue model for the weld stage and study of the effect of variables on the weld structure, plasticine slabs were utilized in a multi-layered sample to enable us for the flow visualization of the weld region.

To compare the analogous result with the actual weld, it was considered to implement a microstructure characterization for the weld plates manufactured during the previous PhD project. The weld samples were selected from A6082-T6 aluminium plates with the weld structures similar to the analogue plasticine. The flow-based weld defects were readily observed in both aluminium and plasticine samples. The flow visualization in the analogue model was validated by the metallographic observations of the AA6082-T6 welded plates. Other

thermomechanical characteristics of the BFSW welds were identified by more advanced microscopic analysis methods like electron microscopy (SEM and TEM), Electron Backscatter Diffraction (EBSD), Atomic Force Microscope (AFM), to provide a better explanation of flow-induced microstructural alterations.

The analysis experiments could provide a variety of new results, which haven't been presented before in the literature of Bobbin-FSW process.

The starting assumption to develop a physical model for the BFSW weld structure was based on the thermo-mechanical nature of the process. It was initially assumed that thermal flow has the same part as material flow in the formation of the solid-phase weld. But, the analogue model indicated the importance of the flow mechanism in the quality of the joining process and immerging of the failed welds. Therefore, it was considered a more role to the material flow and the focus was on material flow visualization through the stirring zone. Between the welding variables, the geometry of the Bobbin tool has the main role in the formation of the material patterns induced through the plasticizing deformation process. The simultaneous advancing movement of the rotating tool and the mechanical stirring of the mass at the proximity of the tool generate a viscoelasticity condition for transverse transferring of the stirred layers between the advancing side (AS) and the retreating side (RS) of the tool. This leads to deposition of the mass in the half-round behind the tool. But during this cycle, the disruption of the integrity of the mass flow leads to a formation of a discontinuity pattern at between the deposited layers of material at the trailing edge of the tool. Identification of the flow-based reasons for the failure is one of the objectives of the development of the physical model of the process.

The main importance of generated heat, from the frictional interaction between the tool and the substrate, can be attributed to the dynamic recrystallization of the weld texture during the re-cooling procedure after the deposition of the stirred mass at the position of the weld-seam.

The first part of the research has a focus on building an analogue model to elucidate the material flow regimes and the origins of the inconsistency in flow failure resulting in emerging of the tunnel void in the body of the weld.

The pilot of the physical studies was built to pursue the thermomechanical characterization of the weld to provide a comprehensive physical model for the microstructural features of the weld structure, where it is corresponding to the defect formation mechanism. Hence, it can provide a better understanding of the requisites of the controlling of the defects.

CHAPTER 2: LITERATURE REVIEW

2.1. Conventional Friction Stir Welding

In this part of the research, a review of the background of the project is presented where the main technique in the context of the work is originated from the conventional friction stir welding.

2.1.1. Process Principles

Friction Stir Welding (FSW) is a new joining technique for solid-phase processing of the metallic structures [1-3], in particular, for soft material with suitable deformability like aluminium [4, 5]. During the FSW process, two metal pieces are joined together by entering a non-consumable rotating pin into the interface of the plates [6, 7]. By a complete contact of the supportive shoulder with the surface of the plates, the rotating pin is inserted into the joint interface whereby an appropriate contact with plates begins the plastic deformation at the touching edges [8, 9].

After complete contact between the pin and the workpiece, the rotating tool starts moving forward through the joint interface [10, 11]. The rotating and advancing motion of the tool along with the weld-line forms the advancing and retreating sides, where the softened and heated material of plates flows around the pin [3, 12]. The plasticized mass at the leading edge of the rotating tool transports to the trailing edge of the tool, where consolidates in form of the solid-phase weld [13]. The magnitude of the rotational speed and travel speed has a key role in the formation and quality of the stirring zone around the tool. Regarding the stirring zone, the side where the travel and rotational speeds are in the same direction is called the advancing side (AS), and the opposite side of the stirring zone where the travel and rotational speeds have different directions is called the retreating side (RS) [14, 15]. The stirring action does not melt the workpiece material to be welded but yields it to plastic state which occurs much below the melting temperature (1/3 Tm) [16]. Hence, the emerging of the solidification defects in FSW welds is not a problem, in comparison to other fusion welding processes [17, 18]. The schematic of friction-stir welding is shown in Figure 2.1.

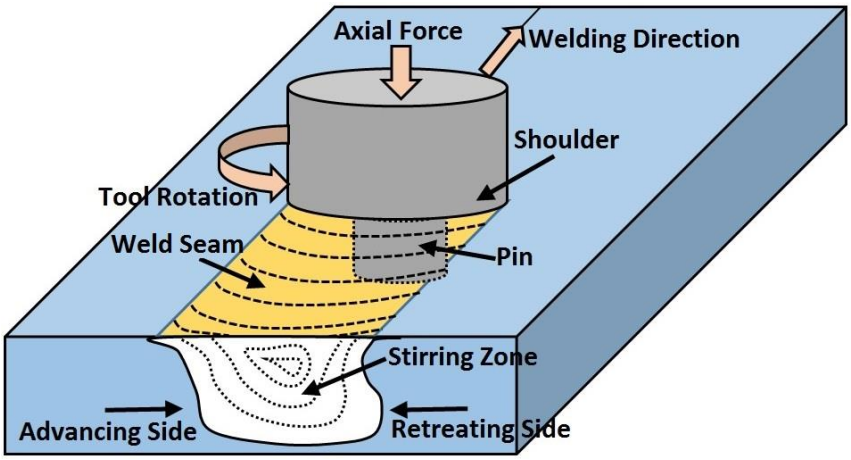

Figure 2.1. Schematic of the conventional FSW process (by A TAMADON).

2.1.2. Process variables

In this part, different variables of the FSW process are discussed to achieve a better understanding of the relationship between different parameters involved in the body of the research.

Joint configurations

FSW applies to many joining positions, the most common of which are the butt-joint and the lap-joint configurations. These joining configurations are shown in Figure 2.2. Another advantage of FSW is the simple required operational control, during preparation and processing [19]. Regardless of the joint configuration, in conventional FSW, the adequate fixturing along with a rigid backing anvil is the most important aspect of the operational control [16]. This is the most time and cost consuming setup prerequisite of the manufacturing process, which needs to be controlled before and during the process to assure the productivity of the process. Furthermore, for the butt-joint position, the workpiece misalignment is a crucial issue which should be avoided during the rigid machinery [20, 21].

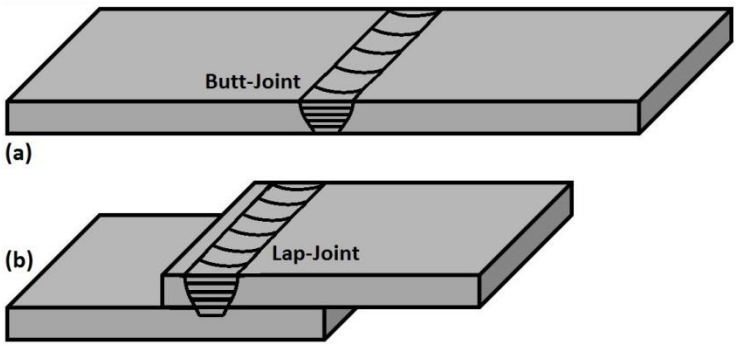

Figure 2.2. Different joint configurations; (a) butt, (b) lap, (by A TAMADON).

Tool design

As the key factor for the generation of the frictional heat, the tool geometry can extremely affect the quality of the weld, during the interaction with the substrate [14, 15]. The flow of plasticized mass at the location of the stirring action in the middle of the weld can be influenced by the geometry of the tool, as well as the linear and rotational motion of the tool [16, 17]. Regarding the tool features, the important geometrical features comprise the shoulder diameter, shoulder surface, and the pin geometry (shape and size), and the material properties of the tool (hardness and roughness) [18, 19].

In addition to the heat generation, the tool must perform many other functions, breaking the surface oxide layers of the workpiece, creating forging pressure to centralize the mass at the position of the stirring, optimum mixing, containing material within the joint during the tool advancement and preventing surface weld flash, uniform formation of the weld layers deposited at the back of the weld, and the as the most important issue, preventing the formation of the defects (such as hole or crack) within the body of the weld [22, 23].

To control these variables, different design innovations were developed to obtain the most effective tool geometry for the optimum condition of the welding. Since then, several studies have been focused on the presenting of new tool geometries and presenting the results of the relevant weld properties, primarily in aluminium alloys [24, 25]. In this regard, the main role of the control of the mass flow during the stirring action was allocated to the pin performance, rather than the shoulder. Consequently, a variety of the probe geometries were introduced (Figure 2.3) for a promoting mixing condition and increase of the dynamic volume during the mechanical stirring. In below, more details of the design aspect for the performance of the tool members are explained [20, 26, 27].

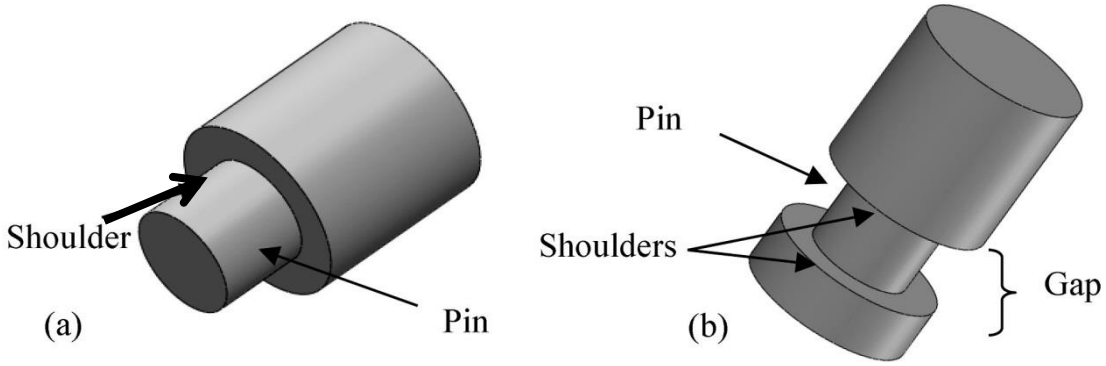

Figure 2.3. Schematic of the FSW tool; (a) Conventional-FSW tool, (b) Bobbin-tool (Courtesy K Sued).

Pin

The geometry of the tool pin (or probe) influences the plastic flow around the tool in which subsequently can affect the final properties of the weld. While the tool

shoulder mostly provides a large material flow near the surface, the pin aided the internal flow layers of the stirred mass. By applying faced pin features or "flats", the material flow increases compared to the cylindrical pin without flats [20, 27]. Moreover, the threaded pin can induce more axial force on the contact surface of the substrate. The flow orientation affected by the pin threads also can refill the discontinuity layers of the stirred mass around the pin, somehow cause a better engagement of the tool and substrate and provide a higher severe plastic deformation by the mechanical stirring mechanism [28, 29].

Shoulder

The tool shoulder has two main roles during the stirring action: i. generating the major portion of the frictional heat at the contact surface between the shoulder surface and the workpiece material. ii. restricting of the plasticized mass at the position of the stirring and preventing from escaping outside of the weld seam [30, 31].

The quality of the shoulder surface is effective on the generation of the frictional heat and subsequent softening of the material at the surface of the workpiece, underneath the shoulder. After the establishment of the flow, the shoulder should adequately grip the plasticized material and keep the stirred mass concentrated at the centre of the weld position [32, 33]. The clockwise rotation of the tool can provide a helical centred-conducted circulation of the mass around the tool. In this regard, the inscribing of the surface scroll features has an intensifying effective to generate the elevated frictional heat. This is similar to the effect of the thread features of the pin, as these features increase the contact area between the workpiece material and the tool surface with extra roughness added to the surface. Moreover, the scrolled features centralize the mass flow underneath the shoulder, also conduct the flow to more internal depths of the stirring region [34, 35].

Dynamics of the FSW process

The main problematic issue regarding the flow behaviour of the FSW is that the shortage of the flow refilling on the AS often results in the emergence of the tunnel void as a discontinuity defect. The helical circulation of the plastic flow around the pin is squeezed backwards where it is transported to the trailing edge of the tool [36, 37].

In this position, several physical changes happen for the flow regime at the proximity of the tool until it is deposited as the weld layer to form the final joint-line. The tool features play a key role in the optimization of the plastic flow to obtain a uniform flow regime. In this regard, the aim is to prevent any material loss or interruption of the flow layers during the mass transportation from the leading edge of the tool and dragging to the trailing edge without any material deficit [38, 39].

In addition to the physical features of the tool, to produce a sound defect-free weld, the stiffness of the accuracy and the machine is effective on the quality control of the

weld. The efficient applying the loads on the tool can prevent any interrupting deflection or deviation from the defined weld-line. Furthermore, moreover, by applying the clamping and fixture facilities the rigidity of the workpiece during the stirring interaction can avoid the excessive vibration and hence protect the relevant plastic flow position from the instability during the process [21, 40, 41].

2.1.3. FSW Weld Structure

Consolidation of the internal flow patterns within the stirring zone forms the main region of the weld, consisting of the bonding layers of the plastic flow streams, transported from the AS and RS borders and mixed at the proximity of the pin [42, 43].

Compared to the fusion welding, this solid-phase weld structure in the FSW process is free of the solidification defects. Also, the plastic deformation and thermomechanical behavior of the weld structure induce an extensive grain refinement within the FSW weld texture. Nevertheless, because of the mechanical and spatial effect of the stirring action within the plasticized material, depended on the distance from the actual position of the toll performance, the material can experience different flow behaviour and heat input flux [44, 45]. This can directly affect the microstructure of the weld, to form different grain size and morphology and caused by distance of the texture from the center-line of the weld. This can be observed within the cross-section of the joint, where four different regions form within the weld region. At the middle of the cross section of the FSW joint, the stirring zone (SZ) is located as the main region of the weld, distinct form the outer weld zones. From the SZ towards the base metal (BM), two transition regions are situated; the thermo-mechanically affected zone (TMAZ) and the heat-affected zone (HAZ). The TMAZ is situated at the direct proximity of the SZ borders, where the base metal grains are deformed but not plasticized within the microstructure [46, 47]. Close to the BM, and adjacent to the TMAZ, the HAZ occurs as the inherent characteristic of all welding process, where the grain size and morphology are affected by the absorption of the heat input from the main welding region. the metallurgical alteration in TMAZ and HAZ can be problematic to cause some structural defects at the neighbouring of the main weld region (SZ) [48-50].

2.1.4 Thermo-mechanical behavior in FSW welding

In the Conventional-FSW process, as a result of the heat generated during friction, the workpiece material in contact with the rotating tool is heated to the plastic condition. This consequently decreases the axial forging force acting on the tool. During the longitudinal movement of the rotating tool through the joint-line, the plastic flow transfers the mass flow behind the tool [51]. This is the crucial step for the formation of a joint at the trailing edge, as the tool leaves the stirring zone location. Hence, the tool design, specifically the geometrical details of the tool components, has a direct role on the structure of the weld, as they are in direct

interaction with the material during the friction, deformation and the yielding of the plastic flow [52, 53].

To evaluate the thermomechanical mechanism during the dynamic interaction between the FSW tool and the substrate, the characterization of the complicated mechanisms occurring within the mass flow can hardly be fully quantified for the stirring process. In particular, for the contact conditions between the tool/workpiece interface, several simultaneous physical phenomena, e.g. heat generation and mass flow transportation (circular, transverse and longitudinal), and the heat flux, happen all in different modes at the leading and trailing edges of the tool [54, 55]. Hence, the presented models have to consider a simplified solving for the heat transfer equation and estimating the thermal flux distribution with neglecting the simultaneous material stirring regimes. The more progressed models are typically constructed on three possible types of methods: computational fluid dynamics (CFD), computational solid mechanics (thermomechanical models) or a combination of both types of fluid and solid models [50, 56]. Regarding the heat generation phenomenon, there is a need to correlate the modelling between the primary mechanical-frictional generated heat and the subsequent heat input during the mass plasticity. Furthermore, for the heat transfer mechanism, a parameter for the convention via dynamic mass flow should be considered in the proposed equation. Therefore, a comprehensive multi-physics heat flow model is required to propose a classification and reliable approximation for the heat generation and subsequent heat flux [54, 55].

2.1.5. Flow-based defects in FSW weld

In general, the FSW welding mechanism suffers from insufficient material flow, during the stirring action. This results in the non-bonding discontinuity or void defect formation as the weld flaws. These flow-based defects can collapse the mass refilling mechanism for the deposition of the weld-line material, and subsequently, deteriorate the strength properties of the final weldment [56]. There are some other common defects during the FSW processes, which caused some difficulties to prevent them during the operational procedure. Some of these defects occur because of the improper selection of the welding parameters, leading to or excessive or insufficient mass and heat flow. However, the formation mechanisms of these defects are not fully understood yet, and the body of the knowledge of the FSW process requires more scientific elucidation of the origins of defects within the weld structure. By understanding of the origins of the defects, and correct selection of the process parameters can obtain a sound weld with the optimum processing productivity [57-59].

Flash defect- at elevated rotating speeds, the stirred mass experiences the excessive frictional heat, generated at the proximity of the rotating pin. The improper engagement between the tool and the workpiece, as well as the insufficient axial forging force and inappropriate performance of the shoulder, leads to the expelling of a large volume of the thermally softened mass. The uncontrolled pumping of the

yielded plastic flow, near the boundary of the pin-shoulder, results in escaping of the mass from under the shoulder, in the form of surface flash at the edge of the weld-line. The inconsistency between the applied pin penetration depth and the shoulder diameter can induce an incorrect flow around the rotating pin plugging through the workpiece thickness. Therefore, the extruding nature of the material flow around the clockwise-rotating pin results in the weld flash appears on the retreating side. At the same time, the decreased plastic flow leaves a cavity-shape discontinuity at the opposite border of the weld, on the advancing side [60-62].

Tunnel defect- By the progressing of the rotating tool along the weld line, the plasticized mass around the pin is transferred layer by layer across the transverse section of the weld seam [63]. Inadequate material mixing, during the stirring, results in the emergence of tunnel void, and failure of the weld bonding. Restriction of the material flowability at the behind of the tool interrupts the mass flow transported from the retreating side to refill at the advancing side border [2, 64]. Therefore, a cavity is created between the pin position and the advancing side of the weld.

The microscopic observation of the material flow around the emerged tunnel defect shows the flow arms appeared in the stirring zone, elongated towards the rotation direction of the tool through the cross-section. The flow arms correspond to the direction of the plastic flow and can elucidate how the flow failure causes the formation of the tunnel defect [65].

2.2. Bobbin Friction Stir Welding

Bobbin friction stir welding (BFSW) is an innovative variant of the friction stir welding (FSW) process, whereby a double-sided rotating tool physically ploughs along the interface of two butted plates [4] without needing the backing anvil and the axial force during the process [66]. The dynamic interaction between the workpiece and the non-consuming tool creates a severe friction condition at the contact interface [67]. Consequently, significant heat is generated due friction which can locally soften the workpiece material sufficient for plastic yielding and stirring at the bonding track [2]. The stirring action arises from the rotation speed (ω) and advance speed (V). While the tool advances along the weld line (Figure 2.4), the mutual interaction of the speeds (ω, V) transports the softened mass from leading edge of the rotating tool to be deposited at the rear or trailing edge of the tool [68].

The side of the weld-seam where the direction of tool rotation is the same as the tool progress is called the advancing side (AS) and the opposite side of the weld-seam is the retreating side (RS) [69]. The region located between the AS and RS borders, named the stirring zone (SZ) [70], experiences a thermomechanical plasticizing and then deposition and consolidation in the weld locus [71]. The adjacent region outside the SZ is the Thermo-Mechanical Affected Zone (TMAZ). The microstructure of this region is formed by the stress-strain fields and heating flux which are induced by the

friction and heat generation effects of the stirring action [72]. The next region between the TMAZ and the Base Metal (BM) is the Heat Affected Zone (HAZ). This region is exposed to thermal fields of the stirring process which alter the microstructure [73].

Comparing with the Conventional-FSW (CFSW), in the BFSW the fully-penetrated pin requires more control during the process, as an inconsistency between the process variables can cause more severe failures. The double opposing shoulders system provide a greater contact surface for the frictional heat generation from both sides of the workpiece [71]. The process also replaces the CFSW backing or anvil support plate with the BFSW rotating shoulder at the lower side of the workpiece [74, 75]. The CFSW case requires a downward axial load [76] on the tooling, whereas the BFSW requires a compression ratio [77] (the variance between the inner edge-to-inner edge biting gap of the shoulders and the actual thickness of the plate). These differences cause differences in the flow regimes of the two processes [64, 78].

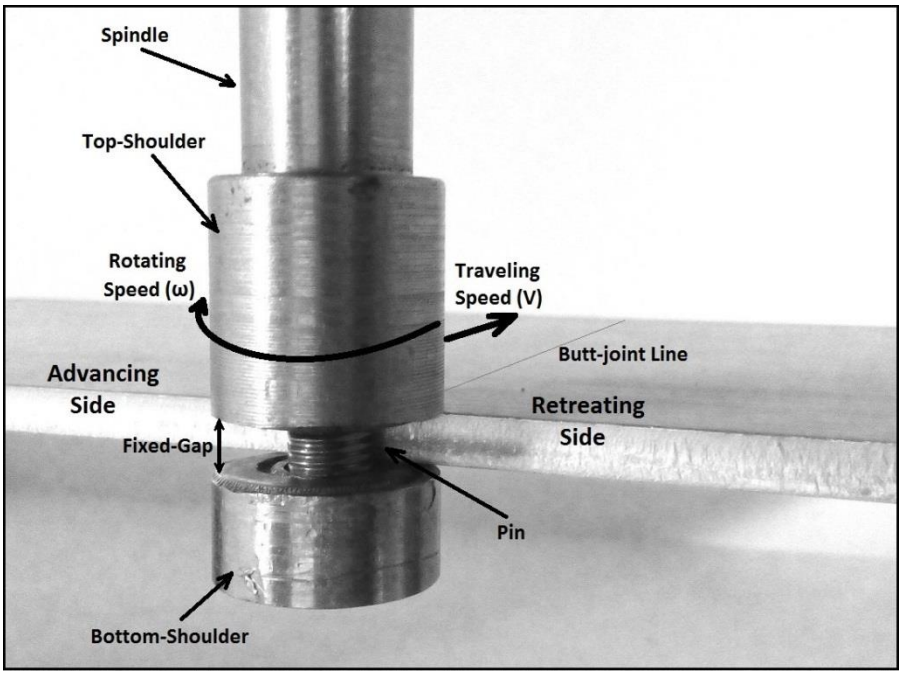

Figure 2.4. Schematic of the BFSW process for a butt-joint position (by A TAMADON).

As the temperature in FSW processes is lower than fusion welding, it is categorized as a metal forming process [46]. The internal flow regimes related to the plasticized mass play the main role in the welding mechanism rather than metallurgical transformations of melt-and-solidification. In general, the FSW technique is proposed for materials with a high capability of the dynamic plastic deformation. Aluminium that responds well to large plastic deformation is a good candidate material for FSW. In particular, marine grade AA6082-T6 aluminium alloy with

good machinability properties would be attractive to be processed by the BFSW, but shows poor weldability in the conventional fusion welding. One of the obstacles to a better understanding of the actual flow regimes is the need to visualise the details of the flow features for the cross section of the weld [70, 79]. This is challenging for AA6082-T6 alloy as the weld region responds poorly to conventional etchant reagents [80]. This problem arises because of the low contrast between grains and grain boundaries for the AA6082-T6 microstructure where the precipitate particles are uniformly dispersed within a supersaturated solid solution treated by artificially ageing per the T6 cycle. Also, severe plastic deformation and grain fragmentation during the BFSW process reduce grain size to ultrafine.

2.2.1. Background

The existing problems in the FSW process including the internal defect can reduce the level of reliability to the process as a valid technique for industrial welding. In this regards, the simultaneous works were started to modify the conventional FSW process to control and elimination of the defects from the weldments. One of the basic hypotheses regarding the refining of the process has been focused on the welding tool. There have been various suggestions for modifications of the tool, for example, TWI proposed again a welding variant as a symmetrical double-sided joining to surround whole the welding region through the thickness of the butt-arranged plates [81]. This welding method can support higher thicknesses of the plates by the increase of the welding speed, hence, the productivity of the welding can significantly approve in comparison with the conventional-FSW for the thick Al-alloy plates [2].

These developed FSW tools have been called the bobbin tools (sometimes named as the self-reacting tools), referring to the shape of these tools, which consist of two shoulders connected by the tool pin as is shown in Figure 2.4. This system consists of a specially designed tool, consisting of two shoulders, one on each side of the workpiece to be joined. The two elements of the tool are connected with the pin, which here runs through the material. Instead of conventional FSW and problems ahead, Bobbin tool Friction Stir Welding (BT-FSW) has the potential advantage of greater heat generation and thermal conservation throughout the weld line and symmetrical flow of heat and material [4]. Also, results show BT-FSW to be better for medium and thick sections than for thin material [5], and other studies have achieved acceptable results for thin plate using bobbin tools as well [66].

2.2.2. Bobbin Tool

The single-piece Bobbin tool generally consists of a top- shoulder, a bottom-shoulder and a fixed pin in the middle. The pin will be modified by adding flat surfaces and threaded feature (several times repeated) on the radial surfaces to help to a uniform flow during welding. Also, a scrolled pattern is inscribed on both shoulder surfaces

to improve the material flow, the direction of spiral for pumping material centred inwards at both surfaces [82, 83].

Compared to the CFSW tools, bobbin tools differ in some features which make them more attractive in certain aspects of the FSW processing. Two rotating shoulders generate the elevated heat input from both sides of the workpiece plate, with much more heat conservation, compared to the inherent heat sink in the single-shoulder tools with the anvil support plate [84].

Moreover, the symmetrical configuration of the bobbin-tool produces a joint with less residual stress compared to the CFSW. The fully-penetrating centred pin in bobbin-tool performs through the joint interface with the complete elimination of root flaws compared to CFSW. This also results in a balanced weld profile through the cross-section, with an almost zero weld forging forces acting on the machine spindle to hold the tool through the weld track (as it is called self-reacting tool). The fully-penetrating bobbin-tools eliminate the lack of penetration at the root of the weld. The increased frictional contact, produced by the bottom shoulder and the elimination of the backing anvil, which acts as the heat sink, elevate the operating temperature, in comparison with the similar conventional welds. To increase the productivity of the process, the welding travel speed needs to be adjusted to enable the process benefiting from this additional heat generation.

On the other hand, there are some difficulties with bobbin-FSW and process development is more delicate for thermal management and flow features. Also, there is very little published in the literature on this process and up to now, the process and tool development has been mostly empirical [20, 83-86]. A transition to a science-based approach is highly necessary.

2.2.3. BFSW Joining Mechanism

The welding mechanism can be explained by several stages which the heat and mass flow can be different:

Circulating flow - the softened material is plasticized by the frictional heat input induced by the rotating tool and simultaneously traverse ahead of the tool from the AS towards the RS border.

Translational flowing- when the rotating tool begins to move forward, there will be a gap at the trailing edge of the tool. This transient space needs to be occupied by the refilling mechanism which transfers the mass flow around the tool, from the leading edge to the trailing edge. Consequently, by the advancement of the tool through the weld-line, the regular mass deposition forms the bonding layers behind the tool, as the weld seam position.

Heat generation- the heat input has two main origins: mechanical friction at the contact surface between the tool and the workpiece; plastic deformation of the material around the rotating tool. Because of the greater surface area at the sub-

shoulder regions, the heat generation is expected to occur predominantly underneath the shoulders.

2.2.4. BFSW Weld Characterization

One of the challenges in the study of the FSW process mechanism is to find an applicable instrument to characterize the weld structure, identify the role of the effective welding parameters to obtain the optimized properties of the weld.

Most of the proposed characterization methods are to be expensive and time-consuming, and hard to present a comprehensive definition from the process mechanism. This can be more difficult for the bobbin-FSW as the effective process variables are not fully recognized yet.

There are plenty of the progressed research works on the microstructure characterization of the FSW welds, with a strong focus on aluminium alloys. By comparing most of the results, it is concluded that there are some similarities between the CFSW and the BFSW processes regarding the weld structure:

The main body of the weld region is the stirring zone (SZ), situated at the centre of the weld structure, generally affected by heavily plastic deformation by the pin action and the subsequent dynamic recrystallization. The grain morphology within the stirring zone is uniformly equiaxed, with a huge reduction in size, compared to the parent material.

At the proximity of the SZ, the strain and the temperature-induced from the middle of the weld can cause some physical changes within the microstructure of the base metal (BM). Adjacent to the SZ, the thermo-mechanically affected zone (TMAZ) forms on either side of the weld borders, advancing side (AS) or retreating side (RS). The absorbed strain and temperature from the stirring action alters the microstructure of this area by the formation of the deformed microstructure, different than the SZ and the BM.

The next region towards the BM is the transition region of the heat-affected zone (HAZ) as the inherent of all welding processes. By affecting from the heat input, and not deformed by the mechanical stirring, the HAZ undergoes the thermal cycles which can change the microstructure compared to the neighbouring regions of the TMAZ and the BM. The comparison between conventional and bobbin outcomes is shown in Figure 2.5.

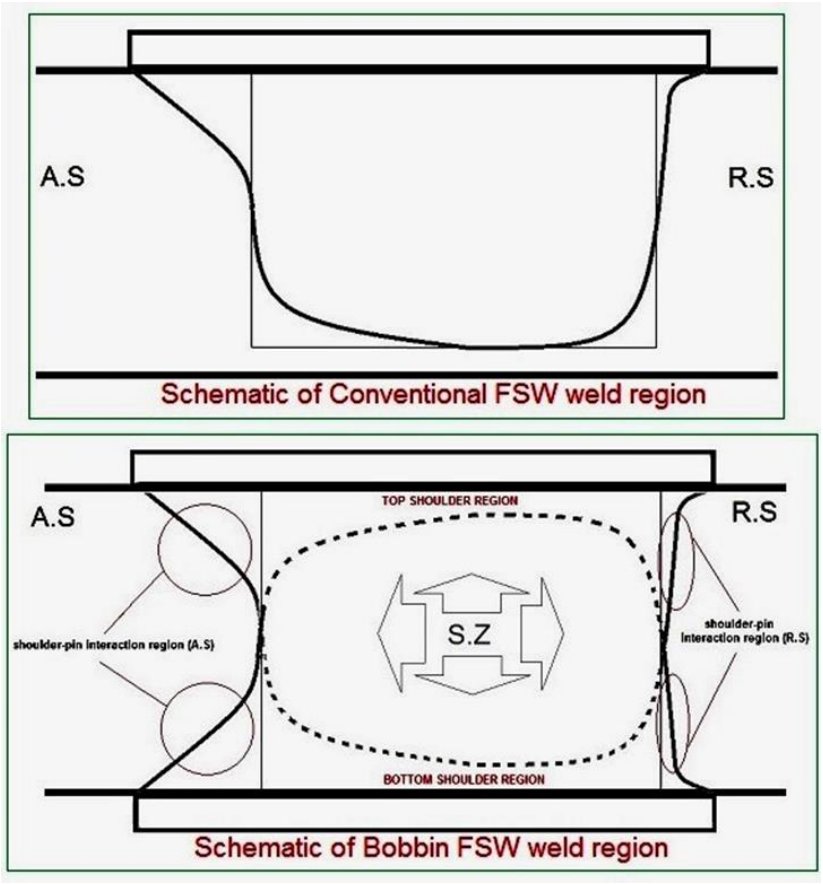

Figure 2.5. schematic of the weld region in CFSW (TOP) and BFSW (BOTTOM) (by A TAMADON).

2.3. Modelling of void formation

It seems that some thermo-mechanical aspects of the FSW process need to be more elucidated in another scheme rather than experimental investigations. As there is no solid theory for controlling of the CFSW and BFSW joints regarding the defects, it has been supposed to carry on the study in a computational modelling phase. The computational modelling rather than experimental trials can provide a predicting pattern for the weld structure to anticipate the modified condition of the welding as well.

Due to the complex content of welding process and interaction of variables as the multiphysics, it is hard and time-consuming for researchers to undertake a comprehensive study of heat and material flow regimes and process settings for FSW techniques. Instead of experimental investigations, some of the other researchers have developed computational modelling methods such as Finite Element Analysis (FEA) [87, 88], Computational Fluid Dynamics (CFD) [89, 90] and Artificial Neural Network (ANN) [91, 92], to present a better understanding of the FSW process.

2.3.1. Flow visualization and mechanism of void formation

The modelling studies have been attempts at different thermomechanical aspects of FSW, to make a better understand and predicting, regarding the effects of process variables in the weld structure. Some works have been simple models focusing on thermal analysis [93], while others have emphasized exclusively on the material flow [94]. In between, others have tried to incorporate both the thermal and mechanical analysis into a robust model [95, 96].

However, there is a need to apply multi-physics modelling by consideration of thermo-mechanical behaviour, transfer phenomena (such as heat and material flow) and microstructure transformation. This is difficult to achieve a reliable model by using the existing mathematical calculations and simulation software.

One of the positive ideas is to collect some patterns about the flow visualization and modelling of the void formation in the weld texture. Majority of results are not achieved by a direct research title focusing on void prediction or void patterns, but as a thermo-mechanical model sometimes there are some discontinuity patterns or stress concentration model which can observe some void features through them. Here, they are collecting in three different groups; finite element method (FEM), computational fluid dynamics (CFD) or smoothed particles hydrodynamics (SPH) based on the modelling method.

In the continuum mechanics, there are two different viewpoints for the explanation of deformation; the Lagrangian formulations and the Eulerian formulations. Briefly, the Lagrangian view is working based on the mesh deformation at the same time as the material, and Eulerian view considers a fixed mesh in the space, and the material flows from one cell to another one. For the Lagrangian formulation, time and material coordinates are independent, and mesh deformation is simultaneous with the material. The Lagrangian method is widely used in structural mechanics, and for the large deformations, calculations for the distorted mesh becomes inaccurate or even fail [97].

In the Eulerian formulation, spatial coordinates track the material flow by a set of fixed points in space. In the Eulerian view, there is no mesh distortion at all which makes it enable to simulate the large deformation or fluid mechanics mechanism. In other hand, high-quality results require a fine mesh, which costs more for an accurate analysis.

To introduce a widely used numerical method for the engineering software, a new formulation has been proposed, as a combination of Eulerian and Lagrangian methods. The Arbitrary Lagrangian-Eulerian (ALE) formulation selects the best results of the Lagrangian and Eulerian methods [97, 98]. The ALE method consists of 3 steps. First, moving of the material nodes to new positions. Second, rezone step that the mesh is modified to obtain a suitable matching to the new location. And finally transferring from the old mesh to the rezoned one. ALE is suitable for metal

forming, where the large deformation could cause severe distortion. Most of the analytical models for ALE formulations are focused on the residual stress, strain rate, or stress concentration during or after the process [61, 65]. CFD models of material/thermal flow path lines around the tool for the Conventional FSW have been shown [22, 63, 76, 79]. Likewise, void discontinuities have been modelled by ALE formulations for the Conventional FSW [50, 57, 64-66, 71, 72, 84].

In the Meshless methods, the solutions are based on moving the smallest number of squares, kernels. They have been applied to structural mechanics like fracture problems, impacts, metal forming or crack propagation [50, 63, 71, 72, 76].

In Smoothed Particle Hydrodynamics (SPH) the domain is represented by a set of particles and each particle individually moves according to equilibrium equations. These particles have a spatial distance by a kernel function. Stability of the configurations in a severe local distortion is the main advantage of the SPH method. By this feature, the method can be used for a range of applications in Solid Mechanics: shock propagation in solids, impact phenomena and metal forming processes (under pressure loads). Note that SPH formulations as a Lagrangian-based system suffer from tensile instabilities. Because of that, during the FSW process and moving of the rotating tool through the weld-line, it can cause a continuous disruption which might overestimate the possibility of the void formation in the weld texture. SPH method is most suitable for the processes with a shocking distortion, impact, crushing or pressure load such as car crash tests, impact tests or forging [57, 64, 65, 84].

SPH models which can show a pattern from possible geometry of the void are not that much developed. Specifically, because the cross-sections are not provided to present a clear flow path lines. Nevertheless, there are some discontinuity patterns through the weld line, which are possible to categorize a collection for meshless methods, see [52, 58, 60, 61]. The majority of the models are for the Conventional Tool. There has been less work on bobbin tools. For an example of SPH to bobbin see [35, 41, 42, 51].

2.3.2. Computational Fluid Dynamics (CFD)

The principles of the CFD method is the interactions between the liquid and solid phases in boundary conditions. The Navier–Stokes equations as a basic problem-solving method of the fluid dynamics, simplifies the problem by defining many single-phase fluid flows. For the FSW process, the CFD model considers the workpiece material as a viscoplastic liquid and the tool as the solid. In this situation, the void defect forms in the boundary conditions area.

Regarding the elucidation of the material flow, the CFD models indicate the most similarity to the aims of the research. Formation of voids in CFD models is based on an Eulerian formulation for the flow regimes [8].

2.3.3. Modeling performance and capability

In the beginning, it was thinking the main method of the project involves computational modelling, to study the material and thermal flow regimes within the weld region in the bobbin FSW process. The Lagrangian-Eulerian formulation in FEM was considered as a promising method to decoupling the solutions for the different physical interactions of temperature evolution and material flow by a sufficiently fast prediction. However, because of the thermo-mechanical nature of the process, severe plastic deformation and complexity of the flow regimes in stirring zone with the geometry of the bobbin tool, evolution of the deformation and plasticized material translation in joining bond, it is relatively hard to cover all the aspects of the BFSW joint formation by the FEM method. FEM has a good explicit for the solid mechanic's problems but it seems that modelling of the BFSW welding as a deformation process with stirring and dynamics of the 3D flow field through the weld-line including with time is more suitable to be developed by the CFD method.

On the other hand, to present an accurate multiphysics approach, near to real circumstances of BT-FSW process, the basic interactions of process parameters should be known in advance. Even by a volume-dependent solving approach like CFD and a strong pilot code like FLUENT or COMSOL, the multi-physics approach for modelling requires a comprehensive elucidation of relationships between effective parameters in creation and elimination of void (tool features, process parameters and material capabilities) as the prerequisite. The thermo-mechanical context of the process, as a solid-phase joining has simultaneously resulted in mechanical work, plastic deformation, friction, heat generation and material displacement. According to particular multiphysics objective of this study, it seems should consider a role for the stress-strain field in the disintegration of material and formation of the void.

By considering of all of these parameters effective in the thermo-mechanical process of joining, there are some difficulties to achieve a reliable computational model using the available mathematical methods and commercial software codes, therefore it is required to continue the research on more understanding of the process variables which can affect the weld structure to emerge the defects. Furthermore, the affecting rate of each parameter in the origination of the defect should be measured to improve the accuracy of the modelling.

2.4 Gaps in the body of knowledge

As the characteristic of the bobbin-tool FSW, it seems to be a Thermo-mechanical process, as a combination of High plastic deformation metalworking, forging and extrusion process, which finally results in a joining between two plates. In fact, due to high mechanical loads, heat generation and material deformation and movement, there are some complexities regarding the thermal management and flow features. For instance, changing the parameters of the process (e.g. feeding rate and rotational

speed), or features of the bobbin tool (size and geometry of pin and shoulder), and thickness and material of the weld plates may lead to unknown-origin defects in the weld region. In other words, there is no solid theory about parameters of process and method of control to achieve the optimum situation. It extends the range of applicable process parameters and overall productivity. Thus, a transition from trial and error to a science-based approach is highly necessary.

On the other hand, there are some difficulties in control of process parameters for bobbin-tool FSW to avoid tool failure and weld defects. Up to now, the process and tool development has been mostly empirical, and also there is very little published in the literature on this process. An overview extracted from the literature is depicted in Figure 2.6 regarding the variables and process parameters effects on the weld quality.

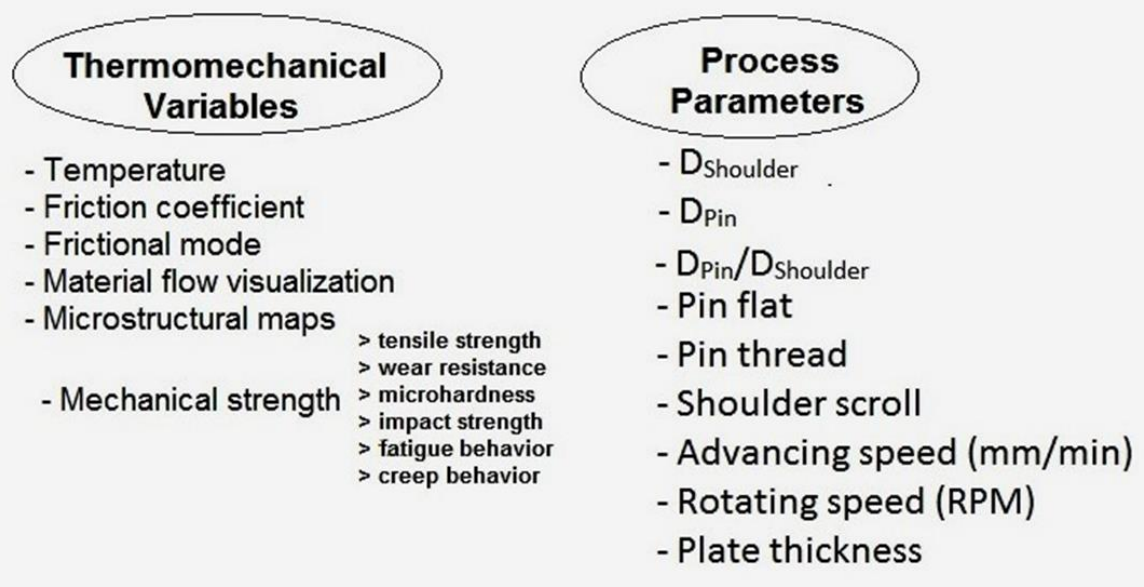

Figure 2.6. Schematic of the thermomechanical principles of the BFSW process (by A TAMADON).

Very few models published in literature explicitly deal with BT-FSW. The main reason for this appears to be the limited availability of technical experiments on BT-FSW process. Still, the focus of the models needs to be modified as the variations of boundary conditions and driving force in the symmetrical treatment of BT-FSW is significantly different from the same in conventional FSW.

All in all, a reliable computational model needs a prerequisite in the understanding of the process variables with a clear rate of affecting in the final weld quality by each parameter. To reach a comprehensive measurement of the parameters for entering to model, there is a shortage of cost and time and still, the result of the work is not clear enough. Thus, it needs to be a little bit conservative to define the objectives, approach and methodology of the research rather than earlier stages of the research.

Specific limitations in the literature regarding material A6082-T6 are difficult to obtain a defect-free weld, identifying the origins of the defects, difficulty in the metallographic analysis because of the poor response to the etching reagents, etc.

2.5. Objectives

There is still a consensus that a free-defect weld structure is the most important output for the BFSW process. This issue can demote the result of performed studies on BFSW as it hasn't been presented yet a solid theory on it to control the weld quality by changing the parameters of the welding. The general area of interest for this particular project is welding of aluminium sheets, and there are many applications for this in marine, automotive, and aerospace fabrication.

Since, the existence of defect can directly affect weld properties, making a reliable weld by BT-FSW process, in a different situation with different parameters, is difficult. On the other hand, the existence of void as a defect is one of the challenges of work during Bobbin-Tool FSW process, something that is more common rather than other types of defects in BFSW welds. A relationship between the variables of the BFSW and emerging of the discontinuity defects is discussed in Figure 2.7.

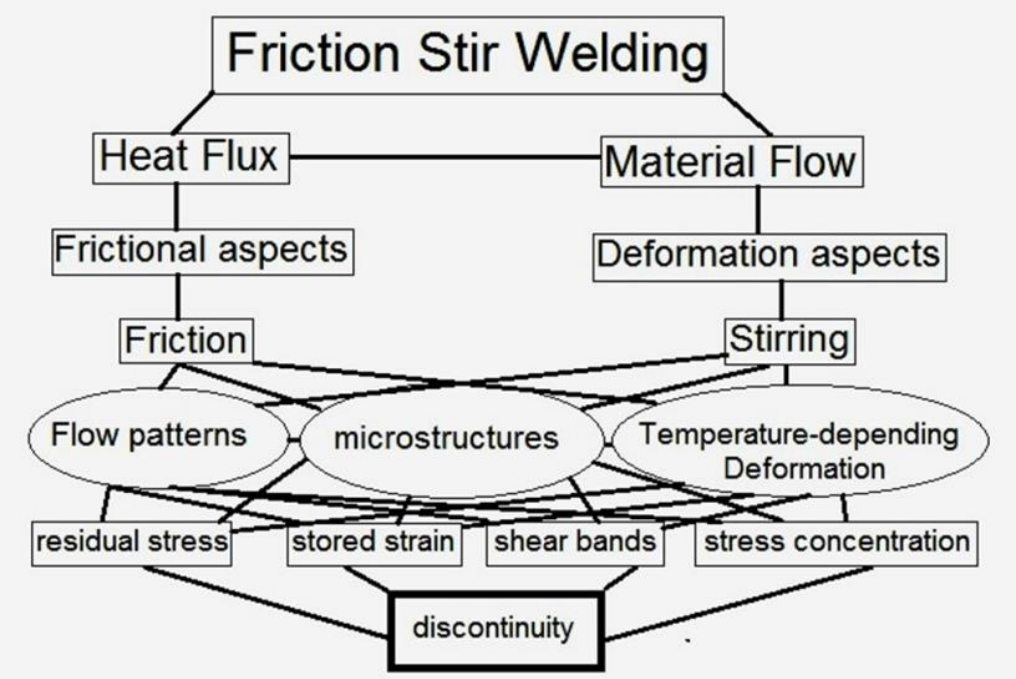

Figure 2.7. Relationship between the parameters in BFSW process (by A TAMADON).

Hence, the objective of this research is to present a model for the mechanism of the void formation in weld region, influential phenomena in the creation of void and

consequently developing a predicting model using flow mechanisms to better understand the formation of the tunnel void in Bobbin-Tool FSW process.

The primary assumption was supporting a multi-physics computational model based on the computational method to be developed for the mechanism of the defect formation. It was supposed the study is focused on the tunnel void as a main defect in the structure the Bobbin-FSW welds, and finally presenting a predicting model for controlling or elimination of the defect from the weld body. The starting hypothesis for the intended multi-physics model was considered by developing of the Finite Element Method (FEM) by adopting the material flow and thermal conduction within the stirring zone of the bobbin FSW welds. But literature review of the FSW processes revealed that possibly the CFD method can show a better result in dynamic flow condition of the plastic deformation through the weld region.

On the other side, by consideration of the process parameters and comparison of the known BFSW process and selected research objective with the publishing works, it found that there is no solid approach for modelling of the void formation for the plasticized aluminium alloy mass during the BFSW process using the current commercial software. It causes possibly ignoring the current commercial codes and starting to develop a special code for the thermomechanical condition of the plastic deformation during the BFSW process and consequently providing the suitable condition for modelling of the voids in the structure of the weld and prediction of the optimum situation where the void formation is prevented during the process. Regardless that how much this aim is possible during a normal PhD program, the reliability of the final model is not clear with the current assumptions of the process. In fact, the BFSW process is still a young joining process with a limited application in the industry and still, there are many gaps in the body of literature which makes it hard to achieve a reliable predicting result for the computational modelling of the weld region and searching of the actual variables during the void formation.

In particular, the current research team during the early assessments of the BFSW could find some other experimental gaps which need to be solved to promote the quality of the joint. The early analogue models conducted by the current PhD student revealed the other aspects of the material flow regimes regarding the relationship between void formation and flow failure. Furthermore, the microstructural observations developed by the PhD candidate revealed some other novel aspects regarding the void content and also some other metallurgical problems such as recrystallization, grain misorientation and thermo-mechanical behaviour of the weld region which can affect the final properties of the weldment. Especially by adding more weld trials and further analysis can evaluate the behaviour of the weld through a physical model which still can be novel in the theory of the void formation, and thermomechanical mechanisms within the weld which can control or remove the flow-based defects from the body of the weld.

Therefore, now the agreement is that the research method should be focused on a physical model based on the welding trials (actual/analogue), microstructure characterization, evolution of the mechanical properties of the joint, and a flow-based approach to study of the thermo-mechanical behavior of the weld during the process, to characterize the effective process parameters in formation and controlling of the void by presenting a conceptual model at the end of the studies.

The nominated physical model as a substitution for the difficulties of the computational model, can capable the research objectives in a physical scheme to understand the origin of the defects by changing of the material, manufacturing parameters, and thermo-mechanical behaviour of the weld region during and after the welding process by physical analysis and mechanical testing.

CHAPTER 3: Approach and methodology

3.1. Approach

In approaching this problem, the proposed approach initially considered applying a computational method. However, it was decided not to proceed along this line because of the existing limitations on an approved frame of the computational modelling for the flow originated defects in the weld structure.

Especially, in literature findings, each research team has been focused on a different method or aspect of the BFSW joint. Therefore, there is a variety of variables for the process and consideration of simplification makes it far from the reality of phenomenon which is exactly happening during the welding process. Hence, the high approximation of the computational model with current assumptions and instruments is difficult or far from the real condition.

After a review on the literature of the computational modelling of the FSW process, it was found that in comparison with the simultaneous characterization the computational model needs more time for implementation and also there is no guarantee to achieve a reliable result at the end of the modelling phase. Therefore, it was decided by passing from the computational phase of the study.

On the other hand, analogue modelling of the process can reveal the internal flow regimes in the weld structure by a focus on the material flow visualization.

Similarly, the metallurgical and thermomechanical characteristics of the weld can be revealed by different characterization methods in a high potential for the publishing of the results to elucidate the flow-based mechanisms during the joining.

It should be noted, up to now (the submission date) six different peer-reviewed papers have been extracted from the progressed findings and also four more submitted manuscripts are under review.

These experimental results have changed the idea of the researcher and the supervisory team and it has been decided that instead of changing of the research stream from experimental scheme to computational modelling, still, the research objectives can follow the structural characterization of the identified gaps to develop a physical model for controlling of the defects mainly originated from failure of the material flow regimes.

The methodology outlines for the rest of research approach are going to be based on analogue modelling in one side and on the other side the in-situ microstructure evolution of the thermomechanical features of the BFSW welding with an emphasis of the material flow aspects within the weld region. For a comprehensive study on the ability of the weld and behaviour of the defects in service, it is required to conduct some metallographic measurements to observe the microstructure details of

the weld. This can also elucidate the mechanical properties of the weld in correlation to the microscopic mechanisms during the joining formation. The summarized details of the research approach are explained in Figure 3.1.

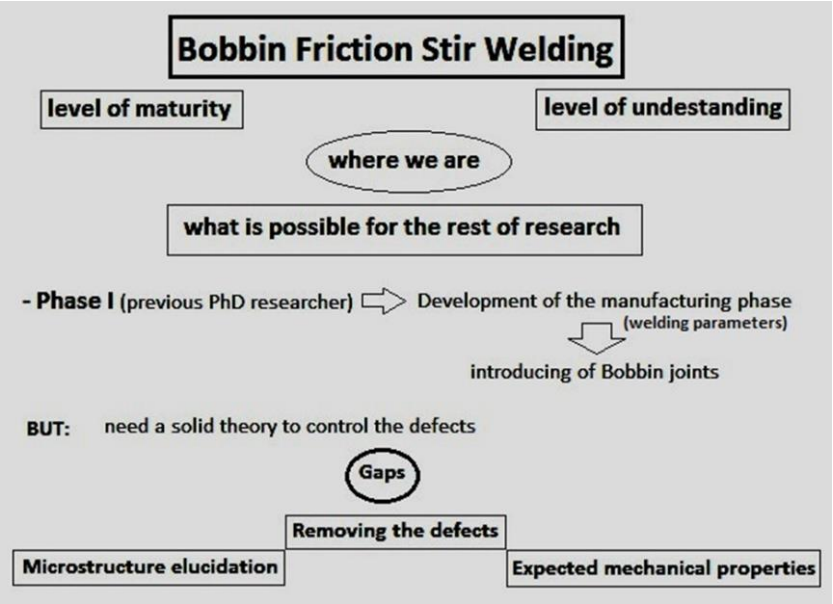

Figure 3. 1. The approach in current research (by A TAMADON).

3.1.1. Analogue Modeling

For the first step to the investigation of voids structure in the weld region, it was intending to have a study on internal material flow regimes and how the failure of the flows causes weld defects. However, the nature of the process makes it difficult to freeze the actual flow, and to validate any model.

A solution to this was to develop an analogue model as an introduction to the flow mechanisms. This provides a means to visualize the plastic deformation, movement and displacement of plasticized material, and probable void patterns to find a definition for flow dynamics relationships.

Instead of aluminium plates and real weld trials, analogue modelling of BFSW was performed using multi-layered colour plasticine. The primary purpose was to see if it is possible to replicate the defect structure known for aluminium plate welding. By fabrication of a plate comprising multiple layers of different colours, the area of examination under BFSW process, and the cross-sections observation afterwards, can provide new insights into a plastic flow model for the welding process.

The first part of the research approved that the plasticine samples has a suitable capability in visualizing of flow-based behaviour of the plasticized material during the BFSW process.

By designing different features of the Bobbin-tool system (e.g. using 3D printing) or changing the parameters of the weld can find a better insight regarding the weld characterization and study of a different aspect of the void formation.

A set of new tools with differences in pin and shoulders features (scrolls, flutes, flats, and threads), have been employed to evaluate the different flow-aspect of the plastic deformation.

Also, by changing of the slabs layered-structure can reveal the different aspects of the stress-strain fields during the process. The material flow visualization in plasticine analogue was validated by the aluminium weldments.

For a comprehensive observation of the thermo-mechanical behaviour of the BFSW process by plasticine analogue, it requires to develop a stabilizing in materials properties of the plasticine. In this regards, because of the limitations of the plasticine, the rest of the research aims can be pursued on the actual weld trials by Al plates.

The material flow patterns from the analogue model can directly show shearing regimes within the plastic mass layers. However, for an accurate study of the thermal behaviour of the weld, it is required to observe physical mechanisms occurring at the transient temperature fields through the weld structure. Compared to the analogue model, a metallographic observation of the grain size and morphology can provide a better explanation of the microstructural evolution of the weld, affected by the thermal history of the process. The elucidation of the thermal history, extending to the plastic deformation mechanism, can give valuable input to the understanding of microstructure formation and the development of thermomechanical features. In this regards, the actual aluminium weld plates are subject of microstructural evolution with a focus on the metallographic measurements. Results are shown in chapters (4-15).

3.1.2. Microstructural Studies and Thermomechanical characterization

By considering the thermal history and material flow mechanism, and the modelling of optimum situations without the existence of voids, now can focus on the time-temperature-displacement relationship for domains of material within the weld. The initial hypothesis is that the time-temperature-displacement evolution is harmonized with observable microstructure.

By correlating the microstructure observations and modelling results, the time-temperature-displacement relationship for domains of weld material helps to construct a physical model to predict the optimized defect-free weld structure with uniformity in the microstructure. For the microstructural observation, the characterization of recrystallization, precipitation and grain misorientation are on the main focus.

The supposed physical model will be completed when a thermo-mechanical study on the microscopic properties of the weld structure is progressed. Measurement of the defects behaviour within the microstructure also can be validated by an in-situ observation of the texture. In this regards, also electron microscopy can evaluate some mechanical properties of the weld structure, for example, the dislocations mechanism in the strengthening of the material or microscopic explanation of the plastic deformation and subsequent dynamic recrystallization can make a robust theory to discuss the origins of defects with a controlling approach.

3.2. Methodology

By neglecting of the computational modelling from the list of research methods for the current PhD research, now the focus of the project is on covering the objectives of the research –flow behaviour, origins of voids mechanism and dynamic recrystallization characteristics- to validate a physical model to explain the thermomechanical nature of the BFSW process. Plasticine analogue elucidates the analogy of the void formation mechanism, and then build a theory for the explanation of the interaction between variables and to achieve an insight for the optimization controls to achieve a free-defect BFSW joint.

Below, the launched techniques and methods as the body of the methodology of the research are explained based on the primary hypothesis and the findings during the work. Obviously, the physical results of these methods are going to build the theory of the BFSW process.

3.2.1. Methodology 01: Analogue modeling of the material flow regimes

For the first step to the investigation of voids in the weld region, it is intending to have a study on internal material flow regimes and how the failure of the flows caused weld defects. However, the nature of the process makes it difficult to freeze the actual flow, and to validate any model.

A solution to this is to develop an analogue model as an introduction to the visualization of the flow mechanisms. This provides a means to visualize the plastic deformation, movement and displacement of material, and probable void patterns to prepare a definition for flow dynamics relationships.

Instead of aluminium plates, analogue modelling of FSW will be performed using coloured layers plasticine. The primary purpose is to see if it is possible to replicate the defect structures known to exist for aluminium plate welding. By fabrication of a plate comprising multiple layers of different colours, area examination under bobbin-tool FSW process, and cut cross-sections afterwards, can provide new insights into a flow model for the welding process.

i. BOBBIN TOOL

To extend the flow aspects of the research, the bobbin tool design in different geometries is one of the main variables of the BFSW process. As a prerequisite, a variety of tool designs (Figure 3. 2) were initially considered for current research.

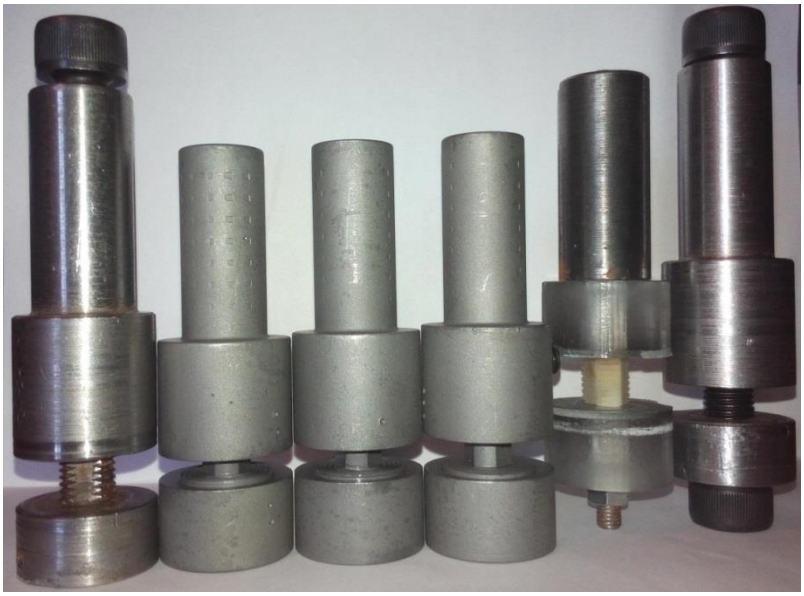

Figure 3. 2. Different bobbin tools manufactured for the current research (by A TAMADON).

Also, a variety of the pin features consisting flats, flutes, and threads were provided to shape different geometries of the pin surface (see Figure 3. 3). By this variety in design, a high angle of novelty in revealing the material flow patterns for the internal and surface flow regimes are achievable.

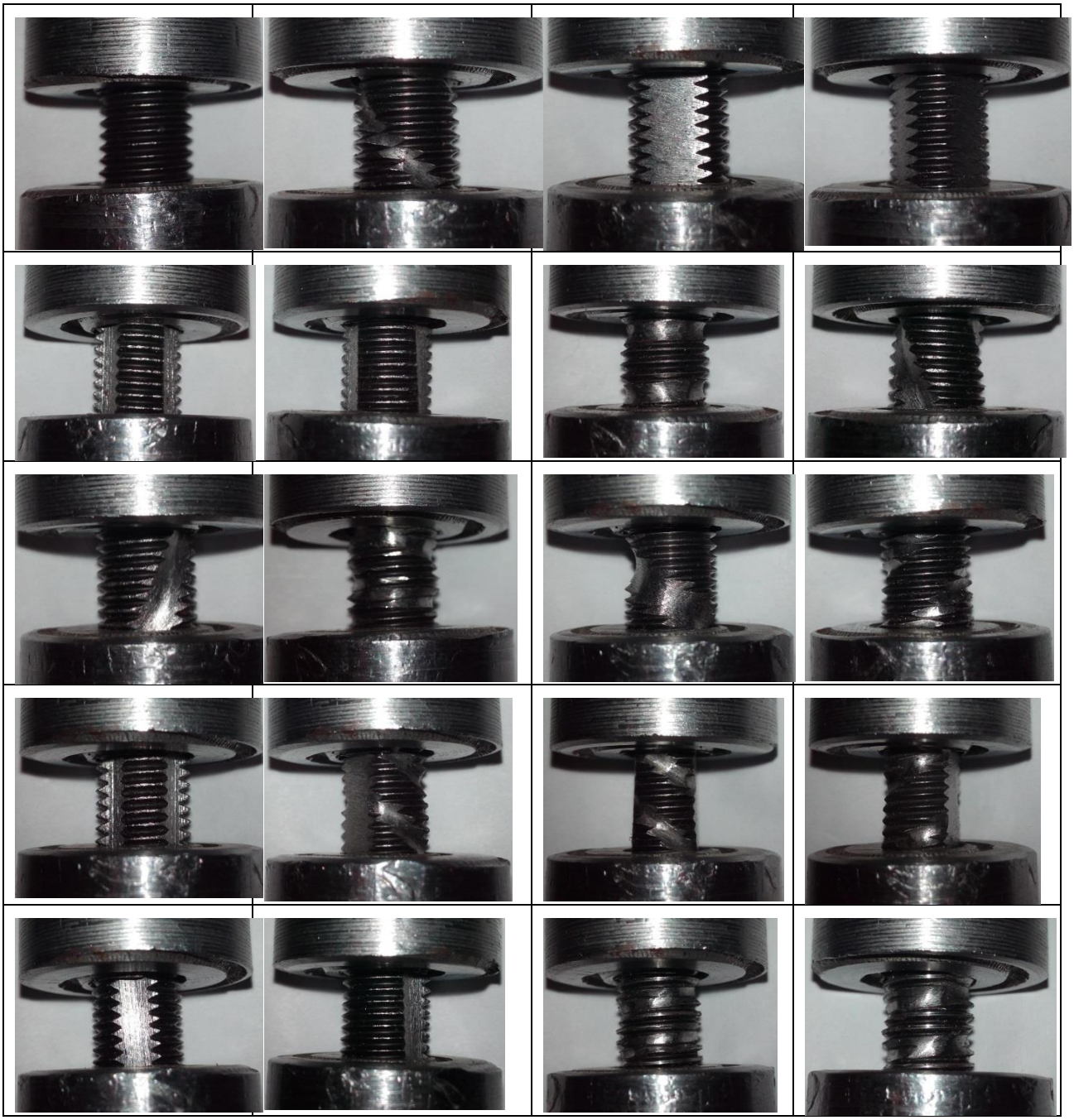

Figure 3. 3. Different features of the pin; threads and flats provided for the analogue model tests (by A TAMADON).

In comparison with the analogue modelling, in actual trials of the aluminium welds, there are fewer changes in tool designs as the RPM and the feeding rate is adaptable. Also, costs of manufacturing, aluminium workpiece, testing time, and next characterization methods are difficult for observation of the effects of all different tool features on the aluminium plates. One of the current solutions is the selection of the best results from analogue modelling where the quality of the weld is significantly high with a minimum possibility for the flow failure and the defect

formation. Afterwards, it can be utilized for the actual aluminium weld trials using the selected features of the bobbin tool. However, for the start of the trials, a full-featured tool design was fabricated in two different alternatives (Figure 3. 4) came from the literature and which can be used for different thicknesses of the aluminium plates.

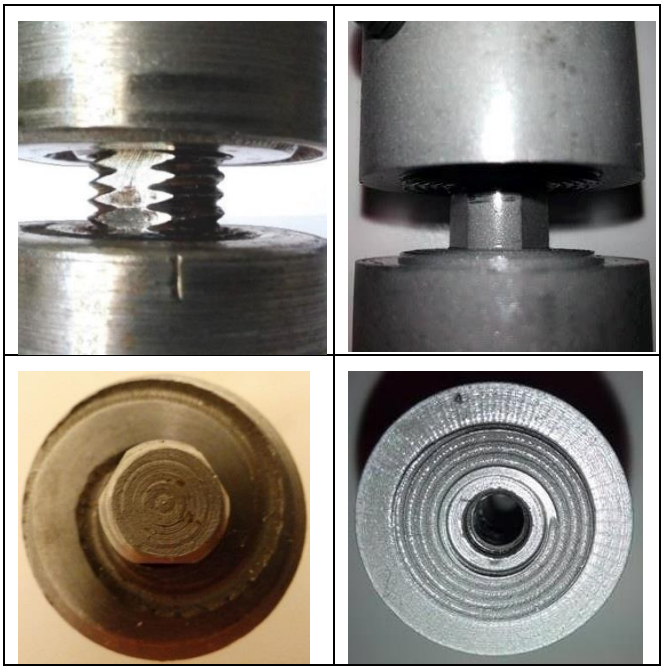

Figure 3. 4. The starting tool features design for the Bobbin tools, employed for the first Al alloy, A6082-T6 welding trials (by A TAMADON).

The geometrical details of the bobbin tool, utilized for analogue and actual welds are shown in Figure 3. 5. As it is shown in Figure 3. 5a, in this research the single piece Bobbin tool was employed in a full-featured design (flats, threads, scrolls).

In comparison with the simple pin, the current pin has been modified by adding three symmetrical flat surfaces one among between three screw-threaded areas with the same size on the radial surface of the pin. The flank angle of thread pitches was considered 10 degrees upwards to provide a better stirring condition. Also, one round clockwise-spiral pattern was inscribed at both shoulders surfaces, scrolled from edge of shoulder to the pin position. Threads and flats on pin and scrolls on shoulders can help to a uniform flow during welding and pumping of material inwards to avoid spilling of mass. For stable preservation of stirred material under the shoulder, diameter (D) ratio (DShoulder/DPin) and compression ratio (the difference between biting gap of the bobbin tool and thickness of the workpiece plate) were considered 5 and 3.75%, respectively.

By consideration of these features, the material of the tool is different for plasticine analogue and real Aluminium welds. To observe the relative stiffness between workpiece and tool, different materials were selected to fabricate the bobbin in for plasticine and aluminium. The bobbin tool for aluminium workpiece is shown in

Figure 3. 5b, made from H13 Hot Work Tool Steel with the hardness of 560 HV in comparison with 100 HV for A6082-T6. Figure 3. 5c illustrates the bobbin tool used for an analogue model which was made by a 3D printing technique. The used 3D printer filament was Polymaker PC-Plus PolyCarbonate which provides a high-performance engineering polymer with excellent impact strength and stiffness.

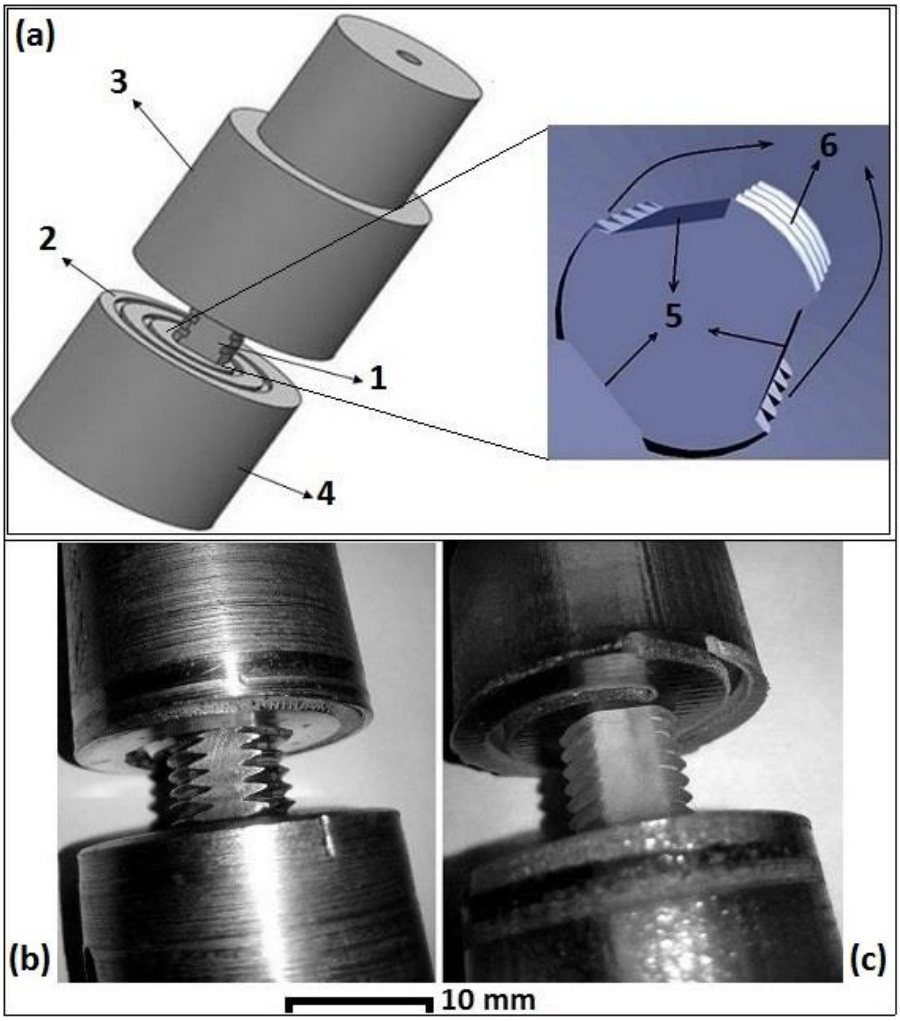

Figure 3. 5. (a) 3D model of Bobbin Tool (Top); 1-Pin, 2-Scrolls, 3-Top Shoulder, 4-Bottom Shoulder, 5-Flats, 6-Threads. Actual Bobbin Tool (Bottom); (b) for H13 Bobbin Tool (Left) for Aluminium, (c) 3D printed Bobbin Tool (Right) for Plasticine samples (by A TAMADON).

ii. WORKPIECE

ANALOGUE MODELLING- To create a multi-layered plasticine block, different colours of the non-drying Newplast plasticine (manufactured by Gordon Harris Ltd, UK) were used. Since the Newplast clay is sufficiently pliable and rheologically firm enough to retain its shape indefinitely, it is widely used for stop-motion clay animation (claymation) techniques, therefore can freeze the flow patterns of the

process similar to the actual metal workpiece. To prepare the multi-layered slabs, different colours of plasticine were manually rolled down to a uniform thickness of approximately 2 mm and then were stacked on top of each other by the thickness of 10mm. These stacked up layers were cut by a thin-cutter of 0.2 mm thickness to the slabs with 100mm (length) x 30mm (width) per piece and set as for butt joint configuration producing weld plate of approximate 100mm (length) x 60mm (width), as the test dimensions. In all the steps of rolling, cutting and welding, Glycerin was used as the lubricant. The plasticine blocks were subject to heat-treatment to improve the adhesiveness between the layers and also to absorb the excess glycerin between the layers. The blocks were heated at a temperature of 60 °C for a period of three hours using a Nabertherm N20/HR oven. The heating rate and the cooling rate of the oven were 1.5 °C/min and 0.35 °C/min, respectively. Figure 3. 6 depicts the heat treatment cycle.

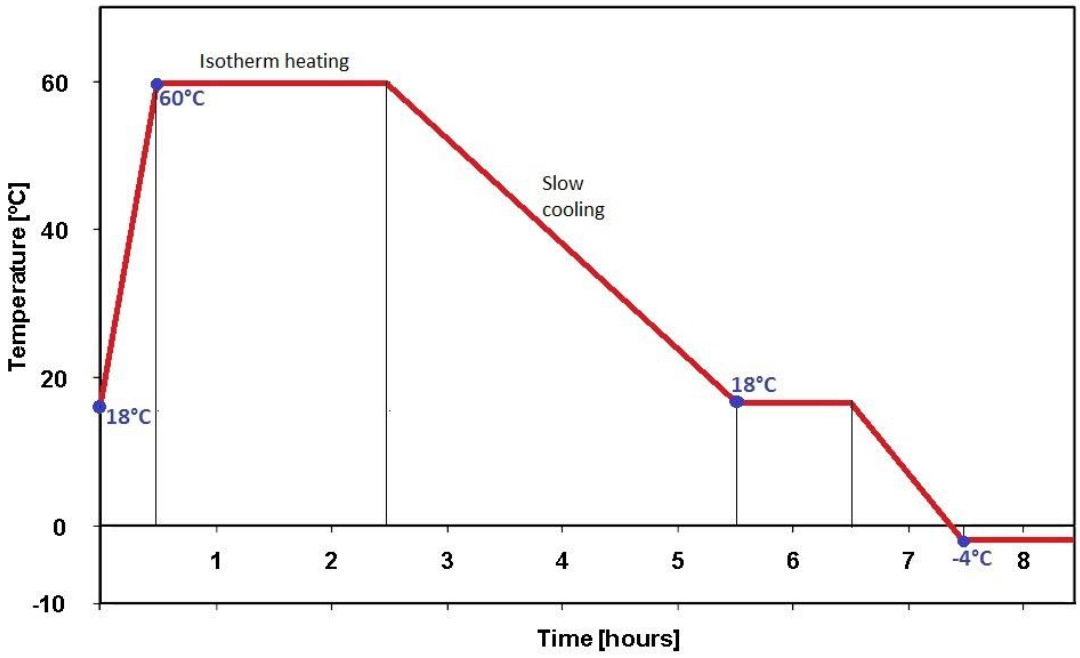

Figure 3. 6. Heat treatment process of the multi-layered plasticine slabs (by A TAMADON).

To determine the most suitable temperature for flow visualization of FSW process, a trial and error extrusion test were performed on the multi-layered plasticine blocks at three different temperatures, namely 18 °C, 4 °C and -4 °C. For the same amount of force, it was witnessed a severe deformation in 18°C block where the disruption marking made it difficult for flow visualization. Compared to the 4°C sample, the -4°C one left an undisturbed dead zone beside the plasticized region of shear fields. To obtain a suitable quality of the material flow visualization during the FSW process, it needs the flow pathlines to be distinguishable from the dead zone, hence -

4 °C is the suitable work temperature of the analogue modelling. See Figure 3. 7 for results.

Figure 3. 7. Plasticine slabs used for the analogue modeling (by A TAMADON).

ALUMINIUM WELDING TRIALS- the first candidate for welding test of the Aluminium plates was the A6082-T6. A high-strength marine-grade aluminium with a high rate of applications in super-structures. But characterization tests revealed that the structure and thermomechanical behaviour of this alloy is not completely possible to reveal, because of a complicated heat treatment cycle during the processing of the sheets. Therefore, it needs to provide some other nominates for the aluminium workpiece, preferably in different strength range and good properties for microstructure characterization and micrographs of the flow feature within the weld texture. It have been nominated three different aluminium alloys with a good microstructural capability, specially the tint metallography and a strength level lower than the A6082-T6 which make the BFSW processing easier than before.

iii. WELDING TESTS

As it is mentioned before and during the first phase of the study (analogue modelling), the welding machine and the welding process parameters for the plasticine analogue and aluminium trials are different, according to the strength of the workpieces.

To conduct the analogue tests a manual milling machine is employed in a minimum range of RPM and the feeding rate. This is because for the disruption prevention and also a good quality of the material flow visualization. The setup of the analogue model test is observable in Figure 3. 8. While in actual trials of the aluminium weld, a CNC machine is employed with a variety of the RPM range and feed rate to investigate the dynamic parameters of the BFSW process through the aluminium joint.

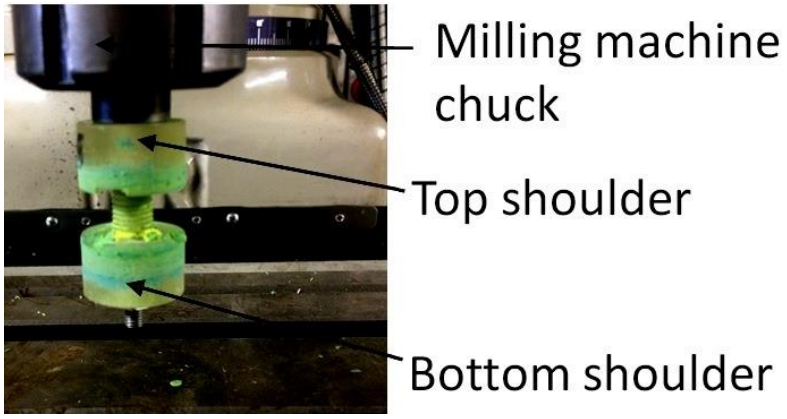

Figure 3. 8. Schematic of the Analogue model of the BFSW plasticine samples, processed by a manual milling machine (by A TAMADON).

The number of the tests for plasticine analogue just is depended on the thickness, pin features (threads-flats-flutes) and scrolls patterns. To achieve the best quality of the material flow visualization, the RPM and feed rate should be considered in the minimum range. On the other hand, because of easy setup for making the samples, manual test condition, and fast and cheap cross-section observations, there are much fewer limitations in the testing in comparison with the real weld trials of the aluminium sample. For the actual weld process, the intent was to explore different processes settings (5x feed rate and 5x spindle speed), the geometry of the bobbin tools, and the metallurgical properties of the weld via metallographic measurements. Nominally this results in several tests. In addition to difficulties for the test setup, a comprehensive characterization analysis for the evaluation of the all physical and mechanical properties of the weld samples is not possible during the normal time of a PhD research, as it requires to process more than 500 samples during the characterization studies. Hence, to save the time and cost this is optimized to reduce testing as follows in Table 3. 1.

Table 3. 1. optimization of the variable during the actual trial of the aluminium tests.

Variables	**Spindle speed (ω; RPM)**	**Feed rate (V; mm/min)**	**Plate thickness (mm)**	**Tool design (Geometry)**	**Alloy grade**	**total**
initial	5	5	3	3	3	+500
optimized	2 sets; (min-speeds) (max-speeds)	2 sets; (min-speeds) (max-speeds)	2, 4 mm 6mm	2 Simple tool Fully-featured	3; 1xxx, 3xxx, 6xxx	~ 50

As the welding test starts with a trial and error, the optimization of the operational parameters and process variables have an empirical basis rather than using an objective function.in addition to the welding speeds (ω, V), and the workpiece material (grade and thickness), the geometry of the bobbin-tool also has a key role in the optimization of the welding process. In this research, three main designs (simple

tool, triflat, and fully-featured; scrolled-threaded-triflat) were applied to identify the optimized welding parameters for the aluminium weldments, see Figure 3.9.

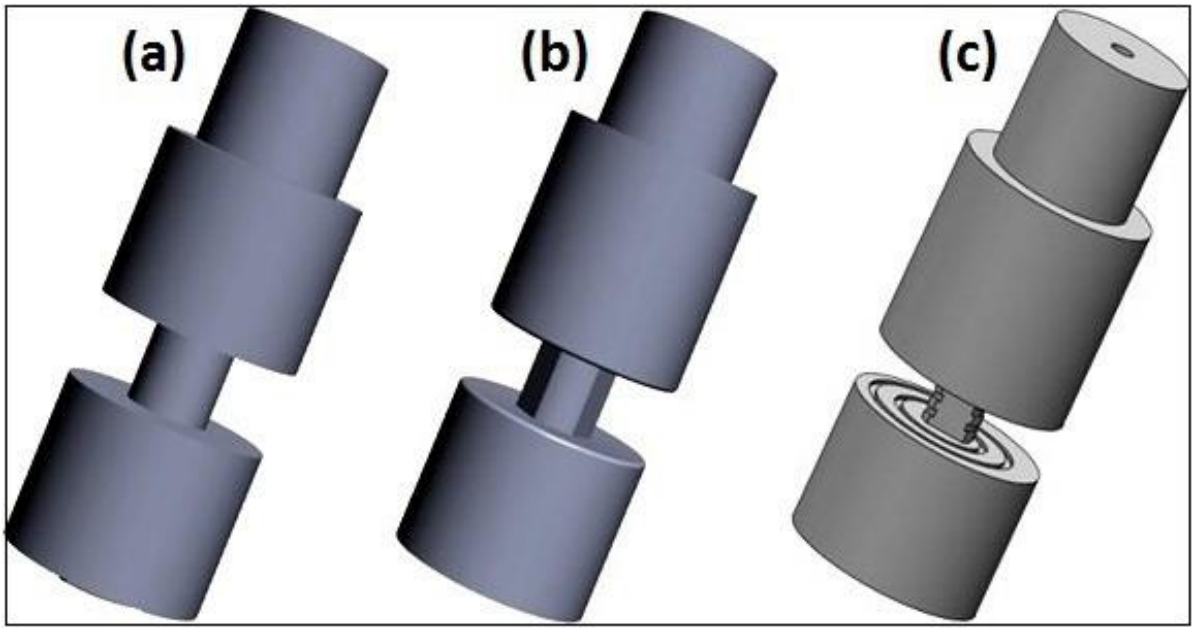

Figure 3. 9. 3D model of the bobbin-tool designs, utilising for the BFSW welding process by the CNC milling machine; (a) simple bobbin-tool, (b) triflat bobbin tool (non-threaded), (c) fully-features triflat bobbin tool (threaded and scrolled). (by A TAMADON).

In this study, the BFSW process was compared between 4 and 6 mm thick Al-alloy sheets and 10mm thick slabs of analogue plasticine as the workpieces. Plasticine shows a good ability in plastic deformation, but due to its much less yield strength in comparison with metals, here should consider a lower strain rate and thicker to achieve a good quality of material flow visualization. The range of spindle speed (RPM), feed rate and thickness of the weld samples were selected by a set of trial and error tests. More details of the welding process for the analogue plasticine and actual Al welds are demonstrated in Table 3. 2.

Table 3. 2. The parameters of the welding process for the Plasticine and Aluminium samples.

Workpiece	Tool Material	Work Temp	$D_{Shoulder}$ (mm)	D_{Pin} (mm)	$D_{Shoulder}/D_{Pin}$	Plate Thickness (mm)	Compression Ratio	ω (rpm)	V (mm/min)	Thread Pitch (mm)
Alalloys	H13 Tool Steel	18 °C	25	5	5	6	3.75%	300-600	300-600	1.2
Multilayered Plasticine	Polycarbonate Plastic	-4 °C	30	6	5	7.5	3.75%	50-100	50-100	1.25

After the welding process, the standard sample fabrication methods were followed according to the standards of tests. For different purposes in metallographic observations, and thermomechanical behaviour of the weld, to study the nature of the flow behaviour, origins of defects and different flow-based mechanisms in the structure of the BFSW welds were investigated.

3.2.2. Methodology 02: Metallurgical Observations

In the majority of the weld samples, tunnel void is the main flow-based defect emerged in the body of the weld. This discontinuity-shaped defect can bring more macro- and micro-features of the material characteristics to evaluate the final properties of the weld. The metallographic measurement is a fast observation method to study the flow-based features of the weld, in correlation with the metallurgic characteristic of the aluminium weld as the grain-properties depended on the alloy.

As material flow has the main role in the formation of the weld region, failure of the flow regimes can be the dominant reason for the formation of the tunnel void. By utilization of different reagents for the revelation of the flow fields in the weld, it has been tried to provide a clue to elucidate the flow behaviour in the weld track and explain how incorrect flow path lines can result from a tunnel void, as discontinuity geometry in the body of the weld.

3.2.3. Metallographic observations; introducing innovative etchants

A6082-T6 alloy was chosen as the workpiece for the first phase of trial experiments. This alloy is a medium-strength Aluminium alloy with excellent corrosion resistance. It has the highest strength of the 6000 series alloys. Alloy 6082 is known as a structural alloy. In plate form, 6082 is the alloy most commonly used for machining. As a relatively new alloy, the higher strength of 6082 has seen it replace the other 6xxx alloys in many applications. T6 is a solution heat treatment and artificially ageing. The T6 tempering is mostly used to improve the machining properties of the alloy 6082. Table 3. 3 shows the chemical composition of the A6082-T6 alloy.

Table 3. 3. Chemical elements of the A6082-T6 aluminium alloy (ASTM standard)

Chemical Element	% Present
Silicon (Si)	(0.70–1.30)
Magnesium (Mg)	(0.60–1.20)
Manganese (Mn)	(0.40–1.00)
Iron (Fe)	(0.0–0.50)
Chromium (Cr)	(0.0–0.25)
Zinc (Zn)	(0.0–0.20)
Titanium (Ti)	(0.0–0.10)
Copper (Cu)	(0.0–0.10)
Other (Each)	(0.0–0.05)
Other (total)	(0.0–0.15)
Aluminium (Al)	Balance

For the microscopic observations, aluminium alloys must be properly prepared to reveal the true metallographic microstructure. In this case, the polishing approach is almost critical. As the followed steps, after the diamond paste and liquid polishing it needs to be polished with the colloidal silica on a pad substrate. This process should be as long as 1 hour with a mild pressure, to provide a mirror surface.

The most common etchants for aluminium are Keller's etch and Kroll's reagent, however, there are hundreds of more specific etchants. For the A6082-T6, there was no success with Keller's reagent to observe the microstructure. The Kroll's reagent were also tried which showed some narrow lines as the borders of the weld region. To develop the etchant solution, a trial and error procedure (by adding or changing of different chemical to the reagent solution) has been done to complete the resolution of the texture. The selection process was done based on the chemical elements of the A6082 alloy. Finally, a range of reagent solutions has been introduced according to the microscopic observation. Note that by increasing of the temperature up to 80 C, or fresh mixing of the chemicals just before the etching, can find a better contrast or resolution in the observations.

There is a known difficulty of visualizing the surface of AA6082-T6. Most of the images in the journal publications are fuzzy, the grains are not visible. The issue is that there needs to be an etchant that can show the grain structure, and none is known. In a previous research project, an attempt was made to develop such an etchant, but this was unsuccessful [81]. The present research returned to this problem and were able to successful product a set of etchants, see Table 3. 4. The details of the method and results are shown in Chapters (9-15).

Table 3. 4. Different groups of reagents with separate sequences of etching processing.

Name of Etchant	Etching Type	Pre-Etching	Etchant Composition
A	General Macrostructure	-	30.0 g NaOH + 100 mL ethanol (3 min, 50 °C)
B	General Macrostructure	-	2.5 mL HF + 2.5 mL HCl + 95 mL H_2O (30 s, 50 °C)
C	General Microstructure	-	0.5 g $(NH_4)_2MoO_4$ + 3.0 g NH_4Cl + 1 mL HF + 18 mL HNO_3 + 80 mL H_2O (90 s, 70 °C)
D	G.B Microstructure	20 g NaOH + 80 mL H_2O (20 s, 50 °C),	Etchant C (60 s, 70 °C)
E	HAZ Microstructure	20 g NaOH + 80 mL H_2O (20 s, 50 °C), then: 30 mL H_3PO_4 + 70 mL ethanol (20 s, 50 °C)	10 g CrO_3 + 2 g Na_2SO_4 + 10 mL HNO_3 + 10 mL CH_3COOH + 1 mL HF + 80 mL H_2O (60 s, 70 °C)
F	TMAZ Microstructure	20 g NaOH + 80 mL H_2O (20 s, 50 °C), then: 30 mL H_3PO_4 + 70 mL ethanol (20 s, 50 °C)	Etchant E (60 s, 70 °C), then: 15 mL CH_3COOH + 85 mL H_2O (15 s, 70 °C), then: 15 mL H_3PO_4 + 85 mL H_2O (15 s, 70 °C),
G	S.Z Microstructure	20 g NaOH + 80 mL H_2O (40 s, 50 °C)	10 mL HCl + 40 mL HNO_3 + 2.5 mL HF + 12 g CrO_3 + 10 mL CH_3COOH + 50 mL H_2O (60 s, 70 °C), then: 20 mL CH_3COOH + 80 mL H_2O (20 s, 70 °C), then: 20 mL H_3PO_4 + 80 mL H_2O (20 s, 70 °C),
H	Micro-flow Patterns	-	2 mL HF + 2 mL HBF_4 + 10 mL HNO_3 + 20 mL CH_3COOH + 33 mL H_2O + 33 mL ethanol (90 s, 70 °C)
I	Polycrystalline Structure	20 g NaOH + 80 mL ethanol (20 s, 50 °C), then: 20 mL H_3PO_4 + 80 mL ethanol (20 s, 50 °C)	2 mL HF + 2 mL HBF_4 + 5 mL HNO_3 + 30 mL CH_3COOH + 60 mL ethanol (90 s, 70 °C)

3.2.4. Metallurgical characterization

The metallographic and microscopic observations can provide more clues for better identification of the weld texture, inhomogeneity of the weld structure, micro-flow visualization and characterization of the micro-sized defects.

The set of innovative etchants can provide a relatively easy characterization for the weld features, e.g. grain distribution, grain boundaries, misorientation or recrystallization through the weld texture. But, a more accurate study of the microstructure beside the phase identification for the precipitates and different phases in the weld texture requires more advanced techniques e.g. electron microscopes, EBSD method or characterization of the elemental composition.

Besides this, some other techniques such as microhardness test, fractography and surface profilometry can reveal more features of the weld and complete the micro-scale characterization of the weld.

For more developed areas of research for evaluation of the thermo-mechanical behaviour of the weld, some high-magnification instruments such as TEM or AFM is required to study the dislocations or precipitates history during the BFSW process.

Characterization Facilities

Optical Microscopy- The macrostructure and microstructure of the etched cross-sections were studied using stereographic and optical microscopy, respectively. The optical microscopy is the first step in the characterization of the grain structure

(grain size and morphology), also visualization of the flow features in macro- and micro-scale.

SEM (including EDS and EBSD)- For a variety of microscopic analysis in higher magnification, the weld samples were examined with the scanning electron microscope (SEM) with two detectors. The electron backscattering diffraction (EBSD) detector was used to create EBSD maps for a different region of the weld cross-section. This analysis can show the grain misorientation as a thermomechanical characteristic of the weld texture also other sub-grain scale details related to the dynamic recrystallization of the weld microstructure are readily indicated by the EBSD technique. The identifying of the chemical composition of the elements in alloy microstructure is possible with the elemental and point maps with energy-dispersive X-ray spectrometer (EDS) detector of the SEM machine.

High-performance electron microscopes (TEM and AFM)- Further characterization of the thermomechanical behaviour of the weld texture affected by the dynamic recrystallization can be characterized by higher resolution of the electron microscopies. The transmission electron microscope (TEM) was used to provide more details of the precipitation mechanism and interaction of the dislocation in sub-micron details. To study of the dislocation mechanism and further elucidation of the sub-micron details of the weld structure, the atomic force microscope (AFM) is a reliable technique to the high-resolution observation of the texture details, down to atomic level.

Utilizing these characterization techniques can help us to build a robust theory on thermomechanical nature of the welding process and the history of dynamic recrystallization within the weld texture.

CHAPTER 4: Formation Mechanisms for Entry and Exit Defects in Bobbin Friction Stir Welding

Chapter Summary: Bobbin friction stir welding (BFSW) is an innovative variant for the solid state welding process whereby a rotating symmetrical tool causes a fully penetrated bond. Despite the process development, there are still unknown variables in the characterization of the process parameters which can cause uncontrolled weld defects. The entry zone and the exit zones consist of two discontinuity-defects and removing them is one of the current challenges for improving the weld quality. In the present chapter, the characteristic features of the entry and exit defects in the weld structure and formation mechanism of them during the BFSW processing was investigated. Using stacked layers of multi-colour plasticine the material flow, analogous to metal flow, can be visualised. By using different colours as the path markers of the analogue model, the streamline flow can be easily delineated in the discontinuity defects compared with the metal welds. AA6082-T6 aluminium plates and multi-layered plasticine slabs were employed to replicate the entry-exit defects in the metal weld and analogue samples. The fixed-bobbin tool utilized for this research was optimized by adding a thread feature and tri-flat geometry to the pin and closed-end spiral scrolls on both shoulder surfaces. Samples were processed at different rotating and longitudinal speeds to show the degree of dependency on the welding parameters for the defects. The analogue models showed that the entry zone and the exit zone of the BFSW are affected by the inhomogeneity of the material flow regime which causes the ejection or disruption of the plastic flow in the gap between the bobbin shoulders. The trial aluminium welds showed that the elimination of entry-exit defects in the weld body is not completely possible but the size of the defects can be minimized by modification of the welding parameters. For the entry zone, the flow pattern evolution suggested formation mechanisms for a sprayed tail, island zone and discontinuity-channel. For the exit zone a keyhole-shaped discontinuity is discussed as a structural defect.

This chapter is a derivative of the following publication:

Tamadon, A.; Pons, D.J.; Sued, K.; Clucas, D. Formation Mechanisms for Entry and Exit Defects in Bobbin Friction Stir Welding. *Metals* **2018**, *8*, 33.

DOI: https://doi.org/10.3390/met8010033.

4.1. Introduction

Since 1991 when the Friction Stir Welding (FSW) was introduced by The Welding Institute (TWI) [99] there have been many studies focussing on the FSW process, properties and weld quality. Despite the development of the conventional-FSW (CFSW) process that plunges a rotating tool into the material interface there are still

some inherent issues. In practice, CFSW is a process with complex and costly setup and produces an asymmetrical weld structure (different microstructure at top and bottom surfaces) where the control of flow regimes is the most crucial variable to achieve a high-quality weld [100, 101]. Although FSW is performed significantly below the melting temperature and the weld region is free of solidification defects, some limitations on tool geometry or process parameters may affect the weld properties by introducing flow-based defects. Bobbin tool geometry is one of the effective variants for modification of the FSW process used to reduce the defects in the weld track. Despite the higher capability in productivity, bobbin friction stir welding (BFSW) has also some inherent problems, for example discontinuity regions at the start and the end of the weld track. The present chapter examines entry and exit defects as the direct consequences of the interaction between the tool and workpiece of the BFSW process.

4.1.1. Literature

The joining mechanism in the FSW process is based on a non-consuming rotating tool (consisting of the single contact shoulder and a penetrating probe) ploughing through the interface of two butted plates, and mixes the materials into a bonding track by heat and stirring [102]. The simultaneous stirring and longitudinal movement deposits the mixed mass behind the probe's position, this forms the weld line [103].

The weld region is distinguished by the flow arms between plasticized and un-plasticized regions, from the surface (shoulder affected flow) to the root of the penetration (pin affected flow) [104]. Improper material flow during the plastic deformation and stirring can cause some structural problems such as lack of penetration, non-uniform stress-strain fields, stress concentration and distortion [104, 105]. Consequently, macroscopic defects in the form of discontinuities or voids develop [104, 105]. Tunnel void [100] and kissing bond [106] are two common defects in the weld track of the FSW processes, originating from the failure of material flow which can significantly reduce the mechanical properties of the weld [107].

To eliminate the defects and reduce the difficulties of the FSW process, the TWI introduced an innovative variant by modifying the tool to a bobbin geometry [4, 66]. The bobbin tool is a symmetrical rotating component consisting of two shoulders, one on each side of the workpiece connected by a pin fully embedded into the workpiece joint [74]. Since two shoulders are reacting together to form the friction stir weld, bobbin-FSW (BFSW) is also known as the self-reacting FSW [67, 108, 109], or double-sided FSW process [110, 111]. Because of two opposing shoulders in contact with the workpiece surfaces, the fixture design is much simpler as a backing anvil is not required [64]. Furthermore, two shoulders create and retain more heat within the working region [64]. These features can enable the BFSW process to join plates with a thickness range of 1.5 mm up to 25 mm [66, 75, 112]. Also, in the BFSW

process a symmetrical joining pattern is expected in the cross section of the weld perpendicular to welding direction, as the fully contained pin can eliminate the incomplete root penetration of CFSW [66]. Among the different bobbin tool designs, the fixed gap between the shoulders, with scrolled surface patterns, allows a relative flow between the shoulders to make a constant force in the stirring zone which can noticeably reduce the material distortion and residual stresses during the process [81].

Although BFSW has been successfully demonstrated, there are still issues to solve before reliable industrial application of this process. Most of the published studies are focused on the process setup [66, 107], tool development [66, 109] or metallurgical and mechanical properties of the bobbin welds [73, 80, 113]. A predictive approach regarding the potential discontinuity defects (i.e. crack or void) is one of the necessities for process improvement which hasn't been described in the literature. Because of the different tool geometry for the BFSW, the material flow is distinct from the CFSW, therefore the variables of the void formation are different to previous observations of the CFSW.

For the CFSW, material flows around and under the pin on the anvil side [102], but in the BFSW process the pin penetrates entirely through the width of joint interface [114]. Because of the differences in size and geometry of the shoulder and pin, material flow in the CFSW process is asymmetrical while in the BFSW the bilaterally shoulder-surrounded weld region creates a symmetrical hourglass cross section pattern [70, 80]. However at a closer inspection it is observed that the BFSW cross section is not symmetrical: the top and bottom surfaces are not always identical, as there is a vertical flow within the joint if the pin is provided with threads; the advancing side is not symmetrical with the retreating side regarding microstructure and extent of heat affected zone; and the defects are not arranged randomly or symmetrically across the section. This difference in flow pattern during the joining process can result in various possibilities for explanation of the defect formation mechanism.

Another difference between the CFSW and the BFSW is how the tool enters into the body of the workpiece. For the CFSW, the weld typically starts from inside the extremities of the workpiece by plunging, perpendicular to the material surface, the rotating pin into the join line and vertical removal of the tool at the completion of the weld. Hence, there is no loss of material. Conversely, BFSW tools cannot be plunged directly into the material so for an internal entry, within the extremities of the plate, a hole must be made and the tool assembled through the plate by fixing the outer shoulder. This method can be hard to implement and in some cases causes distortion of the workpiece. Also, discontinuity of the weld entry and exit features results as material has been removed from the weld line. Furthermore, with complex pin geometries, such as adding thread features or with machined flats, assembly of the pin and shoulders in position may not be straight forward. These limitations result

in the use of the fixed bobbin tool as a single piece component and welding starts from outer edge of the workpiece where the bobbin tool enters the workpiece interface to create a butt joint. Similarly, the tool exits from the material extremity. Entry and exit from beyond the material extremities results in the defects.

For BFSW, as a recent alternative, most of the work is focused on the material performance [115, 116] or attempting to explain the formation mechanism of the internal defects based on a metallurgical observation [80, 115-117]. Regarding CFSW, empirical observations still haven't reached a consolidated theory for the development of defects. The presented computational models also have insufficiencies in explaining the FSW process as a thermo-mechanical phenomenon [35, 118], but these efforts have not yet yielded a consolidated theory for the development of defects. The numerical simulation approach tends to assume a fluid continuum, which is intrinsically limiting since it is evident that the material is transported around the tool in batches (for tools with flats), and the voids are failures in packing (rather than negative pressure regions per se). Consequently the formation of defects is a challenging situation to simulate. Therefore, more studies need to be done by both numerical methods and physical models and experiments to clarify the nature of the FSW process and control of defects.

Published research in the field of the BFSW focuses on the body of the weld where the weld-line is a stable bond [119, 120]. While studies of the microstructure [80, 111] or internal flow of the weld [38, 121] exist, study about the entry zone and the exit zone formation has been neglected in the literature. A characteristic of BFSW is the entry zone has a flashing protrusion prior to the weld stage [81]. Extension of this tail-shaped discontinuity to the weld-line can lead to more defects in the weld and even result in failure of the welding procedure. In addition, shrinkage where the tool exits the workpiece [109] is another defect for fixed bobbin FSW, this disruption mechanism needs to be explained and eliminated. Shortage of information about plastic flow regimes and changes in stress-strain fields in the entry and exit zones of the bobbin weld are the motivations for this chapter.

4.1.2. Approach

The purpose of this chapter is to explain the formation mechanism of the entry and exit defects of BFSW by studying the flow features of the weld. The direct observation of the material flow behaviour in the weld is inherently difficult for a homogenous structure like the metal workpiece as it requires time consuming cutting, etching and polishing of the cross sections [80]. Alternatively, the approach taken was to confirm a plasticine analogue modelling process produces comparative weld defects to aluminium welds and then visualise flow patterns for various welding parameters using the plasticine analogue model. Plasticine was chosen because layers of different colours could be stacked and after welding the redistribution of the material is plainly visible. In contrast it is not possible with homogeneous metallic substrates to see the displacement of the material after

welding. The comparative tests of BFSW were conducted using layered plasticine and aluminium AA6082-T6, for the same tool geometry although feed rate and rotational speed are different. Preparing the plasticine plates required pre and post processing as described in the next section.

4.2. Materials and Methods

4.2.1. Tool Design Features

A full-feature fixed bobbin tool as per [64] was used. This comprised a pin with three flats and a thread, along with top and bottom shoulders having clockwise and counter clockwise scrolls, (Figure 4.1a). For welding of the 100 HV hardness aluminium plates the tool was manufactured from H13 tool steel with hardness 560 HV (figure 4.1b). For softer plasticine the tool was economically made of additive manufactured Stratasys VeroClear™ material having no post-processing, figure 4.1c.

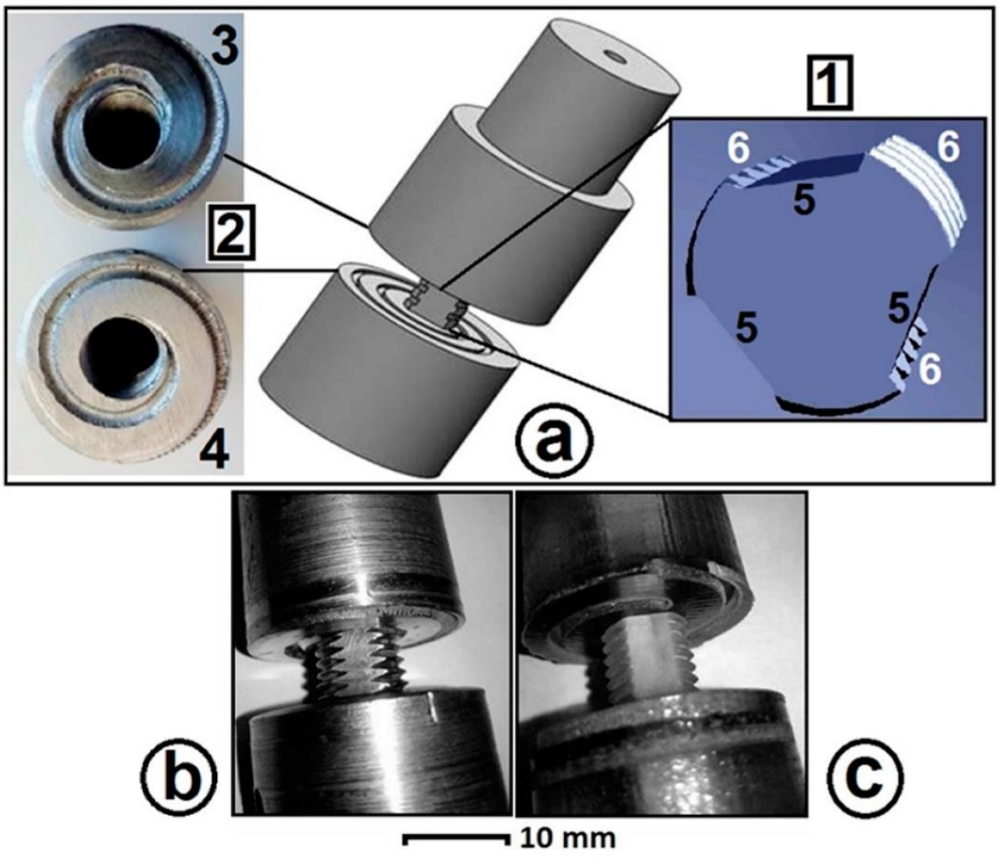

Figure 4.1. Schematic of the Bobbin Tool employed in experimental tests: (a) 3D model of the bobbin tool; 1-pin, 2-open end scrolls, 3-top shoulder, 4-bottom shoulder, 5-flats, 6-threads; (b) H13 steel bobbin tool for aluminium; (c) 3D printed bobbin tool for plasticine;

The pin features were three symmetrical flat surfaces machined onto a screw threaded shaft. The thread provides a better stirring [122]. The flat features allow a vertical flow around the pin to prevent the threads from clogging while stirring the material [122]. A 360 degree spiral pattern was inscribed on each of the shoulder surfaces, with the design intent being that the mouth of the spiral (on the outside edge) would capture substrate material and feed in inwards to the weld region. Alternatively this may be considered a dynamic seal resisting material escaping as flash from the weld. These spirals have opposite hands so that the upper and lower shoulders, which are rigidly connected, engage in similar relative motion to their respective surfaces.

These started from the edge of the shoulders and ended in the vicinity of the pin location. Direction of the scrolls compared with the tool rotation provides a circulation towards the centre. Threads and flats on the pin and scrolls on shoulders improves the stirring by driving the lateral motion and pumping of material inwards, this avoids spilling [64]. For a stable preservation of stirred material under the shoulder, the diameter (D) ratio ($D_{Shoulder}/D_{Pin}$) and compression ratio (difference between biting gap of the bobbin tool and thickness of the workpiece plate) were 5:1 and 3.75%, respectively [123]. Table 4.1 shows more complete details of the bobbin-tool for the plasticine and aluminium tests.

Table 4.1. The parameters of the welding process for the plasticine and aluminium samples.

Workpiece	Tool Material	Work Temp	$D_{Shoulder}$ (mm)	D_{Pin} (mm)	$D_{Shoulder}/D_{Pin}$	Plate Thickness (mm)	Compression Ratio	Feed ω (rpm)	Speed V (mm/min)	Thread Pitch (mm)	Number of Threads
AA6082-T6	H13 Tool Steel	18 °C	25	5	5	6	3.75%	400	350	1.2	5
								450	350		
								600	400		
								600	400		
								650	400		
Multilayered Plasticine	VeroClear plastic	-4 °C	30	6	5	10	3.75%	75	50	1.43	7

Welding Process Parameters

The BFSW processes were compared between actual welds of 6 mm thick AA6082-T6 Al alloy plates with the weld of slabs of 10 mm thick plasticine. The features of the tools were the same, but the shoulder gap differs to accommodate the different substrate thicknesses. A 6mm plasticine slab thickness was tested, but it did not have enough strength to prevent slumping under self-weight at room temperature.

Alternatively, it was considered an increase in thickness of the plasticine slabs with a lower work temperature would provide sufficient consolidation for the analogue samples.

A compression ratio of 3.75% was selected for both materials, based on [67],[109],[111],[123]. Compared with CFSW, a degree of compression assists the flow during the BFSW where the downward axial force of CFSW is removed [4]. 3.75% compression ratio for plate thickness less than 10 mm can create sufficient shoulder forging force during the stirring process and also prevent the ejection (spilling) of the material in the form of flash defects [67],[123].

The welding parameters (feed rate and rotating speed) were different for the two substrates. The feed and spindle speed range for aluminium were selected based on the works of [67],[109],[111],[123]. For the analogue tests, the feed and speed were selected based on the minimum speed sufficient to create bonding. Because of considerably lower mechanical strength of the plasticine compared with metals, the analogue samples are only applicable for flow visualization. The process parameters for the plasticine analogues were sufficient to provide a high quality joint and to reveal the flow paths. Although the initial purpose of the research was to perform several sets of dynamic variables for the analogue model, the plasticine was unable to be welded at speed and feed much above the slowest parameters of the milling machine available (ω =75 rpm, V=50 mm/min) hence only this one set of processes parameters were used here.

The speed set of ω=400rpm & V=350mm/min were used as the minimum speeds required to create a weld bond with a tunnel defect in aluminium, and hence comparable to the defect structure observed in plasticine. Lower speeds in this aluminium did not result in a bonded weld, and higher speeds resulted in better welds (with fewer or less extensive defects).

The orientations are designated as follows. The substrate material is laid flat. The origin is at the centre of the tool axis at the intersection with the plane of the upper surface of the substrate. The x-axis is in the direction of feed V hence also the locus of the weld line. The y-axis is in the plane of the substrate and perpendicular to the locus. Positive y is towards the true–right (on the right when viewing when watching the tool from behind) and the rotation convention also makes this the retreating side. The z-axis in downward into the plane of the substrate. The tool rotation ω is designated clockwise when viewed from above. This means that the advancing side (AS) is on the true-left of the locus (-y) and the retreating side (RS) is on the true-right (+y).

For ease of interpretation the analysis always (unless stated otherwise) present plan views with the x-axis upwards on the page, i.e. weld entry at bottom of the image. Consequently when viewing the top surface the AS is consistently on the left, and the RS on the right, see for example Figures 4.4, 4.6a, 4.7, 4.9. When viewing the bottom surface the AS is on the left and the RS on the right, see Figure 4.6b, 4.9.

4.2.2. Methods for Conducting Plasticine Tests

Creating a layered plasticine slab

In order to create a multi-layered plasticine block, different colours of the non-drying Newplast plasticine manufactured by Gordon Harris Ltd, UK were used. Since the Newplast clay is sufficiently pliable and the rheology firm enough to retain its shape indefinitely, it is widely used for stop-motion clay animation (claymation), therefore it can freeze the flow patterns of the process similar to the actual metal workpiece. To prepare the multi-layered slabs, different colours of plasticine were manually rolled to a uniform thickness of approximately 2.5 mm and then stacked to attain a thickness of 10mm. These stacked layers were cut by a knife of 0.2 mm thickness to slabs 100mm (length) x 30mm (width). They were set for a butt joint configuration producing a welded plate of approximate 100mm (length) x 60mm (width). In all the steps of rolling, cutting and welding, glycerin was used as the lubricant. For a reliable analogue model, the multi-colour layers should remain consolidated to avoid delamination during the BFSW process. Therefore, the plasticine blocks were subject to heat treatment to improve the adhesiveness between the layers and also to absorb the excess glycerin between the layers. The melting point of the 'Newplast' plasticine was measured to be 87 °C. For the heat treatment, the blocks were heated to 60 °C (>> 2/3 Tm) and held for a period of three hours using a Nabertherm N20/HR oven. The heating and cooling rates of the oven were 1.5 °C/min and 0.35 °C/min, respectively. The heat treatment cycle is shown in Figure 4.2.

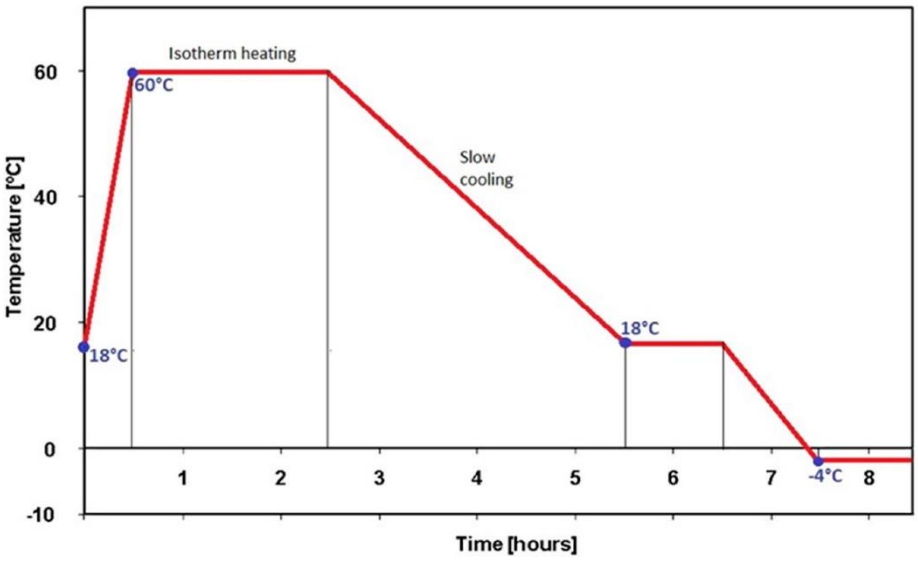

Figure 4.2. Heat treatment process of the multi-layered plasticine slabs.

To achieve the most suitable working properties of the plasticine, various methods were assessed including adding fillers and reinforcement. It was found that the most appropriate option was to perform the weld with the plasticine chilled [123]. To find the most suitable temperature for flow visualization a trial forging test was performed on the multi-layered plasticine blocks at three different temperatures, 18°C, 4°C and -4°C. Cross sections of the internal flow results of the forged trials are shown in Figure 4.3. By considering the melting temperature of the plasticine, the working temperatures were chosen to be much lower to preserve the stability of the sample. Also it should be taken into consideration that during the process the temperature of the sample will increase. For the same force and loading time, severe deformation was shown of the 18°C block and the deformation made it difficult for flow visualization. Compared to the 4°C sample, the -4°C sample left an undisturbed dead zone beside the plasticized region of shear fields. For good quality material flow visualization during a FSW process, the flow path lines should to be distinguishable from the dead zone, hence -4°C was chosen. This temperature also benefited the resistance to delamination or tearing.

Conducting tests with plasticine

Rotating speed ω (75 rpm) and feed velocity V (50 mm/min) were determined by conducting a series of tests to show the formation of a stable weld-line. The plasticine weld samples were run using a manual milling machine (OKUMA, MX-45VAE Model) with motorised longitudinal feed. The slabs for the analogue model of the weld were rigidly fixed between clamp bars and care was taken to ensure that no lateral movement during the welding process occurred. The scroll features on the surface of the shoulders were clockwise and anticlockwise for the upper and lower shoulders, respectively with relation to the direction of the tool rotation. More details of the welding process for the analogue plasticine are shown in Table 4.1.

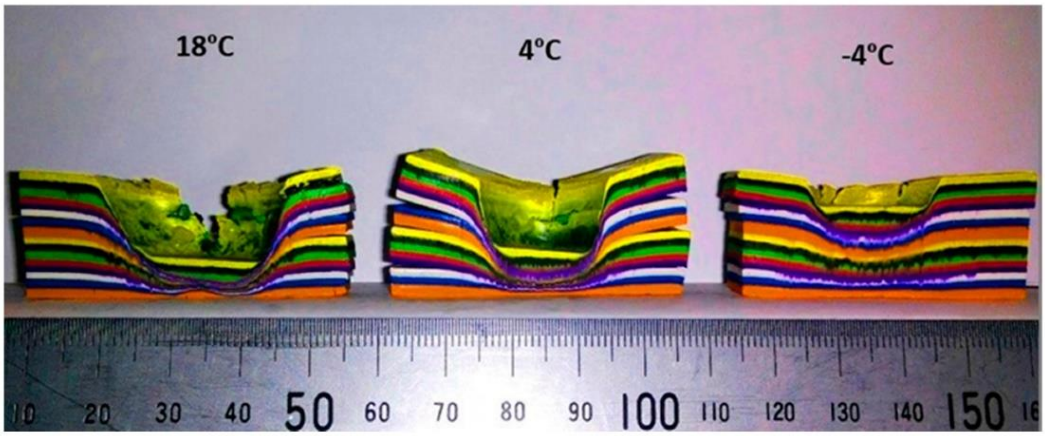

Figure 4.3. Cross section of the internal flow pattern of forging trials for the plasticine samples at 18°C, 4°C and -4°C working temperature.

4.2.3. Methods for Conducting Aluminium Tests

For the comparison of the analogue model with the real weld, 6 mm thick of AA6082-T6 aluminium plates were cut to 250 (length) mm x 75 mm (width) per piece and set for a butt joint configuration. Since the aim of the chapter was to evaluate the evolution of the weld in comparison with the analogue model of the bonding layer, a variety of spindle speed ω (400-650 rpm) and feed rate V (350-400 mm/min) were conducted to validate the joining process. There was no preheating or post-weld processing for the BFSW welded aluminium plates. Table 4.1 shows more details of welding operation for the aluminium samples.

The aluminium weld trials were conducted on a 3-axis CNC machining centre (2000 Richmond VMC 600 brand) with a Fanuc control unit and 14-horsepower spindle motor capacity. The direction of tool rotation was clockwise, as per the analogue tests. The plates were held by strap clamps and supported at the outer faces to be sufficiently rigid.

Characterization Methods

The weld characteristics and striation flow patterns of the entry and exit defects were examined using conventional fractography techniques for both the plasticine analogue and aluminium welds. For consistency of the visual observations, all photographs were recorded using a high resolution digital camera (Fuji Fine- S9500) Pix. To avoid having any shadows on the concave surfaces the photographs were taken under two fluorescent lamps.

4.3. Results

4.3.1. General Appearances of the BFSW Weld

The similarities between the analogue plasticine model and the aluminium welds are revealed in Figure 4.4 showing the material flow features of the entry and exit zones. The photographs were taken from the top surface of the weld samples (spindle side). The entry defect consists of a distinctive ejected tail (region 1), protruded from the retreating side (RS) and an adjacent discontinuity (region 2) penetrating the advancing side (AS) of the weld-line. The exit zone (region 3) shows a keyhole feature where the tool leaves the workpiece. The direction of the tool rotation relative to the weld-line is shown by two concentric circles representative of the shoulder (outer circle) and the pin (inner circle). The weld (region 4) is located in between the entry and exit zones. There is a similarity of size of the entry spray and the exit hole, indicating a similar amount of material is lost from the entry zone and the exit zone.

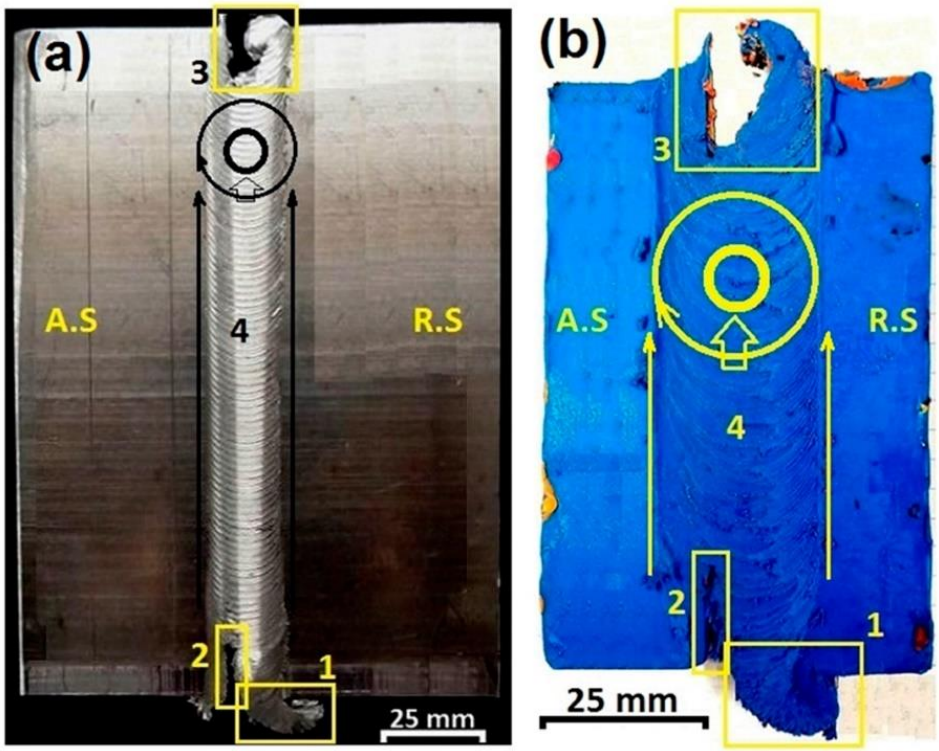

Figure 4.4. Top surface of the weld samples; defect features and the direction of the tool relative to the weld-line: (a) Aluminium plate; and (b) plasticine model; (1) the entry spray, (2) tunnel void discontinuity, (3) the exit zone, (4) weld-line track.

More significant footprints of the shear layers in the formation of the entry and exit zone defects are highlighted in Figure 4.5. The trace of threads during rotation and movement of the pin are demonstrated in Figure 4.5a and Figure 4.5b for the entry and exit zones, respectively. Also, a corresponding schematic of the shear flow around the pin is drawn in Figure 4.5c and Figure 4.5d. Regarding the entry zone (Figures 4.5a and 4.5c) the thread marks have an intersecting layout which is stretched on a convex face from the AS to the RS. The arrangement of diagonal lines of the thread marks from the middle outwards also shows the simultaneous effects of the pin and shoulders on plastic deformation. Another problem in the entry zone Figure 4.5a is the channelling discontinuity line close to the position of the bottom shoulder which can be recognized as the elementary step of the tunnel void formation. Tunnel void is a visible macro-size defect of the FSW process, resulting in a large discontinuity running along the weld-line occurring on the surface or subsurface [124, 125]. There is no solid theory to explain the formation mechanism of the tunnel void. However, it has been suggested that some flow based problems during the process, such as improper plunge of the pin or ineffective stirring between the AS and the RS, can generate a nonbonding region in the weld structure [70].

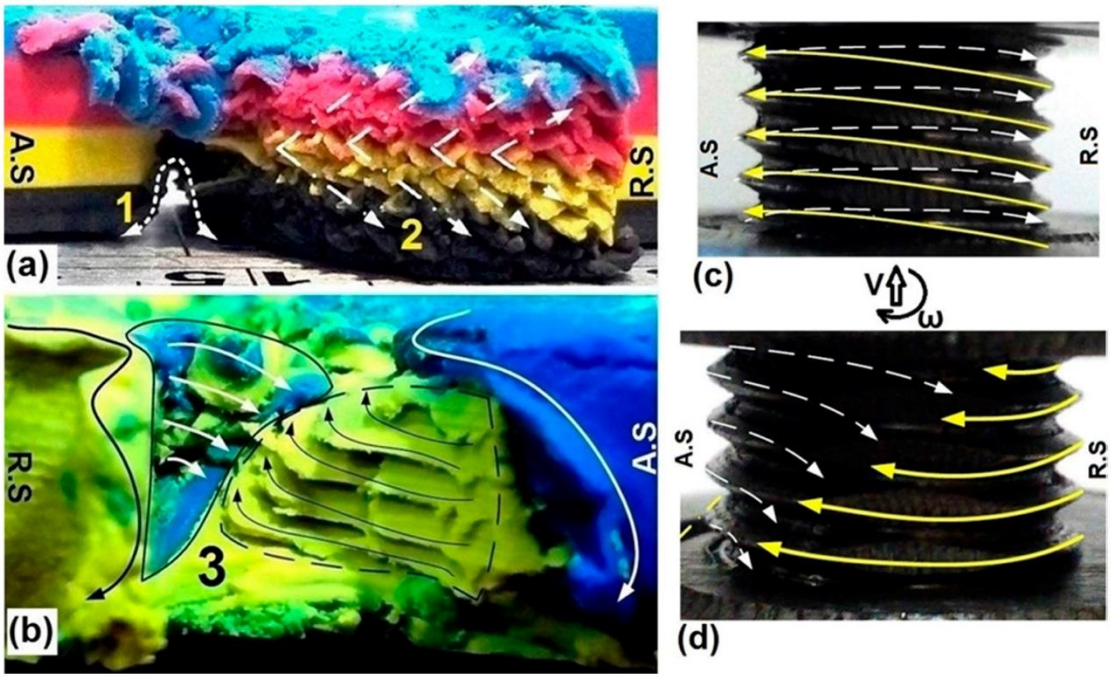

Figure 4.5. (a) Effect of threads in the entry zone for plasticine samples; and (b) the exit zone, replicated in analogue model; (1) tunnel void, (2) schematic of the shear-bands in the entry zone, (3) schematic of the shear-bands in the exit zone. (c), (d) schematic of the shear flow around the pin for the entry zone and exit zone, respectively.

At the end of the weld-line, the rotating pin leaves a concave curve at the exit zone location. As the Figures 4.5b and 5d show, the thread traces are again clear in the form of shear flow patterns. As the pin leaves the workpiece, the intensification of the laminar shear stresses around the pin causes a disruption in the efficient flow circulating between the AS and the RS [126], consequently the joining bond has failed.

At this stage, because of the different position and shape of the entry and exit defects it seems that the formation mechanisms of them differ, thus they will be discussed separately.

4.3.2. Entry Zone

Figure 4.6 shows the top surface (Figure 4.6a) and bottom surface (Figure 4.6b) of the entry zone for a plasticine sample. It is clear the colour of the entry spray on both top and bottom surfaces is the same colour of the RS material top and bottom layers respectively. As one of the principles of the FSW theory it has been assumed that the joining bond is a result of a mutual material flow circulation from the AS to the RS and simultaneously the RS to the AS [127, 128]. This shows for the fixed- bobbin tool FSW process the early steps of the bobbin tool entering the workpiece the material flow from the RS to the AS is disrupted and the plasticized mass flows outwards of

the workpiece. The main reason for the material ejection in the entry zone can be attributed to the free surface at the trailing edge of the tool and absence of a solidified mass blocking the flow.

Beside the sprayed tail, there is an island zone laterally deflected to the advancing side with a granular appearance. This region has a smaller amount of shredded material which is picked up by the tool and transferred to the advancing side. The material colour of the mass reveals that the island region came from the AS layers. Therefore this island is formed by slipping of the AS mass as the tool enters into the workpiece, or is the result of a successful circulation of the mass from the AS to the RS, and simultaneously from the RS to the AS.

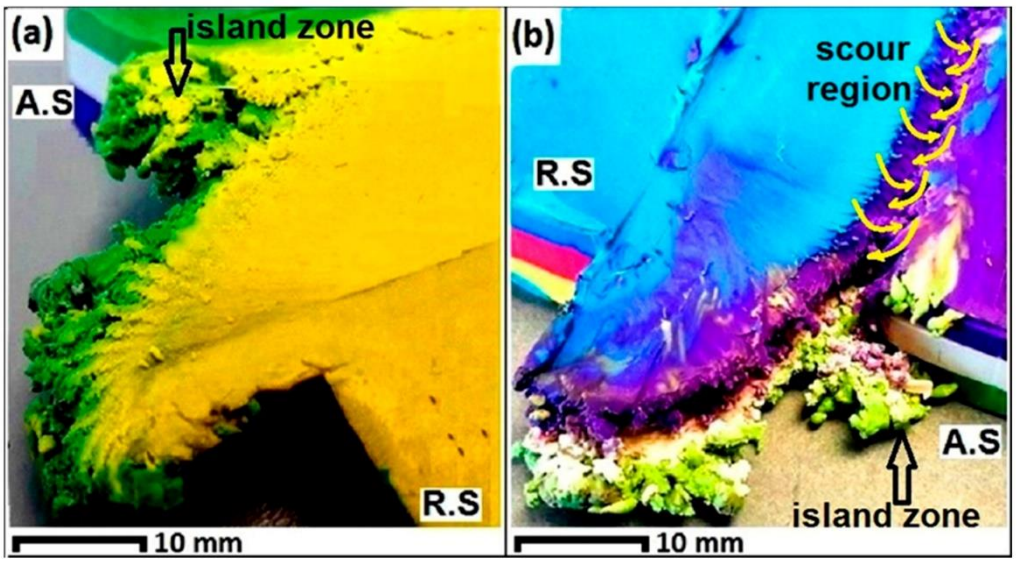

Figure 4.6. The stage of the entry zone for plasticine samples: (a) top view; (b) bottom view.

As it is shown in Figure 4.6b, the bottom surface of the analogue model, the tunnel void has formed a continuous channel pattern. It starts from the entry zone and extends along the side of weld-line, offset by approximately half of the pin diameter toward the advancing side. Here, the underside channel discontinuity is located at the typical position found for aluminium [77, 129, 130]. In the structure of FSW welds, complexity of the material flow fields at the triple junction cause a condition for promoting the localized discontinuity defects such as tunnel void or macro-channel [77, 129, 130]. Sometimes this disarrangement can reach the surface as seen in Figure 4.6b, but mostly it is observed as a macro-size internal defect.

The analogue model of the BFSW joint shows the tunnel defect emerging with a scouring action on the bottom surface of the substrate (Figure 4.6b). As a starting hypothesis, the scour region can be the outcome of flow eddies where the linear and rotation motions are combined during the transportation mechanism. However, for

a better explanation of the scoured area, study of the flow field around the tool is required. The occurrence of the scour region will be explained in more depth after presenting the metal trial results; this provides a robust comparative observation of scouring features between plasticine and aluminium samples.

Figure 4.7 shows the material flow behaviour in the formation of the entry zone with the ejected sprayed tail, the island zone and a nonbonding discontinuity. In general, the entry defect can be characterized as a disordering of the plastic deformation which stabilises as the tool travels completely into the plate. This effect occurs when the shoulders and pin start to engage with the material, but the tool is not fully surrounded by solid material. In this condition, as the rear side of the tool is open, the material is not stirred but instead ejected to the trailing edge where it finally forms a sprayed tail at the free edge of the entry.

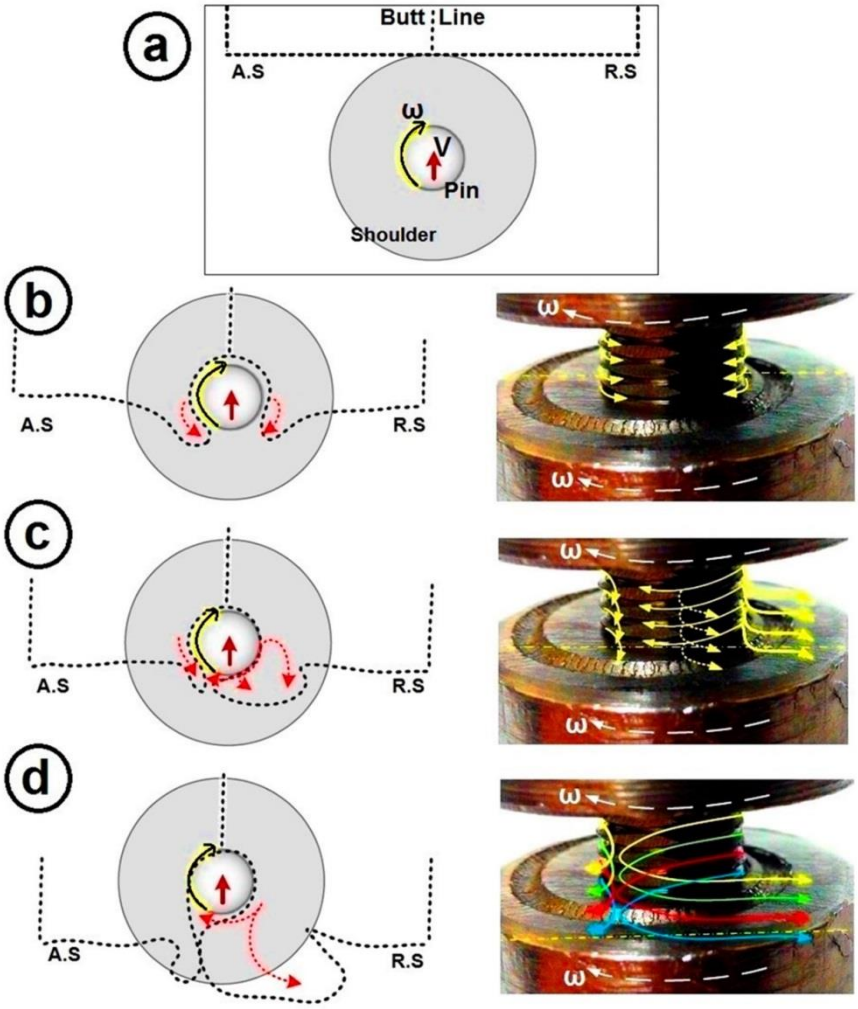

Figure 4.7. Schematic of formation of the entry region at the rear of the pin: (a) relative position of the tool and workpiece; (b) initial contact between the rotating tool and workpiece; (c) formation of the ejected spray by rotation of the tool inside the workpiece; (d) final profile of the mass ejection and formation of the entry defect consisting of a curved tail, island zone and a nonbonding discontinuity.

Figure 4.7a shows the schematic of the tool position relative to the AS and the RS, with rotating and longitudinal (ω and V) relative to workpiece. According to the Figure 4.7b, as the tool enters through the substrate it ejects the ploughed material towards the trailing edge, both at the advancing side and the retreating side. It is shown in Figure 4.7c, the tool is now inside the workpiece and completely surrounded by the plasticized mass. Since the stirring process has not been completely formed yet, some branching patterns are indicated by dotted arrow-lines for the plastic flow around the pin. As the position of the pin is stable inside of the workpiece (Figure 4.7d) the entry zone has been formed completely and the tool keeps going forward through the workpiece. Passing of the tool from the entry zone, the weld track will be formed along the butt line by the typical stirring flow driven from ω and V.

During the stirring process, successive layers of plasticized flow rotate in different strain planes which cause different twisting directions. By movement of the pin, each twisting pattern can create striation layers which, after travelling a defined deflection distance, reach a stagnation point (on the AS rearward of the pin). Consequently, the plastic mass becomes immobilized next to the adjacent accumulated layers and settles/builds up in the form of the final sprayed tail (similar to Figure 4.6a). The consequence of these series of movements and settlements of twisting layers is a stirred zone in the body of the material. Since this branching pattern is affected by movement of the tool, there is a gap between the primary and new position of the striation layers. As illustrated in Figure 4.7d, at the stirring area in trailing edge of the rotating tool, there is a discontinuity region which indicates the original position of separated materials in AS before taking part in stirring. In other words, since the mass cannot travel the main route of the stirring, this discontinuity is left as the footprint of the unstable circulation of the plastic flow during the early steps of the stirring process. The ejected spray which is curved back towards the workpiece is the plasticized twisting mass. Gradually as the tool plunges into the workpiece, the deposited material at the trailing edge acts as an entry backing plate for the circulating mass and therefore the tail changes from a curved to a straighter profile in the plan view. The similar region in the AS (Figure 4.7d), referred to as the island zone, consists of the mass that did not take part in stirring (remained from the primary embedment of the pin into workpiece) or the twisting layers which have strayed away during the stirring cycles.

Figures 4.8 and 4.9 show the top view and bottom view of the entry zone for the aluminium plates in different rotating and longitudinal speeds (ω and V), respectively. These weld tests were performed to investigate the material flow details in the entry and exit zones. For AA6082-T6 plates with 6mm thickness, the minimum ω and V for creating a join was 400 rpm and 350 mm/min, respectively. Generally, by increasing ω and V, the volume of ejected spray and length of the discontinuity line were decreased, but there was also an increase in the size of the

shredded island zone (Figures 4.8 and 4.9). At (ω=500rpm) and (V=350mm/min) the entry spray and discontinuity defect size was minimised. As ω and V are increasing, the volume of the ejected spray decreases on the RS, but a multi-branched pattern of the spray started to grow in the AS with a further increasing size of discontinuity line.

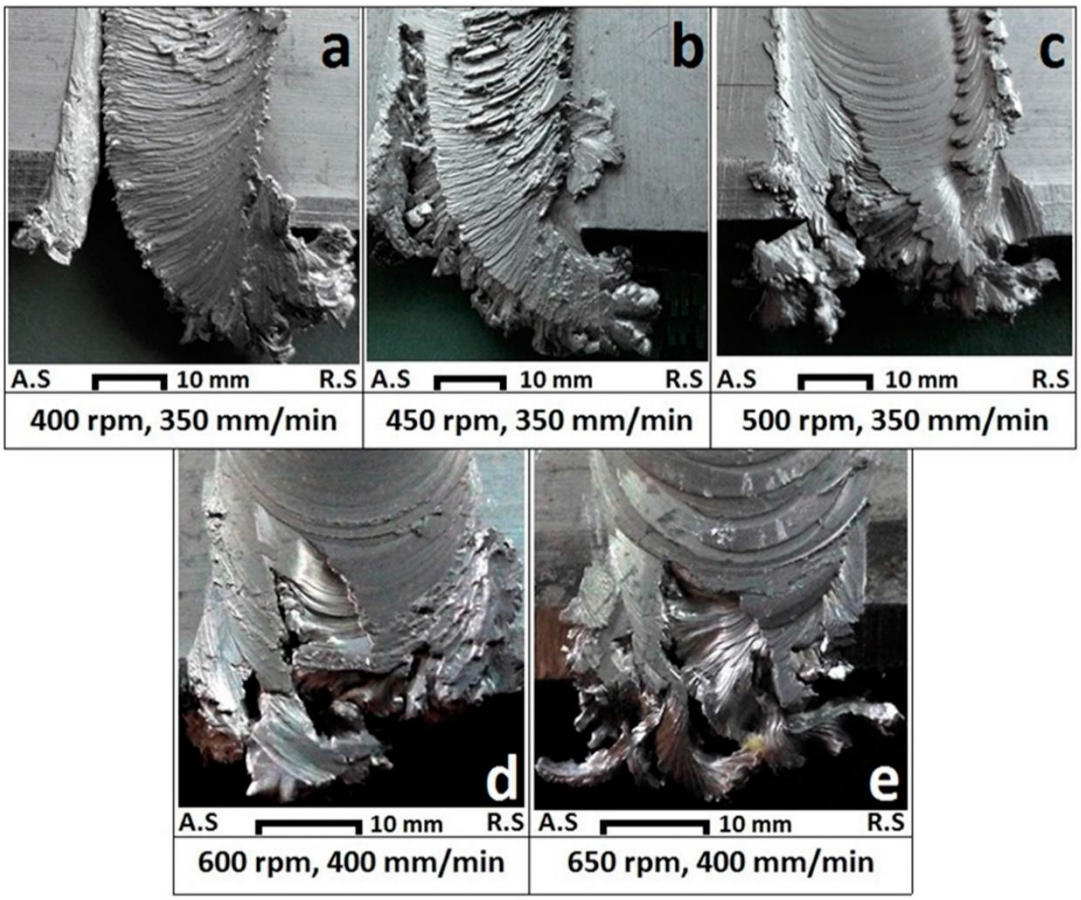

Figure 4.8. The entry region for aluminium weld samples, in different (ω/V) ratio (Top view).

In Figures 4.8 and 4.9, images a-c are for feed V=350 mm/min and the rotation speed ω was varied from 400 rpm to 500 rpm. At rotation speeds higher than 500 rpm the size of the shredded particles at the entry zone was increased and the weld was not formed, hence this was deemed a non-viable process setting. The common practice in these situations is to compensate by increasing the feed, on the basis that heat input is increased by faster rotation speed but decreased by faster feed speed. Hence images d-e are for feed V=400 mm/min and the rotation speed ω was varied from 600 rpm to 650 rpm. Thus, increase of speed alone does not eliminate the entry defect, only by an optimum combination of ω and V can the size of the entry defect be minimized.

Regarding the scour region, in Figures 4.8a and 4.8b, also 4.9a to 4.9c, this flow feature exists on the edge of the tunnel void channel for both the aluminium and plasticine samples. The scour region on samples (400 rpm, 350 mm/min) and (450

rpm, 350 mm/min) is evident on the surface. Figure 4.10 shows the scoured channel discontinuity for aluminium and the analogue plasticine.

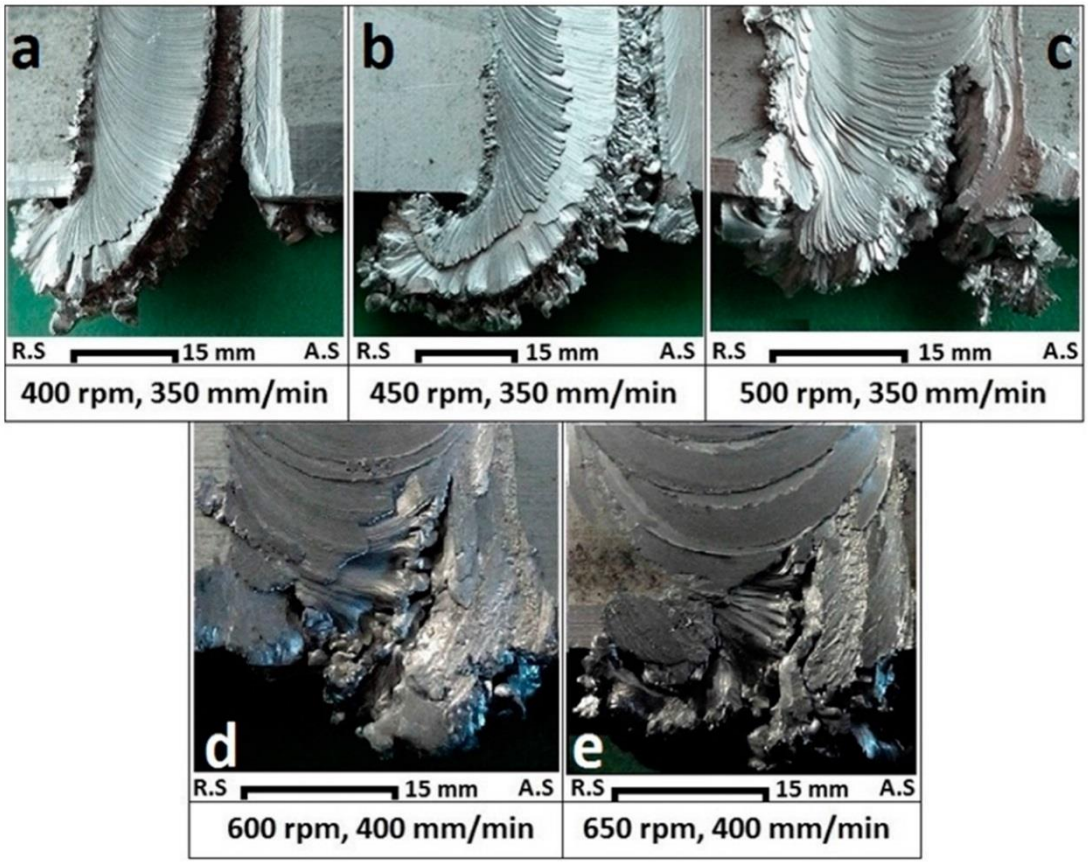

Figure 4.9. The entry region for aluminium weld samples, in different (ω/V) ratio (Bottom view).

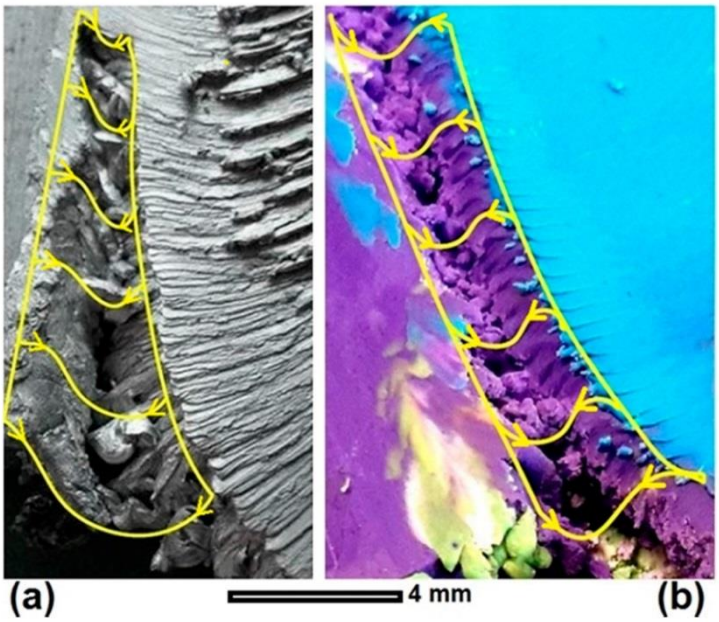

Figure 4.10. Schematic of the entry scour region for the channel discontinuity: (a) aluminium weld; and (b) analogue plasticine.

The scour region results from the dynamic interaction between the tool and workpiece. The ejection of material from the weld zone at entry causes a mass deficit to persist further along the weld locus. This mass deficit appears as a void on the bottom surface, because the threaded action of the pin pumps material to the top surface. Hence the deficit appears as a scour. This is progressively closed in as the tool moves forward.

The flow circulation from the RS towards the AS at the bottom shoulder transports material to the trailing edge of the tool. Here it is smeared into the void, and progressively fills it in. This results in the formation of the streak-like patterns at the edge of the channel which are stretched onto the bottom surface of the weld.

Another variable for BFSW weld quality that has not been considered before is the speed ratio; (rotational speed/traverse speed) or (ω/V). The speed ratio is representative of revolutions per tool traverse distance (rev/mm) which can be a key factor for integrity of the flow regimes during the stirring process between the AS and RS. An incompatible speed ratio can cause the failure of the weld in the early stages of the process or cause structural defects through the weld-line such as tunnel void or macro-cracks. According to principles of metal forming, plasticizing depends on the heat generated at the contact area between the tool and material [131]. In this situation the tool geometry and the rotational speed of the tool (ω) activate the shear layers required for the plastic deformation. The ω directs the material in a rotational direction, which corresponds to a mutual horizontal flow between AS and RS. Differences in ω affect the rate of plasticizing around the tool and also the overall mass flow driven by the stirring [131]. At the same time the longitudinal motion of the tool creates sufficient working space for transporting the mixed plastic flow behind the pin.

The speed ratio (ω/V) has several implications. First, the higher speed ration implies the elevated rotational speed compared to the feed rate. This intensifies the frictional heat generated at the interface of the tool surface and the workpiece material. Greater heat input is obtained by faster rotation speed ω and decreased feed speed V, i.e. larger values of ω/V. However the relationship between heat and weld quality is not straightforward: greater heat is generally associated with more defects. Rate at which welds are produced, an important consideration in production economics, is determined by feed speed (V), hence favours lower ratios of ω/V.

Further considerations arise when considering the entry zone. At the point of entry a high ω/V increases the ejection of material out of the weld zone. The higher ω more violently expels material per images a-c in Figures 4.8 and 4.9, including as detached strips and granules that fail to build the adherent structures that limit subsequent ejection. The lower V is presumed to prolong the opportunity for the tool to discharge material. The ejection of material results in a deficit of material in the cross

section further along the weld locus, which causes discontinuities in the flow around the tool and in the packing of material.

The packing occurs in the wake of the tool, on the advancing side. The mechanism for this is relatively complex and incompletely understood. The explanation is that the transport of material around the pin is in batches, with the source material arising from a sector from 9 o'clock (advancing side) to 3 o'clock (retreating side) when viewed from above with 12 o'clock being the x-axis. The batches arise due to the flats on the pin and the slip-stick motion of the tool. The latter occurs to some extent even with smooth pins, is attributed to the dynamic interaction between tool deflection and plasticity in the substrate [15], and is evident in the shoulder marks on the surface (especially those intersecting circlular striation marks that show deviation in tool concentricity). Inside the weld the material is moved in a circular motion (clockwise in the present situation), and deposited in the wake of the tool. The most difficult area to fill is the advancing side near 9 o'clock, because this is where the tool is simultaneously laying down the processed material (from say 7 o'clock to 9 o'clock) and extracting fresh substrate (from 9 o'clock onwards). Microscopy studies show that this is the region where there are many folds of material evident in flow features, and different crystal characteristics [24]. This is also where voids are commonly found. Consequently when finding weld defects in the cross section at the approximate position of the AS edge of the pin, it mainly attributes to insufficient material, in turn to loss of material.

Our primary interest here is in the entry feature, but it should be noted that material may be lost in other ways, such as rind/flash, and small chips of material that fall out the bottom of the weld. The greater the material deficit in the weld cross section the greater the defect problem, and in extreme cases a tunnel defect is observed. There is a direct continuation of the scour region (see Figure 4.9 a-b) at entry to the tunnel defect further along the weld locus, and attributing this to a single underlying mechanism of loss of material at entry. The reason for the tunnel defect being at the bottom surface as caused by the threads on the pin, is attributed to upwards pumping of material, see Figure 4.5.

Loss of material is exacerbated by higher values of ratio ω/V. The different ratios used for the aluminium tests are shown in Figure 4.11. Due to experimental limitations, it was not possible to get this grade of aluminium to join at all for $\omega/V <$ 1.15 rev/mm. The best welds (but by no means defect free) were obtained towards the centre of this range at ω/V = 1.43 rev/mm. At higher ratios the weld quality deteriorated, as evident in large entry scour and extended tunnel defect.

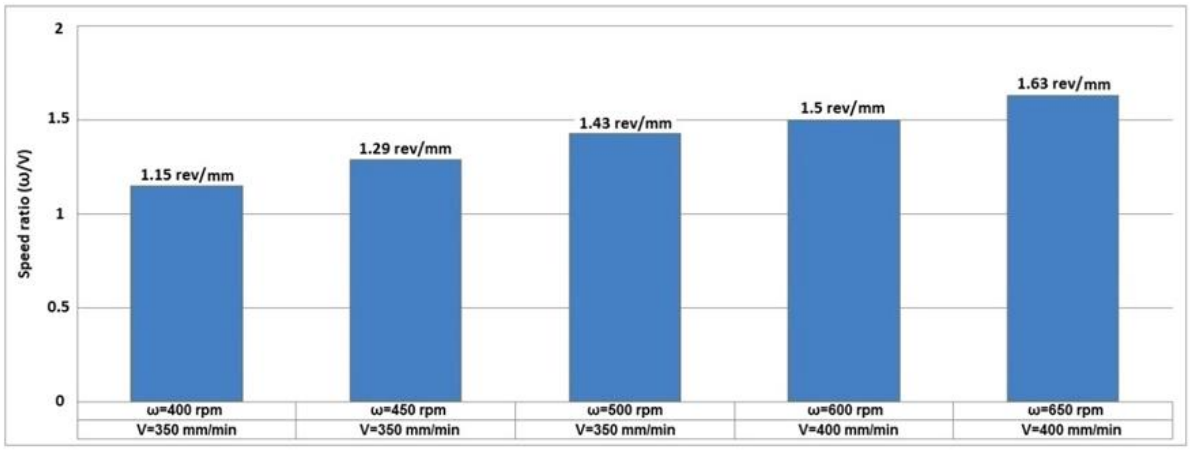

Figure 4.11. Speed ratio (ω/V) for different aluminium weld rates.

The ratio of 1.43 rev/mm for aluminium is similar to the speed ratio of 1.5 rev/mm of the plasticine samples (ω=75 rpm and V=50 mm/min), and resulted in comparable flow features. This suggests that the formation of the features was determined primarily by geometric mechanisms of flow, rather than material properties or absolute values of welding parameters.

The ratio (ω/V) is effectively a shear rate, where the plasticized mass can flow around the tool in two different frictional modes; sticking contact mode or slipping contact mode [131, 132]. An optimum (ω/V) causes a sticking mode when the shear rate is greater than the threshold value to transport the mass crossing AS-RS [131-133]. This means that the plastic flow is continuously transported into the stirring region without any local discontinuity of the streamlines – though this is an idealization. In practice the flats on the tool move material in discrete batches. The equilibrium stirring is achieved when material is continuously transported in from AS to RS at the front of the tool, and RS to AS at the rear. The combined effect of rotation (ω) and longitudinal travelling (V) can cause a transitional sticking/sliding model for the contact mode between the tool and material [134], hence the empirically observed slip-stick motion [109]. The slip-stick causes high frequency dynamic forces in the tool-substrate-machine system, and also explains the striation lines on the outer weld surface (weld crown).

To provide longitudinal conservation of mass across the cross section of the weld, it is necessary for new material to be added to replace that lost at the entry spray. Here in BFSW, the compression ratio for the shoulder gap provides the required make-up material. However the compression is necessarily small due to the stiffness of the substrate, hence it takes some distance of horizontal weld travel before the tunnel defect is closed. Hole-entry avoids the entry spray, hence results in fewer tunnel defects, but has other difficulties due to the need to assemble the tool into the hole. A bobbin tool that is assembled or adjustable tends to have less stiffness than a one-piece tool, and hence greater design challenges.

The material loss is less severe in the CFSW case because the tool may be plunged deeper into the substrate to compensate. Also the CFSW tool may be inclined so as to wedge material into the weld. Furthermore it is competitively simple to start the CFSW process in a drilled hole. All these actions avoid loss of material or increase the amount of material available in the weld region. However for CFSW a large force is required down the axis of the tool to hold it into the material. This is necessary to contain the compressed material within the weld. The single side conventional friction stir welding tool must be provided with this force, whereas the bobbin tool carries the force internally via the pin. A one-piece bobbin tool has greater stiffness than one that is assembled or adjustable. Hence tools suitable for hole-entry have benefits and disadvantages.

In summary, the results propose that any material lost from the weld cross section is at risk of causing subsequent defects. Consequently one of the key quality issues with BSFW is identified as the need to reduce the loss of material, especially the potentially large volumes of material lost at entry.

4.3.3. Exit Zone

Regarding the exit zone, the aluminium and plasticine welds show similar defect features. Unlike the entry zone, the approximate size of the exit zone did not change by varying ω and V. Figure 4.12 shows the Top view, Bottom view and Side view of the exit zone for the optimum aluminium weld (ω=500rpm, V=350mm/min) where the entry defect was minimized. Figure 4.13 shows the comparable flow features in the exit zone of the analogue model.

Both the alumiunum and plasticine welds show similar features at the exit zone, despite different welding parameters.

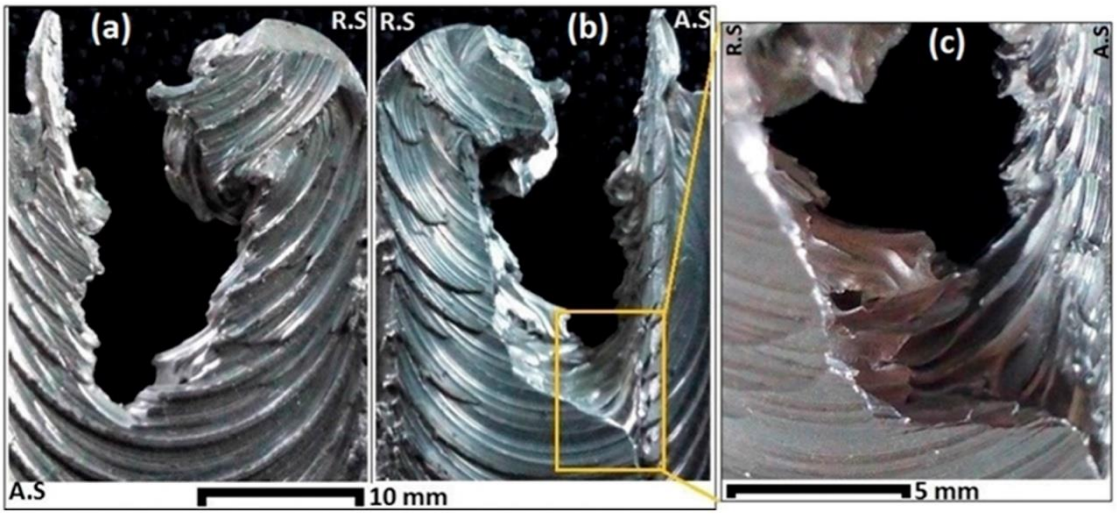

Figure 4.12. The exit zone for an aluminium weld: (a) Top view; (b) Bottom view; (c) End view.

In both materials the tool leaves the workpiece by a disruption in the body of the weld. The arrows on the top and bottom surface of the workpiece (Figures 4.13a and 4.13b) reveal the last trace of the shoulder on the surface in which material is transported from the RS to the AS before the start of the disruption, however the circulation system is not able to continue the primary circulation from the AS to the RS. The end view (Figure 4.13c) also shows the shear layers of the exit zone, where the last traces of the pin threads of the tool leaves the material. Figure 4.13c, similar to Figure 4.5b, shows a layered pattern in curvature of the side view which is attributed to the threads and flats on the pin and their effect on the plastic flow during the stirring.

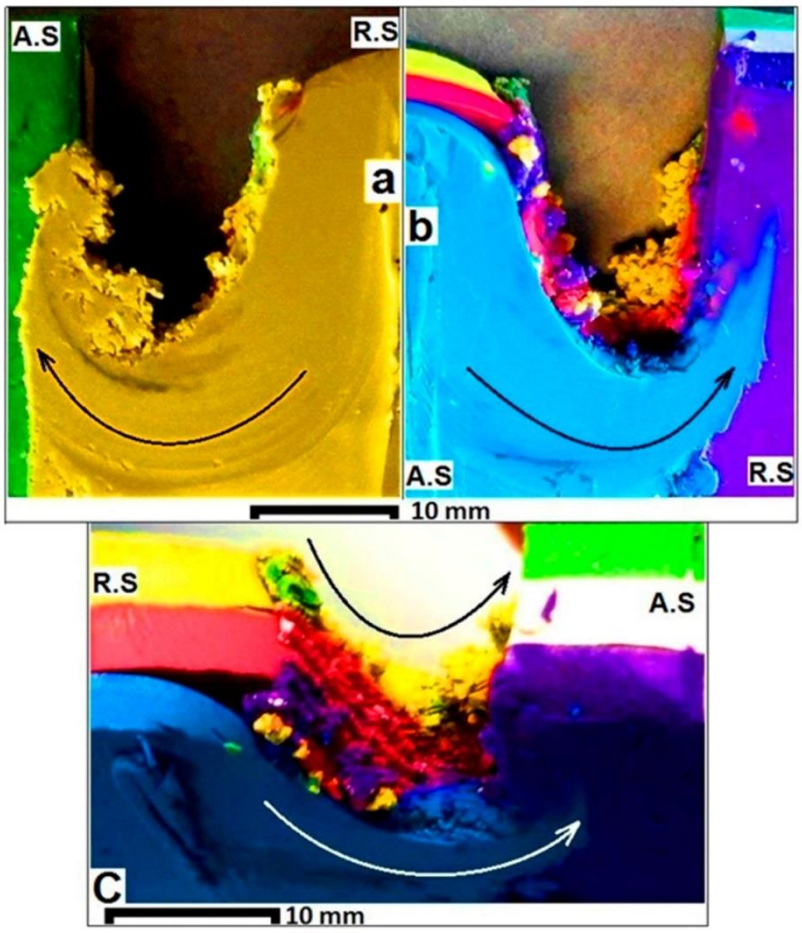

Figure 4.13. Exit zone at the analogue model: (a) Top view; (b) Bottom view; (c) End view.

The proposed disruption mechanism for the exit zone defect is shown in Figure 4.14. Starting with Figure 4.14a, as the material mass in front of the tool loses its stiffness because of the shortage of forward material, the circulation of the material in a path line behind the tool is also irregular. Thus by forward motion of the tool and plastic

deformation, the material bulges out and a hole is left behind. In Figure 4.14b the leading edge of the pin arrives to the free surface and starts to leave the plate. Here, material either side of the tool separates, creating of a wishbone-shaped or keyhole disruption. Figure 4.14c and Figure 4.14d show the exit of the pin from the shoulder from the workpiece. For the shown clockwise rotation of the tool, the AS edge is stretched more than the RS, and simultaneously the shredded mass in the RS is compressed back towards the workpiece. As the exit zone is related to the contact mode between the tool and the workpiece, even for different (ω/V) speed ratios the exit disruption will always be present. Therefore, it is confirmed that the exit zone defect is an inherent feature of the process whether using a simple or complex bobbin tool with different welding parameters.

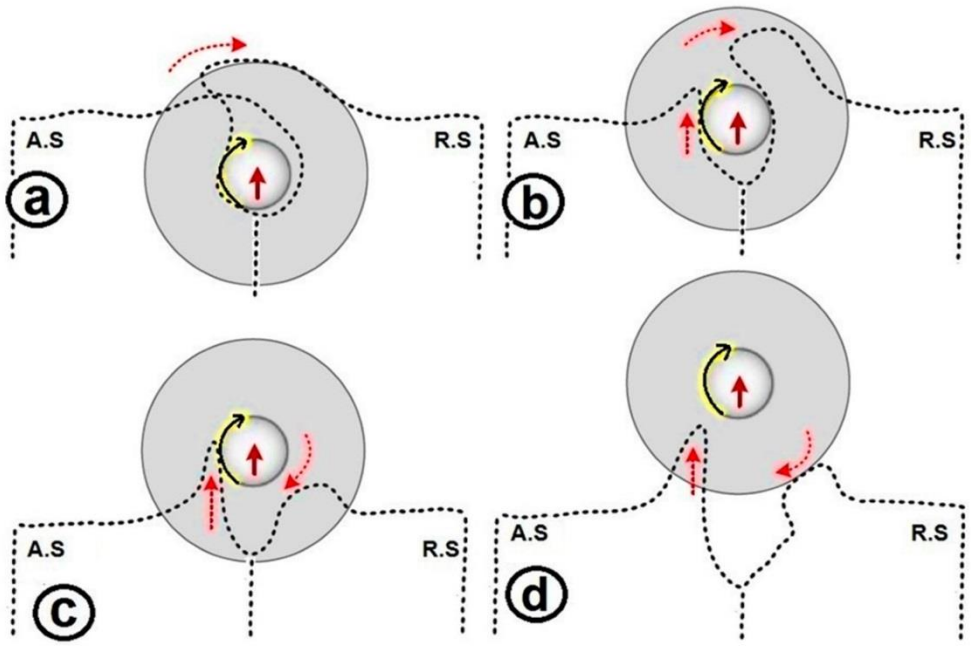

Figure 4.14. Schematic of the progression of material disruption in the exit zone.

4.4. Chapter Discussion

4.4.1. Outcomes

By experiment, it has been shown that plasticine analogue modelling of the BFSW joints can replicate the process and assist with explanation of the flow regimes at the entry and exit defects. Plasticine as a physical analogue can demonstrate reliable flow visualization for the plasticized material during the process [133, 135]. The similar formability behaviour of the plasticine to some metals makes it possible to be used for modelling of the shear flow patterns during the severe plastic deformation [29, 30]. A plasticine model with multi-coloured layers can reveal the actual flow patterns during the FSW process without needing to prepare and etch metal sections [73, 80, 113].

The flow visualization findings showed a disruption for the shear bands of the plastic deformation in the boundary layers around the pin. Consequently, the flow interruption can cause the entry and exit defects for the BFSW process. In particular, for the entry defect a change in frictional mode from sticking to slipping during the stirring between the RS and the AS can cause the escaping plastic flow from the joint position to the edge of the workpiece, this forms a sprayed tail. The tunnel void discontinuity appeared as a channel at the bottom surface of the weld on the AS. Although, further characteristics of this defect need to be investigated by observing the internal flow and making and examining cross-sections through the weld. At the exit zone, as the tool approaches the edge of the workpiece, the uniform circulation between the AS and the RS is disrupted. As the tool leaves the workpiece, a keyhole-shaped rupture is formed which is the exit defect.

It was found that defects of both the entry and exit zones are inherent features of the BFSW process. The weld trials for AA6082-T6 showed that an optimized speed ratio (ω/V) can minimize the size of these defects.

Limitations of the study

As delamination can cause misinterpretation of the flow failure patterns, it would be better if the layered sample had sufficient in-plane resistance to shear stress. This is mitigated by process control during the preparation of the plasticine sample, but this is not always perfectly achieved.

Other limitations relate to representation of heat flow and grain growth. Although plasticine is an amorphous solid it can stay solid after the forming process to duplicate the flow patterns. FSW is a thermo-mechanical process, but because of poor thermal properties of plasticine, study of the thermal history of the weld during the process would be difficult using plasticine analogue modelling. Also, due to the non-metallic and non-crystalline structure of plasticine, study of metallurgical transformation of weld structure, such as microstructure deformation and grain growth is not possible.

4.4.2. Implications for future research

This chapter was limited to the description of the visual observation of the surface flow features, but more detail can be learnt by examining the internal flow features of cross-sections through the weld. Future work may be directed to extracting cross sections from different locations of the weld zone. These may be useful for studying the material transport and consequently lead to a better understanding of the causes of weld defects.

Another possible line of future investigation could be to make use of analogue modelling to quickly evaluate different process parameters and tool geometry. This is because analogue modelling is faster and quicker than welding aluminium. Also, the cross sections are quick to obtain with analogue modelling, and the colours allow the flow to be immediately revealed, something which is not easily done with

aluminium– no combination of etchants can identify the origin of material seen in a cross section.

Another option for further research and flow visualization could be red, green and blue (RGB) colour analysis. This may model the origin of the interlaced materials and the different mass fractions [133].

4.5. Chapter Conclusions

BFSW of AA6082-T6 aluminium plate and corresponding plasticine analogue model were performed to evaluate the features of the entry and exit zones. By varying the rotating and longitudinal tool speed for both of the aluminium and analogue model welds, the entry defect and the exit defect could not be completely eliminated. However, using an optimum rotating and longitudinal tool speed the size of the entry defect can be reduced, although the size and the shape of the exit hole remained similar.

The material flow studies introduced two formation mechanisms for the entry defect and the exit defect. For the entry zone, as the bobbin tool enters into the workpiece from the free-edge of the butt-joint position, the material flow is disrupted from RS to AS. Consequently, the plasticized mass flow makes a spray zone outside of the workpiece at the RS position along with a discontinuity-line at the AS position of the weld-line.

Existence of the entry and exit defects on the analogue model of the plasticine, and/or in trials with the fully featured tools (threads, flats, scrolls) and in different welding parameters (ω, V) shows that these defects are permanent characteristics of the fixed bobbin-friction stir welding process for edge-entry.

Exiting of the fixed-bobbin tool from the weld line can cause a spontaneous disruption hole due to the lack of material ahead of the pin and dominance of shear flow patterns at the edge of the workpiece and the pin. Accordingly, the bobbin tool leaves the weld-line with a wishbone-shape, referred to as the exit defect.

The research demonstrates that with lowering of the rotating and longitudinal speed of the tool, the multi-layered plasticine analogue model allows visualisation of the plastic flow of the material. Also, it accurately replicates the localized disruption for the positions of the severe plastic deformations in the BFSW process.

CHAPTER 5: Anatomy of Bobbin Friction Stirred Weld; AA6082-T6 Aluminium Plate and Analogue Plasticine Model

Chapter Summary: Material flow transportation around the rotating tool and the mass deposition at the backside of the tool are critical characteristics of friction stir welding. To achieve an optimized weld structure, the history of the plastic deformation needs to be identified with a flow-based elucidation. In this chapter, an analogue model was applied to evaluate the formation of a banded structure using the bobbin tool, with a focus on the interaction between the tool-workpiece. The flow visualization in plasticine analogue was validated in comparison with the aluminium welds. The plastic flow mechanism was visualized both at the surface and cross-section of the weld-seam. The cross-section of the weld shows the details of the formation of tunnel voids, caused by the failure of flow regimes. A physical model of the material flow was proposed to explain the formation mechanism of the tunnel void as a discontinuity during the mass refilling at the rear of the tool.

This chapter is a derivative of the following publication:

Tamadon, A.; Ds, K.C.; Pons, D.; Sued, M.; Clucas, D.; Wong, E. Analogue modelling of bobbin tool friction stir welding. In Proceedings of the International Conference on Innovative Design and Manufacturing, Auckland, New Zealand, 14–16 September 2016.

5.1. INTRODUCTION

Bobbin-tool with a double-sided configuration is an innovative tool variant for friction stir welding (FSW), suitable for solid-phase joining of aluminium alloys [1, 2]. By modification of the FSW tool, bobbin friction stir welding (BFSW) has significant advantages to process butt-joint welds through the asymmetrical shape in cross-section [5, 66, 81]. The double rotating shoulders in bobbin-tool can generate more heat compared to the single-shoulder conventional-FSW (CFSW) tool with a stationary backing anvil acting as a heat sink [38]. This enables the BFSW process to weld different thickness of workpiece with a simple process setup, in a shorter processing time/speed [37, 38]. Recently, the significant potential of the BFSW has been applied for processing of high-strength aluminium alloys, e.g. 6xxx-series, which suffer from poor weldability [64, 66]. However, this is a new technique and producing excellent joints without the presence of defects requires extensive investigating to identify the optimum welding parameters [137, 138]. Since there is no solid theory about the details of the BFSW mechanism, this is also subject of recent research to identify the role of the process variables affecting the weld properties [137-139].

In general, there is an agreement that the tool components (top and bottom shoulders and centred pin) are responsible for the friction action and subsequent heat generation [28, 37, 136]. By advancing the rotating tool through the initial butting interface position, the continuous plastic deformation and mixing of the material flow regimes from both sides of the tool (advancing side and retreating side) forms solid-phase joining at the position of the stirring zone [15, 20, 27], Figure 5.1. The welding process parameters (rotational and transverse speeds) and the tool geometry (thread, flat, scroll) are mainly responsible heat input and formation of the stirred-based flow regimes, rather than plausible metallurgical procedures during the interaction between the tool and the workpiece [28]. However, the microstructural observation indicates the existence of some discontinuity defects (e.g. voids or crack) within the weld structure, which can severely deteriorate the mechanical properties of the weldment [34, 140].

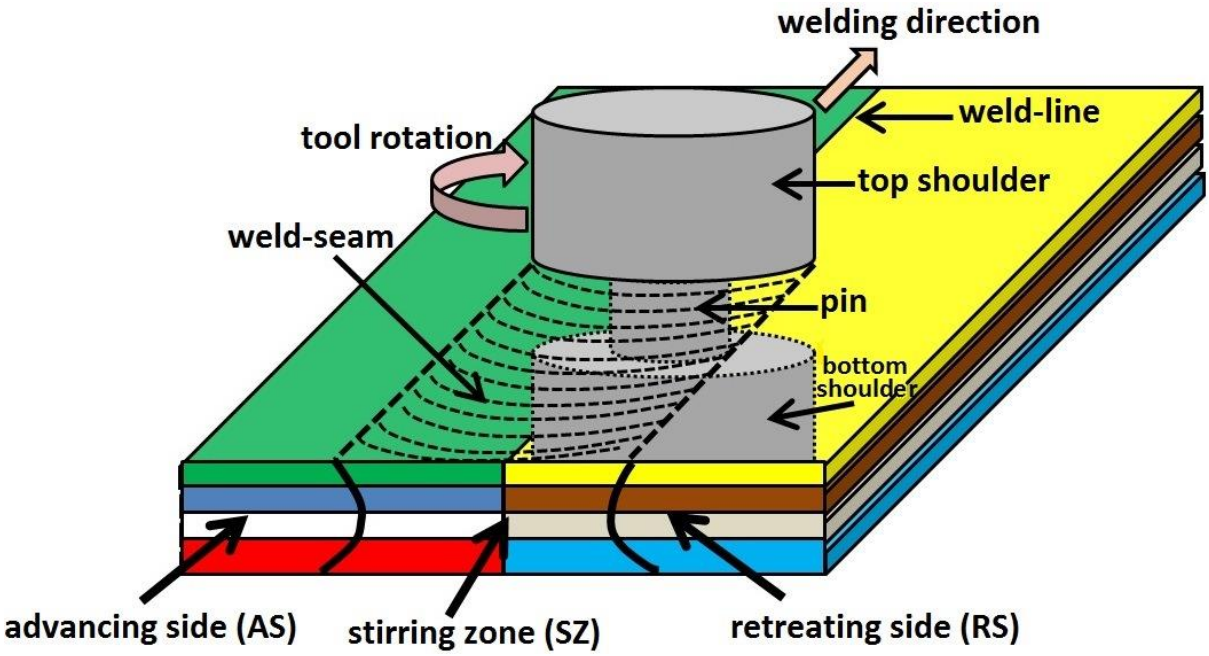

Figure 5.1. Schematic of the interaction between the bobbin tool and the substrate (multi-layered plasticine slab), with details of the weld structure.

These defects can emerge because of a limitation in the consistency of the welding parameters or inaccuracy in control of the operation setup. Thus, insufficient heat input, or poor engagement of the tool-substrate result in failure of the flow regimes during the stirring action [37, 38]. Subsequently, unsuitable interaction of the operating variables cannot provide the required homogeneity in plastic deformation, arising the physical defects within the structure of the welded joints [13].

Characterization of the flow-based details of the weld structure can indicate the quality of the weld in correlation to the welding variables [136, 138, 139]. In a general

flow mechanism in FSW, the formation of the joint requires a level of deformation and mixing of the material from both sides of the interface [137]. By considering the movement of the rotating tool, it is also essential to understand the actual nature of the material flow under the tool shoulders, transferring from the leading edge of the tool to the trailing edge around the pin [136]. This is a crucial aspect of the flow mechanism in FSW which is supposed to be responsible for the completeness of the stirring and deposition procedures to produce a sound weld [65].

Flow visualization can explain the plastic flow mechanism near the position of the tool. However, the demonstration of the actual flow pattern in the FSW process is difficult. The complex interaction between the rotating tool and the abutting base metal results in chaotic flow [141]. This can interrupt the identifying of the actual flow mechanism by misinterpretation of the banded shear structures in the form of plastic flow lines [142].

For the weld samples, the common etching technique is used to visualise flow mixing with suitable contrast [140]. However, visualizing the shear bands is dependent on the suitable response of the metal to the etchant reagent, which is difficult to achieve for some of the aluminium grades, e.g. 6xxx-series [140]. Physical problems in metallographic methods cause laborious time-delay costs in research. Therefore, the material flow visualization should be facilitated by alternative methods providing good contrast within the flow patterns.

Among various flow visualising techniques, the plasticine analogue has a suitable similarity to the etching results to produce a reliable physical model for the weld structure [138]. Plasticine analogue is an easily-prepared sample to be used for the visualization of the metal forming processes, for showing the detailed patterns of plastic deformation behaviour [137]. The contrast in coloured-layers of the plasticine can demonstrate the slip-lines patterns, representative of the shear bands in the flow fields of the material in the plasticity region [143]. Nevertheless, because of inherent differences with the metallic structure, the accuracy of the produced flow patterns in plasticine analogue needs to be validated by comparing with the actual weld samples [139].

This chapter studies the anatomy of the BFSW weld structure with a focus on the flow features responsible for the formation of the defects within the plasticized weld material in interaction with the bobbin-tool. The mixing behaviour of the material flow lines in the stirring zone is visualized by an innovative plasticizing flow model using plasticine analogue.

To identify the effect of the welding variables on the stirring flow behaviour, also validation of the plasticine analogue model, a set of AA6082-T6 welding trials were experimentally produced by the bobbin-tool. The metallographic observations reveal more details of the flow mechanism during the tool-substrate interaction. Based on the flow visualization, the authors propose a physical model for the formation of the

tunnel void, attributed to the flow-based origins of the weld failure arisen by the inconsistency in welding variables during the process.

5.2. MATERIALS AND METHODS

For both plasticine analogue tests and actual aluminium welds, a full-featured fixed-gap bobbin tool was used. The tool was made of H13 tool steel with two symmetrical scrolled shoulders at top and bottom and a tri-flat threaded pin in the middle. All these features were inscribed in a clockwise, as per the direction of rotation of the tool, to provide a better lateral mixing motion, avoiding material escaping or pin clogging during the stirring. Also, inwards circulation during the clockwise rotation of the tool pumps materials towards the centre and avoids mass spilling during the advancing movement. For a rigid engagement of the tool and the substrate, a compression ratio of 3.75% (the difference between the distance of the shoulders and the thickness of the workpiece plates) was used. This can induce a better shoulder forging effect, similar to the spindle forging axial force in CFSW, whereby restraining the stirred mass under the shoulder and protect the stirring process from the material ejection and emerging flash defect at the surface of the weld.

The BFSW process comparison was conducted on the welding workpiece of 6mm thick AA6082-T6 aluminium plates and multi-layered plasticine slabs of 10 mm thick. The multi-layered plasticine slab with thicknesses below 10 mm suffered from stable inconsistency during the stirring. Alternatively, to provide sufficient consolidation for the analogue slabs, an increase in the thickness of the plasticine samples was considered. Moreover, to guarantee enough material preservation, also preventing slumping under the shoulders, for analogue samples the working temperature was lower (0°C), compared to the aluminium plates (room temperature, 18°C).

To evaluate the flow features within the weld structure, a variety of speeds - rotational speed; ω (rpm) and advancing speed; V (mm/min)- were applied to produce different flow regimes based on the tool-substrate interaction.

For aluminium plates, after running trials, the set of speeds of V (300 and 400 mm/min) and ω (650, 800 and 1000 RPM) were performed to obtain the welds with no failure or material loss through the weld-line. However, although the speed sets were able to create a bonded weld, some partial defects were observed which can affect the weld quality. These defects are the subject to be studied by a comparative flow-based analogue model in plasticine samples.

Because of the considerably lower mechanical strength of plasticine compared to metal, the welding speeds set, rotational spindle speed (ω) and longitudinal feed rate (V), in analogue tests were much lower than the aluminium trials. The welding speeds in plasticine samples were chosen only enough to achieve a joint with the possibility of the flow visualization. Hence, the set of speeds for analogue plasticine samples was V (40 and 50 mm/min) and ω (50, 75 and 90 RPM), just above the

slowest available speed of the milling machine. Welding speeds higher than these, cause extensive defects and fast rupture in the plasticine samples.

To explain the welding condition, the substrate was laid flat in a butt-interface position, with no gap between at the joint line. The tool entered the plate from the locus of the butt-interface. With a view from behind of the tool, the centre of the tool is tangent to the intersection plane of the workpiece, while the shoulders are evenly in contact with the top and bottom surfaces of the plate. The tool rotation was clockwise from the top view, perpendicular to the locus. This means that the advancing side (AS) is situated on the left, and the retreating side (RS) is on the right of the tool , both in the surface plane and cross-section of the weld-line.

The plasticine weld tests were run using a manual milling machine (MX-45VAE Model, OKUMA brand, Nagoya, Japan). The aluminium weld trials were performed on a 3-axis CNC machining centre (2000 Richmond VMC Model, 600 Group brand, Sydney, Australia) with a 14-horsepower spindle motor capacity. Figure 5.2 shows the operational details of the BFSW process for the plasticine analogue. For both sets of samples, the bobbin tool had a clockwise rotation corresponding to the welding direction. To ensure no lateral movement during the BFSW process, the samples were rigidly fixed by the clamp bars in the fixture, with no gaps between the AS and RS workpieces.

After performing a 150mm single-pass weld-line, samples were cross-sectioned perpendicular to the welding direction to produce the specimens for the metallographic analysis and flow visualization.

The flow patterns in plasticine analogue samples were observed by a high-resolution bridge digital camera (FinePix S9500 Model, Fujifilm brand, Tokyo, Japan). The digital photographs were recorded under a fluorescent lamp to avoid any shadows in pictures.

The AA6082-T6 weld cross-sections were ground and polished by a standard mechanical polishing to obtain a mirror surface with roughness below 1μm. To show the metallographic details of the weld, the cross-section specimens were then etched by a reagent solution with the chemical composition of (0.5 g $(NH_4)2MoO_4$ + 3.0 g NH_4Cl + 1 mL HF + 18 mL HNO_3 + 80 mL H_2O). The etching was done by direct immersion of the surface samples in an ultrasonic bath for 90 s, at 70 °C. After washing the samples and drying under hot air, the cross-section of the aluminium welds was observed by a stereo microscope to show the material flow details.

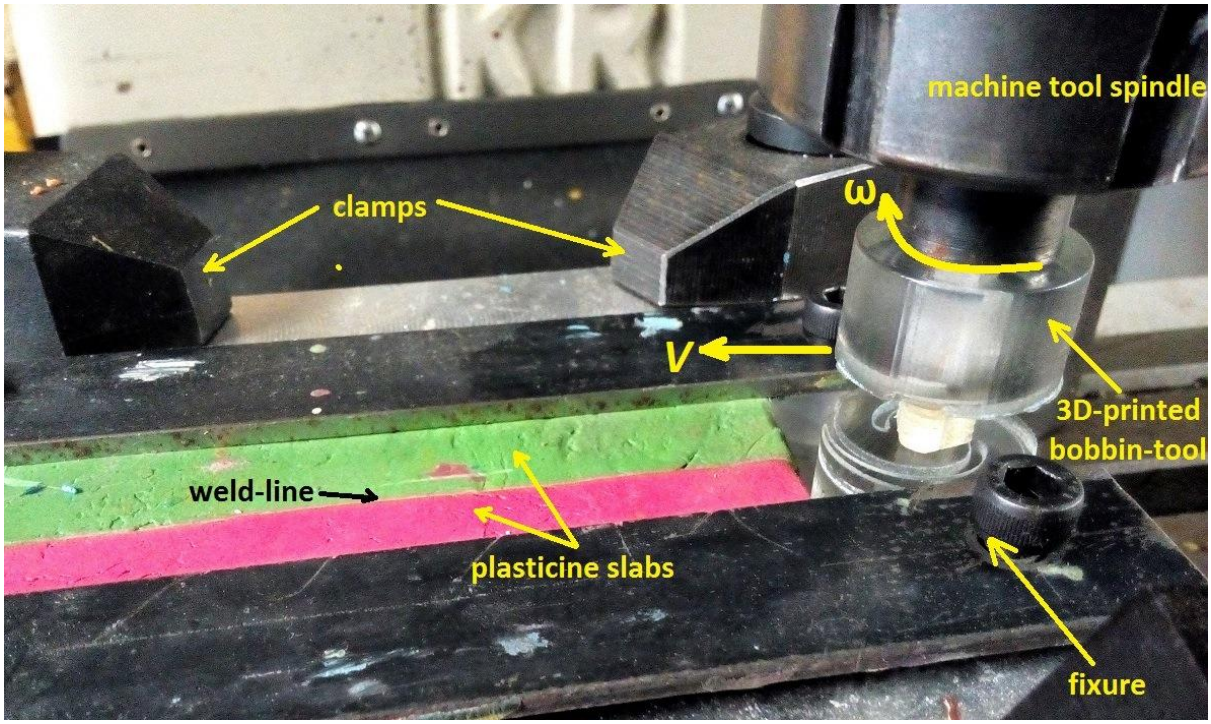

Figure 5.2. The operational details of the BFSW process for the plasticine analogue.

5.3. RESULTS

5.3.1. Similarities in Entry geometry

The plasticine sheets were subject to bobbin friction stir welding (BFSW), and the produced identical structural anatomy to aluminium, where similar features were observed, regarding the size and shape of the patterns, see Figures 5.3 and 5.4. For the beginning of the weld, these include the entry spray on the retreating side (RS) and a remained channelled discontinuity on the advancing side (AS), representative of the tunnel void. Note the relative sizes of these two sprays in analogue and aluminium welds are approximately the same. As the clockwise-rotating tool enters the substrate, it ejects material into the air at its rear and onto the retreating side. Hence the large spray at the entry location protruded to the RS. A smaller amount of material is picked up by the tool and transferred to the advancing side (see Figure 5.4). Note also the similarity of the surface patterns. This is characterized by a shredded appearance, which is attributed to the threads and flats on the tool. Also, the face is concave. These features are the same in both materials. Likewise the tunnel defect, both its location (underside), laterally deflected to the advancing side, and its granular internal surface is the same.

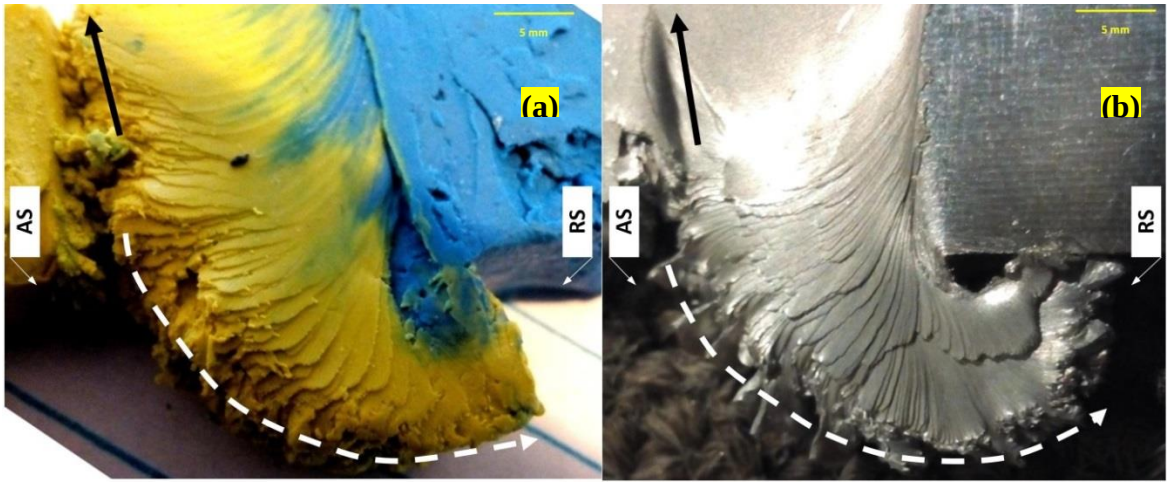

Figure 5.3. Macroscopic structural features of entry-zone sprayed tail, produced via bobbin friction stir welding, (a) plasticine (50 rpm, 50 mm/min) and (b) aluminium 6082-T6 (650 rpm, 400 mm/min), in both cases Figure 5.3 shows the top-view.

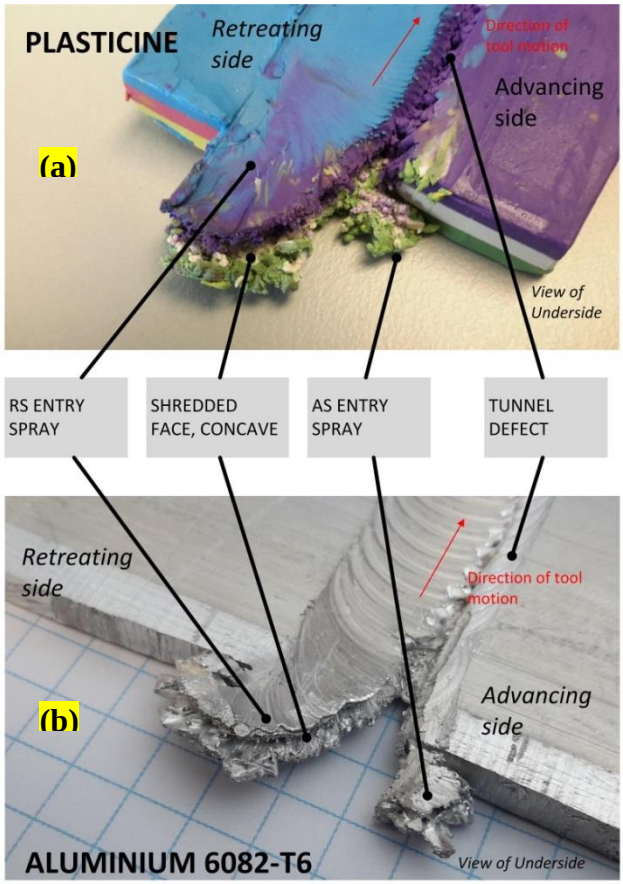

Figure 5.4. Macroscopic structural features of bobbin friction stir welding, (a) plasticine (75 rpm, 50 mm/min) and (b) aluminium 6082-T6 (650 rpm, 400 mm/min), in both cases rotation is clockwise viewed from above, though this view is from below. Figure 5.4 shows the common features. (Figure 5.4 is an adaptation of Figure 4.6(b).

It is concluded that the plasticine faithfully represents the structural anatomy of BFSW in aluminium. The analogue methodology, therefore, has the potential to explore flow behaviours in BFSW. The capability of the plasticine analogue in producing of the geometric features of the BFSW weld makes it a suitable candidate to be used for analogue modelling of the BFSW. Regarding the production of the flow pattern, it also has good potential to produce the identical analogue model of the internal features, which will be shown in the following.

5.3.2. Weld surface under the shoulder

To understand the flow mechanism induced by the shoulder, the weld surface can be the initial place for observations. The overall surface flow at the surface field pitch is demonstrated for aluminium and plasticine model in Figure 5.5.

The typical surface appearance of the FSW weld is a periodic pattern of the circular ripples, pitched towards the initial starting position of the tool rotation. These surface weld pitches are a direct outcome of the shoulder action at the surface of the workpiece, formed by the material deposition at the rear circumferential of the shoulder (trailing edge of the tool). By the advancement of the tool, the stirred massed at the leading edge of the tool undergoes traverse transportation between the AS and RS of the weld section.

The combined relative motion of the tool (rotating and advancing) is responsible for this ripple pattern by a successive revolution and overlapping between the deposited pitch layers. The thickness of the pitch layers is depended on the speed ratio of the FSW tool, (ω/V or RPM/mm), which is defined as the revolution per distance.

To understand the overall planar flow, a comparison between the aluminium weld surface and the analogous plasticine sample are shown in Figure 5.5.

For both samples, the effect of the shoulder action on the weld surface is experienced by a relative effect of the speed ratio (distance/rev). The surface flow visualization shows a flow patch pattern at the RS edge of the weld. The interpretation attributes this feature to the lateral revolution of the tool after deposition of the mass layers at the trailing edge, with a simultaneous forward movement which induces an opposite flow between the direction of V and ω at the rear edge of the shoulder. The formation mechanism of this flow patch patterns (later called as “surface pitch ripples”) is elucidated in Figures 5.6 a,b which an aluminium weld sample with intensified flow patch patterns at the RS is compared with the colour-layered plasticine model. The plasticine analogue reveals the plan view of the top surface (horizontal section), cut in the vertical depth of 1 mm. Both samples experienced similar flow patterns at the RS vicinity of the shoulder. Figures 5.6c reveal the turbulent flow caused by inconsistent tool parameters, whereby induces a flow with disordering in size and distance of the successive flow patches. As it is shown in

Figure 5.6d, by continuing of the flow tribulation, the increase in the size of these flow patches causes a strain field for the material in stirring zone, where can form a tunnel defect discontinuity in the stirring zone (SZ) towards the AS. The helical flow distribution during the material mixing can provoke a macro-scale discontinuity defect in the weld. The horizontal section shows the bending shape of the material flow patterns, was affected by the circumferential velocity at the trailing edge of the shoulder. While the clockwise rotating tool moves forward, it causes a bending direction for the backward accumulated layers by a transverse extruding towards the advancing side. For a better understanding of the shoulder-tool flow interaction, the flow visualization should be shown in more depth from the weld surface, by observation of the weld cross-sections.

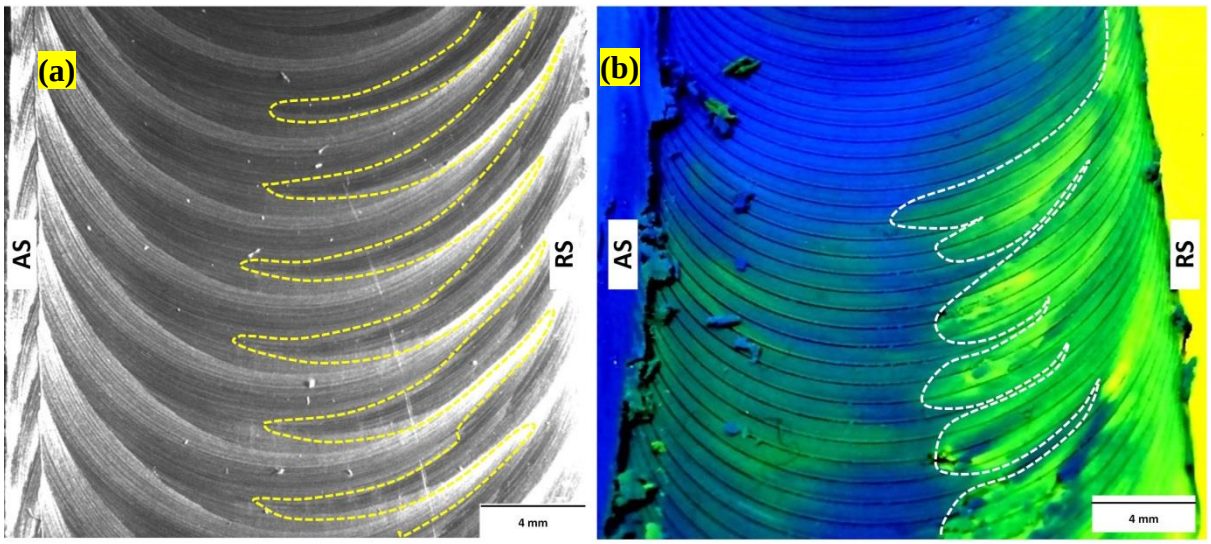

Figure 5.5. Surface flow patterns of the BFSW weld samples; (a) aluminium 6082-T6 (650 rpm, 400 mm/min), and (b) plasticine (50 rpm, 50 mm/min), in both cases Figure 5.5 shows the top-view.

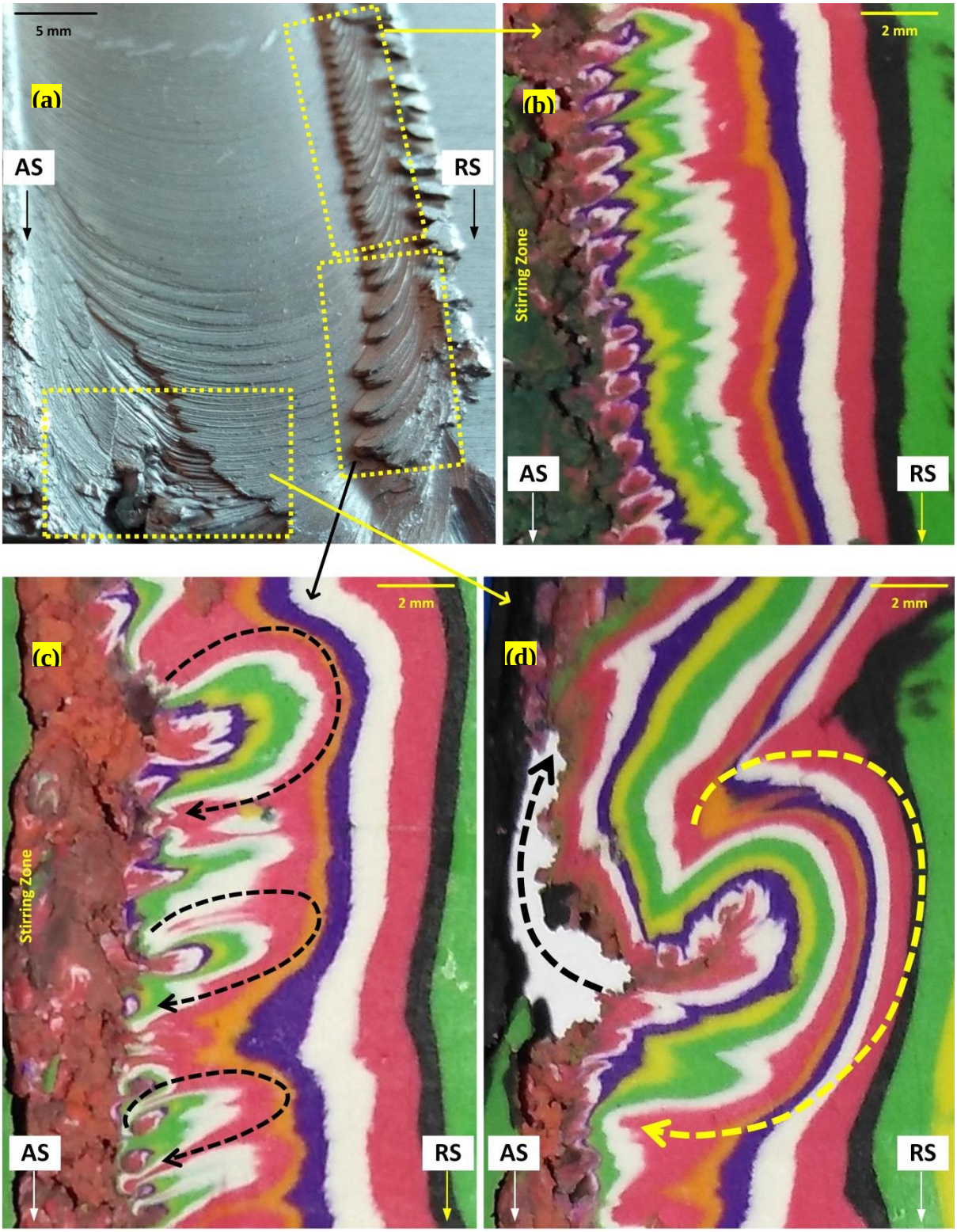

Figure 5.6. Surface flow patterns of the BFSW weld samples on plasticine (50 rpm, 50 mm/min) and aluminium 6082-T6 (650 rpm, 400 mm/min), in both cases Figure 5.6 shows the top-view.

5.3.3. Cross sections

Macroscopic features across the weld as a whole

To observe a better contrast for the internal material flow features within the cross-section of the weld, the analogue plasticine samples with a multi-colour layered structure were used, compared to the aluminium single thickness welds. The differencing of the flow patterns through the weld cross-section can reveal the material transportation mechanism between the AS and the RS during the stirring action. Even though, this analogue model has a potential to be used for flow modelling of the laminate materials. Figure 5.7 shows the comparison of the internal flow features within the transverse sections of the plasticine analogue and aluminium weld samples. The samples were cross-sectioned perpendicular to the welding advancement direction.

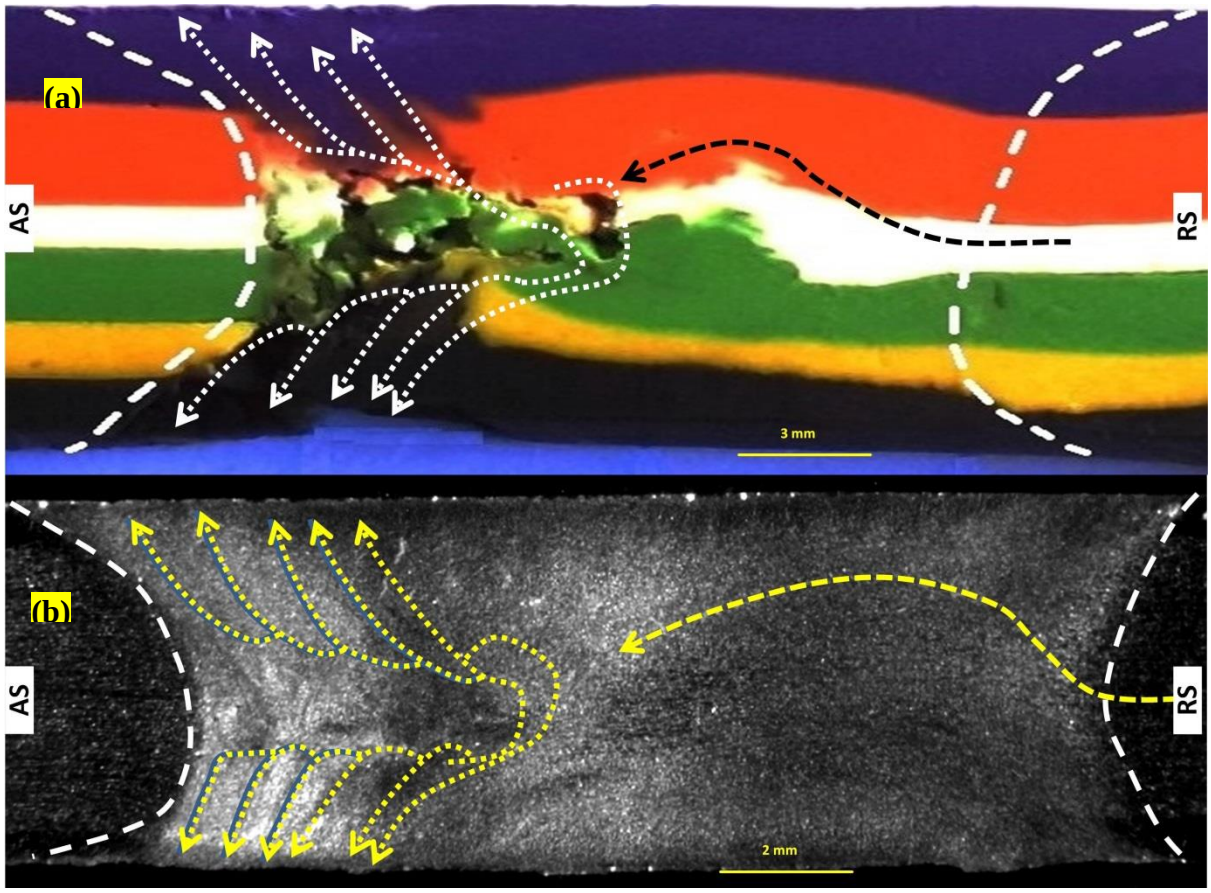

Figure 5.7. Cross-section of the BFSW weld, (a) plasticine sample (50 rpm, 50 mm/min) and (b) aluminium weld (650 rpm, 400 mm/min).

As a general characteristic of the weld flow, there is a common characteristic as the flow layers are bending into advancing side border compared to the retreating side. Consequently, the mixing of the material in a deeper region of the cross-section is wider for the AS rather than RS. This can be due to the stronger shearing action in the AS proximity of the rotating tool. This makes it slightly harder to assure the

uniformity of the mass flow at the AS, where the tunnel void forms in the form of the flow discontinuity (Figure 5.7a).

Another interesting flow feature which can be visualized by the analogue model is the sub-shoulder flow pattern with an independent flow behaviour compared to the deeper region affected by the pin performance. Although some flow features are visible in Figure 5.7a, it would probably be more apparent at higher welding speeds, where the flow dispersion can be more visible by the intensified shearing.

The material flow around the pin can be better observed at elevated speeds, both feed and rotation. By elevating of the speed the distributed, area of the circumferential flow around the tool increased. However, faster rotation of the pin causes more slip between the mixing layers of the stirring mass. During the mass transportation, the improper flow regimes can be distinguished at the higher speeds, where it results in the formation of the discontinuity defects (e.g. tunnel void). In Figure 5.8, the tunnel defect is observed in the middle part of the cross-section, for both analogue plasticine and aluminium weld. Insufficient material mixing limits the integrity of flow during the mass transportation behind the tool. Therefore, the slip condition during the flow deposition interrupts the integrity of the layers and forms a tunnel void discontinuity. In this situation, the downward flow is less, causing more refilling failure problems at the bottom part of the cross-section. Combined shearing of the material flow at the sub-shoulder regions induces a continuous vortex-like flow which is affected by the pin motion at the lower parts near the mid-SZ. By the simultaneous rotational and advancing movement of the pin, this vortex-like flow pushes the material to the leading edge of the tool in AS and pulls the mass from the RS into the trailing edge of the tool. Because of the similar direction of the rotation and advancing movement of the tool in AS, the multi-circulation of the mass around the tool causes a periodically repeated transformation pattern, observable as a blipped-shape pattern at the AS. This is similar to the onion rings pattern at the conventional-FSW weld structure.

Figures 5.9-5.11 compare the weld cross-sections for different welding speeds (ω, V). Also, using the bi-colour plasticine slabs, the tool-driven flow patterns at the sub-shoulder region are revealed by a better contrast, compared to the aluminium weld samples. The macroscopically mixed region situated between the AS and RS distinguishes the flow features of the stirring zone in a large-scale for different welding conditions. In all the stirring condition, it is noticeable that the flow-arm features across the weld are originated from the AS near the sub-shoulder area. However, by continuing the mixing towards the RS, it indicates that the interface at the mid-SZ has been slightly changed. It can be observed at the butt-interface from top to downward, the material flow penetrated from the AS into RS. This flow behaviour is also observable in the aluminium welds. Moreover, the existence of an unwelded region near the bottom surface of the workpiece is representative of an inconsistency in flow mixing regarding the bottom shoulder. It is unlikely, that the

colour mixing in the sub-shoulder region near the top surface of the workpiece verifies the sufficiency of the flow mixing induced by the pin and top shoulder.

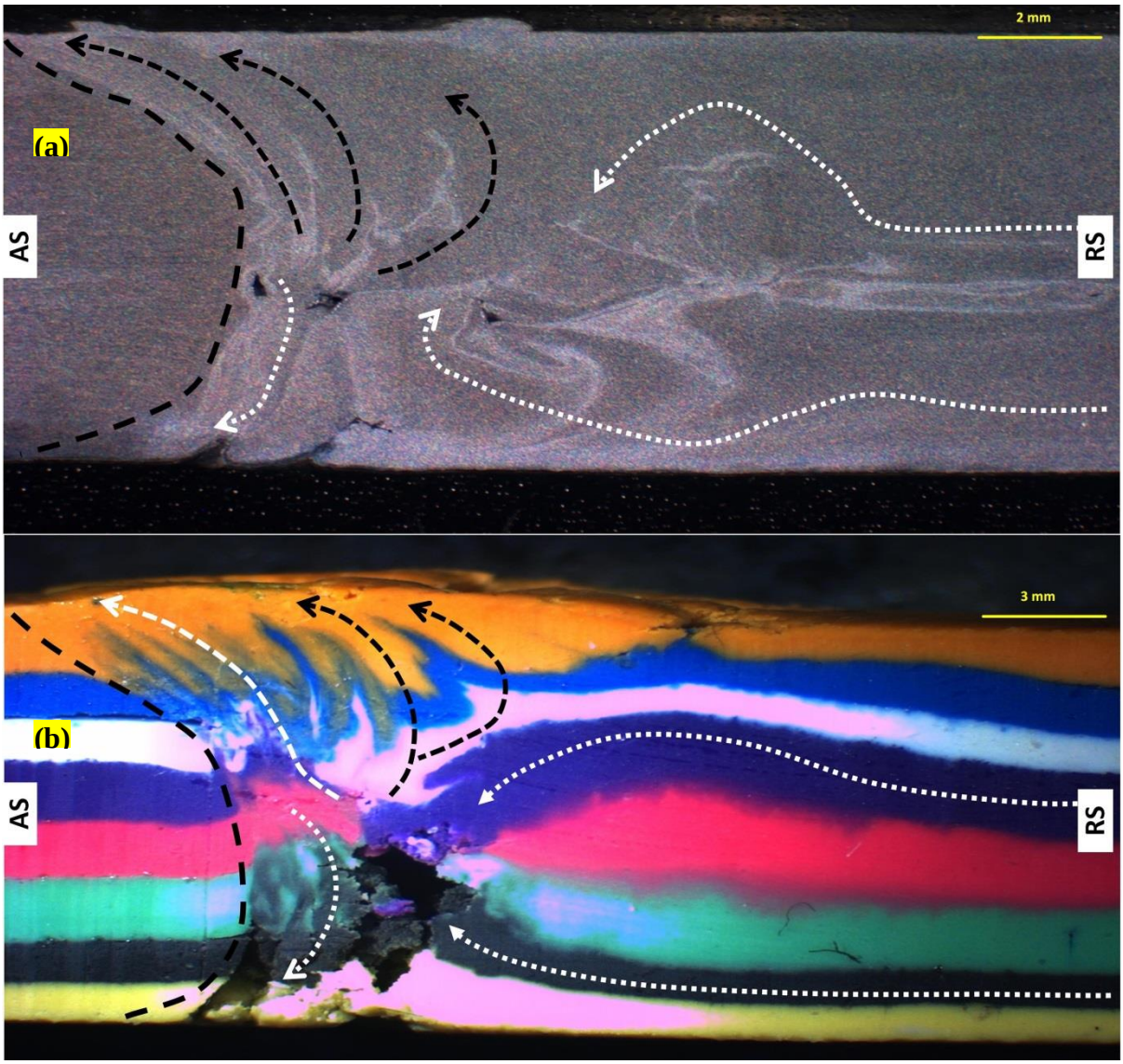

Figure 5.8. Blipped-shape pattern at the mid-thickness pattern, pulled upward and downward, repeated along AS-to-RS, which can be shear layers around the pin, elongated to top and bottom shoulders. (a) aluminium sample, (b) plasticine analogue.

Figure 5.9 (for the plasticine analogue) shows a mixing region underneath the top shoulder, which is consistent with the aluminium weld. Similar to this flow feature, a narrow mixed area also is observed near the bottom shoulder. It can be explained that the difference in the performance of the top and bottom shoulder is probably responsible for the movement of the flow interface compared to the primary position of the butt-interface. By consideration of this different performance, the further action of the tool, specifically in higher speeds, can cause an unsuitable flow

mechanism around the pin, which results in discontinuity within the SZ mixing region. Regarding the welding speeds, it should be noted that the elevated RPM has a more significant role in stirring action, compared to the travelling speed. Hence, the material around the rotating pin and underneath the shoulders undergoes multi-circulation while travelling forward. This increases the mixing rate during the stirring. In this condition, if the feed rate during the forward motion does not properly support the flow around the pin, the integrity of the flow lines can be deteriorated by emergence of the discontinuity between the stirred layers of the mass.

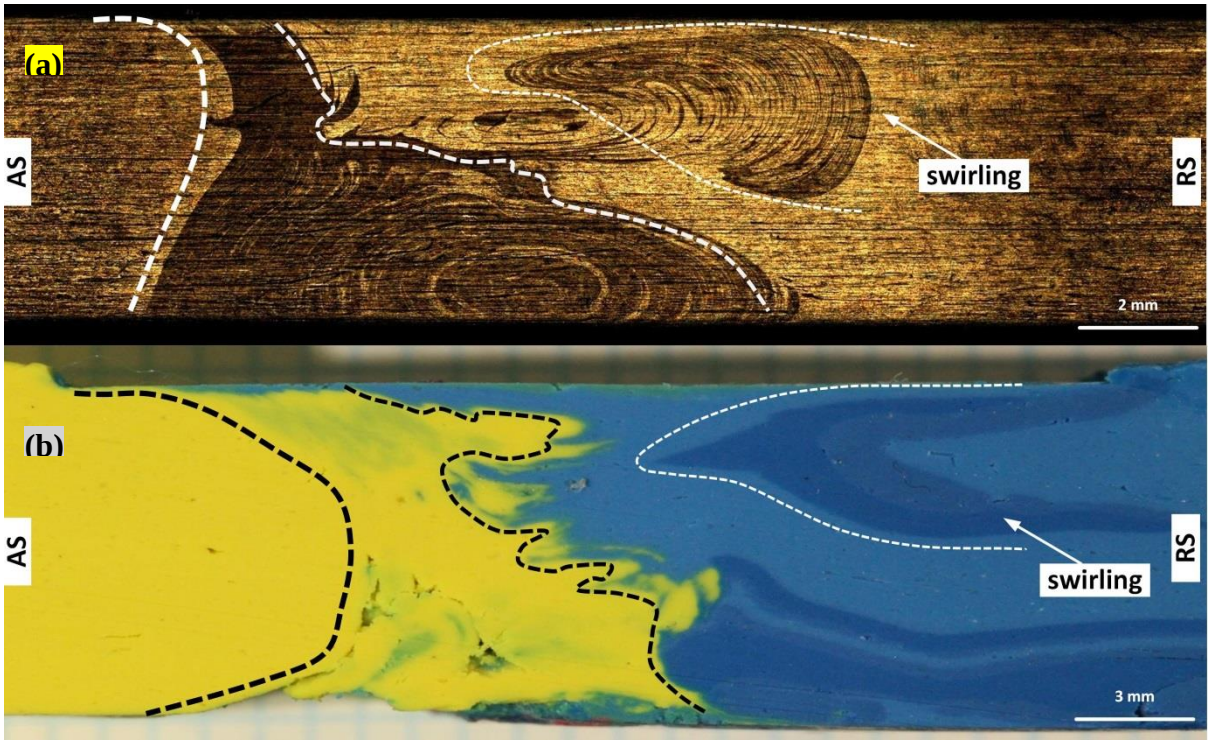

Figure 5.9. Blipped-shape pattern at the mid-thickness pattern, pulled upward and downward, repeated along AS-to-RS, which can be shear layers around the pin, elongated to top and bottom shoulders. (a) aluminium weld, (b) plasticine analogue.

The increase of the rotational speed can increase the influence of the shoulders in inducing of the frictional flow. This can lead to a large-scale mixing effect in the sub-shoulder region at the top and bottom face of the workpiece. By applying a suitable value of the compression ratio, the flow will be prevented from ejection and formation of the flash defect. Alternatively, the internal flow can be transmitted from the sub-shoulder region into the central area of the SZ, with an elliptical mixing pattern (Figure 5.10). This feature can be also attributed to the onion ring pattern observable in the CFSW welds. The interpretation is that at the higher rotational speeds, the sub-shoulder regions induce more flow into the SZ, and the pin circulates the stirred mass several times by a lateral motion. Subsequently, the flow

pattern at the mid-SZ can form an ellipse pattern elongated from the AS towards the RS, corresponding to the clockwise rotation of the tool.

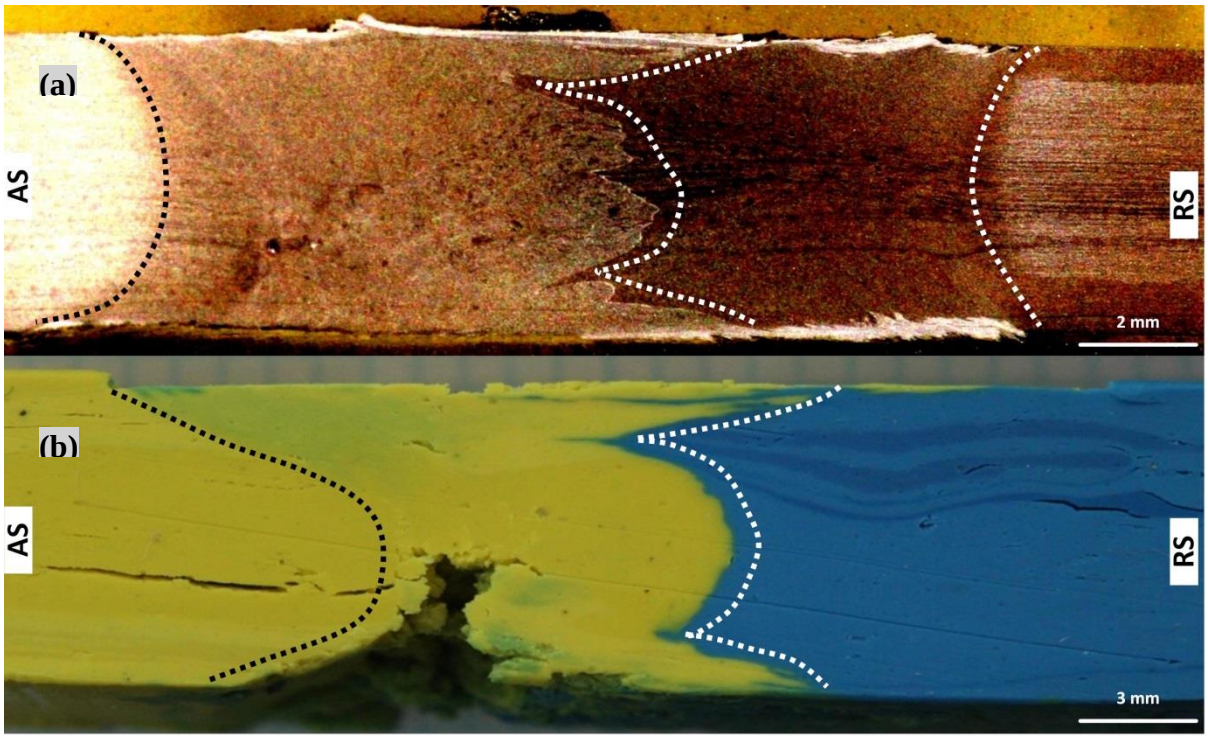

Figure 5.10. Elliptical mixed pattern at the mid-thickness pattern, pulled upward and downward, repeated along AS-to-RS, for both aluminium and plasticine samples.

There is a thin surface layer that is smeared over the top and bottom surfaces. The plasticine identifies that this is an approximately equal mix of material from the advancing and retreating sides. This is most evident in Figure 5.11. This is consistent with the wide-accepted function of the shoulder. There is a deeper mixing under the shoulder, which appears on the AS, upper region only. This comprises multiple jagged flow arms. The plasticine shows this comprises layered fragments of the AS material (upper layer). What is interesting in Figure 5.11b is the narrowness of these flow-arm layers which shows the preciseness of the analogue model in the visualization of the partitioned flow behaviour at the sub-shoulder region of the stirring zone.

In Figure 5.11, the sub-shoulder flow patterns have been visualized through the cross-section of the weld. As it was suggested in Figure 5.8, the stirring action of the pin in the sub-shoulder region has an effective role in the formation of the flow bands. By the rotation of the tool, the flow patches of the stirred mass are formed at the interface of the threads-flats and entered into the stirring flow between the AS and RS. The simultaneous rotation and advancement of the tool lead to deposition of

the mass at the trailing edge of the pin, this is where the shoulder-driven flow plays the main role in direction and deposition of the stirred mass by the ejection from the tool position and adding it into the periodic deposited layers at the weld-line. This is where the flow-arm patterns form underneath the shoulder. A remaining question is about the actual visualization of the flow arms. The proposed interpretation is that the actual direction of the flow arms is parallel to the cross-section plane where the mass flow is transported between the RS towards the RS at the trailing edge of the tool. Different cross-sectioning of the weld samples parallel to the weld-line direction might be useful to find more details of the flow lines.

Finding: Mixing under the shoulder

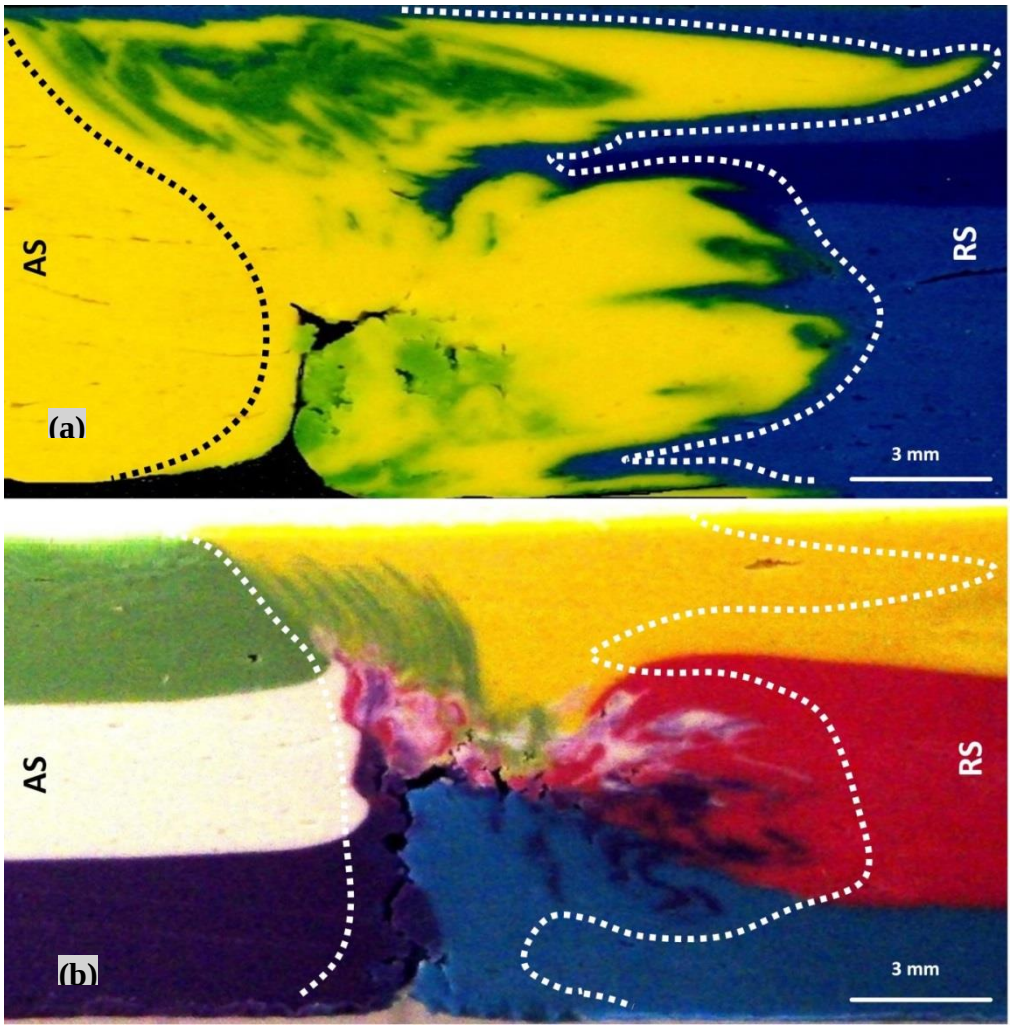

Figure 5.11. Mixing flow lines under the shoulder. Blipped-shape pattern at the mid-thickness pattern, pulled upward and downward, repeated along AS-to-RS, which can be shear layers around the pin, elongated to top and bottom shoulders.

The clockwise direction of the tool rotation causes an asymmetric material flow circulation through the stirring zone. This causes the plastic flow to be dispersed

through different directions at the proximity of the tool, where the mass layers undergo different levels of deformation and intermixing. During the tool-workpiece interaction, the portion of the plasticized mass is transported in a circulating pathway around the tool, from the leading edge undergoes a chaotic flow and is squeezed to the trailing edge where it is deposited in the weld-seam. At the trailing edge, the flow packets are dispersed into the RS layers to migrate across the centre-line of the weld section, to settle at the AS hourglass-border. However, by approaching the centre-line, the RS flow layers are deflected and mostly cannot complete the refilling circulation to be deposited at the AS border wall. This is where the flow discontinuity is most likely to occur.

5.3. Chapter Discussion

The analogue model showed the tool performance causing a variety of the flow patterns inconsistency during the stirring action, which can be critical to the emergence and propagation of flow-based discontinuity defects through the structure of the weld. The intercalated regimes or vortex-like flow structures were illustrated in different positions of the SZ which are extraordinary solid-state features in the plastic region of the BFSW welds. The intercalated flow lines with the multi-colour layers of the analogue plasticine can develop the perception about the plastic flow mechanism in BFSW as a solid-state joining process. The plastic deformation pattern shows a turbulent flow around the tunnel void defect which is elongated from the surface and pulled up towards the centre of the stirring zone. The cascading shape of the plastic flow arms at the hourglass-border can be attributed to the shear stress field introduced by the pin and intensified at the sub-shoulder region. The jagged features in the tunnel defect are attributed to shear bands emerged by the failure of the material flow.

Furthermore, it should be noted that the flow failure during the continuous revolution of the tool can interrupt the homogeneity of the periodic deposition of the layers at the trailing edge of the tool. This can cause an un-bonded condition between the deposited layers and leads to emergence of the flow-based discontinuity defects. This has been shown in Figure 5.12 for the macro-etched cross-sections of the weld, for the similar welding conditions with and without emergence of the defect. As it is shown for the advancing side of the weld cross-section, the defect-free weld (Figure 5.12b) possesses uniform flow lines dispersed from the weld centre (at the position of the tool) towards the AS border. Because of the forging effect of the rotating shoulders, the flow lines are directed towards the top and bottom shoulders. This is required to form a bent-shaped hourglass border at the boundaries of the stirring zone. In Figure 5.12a, the failure of the flow regimes leads to dispersion of the flow lines from the centre of the weld towards the AS border. Therefore, the un-bonded layers of the deposited mass form the open tunnel void. Tunnel defect is representative of the continuous discontinuity at the bottom side of the AS weld

region. There is no solid theory regarding the flow-based mechanism of the tunnel void formation, as some interpretation provided in this chapter. However, it needs to be investigated in a more advanced level to recognize the origination of the defect to prevent it to form in the body of the weld. It seems that a defect-free joint can be achieved by optimizing the rotating speed, longitudinal speed and the compression ratio.

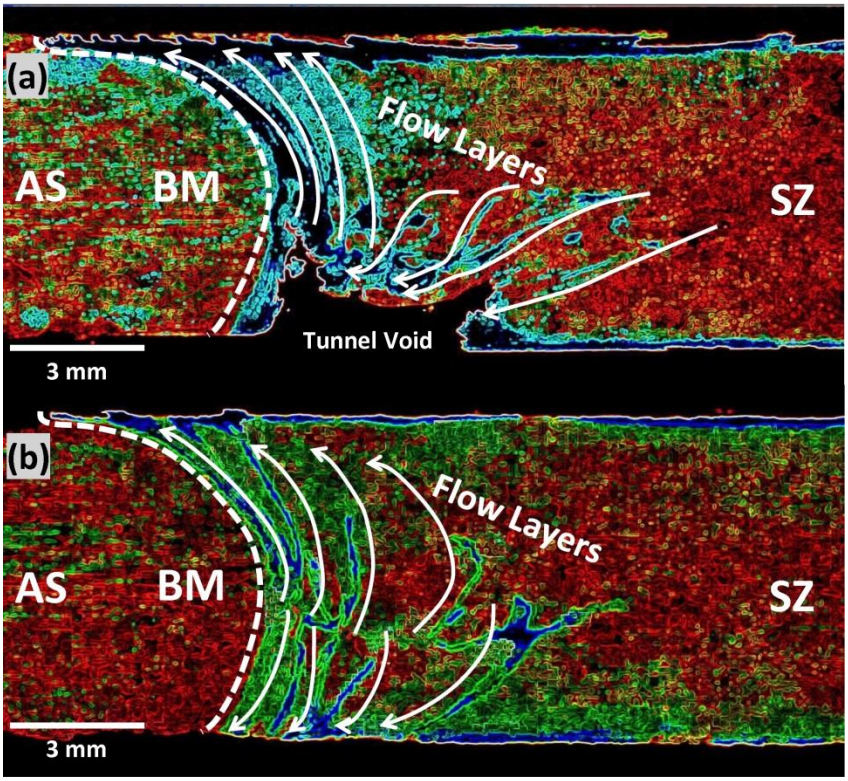

Figure 5.12. . The proposed flow patterns at the AS location of the stirring zone, drawn at the weld cross-section (etched and observed under polarized illumination); (**a**) in presence of the tunnel void (w = 400 rpm, 350 mm/min), and (**b**) for a defect-free sample (w = 650 rpm, 400 mm/min).

Figure 5.13 shows a physical model for the occurrence of the tunnel void, based on the flow-based approach applied in analogue modelling. The picture of the actual void at the beginning of the formation at the entry zone of the weldment is shown in Figure 5.13a. It suggests that the flow lines during the transportation from the RS to AS and deposition at the trailing edge of the tool, deviate by the sub-shoulder flow effect. This stretches the flow lines upwards and downwards of the cross-section. The inconsistency of flow deposition can easily deteriorate the integrity of the refilling of the stirred layers and cause an un-bonded discontinuity at the end of the flow path lines in AS border.

Figure 5.13b provides a general schematic of the flow regimes at the stirring zone of the BFSW process, where the flow patches at the proximity of the pin begin to form the plasticized mass until finally are deposited at the back of the tool and form an hourglass-shaped stirred zone at the cross-section of the weld.

Based on the visualisation of the flow layers at the cross-section of the weld, it suggests that the reduced integrity and the consolidation of mass flow line during the transportation can lead to dispersion of the flow lines and cause a discontinuity in the form of the tunnel void at the AS position of the weld, where the stirred plasticized mass is directed to be deposited there. The further analysis of the tunnel void position is necessary to reveal the nature of the formation of this flow-based discontinuity at the weld structure. However, the suggested flow-based model suggests that the failure in the integrity of the mass transportation during the refilling mechanism between RS-to-AS at the trailing edge of the tool play a key role in the formation of the tunnel void.

The tunnel defect occurs at the AS because this is the last region for the deposition of material at the trailing edge of the tool. The tunnel occurs at the bottom because the threads on the pin pump the flow upwards. The tunnel is further intensified by the loss of material from the cross-section, where this loss primarily occurs at edge entry.

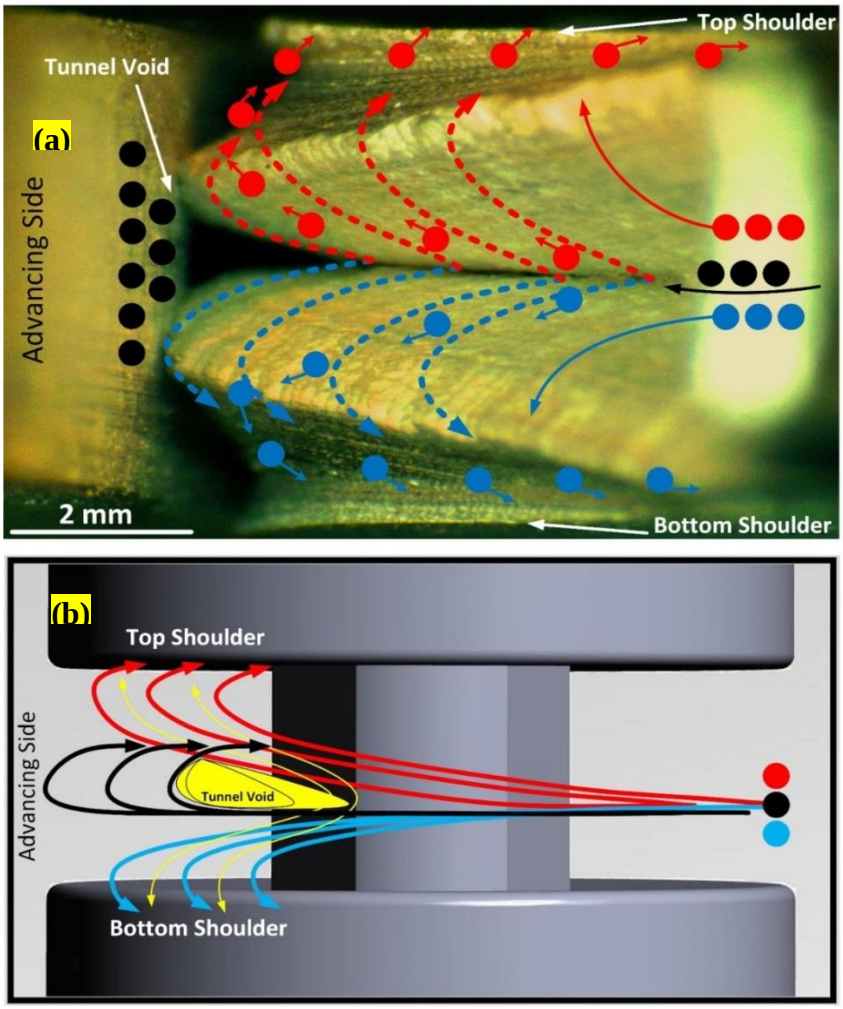

Figure 5.13. The proposed flow model for the formation of the tunnel void at the AS location of the stirring zone. (a) physical model at the position of the tunnel void, (2) schematic of the proposed model for the formation of the tunnel void within the flow lines around the rotating in.

5.4. Chapter Conclusions

The flow behaviour during bobbin friction stir welding was visualized using the plasticine analogue supplemented with the aluminium welds. The weld tests demonstrated the surface and internal flow features obtained from the interaction between the rotating tool and the substrate. The flow visualization detected the origins of the discontinuity defect between the layers of the stirred mass, deposited at the rear of the tool. The transverse transportation of the plastic flow, between the retreating and advancing sides, creates the mass refilling mechanism as the result of the stirring action. The flow failure around the pin can deviate the mass refilling, causing the occurrence of the tunnel void discontinuity. A flow-based model was proposed to elucidate the formation mechanism of the tunnel void at the trailing edge of the tool near the advancing side of the weld seam.

CHAPTER 6: Structural Anatomy of Tunnel Void Defect in Bobbin Friction Stir Welding, Implemented by the Analogue Modelling

Chapter Summary: The potential position for defects in the structure of Bobbin-Tool Friction Stir Welds was studied by analogue modelling. The welding process was simulated on layered plasticine slabs instead of metal plates. Observations in the modelled structure show a high possibility for a continuous channel void like a tunnel-shaped defect in the entry zone of the weld, which mirrors metal welding. The anatomy of tunnel defect in the entry zone is explained according to the mechanics of material during the plastic deformation process.

This chapter is a derivative of the following publication:

Sued, M.; Tamadon, A.; Pons, D. Material flow visualization in bobbin friction stir welding by analogue model. In Proceedings of the Mechanical Engineering Research Day 2017, Melaka, Malaysia, 30 March 2017; Volume 2017, pp. 1–2.

6.1. Introduction

Friction stir welding (FSW) is a solid-state joining method whereby instead of melting the material, a rotating tool ploughs through the interface of the two plates to be joined. The bonded structure is obtained by mixing the material, softened by heat and stirring, generated from friction between the rotating tool and the workpiece [3]. There is a class of FSW tools called bobbin tools [4, 64, 66], consisting of two shoulders, one on each side of the workpiece surfaces, connected by the tool pin (Figure 6.1). Recent welding trials using this symmetric tool configuration (comprises two shoulders connected by an axial pin) have highlighted some of the benefits for a fast and less complicated process, compared to the conventional FSW [5].

One of the critical problems in bobbin friction stir welding (BFSW) is to provide an applicable instrument for optimization of the joining parameters and their side-effects on final quality of the weld [81]. This situation is crucial for bobbin-tool technique as the process settings are still in the early stages of study.

The general area of interest for the BFSW process is welding of light-alloys sheets, where there are many applications for this in marine, automotive, and aerospace fabrication processes [20, 83, 86]. Since, existence of defects can directly affect weld properties, making a reliable weld by the FSW process, in different situations and

with different parameters, is difficult. Existence of a void as a defect is one of the challenges of work during bobbin-tool FSW process [136, 139]. The objective of this chapter is to elucidate the origins of the formation mechanism of a typical tunnel void in the weld region. Identification of the influential phenomena in the creation of a void is required in developing a multi-physics model, based on the principles of fluid mechanics.

Bobbin-tool FSW appears to be a thermo-mechanical process as the frictional heat combined with the high plastic deformation is used for the joining process during the rotation and movement of the bobbin tool [141, 142, 144]. Also, changing the parameters of the process (e.g. feeding rate and rotational speed), or features of the bobbin tool (size and geometry of pin and shoulder), or the thickness and material properties of the weld plates may lead to unknown origin defects in the weld region [136, 139]. In other words, there is no solid theory about the parameters of the process and method of control to achieve the optimum machine settings. Developing a comprehensive theory describing the process will extend the range of applicable process parameters and overall productivity. Thus, a transition from trial and error to a science-based approach is required to link the welding mechanism and operational variables.

For the first step in the investigation of weld region voids, it is intended to study the internal material flow regimes and how the failure of the flows causes weld defects. However, the nature of the process makes it difficult to freeze the actual flow to validate a model [138]. In order to present an accurate multi-physics approach, near to real circumstances of the BFSW process, the basic interactions of the process parameters should be known in advance. Using an analogue model of the process and elucidation of relationships between effective parameters in creation and elimination of a void (tool features, process parameters and material capabilities), it presents the prerequisites of a numerical solution to effectively model the multi-physics of the situation. The starting hypothesis for BFSW Joining is based on a thermo-mechanical context of the process, as the solid-phase joining is simultaneously a result of plastic deformation and material displacement.

Instead of aluminium plates, analogue modelling of FSW was performed using coloured layers and grids of plasticine. This provides easier flow visualization compared to the metallographic measurements of the aluminium welds. The objective is to see if it is possible to replicate the defect structures known to exist for aluminium plate welding. By fabrication of a plate comprising multiple layers of different colours, external area examination during and after the bobbin-tool FSW process, and subsequent post processing by cutting and viewing the cross-sections , can provide new insights into a flow-based model for the weld process.

6.2. Materials and Methods

For better visualization of the welding process, multi-layered plasticine slabs were used as the weld workpieces. Different colours of plasticine manufactured by New Clay Products – United Kingdom, were rolled to a uniform thickness of approximately 1.25 mm by a cylinder-shaped roller and using glycerine as the lubricant.

Layers of different colours of plasticine were stacked on top of each other to create the test piece thickness of 10 mm. The slabs were subjected to heat treatment to improve the adhesion between the layers and also to diffuse the remained glycerine between the layers. The blocks were held at a temperature of 60°C for a period of two hours. The hot blocks of plasticine cooled gradually to -4°C as it was used for the processing in the room temperature.

To validate the plasticine analogue, an aluminium plate also was welded by the bobbin tool.

The single-piece bobbin-tool consists of a top-shoulder, a bottom-shoulder and a fixed pin in the middle. The feature details of bobbin tools will identical for welding of both the aluminium and plasticine plates. However, the analogue models were tested by a 3D-printed plastic tool made on a Stratasys Connex machine, while the aluminium welds were performed by a metal tool made of H13 tool steel. The plastic-made tool has a better consistency with the non-metallic plasticine samples, and the steel-made tool is strong enough for processing of the aluminium plates.

The trials used a CNC milling machine (OKUMA, MX-45VAE Model). The weld workpieces were rigidly fixed between clamped bars and care was taken to ensure that no lateral movement during work occurs.

Based on prior experimentation, to achieve a uniform welded joint, the welding parameters, rotational speed (ω) and feeding rate (V), were selected in a range sufficient for the establishment of a bonded weld. In this regard, the plasticine analogue samples were processed under welding speed set of (ω= 50 rpm, V= 50 mm/min), as these were the minimum speeds of the milling machine. The aluminium sample was processed under speeds of (ω= 650 rpm, V= 400 mm/min). There was also a difference in the thickness of the workpieces, because of the limitation of the material instability under the processing condition. While the aluminium plate shows suitable processing in 6 mm thickness, the thickness of the analogue slabs increased to 10 mm to improve the stability of the layered plasticine during the process.

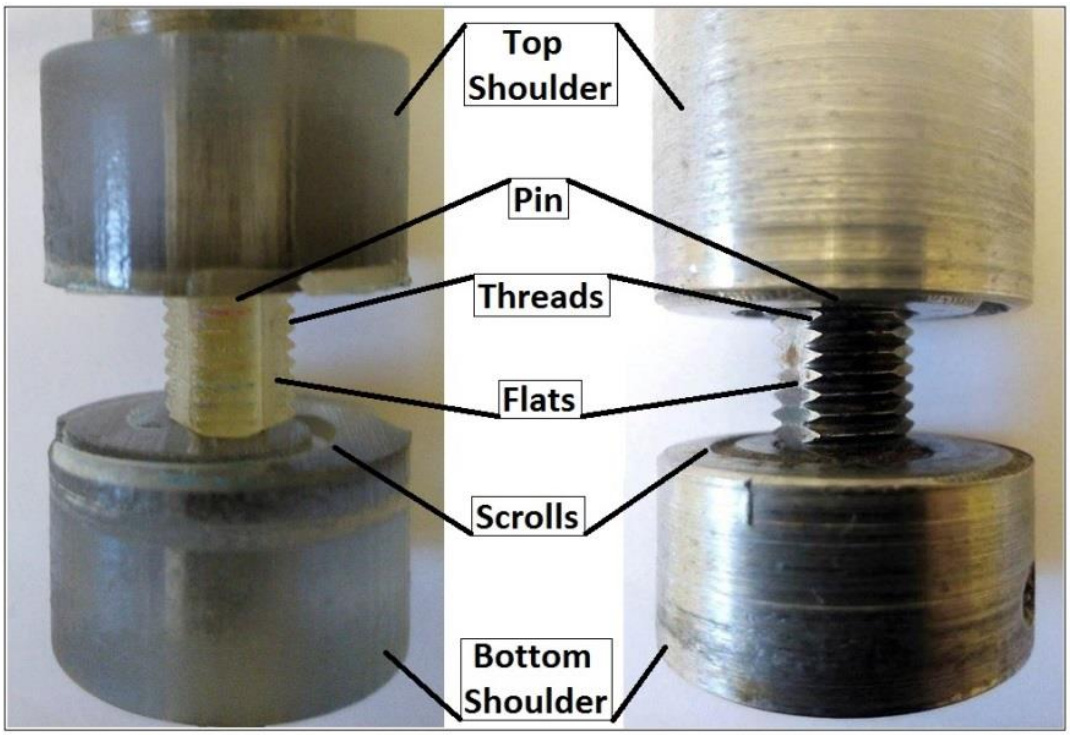

Figure 6.1. The apparent geometry features of the bobbin tools used for the analogue and aluminium welds; (a) 3D-printed plastic tool utilised for the plasticine analogue, (b) H13 steel tool for the aluminium welding.

The dynamic analysis of the forces as the process response during real-time welding was recorded using the LabVIEW software. By a current (*I*) clamp meter, the signal trend recorded by the load cell transducers can analyse the variation in displacement under the material flow inconsistencies during the process.

After 100 mm advancement of the weld-line, the samples were taken for flow visualization and cross-sectioning. The weld characteristics and striation patterns were investigated by visual observation using a high-resolution digital camera (Fuji Fine-Pix S9500) for the plasticine analogue samples. Regarding the aluminium welds, the flow patterns of the cross-sections were delineated by a conventional metallographic procedure, etched by the Keller's reagent, and the optical microscopy observation using the stereoscopic microscope (Olympus Metallurgical Microscope, Tokyo, Japan).

6.3. Results and Discussion

Figure 6.2 shows the physical appearance at the top plan view of the analogue plasticine sample after welding with the 3D printed plastic tool. The relevant dynamic force changes measured in longitudinal and traverse directions of the weld-line also are presented beside the weld analogue. The welded samples show two main defects at the entry and exit zones, as the inherent of the butt-joint bobbin weld. The welding process by the bobbin tool, there are three stages; entry, welding

zone and exit. The related areas for these three parts can be identified in the analogue model by the material movement patterns. The weld stage is located between the entry and exit. The entry can be characterized as a sudden high deformation which decreases over time before becoming stable as the tool travels completely into the plate. The exit phase is when the leading edge of the tool first starts to leave the plate, and material deformation decreases steadily with a sudden last drop of plastic deformation and disintegration of the material. The physical size of defects is corresponding with the dynamic changes of the load during the process.

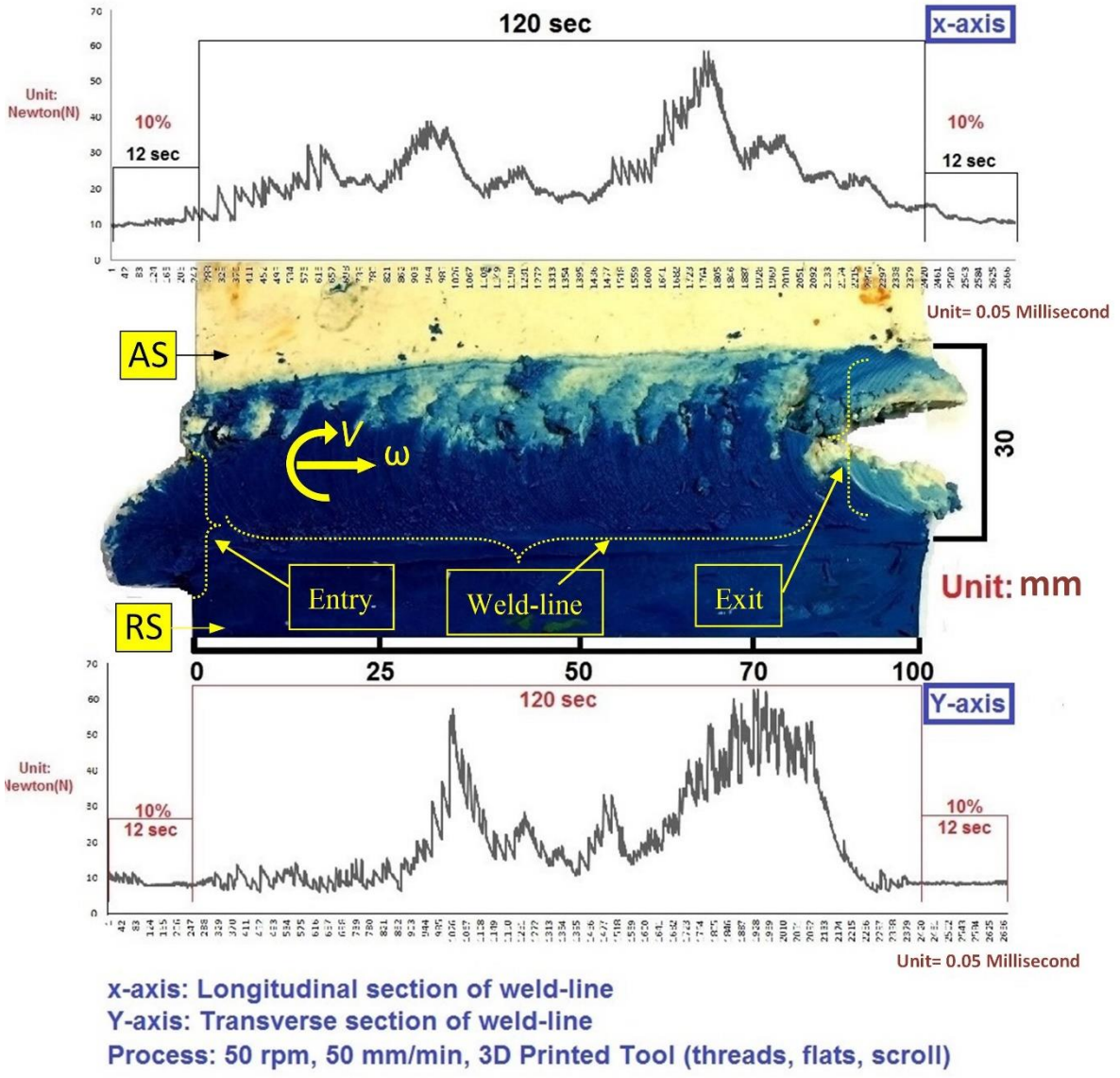

Figure 6.2. Photograph of the BFSW section sample (Top Surface): Plasticine Model. (a) entry zone of weld. (b) exit zone of weld. (c) weld-line body.

The surface appearance of the weld-seam shows a continuously-repeated pitch ripple pattern, which is related to the shoulder performance during the advancement of the tool through the weld-line interface, see Figure 6.3. The comparison between these surface pitch ripples in analogue plasticine and aluminium welds shows high

similarity in shape and size. Therefore, the formation mechanism of these circular surface patterns is relevant to the tool features and flow interaction underneath the scrolled shoulder. As a general interpretation, these pitch ripples are produced by the final ejection of the depositing mass layers at the trailing circumferential edge of the shoulder, during the longitudinal travelling of the tool. Although the pitch patterns have similar shapes in both analogue and metal samples, the actual size of the ripples can be defined by the speed ratio of the tool (relative feeding rate per rotation; distance per revolution). However, the overlapping of the combined successive revolutions makes it hard to provide an accurate measurement of the distance between the pitch layers to determine the optimised condition for the curved patterns of the weld surface.

The 3D printed plastic tool has a suitable mechanical consistency in its interaction with the substrate, regarding the observation of the physical changes in flow mechanism as the tool travels forward. The sample is suspected to contain more internal defects within the weld structure. Therefore, several extra samples were tested with the same tool features in different colour patterns and under similar welding parameters to reveal more details of the internal flow mechanism during the bobbin friction stir welding.

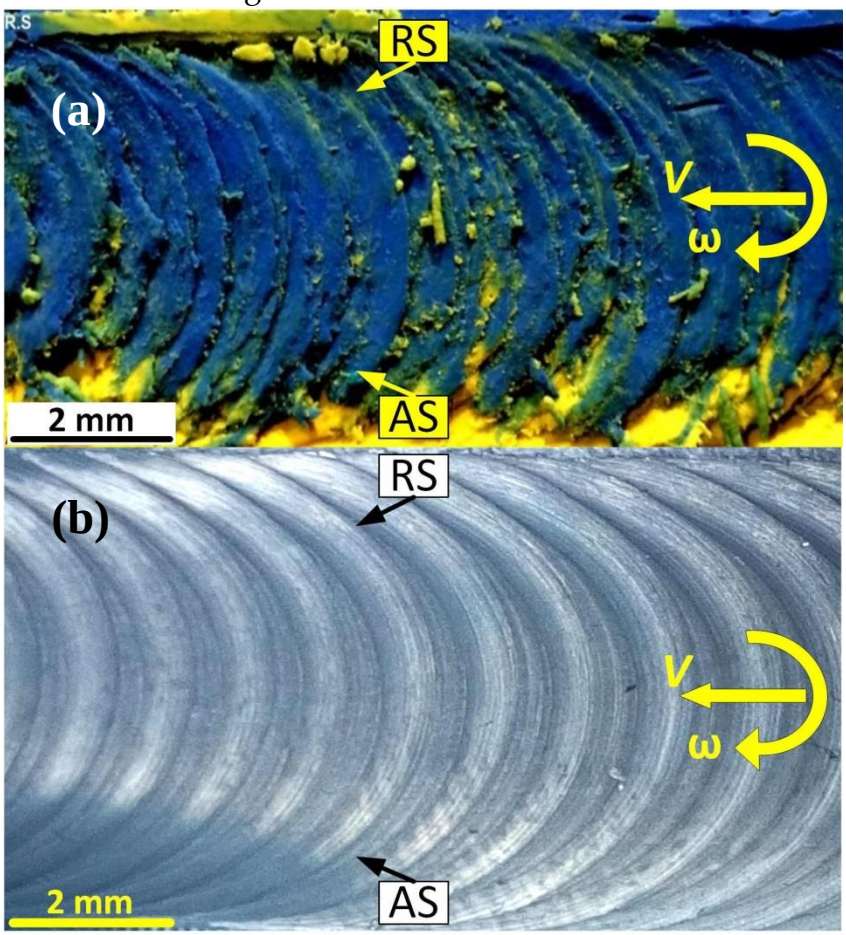

Figure 6.3. In-situ model of the surface pitch ripples as the surface pattern through the weld-line; (a) plasticine analogue, (b) aluminium weld surface.

Figure 6.4 shows the cross-section of the plasticine weld in a multi-layered slab. The further details of the flow behaviour at the cross-section of the analogue plasticine are observed in Figure 6.4b. The analogue model of the weld suggests a possible position for the tunnel defect between the entry zone and the exit zone of the weld (Figure 6.4a). Also, the nucleation of the defect in correspondence with the material flow interaction in the middle of the stirring zone is visible (Figure 6.4b).

The previous research confirmed that the tunnel void originally forms at the entry zone. By including the flow visualization from the actual aluminium sample, compared with the analogue model, can construct a better understanding of the history of the flow interaction during the stirring process. Figures 6.5 and 6 are showing some magnified views of the entry zone in aluminium weld sample. The flow patterns at the entry demonstrate the plastic deformation patterns caused at the substrate in interaction with the rotating tool. According to Figure 6.5, the initial deformation process at the entry zone contains highly plastic deformation in an unstable mode. As the unstable rotating tool passes through the weld-line, the plasticized mass underneath the shoulder escapes outwards the workpiece, whereby forms the spray zone at the entrance position of the tool. Because of the instability of the deformation, the plasticized mass curves from the Advancing Side (AS) and stretched to the Retreating side (RS) of the clockwise rotating tool. The large discontinuity at the AS of the weld-line is the plausible position of the tunnel void as a flow-based defect.

The surface weld pattern typically shows a mixing pitched patterns as a result of the intercalation of the plasticized mass layers from both of the interface (AS and RS) come together to form the joint-line. The curved flow layers at the surface area of the entry zone can be the starting of these pitched surface patterns. Figure 6.5 reveals the twisting flow pattern of the plastic deformation in the entry spray of the aluminium weld. The striation lines of the plastic flow consolidated at the surface of the entry spray suggests that during the tool-substrate interaction, the simultaneous rotation and movement of the tool along with the edge of the workpiece caused a driving force for the strain planes underneath the shoulder. Because of the stirring action, the strain planes rotate with a twisting flow pattern. In this twisting flow mechanism, each plane after travelling a specified distance, can transform its driving force to the neighbouring planes and become settled. Spatial location for each plane in the settlement position is in a different geometry in comparison with the original position. The consequence of these series of movements and settlements of the strain planes is a stirred zone in the body of the weld region.

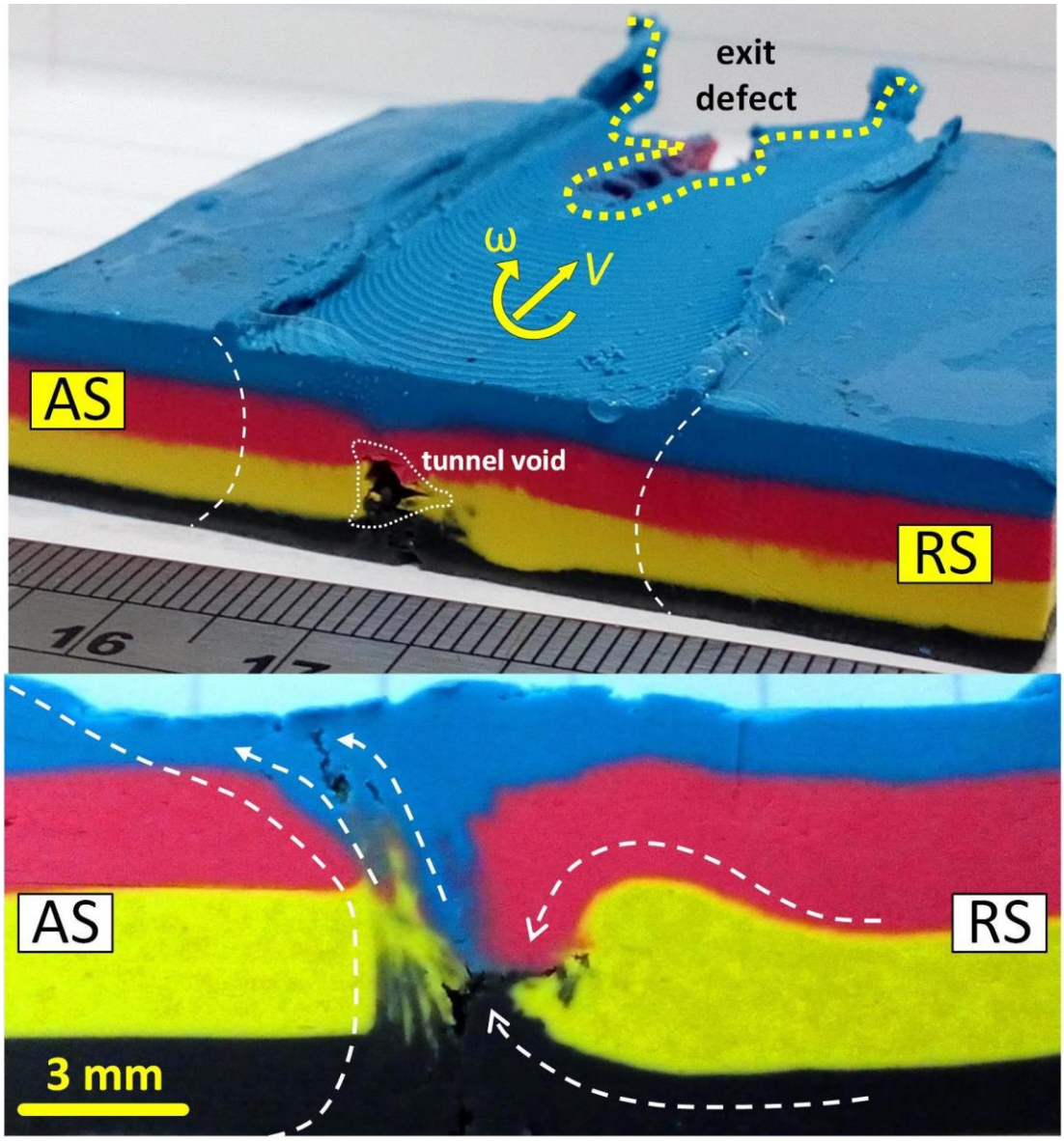

Figure 6.4. Photograph of the BFSW section sample (Bottom Surface): a model for the possible position of tunnel void (plasticine analogue).

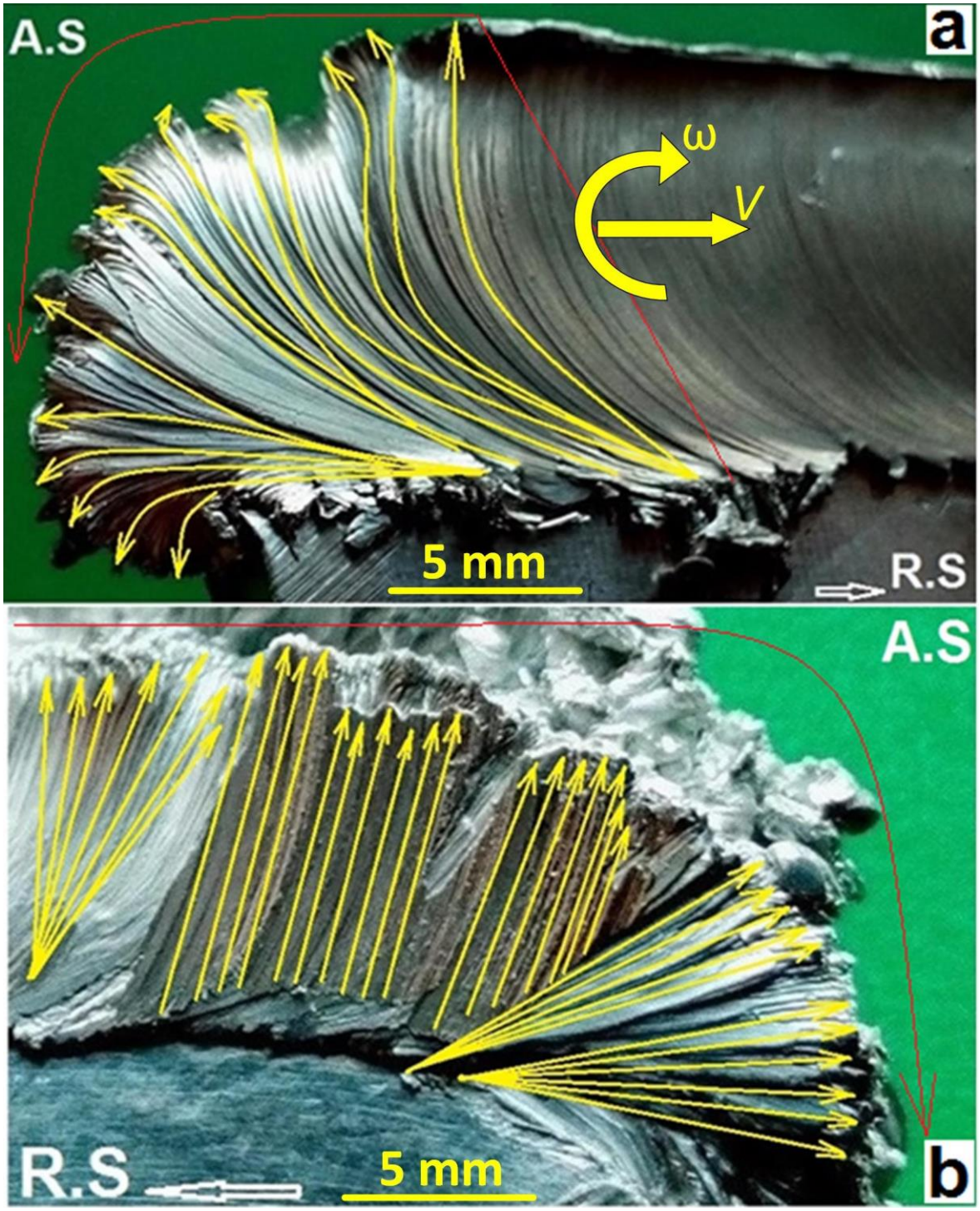

Figure 6.5. Flow patterns of plastic deformation in the entry zone (aluminium weld).

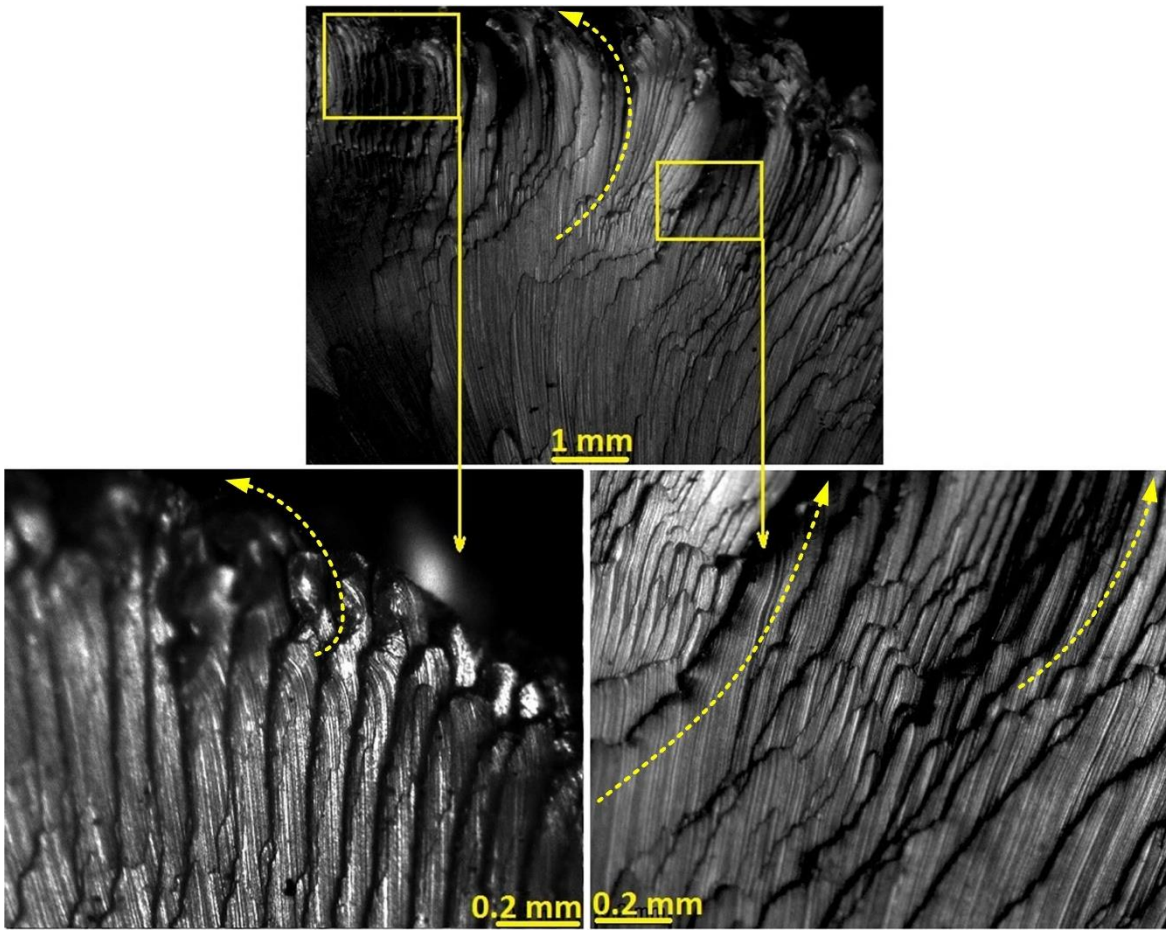

Figure 6.6. Twisting model for the plastic deformation in the stirred zone of the entry spray.

Since this twisting pattern caused a movement, there is a gap between the primary and new location of the planes. As it is illustrated in Figure 6.6, by pushing the stirring front to the entry zone (region c), a channelled flow in the neighbourhood regions of the advancing side forms which are representative of the original position of materials before taking part in a stirred zone. In general, the surface flow lines are on a curvature direction from the advancing side towards the retreating side, according to the clockwise rotation of the bobbin tool. However, because of the scroll patterns inscribed on the shoulder surface, there is a bunching of the segmented contours which are formed as a continuous succession of the deposited mass. All of these successive segments are formed the spray region of entry zone. This continuous twisting movement can finally form a stirred zone for the bonding of the interface whereas there remains a tunnel defect as the footprint of unstable plastic deformation during the twisting pattern of plastic flow mechanism at the beginning of the stirring action.

For further analysing of stirring action inside the workpiece, the material mixing phenomenon at the cross-sections of the plasticine analogue is shown in Figure 6.7.

Figure 6.7 shows the material flow in three regions of entry zone, the body of weld and exit zone. Instead of one cross-section perpendicular to the welding direction, samples were cut at the AS and RS of the stirring zone at 45° angle on the welding direction. Figures 6.7a,b show the cross-sections of the entry zone at the AS and RS, respectively. Figures 6.7a,e reveal the flock-shape patterns on the AS of the stirring zone, representative of the pin profile at the entry and exit zones, respectively. By the interaction between the threaded pin and the substrate, the material forms a vortex area near the bottom surface and a lamellar structure underneath the top shoulder. The RS cross-section shows an arc flow for the stirring zone with a curved wave mixing pattern at the position of the pin. Similar flow patterns are also visible in the exit zone, observed in Figures 6.7e,f, for the AS and RS of the weld-line, respectively. In both entry and exit zones, the birds-flock swarm pattern at the AS of the weld is representative of direct interaction between the threaded pin and the workpiece material which is inscribed around the hole defect because of the shortage of the refilling material to provide the integrity of the mass circulation.

The literature reports the middle of the stirring zone as the onion ring pattern. By generating a continuous refilling flow behind the tool, the plastic layers from the onion ring flow pattern at the contact region of the pin and the stirred mass. The flow trend for the onion rings can be conducted by the angle of the pin threads which result in a curved lamellar structure. Figure 6.7c,d, shows the flow patterns formed in the form of onion rings for the AS and RS cross-sections. Although both patterns demonstrate a similar curved lamellar pattern, the RS onion rings have better integrity between the flow layers. It implies the flow consistency at the leading edge of the pin, where the plasticized mass is transferred from AS to RS. The simultaneous advancement and rotation of the tool cause a flow complexity at the trailing edge of the pin (AS-to-RS transportation) whereby form a turbulent vortex flow deposited towards the AS. This is visible in all sections of Figure 6.7 that the flow lines in RS (Figures 6.7b,d,f) possess a more steady shape compared to the AS (Figures 6.7a,c,e). The discontinuity pattern at the AS region of the entry and exit zones represent the formation of the open tunnel void as the most common defect emerging at the BFSW weld structure.

To validate the internal flow visualization of the BFSW weld obtained by the analogue plasticine, it needs to compare these flow patterns with the actual weld samples. Figure 6.8 shows the etched weld samples selected from the AS and RS cross-sections of the entry zone, similar regions in Figures 6.7a,b, respectively. In the case of the AS, Figure 6.8a demonstrates an open void surrounded by the birds-flock swarm patterns, similar to Figure 6.7a. as the tool passes from the entry zone, the void deficiency emerged at the AS interface. However, the forging effect of the tool at the RS generates a refilling effect whereby it forms the onion ring pattern in the stirring zone, see Figure 6.8b. The flow lines at the RS interface shows a lamellar structure, moving with a horizontal trend from the top surface underneath the top shoulder to the centre of the stir zone. This flow detail in the RS (Figure 6.8b)

indicates an optimized refilling at the trailing edge of the tool without void occurrence. It confirms that for integrity in the refilling mechanism, the simultaneous performance of the pin and shoulder should generate an overlapped mass flow which can cover the material deficit after the tool leaves the stirring position.

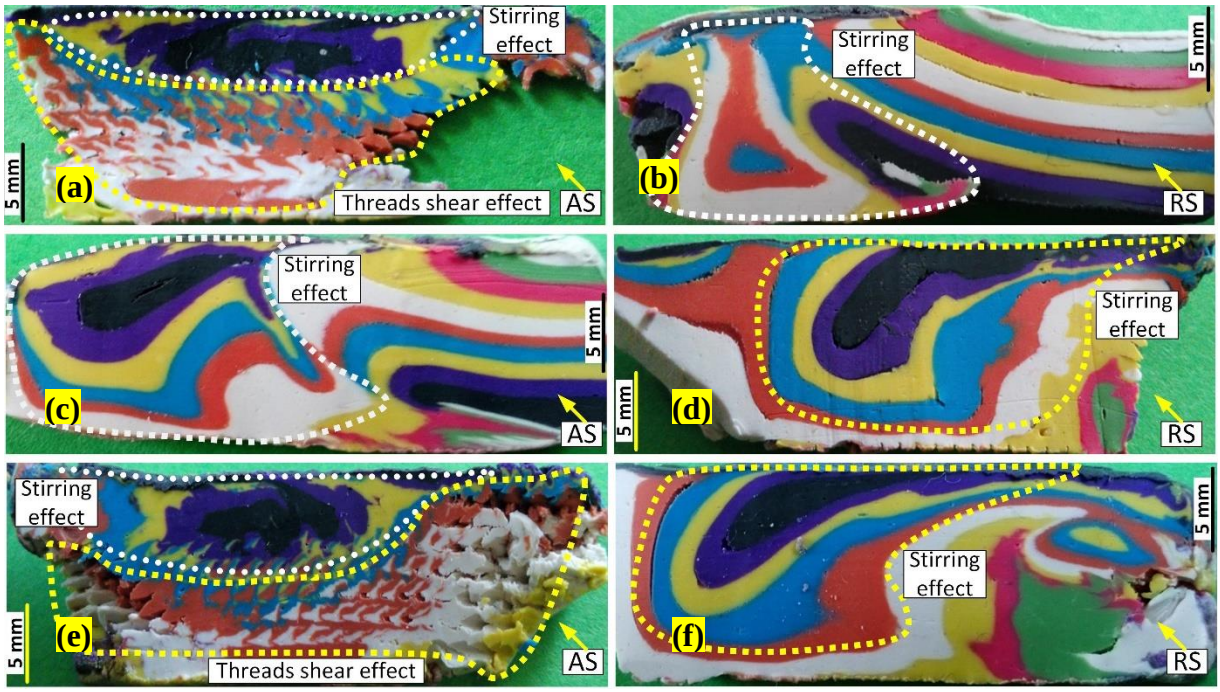

Figure 6.7. The cross-sections of the stirring zone showing the internal flow details for the plasticine analogue sample; (a, b) cross-sections of the entry zone; the AS and RS transverse sections, respectively; (ac, d) cross-sections of the mid-weld; the AS and RS transverse sections, respectively; (e, f) cross-sections of the exit zone; the AS and RS transverse sections, respectively.

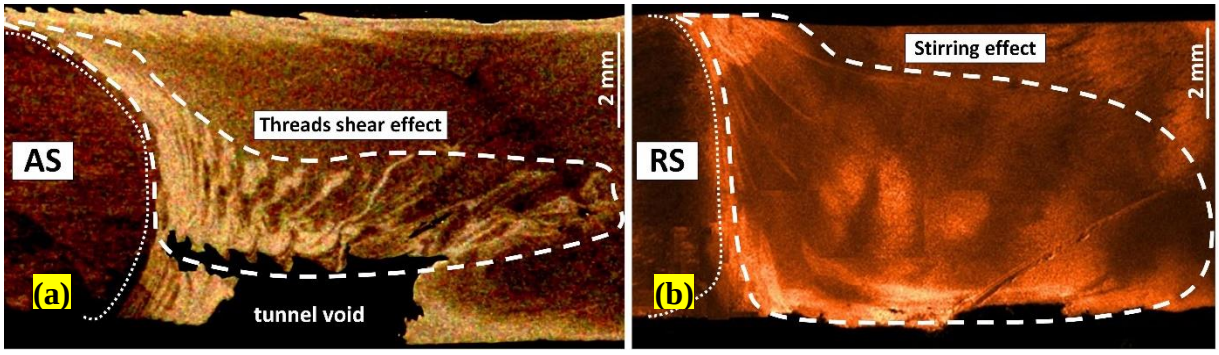

Figure 6.8. The cross-sections of the stirring zone showing the internal flow details for the AA6082-T6 BFSW weld sample; (a, b) the entry zone; the AS and RS transverse sections, respectively.

During the FSW process, the first evidence of plastic deformation and material flow needs to be explored in the entry zone. In the entry zone, even before entering the pin into the workpiece, the flow regime is affected by the rotating movement of the shoulder. Since the position of the shoulder edge is located ahead of the pin, therefore the first stage of the entry zone as the ejected spray is the consequence of the pure plastic flow imposed by the shoulder. It should be noted that the flow features in the spray zone outside of the workpiece, is totally different from the surface flow features of the weld track.

Figure 6.9 shows the metallographic observations of the plastic internal flow patterns at the body of the weld with a focus on the tunnel void region. Figure 6.9a demonstrates the tunnel void occurred at the spray region at the beginning of the entry zone. The angle of view imaging can portray more details of the plasticized mass, accumulated outwards of the weld-seam. Because of the absence of the pin in the plastic deformation, spray region is sagging to the one side (bending towards the RS). As there is no backup material behind the movement direction, the mass is plasticized between two shoulders and then through the shoulders gap is ejected outside.

To be more focused on the flow history around the tunnel void, a 3D photomontage of the stereoscopic images, depicting the left-eye and right-eye views of the tunnel void position is shown in Figure 6.9b. According to the stereograph pictures of Figure 6.9b, the surface pitch ripples features are also observed as the curved flow induced by the shoulder rotation in a circle route between the AS and the RS. Regarding the weld cross-sections, the wavy flow layers accumulated at the circumferential edge of the tunnel void elucidates turbulent flow regimes strayed in random directions causing the flow discontinuity.

The origins of these dispersed flow lines can be attributed to the plasticizing rotation of the shoulder in contrary with the pin-induced flow at the trailing edge of the tool, while the plasticized layers of the stirred mass are depositing to form the weld-seam. Therefore, incomplete refilling at the AS forms a kinked-shape discontinuity at the weld-track known as the tunnel void.

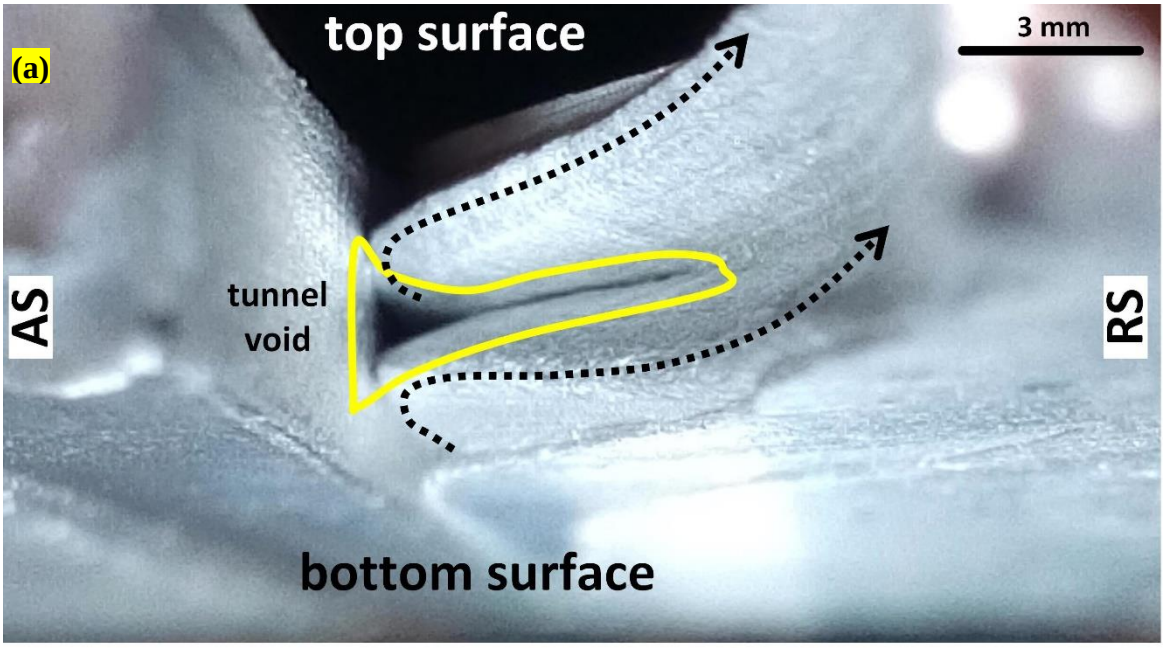

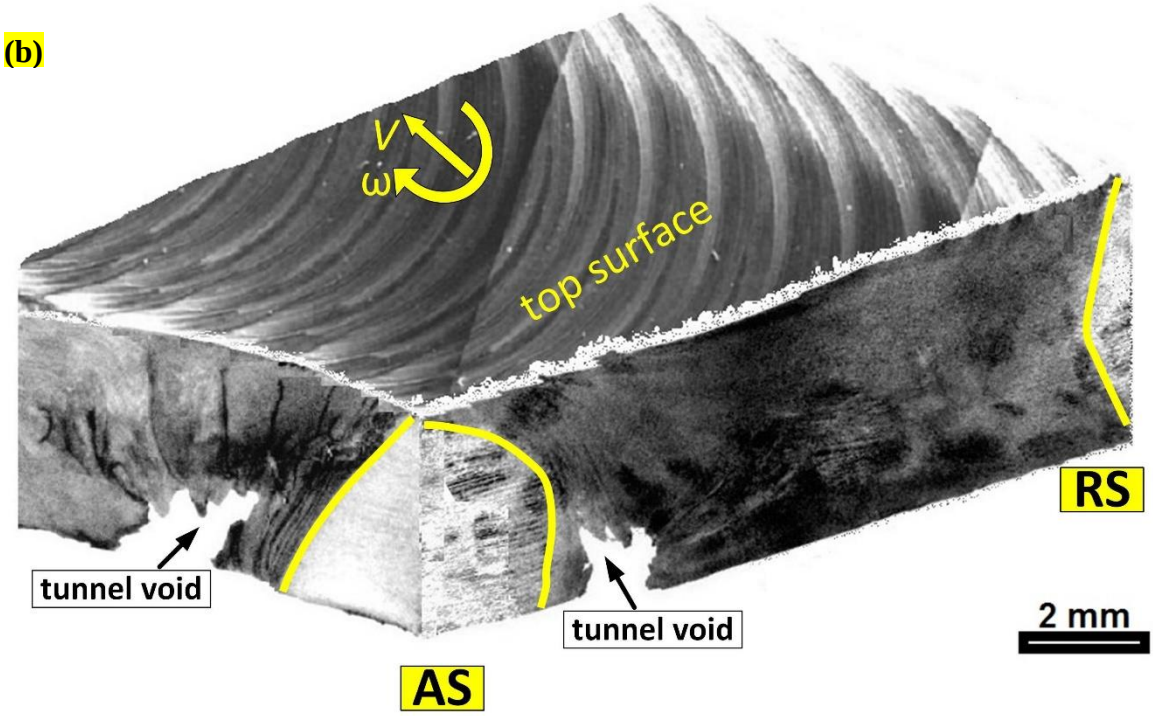

Figure 6.9. Details of the apparent features of the tunnel void within the AA6082-T6 aluminium weld; (a) tunnel void emerged at the entry location of the weld, (b) photo-montage pattern of the tunnel void within the weld structure, revealed in cross-section and side view of the weld.

6.4. Chapter Discussion

The main aim of this chapter was to predict the position of the tunnel defect based on the analogue model to elucidate the flow-based formation mechanism. Based on the analogue flow visualization at the cross-section, a simplified physical model can

summarize the general flow behaviour of the process during the interaction between the tool and the substrate. The tool features in Bobbin-FSW process generate a specific inherent flow interaction around the tool, compared to the Conventional-FSW. Although different defect geometries (open tunnel\void) were observed in flow visualization of the analogue model, the flow mechanism is proposed to be similar. By comparing the weld cross-sections in plasticine analogue and aluminium weld, it was found that the tunnel defect is commonly formed at the advancing side of the tool near the bottom surface. This can be attributed to the sequence of the material transportation relevant to the tool features and the welding process setup.

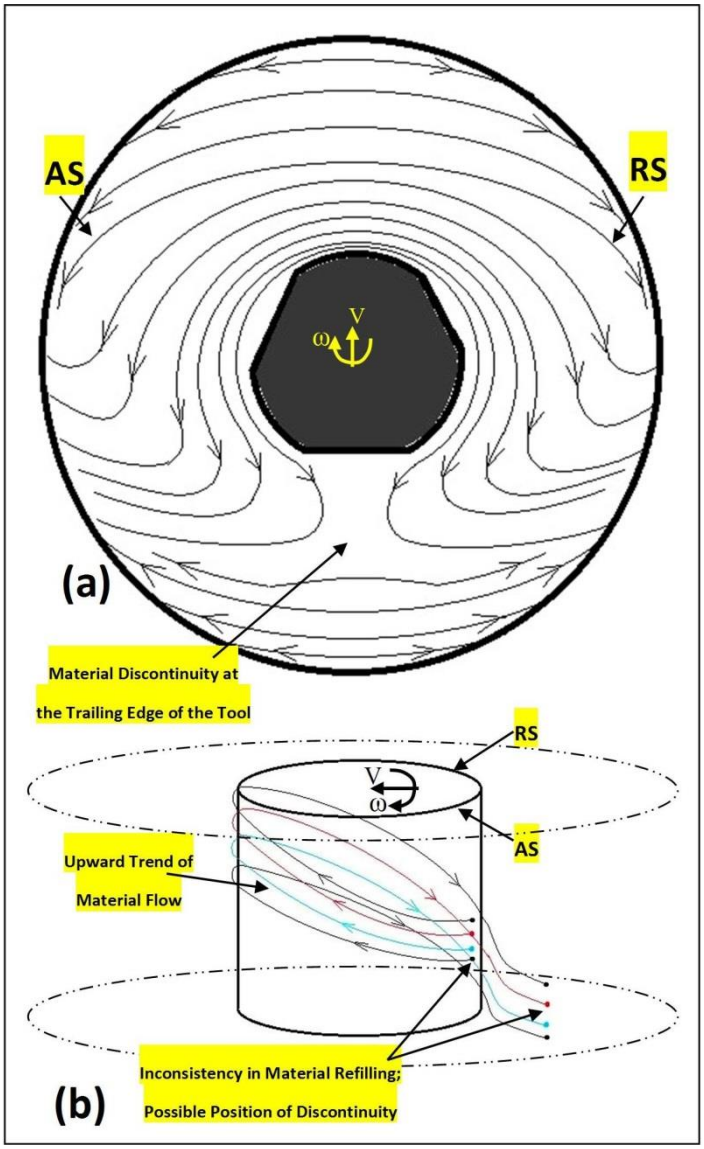

Figure 6.10. The schematic of the flow features under the shoulder, around the pin; (a) top view of the flow model under the shoulder, (b) side-view of the flow lines around the rotating pin.

Figure 6.10 presents the details of the flow lines at the proximity of the tool components (shoulder and pin). The plain view of the plastic flow underneath the shoulder is shown in Figure 6.10a. It is shown that by entering the pin to the substrate, the materials undergo a local discontinuity caused by the shearing effect of the rotating tool. After circulating of the plastic mass around the pin, the stirred materials are being deposited at the trailing edge of the tool. In this situation, the flow inconsistency can cause a mass deficit between the deposited layers, resulting in void occurrence. It seems that the rotating pin has more responsibility regarding the internal flow features within the stirring zone. Hence, for a better explanation, the mass flow pattern around the pin is drawn in Figure 6.10b. The side view of the tool in Figure 6.10b shows that the clockwise rotation in the presence of threads on pin pulls the mass flow upwards. Therefore, the upward trend pumps material vertically from the advancing side to the leading edge of the tool, and simultaneously the fresh material of the retreating side are swept to the trailing edge of the tool. This helical flow path for transportation of the stirred mass cause a refilling inconsistency, in the form of the escape of the material at the backside of the tool, which increases the possibility of the material deficit at the bottom of the advancing side where the material is expected to be deposited after the circulation around the pin. This is where the incomplete filling deficit and eventually a tunnel void emerge as the discontinuity defect between the deposited mass layers.

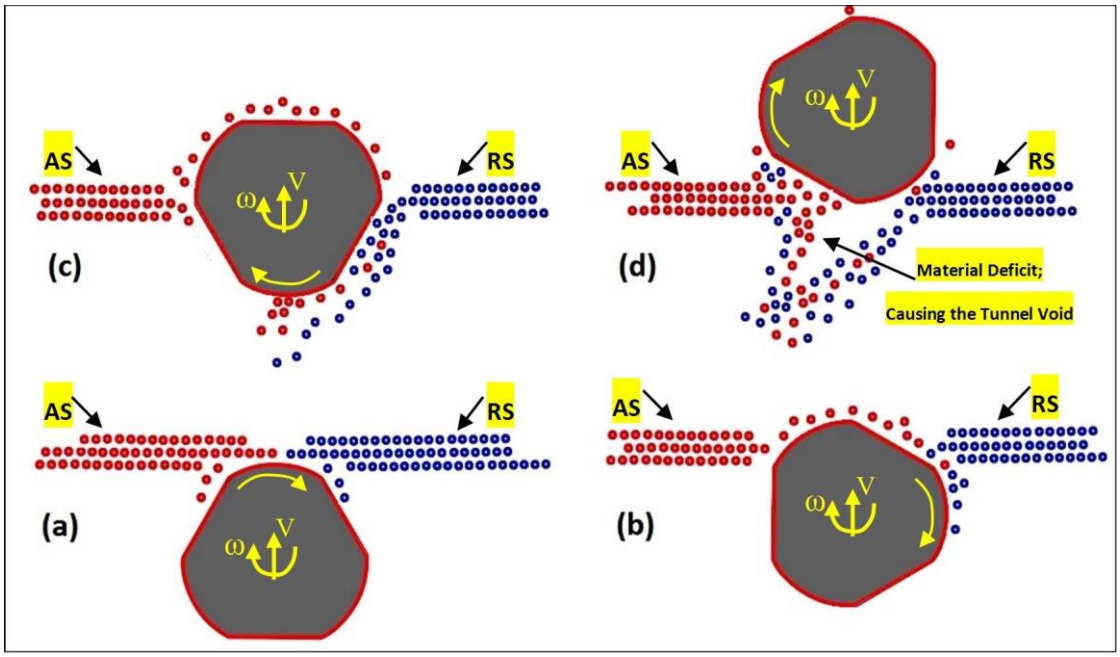

Figure 6.11. The proposed physical model for the material flow regimes in interaction between the pin and the workpiece material; (a) initial contact between the rotating tool and the workpiece material, (b, c) entering of the pin into the substrate mass, start of the plastic deformation, (d) fully embedment of the pin into plasticized mass of the substrate with a tunnel void discontinuity formed at the trailing edge of the tool. (All schematic flow patterns are presented at the top-view of the pin and substrate).

The pitch threads have a positive influence in stirring performance by the increase in velocity of transportation and a helix angle and thus better plastic flow condition at the leading edge of the tool. However, this helical flow path affects the efficiency of the adhesion of the material to the pin during the transportation at the trailing edge of the tool, between AS-to-RS. This is consistent with the cross-section observations where clearly identifies that the turbulent-like flow features at the advancing side towards the bottom surface form an open tunnel void defect.

The schematic of the dynamic material flow can be shown around the rotating pin in plain view to elucidate the pin-material interaction with a focus on void formation mechanism. Figure 6.11 demonstrates the sequence of material flow around the pin, based on the flow behaviour identified in this work. Referring to the flow visualization developed in this work, by the clockwise rotation of the tool, the material at the AS is stirred and transported to the RS.

By entering the tool into the substrate, the pin grabs the material from the leading edge of the tool, see Figure 6.11a. By further advancement of the tool trough the butt-interface locus, the sharp edges of the pin (threads-flats) dig into the workpiece material (Figures 6.11b). This yields more plasticized mass at the trailing edge of the pin. The clockwise rotation of the pin causes an opposite mass flowing at the retreating side of the tool, squeezing the transported material from the leading edge backwards at the trailing edge of the pin (Figure 6.11c). However, due to the opposite direction of the rotational and advancing movement of the pin at the retreating side, the plastic flow tends to escape from the edge of the pin surface during transport to the back of the tool. This lateral escaping mass from the pin surface causes a slipping mode in material transportation which decreases the compression and integrity of the flow layers at the trailing edge. This explains the flow failure by observing a discontinuity pattern in RS-to-AS recirculating flow path as the potential position for the formation of the tunnel void and emerging of the incomplete weld (Figure 6.11d).

By repeating this flow inconsistency behaviour during successive rotation of the pin, the deficit in material flow forms a channel-shaped tunnel void as a flow-based defect. In addition to the tool geometry, it seems that the lack of mixing and insufficient material refilling at the AS also are effective in the evolution of the tunnel. This can be overcome by applying higher welding speeds (both rotational and advancing velocity).

6.5. Chapter Conclusions

This chapter illustrates an original contribution by introducing an analogue modelling process of BT-FSW to visualize deformation and joining of the material. The method is applicable to identify the flow characteristic of the weld and present probable formation mechanism of the discontinuity defects for the processed material. The reported results point out a very strong model based on the flow

visualization by the plasticine analogue during the friction stir welding process. Results show that the main reason for the tunnel defect is the instability of the plastic deformation during the entering of the tool into the body of the workpiece material at the entry zone. This highly plastic embedding occurs with the ejection of material as a spray in the entry zone of the weld and consequently, the tunnel defect is left in the place of the material loss. By identification of the origins of the void formation, it was concluded that a defect-free weld should be able to establish the uniform flow integrity within the stirring zone. This can result in a stable mass refilling process at the trailing edge of the tool, where the mass deposition forms the weld seam with no discontinuity flaw within the bonding layers.

CHAPTER 7: Analogue Modelling of Flow Patterns in Bobbin Friction Stir Welding by the Dark-Field/Bright-Field Illumination Method

Chapter Summary: The flow-inducing effect of the bobbin-tool features (tri-flat pin and scrolled shoulder) were replicated by a simple analogue model for aluminium welds by layered plasticine samples. Flow patterns of the weld zone were clarified by a typical stereomicroscopy instrument assisted by dark-field/bright-field illumination. The effects of the pin features, specifically threads and flats in centre of bond zone and scrolled shoulder in sides of stirred zone, were identified. This study shows that internal flow features for BFSW welds is transferable from the friction stir welding process to the functional metal forming processes such where the shearing can extensively affect the microstructure.

This chapter is a derivative of the following publication:

Donthi Sudarshan, K.C.; Tamadon, A.; Pons, D.; Sued, M.; Clucas, D.; Wong, E. Preparation of Plasticine Material for Analogue Modelling. In Proceedings of the International Conference on Innovative Design and Manufacturing (ICIDM 2016), Auckland, New Zealand, 24–26 January 2016.

7.1. Introduction

Friction stir welding (FSW) is a process whereby a weld is formed by a plastic deformation involving a rotating tool being driven through two pieces of substrate material [1, 2]. The general area of interest is welding aluminium sheet, and there are many applications for this in marine, automotive, and aerospace fabrication [3, 5]. Weld properties are as good as or better than those from conventional thermal processes, but making a reliable weld is challenging.

One of the difficulties in study of the FSW process is to understand the internal material flows. The work of Sued [64, 81] provided new insights into the flow mechanisms and how the failure of the flows caused weld defects. However the nature of the process makes it difficult to freeze the actual flow and this makes it difficult to validate any model. A solution to this, and the subject of the current chapter, is to use plasticine as an analogue to aluminium. The objective is to create a plate comprising multiple layers of different colours. This provides a means to cut cross sections afterwards and see where the colours have been displaced in stirred zone of FSW weld. This is useful to take the results of flow patterns further by developing a multiphysics model of the weld zone. Others have used plasticine in

this way, so the idea itself is not novel. However others are secretive about the way they have done this.

The research question is to discover how to perform analogue modelling of FSW using colour layers and grids of plasticine, and then apply this empirically to determine the material flow inside the weld, induced by the geometrical tool features. The area under examination is bobbin friction stir welding (BFSW). In this regard, the actual bobbin-tool FSW process was conducted on the plasticine slabs instead of aluminium plates. The microstructure of weld will be studied by using a typical stereomicroscopy using dark-field/bright-field illumination to find a better explanation for flow regimes within the BFSW weld structure.

7.2. Experimental

The welding process was done by a single piece bobbin tool that consists of a top-shoulder, a bottom-shoulder and a fixed pin in the middle, Figure 7.1. The pin was modified by adding three symmetrical flat surfaces and a threaded feature on the radial surfaces to help uniform flow during welding. The feature details of the bobbin tool will be replicated on the multi-layered plasticine workpieces. By using different colours of plasticine it is easy to distinguish the material flow trajectories.

In order to create a multi-layered plasticine block, different colours of plasticine manufactured by *New Clay Products* – United Kingdom were used. Each colour of plasticine was manually rolled down on a flat plate to a uniform thickness of approximately 1.25 mm. Layers of different colours of plasticine were stacked on top of each other to form the 10 mm thick slab. The plasticine blocks were subject to heat treatment to improve the adhesiveness between the layers. The blocks were heated to a temperature of 60ºC for a period of two hours. The heated blocks of plasticine were cooled gradually to -4ºC as the working temperature. The trials were run using a CNC milling machine (OKUMA, MX-45VAE Model) in a steady-state of 50 rpm for the clockwise tool rotation (ω) and 50 mm/min as the feeding rate (V). To conduct the process easily, glycerine was used as the lubricant between the bobbin-tool and substrate. The flow patterns of the BFSW weld region were studied at the cross-section of the analogue plasticines by a dual-power stereo microscope (Olympus Metallurgical Microscope, Tokyo, Japan), facilitated by a dark-field/bright-field objectives exposure.

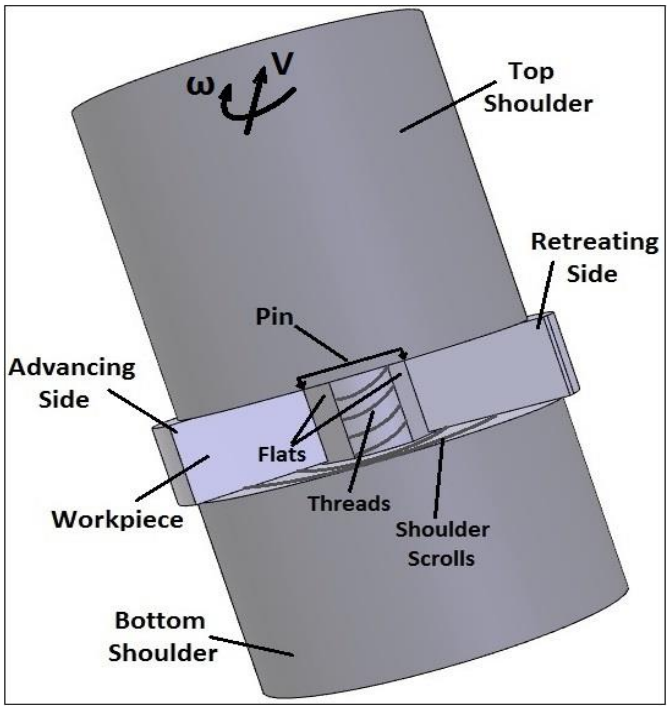

Figure 7.1. 3D schematic of the bobbin tool with a tri-flat pin in interaction with the workpiece.

7.3. Results and Discussion

After the welding process, samples were cut with a wire cutter and the cross sections were investigated using a stereomicroscope. To clarify voids and cracks inside the structure, the dark-field/bright-field Illumination method was used. Using this technique a variety of flow patterns in different zones of weld were extracted. As the tool rotation was clockwise, in all cross-sections the advancing side (AS) of the weld is situated on the left side of the weld region, and the retreating side (RS) is located on the right.

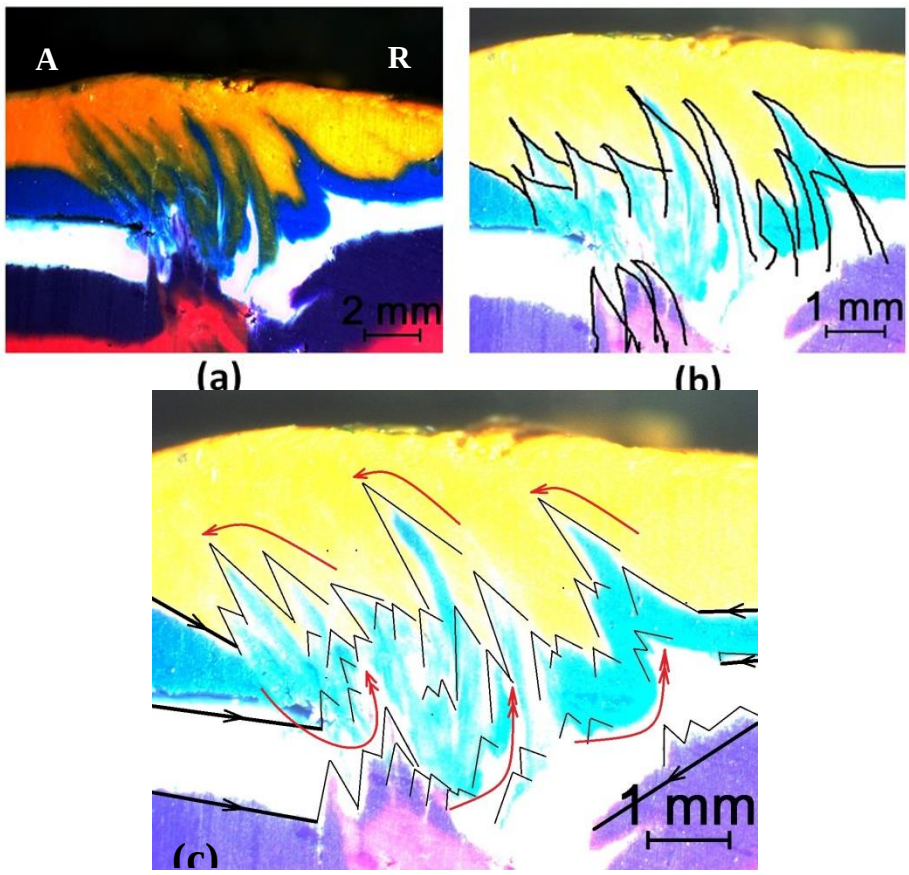

Figure 7.2. Flow patterns representative of stress concentration; (a) dark-field exposure, (b) bright-field exposure, (c) proposed shear flow existing through the stress concentration region. Sample processed in (V=50mm/min, ω=75rpm). Figure 7.2(a) is an adaptation of Figure 5.8

Figure 7.2 illustrates the stress concentration patterns as a result of the interaction of the shoulder and pin with the material. Because of higher stresses caused by the shoulder surface, branches are stretched from centre of stirred zone to the sub-surface area.

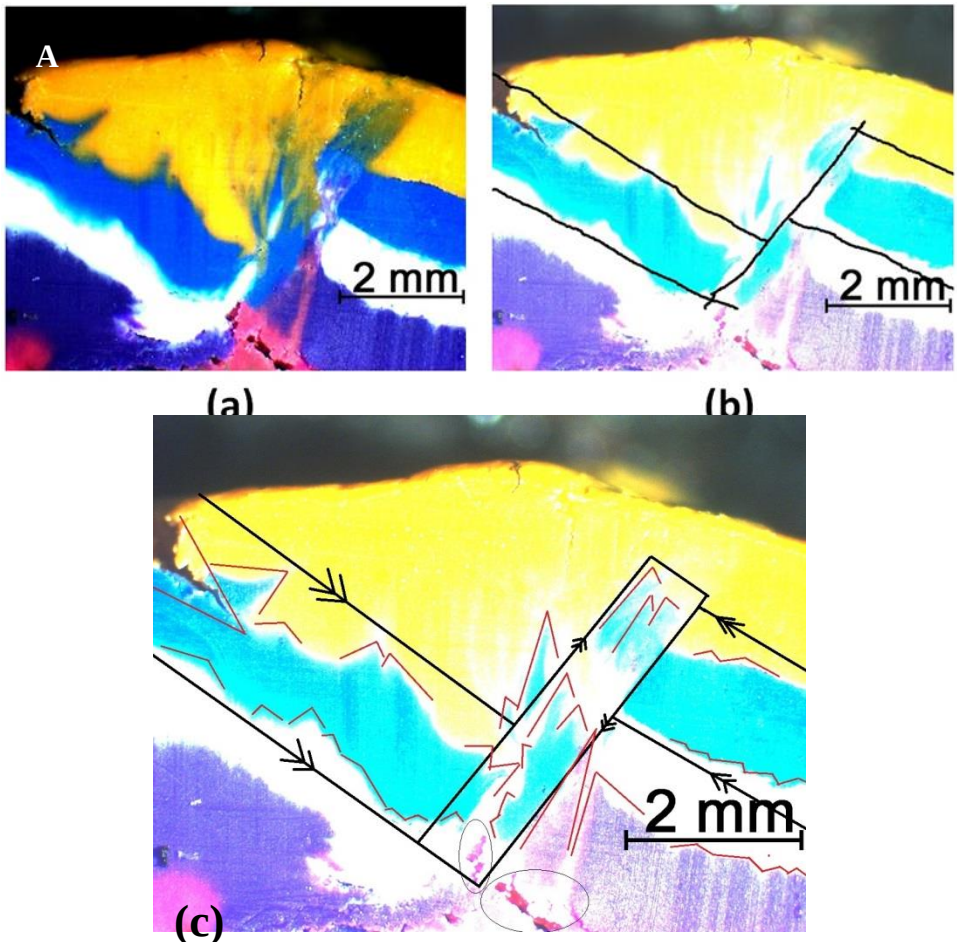

Figure 7.3. Flow patterns representative of plane strain, induced by the shearing; (a) dark-field exposure, (b) bright-field exposure, (c) interaction of the flow layers between the orthogonal strained planes.

As the stress concentration expands through the stirring-zone breadth, the focus points in the structure connect together to create plane strains. The pattern of these plain strain regimes is observed through Figure 7.3.

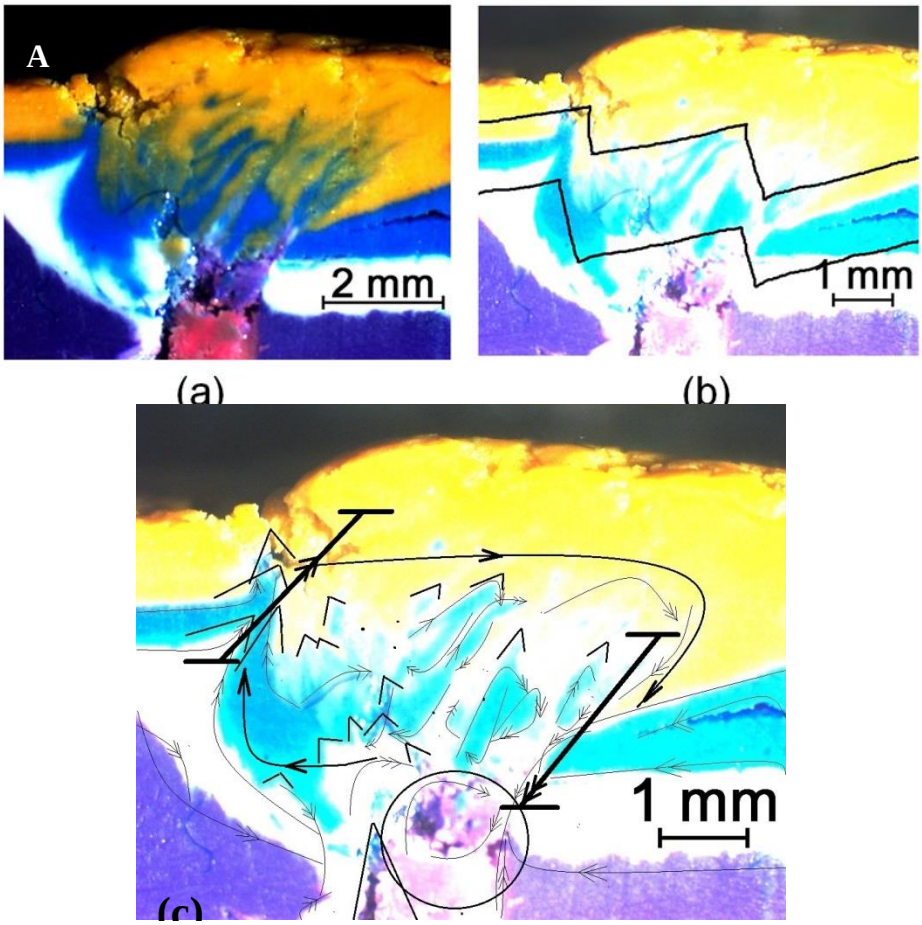

Figure 7.4. Transformation of the flow patterns from plain strain to shear planes; (a) dark-field exposure, (b) bright-field exposure, (c) tangled shearing flow features with a swirling pattern through the shear planes.

Due to the cyclic nature of FSW process, plane strain filed converts to the shear planes. Figure 7.4 shows a pattern for the transformation of plain strain to shear planes.

In BFSW process, the complex pin and shoulder generates a high rate of plastic deformation in the network. Rotation of the tool through the material shows it reduces the shear rate. Consequently, a rotating flow will be created in the structure. This vortex nature can damp all the stress-strain planes in a steady-state flow. As the rotation of the tool is conducted in the interface of two plates, stirring also mixes the materials into a bonded structure which is called the nugget zone (see Figure 7.5).

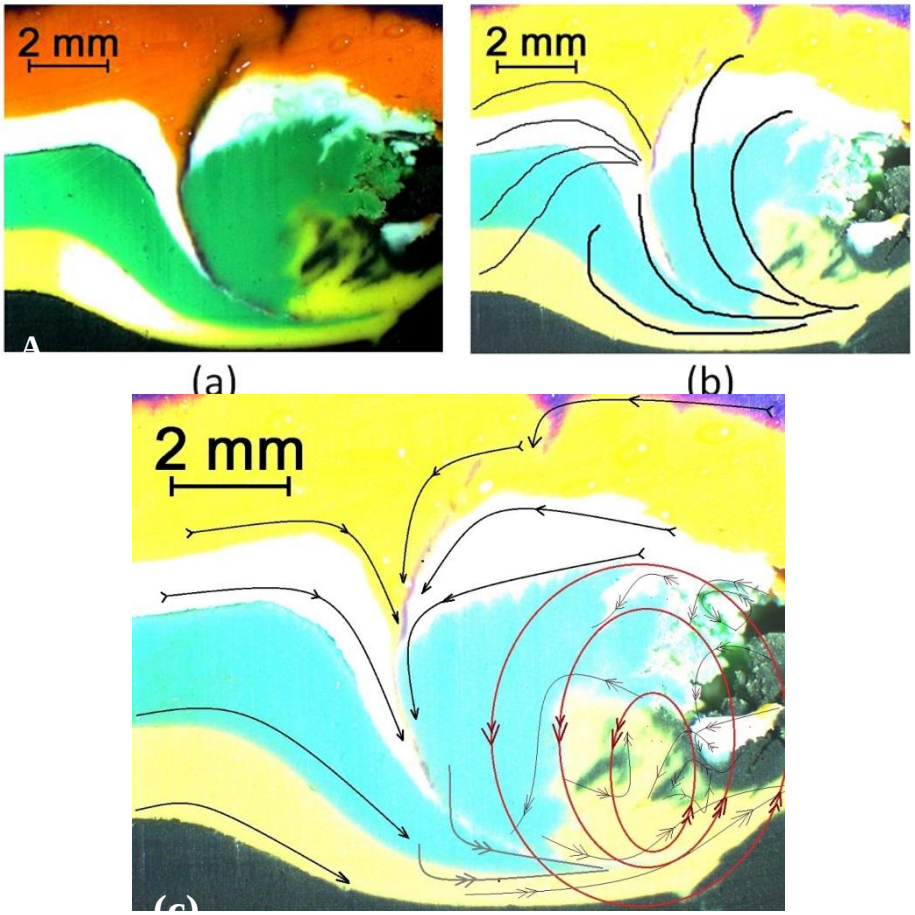

Figure 7.5. Vortex patterns; destruction of shear planes in circulating flow; (a) dark-field exposure, (b) bright-field exposure, (c) turbulent shear flow behaviour in severe plastic deformation filed.

7.4. Chapter Conclusions

This chapter illustrates an original contribution by introducing analogue modelling of the BFSW process to visualize plastic deformation and joining of material. The method is applicable to explain material flow trajectories during welding. Failure of flow regimes in each step of the joining process can cause defects in the structure. A successful flow regime can result in a sustainable jointing bond through the stirring zone. Also it is suggested that a flow pattern for the formation of the nugget zone or stirring area as a feature for FSW welds.

CHAPTER 8: Structural Defects in dissimilar BFSW weld: Hybrid Joint of AA6082-T6 Aluminium Alloy and Commercially Pure Copper

Chapter Summary: The purpose of this chapter is to examine the flow features of a fractured welded plate. The welding method used is Bobbin Friction Stir Welding (BFSW), and the joint is between two dissimilar materials, aluminium alloy (AA6082 T6) and pure copper. Weld samples were cut from along the weld line, and the cross-sections were polished and observed under an optical microscope (OM). Particular regions of interest were examined under a scanning electron microscope (SEM) and analysed with Energy Dispersive X-ray Spectroscopy (EDS) using the AZtec software from Oxford Instruments. The results and images attained were compared to other similar studies. The reason for fracture was mainly attributed to the welding parameters used; a higher rotational speed may be required to achieve a successful BFSW between these two materials. The impact of welding parameters on the Al-Cu flow bonding and evolution of the intermetallic compounds were identified by studying the interfacial microstructure at the location of the tool performance.

8.1. Introduction

8.1.1. Context

Aluminium to copper dissimilar welds are a highly applicable hybrid joint, necessary for high-tech industrial applications, where needed to meet specific ductility or weight requirements, as well as providing thermal and/or electrical conductivity, with corrosion resistance [49]. The examples of high-performance Al-Cu welds include electronic industries, transportation vehicles, energy industries, and aerospace components [62].

Nevertheless, regarding the weld quality, there is a challenge in joining these two incompatible materials, due to their distinct physical and chemical characteristics. In general, fusion welding is not a recommended process as a large number of Inter-Metallic Compounds (IMCs) are formed in this process, and a decent weld is difficult to achieve [49].

IMC's in fusion welding are uncontrolled metallurgical defects emerging during the solidification, which deteriorate the expected welding properties by lower strength, brittleness, and electric resistance [25]. In such instances, to avoid the solidification problems, other types of welding methods without a liquid phase, including Friction Stir Welding (FSW), are more suitable for dissimilar joints [145]. FSW is a solid-phase welding method, where processing temperatures are below the melting point of the workpieces [5]. Moreover, no filler metal is used, therefore, the weld region is

free of solidification cracking or porosity [1, 2]. Besides that, no gases or fumes are produced during the FSW operation compared to fusion welding. Since the working temperature is well below the melting points, the FSW can provide better control on the formation of IMCs [20]. Also, because of the automation of the operation, the welding parameters can be applied with a high level of accuracy [86], which is required to remove any possibility of the operation error, affecting the final quality of the weld.

FSW was introduced by The Welding Institute (TWI) in 1991 [2], for solid-state welding plates of same or dissimilar materials [1]. By rotating a non-consumable tool between the joint interface and driving along the weld direction, frictional heat generation and sufficient shearing force induced by the rotating tool, result in plasticizing and mixing the mass at the interface of the tool-substrate [136]. The frictional interaction at the surface contact between the tool and the workpiece (as the substrate), causes the heat input with -no external heat source- which provides the plasticity of the materials [141], required for the mass flow within the stirring zone (SZ) of the weld [138, 144].

Bobbin Friction Stir Welding (BFSW) covered in this study uses a bobbin tool; this offers better stability during the welding process [139, 140]. Although, the main issue to obtain a sound weld by the BFSW technique, is a fully connect between the AA6082- aluminium alloy and Copper (Cu) without any discontinuity through the weld-seam position.

8.1.2. Literature Review

Bobbin friction stir welding

Bobbin tools were developed to improve a few aspects of conventional FSW [81]. The tool consists of two symmetrical shoulders on the workpiece surfaces, connected by a centred pin embedding in the butt-joint-line interface [4]. A conventional FSW (CFSW) tool consists of one shoulder and the penetrating probe, requiring a backing anvil bar for support. This can act as a heat sink, also would have the potential to generate defects in the weld root [12].

A double-sided tool (bobbin tool) overcomes these issues as the tool itself supports the joint, and the root region is removed by a rotating bottom shoulder with participating in heat generation and conservation, instead of backing anvil in CFSW which act as a chill [55]. BFSW will also provide an even heat input across the weld resulting in low distortion, can accommodate thickness variation, would have low axial forces on the fixture and machine, and provides ease of control due to the force exerted by the shoulders [36, 38].

When the tool is rotating and traversing through the joint-line, the pin pinches material from both sides and forges them together at the SZ [137, 138]. This plasticises the material, and subsequently by the advancing of the tool, results in

forming the weld-seam by repeated deposition of the stirred layers, transported to the trailing edge of the tool [3, 27]. By acting of two rotating shoulders, BFSW provides sufficient heat for plastic flow between the Al and Cu faces; more effective than conventional FSW [37, 136].

Dissimilar joints: soft materials

Many methods are used to join two different materials together; these could be categorised as per their joint formation mechanism, which can be mechanical, a chemical reaction, an application of thermal energy, or a combination (hybrid process). FSW is a combination of thermal and mechanical joining, where the frictional heat generated by the mechanical performance of the rotating tool softens the material, and the further stirring action mixes and bonds the material.

FSW achieves the solid-state joining of two dissimilar materials at a working temperature much below the melting points (1/3 T_m) [35, 46]. The structure of the FSW joints comprises of four typical subdivisions. The main weld region is the stirring zone (SZ), situated at the weld centre and is directly formed by the tool action [63, 83]. As the heat generation and the deposition of the plastic mass occurs in the SZ, this region experiences full dynamic recrystallization (DRX) as it cools down after the welding process [141, 144].

The thermo-mechanically affected zone (TMAZ) at the proximity of the SZ, is the interface between the stirred mass and the solid region at the work-piece. The TMAZ is where the material microstructure is affected by the shear strain induced by the mechanical performance of the tool, as well as the heat flux absorbed from the friction effect [145]. The heat-affected zone (HAZ) is the next region between the TMAZ and the base metal (BM) [7]. HAZ is a common characteristic between all thermal welded joints, influenced by the heat input, affecting the microstructure and mechanical properties. Both the HAZ and TMAZ are known as the transition region in the FSW weld structure, situated between the SZ and the BM [85].

It should be noted that a defect-free interfacial in dissimilar joints is difficult to achieve due to the narrow weldability window. Adjusting the process parameters to achieve an optimized flow, as well as controlling the high chemical interaction between the base metals would be required to obtain a successful hybrid joint [51].

Dissimilar joints: partnerships with copper

In many works studying the dissimilar FSW processing of aluminium-copper alloys, joint efficiency of the weld was noted to be less than 100%. The weld microstructure can be divided into two areas: under the shoulder where the SZ and TMAZ are, and outside the shoulder where the HAZ is situated next to the parent material [31].

According to the theory of the FSW process, in an Al-Cu joint, by considering of the clockwise rotation of the tool, it suggests to consider the aluminium plate at the advancing side (AS), and the copper plate at the retreating side (RS) of the weld. This

configuration can provides better tool performance in interaction with the workpieces, as the tool first softens the workpiece with higher density (Cu) at the AS, and then transport the plasticized mass towards the lower density material (Al) at the RS of the weld. As in a clockwise tool rotation, both the heat input and the mass transposration has a AS-to-RS flow direction, the TMAZ shows a wider breadth on the RS (Al-side) than in the AS (Cu-side). This is noted to be due to the tool offset creating more mass circulation, steering at the Al-side (retreating side), while the lower peak temperatures at the Cu-side (advancing side) will not affect the Cu grains [82]. Similarly, the width of the HAZ usually is larger on the Al-side. This is caused by intense heat but with no grain deformation and would have less hardened coarse grains.

The microstructure in the SZ of dissimilar FSW shows a intercalated vortex pattern of the lamellae flow lines as the stir-induced shear bands. The stirring action creates swirl-like patterns at the bottom of the weld, while at the upper part of the nugget zone, a composite-like structure is formed. This can be similar to the onion ring structure as a typical inherent of the material flow patterns, found in the SZ of the FSW joints [30].

The formation of Intermetallic compounds (IMCs) in Al-Cu welds is a major issue, as IMCs are hard and brittle, and would decrease the quality of the weld by creating irregular and fragmented defects. It is normal to find continuous thin layers of IMCs at the Al-Cu interface that would result in a complete joint free from defects, but the brittleness of the IMCs would still make this the weakest zone. Moreover, micro-hardness of the weld nugget is also affected by the IMCs. Commonly found IMCs in Al-Cu FSW joints are $CuAl_2$, Cu_9Al_4, Cu_3Al and CuAl, Al_2Cu and γ_1-Al_4Cu_9 phases were found to be formed in an Al 6082-T6/ Cu FSW [146].

Regardless the metallurgy of the weld, in FSW process, the weld configuration and the welding operational parameters play a major role in creating a good joint, or on the other side, the occurrence of the physical defects within the weld structure. Placing the copper plate on the retreating side in a butt-joint during conventional FSW has been shown to cause macro-size voids or the open tunnel void, while placing Cu on the advancing side would allow for a defect-free weld. A tunnelling defect appears as a continuous pattern of voids beneath the shoulder and above the root of the weld in FSW [147].

High transverse welding speed and low tool rotational speed would also cause voids and tunnelling defects, due to the insufficient heat input and material flow required for a steadily mass transportation during the stirring action. Very low rotational speeds could also cause pores, which are large voids about 0.1-0.5 mm in diameter [53, 59].

On the other hand, extreme process temperatures would create high copper diffusion in the aluminium matrix, leading to more and larger IMCs formation, hence an increase in hardness, more cracks, and lower ultimate tensile strength

(UTS) [49]. Macro- and microcracks could also be caused by poor metallurgic bonding between the large copper particles in an aluminium matrix, emerging a large discontinuity through the joint-line [61].

Issues that need addressing

Early efforts in Al-Cu FSW were focused on conventional-FSW for lap-joints or spot-welds; the published literature shows insufficient information regarding Al-Cu butt-joint welds by BFSW. In this regards, the aim is to identify the flow stability of the weld, as well as to characterize the formation of possible intermetallic compounds through the weld structure. It should be noted that the stability of the joint in FSW is challenging to achieve a defect-free interfacial dissimilar joint. In addition to an optimized flow, the control of the high chemical interaction between Al-Cu base metals is another consideration required to obtain a successful hybrid joint. This paper studies a butt-weld joint between AA6082-T6 and commercially pure copper plates using the BFSW method, by applying a fixed-gap bobbin-tool. The Al-Cu hybrid weld structure is subject of microscopic characterization, focusing on the material flow evolution in the SZ area. The impact of welding parameters on the Al-Cu flow bonding and evolution of the intermetallic compounds were identified by the interfacial microstructure at the position of the tool performance. The microscopic flow characterization can help to present a physical model for the elucidation of the material flow interaction at the proximity of the rotating tool in interaction with the mixing mass from Al-side and Cu-side of the weld.

8.2. Materials and Methods

8.2.1. Purpose

This chapter aimed to evaluate the internal flow mechanism observed in the Al-Cu weld structure and analyse the microscopic features within the Stir Zone (SZ). By comparing the internal microflow patterns between the cross-sections, the origins of the failure will be identified.

8.2.2. Materials

The BFSW process was conducted between the two dissimilar materials: pure copper (Cu), and a 6xxx series marine-grade aluminium alloy (AA6082-T6). The aluminium alloy AA6082-T6 was used as one of the strongest structural Al grades with excellent corrosion resistance, that is to provide similar conditions in tool interaction and chemical reactions during the process, in comparison with the copper.

8.2.3. Welding

Welding parameters are shown in Table 8.1. Chemical composition of the aluminium alloy is shown in Table 8.2.

Table 8.1. Parameters of the BFSW trial for the AA6082-T6-Cu plates.

Welding Parameters	amount
$D_{Shoulder}$ (mm)	21
D_{Pin} (mm)	7
$D_{Shoulder}/D_{Pin}$	3:1
Plates Thickness (mm)	6
Compression Ratio	3.75%
Spindle Rotational Speed, ω (rpm)	800
Feed Rate, V (mm/min)	400
Pin Thread Pitch (mm)	1.5
Number of Pin Threads	4

Table 8.2. Chemical composition of AA6082 T6.

Alloy 6082	
Chemical Element	% Present
Silicon (Si)	(0.70–1.30)
Magnesium (Mg)	(0.60–1.20)
Manganese (Mn)	(0.40–1.00)
Iron (Fe)	(0.0–0.50)
Chromium (Cr)	(0.0–0.25)
Zinc (Zn)	(0.0–0.20)
Titanium (Ti)	(0.0–0.10)
Copper (Cu)	(0.0–0.10)
Other (Each)	(0.0–0.05)
Other (total)	(0.0–0.15)
Aluminium (Al)	Balance

The bobbin-tool used was a fully-featured tri-flat pin with spiral scrolls on the shoulders (Figure 8.1). The tool was fabricated form H13 tool steel (560 HV hardness).

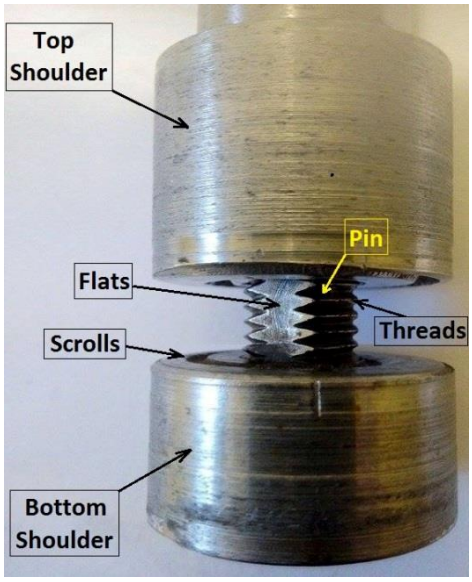

Figure 8.1. The bobbin-tool used for the Al-Cu welding trial.

The samples preparation procedure was followed with the method of previous works [145]**.** The BFSW welding trial was conducted by a 3-axis CNC machine (2000 Richmond VMC Model, 600 Group brand, Sydney, Australia) while the bobbin-tool was installed on a spindle motor (Fanuc control unit) with 14-horsepower capacity. The aluminium and copper plates were arranged in the butt-joint position (copper plate of the left (AS), and aluminium plate on right (RS), compared to the advancing movement of the tool through the joint-line), rigidly fixed by strap clamps, and no gap between the plates. The welding operation was done in room temperature, without any preheating, post-heating or post-cooling treatments. The tool spindle rotation was in the clockwise direction, relative to the plan view of the weld-line. During the process, the applied rotational and advancing welding speeds were kept (ω = 800 rpm) and (V = 400 mm/min), respectively. Schematic of the welding process and interaction between the tool and the workpieces are shown in Figure 8.2.

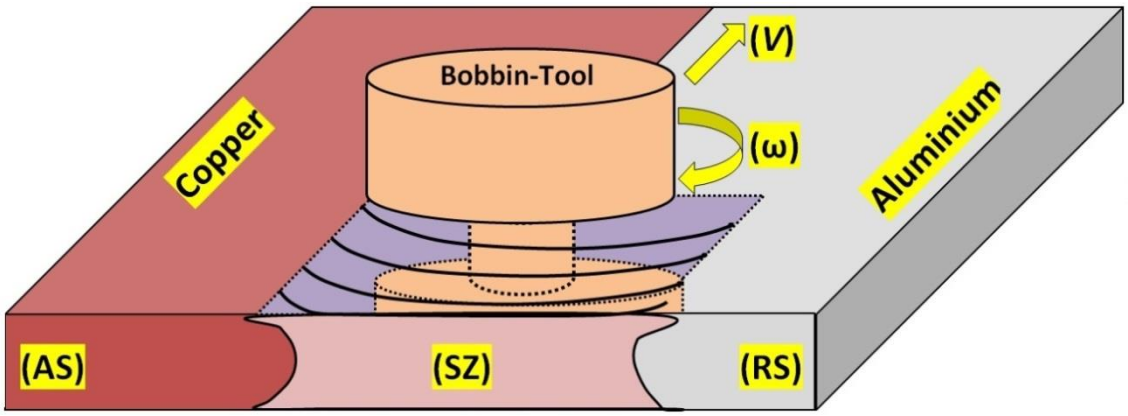

Figure 8.2. Schematic of the BFSW process; the bobbin tool in interaction with the AA6082 T-6 and copper plates.

8.2.4. Sample preparation

The Al-Cu welded plates were 6 mm in thickness. The plates were wire cut by an electro-discharge machine across the failed weld-seam areas on different cross-sections, perpendicular to the welding direction. The weld length from the edge of the plate until the centre of the failure area was approximately 45 mm. Individual samples cut were about 20mm in width, and 5-20mm in length (6mm thick).

For ease of handling, the samples were mounted in thermoplastic resin, and then ground using silicon carbide (SiC) papers of 180-grit, 400-grit, 600-grit, 800-grit, and 1200-grit fitted on a rotating wheel disc, spinning at 200 rpm. Water was used as a lubricant during grinding, and samples were rotated in 90-degree iterations till all scratches from the previous grit vanished.

The micro-polishing was done using a micro-cloth pad in a series of 9-3-1 μm diamond pastes. Final polishing was done using a 0.06 μm micro-cloth pad at 150 rpm and 5 lbs/sample for 5-15 minutes, using a Buehler brand MasterMet colloidal silica.

Samples were rinsed with cold water, ethyl alcohol, and dried under warm air, then the mirror-surface observed under an optical microscope after each polishing round or as deemed necessary.

8.2.5. Optical microscopy (OM)

The prepared cross-section samples were examined under a light optical microscope (Olympus Metallurgical Microscope, Tokyo, Japan) using the polarized exposure. Due to the contrast of colour between the copper and aluminium alloy, etching was shown to be unnecessary for this study, as the flow patterns within the BFSW weld region were demonstrated clearly.

8.2.6. Electron microscopy

For the metallurgical analysis, the scanning electron microscopy (SEM) was used, equipped with further elemental analysis using an energy-dispersive X-ray spectrometer (EDS) detector. The SEM observations were studied with a (JEOL 6100, JEOL Inc., Peabody, MA, USA) machine. The EDS elemental mapping for the spatial distribution of the composition and the similar point analysis of elemental weights were measured by an EDS detector (Oxford Instruments plc, Abingdon, UK), with the working voltage of 20 kV. The analysing software for processing of EDS data was AZtecLive & Ultim Max (X-Max version, Oxford Instruments plc, Abingdon, UK).

8.3. Results

8.3.1. Copper-aluminium overview of weld

The Al-Cu BFSW weld plate is shown in Figure 8.3. A continuous fracture line is observed in the middle of the weld-line, representative of the improper situation of the weld. Nevertheless, the weld structure can reveal the origins of the failure, identifying how the interaction between the tool and substrate results in the occurrence of structural defects. Moreover, the internal flow patterns are useful to evaluate the performance of the applied operational welding parameters in emerging of the discontinuity defect depended on the flow failure within the weld region. The further microscopic measurements of the weld were progressed on the cross-sections of the weld. In this regards, the weld samples were selected from different sections along the weld, as shown in Figure 8.3.

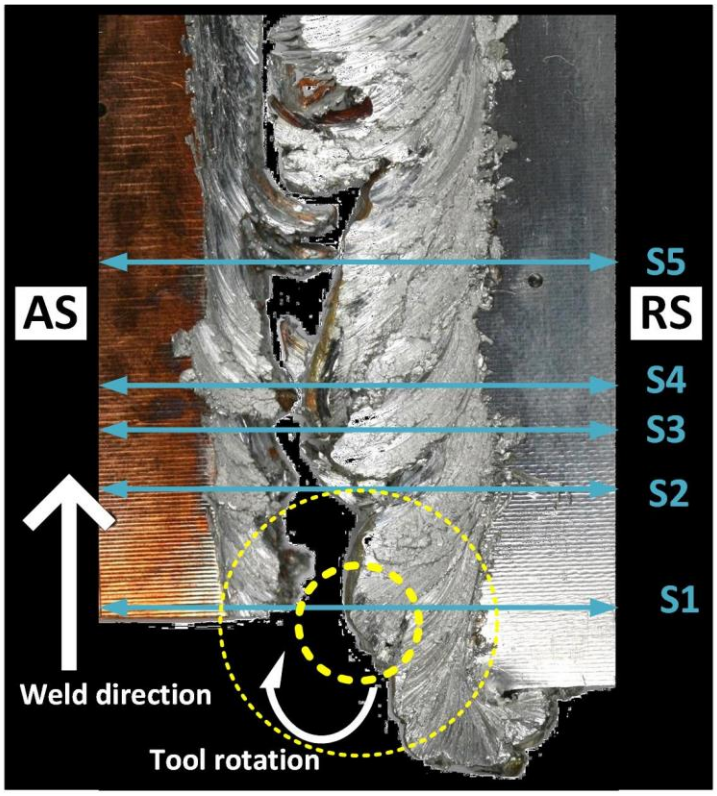

Figure 8.3. Visual surface analysis of the Al-Cu hybrid BFSW weld. The top-view of the weldment; copper plate on the AS (left) and AA6082-T6 aluminium plate on the RS (left).

8.3.2 Cross-sections; Cu-side (AS), Al-side (RS)

The multiple cross-sections are shown in Figure 8.4, according to the selected sections (S1 to S5) from the weld plate shown in Figure 8.3. These represent different flow patterns within the weld cross-section, as the rotating tool moves forward along the weld line. The interaction between the cupper and aluminium flow layers are different on the Cu-side (AS) and Al-side (RS) of the weld.

In all cross-sections in Figure 8.4, the weld structure shows large internal cracks in the middle of the stirring zone, leading to the spontaneous fracture, and subsequently, the failure of the final weldment. The material loss at the position of the failure in mid-SZ, interrupt the flow-lines at the middle of the weld region. However, the deposited dissimilar flow layers at the AS and RS borders, and near the top and bottom surfaces near the sub-shoulder regions, can give some useful insights about the flow mechanism during BFSW processing of the dissimilar welds.

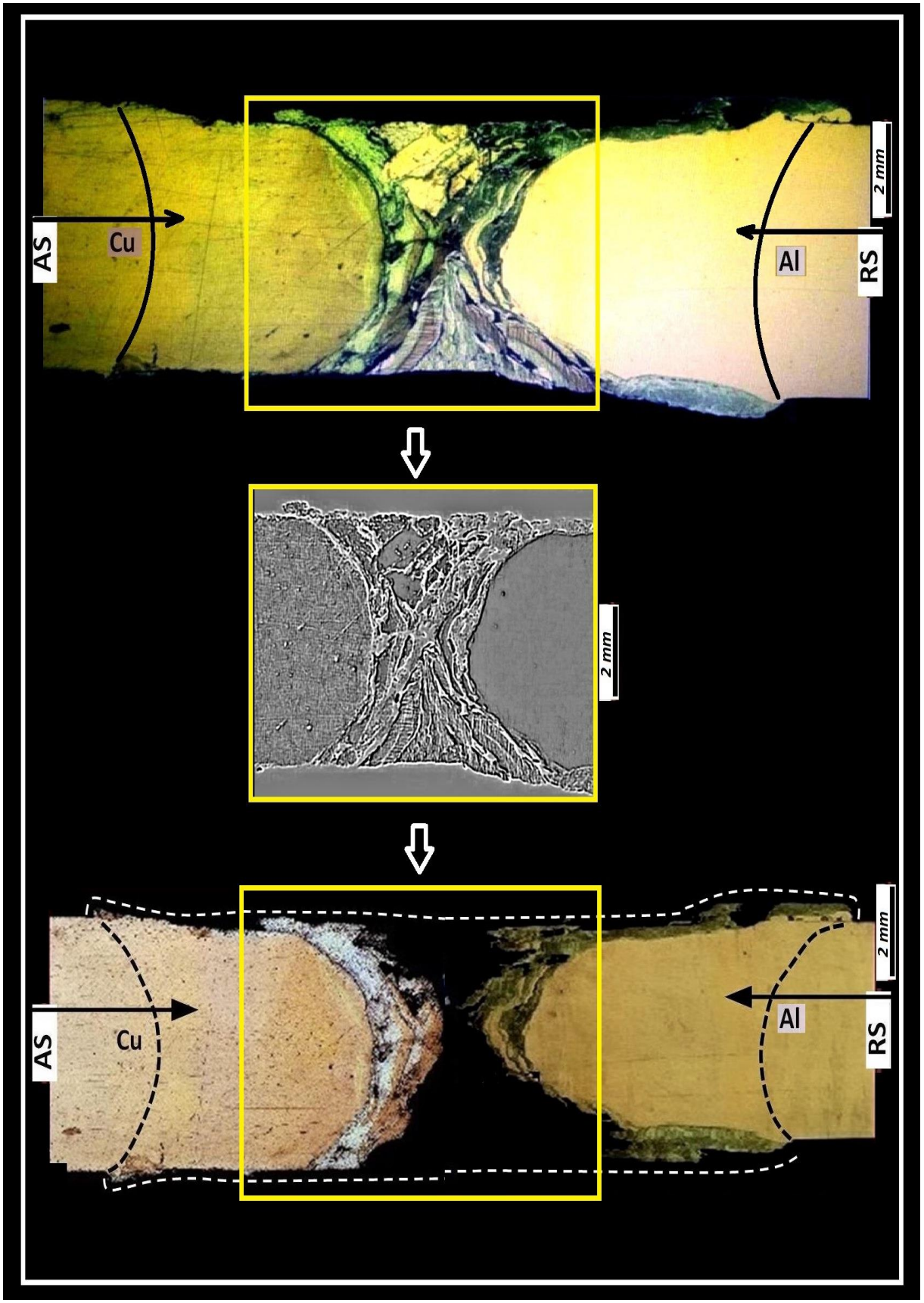

Figure 8.4. Cross-sections on the hybrid weldof Al-Cu BFSW, representative of dissimilar flow interaction between the aluminium and copper mass layers; Cu-side (AS) and Al-side (RS).

Because of the suitable contrast between the copper and aluminium mass flows, the samples can provide a clear flow visualization without using any etchant reagents. In below, some more microscopic details of the microstructure for both Al-side and Cu-side of the hybrid weld will be observed with a focus on flow mechanism and metallurgical explanation of the weld failure.

A general observation of the progression along the weld is that there are large pieces of copper that are firmly bonded to the aluminium (from mid-SZ towards the RS). Within these are regions of pure copper and areas of intermetallic, which could indicate a well-stirred zone. There are also large areas of IMCs underneath the shoulders that are predominately aluminium with small fragments of copper. All these IMCs have a lamellae structure to them, and this is especially pronounced under the shoulders. Multiple alternating large bands of copper and aluminium are also noticed throughout the weld region near the AS border. The general flow features trend apparent on the Cu-side at the AS border is the solid copper to be intact up to the hourglass border, with a thin layer of aluminium rich material under the shoulders. There is also a fragmented area inwards of the hourglass border, with poor adhesion.

8.3.3 Detailed examination of regions of interest through the weld cross-section

The stirring zone has multiple morphological features that can be identified in Figures 8.5-8.10: large deposits of material; both Al and Cu, a stirred area at the sub-shoulder regions with fragmented material within it (intermetallic region), large voids, and the formation of lamella patterns as the intermixing between the Intercalated layers of Al and Cu.

Al-side (on the RS border)

Figures 8.5 and 8.6 show the formation of intermixing stirring zone at the Al-side of the weld towards the RS border. Two main microscopic features of the material formability at the SZ are lamellae-layered flow patterns and the IMCs regions near the sub-shoulders (Region 1, Figure 8.5), and deposited lamellae patterns in a large Cu fragmented pieces (Region 2, Figure 8.5).

The Fragments of copper particles are observed in an Al matrix near the shoulders. This formation of material near the shoulders seems to be consistent throughout the weld sections, as highlighted as the Region 1, in Figure 8.5. The lamellae formed swirl patterns but are bounded in the Cu matrix and do not extend to the Al matrix. The small copper particles have finer lamellae structures, which could be interpreted as material that has been processed multiple times around the tool. Similarly, in Figure 8.6, IMCs and lamellae formation as observed are mostly visible in the middle of the stirring zone and far from the RS border; where the fragments of copper particles are noted to be in the Al matrix. The large pieces of copper near the RS border (Al-side) appear with a formation of lamellae structured intermetallic compounds within them. However, the deposited pieces of copper at the middle of

the SZ, are deposited with large discontinuity crack between the and the Al-matrix. This can be related to the viscoplasticity of the Al- and Cu- mass layers, during the stirring, and differences in density and thermal expansion of them within the dissimilar joint.

Cu-side (on the AS border)

Figure 8.6 showed the large pieces of copper are gradually detached from the base metal in the SZ, approximately where the pin is crossing through. Simultaneously, the stirred aluminium appears to be attached to the Cu base metal, connecting to the copper pieces, though still showing large voids in between (Figure 8.7). Copper particles in an aluminium matrix are commonly observed, but the reverse is not often found. Figure 8.8 shows Al pieces found in a Cu matrix (Region 1, Figure 8.7). These are larger in size compared to what is seen of the Cu particles in an Al matrix, and it appears they seeped in through the cracks in the copper matrix rather than being shaped in it. Moreover, small copper particles (less than 10μm in size) appear to be distributed in the Al matrix (Figure 8.8, Region b). In Figure 8.9, a clear division is seen between the large pieces of copper and aluminium. What is more apparent is the lamellae layers of copper, dispersed within the Al-matrix (Region 2, Figure 8.7). These individually separated copper pieces in the Al-matrix can be a plausible place for the formation of IMCs.

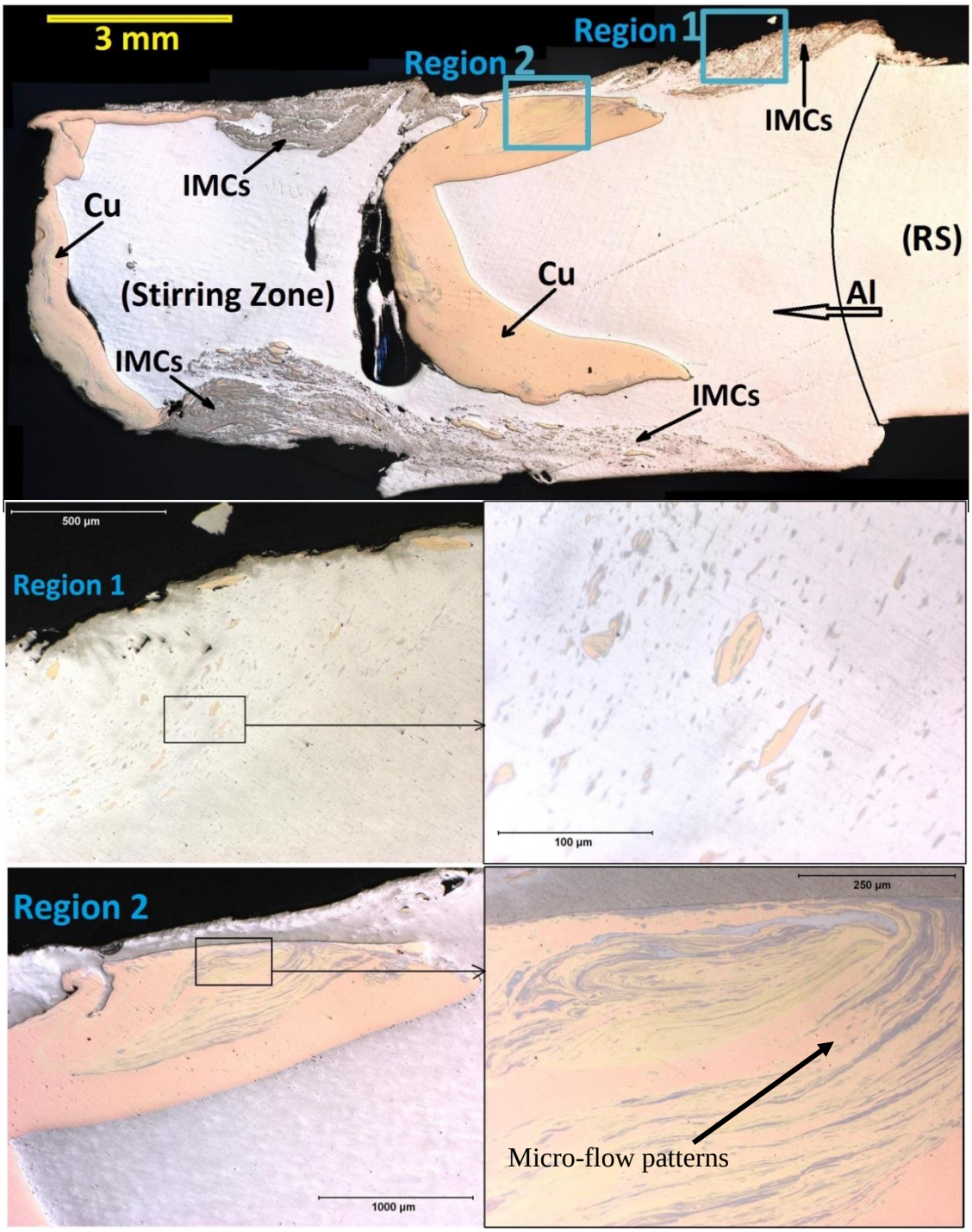

Figure 8.5. Optical micrograph of the weld cross-section from Al-side location (sample S1 from Figure 8.4). Regions of interest. **Regions 1;** formation of intermetallic compounds (IMCs). **Regions 2; l**amellae formation in a Cu packet.

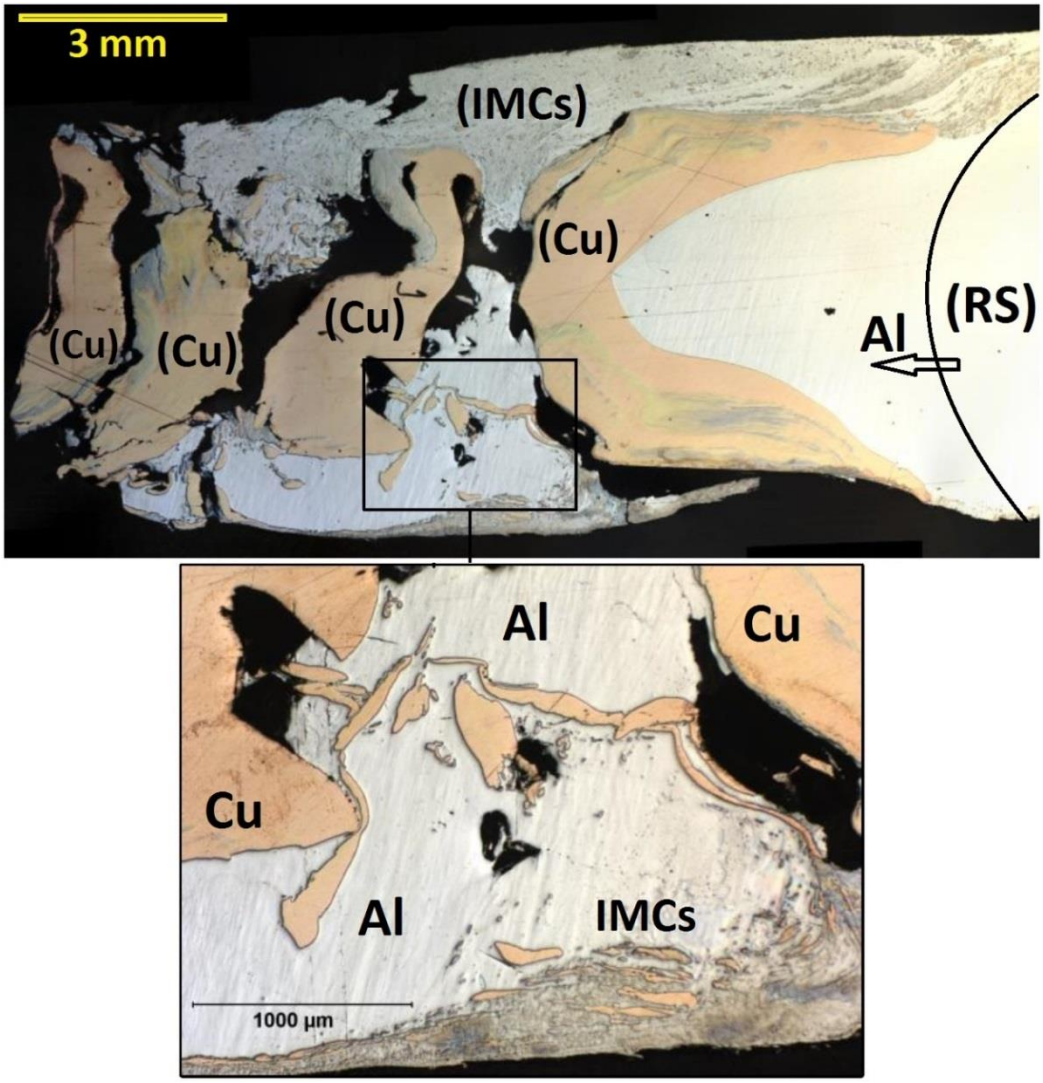

Figure 8.6. Large copper particles in the mid-thickness region. Al-side, (sample S4 from Figure 8.4).

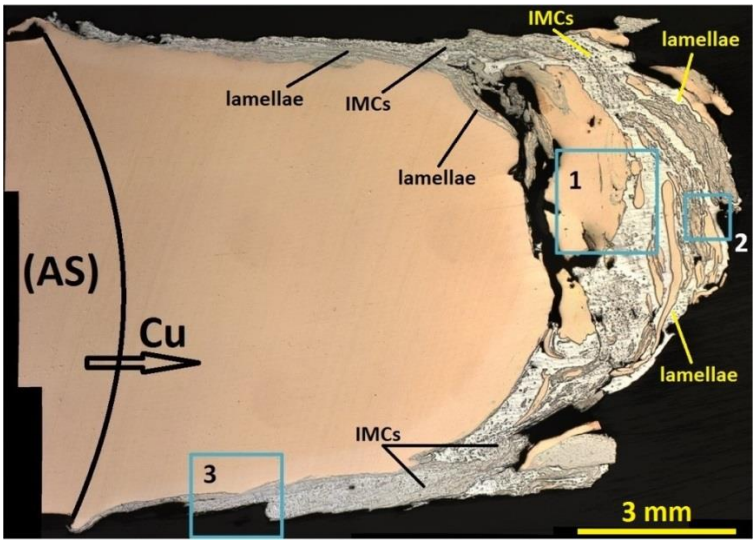

Figure 8.7. Advancing side, Cu. (sample S5 from Figure 8.4).

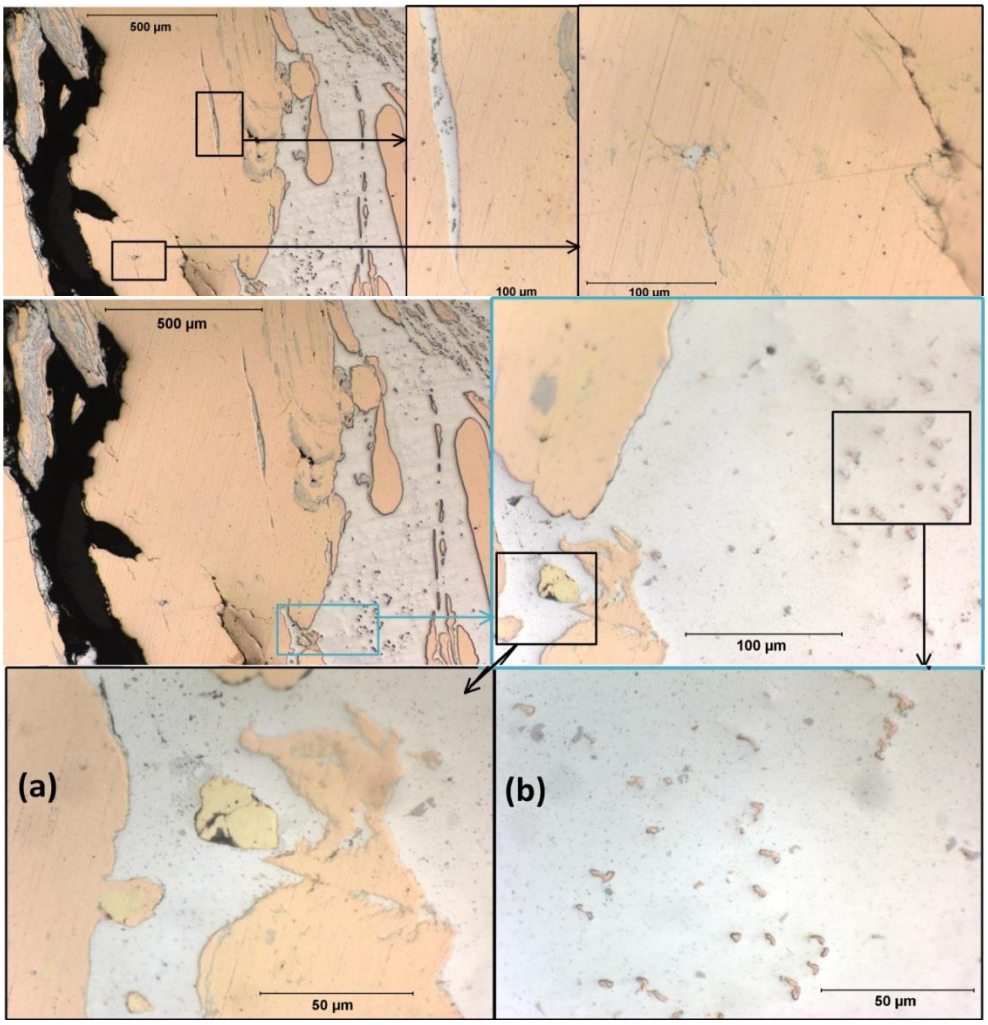

Figure 8.8. Al particles in Cu (Region 1 from Figure 8.7). (a, b) Cu particles in Al matrix.

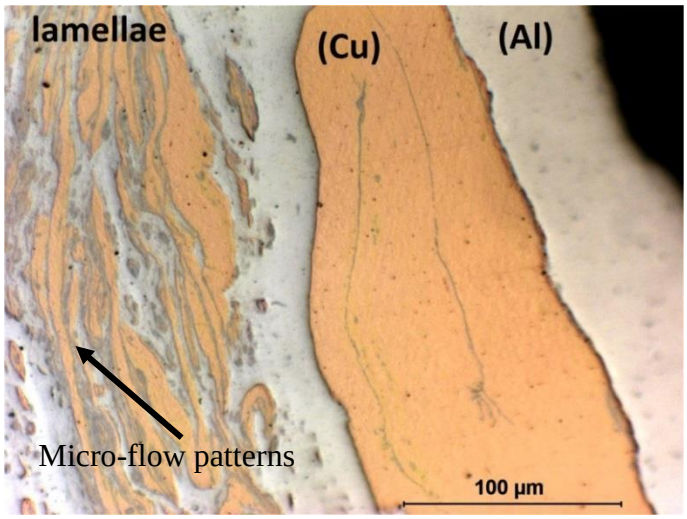

Figure 8.9. Intersection, Cu lamella formation in between Cu- and Al- large particle lumps. (Region 2 from Figure 8.7).

The sub-shoulder region on the Cu-side of the SZ (region 3 from Figure 8.7) indicates fragmented particles pattern similar to the Al-side (Figures 8.5 and 8.6). The magnified micrographs of the sub-shoulder region of the Cu-side are shown in Figure 8.10. An aluminium mix is observed integrated with the pure copper matrix through a structured lamella division. As the sub-shoulder pattern moves away from the centre, the stirred aluminium changes from a lamella structured formation with the copper, to having copper particles within the aluminium matrix. The small copper particles show signs of intermetallic formation within them. This seems to be a consistent formation as shown in the Cu cross-sections taken from different weld sections (observable in Region b, Figure 8.8). Cracks are also noticed in this area, as it is appearing between the lamellae formed structure and the IMCs distributed particles.

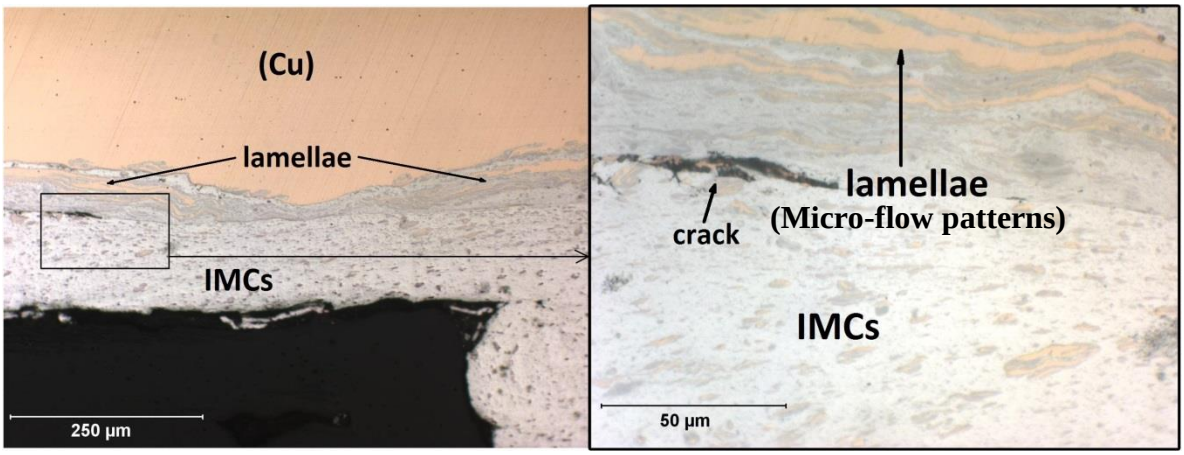

Figure 8.10. Sub-shoulder region from Cu-side of the stirring zone, located on the AS border of the weld. (Region 3 from Figure 8.7).

8.3.4. Electron microscopy

For further evaluation of the microscopic features driven from the flow interaction, the SZ was analysed by the SEM and relevant EDS mapping.

Based on the observation of the optical micrograph image, the small particles in the Al matrix appear to us as Cu pieces; this has been confirmed by the SEM-EDS results (Figures 8.11-8.14).

Figure 8.11 demonstrates the microscopic details of the SZ with a focus on the sub-shoulder region, where the dispersed Cu-based particles from the AS enter through the stirred zone, with a higher concentration at the sub-shoulder region. The relevant EDS elemental map (Figure 8.12) confirmed that copper is the main element of the composition of these dispersed particles. This is following the nature of the stirring action which provides a stirred mass without uncontrolled reaction between the mass compositions.

The stirred mass at the mid-SZ region shows a layered deposited pattern, typically named as the lamellae swirling pattern. This is a direct outcome of the stirring at the proximity of the pin position. The shearing induced by the features of the pin threads could be responsible for this layered deformation. The changing of the colour between the copper and aluminium through this pattern implies the formation of an intermetallic layered band. To confirm this hypothesis, observed lamellae patterns were analysed by EDS elemental mapping and point point (Figures 8.13 and 8.14, respectively) to analyze the chemical composition of the mass. The EDS elemental map (Figure 8.13) shows an extreme mixing of the mass between the Al and Cu, as the colour contrasts of these two elements illustrate a proper level overlapping, with similar colour contrast. The elemental point analysis of the lamellae pattern also confirms that, although this region belongs to the Cu mass, a suitable level of mixing of Al alloy particles was observed from the analysed layers. Therefore, efficient mixing of the Al and Cu in this lamellae region have occurred.

A lamellae formation in a Cu matrix was also observed under the SEM. The EDS elemental map results show that both Al and Cu are present, but are in the form of IMCs. The elemental point analysis (Figure 8.14) presents findings of the percentage of individual materials; it shows that Cu is the major material, while the presence of carbon and aluminium are also high.

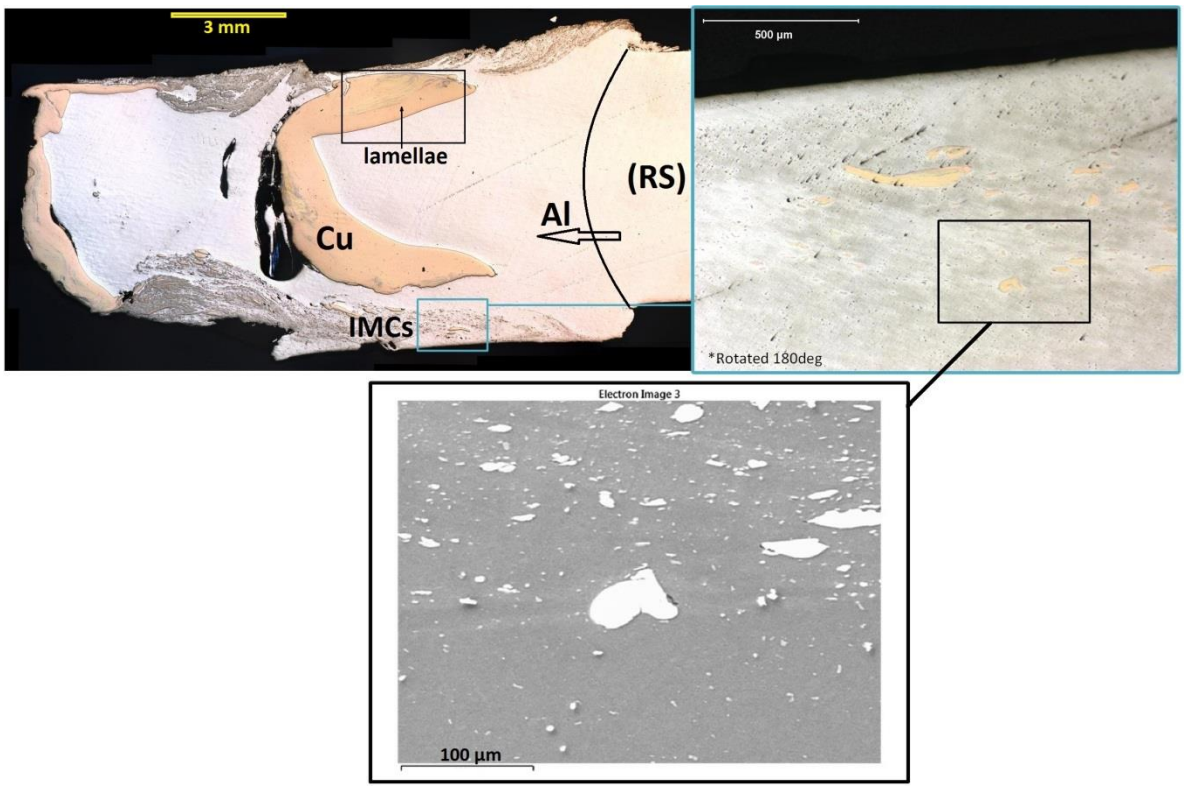

Figure 8.11. SEM image of IMCs situated at the sub-shoulder region from the Al-side (near the RS border).

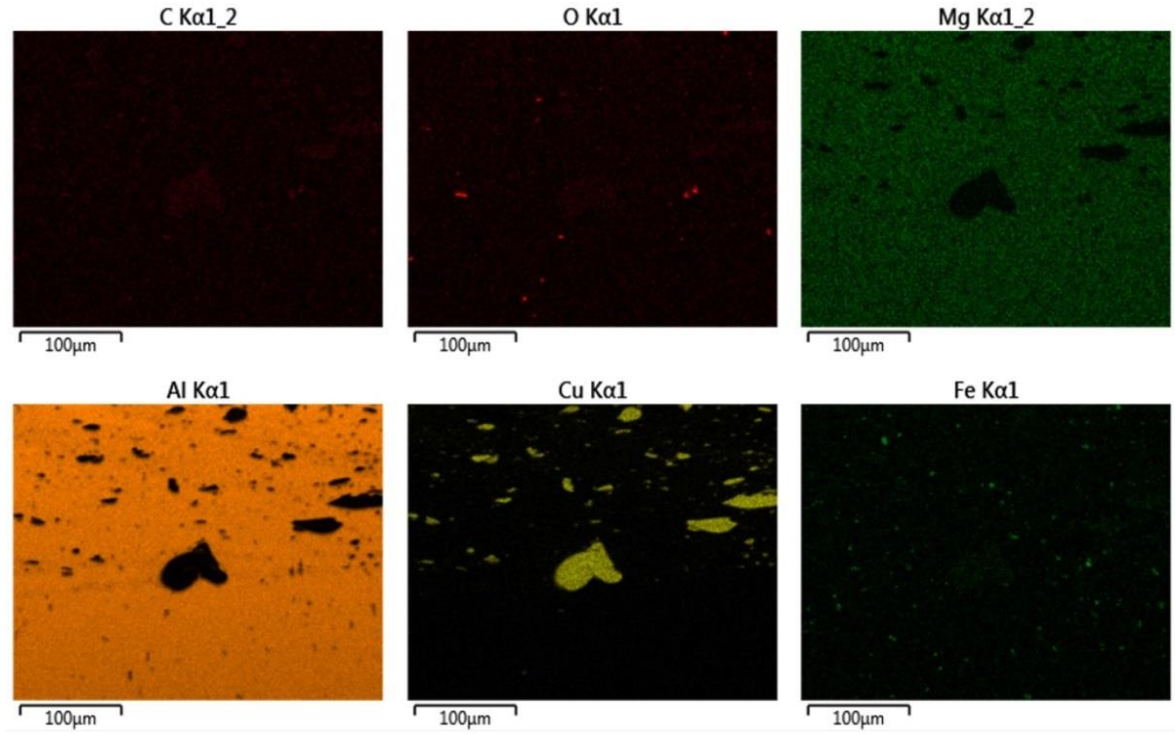

Figure 8.12. Results of the EDS elemental map, for the sub-shoulder IMCs particles, shown in Figure 8.11.

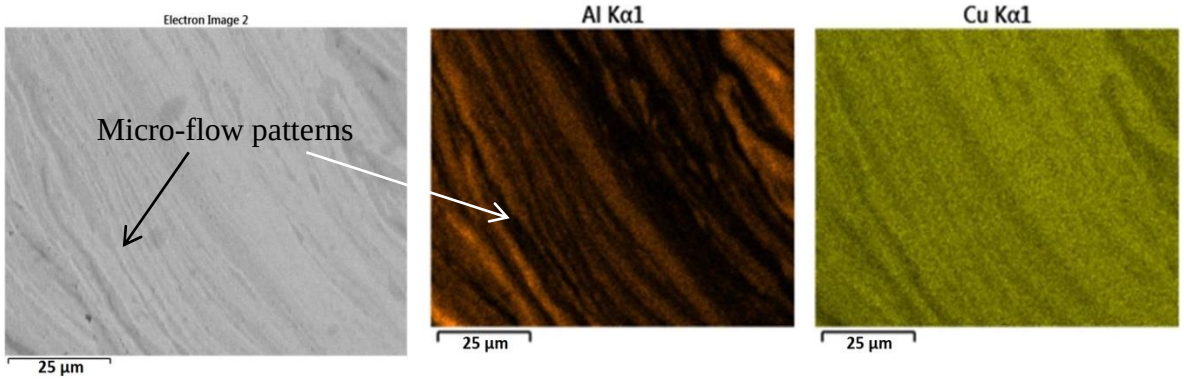

Figure 8.13. The EDS elemental map for the lamellae pattern formed within the copper lumps within the stirring zone, shown in Figure 8.11.

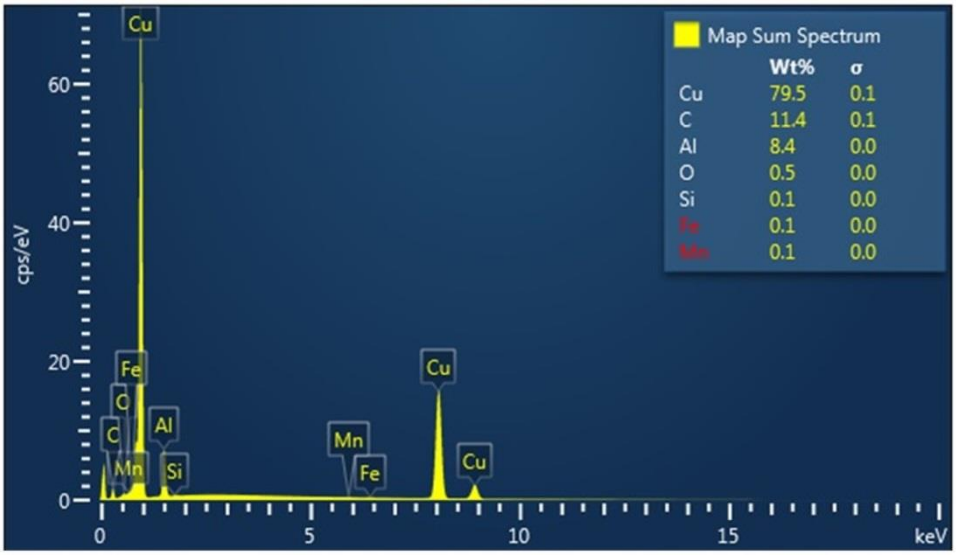

Figure 8.14. The EDS elemental point analysis for the lamellae pattern in Figure 8.13. The chemical composition of elements is listed by the weight percentage.

8.4. Chapter Discussion

8.4.1. Metallurgy of the weld

The microscopic measurements of the Al-Cu hybrid BFSW weld were investigated by optical and electron microscopy. The micrographs from the stirring zone both in Al-side and Cu-side identified different flow-based intermixing layers, IMCs compounds, and intercalated lamellae morphologies of swirling bands within the dissimilar weld breadth. The EDS analysis characterized the chemical composition of Al-Cu complexity structures of IMCs and lamellae layers, found within both the AS and RS borders of the dissimilar weld. Most of the time, these microscopic features are observed as a mixture together, which makes it hard to accurately recognise the specific regions for the original formation of each within the stirring zone. However, the IMCs are mostly detected in the sub-shoulder regions, between the fragmented Cu particles, or between the swirling lamellae layers.

Although the cross-section micrographs revealed the details of the intermixing patterns as the result of the plastic deformation in the interaction between the tool and the Al-Cu substrates, the stirred structure still could not achieve a fully homogeneous mixture. This is the main challenge during the BFSW processing of the dissimilar Al-Cu weldment. More specifically, regarding the copper mass entered into the stirring zone, the interaction between the plastic layers shows large pieces of copper-lumps with lamellar intercalated features deposited within the weld structure towards the RS (Al-side). Far from the middle of the stirring zone, the fragmentation of Cu particles at the sub-shoulder leads in formation of a vortex-shaped mixture near the top and bottom surfaces of the cross-section, consists of rich IMCs phases.

Formation of large voids and cracks within the stirring zone were also inevitable in observed processed cross-sections. These discontinuity defects mostly occurred at the boundary layers between the Cu and Al interface. This can be originated from the inefficient or inadequate mixing plastic flow between the Cu and Al mass layers entering into the stirring zone, from the AS and RS borders, respectively.

Moreover, the different density of the Al and Cu mass, and the brittle nature of the IMCs phases distributed through the stirring zone can also intensify the formation of the discontinuity layers between the dissimilar deposited layers.

Irregular distribution of Al- and Cu-layers, and formation of IMCs-rich morphology (flake-shaped phase) causes insufficient refilling during the mass-circulation at the proximity of the rotating tool. Therefore, the inadequate intermixing of the flow layers interrupts the integrity of the flow deposition at the trailing edge of the tool. Therefore, the weld-seam forms with some internal flow-based defects, e.g. voids or cracks.

8.4.2. Flow mechanism around the rotating tool

The main challenge during this chapter was to obtain a defect-free joint for comparison. However, existing weld defects within the weld seam can explain the defect formation mechanism with a flow-based approach in relationship with the tool features and interaction between the tool and substance.

The transportation of the copper mass packets around the pin was observed in a unique material flow pattern, not previously identified in the literature. Based on the microstructure observations, here, the results propose a flow-based explanation for the mass flow transportation mechanism around the rotating pin. The sequence of the flow mechanism demonstrated in Figure 8.15.

Reference to Figure 8.15a; the clockwise tool rotation begins the mass flow at the AS by grabbing copper mass via pin features (threads-flats). The threads-flats features of the pin provide an efficient frictional condition at the surface of the rotating pin, which increases the adhesion of the material to the pin and its transportation and release, to pack the material towards the retreating side. As the tool travels through the interface, the copper mass at the leading edge of the pin experience transverse transportation towards the RS. Simultaneously, the aluminium mass at the RS undergoes a reverse flow towards the trailing edge of the pin, opposite to the tool travel direction, see Figure 8.15b. The relocation of the aluminium mass, makes extra space for the yielded copper mass to have more lateral thrust towards the RS to refill the primary locus of the aluminium. In this regards, the features of the flat pin would capture more volume of the copper mass and contribute to mass transportation. The copper mass packet would arrive from the AS to the RS of the pin; it is now surrounded by the aluminium mass thoroughly (Figure 8.15c). The extra mass-circulation around the pin intensifies the thrust of the copper mass packet stuck to the pin and eventually separates it from the position of the pin.

Consequently, large volumes of the copper packets get deposited at the retreating side Figure 8.15d, due to the combination of the clockwise rotation and forward movement of the tool which creates two opposite flow directions at the RS of the pin. The rotating pin continues the stirring action whereby the mass-circulation continues from the retreating side to be deposited at the advancing side. However, the deposition of the copper mass packets, swept at the RS, makes it hard for the pin to laterally displace them again to the backside of the pin to complete the circulation towards the RS. This can cause a deficit in the material flow at the trailing edge of the tool in the form of incomplete RS-to-AS mass transportation. This is where the loss of the mass occurs near the AS. At the same time, the further tool travel consolidates the stirred mass deposited behind the tool, with a discontinuity defect indicating a weak joint.

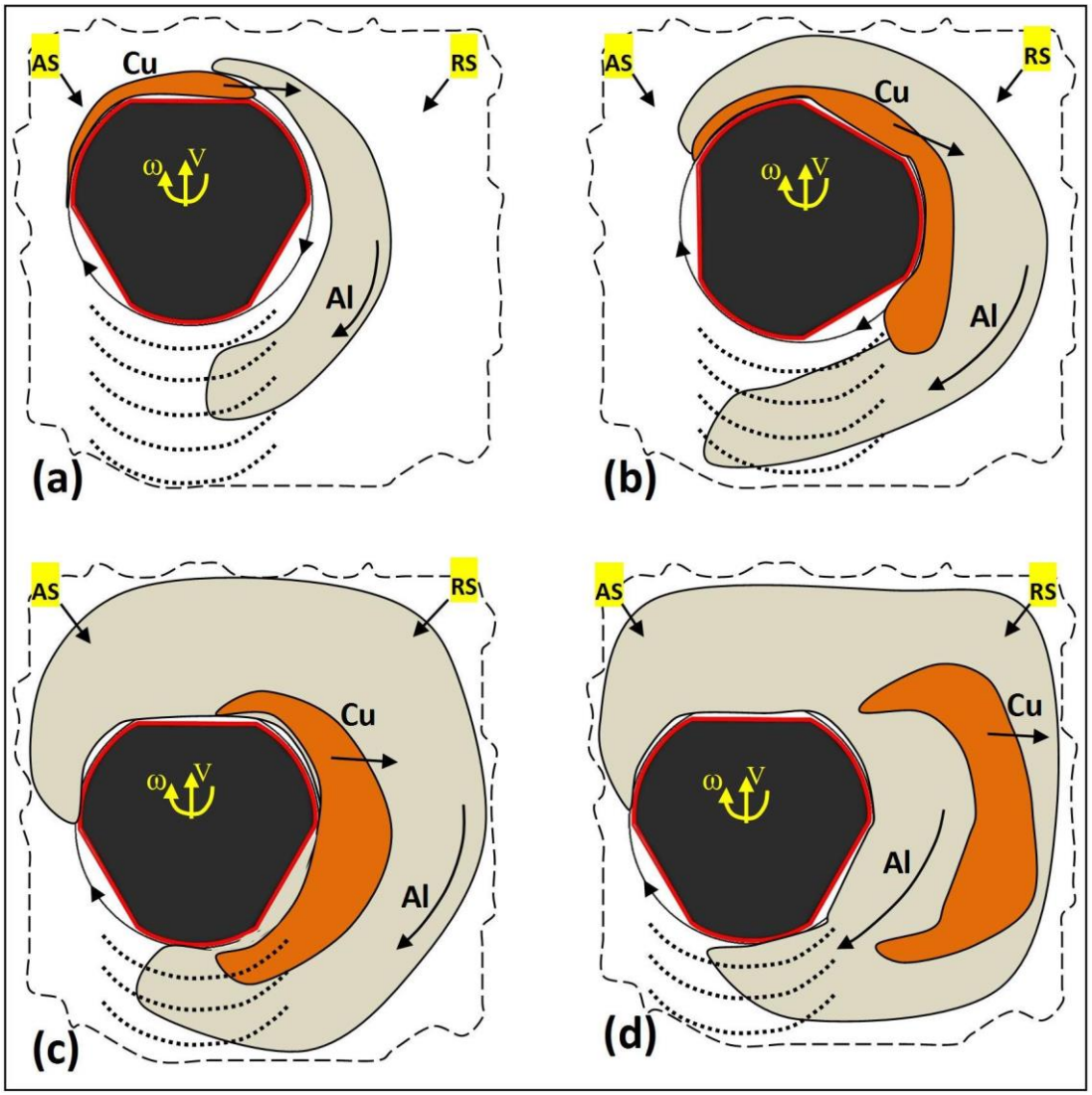

Figure 8.15. (a-d) Sequence of the mass flow transportation around the rotating pin in interaction with the Al-Cu plates.

Based on the flow mechanism in the BFSW process, there are two main regions induced by plastic deformation that identify as part of the SZ.

(1) The sub-shoulder region; where the top and bottom shoulders are acting upon the workpiece, these sub-shoulder regions are induced by plastic deformation caused by the tool rotation. The typical flow features induced by the top and bottom shoulders are demonstrated in Figure 8.7 and Figure 8.13, respectively.

(2) Mid-thickness region; which undergoes a dominant flow induced by the pin action. The most evident flow feature in this region is the lamellae-shaped swirling flow patterns within the copper mass deposited towards the Al-side (RS), see Figure 8.8 and Figure 8.12. This flow complexity can be related to the geometric features of the pin, specifically the threads which can induce a micro-circulation through the stirred layers of the mass.

Besides the mechanical friction action from the shoulders, the shoulder surface has a spiral scroll feature that would cause more localised deformation near the surface of the workpiece. The outcomes can be observed as a turbulent flow regime at the sub-shoulder areas with fine mixing of Cu particles in the Al matrix. The uniform dispersion of the Cu particles at the Al-side (RS) is evident; this can attribute to the deformation induced by the shoulder scrolled surface, as well as the deformability of small pieces of copper. This formation aligns with another work [145], where the FSW tool offset towards the Al-side meant that smaller copper particles are mixed in and a better interface is created.

The EDS results in Figure 8.15 implies that some shredded Cu particles exist without reacting to the elements of the AA6082-T6 alloy. This can be attributed to the fast cooling at the sub-shoulder region, where the mass is in contact with the free-air once the tool leaves the location of the stirring action. To identify the history of the dynamic recrystallization at the sub-shoulder region, further metallurgical characterisation is required to analyse the composition and microstructure of the Cu dispersed particles with a focus on the plausible formation of the intermetallic phase at the interface of the Cu-Al phases. This is an interesting subject for future studies, as the larger copper particles contain some lamellae-shaped pattern in the middle, which indicates presence of intermetallic compounds.

The clockwise transverse transportation of the plasticised mass from the AS towards the RS around the proximity of the rotating tool causes a circulating flow condition which can be responsible for the lamella pattern. As the generated heat at the middle of the SZ is in a higher rate compared to the sub-shoulder region, there are more suitable conditions for atoms to interact together and form intermetallic compounds, such as the ones within these lamella regions. This has been presented in Figure 8.13 and Figure 8.14, confirming the existence of the intermetallic compounds at the position of the lamella patterns.

Previous studies have shown that Cu malleability is not enough to achieve a proper mechanical stirring (Cu requires a homologous temperature close to 0.8), hence detached large Cu particles would be harder to flow in the Al matrix, this is shown clearly at the mid-thickness region (see Figure 8.6).

8.4.3. Implications for dissimilar welding processes

The difference in density, strength, and the viscoplasticity of the stirred materials would cause defects in solid-state welding. The chipped formation of the large copper pieces embedded within the Al matrix is an example of defect due to difference in deformability.

The weld examined in this research showed a discontinuity line at the interface of the weld. This could mean that the applied welding operational parameters led to the failure of the weld. The origins of the welding failure can be attributed to the insufficient flow circulation at the SZ to transport the Al and Cu in a uniform flow path and provide a homogenous mixing regime at the trailing edge of the tool, where the mass deposited as the final joining layer.

There are some possibilities which can affect the stirring action to fail the flow regimes. Stirring is a mechanical action leading to plastic deformation of the workpiece material, but the macro observation of the cross-sections shows a poor deformation pattern for the Cu material deposited in SZ. The existence of some large chunky-shaped pieces of copper suggests poor deformability of the Cu mass under the applied operation condition. Higher density and hardworking strength of the copper compared to the Al-alloys can explain the inconsistency in the deformation of the Cu under the same stirring condition induced by the tool. Therefore, the unsuitable viscoplasticity of the Cu stirred mass can lead to failure of the plastic flow transportation between the AS and RS at the position of the tool rotation.

8.4.4. Limitations of this work

The main limitation was that a successful weld is not available for comparison. Ideally, multiple welds might be performed to provide the means to compare flow regimes. In this regard, the welding speeds (rotational and feed rate) can also be modified to induce a higher rate of plasticising through the stirred mass. Furthermore, the tool geometry also can be modified to provide more efficient material transportation flow between the AS and RS during the rotation and mass-circulation around the pin.

8.4.5. Implications

Further analysis of the current samples can be conducted. Studying the grain boundaries using the developed metallographic etchants, as well as additional analysis using the Electron Backscatter Diffraction (EBSD) methods, would contribute to understanding the weld better.

Possible future research topics that might be helpful for better understanding BFSWing of dissimilar materials could be regarding the material processing mechanism in dissimilar Al-Cu BFSW processes, and characterisation of other regions of the weld can be useful to build a more comprehensive theory. Further analysis of the intermetallic compositions in a different region of the weld can also elucidate the metallurgical aspect of the BFSW welding process for dissimilar joints of Al-Cu.

8.5. Chapter Conclusions

This research inspected a dissimilar hybrid butt-joint of Al-Cu processed by the BFSW technique. This chapter aimed to examine the flow-based features of the materials mixing occurring during the stirring mechanism in the weld region. The colour contrast between the aluminium and copper provides a suitable level of flow visualisation without applying any etchant reagent for the cross-section of the weld. This allowed the microscopic measurements to study the flow features of the weld in a direct scheme. The microscopic details of the weld region were analysed by the metallographic measurements using optical and electron microscopes. The observed flow features of the Stir Zone (SZ), and the trace of the intermetallic formation confirmed the mixing of the Aluminium and Copper under the rotating bobbin tool. However, inconsistency of the flow regimes and insufficient engagement of the tool and substrate led to the failure of the weld by creating a discontinuity near the Cu-side. By comparing the internal microflow patterns between the samples of the broken joints, it is possible to look for signs of what may improve the welding process or reasons for the joint failure, as the outcome of the improper interaction between the tool and substrate.

CHAPTER 9: Development of Metallographic Etchants for the Microstructure Evolution of A6082-T6 BFSW Welds

Chapter Summary: The solid-phase joining of A6082-T6 plates by bobbin friction stir welding (BFSW) is problematic. Better methods are needed to evaluate the microstructural evolution of the weld. However conventional Al reagents (e.g. Keller's and Kroll's) do not elucidate the microstructure satisfactorily, specifically regarding grain size and morphology within the weld region. Innovative etchants were developed for metallographic observations for optical microscopy. The macrostructure and microstructure of A6082-T6 BFSW welds were clearly demonstrated by optical microscopy analysis. The microetching results demonstrated different microstructures of the Stir Zone (SZ) distinct from the Base Metal (BM) and Heat Affected Zone (HAZ) & Thermo-mechanical Affected Zone (TMAZ). The micrographs showed a significant decrease in grain size from 100μm in BM to ultrafine 4-10 μm grains for the SZ. Also, the grain morphology changed from directional columnar in the BM to equiaxed structure in the SZ. Furthermore, thermomechanical recrystallization was observed by the morphological flow of the grain distortion in HAZ and TMAZ. The etchants also clearly show the polycrystalline structure, microflow patterns, and the incoherent interface around inclusion defects. Chemical compositions are identified for a suite of etchant reagents for metallographic examination of the friction-stir welded A6082-T6 alloy. The reagents have made it possible to reveal microstructures not previously evident with optical microscopy.

This chapter is a derivative of the following publication:

Tamadon, A.; Pons, D.J.; Sued, K.; Clucas, D. Development of Metallographic Etchants for the Microstructure Evolution of A6082-T6 BFSW Welds. Metals 2017, 7, 423.

DOI: https://doi.org/10.3390/met7100423.

9.1. Introduction

Friction stir welding (FSW) was introduced by the welding institute (TWI) [74, 148] as a solid-state joining process whereby a rapidly rotating tool is physically moved along the interface of two plates [4, 67]. As the weld-line bond is formed, the material from the advancing side (AS) and retreating side (RS) mix together to form the bonding layer [66], in a solid phase mixing process. A material that would be attractive to weld with the FSW method is aluminium 6082-T6. This grade, particularly the T6 condition, is important in ship-building and marine structural

applications. However the material suffers from poor weldability using FSW [149]. One of the obstacles to better understanding the poor weldability is the difficulty of visualizing the microstructure of the weld region [78, 149-151]. The material does not respond to many etchants, hence it is difficult to visualize the grain boundaries and the internal flow features [149, 152, 153]. This chapter presents a new method for etching A6082-T6 to show the microstructure.

9.2 Literature

Background to friction stir welding

To increase the productivity of FSW and decreasing of structural defects, various modifications have been progressed on Conventional-FSW (CFSW) [67, 154]. Bobbin friction stir welding (BFSW) is a variant where a symmetrical tool (consisting of two shoulders, one on each side of the workpiece connected by the tool pin) creates a fully penetrated butt joint by stirring and mixing of the plasticised material [64, 81, 155]. The schematic of the BFSW process for the butt-joint position is shown in Figure 9.1a. The process has demonstrated capabilities in industrial applications such as fabrication of spacecraft fuel tanks [74], pressure vessels [66], shipbuilding [81] and marine superstructures [108, 156].

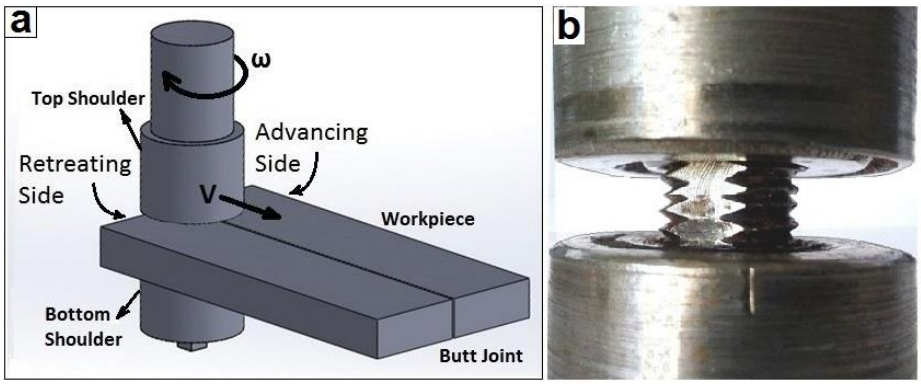

Figure 9.1. (a) Schematic of the BFSW process, (b) Geometric features of the bobbin tool.

Characteristics of aluminium 6082-T6 in BFSW

A6082-T6 is a useful marine grade aluminium alloy with excellent mechanical properties. It is metallurgically stabilized making it suitable for structural applications [81]. It is an Al-Si -Mg alloy which is grain-refined by addition of manganese (Mn) [157]. The standard element composition for the selected A6082 alloy is presented in Table 9.1. Typical material properties for A6082 include weldability, machinability as well as excellent corrosion resistance [110]. Besides, it has the highest strength of the 6xxx series alloys, making it suitable for structural

applications in highly stressed positions including bridges, shipbuilding and marine superstructures [152, 153]. Since A6082 is a heat treatable alloy, strength is reduced in the weld region [75]. An aging or tempering heat treatment is used to stabilize the microstructure and increase the mechanical properties [156].

Table 9.1: Element composition of the A6082 Al alloy (wt%) [158].

Chemical Element	% Present
Silicon (Si)	(0.70–1.30)
Magnesium (Mg)	(0.60–1.20)
Manganese (Mn)	(0.40–1.00)
Iron (Fe)	(0.0–0.50)
Chromium (Cr)	(0.0–0.25)
Zinc (Zn)	(0.0–0.20)
Titanium (Ti)	(0.0–0.10)
Copper (Cu)	(0.0–0.10)
Other (Each)	(0.0–0.05)
Other (total)	(0.0–0.15)
Aluminium (Al)	Balance

The most common temper for A6082 is the T6 heat treatment process, which is a precipitation hardening procedure including three time/temperature cycles; solutionising, quenching and artificial aging [150, 159]. For details of the T6 heat treatment for A6082 see [6, 160]. Solid solution strengthening involves formation of a single-phase supersaturated solid solution via quenching [68]. Unlike ordinary tempering, alloys must be kept at elevated temperature for some hours to achieve uniform precipitation [153], hence "ageing".

Visualising the cross section of BFSW welds

Zones within the weld

The transverse section of a BFSW weld-line reveals three typical zones. The stir zone (SZ) is the center region of the weld and is distinguished by hourglass pattern at the AS and the RS borders of the cross section [38, 74, 111, 121]. In this region, the thermomechanically distorted grains are plasticized and then recrystallized by the stirring action of the tool [121]. The adjacent region is the thermo-mechanical affected zone (TMAZ), created by the thermal and mechanical effects of the friction and stirring [111]. Similar to other welding processes, the heat affected zone (HAZ), an area of the base metal (BM) which has an altered microstructure by heat flux effects during the process, is located between TMAZ and BM [161]. The welding

process may introduce defects at macro- or microscopic level, and these affect weld quality. Microstructure observation of the weld texture consists of a transitional configuration for morphology and grain size distribution is one of the basic steps of weld characterization [113, 150]. Also a comparison between the microstructures of BM and different regions of the weld is necessary.

Metallography

Metallographic measurement is an effective technique to characterize the microstructural details of the various metals or alloys in cross section [68, 162]. In comparison with electron microscope analysis, the etching method is fast and inexpensive. In principle it is able to show grain size, morphology, and distribution [163]. There are different macro-etchant or micro-etchant solutions which can be used by immersion, swabbing or electrolytic processes [72, 164]. Other techniques like electron backscatter diffraction (EBSD) can be used for microstructural-crystallographic characterization to study any crystalline or polycrystalline material, but preparation of the aluminium sample for EBSD is time consuming and the equipment is considerably more expensive than optical microscopes [165].

Metallography of Aluminium alloys

In the case of aluminium alloys, the most common etchants are Keller's etchant (95 ml H_2O, 2.5 ml HNO_3, 1.5 ml HCl, 1.0 ml HF) and Kroll's reagent (92 ml H_2O, 6.0 ml HNO_3, 2.0 ml HF) [163]. Also, anodizing using Barker's reagent (5 ml HBF_4, 200 ml H_2O) and colour etching by Weck's reagent (4 g $KMnO_4$, 1 g of NaOH, 100 ml H_2O) are widely applied to reveal the microstructure and grain boundaries (G.B) [166].

Problem

One of the restrictions of the BFSW weld characterization for the A6082-T6 cross section is the metallographic measurement of the specimens using the available reagents for the aluminium alloys. For A6082-T6 BFSW weld samples, Keller's reagent has been unsuccessful for observing the microstructure [78, 149]. Also, Kroll's reagent only showed some narrow lines at the borders of the weld region [64]. More specifically, thermomechanical evaluation requires that the fine structure of A6082-T6 alloy be delineated in grain-refined regions; and this necessitates that other etchants be used to improve the microstructural observations.

The problem has two causes [167, 168]. First, the tempered structure of A6082-T6 base metal has a uniform and stabilized solid solution [167]. The T6 condition retains the hardening particles in the solid solution as opposed to precipitating them on the grain boundaries where they would increase the contrast. This makes it hard to distinguish the grain boundaries from the grains. Second, the solid phase plastic deformation of the welding process fragments the grains to ultrafine size (in the range of 10 um or below). This further reduces the ability to detect grain boundaries [168].

9.3 Purpose and approach

Purpose

There is a need to develop better etching methods for A6082-T6. Specifically, the etching process needs to distinguish grain boundaries down to the ultrafine size, show the morphological flow originated from the grains fragmentation during the stirring process (which is important for processes involving internal flow), preferably reveal some thermomechanical features at higher magnification (for studying recrystallization), and ideally not require electro-polishing or anodising.

The objective was to develop such an etching solution and process. It was started with the idea that it is necessary to improve the contrast at grain boundaries, and that this might be achieved by a chemical attack followed by a doping process. The details of the doping mechanism need to be described by transition state theory and activated complex which is beyond the scope of this chapter, but as a brief explanation: using some multi-stage reactions the unstable reagents can create an activation of the surface using the metal ions and consequently the ion migration into the grain boundaries can improve the contrasting patterns there.

Approach

To make the etchant solution, a trial and error procedure -by adding or changing different compositions to the chemical solution was done to compare the resolution of the grain size and morphology. HNO_3 is common between the majority of Al reagents [166, 169, 170]. Also, HF is one of the strongest acids for chemical attack on silicon-containing compounds [169, 170]. Dissolution of the Al_2O_3 film on the Al surface can be progressed by H_3PO_4 [169]. Furthermore, using an alkaline developer (NaOH) can improve the grain boundary contrast [166, 169].

The etching process may be accelerated by higher temperature or immersion in a solution under ultrasonic fields. Depending on chemical composition of the etchants, compounds of solutions can be applied in one-step or multi-step processes. This set of arrangements gives the boundaries a rougher and darker appearance than inside the grain when viewed under the optical microscope.

After completion of the etching process, macrostructure and microstructure of the weld can be studied by using a stereomicroscope and light-optical microscopy analysis, respectively. In this part, besides demonstrating the recrystallized microstructure of the weld region in the SZ, the main focus was on a thermomechanical comparison of grain size, morphology, and flow distribution in BM, HAZ and TMAZ and SZ different regions of the weld. Also, by showing the results related to the recrystallization and a morphological flow gradient for the grain distortion from the BM towards the SZ, the thermo-mechanical behavior of the BFSW process can be explained.

9.4 Materials and Methods

Experimental welding process

In this chapter, the BFSW process was done on 6 mm thick A6082-T6 Al alloy plates for the base metal. The plates were cut into two pieces of 250 (length) mm x 75 mm (width) and set for a butt joint.

Figure 9.1b demonstrates the geometric details of the fixed bobbin tool, utilized for this research. The threaded pin was modified by adding three symmetrical flat surfaces (tri-flat) to provide a more homogenized stirring condition. Also, a 360 degree inward-flowing spiral pattern was inscribed on both shoulders surfaces, i.e. a scroll feature. Diameter (D) ratio ($D_{Shoulder}/D_{Pin}$) and compression ratio (difference between the biting gap of the bobbin tool and thickness of the workpiece plate) were 3 and 3.75%, respectively [123]. These features are believed to assist the flow during welding [70]. The bobbin tool was made from H13 Hot Work Tool Steel with hardness 560 HV. The rotational speed and feed rate were 600 rpm and 400 mm/min respectively, which were selected to give a successful weld. The direction of tool rotation was chosen clockwise, similar to the scrolled features on the shoulder surfaces. Table 9.2 gives details of the geometry and process parameters.

The trials were run using a CNC milling machine (OKUMA MX-45VAE). The weld workpieces were rigidly fixed between clamped bars. The temperature of the tool and workpiece was 18 °C at the beginning of the test, and there were no preheating or post-weld processes before or after the welding process. For more details of the BFSW process for A6082-T6 plates see [64, 155]. After welding the joint was cross sectioned by wire cut in the middle of the weld-line, to provide specimens for the metallographic measurements.

Table 9.2: Parameters of the welding process for the A6082-T6 samples.

Parameter	Value
$D_{Shoulder}$ (mm)	21
D_{Pin} (mm)	7
$D_{Shoulder}/D_{Pin}$	3
Plate Thickness (mm)	6
Compression Ratio	3.75%
Spindle rotational speed ω (rpm)	600
Feed rate (mm/min)	400
Thread Pitch (mm)	1.75
Number of Threads	4

Metallography and etchants

For optical metallography (OM) the preparation procedure was to mount the aluminium samples in a thermoplastic hot pressed resin. The mounting material was chosen for its resistance to physical distortion and it is chemically inactive to lubricants, solvents and etchants. Next, the grinding and polishing of the specimens was performed via standard metallographic techniques to achieve a fine smooth surface for etching [169, 170]. For uniform polishing the grinder consisted of a rotating wheel fitted with a series of 400-grit, 600-grit, 800-grit and 1200-grit silicon carbide (SiC) papers revolving at 200 rpm and 5 lbs/specimen for 15 minutes/wheel. Samples were lubricated with a stream of water and were rotated in 90 degree increments until all the scratches from the previous grinding direction had been removed. For micropolishing, specimens were polished first on a Microcloth pad with a series 6μm to 0.5μm diamond pastes and finally finished using 0.05μm Struers OPS colloidal silica at 150 rpm and 5 lbs/specimen for 5 minutes. The lubrication was white spirit (paraffin oil) during the micropolishing. After each polishing wheel, the specimens were rinsed with cold water and ethyl alcohol and dried with warm air.

After polishing, samples were at first etched with conventional Keller's and Kroll's reagents as an early comparison. The etching involved immersion of the polished specimens for 15s at room temperature. Inspection showed that neither of these reagents clearly delineated the grain boundaries. This failing is consistent with the literature for this material. Despite increasing temperature and immersion time there was no significant improvement in microstructure definition. As shown in Figure 9.2, even in severe chemical attacking of the surface and emergence of pitting, Keller's and Kroll's reagents could not produce good grain contrast for the weld samples.

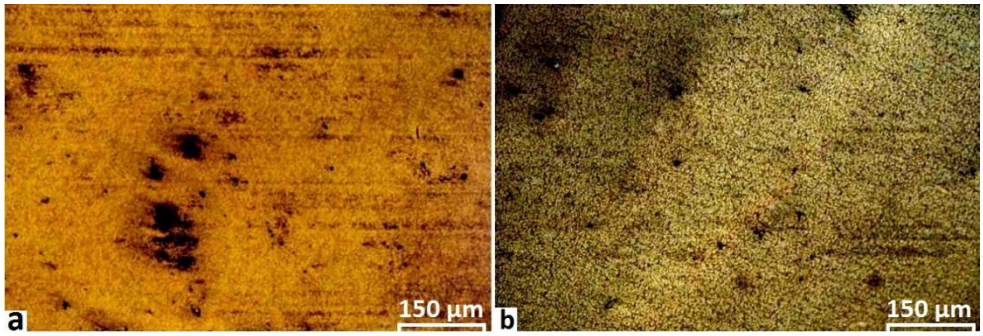

Figure 9.2. Etched surface of the A6082-T6 weldments, (a) the Keller's reagent and (b) Kroll's reagent. These reagents are unsuccessful at elucidating the microstructure for this material.

The second part of the metallography method was focused on modification of reagents for macroetching and micoetching.

A number of candidate etchants were developed, or more accurately a set of specific chemical solutions each with a sequence of application (process). The chemical perspective considered the following factors:

- NaOH is used to reveal grain structure. Likewise HF.
- H_3PO_4 dissolves the Al_2O_3 oxide layer.
- CH_3COOH is used to dilute the solution and reduce pitting attack. CH_3COOH also has a positive effect in delineation of fine features (e.g., in stirring zone).
- The process perspective considered the multiple steps. There is a need for a stage to remove the oxide film, followed by another stage to delineate the grain boundaries. Temporal or sequence factors that were considered were:
- Duration of immersion.
- Increasing the temperature up to 70 °C during etching.

Immersion in ultrasonic bath can improve the uniform etching and also help remove the oxide layer. However in this case, the conventional immersion was used for all etchants.

Our optimisation method involved setting the chemical composition first, then etching until reaching an over-etched surface. Then the etching time and temperature progressively were reduced until the surface features become clear.

The results are shown in Table 9.3, which describes the composition and other conditions of chemical solutions for different applications.

Table 9.3: Different groups of reagents with separate sequences of processing.

Name of Etchant	Etching Type	Pre-Etching	Etchant Composition
A	General Macrostructure	-	30.0 g NaOH + 100 mL ethanol (3 min, 50 °C)
B	General Macrostructure	-	2.5 mL HF + 2.5 mL HCl + 95 mL H_2O (30 s, 50 °C)
C	General Microstructure	-	0.5 g $(NH_4)_2MoO_4$ + 3.0 g NH_4Cl + 1 mL HF + 18 mL HNO_3 + 80 mL H_2O (90 s, 70 °C)
D	G.B Microstructure	20 g NaOH + 80 mL H_2O (20 s, 50 °C),	Etchant C (60 s, 70 °C)
E	HAZ Microstructure	20 g NaOH + 80 mL H_2O (20 s, 50 °C), then: 30 mL H_3PO_4 + 70 mL ethanol (20 s, 50 °C)	10 g CrO_3 + 2 g Na_2SO_4 + 10 mL HNO_3 + 10 mL CH_3COOH + 1 mL HF + 80 mL H_2O (60 s, 70 °C)
F	TMAZ Microstructure	20 g NaOH + 80 mL H_2O (20 s, 50 °C), then: 30 mL H_3PO_4 + 70 mL ethanol (20 s, 50 °C)	Etchant E (60 s, 70 °C), then: 15 mL CH_3COOH + 85 mL H_2O (15 s, 70 °C), then: 15 mL H_3PO_4 + 85 mL H_2O (15 s, 70 °C),
G	SZ Microstructure	20 g NaOH + 80 mL H_2O (40 s, 50 °C)	10 mL HCl + 40 mL HNO_3 + 2.5 mL HF + 12 g CrO_3 + 10 mL CH_3COOH + 50 mL H_2O (60 s, 70 °C), then: 20 mL CH_3COOH + 80 mL H_2O (20 s, 70 °C), then: 20 mL H_3PO_4 + 80 mL H_2O (20 s, 70 °C),

H	Micro-flow Patterns	-	2 mL HF + 2 mL HBF_4 + 10 mL HNO_3 + 20 mL CH_3COOH + 33 mL H_2O + 33 mL ethanol (90 s, 70 °C)
I	Polycrystalline Structure	20 g NaOH + 80 mL ethanol (20 s, 50 °C), then: 20 mL H_3PO_4 + 80 mL ethanol (20 s, 50 °C)	2 mL HF + 2 mL HBF_4 + 5 mL HNO_3 + 30mL CH_3COOH + 60 mL ethanol (90 s, 70 °C)

After etching, the samples were washed under a distilled water stream, rinsed in ethanol, and then dried with warm air. The macrostructure and microstructure of the etched samples were studied under stereograph microscope and optical microscope, respectively. Results are reported below. The images are all for one welded sample, that has been re-polished and re-etched each time. It shows that these various etchants are useful in elucidating different aspects of the microstructure.

9.5. Results

Macrostructure

The macrostructure in the cross-section of a BFSW joint, processed by etchants A and etchant B are shown in Figure 9.3. The etchants readily reveal the SZ hourglass pattern for the cross-section of the weld and the flow patterns. In Figure 9.3a the AS border is more visible rather than the RS side. Employing etchant B makes the position of the RS border more visible, see Figure 9.3b. Even so there is a blurring of the RS border. This is attributed to the tendency for the tool to aggressively remove substrate material from the AS and subsequently backfill the region with heavily worked material, hence making the AS more defined by comparison with the RS.

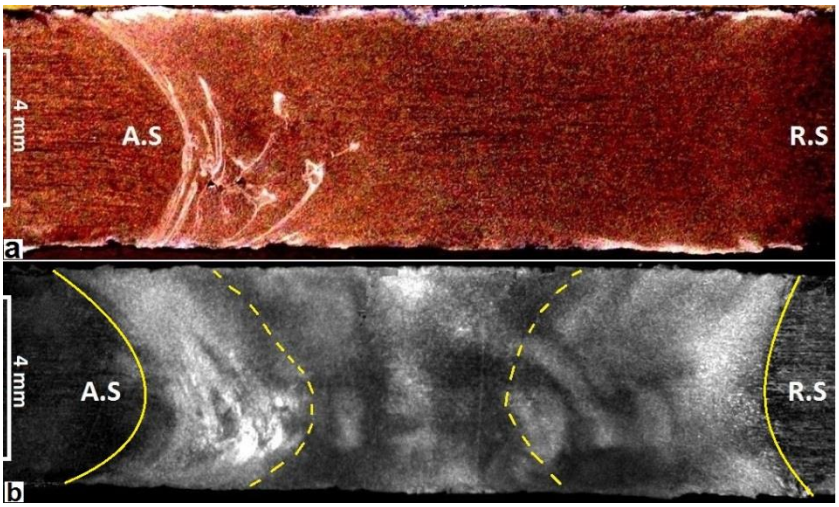

Figure 9.3. Macrostructure of the cross-section of the BFSW joint for two different etchants, (a) etchant A, and (b) etchant B. The pictures belong to the same sample and the same location of the cross section, after re-polishing and re-etching the surface.

The flow eddies are best seen with etchant A, see Figure 9.3a. These features are attributed to the transportation mechanism inside the weld. The transportation mechanism is proposed to be as follows, extending on [155]. The flats on the tool scour out packets of material from the substrate – this work is most aggressive conducted on the advancing side because this is where the combined linear and rotation motion is greatest relative to the substrate, hence this is also the hottest side. However material is also scoured from the leading edge and the retreating side, as this is necessary for linear tool progression through the substrate. The rotation of the tool (clockwise from above), moves the material in the same rotational direction, which corresponds to a horizontal flow from right to left in the wake of the tool (which is always where the post-weld section is taken). Consequently packets of material are moved round the weld from the advancing side, through the retreating side and back to the advancing side where the flow stalls. The stall occurs because the packets move into a region immediately downstream of the scouring action, while the flats scour out fresh material. The packets are thus packed into the downstream AS, and the boundaries between these packets are believed to correspond to the bright lines in Figure 9.3a. According to this explanation the flow of material is orthogonal to the bright lines, not along them. Hence it is incorrect to call them flow lines – rather they are boundaries between flattened packets of material. It is generally evident, in this and other samples not shown here, that the lines are primarily vertical, which is consistent with the above explanation. Also the spacing between lines is observed to be smaller closer to the advancing side wall, and this too is consistent with the packet transportation mechanism. An additional complexity is introduced by the threads on the tool. These transport the material downward [155], hence explaining why the packet boundaries are preferentially located at the bottom of the AS.

The results attribute the internal void defects, which are evident in the figure 9.3a, to intermittent stalling of the flow. This is explained as the periodic passage of the flats on the tool causing momentary vacuum - hence the horizontal flow sometimes stalls into a low pressure situation, i.e. the packing pressure is absent.

The macroscopic aspects of BFSW joint show no grain structure in the macro-etch. As subsequent results show, this is because of the fine grain size that arises in this material. However to see these grains requires one of the micro-etch processes, which are describing next.

Microstructure

The etchant C was found to be effective at revealing the optical microstructure. Figure 9.4 shows the BFSW weld cross-section from BM towards the SZ for both of AS and RS. The etchant differentiates between the grains of the HAZ and TMAZ. In

both cases the grain morphologies show a change in grain direction from columnar in the BM, to an ultrafine structure in the SZ.

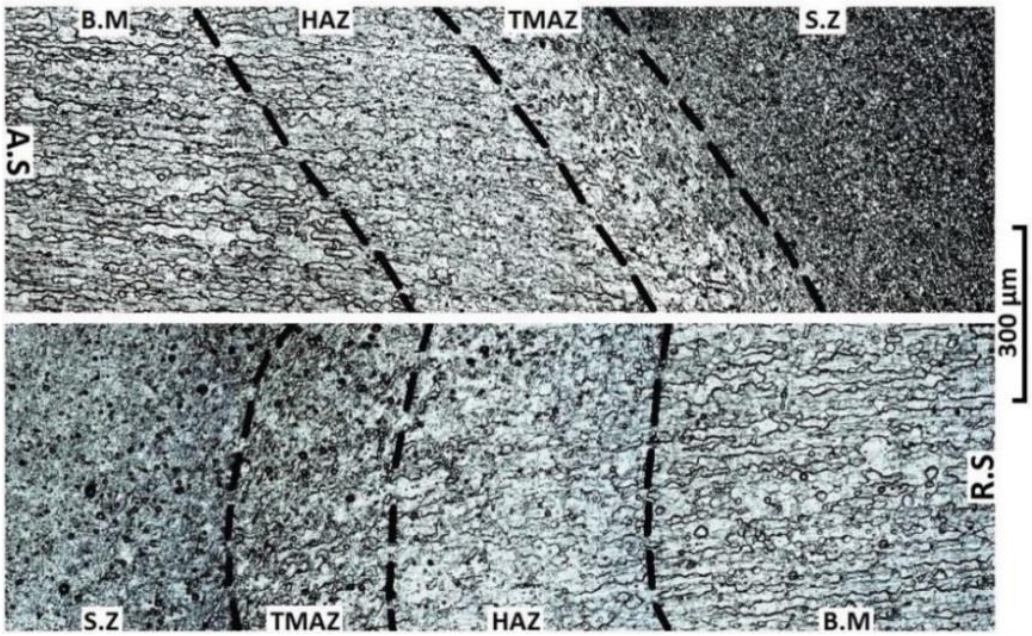

Figure 9.4. Microstructure of the grain distribution in the AS (top) and the RS (bottom) of the A6082-T6 weld (processed by etchant C).

Higher magnification of the BM and SZ regions show the differences in grain morphology and size distribution, see Figure 9.5. Fine grains of the SZ have spherical morphology with an average size less than 10µm, while the grain size for the BM is in the range of 100µm. Also, the directional grains in the BM (as a result of the primary rolling process on the sheets) have changed into equiaxed grains in the SZ with a narrow range distribution. These features are indicative of dynamic recrystallization during the thermo-mechanical regime experiences in the welding process.

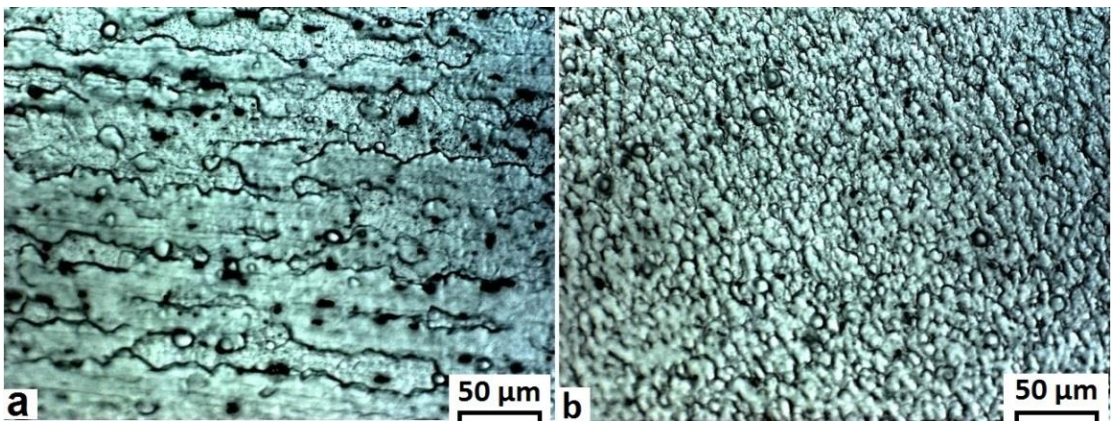

Figure 9.5. A comparison between (a) the BM and (b) the SZ for the A6082-T6 weld cross-section (processed by etchant C).

Grain boundaries

To obtain better contrast of the grain boundaries the etchant D was developed. The microstructure of different regions of the BFSW weld are shown in Figure 9.6. Here the grain recrystallization and transition gradient of morphological flow are more visible. A parallel columnar grain distribution indicating the rolling process in the base material is clear in Figure 9.6a. The HAZ shows a recrystallization of grains in Figure 9.6b. The TMAZ in Figure 9.6c shows a significant grain distortion which is attributed to the strain field.

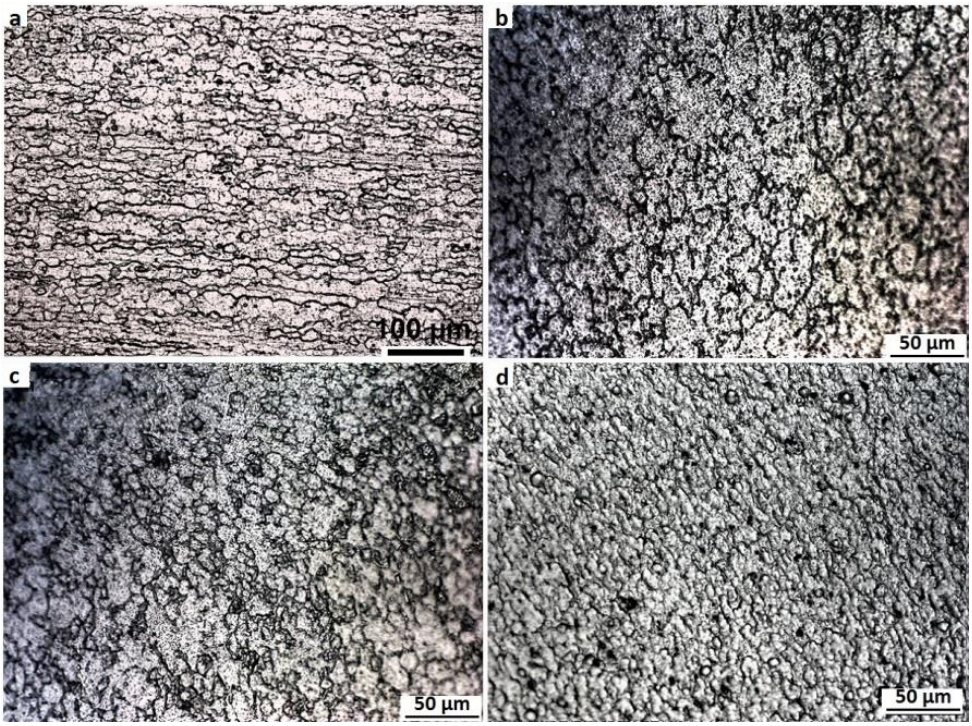

Figure 9.6. Microstructure of different regions of a BFSW A6082-T6 weld processed by etchant D; (a) BM, (b) HAZ, (c) TMAZ, (d) SZ.

It should be noted that there are some dark areas in the micrographs of Figures 9.6b and 6c in the HAZ and TMAZ, respectively. During the etching process some stains are visible in the HAZ and the TMAZ. At first glance these might be assumed to be artefacts of over-etching. However these are instead representative of flow features with different grain morphologies and sub-grain boundaries. They are unlikely to be precipitates as precipitation in the stabilised microstructure of A6082-T6 alloy needs more temperature and time, higher than that provided by the BFSW process.

In the SZ, Figure 9.6d, there is a fine homogeneity to the grain structure. This is a consequence of the recrystallization caused by the mechanical stirring mechanism. The stirring reduces grain size to less than 10 microns (see below) with low anisotropy (equiaxed grain structure).

Morphological flow of grains (thermomechanical distortion, fragmentation and recrystallization)

For a finer scaled study of recrystallization and transition of grain morphology for the microstructure of A6082-T6, several additional etchants were developed.

Etchant E is effective for microetching of the HAZ. Using a colour etchant can demonstrate the morphological flow of grain in an inhomogeneous transitional microstructure. Results are shown in Figure 9.7 for four different regions; AS and RS, and adjacent to the top shoulder and bottom shoulder. The micrographs show a layered structure with the colour contrast representing different gradients of the morphological flow for the grain distortion between the layers.

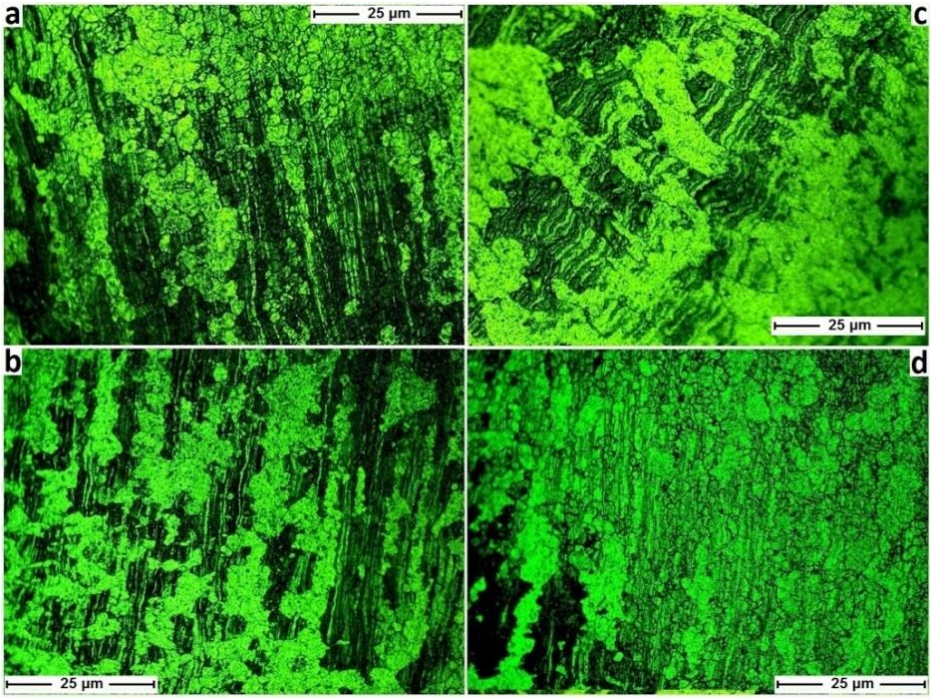

Figure 9.7. Morphological transition of grain flow in the HAZ processed by etchant E: (a) top shoulder-AS, (b) bottom shoulder-AS, (c) top shoulder-RS and (d) bottom shoulder-RS.

Etchant F was developed for microetching of the TMAZ. As before results are shown for four different regions; AS and RS, and adjacent to the top shoulder and bottom shoulder. See Figure 9.8. The dynamic nature of the mechanical and thermal trajectories causes each layer to have a different recrystallization history in comparison with the neighbouring layers.

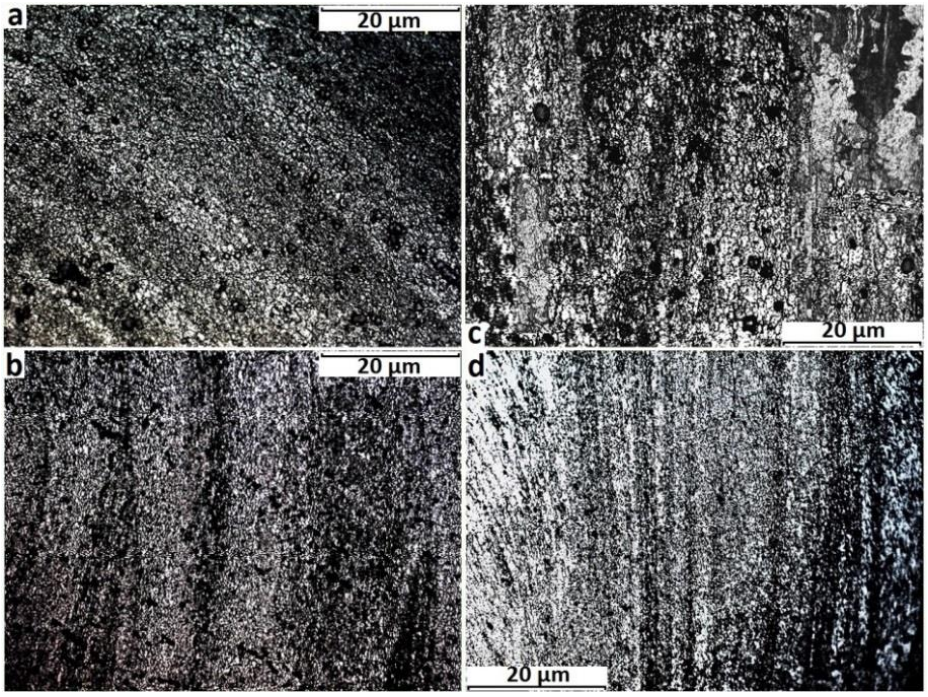

Figure 9.8. Morphological transition of grain flow in the TMAZ processed by etchant F: (a) top shoulder-AS, (b) bottom shoulder-AS, (c) top shoulder-RS and (d) bottom shoulder-RS.

Both HAZ and TMAZ the micrographs show a layered structure. Comparison between different regions of the HAZ or TMAZ shows that generally the grains in the RS are coarse and the layers are interwoven, while in AS the layers have a more uniform structure. For further characterization of the grain orientation it would be appropriate to use XRD analysis or EBSD.

Etchant G was developed to reveal finer details about the individual grain boundaries, as opposed to the grain morphology. Results for different areas of the SZ are shown in Figure 9.9. For all these micrographs the equiaxed polycrystalline structure are visible with a narrow grain size range of distribution. The ultrafine equiaxed structure of the grains is attributed to the plasticisation and stirring of the welding process.

The grain size in the middle of SZ (Figure 9.9e) is slightly bigger. This may be because it is furthest from the free surface of the workpiece hence experiences higher heat conservation. The grain boundaries are more pronounced on the AS (Figures 9.10 a,b).

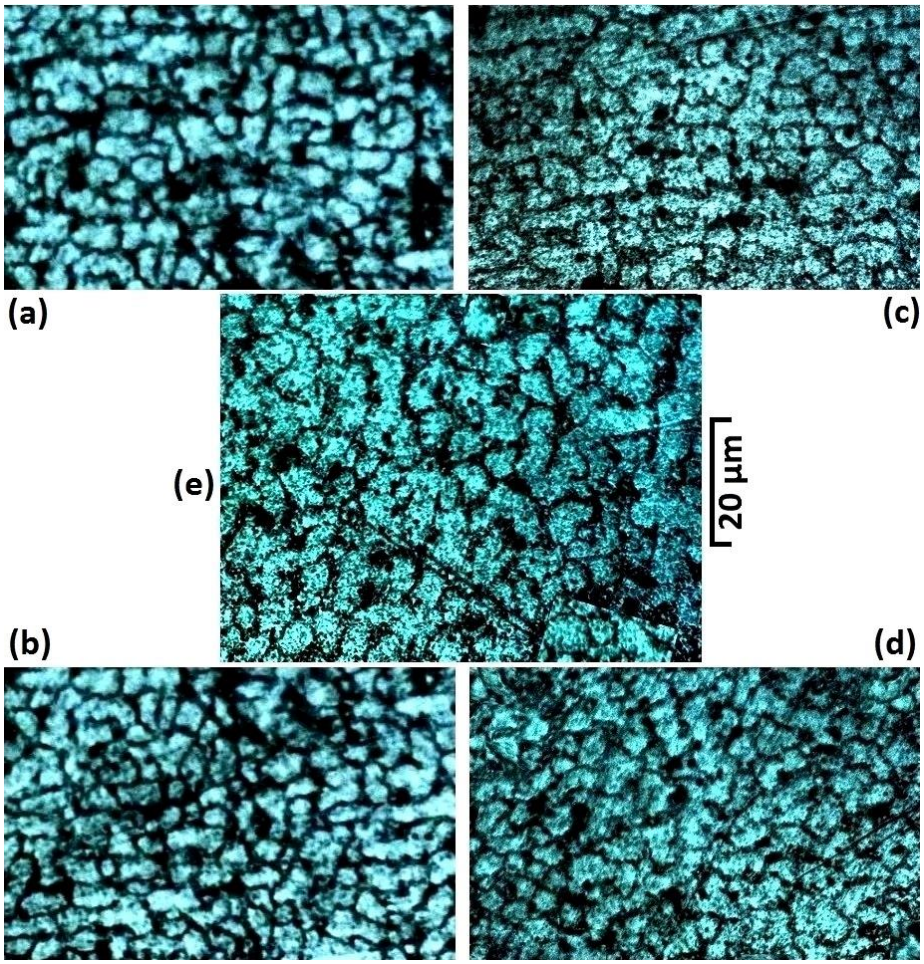

Figure 9.9. Equiaxed polycrystalline microstructure in different areas of the SZ, (10a) top shoulder-AS, (10b) bottom shoulder-AS, (10c) top shoulder-RS, (10d) bottom shoulder-RS and (10e) middle of SZ (all processed by etchant G). The average grain size in the SZ is smaller than 10µm, but in the centre of the SZ the grains are larger.

High magnification observations: microflow patterns, polycrystalline grain distribution

We are interested in elucidating the microflow patterns for this material, which have not previously been shown in the literature. As shown above, the grains are of a fine size of 4-10 microns, which makes etching difficult. To address this problem, the etchants H and I were developed. These are able to reveal the microflow patterns of the stirring (etchant H) and then the polycrystalline distribution in microstructure for the same position (etchant I), see Figure 9.10. The microflow patterns are provided by etchant H being designed to have a high sensitivity to the stress-strain fields. The vortex style of the microflow shows the stirring motion of the process. The plasticised material is solidified after severe deformation under rotation and movement of the tool.

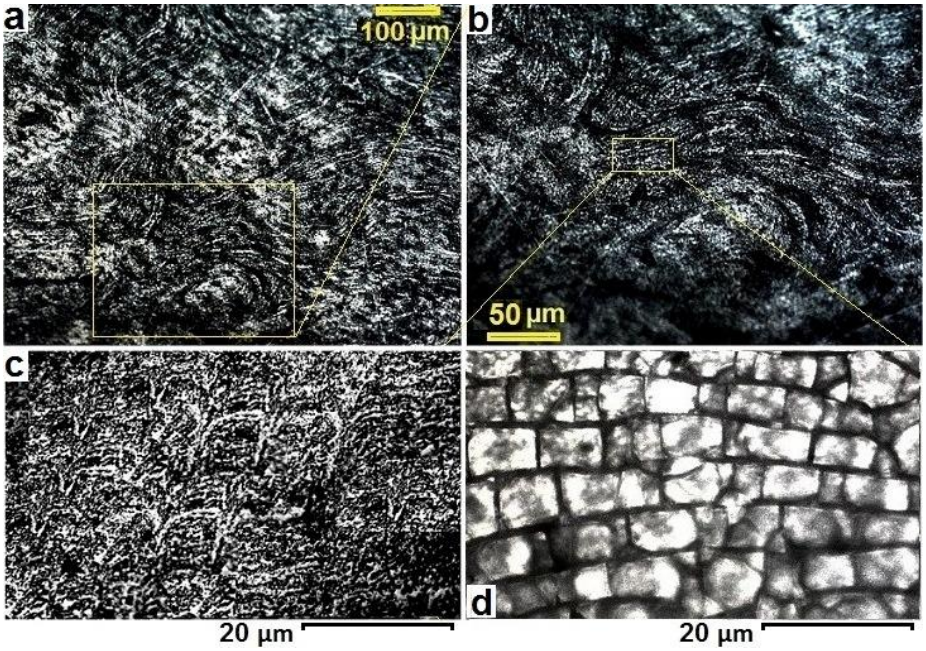

Figure 9.10. The micro-patterns in the SZ at progressive magnification (a) to (c) using etchant H, and (d) the mosaic crystallites for the same location of (c) processed by etchant I.

Figure 9.10c reveals a cusp pattern to the microflow, though this is only evident at higher magnification. The micrograph of Figure 9.10d processed by etchant I shows the polycrystalline patterns of the grain distribution for the same area and magnification as Figure 9.10c. This demonstrates that the different etchants selectively enhance different features in the material.

Figure 9.10d emphasises the polycrystalline morphology, and the results are interpreted as the grains having the same crystalline arrangement and grain size distribution. The cusp patterns of Figure 9.10c are resolved into grain boundaries in Figure 9.10d, indicating a coherent interface between the crystallites.

Coherent interfaces

Inclusion particles are not uncommon in FSW [171]. These particles can be external inclusions which entered to the weld region, probably by breaking of the oxide surface layer during the stirring process [171, 172]. Sometimes the crushed particles from breaking of the oxide surface layer cannot escape from the shoulder's rotation and are sucked into the stirring region. As the lattice parameter of the Al_2O_3 is different to Al solid solution, these oxide particles form the non-metal inclusions [172].

Similar to slag inclusions in fusion welding these structural defects cause local interruptions in the microstructure [170, 173]. These defects are clearly

distinguishable inside of the weld region underneath the surface and can be identified by streak-like segregation and gas blisters in their immediate proximity [171-173]. As a result, inclusions can be harmful for the structural integrity and may decrease the strength characteristics of the weld. But by formation of a viable interface layer, they can remain in the structure [171]. Accurate quantification of the interface layer is performed by means of electron microscopy and composition analysis; however here one such inclusion were examined in the sample.

Using etchant I, Figure 9.11 reveals the coherent-incoherent interface for the inclusion particles with a clear lattice mismatch within the SZ. The oxide inclusion particles were trapped in the sub-surface region of the SZ, close to the top shoulder position, see Figure 9.11a.

Figures 12-b and 12-c show a higher magnification in the interface of the inclusion (dark mass) with the SZ microstructure. Obviously the inclusion itself has an incoherent interface with the parent phase (SZ mass). Initially, the broad and curved layers surround the inclusion as the incoherent interface layer. This is similar to a primary adjustment between the external particle (oxide inclusion) and the solid solution lattice during the solidification. However the interface bonding is non-uniform and can create some discontinuity e.g. microcracks, during the cooling due. To increase the conformity, during the recrystallization process a secondary semi-coherent layer is formed between the wavy-shaped incoherent layer and the stirred mass to make a compromise between the SZ microstructure and the external inclusion. Microstructural study of the coherent/incoherent interfaces usually needs to be analyzed by the transmission electron microscopy (TEM) technique, but here etchant I provides a quick measurement using optical microscopy.

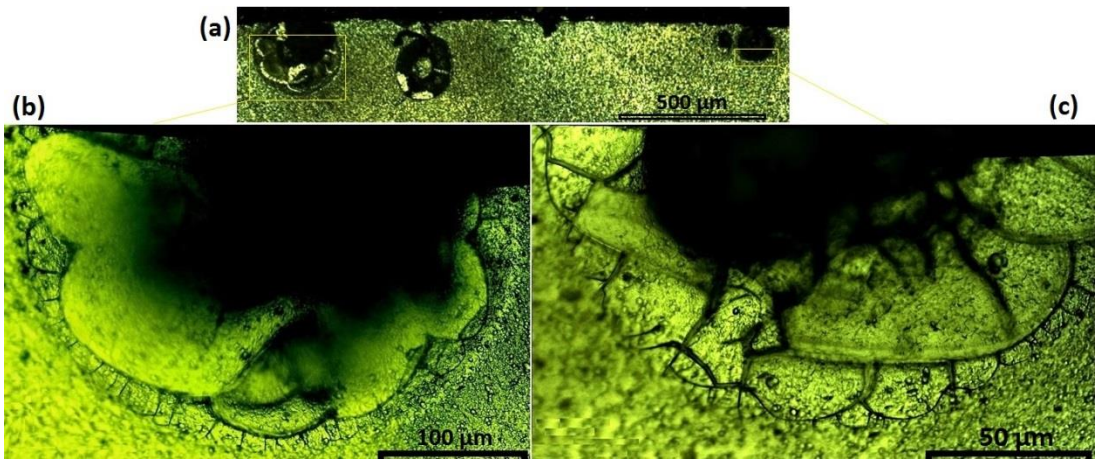

Figure 9.11. Crystalline incoherent-semicoherent interface of the oxide inclusions with the SZ lattice (processed by etchant I).

9.6. Chapter Discussion

This work makes several novel intellectual contributions. The first is the development of a suite of etchant reagents for metallographic measurement of the friction-stir welded A6082-T6 alloy. The reagents have made it possible to reveal the grain boundaries and grain distribution with an ultrafine size within a BFSW weld region. This has not previously been shown to be possible in the literature for the optical microscopy.

Observation of these micropatterns for FSW has not previously been shown using metallography methods, especially not for this grade of material. Development of these innovative etchants creates a high contrast between grains and grain boundaries; and this reveals micrographs which are usually visible only by electron microscope technology. Being able to show these with conventional optical microscopy is a novel contribution.

Another contribution is the elucidation of the grain size distribution and morphology for the BFSW weld, particularly the identification of polycrystalline structure. The ultrafine grain microstructure with a narrow range of distribution was found in the stirring zone, and were able to visualise this at high magnifications. The grains in the stirring zone show a reduction up to 10 times finer than the base material grain size.

The present chapter shows that it is feasible to use optical microscopy, with suitable reagents, to inspect multiple aspects of the thermomechanical nature of the BFSW process. e.g. dynamic recrystallization, morphological flow of the grain distortion and degree of interface coherency in solid solutions. Naturally these phenomena can be comprehensively examined with the EBSD and electron microscopy techniques, nonetheless there is value in the simpler and less expensive optical methods shown here.

One issue is regarding the T6 heat treatment process and how it may be affected by the thermomechanical behaviour of BFSW. The obtained results show that the A6082-T6 columnar structure in the base material is changed to ultrafine equiaxed grains in the stirred zone. Since the microstructure has been changed with a massive increase in density of grain boundaries (the preferable position for hardening participates) there is uncertainty about the stability or otherwise of the T6 properties. The present chapter does not answer that question, though it does show that the BFSW process significantly affected the microstructure of the T6 heat treatment at the HAZ, TMAZ and SZ. Further work would be required to address this question, possibly using EBSD, phase characterization of participates in grain boundaries, or microhardness evaluation of different regions of the weld. This is left for future research.

Although the new etchants have demonstrably improved capability for microscopic observations, the process does require a fine surface polishing to show the

microstructure details at higher magnifications. On its own this is not a detriment as such finishes are generally expected for such magnifications. It will be noted that the etchants and associated procedures obviate the need for electropolishing or anodising, hence provide a significant economy over those processes.

Warning - it should be noted that the etchants are more toxic than typical Al reagents. Hot immersion of samples may cause emission of toxic vapours, so the operator is advised to use a proper ventilation system and apply personal protective equipment (e.g. mask, polymer gloves and safety glasses) to protect the skin, eyes and respiratory system. The waste chemicals after etching should not be put down the drain because it can get into water system and be hazardous for human consumption and environment.

A number of lines of enquiry for future research have been identified above. To which it can add additional ideas such as develop new reagents for colour metallography with sensitivity to the material flow and heat flux. Such reagents could provide a better understanding about the thermo-mechanical aspects of the process and also reveal the failure mechanism of the flow regimes around defects such as the tunnel void or kissing bond that is so prevalent in this grade of material.

9.7. Chapter Conclusions

A new suite of etchants have been developed for macro- and micro-etching of A6082-T6 bobbin welds. The etching provided the microstructures reasonably free from pitting and observable to high magnification using optical microscopy. The microstructure of the grain boundaries was revealed for the different regions within the weld: HAZ, TMAZ and SZ. Results showed the grain size variation with distinct morphological patterns. This is an advancement on the level of detail apparent in the published literature, and makes it possible to conduct optical microscopy where previously only more expensive methods were suitable.

The polycrystalline structure of the SZ showed a large decrease in grain size in comparison with the BM. While the columnar grains of the BM are about 100 micrometers, this is changed in SZ to an equiaxed structure with average grain size under 10 microns. The grain boundaries and morphological flow gradient of grains from the BM towards SZ indicated a past recrystallization process which was attributed to the thermo-mechanical regime of the BFSW process. Etchants were able to elucidate microflow patterns and crystalline coherency of the interface at a high level of accuracy for high optical magnification.

CHAPTER 10: The effects of processing BFSW parameters and entry conditions on the microstructure of AA1100 and AA3003 Aluminium Alloys

Chapter Summary: The influences of processing parameters and tool feature on the microstructure of AA1100 and AA3003 aluminium alloys were investigated under bobbin friction stir welding (BFSW). The research includes the flow visualization and microstructural evolution of the weld texture using the metallographic measurement. Results indicated that the operational parameters of the welding (e.g. feed rate, rotating speed) and the geometry of the tool can directly affect the flow patterns of the weld structure. The microscopic details revealed by the optical and electron microscope implies on the dynamic recrystallization including grain refinement and precipitation mechanisms within the stirring zone of the weld region. As two BFSW tools were utilized in different series of Al alloy, the microscopic comparison attributed on better performance of the fully-featured tool (comprises a tri-flat threaded pin and scrolled shoulders) for the formation of thermomechanical features within the weld texture, compared to the simple tool without inscribed surface features.

10.1. Introduction

Bobbin Friction Stir Welding (BFSW) is a new joining technique [1, 4, 5] which has been achieved many attraction to be utilized for solid-state processing of deformable materials, e.g. aluminium alloys [66]. Nevertheless, compared to convention FSW (CFSW) [3], the BFSW technique is a relatively new process [36-38], where the process parameters and variables, effective on the quality of the weld, need to still be fully understood.

Regarding the quality control of the weld, the CFSW has also inherent problems which need technical consideration to obtain a sound weld [12, 14, 16]. For instance, regarding the stirring zone (SZ), the improper engagement of the pin tool and the workpiece causes incomplete penetration to occur discontinuity defects within the weld structure [13, 34, 35]. Moreover, the vibration disturbance needs to be avoiding during the process, which requires anvil and clamping rigidity design [17]. The BFSW techniques as a self-reactive FSW process does not necessarily require the

complex and relatively costly fixture and backing anvil to compensate the reactive forces inducing the sufficient and effective material flow within the SZ [64]. Unlike BFSW, CFSW does require the exact plunged depth for the tool so that the formation of the root flaws can be avoided [2]. However, not only BFSW, but also FSW are excellent candidates to join the aluminium alloys as the other processes of welding such as fusion welding hardly utilized on such kind of active alloys [4]. Porosity and hot cracking are usually appearing if the aluminium alloys are fusion welded [86].

BFSW is known as a variant of FSW, however, it has very different characteristics within the weld structure, where the plastic flow regimes and the relevant microstructure is entirely different from the physics accepted for the Conventional-FSW process [86]. The general geometry of BFSW's tool consists of two cylindrical shoulders with a pin in the middle. By rotation of this single-piece tool, the mechanical interaction between the tool components and the workpiece generates the frictional heat in the contact surfaces [20]. Because of replacing of the backing anvil (in CFSW) with a rotating bottom shoulder (in BFSW), the heat input and the plastic flow in BFSW are elevated compared to CFSW [28, 38]. Moreover, the axial force required in CFSW is not essential to be provided in BFSW, as the compression ratio (the variance between the actual thickness of the workpiece and the biting gap at the edge of shoulders) provides enough engagement between the mass and the tool during the stirring action, while the rotating tool moves forward towards the butt-joint interface [36]. The geometry of the bobbin-tool can provide approximately symmetrical microstructure as the tool is perpendicular to the welding direction, and simultaneously rotates and advances between the advancing side (AS) and rotating side (RS) of the welding locus [37]. Eventually, the interaction between the tool and the workpiece at the working region (stirring zone, SZ) forms a symmetrical flow-pattern in the top and bottom portions of the SZ, at the proximity of the rotating tool [140]. This is observable as an hourglass pattern at the cross-section of the weld, which is different from the basin-shaped pattern of the weld-region in CFSW weld samples [136, 138]. The special double-sided bobbin- tool design can work on a material which has up to 25mm thickness, because of sufficient heat which is created and maintained by the double rotating shoulders, connected by a centred-pin in the middle [81]. However, all these, add more complexity in flow-structure and microscopic details of the BFSW weld [141, 144], compared to the CFSW. Thus, there is more investigation needing to be done, regarding identifying the effective variables of the BFSW process, to obtain the defect-free weldment under optimized welding condition.

To achieve the higher quality in the manufacturing, the variables of the process, for instance, the design of the tool, appropriate processing parameters and the simulation of material flows are needed to be optimized. In this chapter, the potential development of BFSW is subject of investigation, where the weld structure and internal flow details are practicality studied for two different grades of aluminium alloys. By applying different welding speeds (rotational and advancing),

and different bobbin-tool designs, the effect of the tool's features and processing parameters are compared on AA1100 and AA3003 aluminium plates with the same thickness. The metallographic analysis (optical and electron microscopy) can reveal the details of the microscopic evolution and flow mechanism within the weld region.

The comparison between the microscopic characteristics of the weld region, internal flow features, and the anatomy of the occurred defects (e.g. tunnel void) can give better understanding from the mechanism of the bobbin friction stir welding. The alteration of the weld microstructure in the middle of the stirring zone, compared to the transition regions (thermomechanically affected zone and heat affected zone) can explain the mechanical grain refinement caused by the stirring action. Also the void formation originated from the inconsistency of the welding parameters can explain the insufficient material flow within stirring zone, induced by the rotating tool. Therefore, obtaining a defect-free weldment with a uniform grain structure can indicate the optimum welding parameters for the BFSW process.

10.2. Materials and method

10.2.1 Characteristics of AA1100 and AA3003 Aluminium Plates

AA1100 is a commercially pure aluminium alloy from the 1xxx series of wrought aluminium-based alloys. The AA1100 alloy with a standard element composition was chosen as the best candidate for the FSW process, because of excellent deformability characteristics. The chemical purity and stabilized microstructure can easily reveal any flow-based defects or weld contamination during the FSW process. If the applied welding parameters lead to unsatisfactory results for this alloy, it will not be suitable to obtain a sound weld for other grades.

AA3003 from 3xxx series is considered as a wrought aluminium alloy with good machinability, formability, weldability, the resistance of atmospheric corrosion, and moderate strength. AA3003 is wildly used in a range of industries such as chemical and food industries, as well as many building products. Even though AA3003 belongs to the wrought aluminium-manganese family, it is a non-heat-treatable alloy, and the microstructure cannot be adversely affected by the plastic deformation or heat-input during the FSW process. Compared to the 1xxx series, the AA3003 has higher tensile and elongation strength at the situation of elevated temperature. All these make it a good candidate to be investigated for the microstructural and flow-induced properties under FSW processing.

The chemical composition of the AA1100 and AA3003 aluminium alloys, analysed in elemental details, are listed in Tables 10.1 and 10.2, respectively.

Table 10.1. Chemical composition of the AA1100 aluminium alloy, measured in elemental detail (wt. %).

Chemical Element	Composition (wt.%)
Zinc (Zn)	0.006
Manganese (Mn)	0.016
Silicon (Si)	0.138
Copper (Cu)	0.009
Chromium (Cr)	0.03
Iron (Fe)	0.182
Magnesium (Mg)	0.007
Aluminium (Al)	Balance

Table 10.2. Chemical composition of the AA3003 aluminium alloy, measured in elemental detail (wt. %).

Chemical Element	Composition (wt.%)
Zinc (Zn)	0.1
Manganese (Mn)	1.2
Silicon (Si)	0.6
Copper (Cu)	0.12
Iron (Fe)	0.7
Cobalt (Co)	0.1
Zirconium (Zr)	0.1
Aluminium (Al)	Balance

10.2.2. The Features of the Bobbin-Tool

The significant features of the bobbin-tool comprise a pin, connected between the top and bottom shoulders. For a uniform flow regime induced by the tool action, the pin is required to have a symmetrical design. To increase the efficiency of stirring action, the thread feature is usually required as it can benefit the vertical material flow circulation at the proximity of the pin. However, it cannot be excessively coarse on the pin, because of the consequence of excessive flash, or clogging by the plastic mass. The existence of grooves could create vertical resistance and cause remnants of

material on the pin, which is also known as cutting effect. As a result, while the tool is keeping adequate heat to break the boundary of grains when it transverses to certain welding directions, the material in SZ does not fully bond with adjacent portions. Also, threads in the pin should be designed either only on clockwise or anti-clockwise, otherwise the material flow could be stalled or delivered from the centre to the surface and increase defects such as incomplete joints, voids and beads, as inappropriate flows are produced by multi-directional threads. The flat feature helps the bonding process, which has a similar function during the stirring as the thread but in the horizontal direction [139]. Another well-known feature is the scrolled patterns which inscribe a spiral pattern on each side of the shoulder surface. The process of recrystallization and reforming grains is affected significantly by the shoulder, as the heat which is created from the friction of the shoulder and also the pin. The spiral scrolls on the shoulder, similar to the pin threads can conduct the mass flow inwards centred, and avoid the escaping of the plastic mass from underneath the shoulder, while the rotating tool moves forward through the weld-line. Consequently, the compression ratio for the spacing of the gap between shoulders is particularly important to produce the compression of the mass flows mixing from the AS and RS at the proximity of the pin, while the rotating tool travels forward.

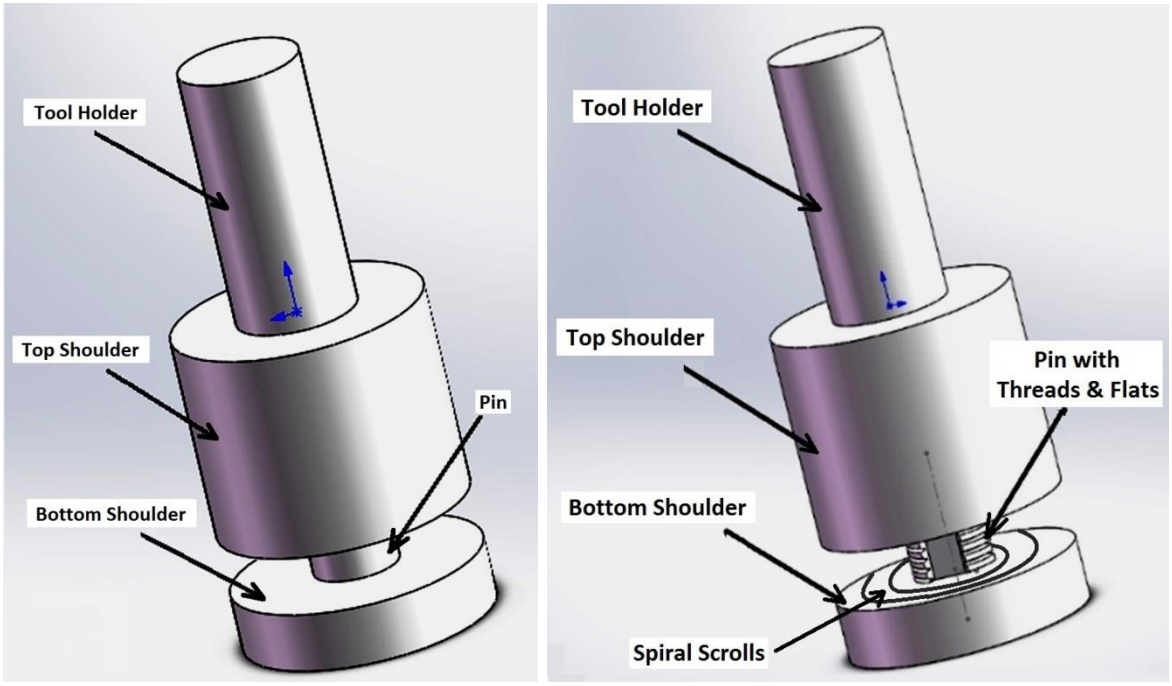

Figure 10.1. 3D schematic of the bobbin-tools, utilised for the welding of the aluminium plates; (a) single-piece bobbin-tool without ant surface features, utilised for BFSW processing of the AA1100 aluminium plates, (b) fully featured (threaded tri-flat pin, with scrolled shouldered) fixed-gap bobbin-tool, used to weld the AA3003 aluminium plates.

The certain two types of BFSW tools are applied in the experiment of this chapter, while the tool dimensions are the same and the surface geometrical features are different (Figure 10.1). A single-piece bobbin-tool without any surface features were utilized for BFSW welding of AA1100 plates, as it is considered the basic soft material to show the principles of this solid-state processing (Figure 10.1a). A fully-featured fixed-gap bobbin-tool comprises a tri-flat threaded pin, and scrolled shoulders were considered for the processing of the AA3003 plates (Figure 10.1b). Both bobbin-tools were made of H13 tool steel, with hardness of 560 HV. The geometrical details of the bobbin-tools are listed in Table 10.3.

Table 10.3. Geometrical details of the bobbin-tools utilised for BFSW processing of AA1100 and AA3003 aluminium plates.

Bobbin-tool	Simple tool (used for AA1100)	Fully-featured tool (used for AA3003)
Tool holder	12mm(diameter), 26mm(height)	12mm(diameter), 26mm(height)
Top shoulder	18mm(diameter), 20mm(height)	18mm(diameter), 20mm(height)
Pin	8.5mm(diameter), 5.8mm(height)	8.5mm(diameter), 5.8mm(height)
Bottom shoulder	18mm(diameter), 7mm(height)	18mm(diameter), 7mm(height)
Number of threats	3	Non
Number of flats	3	Non
Compression ratio	3.75%	3.75%

10.2.3. Welding Processing

The AA1100 and AA3003 aluminium plates of 6 mm thickness were used separately as the workpiece material for two sets of 1xxx and 3xxx welding trials, respectively. For each welding test, two plates were arranged side-by-side, with the dimensions of

250 mm (length) x 75 mm (width) x 6 mm (thickness), in the butt-joint position with no gap between the plates. To compare the weld structure in different condition of the welding process, a variety of the welding speeds (clockwise rotational/spindle speed; ω and advancing longitudinal speed/feed rate; V) were applied for the study of the weld texture and flow behaviour in different stirring regimes. In this regards, a set of tests were run in ω (350–600 rpm) and V (150–400 mm/min). Six sets of speeds (ω, V) were selected for AA1100 and AA3003 plates, applied in identical welding condition, only with different bobbin-tool designs for each grade. Table 10.4 presents the condition of welding trials in detail. A 3-axis CNC machine (model MX-45VAE, OKUMA brand, Japan) was utilized for welding of the plates, rigidly fixed under the fixture and strap clamps, with no pre-heating or post-heating treatment during the process. After conducting a single-pass weld-line, the weldments were cut along the transverse direction, at the middle of the weld locus, to select the weld cross-sections for the metallographic measurements.

Table 10.4. The specification of the operation parameters for the AA1100 and AA3003 BFSW weld sample.

Welding Speed Sets		**Aluminium Grade**		**Tool feature**	**Tool Material**	**Tool Entry**	**Working Temperature**
ω (rpm)	***V* (mm/min)**						
350	150	AA1100	AA3003	Simple single-piece bobbin-tool (AA1100)	H13 Tool Steel	Plate Edge	18 °C
400	200						
450	250						
500	300			Full-featured fixed-gap bobbin-tool (AA3003)	H13 Tool Steel	Plate Edge	18 °C
550	350						
600	400						

10.2.4 Metallography

To achieve the great standard of smooth mirror surface for etching and metallographic measurements, all the samples were ground and micro-polished manually. Then, using different etching solutions the microscopic details and flow structures were revealed. By using the light optical microscope (Olympus Metallurgical Microscope, Tokyo, Japan), and Scanning Electron Microscope (SEM) machine (JEOL 6100, JEOL Inc., Peabody, MA, USA) equipped with the Electron Backscatter Diffraction (EBSD) detector (HKL Nordlys III, Oxford Instruments plc, UK), the details of the microstructure were analysed via micrograph images. The details of the metallographic measurement are introduced in the next part, as Figure 10.2 briefly shows the analysing procedure.

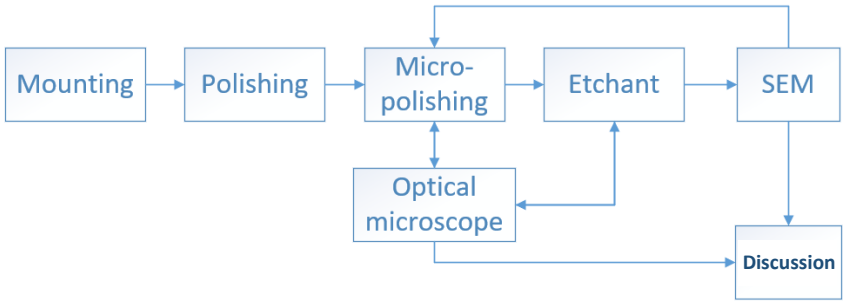

Figure 10.2. The flow of the metallography procedure indicated how the trial is done.

Sample Preparation (grinding and polishing)

The cross-section samples were mounted using EpoFix resin to be safe from any physical distortion and increase the efficiency of the polishing procedure. The mixed resin powder and hardener were cast in a cylindrical mould container, while the sample was placed faced down in the container, fully covered by the resin material. Buehler Grinder was run for the entire process of grinding and miro-polishing of the mounted samples. Initially, the trial of grinding was conducted via the fixture (Figure 10.3) followed by the manual polishing, according to the instruction listed in Table 10.5. The smooth mirror surface was attained even though the micro-polishing procedure with a series of Polycrystalline Diamond Suspensions (PDS) from 9μm to 0.6 μm (1sec. spray and 30sec. off). For the final step of micro-polishing, the samples were polished with a micro-cloth pad with Master Met (Colloidal Silica Polishing Suspension) and the stream of water instead of PDS. The final polished samples were washed by ethyl alcohol, and then dried under hot air.

Figure 10.3. Grinding of mounted samples; (a) Fixture of the grinder; (b) Specimens used automatic grinding.

Table 10.5. Details of grinding and polishing procedures for the samples preparation required for metallographic measurements.

Grinding stage	Surface	Rotating speed	Direction	Force on sample	Time
	P180-grit	120 rpm	+90°	Around 6 Lbs.	2 min/pad or till plane
	P280-grit				
	P400-grit			Around 5 Lbs.	3 min/pad or till plane
	P600-grit				
Polishing stage	Polishing suspension	Rotating speed	Direction	Force on sample	Time
	9 μm PDS	120 rpm	+90°	Around 5 Lbs.	3 min/ PDS or till smooth surface
	6 μm PDS				
	3 μm PDS				
	1 μm PDS				
	0.6 μm PDS			Around 8Lbs	3 min/ PDS or till mirror surface
Final micro-polishing stage	(MasterMet)				3 min

Etchants

The AA1100 weld samples were etched by a direct immersion the Keller's etchant (95 mL H_2O, 2.5 mL HNO_3, 1.5 mL HCl, 1.0 mL HF), for 30 seconds in 50°C temperature. The AA3003 weld samples were etched using a reagent solution of (25 mL CH_3OH, 25 mL HCl, 25 mL HNO_3, and 1 drop HF), for 60 seconds in 70°C temperature.

10.3. Results

10.3.1. Material flow Mechanism

Figures 10.4 and 10.5 show the macro-etched cross-sections of the AA1100 and AA3003 weld samples, respectively. In each set of cross-section, different welding

speeds were tested to compare the differences in internal flow features within the weld structure, altered by the various stirring condition.

As shown in Figure 10.4 for the AA1100 BFSW welds, the plastic flow patterns are observed at the centre of the SZ towards the AS border. These flow patterns are actually revealing the flow lines of the deposited mass at the traverse section of the trailing edge of the tool, once it leaves the location of the stirring action.

Three different flow patterns can be generally categorized from the macro-etch observations of the AA1100; S-line-shape flow (Figures 10.4a,b), ellipse-flow (Figures 10.4c,d), swirling-flow (Figures 10.4e,f). As shown by hatch-lines in the middle of the SZ (Figures 10.4a,b), the S-line in lower speeds represents the stirring action with a concentration at the proximity of the tool. The flow pattern has more depth in the mid-SZ, rather than the sub-shoulder areas, therefore the S-line flow is mostly induced by the pin action at the centre of the weld breadth. By the increase in welding speeds, the plastic flow pattern changes to an ellipse-shaped flow, which extends from the centre of the weld towards the underneath of the shoulders (Figures 10.4c,d). The ellipse flow shows a more uniform thermomechanical deformation feature, compared to the primary S-line flow pattern. The third flow pattern at the butting surface of the AA1100 weld is the swirling flow lines. This splitting shaped of the flow lines is mostly similar to the onion ring patterns of the CFSW weld. The macrostructure of the BFSW welds (Figures 10.4e,f) shows the segregation bands morphology a the middle of the SZ, elongated towards the top and bottom shoulders. It is attributed to the increase of the welding speeds, where the shoulder (because of more contact surface, compared to the pin) has a dominant role in stirring action. Therefore, the blipping flow patterns of the swirling plastic region are revealed in the sub-shoulder regions. The flow partitioning within the swirling structure reduces the integrity of the flow regimes. This leads to emerging of some discontinuity defects, e.g. tunnel void, within the stirring zone, as it observed in Figures 10.4e,f.

Figure 10.5 shows the weld cross-sections of the AA3003 aluminium alloy in deferent sets of speeds, similar to the AA1100 samples, processed by a fully-featured bobbin-tool. The lack of plastic flow at the stirring zone of the weld implies to the homogeneity of the mass flow induced by the proper tool performance. The fully-featured tool can create a more severe frictional heat because of the increased contact surface between the tool components and the workpiece materials. Therefore for the AA3003 samples, the heat input generated at specific welding speeds is higher than the stirring action occurred in AA1100 samples. This can form a more uniform plastic deformation, with more sufficient intermixing between the plastic layers flowing within the stirring zone. Therefore, the flow band structures are mostly unified without any segregation effect which can be delineated with etchant reagent. However, still, the hourglass borders of the stirring zone are distinct from the base

metal region, distinguishing the intense plastic deformation through the etched cross-sections.

However, at the elevated speeds (Figures 10.5e,f), the segregated flow-arms are observed widespread around the emerged tunnel void towards the AS border. This can be because of the higher strength of the material (AA3003, compared to AA1100), affecting the viscoplasticity of the plastic mass at higher speeds. Moreover, the elevated welding speeds can cause a relative flow inconsistency at the leading and trailing edge of the rotation tool. The simultaneous rotation and advancement of the tool along with the joint-line causes a plasticized mass flow circulating around the rotating pin which needs enough time to spatially be deposited at the trailing edge of the tool. The elevated feeding rate probably interrupts the refilling mechanism of the mass the AS position of the weld, therefore the flow discontinuity occurs the tunnel void defect at this region, which is revealed in Figures 10.5e,f.

The tunnel void opens by the increase of the welding speed, surrounded by the flow patterns elongated upwards and downwards on the AS border. At the elevated speeds (rotational and advancing), the plastic mass flow is mostly transferred by the shoulders action, rather than pumping by the rotating pin in the middle of the SZ. Therefore, as the pin action is not sufficient same as two symmetrical shoulders, the refilling mechanism cannot form uniform flow integrity during the mass deposition at the trailing edge of the tool. This causes a gap between the flow layers near the pin abutting, where is the location of the tunnel void discontinuity, while the surrounding flow-arms are gradually elongated to both top and bottom sub-shoulder surface regions.

For both AA1100 and AA3003, the material flow patterns in maximum speeds (600 rpm, 400 mm/min) have the best resolution within the SZ matrix. The visualization of the micro-flow patterns in higher magnification can reveal more details of the flow mechanism during the stirring action of the weld. Figure 10.6 shows two typical flow pattern selected from the stirring zone of the AA1100 and AA3003 welds, both processed at (600 rpm, 400 mm/min) speeds, but with different bobbin tools. Figure 10.6a demonstrated the swirling flow pattern for the AA1100 sample. Figure 10.6b shows the blipped flow pattern for the flow-arms within the SZ of the AA3003 weld sample. Both layered flow patterns show an onion ring shape, similar to the CFSW weld. However, the shear bands are mostly bending as extending upwards and downwards towards the sub-shoulder regions. Higher magnification of the flow-arms for both samples (Figure 10.6c,d) reveal similar morphology for the micro-flow packets forming the deposited mass layers. This implies on the similarity of the stirring flow mechanism in both samples with different material and tool features. In fact, it shows the micro-flow mechanism mostly is depended on the welding speeds rather than the workpiece material or geometrical features of the tool components. However, in macro-scale, the flow patterns can have different shapes.

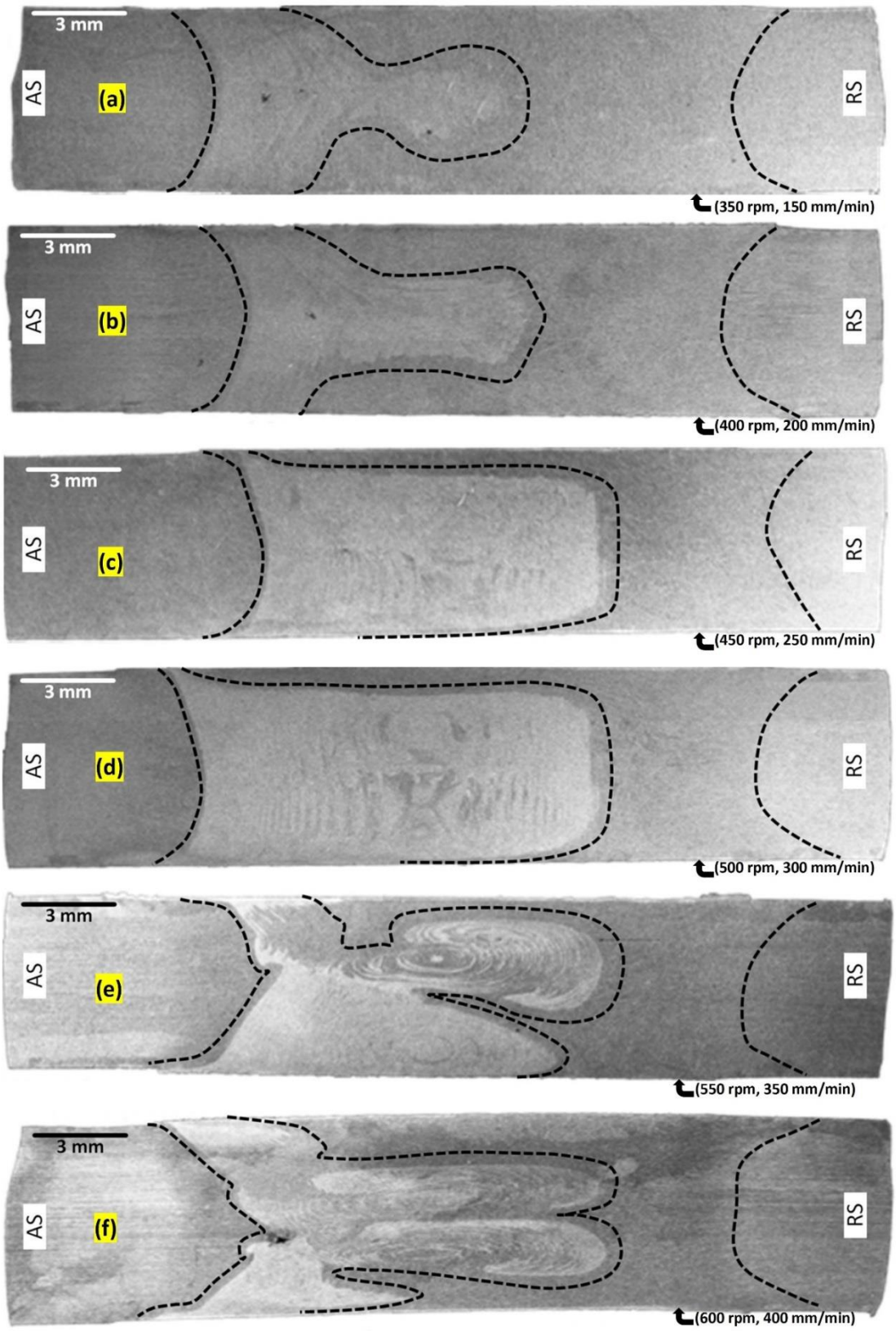

Figure 10.4. Macro-etched cross-section of the AA1100 BFSW weld samples in different welding speeds; (a) 350 rpm, 150 mm/min, (b) 400 rpm, 200 mm/min, (c) 450 rpm, 250 mm/min, (d) 500 rpm, 300 mm/min, (e) 550 rpm, 350 mm/min, (f) 600 rpm, 400 mm/min.

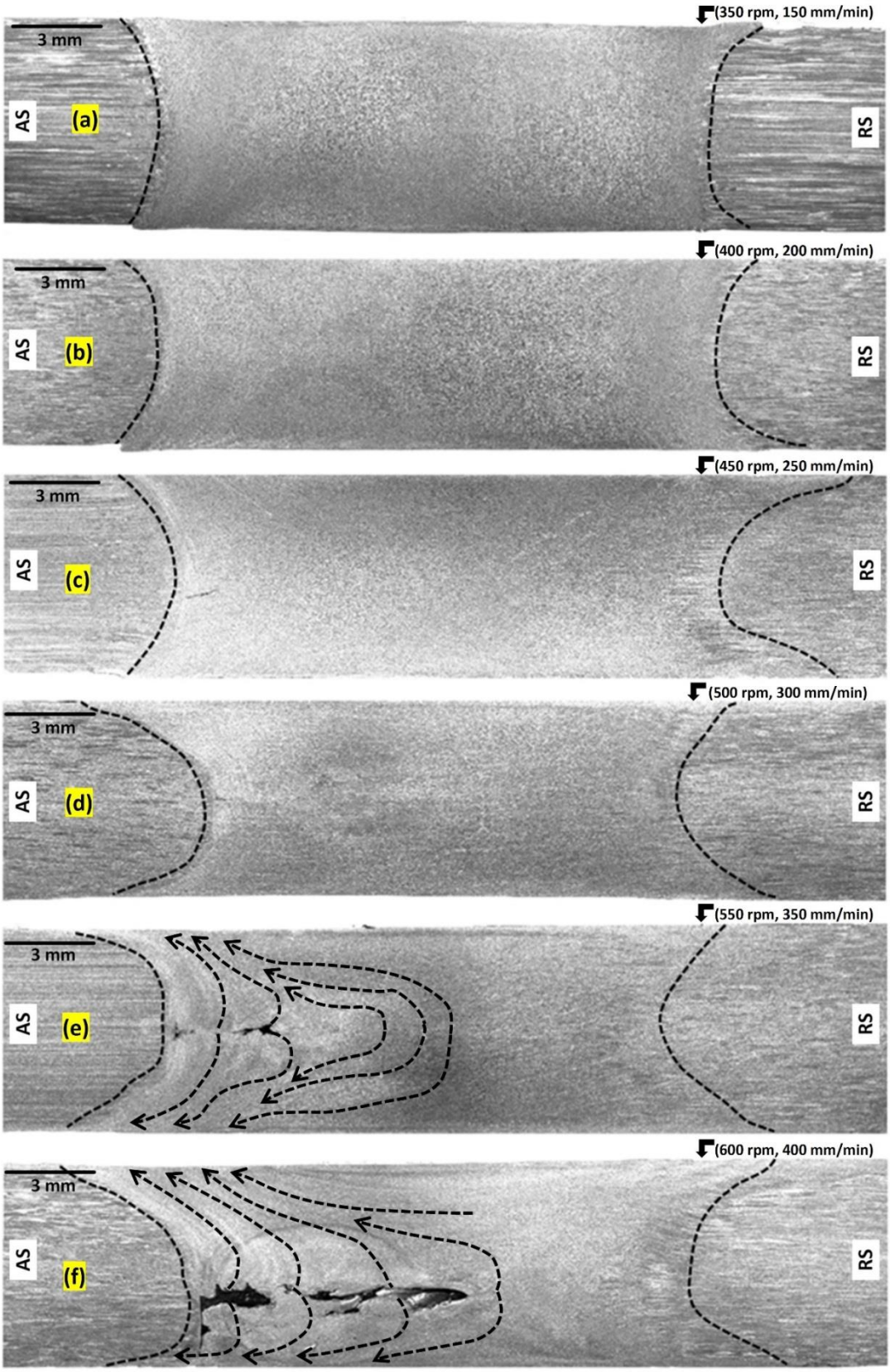

Figure 10.5. Macro-etched cross-section of the AA3003 BFSW weld samples in different welding speeds; (a) 350 rpm, 150 mm/min, (b) 400 rpm, 200 mm/min, (c) 450 rpm, 250 mm/min, (d) 500 rpm, 300 mm/min, (e) 550 rpm, 350 mm/min, (f) 600 rpm, 400 mm/min.

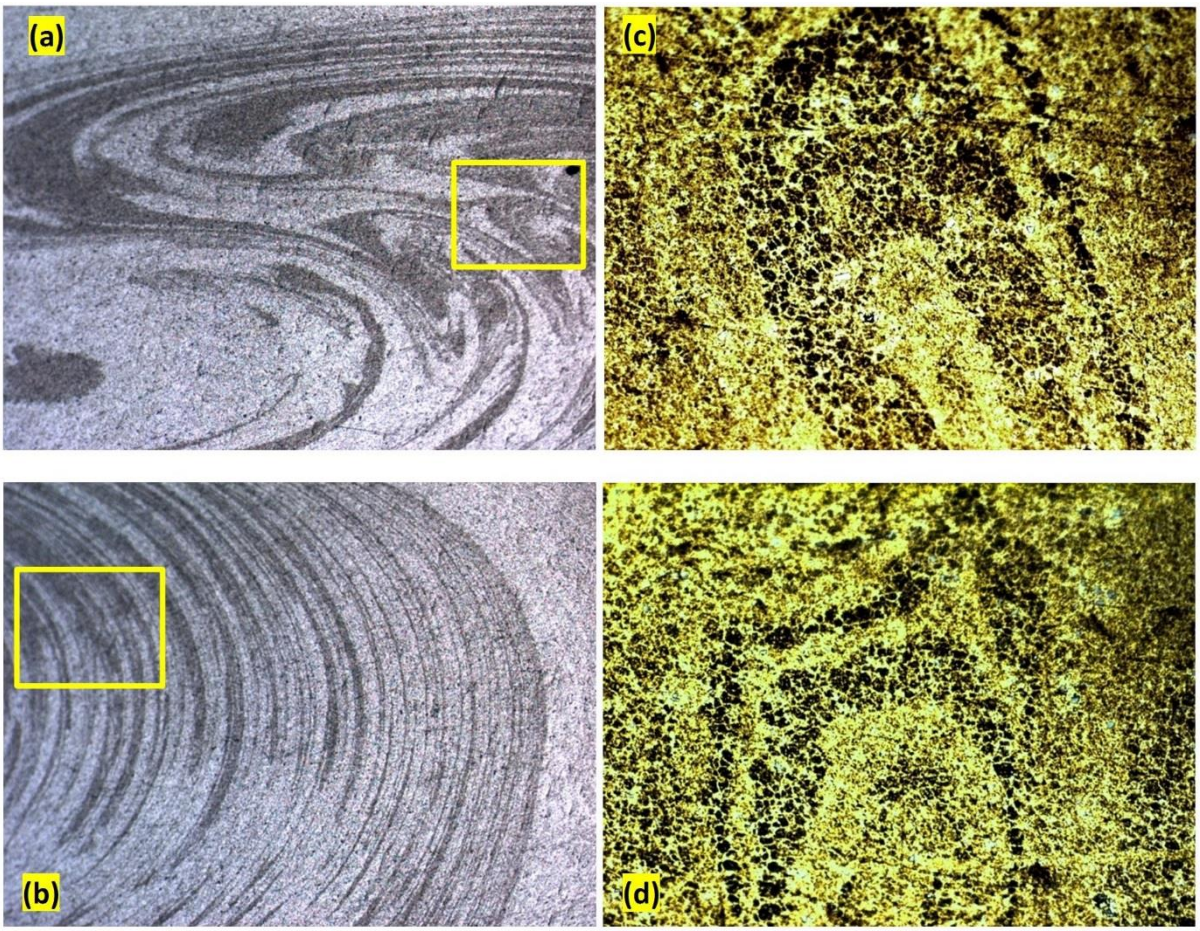

Figure 10.6. Optical microscopy of micro-flow arms for the AA1100 (a, b) and AA3003 (c, d) weld samples, both processed at the welding set of (600 rpm, 400 mm/min).

Figure 10.7 shows the schematic of different plastic flow mechanisms observed in the stirring zone of the AA1100 and AA3003 BFSW weld samples. These schematic flow patterns are drawn based on the macroscopic observations of the weld cross-sections in Figures 10.4-10.6. The dark hatched-lines are representative of the shearing bands forming the flow-arms existing within the plasticised mass between the mid-SZ and the AS border. The arrows elucidate the refilling process at the trailing edge of the tool during the deposition of the stirred mass. Different processing condition comprises the geometrical features of the bobbin tool, welding speed or workpiece material, can influence the nature of the plastic flow mechanism in macro-scale and construct different flow pattern morphologies within the cross-section of the SZ. The backward flow profile is the inherent pattern observable from the metallography of the weld; therefore, regardless the flow situation at the leading edge of the tool, the proposed interpretation only considers the flow transportation related to the mass deposition behind the tool, from the RS towards the AS. The details of the formation mechanism of the flow-induced defects are also absent in provided flow

interpretation, as there was not enough elucidating evidence for it in performed microstructural observation.

The flow bonding is the general result of the simultaneous effect of the tool components (symmetrical shoulders and the centred pin), generating the plasticization and shearing through the stirring mass. The heat input as the direct outcome of the mechanical stirring softens the mass and the subsequent rotation and movement induced by the tool activate the shearing flow through the yielded mass. The intercalation of the plasticised layers forms the intermixing between the bonding layers transported to the trailing edge of the tool. In this situation, the rotating tool can cause a repeatable periodic structure within the depositing mass layers. The uniformity of these flow patterns depends on the consistency of the mechanical shearing bonds induced by the tool components (pin and shoulders) and the relevant homogeneity in material positioning. In this chapter, three flow patterns were observed within the stirring zone at the cross-sections of the weld; S-line flow pattern (Figure 10.7a), swirling flow pattern (Figure 10.7b), and blipped ellipse-shaped flow pattern (Figure 10.7c). All these three patterns were observed for the AA1100 samples, while the AA3003 weld samples only demonstrated the blipped pattern at the highest applied speeds. For the AA1100 the maximum welding speeds led to the formation of the swirling flow pattern, elongated towards the sub-shoulder regions. This attributed to the effect of the shoulder rotation which is dominant in higher speeds, compared to the pin rotation in inducing of the mass flow. The shoulders have a wider contact surface with the workpiece material, and the intensified speeds can generate more frictional heat, and inducing more stirring flow. This is a general interpretation, and the flow mechanism can be affected by the materials properties or the geometrical features on the tool surface (threads, flats, scrolls).

The effect of each welding parameter cannot separately be elucidated, as the macrostructure results cannot distinguish the combination of the welding parameters roles on the flow mechanism. However, the higher resolution of the flow patterns in higher speeds implies the importance of the welding speeds compared to the tool geometry and mechanical behaviour of the material. Splitting of the flow (flow segregation or partitioning) in higher speeds also shows the greater role of the shoulder performance, compared to the effect of the rotating pin. This is where defects occur at higher speeds, as the pin cannot adopt the mass transportation inconsistency with the flow induced by the shoulders. Therefore, interruption of the integrity between the deposited flow layers fails the refilling and emerging of the tunnel void discontinuity between the pin position and the AS border.

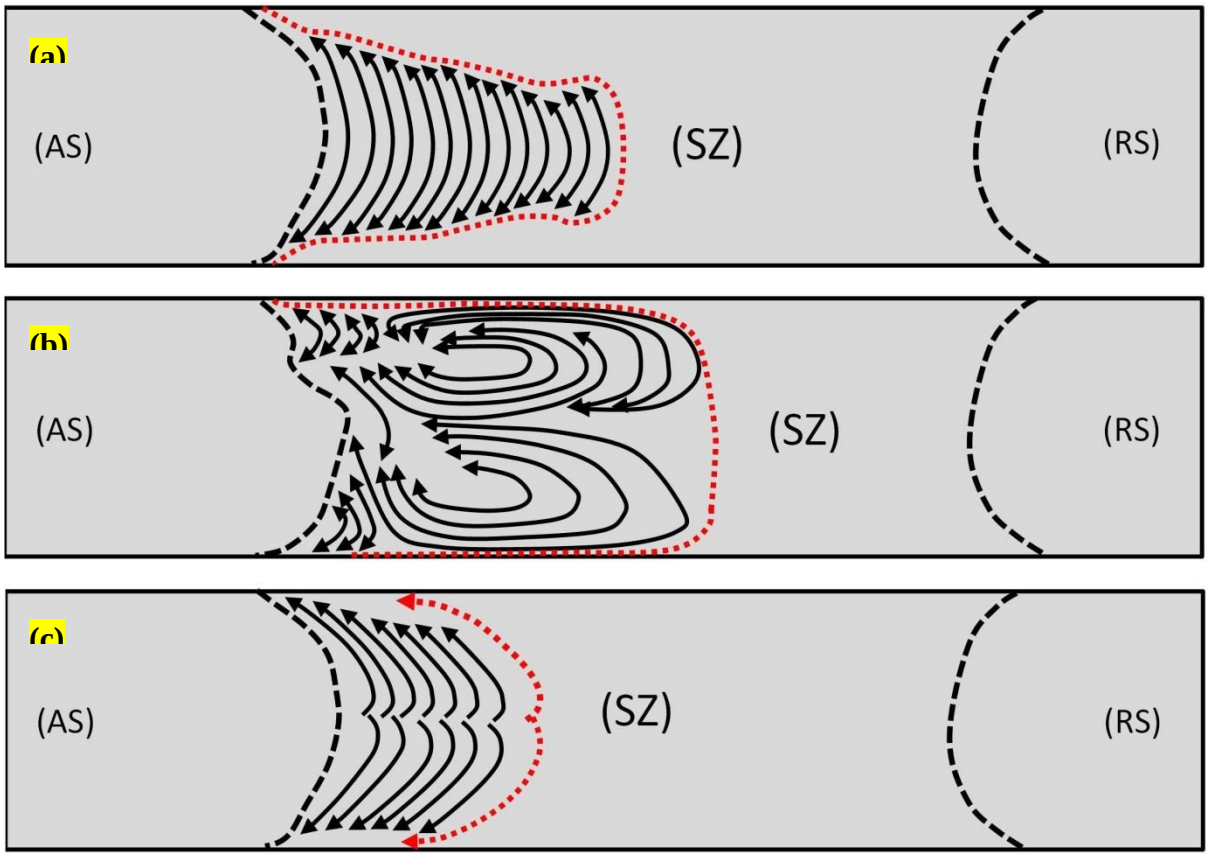

Figure 10.7. Schematic of the flow patterns formed during the BFSW process within the SZ, observed for the AA1100 and AA3003 samples in this research; (a) S-line flow pattern, (b) Swirling-shape flow pattern, (c) blipped ellipse-shaped flow pattern

10.3.2. Microstructure Evolution

Optical microscopy

Figure 10.8 shows the optical microscopy measurements for the microstructure of the mid-SZ for the AA1100 and AA3003 weld samples at (600 rpm, 400 mm/min) speeds set. The fine-grained morphologies show the equiaxed recrystallization, under the tool performance and the induced severe plastic deformation. However, due to the magnification limitation of the optical microscopy, the grain boundary contrast is not pronounced enough, for the uniform ultrafine grains of the mid-SZ. Hence, to overcome these limitations (magnification and resolution and contrast between the microscopic details of the grain structure), the electron microscopy was utilized for the rest of the microstructure observations.

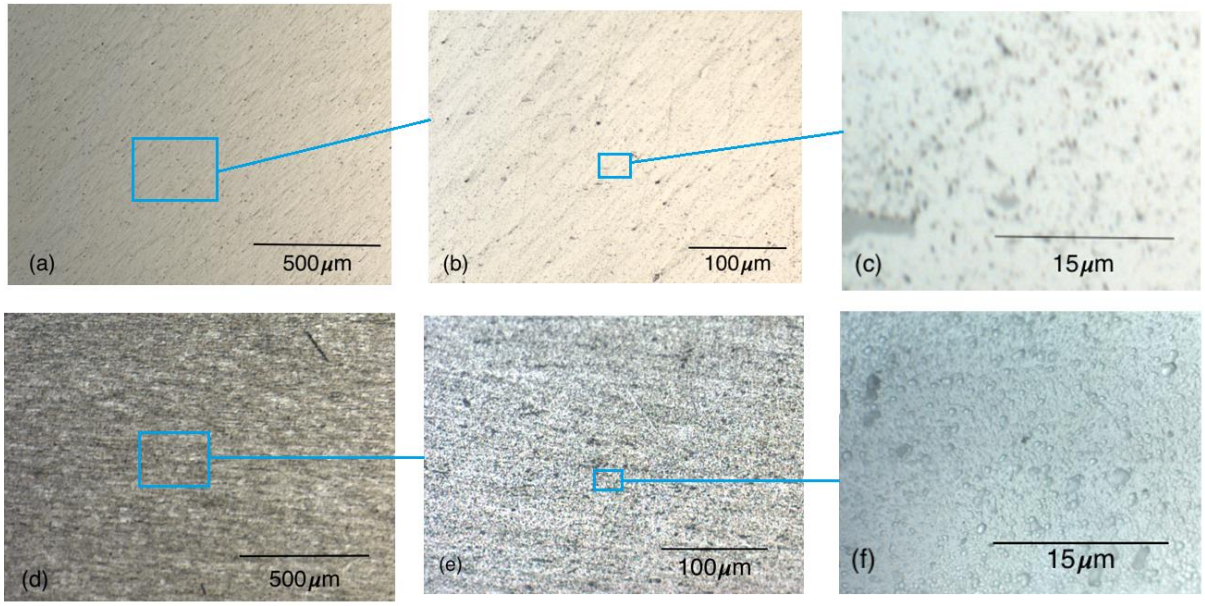

Figure 10.8. Optical microscopy of the etched cross-section of the aluminium weld samples, at the mid-SZ; (a, b, c) the AA1100 weld sample, and (d, e, f) the AA3003 weld sample, selected regions at different magnifications. Both aluminium weld samples were processed at the welding speeds set of (600 rpm, 400 mm/min).

SEM micrographs

Figures 10.9 and 10.10 show the SEM micrographs from selected frames of the mid-SZ, for the AA1100 and AA3003 weld samples, respectively. According to the material flow visualization, for each alloy, three sets of speed -(400 rpm, 200 mm/min), (500 rpm, 300 mm/min), (600 rpm, 400 mm/min)- were chosen for the SEM analysis. The comparison between the microstructures shows that the grain morphology has a similar trend with the increase of the welding speeds. Although the dynamic recrystallized structure was formed for all the samples, the differences in apparent surface roughness showing more severe plastic deformation has been increased by elevating the welding speeds. Figure 10.9c and Figure 10.10c demonstrate a morphological comparison of the AA1100 and AA3003 samples in the maximum speeds (600 rpm and 400 mm/min), respectively. The micrographs indicate that within the deformed structure, more severe recrystallization occurs in AA3003 sample, compared to the AA1100. This can be attributed to the mechanical tool action, where the fully-featured bobbin tool applied for AA3003 (comprises a tri-flat threaded pin and scrolled shoulders) enables to induce more uniform plastic deformation during the stirring process. The etched samples containing some pitting features which make it hard to observe the grain boundaries for precipitation details within the microstructure. Therefore, SEM imaging needs to meet more advanced imaging modes to increase the resolution of the microscopic details.

SEM images produced by the secondary electrons (SE) can provide better contrast in surface topography, therefore are enables to show the grain boundaries in ultrafine

microstructures. The secondary electron imaging (SEI) applied in Figure 10.11, shows the morphology of the mid-SZ area for AA1100 and AA3003 weld samples processed in speeds set of (600 rpm, 400 mm/min). The grain boundary contrast is shown for both samples, where it shows the average grain size of the 5µm for the dynamic recrystallized structure of the stirred zone. The grain boundaries network for the AA3003 samples shows a better contrast compared to the grain, which can be related to the physical properties of the alloy or completion of the dynamic recrystallization (DRX) by the fully-featured tool, compared to the AA1100 sample.

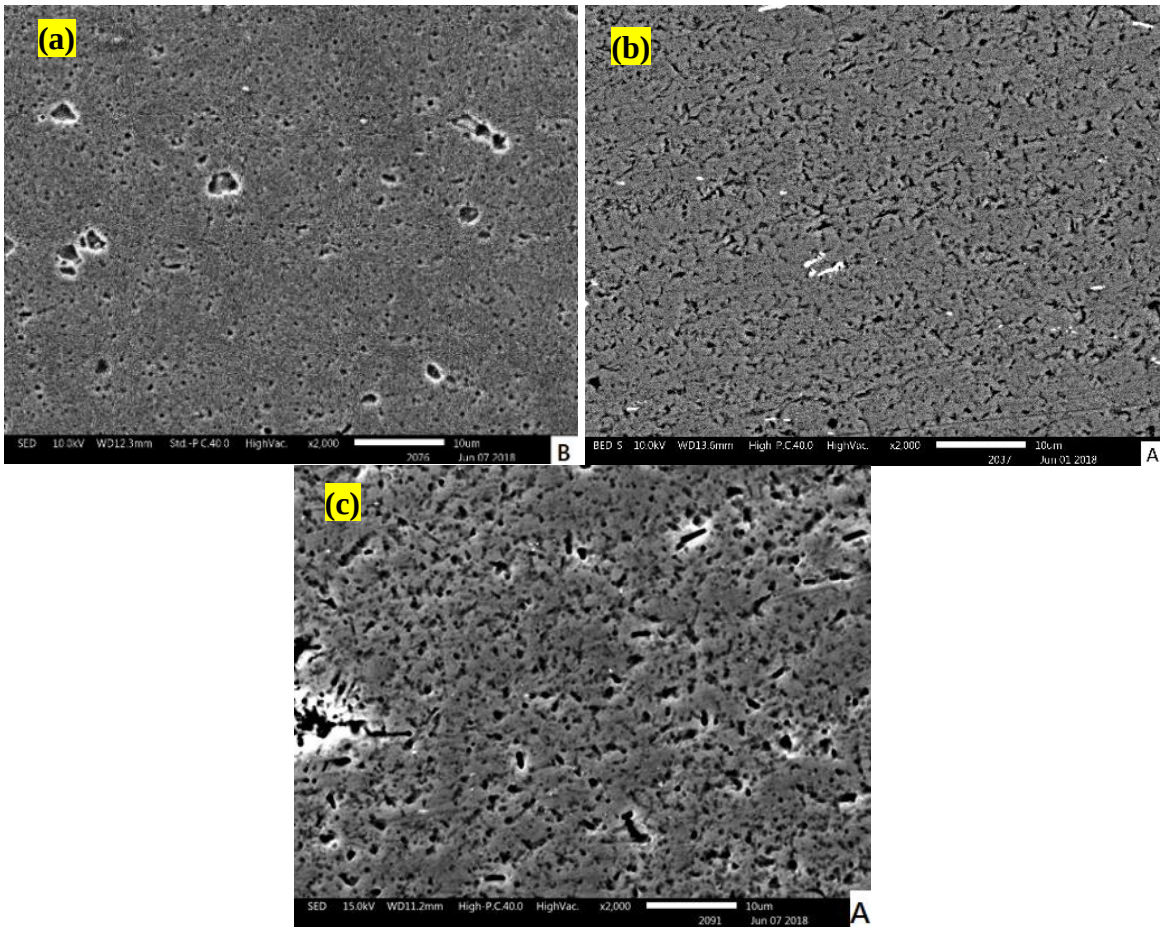

Figure 10.9. SEM micrographs of the AA1100 weld samples, at the mid-SZ region, processed with different sets of speed; (a) 400 rpm, 200 mm/min, (b) 500 rpm, 300 mm/min, (c) 600 rpm, 400 mm/min.

Precipitate particles with the ultrafine structure in a sub-micron scale need higher magnification to be properly observed through the micrographs. Backscattered electrons (BSE) have higher sensitivity in atomic numbers and can provide more details in phase contrast. Therefore, the BSE imaging can show the precipitates distinguishable than the Al-matrix.

Figure 10.12 shows the SEM micrographs in BSE imaging mode, with a better phase-contrast revealing the details of precipitation. The ultrafine precipitates are observed for both AA1100 and AA3003 at the mid-SZ, processed in speeds set of (600 rpm, 400 mm/min). The morphological observations demonstrate three different kinds of

precipitates; ultrafine precipitates in sub-micron scale (zone 1), micro-size precipitates (zone 2), and the corroded particles (zone 3). The nature of the precipitates, chemical composition and formation mechanism is not much clear in this stage. However, it can be concluded that the variety of size and morphology of the precipitates depends on different stages of the grain growth, occurring during the DRX mechanism. The corroded particles (region 3) have been partially removed within the surface area, affecting by the etching procedure. This is happening because of the selective dissolving of the silicon-compounds by the corrosive chemicals of the etchant reagents.

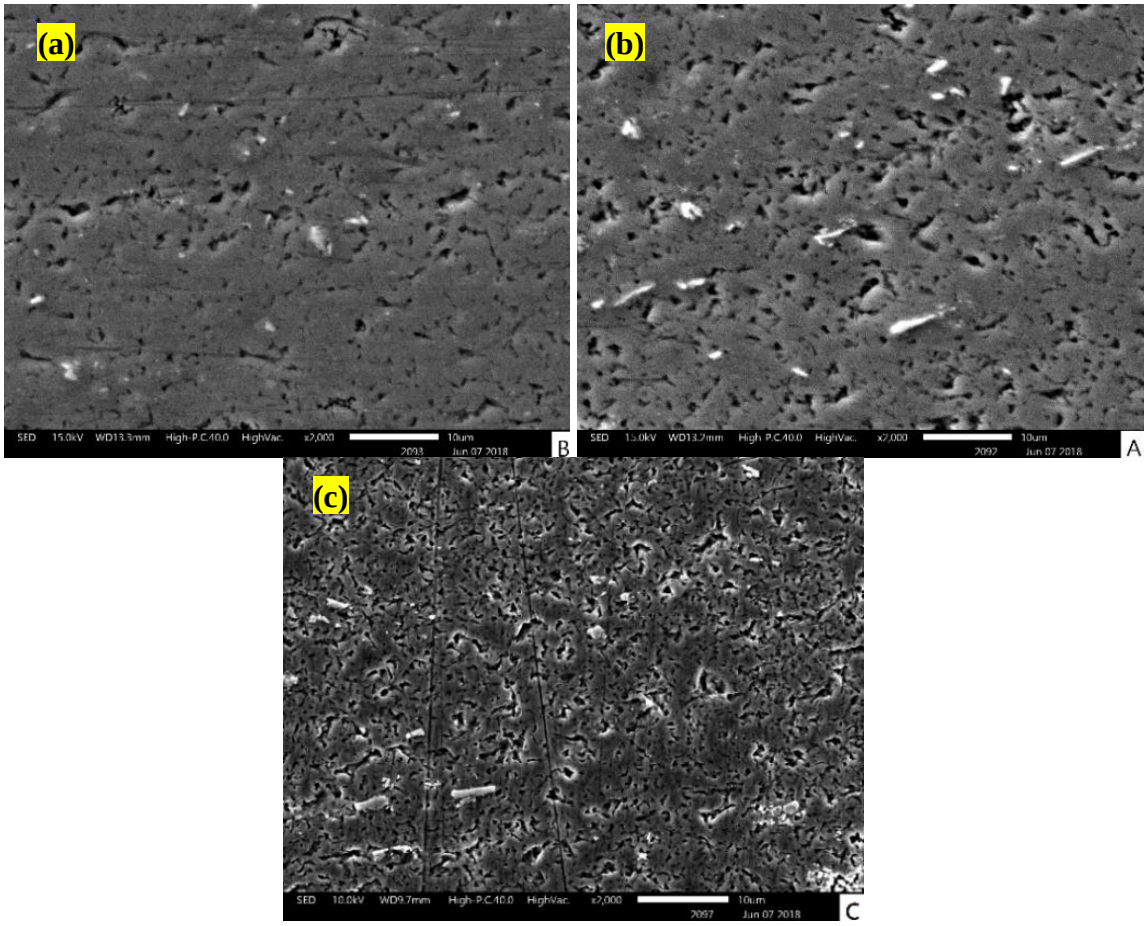

Figure 10.10. SEM micrographs of the AA3003 weld samples, at the mid-SZ region, processed with different sets of speed; (a) 400 rpm, 200 mm/min, (b) 500 rpm, 300 mm/min, (c) 600 rpm, 400 mm/min.

For a more quantitative analysis of the precipitation mechanism, the BSE results data have been processed to measure the details of the particle size and distribution as the secondary phase within the Al-phase matrix.

Figure 10.13 shows the graphs of the BSE data processed by the STATISTICA, elucidating the details of the precipitation; particles size and distribution, for the AA1100 and AA3003 samples, in mid-SZ (extracted from the micrographs in Figure 10.12).

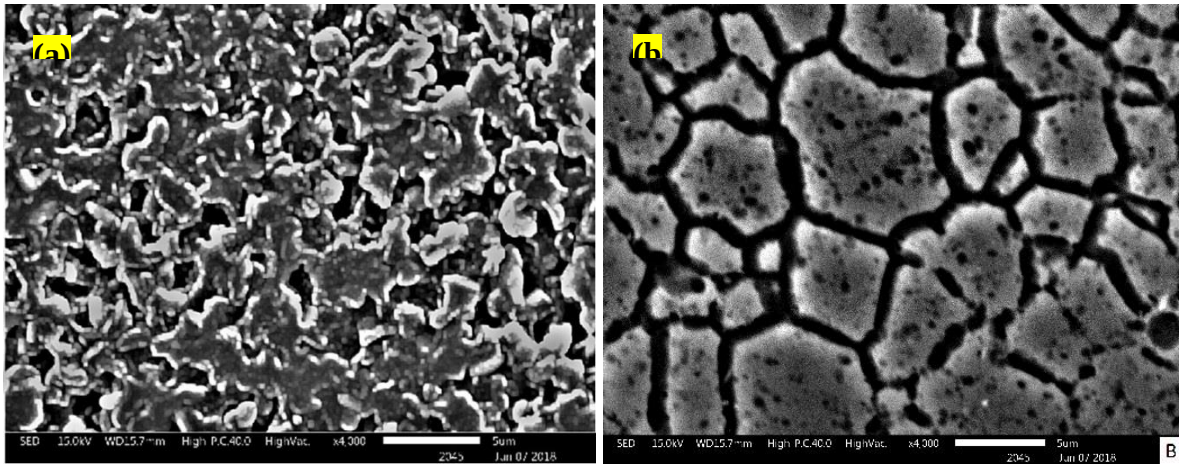

Figure 10.11. The SEM micrographs (SE imaging mode) of the aluminium weld samples, at the mid-SZ; (a) the AA1100 weld sample, and (b) the AA3003 weld sample. Both aluminium weld samples were processed at the welding speeds set of (600 rpm, 400 mm/min).

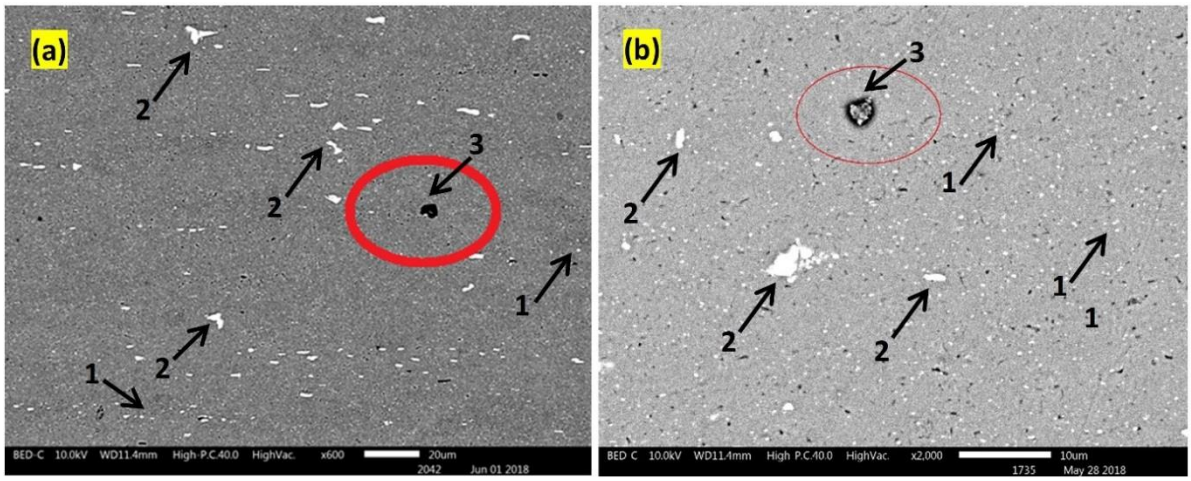

Figure 10.12. The SEM micrographs (BSE imaging mode) of the aluminium weld samples, at the mid-SZ; (a) the AA1100 weld sample, and (b) the AA3003 weld sample. Region 1; ultrafine precipitates, region 2; micro-size precipitates, region 3; corroded precipitates. Both aluminium weld samples were processed at the welding speeds set of (600 rpm, 400 mm/min).

The comparison between the information of the AA1100 and AA3003 samples shows that the average size of the precipitates in AA1100 sample (6.5µm), is more than the AA3003 sample (1µm). However, regarding the area occupied by the precipitates, the AA3003 has more precipitate content (7.5vol.%) compared to the AA1100 (1.8vol.%). This can cause better precipitate hardening effect for the AA3003 sample, as the finer distributed particles (with the average size of 1µm) allocate more volume portion of the structure (7.5vol%). This increases the surface-to-volume ratio of the secondary phase as the hardening particle playing a barrier role in front of the movement of the dislocations [142]. Therefore, the finer precipitates can block more

dislocation, create a pinning effect on the dislocation transitions, and subsequently act as a strengthening mechanism during the grain refinement caused by the DRX.

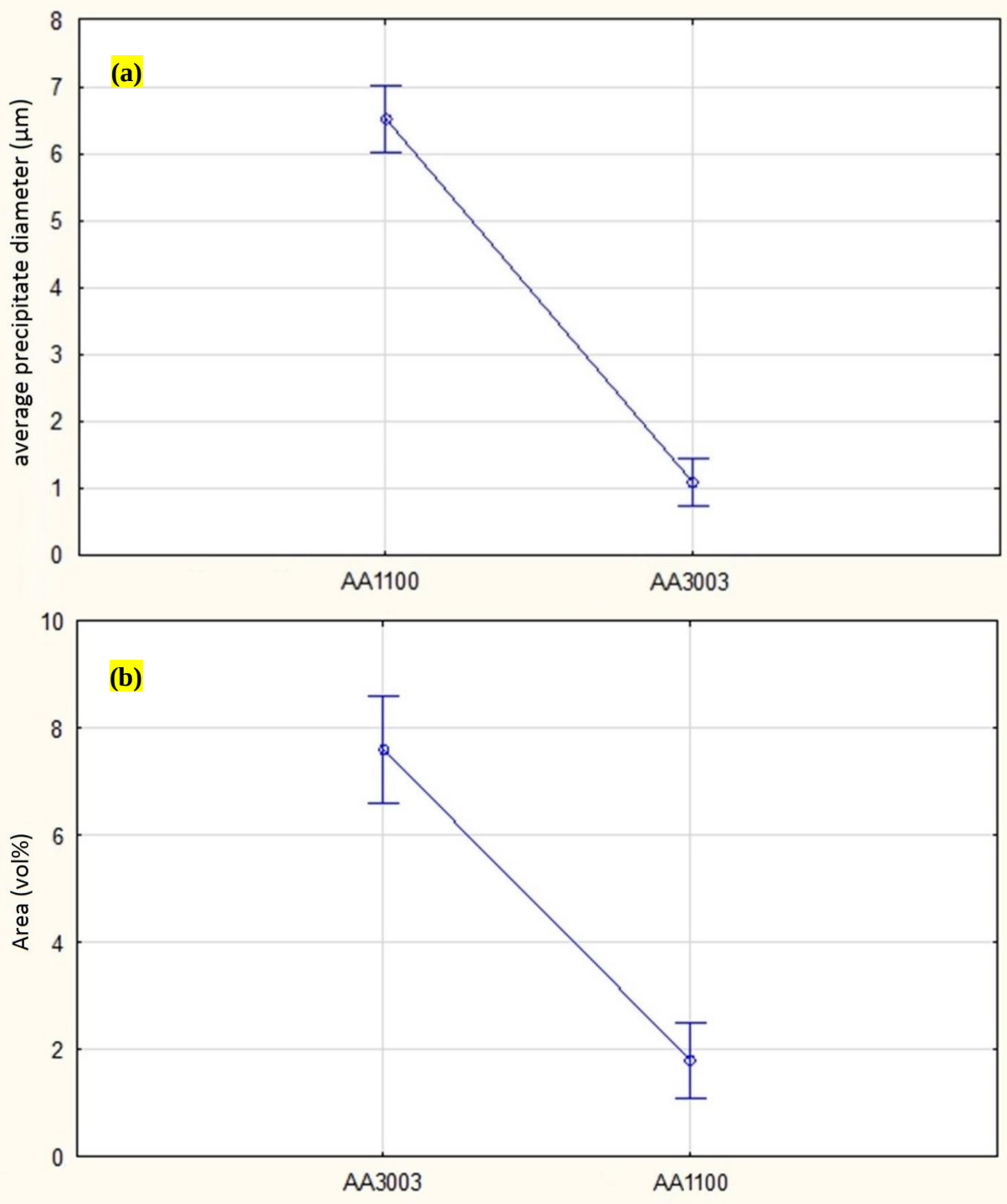

Figure 10.13. Quantitative analysis of the backscattered electrons data, for the precipitation mechanism at the mid-SZ of the aluminium weld samples (AA1100 and AA3003); (a) the average diameter of precipitates in the specimens of AA1100 and AA3003, (b) the area of the precipitates (vol.%) in the specimens of AA1100 and AA3003. Both aluminium weld samples were processed at the welding speeds set of (600 rpm, 400 mm/min).

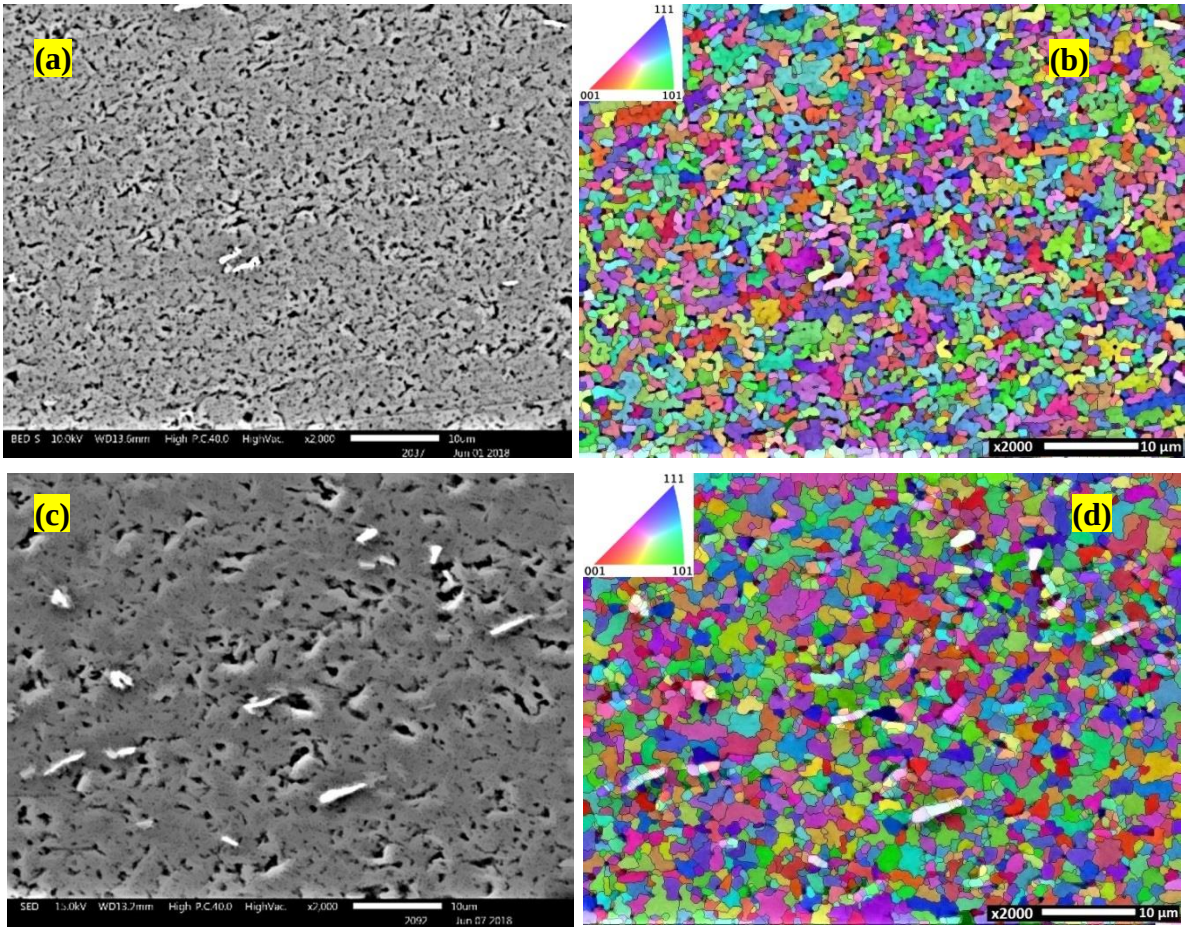

Figure 10.14. The EBSD analysis of the aluminium weld samples, at the mid-SZ; (a, b) the SEM micrograph, and the relevant IPF colour map for the AA1100 weld sample, respectively; (c, d) the SEM micrograph, and the relevant IPF colour map for the AA3003 weld sample, respectively. Both aluminium weld samples were processed at the welding speeds set of (600 rpm, 400 mm/min).

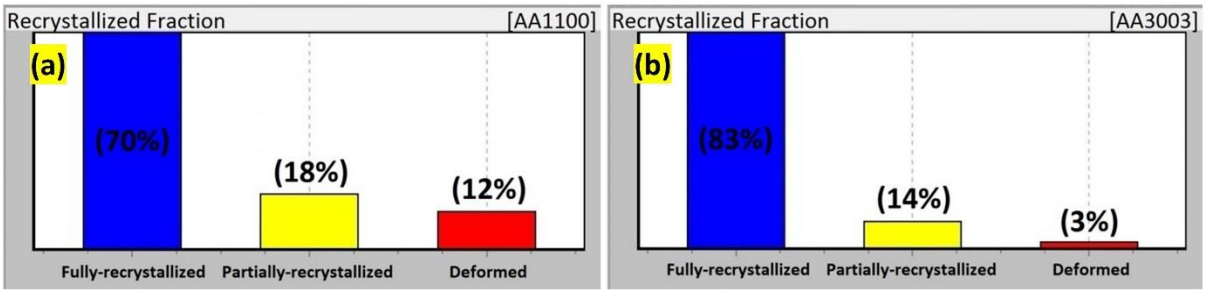

Figure 10.15. Quantitative analysis of the recrystallized fraction for the aluminium weld samples, at the mid-SZ; (a) the AA1100 weld sample, and (b) the AA3003 weld sample. Both aluminium weld samples were processed at the welding speeds set of (600 rpm, 400 mm/min).

Grain refinement and dynamic recrystallization are the direct outcomes of the thermomechanical plastic deformation and the subsequent re-cooling after the stirring process. Alteration in grain boundary network, grain size and morphology and the subsequent precipitation cause a stored-strain, induced through the weld texture, which can cause a crystallographic misorientation within the polycrystalline structure. Electron Backscatter Diffraction (EBSD) analysis gives more crystallographic measurement details of the microstructure, elucidating the grain misorientation in graphical maps.

Figure 10.14 shows SEM micrographs and the relevant inverse pole figure (IPF) colouring orientation map of the microstructure of the mid-SZ for the AA1100 and AA3003 weld samples, both processed at speeds set of (600 rpm, 400 mm/min).

The mid-SZ areas in both samples demonstrate an equiaxed recrystallized grain morphology in average grain size of below 5μm, similar to the SE imaging results shown in Figure 10.11. The mechanical rotation of the tool within the stirring zone fragments the grain structure, followed by a severe plastic deformation intensified by the frictional heat input. The subsequent dynamic recrystallization forms ultrafine equiaxed grains randomly distributed in different crystallographic orientation. The nature of the grain misorientation is not fully understood yet, but it is attributed to the stored strain within the polycrystalline texture during the stirring, releasing during re-cooling and DRX.

In figure 10.15, the analysis of recrystallized fractions of the mid-SZ texture shows that the AA3003 sample possesses more progress in recrystallization (83% fully-recrystallized and 14% partially-recrystallized fraction), compared to the AA1100 sample (70% fully-recrystallized and 18% partially-recrystallized fraction). This implies that under same welding speeds (600 rpm, 400 mm/min), the AA3003 sample (processed by the fully-featured tool) experienced more effective stirring action, compared to the AA1100 sample (processed by the single-piece simple tool).

10.4. Chapter Discussion

The material flow visualization measured within the cross-sections of the AA1100 and AA3003 BFSW weld plates AA6082-T6 revealed varieties of macro-features such as S-line shape, swirling like or blipped ellipse patterns in the SZ. The increase in welding speeds (rotational and longitudinal) moves the flow towards the sub-shoulder regions, where the shoulder flow action seizes the majority of frictional heat generation, because of wider surface contact with the workpiece material, compared to the rotating pin. In this situation, the flow partitioning can interrupt the flow integrity where it eventually can emerge a discontinuity between the deposited mass layers to occur the tunnel vid defect by the failure of the refilling mechanism, near the AS border of the SZ.

Microscopic analysis of the etched samples delineates some thermomechanical features at the mid-SZ region of the weld, where the severe plastic deformation and subsequent dynamic recrystallization form an ultrafine grain structure. The SEM micrographs showed a significant grain refinement, forming the equiaxed morphology with the grain size below 5μm. Also, the EBSD maps confirmed a randomly distributed grain misorientation through the weld texture, which is because of the mechanical stirring action and the subsequent DRX. The DRX mechanism also forms a remarkable precipitation process within the microstructure which can improve the strength of the material by the precipitate hardening effect in interaction with the dislocations in the crystalline lattice of the processed material. The EBSD analysis also approved a high rate of the recrystallization within the SZ of the weld, where the fully-featured tool performed a more progressed DRX within the texture, compared to the single-piece simple tool.

10.5. Chapter Conclusions

This chapter makes the original contribution of identifying different flow mechanisms created by the alteration of the welding variable (operational parameters of the welding (e.g. feed rate, rotating speed) and the geometry of the tool), which are evident within the macro-etched cross-sections of the AA1100 and AA3003 BFSW weld plates. As shown in optical microscopy images, the interaction between the bobbin tool and the aluminium workpiece results in the formation of S-line, swirling like or blipped ellipse-shaped flow patterns within the stirring zone of the weld structure. The overall interpretation is that the mutual interaction of the tool geometry and welding speeds influence the mass flow regimes to form different flow arm patterns during the deposition of the plasticized mass layers at the trailing edge of the tool, where the refilling mechanism happens near the AS border of the weld.

The microscopic confirms dynamic recrystallization progressed at the mid-SZ region of the weld, including grain refinement, the formation of the ultrafine equiaxed grain morphology, with a significant precipitation phenomenon during the stirring action and the subsequent re-cooling procedure. The EBSD analysis of the weld texture confirmed a randomly distributed grain misorientation induced by the mechanical performance of the bobbin-tool during the grain fragmentation of severe plastic deformation during the stirring action. The stored strain released during the DRX can stabilise the grain structure by formation of a uniform grain structure with a significant modification of the grain size and polycrystalline morphology.

Chapter 11: Thermomechanical Grain Refinement in AA6082-T6 Thin Plates under Bobbin Friction Stir Welding

Chapter Summary: Bobbin friction stir welding (BFSW), with its fully penetrated pin and double-sided shoulder, can provide high rates of heat generation. This produces solid-state thermo-mechanical grain refinement. In this chapter, the microstructure evolution of the welded joints of AA6082-T6 obtained using BFSW process was investigated with a focus on grain refinement. Two sheets of the AA6082-T6 alloy were butt welded with a fixed-gap bobbin tool. The microstructure at a mid-weld transverse cross-section was evaluated using optical microscopy and electron backscatter diffraction (EBSD). Significant grain refinement was observed with a decrease in grain size from 100μm in directional columnar grain morphology of the base metal, to an ultrafine size, less than 10μm, for the equiaxed grains in the stirring zone. The EBSD results showed that by BFSW processing secondary phase precipitation patterns were produced which are distinct from the primary artificial age-hardening precipitates created by the T6 tempering cycle. The severe plastic deformation and heat generation appear to accelerate dynamic recrystallization and precipitation during the BFSW process. The microstructural studies confirmed that the BFSW process can provide a highly efficient thermodynamically activated grain refinement in the solid-state without requiring additional processes such as heat treatment or external means of grain refinement.

This chapter is a derivative of the following publication:

Tamadon, A.; Pons, D.J.; Sued, K.; Clucas, D. Thermomechanical Grain Refinement in AA6082-T6 Thin Plates under Bobbin Friction Stir Welding. Metals 2018, 8, 375.

DOI: https://doi.org/10.3390/met8060375.

11.1. Introduction

11.1.1. Context

The friction stir welding (FSW) process was invented and patented by The Welding Institute (TWI) [99] to create a solid-state bonding by a non-consumable tool that rotates and mechanically travels through the workpieces to be joined. The initial design was for a single-shoulder tool, hence conventional-FSW (CFSW). TWI then introduced a further improvement in the form of a tool with two shoulders which penetrated through the whole weld section [4, 66, 67]. This bobbin FSW (BFSW)

process is a cheaper manufacturing technique with potentially higher productivity. Also it is highly repeatable, offering a rapid butt-joint by using a double-sided and fixed-gap bobbin tool [66]. The formation of the weld occurs through the mixing of the plasticized mass. Due to the combination of tool rotation and forward linear motion, there is an advancing side (AS) and a retreating side (RS). This results in different internal flow trajectories and the formation of a bonding layer in a solid phase process [167].

The greater heat generation in BFSW compared with CFSW has considerable effect on the thermal experience of the grains, and consequently can benefit the microstructure. The solid phase plastic deformation implemented in the BFSW process has a good potential for a thermomechanical grain refinement [174, 175]. However it is difficult to realise these benefits in some materials. A specific example is marine grade AA6082-T6 aluminium alloy, which suffers from poor weldability when used in thin plates. This chapter presents a set of microscopic analysis of this alloy, investigating the dynamic recrystallization and precipitation as the principles of the grain refinement during BFSW process.

11.1.2. Background

Friction Stir Welding is a solid-phase joining technique whereby the combination of the pressure (from the forging force of the tool) and the heating (caused by the friction between the tool and the workpiece) produces a high-strength bond, hence avoiding solidification defects [69]. During the FSW process, the deformed metal is changed from a solid phase into a mushy-like state. This thermomechanical stirring of the plasticized mass eventually leads to formation of a welded joint under the pressure and heat input [176, 177].

While most FSW research is widely performed via conventional FSW tools, there are possible benefits of using the bobbin tool which make this attractive to implement as part of the FSW process [2]. BFSW develops a double-sided weld with the advantage of the elimination of the root flaws in butt joints and also the removal of the need for a backing anvil or heavy fixturing as part of the process set-up. This results in less component distortion than CFSW due to a more uniform/balanced heat input. In addition, for a fixed-gap bobbin tool there are only two process variables to control: rotation speed (ω), and travel speed (V) [123, 155]. In BFSW the backing anvil of CFSW is replaced by a self-reactive bottom shoulder and the axial engagement force (to keep the tool in the substrate) is compensated by a self-adaptive compression ratio at the shoulders gap [123].

Based on the BFSW trials it has been suggested that as the tool rotates through the workpiece, the created friction leads to an increase in temperature in the material around the tool which promptly yields a plasticized zone [178]. This is the stirring zone. As the tool progresses through the weld-line, the stirred mass is squeezed (extruded) under the pressure of the shoulders and consolidates behind the pin to

form a bond [179, 180]. As opposed to fusion welding, no melting happens in the FSW process and the final weld-seam forms in a fine-grained microstructure without any solidification.

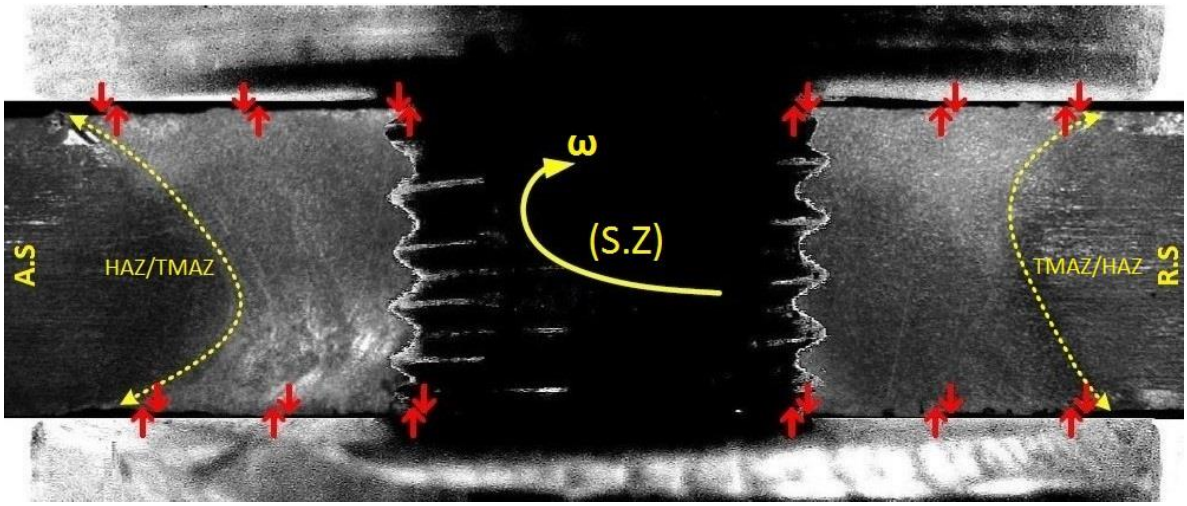

Figure 11.1. Schematic of transverse cross-section of the BFSW weld; dynamic interaction between bobbin tool and AA6082-T6 butted substrate during the stirring. The dotted lines denote the location of the hourglass borders as the inherent feature of the BFSW weld. The red arrows are representative of the compression ratio and the consequent axial forging force generated by stirring.

The BFSW process was originally developed for specific industrial exploitation, e.g. implementation in aerospace, transportation and marine industries [81]. Successful welding of aluminium alloys is one of the main advantages of this technique, compared to the more demanding setup requirements for fusion welding. The marine grade AA6082-T6 aluminium is an attractive industrial choice to process with the FSW technique. Suitable machinability and excellent corrosion resistance have seen the application of AA6082-T6 in shipbuilding and bridges [181].

However, in practice the FSW process causes macrostructural flaws in AA6082-T6 resulting in poor performance after welding [10]. Unfortunately for problem-solving purposes, the AA6082-T6 material responds poorly to conventional etchants which are commonly use for the metallography of aluminium alloys [80, 182]. This makes it difficult to observe the microstructure of the weld: the grain boundaries and internal flow features are difficult to resolve [70, 80]. Therefore, determining the origins of defect is problematic. Consequently it has been necessary to modify the composition of etchants and the process of application, and these techniques have only recently become available [80].

AA6082-T6 is an Al-Si-Mg alloy which has a stabilized microstructure by addition of manganese (Mn) [166]. The typical element composition is given in Table 11.1. The thin plates of wrought AA6082-T6 are rolled and then tempered during T6 heat treatment cycle to stabilize the microstructure and improve the mechanical

properties [159]. The T6 is a precipitation hardening tempering including three time-temperature cycles; first solutionising of the primary microstructure, quenching of the grains, and finally an artificial ageing by tempering heating [172]. Details of the T6 tempering for AA6082 are available [80, 183]. In general, quenching can form a single-phase supersaturated solid phase, this can cause a solid solutionising strengthening [72]. The heat input during the BFSW processing can change precipitation hence alter the T6 condition [64]. Therefore, the BFSW process may cause detrimental effects on the metallurgical and mechanical properties of the AA6082-T6 workpiece.

Performance assessment and optimization of the AA6082-T6 BFSW welds need to be evaluated by metallurgical analysis of the grain microstructure and phase characterization to see how much the artificial aging properties are affected by the process condition/parameters.

Microscopic observation of the BFSW weld reveals that the grain size and distribution of the weld region is typically affected by a plasticity-induced transition in morphology [184]. In general, there are three typical zones through the macrostructure of the cross section of the BFSW weld. The central region of the weld, which is the location of the direct interaction of the pin and the workpiece, is termed the stir zone (SZ). It is characterized by the hourglass borders (Figure 11.1) at the AS and the RS of the weld [70]. In SZ, the distorted and fragmented grains are thermomechanically plasticized by the rotation of the tool and then the stirred mass dynamically recrystallized after consolidation and cooling of the weld mass [71]. The next region after the SZ towards the base metal (BM) is the thermomechanical affected zone (TMAZ). The effects of the complex interaction between the friction, heat input and stirring action create a different thermal and mechanical induced microstructure at the proximity of the SZ [72]. Similar other weld types, the heat affected zone (HAZ) is a region of the base metal closer to the weld, and experiences some thermal flux effects during the welding which creates a transitional microstructure [73].

Grain refinement is a metallurgical process which makes the alloy stronger (strength, ductility and toughness) by increasing the number of grains, or modifying the grain morphology. Grain refinement can be achieved by heat treatment, adding alloying elements to the liquid phase during solidification, or plastic deformation (thermomechanical work). These can activate recrystallization mechanisms or change the grain growth behavior through the microstructure. In all these processes, by increasing the density of grain boundaries (G.B), the dislocation defects are blocked which leads to strengthening within the polycrystalline structure. Al alloys respond well to thermomechanical processing whereby the grain refinement can be dynamically obtained with control of the grain morphology as well as limiting grain growth.

In some specific alloys (e.g. 6xxx aluminum alloys), the strengthening mechanism can be via precipitation as the secondary phase. Nucleation of the hardening precipitates in a fine distribution -which are embedded in crystalline lattice of the solid solution- can form obstacles against dislocation movement, this acts as another strengthening mechanism.

11.1.3. Purpose and Approach

The heat-treated microstructure of AA6082-T6 contains a uniformed and stabilized solid solution which has been super-saturated by the artificial age-hardening. The T6 tempering condition retains the hardening particles in the solid solution matrix as opposed to precipitating them in grain boundaries where there are natural sites of nucleation. However it is expected that the solid phase plastic deformation of the BFSW process fragments the grains to ultrafine and changes the T6 microstructural properties. Published research on microscopic studies of friction stir welded alloys suggests that a form of grain refinement can happen during the CFSW process [22, 24, 174], however it has not been recorded in the literature for the BFSW technique.

To activate the grain refinement mechanisms in solid phase processes, heat and mechanical work are obviously two main prerequisites. Based on the thermomechanical nature of the process, BFSW can be a good candidate to develop grain refinement.

The aim of this chapter is to evaluate the grain refinement mechanism in AA6082-T6 BFSW welds by studying microscopic transformations within the weld texture. The starting hypothesis is that the driving force for this grain refinement is supplied by grain fragmentation, plastic deformation, and stored strain within the polycrystalline lattice structure which increases the density of grain boundaries and blocking of dislocations motion through the microstructure.

The direct observation of the ultrafine grain microstructure is inherently difficult using optical microscopy. More specifically, describing of the thermomechanical behavior of the weld needs the fine structure of AA6082-T6 alloy to be revealed in the deformed regions to show the weld texture evolution; grain orientation, size and morphology, based on crystallographic characteristics. The electron backscatter diffraction (EBSD) was used for crystallographic measurement of the microstructure because optical microscopy could not provide enough contrast and resolution to visualise all the microscopic details required for a precise measurement. Note that in optical metallography, the phase contrast is not easily distinguishable and occasionally the contrast which comes from different etch rates causes a misdiagnosis even on the same material. Hence, using the EBSD as microstructural-crystallographic characterization method can provide a more reliable study of the history of metallurgical transformation phenomena during the BFSW process.

11.2. Materials and Methods

11.2.1. Welding trials

In this chapter, the BFSW process was performed on AA6082-T6 Al alloy plates with the thickness of 4 m. The standard element composition of the parent metal is presented in Table 11.1.

Table 11.1. Element composition of the AA6082 Al alloy (wt.%) [169].

AA6082-T6	
Chemical Element	% Present
Silicon (Si)	(0.70–1.30)
Magnesium (Mg)	(0.60–1.20)
Manganese (Mn)	(0.40–1.00)
Iron (Fe)	(0.0–0.50)
Chromium (Cr)	(0.0–0.25)
Zinc (Zn)	(0.0–0.20)
Titanium (Ti)	(0.0–0.10)
Copper (Cu)	(0.0–0.10)
Other (Each)	(0.0–0.05)
Other (total)	(0.0–0.15)
Aluminium (Al)	Balance

A full-feature bobbin tool with a fixed-gap configuration as per [64, 185] was utilized for the weld trials. The tool features include a threaded pin modified by adding three symmetrical flat surfaces (tri-flat), with top and bottom shoulders. Each shoulder had a scroll, which is a spiral groove that is oriented (clockwise or counter-clockwise as appropriate) to feed material into the centre during rotation (Figure 11.2). In proportion to the 100 HV hardness of the aluminium plates, the welding tool was fabricated from H13 tool steel (560 HV).

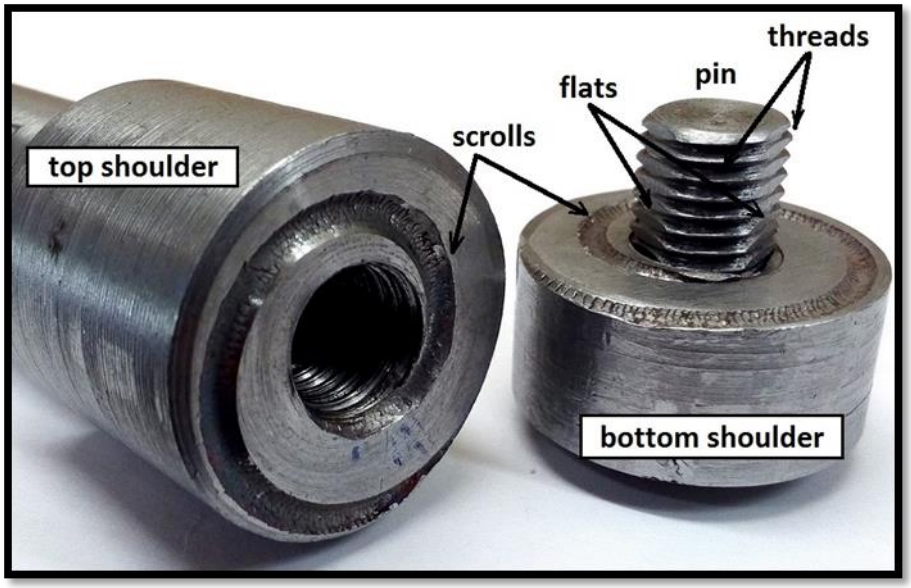

Figure 11.2. Configuration of the bobbin tool utilized for the AA6082-T6 weld trial.

The design intent of these features is that the threaded surface of the pin provides a more homogenized stirring condition and creates vertical flow around the pin [70]. The flat features grasp base material, and prevent clogging of threads by the stirring material [155]. The 360 degree spiral scrolls pump material towards the centre of the pin to seal the weld region [18]. The diameter (D) ratio ($D_{Shoulder}/D_{Pin}$) were selected as 3:1, consistent with those other references. A degree of compression of the base material is required, to make up for mass that is lost to the cross-section from flash and chips that may escape (especially at commencement). The compression ratio is the difference between the gap of the bobbin tool and the thickness of the workpiece plate, relative to the plate thickness, and was set at 3.75% [81]. More details of the bobbin-tool features used for the aluminium weld trials are listed in Table 11.2.

Table 11.2. Parameters of the BFSW trial for the AA6082-T6 plates.

Welding Parameters	amount
$D_{Shoulder}$ (mm)	21
D_{Pin} (mm)	7
$D_{Shoulder}/D_{Pin}$	3
Plate Thickness (mm)	4
Compression Ratio	3.75%
Spindle rotational speed, ω (rpm)	600
Feed rate, V (mm/min)	400
Thread Pitch (mm)	1
Number of Threads	4

The weldment plates were cut into two plates with dimensions of 250 mm in length and 75 mm in width and set side-by-side for a butt weld. The feed rate (V) and rotational speed (ω) were optimized based on the works of [64, 80, 155, 183]. For this aluminium grade, lower speeds imposed more violence on the tool and did not create a stable weld, and higher speeds led to poorer weld quality in the forms of structural defects (e.g. tunnel void or kissing bond discontinuities).

The aluminium welds were manufactured by a 3-axis CNC machine (2000 Richmond VMC Model, 600 Group brand, Sydney, Australia) with a Fanuc control unit and motor capacity of 14-horsepower spindle. The direction of tool rotation was clockwise, and the plates were fixed rigidly by strap clamps at the corners. The welding was done in open air with the work temperature of 18 °C at the beginning of the test and no preheating or post-weld heating for the plates. After BFSW process, the metallography specimens were selected from the middle of the weld-seam.

11.2.2. Metallography

To make the metallography samples, the weld cross-sections were mounted in thermoplastic hot-pressed resin. Next, the mounted samples were polished by the typical metallography preparation to provide a smooth mirror surface for etching [166]. After micro-polishing of the surface down to 0.5 μm, specimens were etched to identify the grain boundaries. Ultrafine optical observations were achieved, including the grain morphology. This reveals details of the dynamic recrystallization within the weld texture. The etchants typically used in the literature are Weck's and Keller's reagents. However the published results in the literature only show grain boundary patterns, and fail to show adequate results at higher magnification, hence cannot show grain refinement features, dynamic recrystallization and precipitation. Instead these finer features generally require electron microscopy. Recent published work [80] has demonstrated that it is possible to observe these microscopic features using more sophisticated etchant processes. The compositions of etchants of [80] was adapted by emphasizing the etchants compositions that were expected to elucidate grain boundaries and intermetallic compounds.

Our developed etching method comprises a multiple-step immersion of the specimens in an ultrasonic bath at 70 °C during etching. The composition of the reagents and other conditions during the etching (pre-etching, time and temperature) are shown in Table 11.3.

Table 11.3. Different chemical solutions for etching with separate processing procedures.

Name of Etchant	Pre-Etching	Etchant Composition
A	-	0.5 g $(NH_4)_2MoO_4$ + 3.0 g NH_4Cl + 1 mL HF + 18 mL HNO_3 + 80 mL H_2O (90 s, 70 °C)
B	20 g NaOH + 80 mL H_2O (20 s, 50 °C),	Etchant A (60 s, 70 °C)
C	20 g NaOH + 80 mL H_2O (20 s, 50 °C), then: 30 mL H_3PO_4 + 70 mL ethanol (20 s, 50 °C)	10 g CrO_3 + 2 g Na_2SO_4 + 10 mL HNO_3 + 10 mL CH_3COOH + 1 mL HF + 80 mL H_2O (60 s, 70 °C)
D	20 g NaOH + 80 mL H_2O (20 s, 50 °C), then: 30 mL H_3PO_4 + 70 mL ethanol (20 s, 50 °C)	Etchant C (60 s, 70 °C), then: 15 mL CH_3COOH + 85 mL H_2O (15 s, 70 °C), then: 15 mL H_3PO_4 + 85 mL H_2O (15 s, 70 °C)

After etching, the specimens were rinsed with distilled water, cleaned by ethanol, and dried with hot air. Then typical optical microscope was used for the microscopic observation of the etched cross sections.

11.2.3. Electron microscopy

For the electron microscopy analysis, the mounted specimens were re-polished using 9, 3, and 1μm diamond paste with a final polish of 0.06μm colloidal silica. An HKL Nordlys III EBSD detector was used to create EBSD maps for different region of the weld cross section, using a JEOL 6100 scanning electron microscope (SEM) with Oxford Instruments Aztec software. As the stirring was conducted over the weld locus, the grain size of the sample varied greatly from BM through to the centre of the weld. Thus to maintain a constant number of pixels for EBSD mapping and estimation of grain size, for small grain-sized regions, a magnification step size of 0.75μm with an overall acquisition area of ~1/16 mm^2 was used. Alternatively, for large grains of BM region, a step size of 3μm with an overall acquisition area of 2 mm^2 was used. All other control parameters such as binning, probe current, accelerating voltage, and exposure time were held constant. EBSD maps with obscured clarity of the Kikuchi diffraction patterns were rejected. By altering the step size, the average indexing rate of all collected samples was 97.5 %, where the unindexed pixels were filled in using traditional clean-up procedures with HKL Tango software. The elemental maps of different weld samples were subjected to an analysis using an SEM equipped with energy-dispersive X-ray spectrometer (EDS) detector. The working voltage for EDS mapping of the aluminium samples was 20 kV.

11.3. Results and Findings

The typical microstructure distributed in different regions of the BFSW joint is depicted in Figure 11.3 for the transverse cross-section of the AA6082-T6 weld. The micro-etched samples readily reveal the grain boundary (G.B) contrast which makes it possible to study the polycrystalline lattice and the grain morphology in different regions of the weld (HAZ, TMAZ, SZ) compared with the BM.

11.3.1 Optical microscopy

The optical micrographs in Figure 11.3 demonstrate a variety of grain morphologies from BM towards the SZ with a significant change in grains size. The optimized microscopic resolution and contrast also distinguishes between the grains of the HAZ and TMAZ which are hardly distinct in macroscopic measurements. The columnar morphology of the BM grains changes to equiaxed grain structure with an ultrafine size in the SZ.

Grain refinement

The comparative microanalysis between BM and SZ regions confirms a distinct modification in grain size and morphology. The 100μm directional grains of the BM are converted to fine spherical grains in a narrow range distribution less than 10μm in the SZ. These transitions in grain size and morphology may contribute to dynamic recrystallization through the SZ. It should be noted that the G.B patterns in the BM is not delineated continuously and in some places is hardly distinguishable from the grains. This feature may be due to the T6 temper making a uniform/homogenized lattice with motion of the grain boundaries. The grain growth phenomenon can change the shape and location of the grain boundaries (without the need of an applied shear stress) which is emerged by the discrete lines or disconnections in the plane-view micrographs as the characteristics of the motion of the G.Bs plane orientations.

It should be noted that the stirring reduces grain size to less than 10 microns with low anisotropy (equiaxed grain structure). Therefore, as a consequence of the recrystallization caused by the mechanical stirring mechanism, a fine homogeneity is observable through the microstructure of the SZ. This ultrafine condition is likely to contribute to the lack of success with simple conventional etchants.

It should be noted that there is a transitional region between the BM and SZ, showing a different morphologic grain structure. HAZ and TMAZ regions as the interface between BM and the SZ illustrate a plasticity-induced microstructure. The grain structures of the HAZ-TMAZ are refined, but the observed elongated grains are almost identical to the deformation-induced thermal and strain fields which are directed from the SZ outwards. The dynamic recrystallization and transition gradient of the grain morphology for the HAZ and TMAZ regions are shown in micrographs Figures 11.3b,c. The TMAZ in proximity of the weld region shows

significant grain distortion which is directly attributed to the strain field caused by the mechanical work and heat generation in the SZ. The next region, HAZ, is in the first instance only affected by the heat flux conducted from the SZ. The micrograph shows different morphology and smaller grain structure compared to the base material, but has similarities to the thermo-mechanical affected zone in terms of the grain size and morphology. This was interpreted as a thermal-induced reduction in grain size via activation of sub-grain boundaries and formation of new boundaries. It is also possible that strains may be induced in this region during post-welding re-cooling, and this may affect the development of grain attributes.

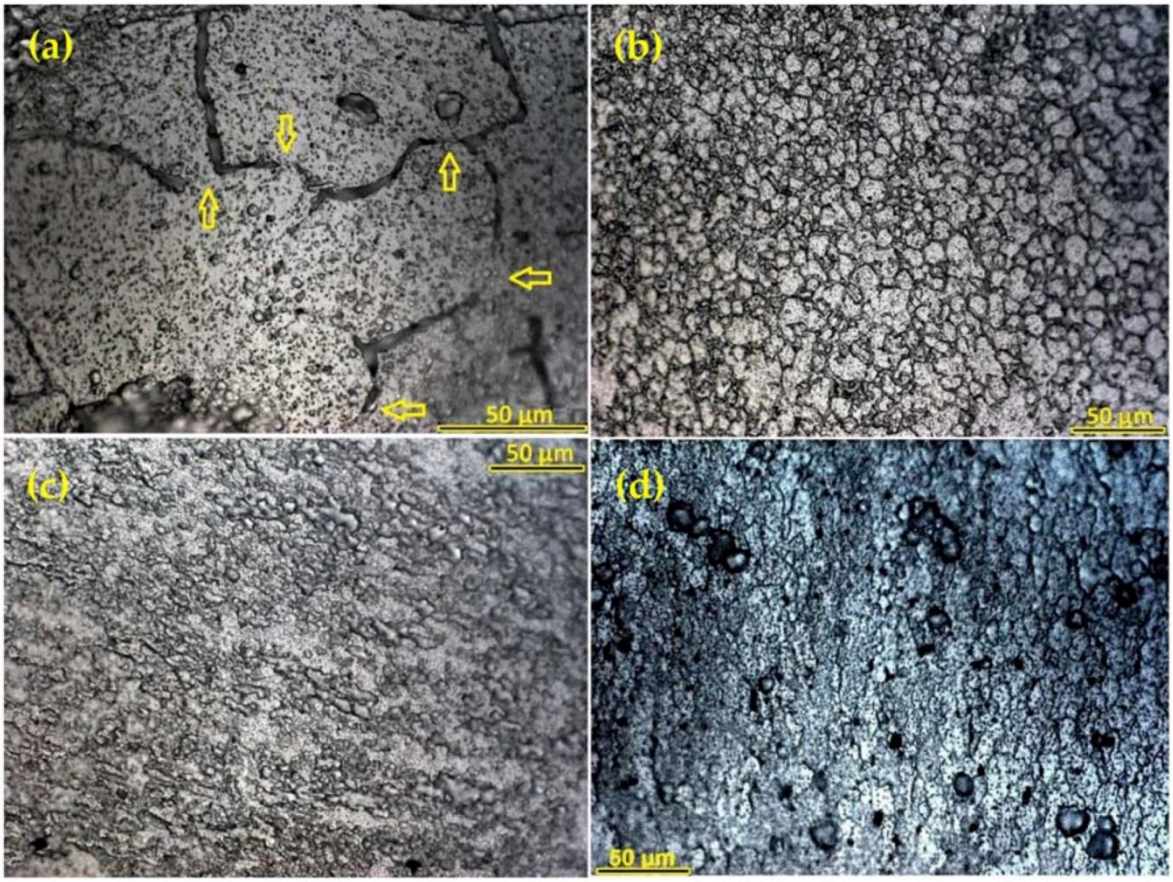

Figure 11.3. Microstructure of different regions of a BFSW A6082-T6 weld, processed by etchant A; (a) BM. The yellow arrows show the motion of G.B.; (b) SZ; (c) Heat Affected Zone (HAZ); (d) Thermo-mechanical Affected Zone (TMAZ).

It seems that the transitional region of HAZ/TMAZ is the place that most illustrates the thermomechanical nature of the BFSW processing. In this regard, additional etchants (see A, B, C, D in Table 11.3) were developed with higher discrimination to reveal more details of the recrystallization and transition of grain morphology through the microstructure of AA6082-T6 in a finer scaled microscopic observation.

Figure 11.4 shows the transitional structure of TMAZ in the vicinity of the SZ revealing a tapered pattern representative of the morphological flow of grains in an

inhomogeneous microstructure. Adjacent to the SZ a poor distribution of G.B (washed pattern) is observed which is representative of a transformed grain structure (bulging recrystallization) at the entrance of the weld region.

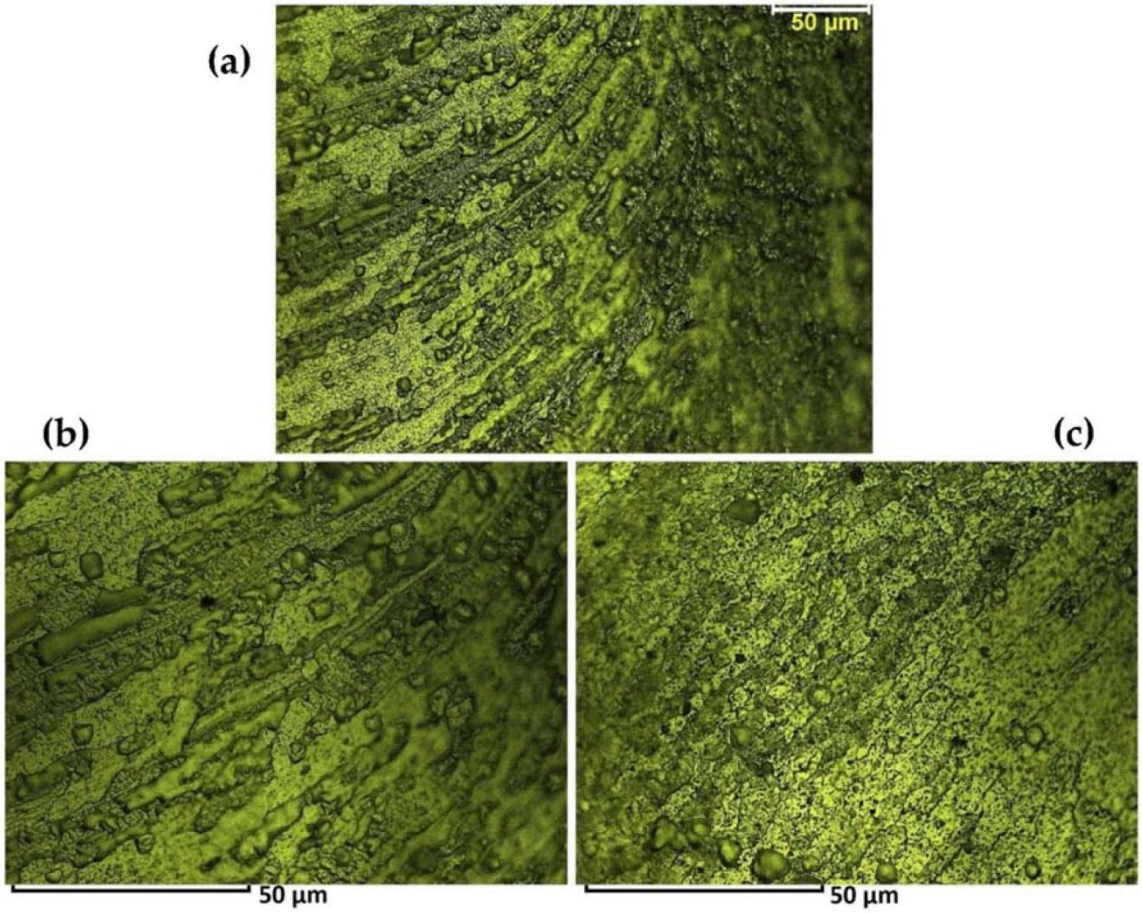

Figure 11.4. Morphological transition of grain flow in the TMAZ processed by etchant: (a) overview; (b) higher magnification view of the region closer to the heat affected zone; (c) higher magnification view of the region closer to the stirring zone.

The bulging recrystallization (BLG) is characterized by small recrystallized grains along grain boundaries which have been exposed to mechanical shear stress, see bottom right of Figure 11.4c. A limited crystal plasticity and an increase in temperature (both induced by the stirring) makes the grains bulge into each other, which results in stress relieving and the release of strain stored in the weld texture. The imposed stress-strain fields can also drive different grain boundary motion mechanisms which will be describe in the following.

Closer to the HAZ region, the micrograph shows a contrasting curved layered structure representing different morphological gradients of the grain distortion between the layers, see Figure 11.4b. The dynamic nature of the stirring flow causes each plasticized layer during the stirring to have a different thermal and mechanical

history, which affects recrystallization. Irrespective of whether grain boundaries are planar or curved, this distinct transition morphology is evidence of the grain misorientation for the TMAZ microstructure.

Complexities of the microscopic details inside of the grains are generally evidence of the transformation history which has been preferentially located for the microstructure, and can reveal the grain structure evolution in each specific region of the weld (HAZ, TMAZ or SZ). These different grain morphological features are representative of the transportation mechanism inside the weld which likely stabilizes the microstructure.

The microstructure of HAZ/TMAZ region was further analyzed with a different reagent C suitable for high magnification details revealing inner regions of the grains. Subsequent results are shown in Figure 11.5. Two other transformation features arise in HAZ/TMAZ material as described below.

Figure 11.5a reveals a discontinuity pattern for the grain boundaries. This is superficially similar to the effect seen in the base material (Figure 11.3a), but here the features are at smaller scales. This is interpreted as due to the grain boundary migration (GBM) in the form of the movement of the boundary separating two grains. The driving force for grain boundary migration originates from the elastic strain energy stored as dislocations, which in turn is attributed to the shear forces generated during welding. However temperature is an inherent prerequisite for the mobility of the boundary, as well as the impurity content of both the grains and the boundary. Nevertheless, at higher temperatures, grain boundaries are free to sweep across entire grains.

The microscopic studies suggest a possible mechanism for the grain boundary migration: the applied shear force acts on the disordered boundaries of the now-smaller grains, and causes those boundaries to advance into the grain. The stepping/motion mechanism is accelerated at triple junction points of grain boundaries [186]. The GBM effect is evident in Figure 11.5a as the discontinuities in grain boundaries.

The outcome of the process is the induction of internal strain and formation of sub-grain boundaries in the same and adjacent grains, and this is evident in Figure 11.5b as the aligned regions. Sub-grain boundaries (SGBs) are a thermomechanical feature, leading to reduction of internal stresses specifically in two-dimensional crystals. Strain field mapping of the crystalline structures introduces dislocations which is consistent with the considerable strain along the grain. The observed dynamics demonstrate when dislocations cannot reach the grain boundaries, the array of dislocations arrange themselves in an aligned order inside the grain and form the sub-grain boundaries as the low-angle grain boundaries (LAGBs). The accumulation of dislocation cores at the sub-grain boundary creates a low-energy barrier for grain misorientation resulting in a strain free grain.

From the thermomechanical viewpoint these microscopic features (BLG, GBM and SGBs/ LAGBs) are a direct result of the mechanical work (the rotation of the tool) and the stored strain induced by the deformation. These structural features potentially adversely affect the mechanical strength properties of the HAZ/TMAZ region, but in another way are positive because they assist the dynamic recrystallization process and hence avoid microscopic failure or embrittlement.

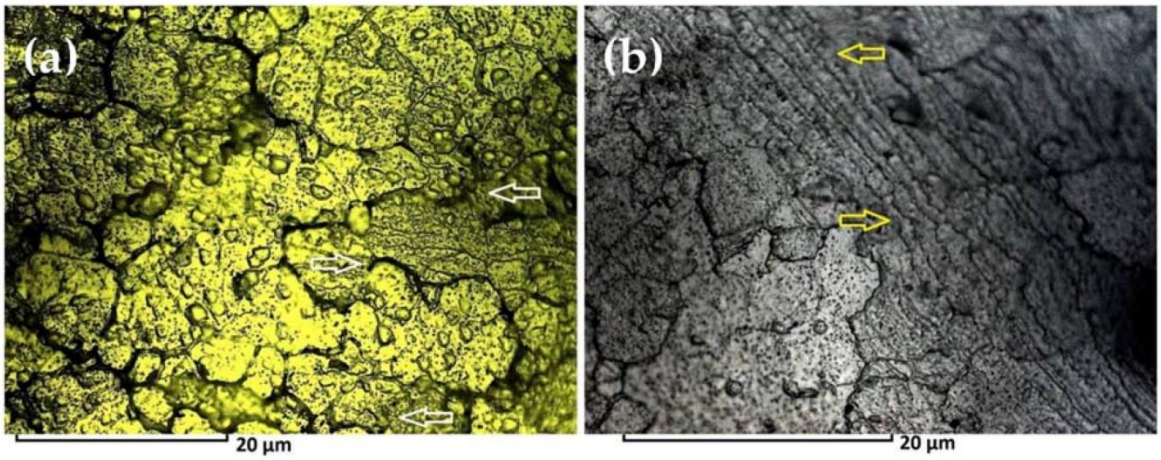

Figure 11.5. Thermomechanical features in TMAZ region, processed by etchant C; (a) Grain Boundary Migration (the location is highlighted by the white arrows), (b) Subgrain Boundaries (yellow arrows).

Glass-metal features

The other consequence of the thermomechanical processing of the polycrystalline structure is related to the SZ microstructure. As Figure 11.6a reveals the fine-grained homogenized structure of the SZ, some uncommon blister-like stain patterns are visible within the weld region, near the surface. At first glance these might be misdiagnosed as over-etching artefacts or impurity particles, but this is unlikely as they are an integral part of the microstructure. They are unlikely to be precipitates as their size are more than typical. This is not pitting as the structure is filled rather than an open void expected of a pit. It is also not an inclusion as these appear in identifiably different ways for this alloy [80]. Figure 11.6b shows a higher magnification of this segregated spherical mass within the SZ. The interpretation is that these granular areas comprise the amorphous structure of metallic-glass. The blurred microscopic region has a glassy/amorphous structure with a central shrinkage core in the middle of the sphere. This is typical of the formation of amorphous phase comprising a local shrinkage and lattice mismatch with the crystalline lattice [187-190]. Hence it is proposed that an element of localized melting has occurred, with a fast cooling rate. This is consistent with the observed superficial location of these structures, where proximity to air may cause faster cooling, though cooling rates were not measured.

Most alloys have a crystalline lattice structure in their solid state structures with long-ordered arrangement of atoms. Sometimes, after thermal processing when the

cooling rate is non-equilibrium, there is not enough time for crystals to form and the mass is locked in a glassy state. In this situation, the result is an amorphous or non-crystalline metal structure with a disordered atomic-scale structure or glass-like structure. There are occasional reports in the literature of a process in which a metallic-glass structure was formed by the FSW technique. This is observable as an amorphous layer formed by a self-propagating reaction due to the mechanical alloying effects [191-194]. The present results (Figure 11.6) show multiple amorphous regions that are distinct from the polycrystalline texture of the stirring zone. As mentioned above, it is believed that these are amorphous glass-metal features.

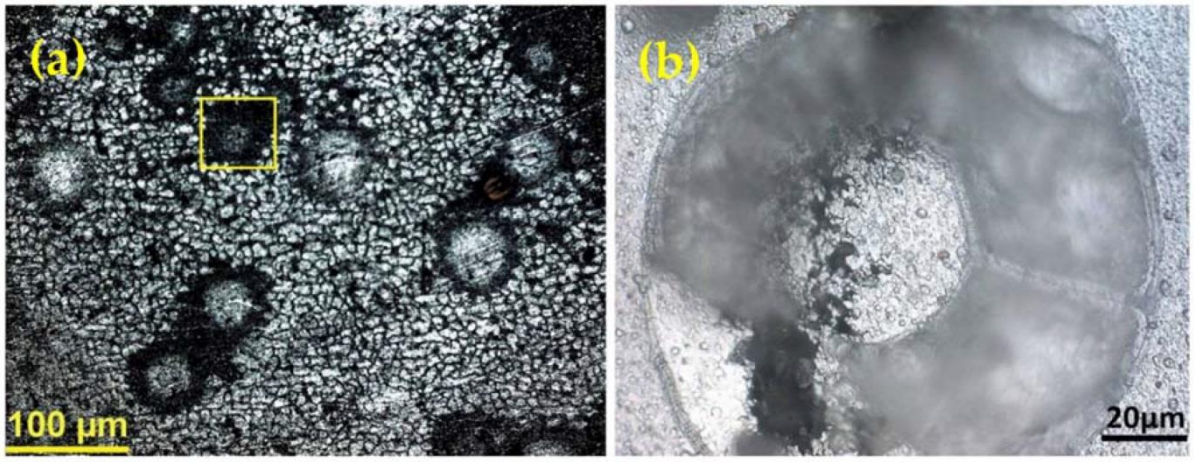

Figure 11.6. (a) Spherical blister-like stains within the microstructure of SZ, processed by etchant D; (b) Magnified feature of the blister-like patter, revealing a structure similar to the metallic-glass phase. The yellow rectangle shows the progressive area of magnification from (a) to (b). These features are interpreted as evidence of localized amorphous structure.

The structures were observed in only one of the weld samples. However the processes conditions under which this occurs are unknown. The structures have a random distribution in the sub-shoulder region. As evident in Figure 11.6a, the structures are separate from each other. They have an average grain size of 50 µm.

The spherical structure appeared after etching, and were best observed when etchant D was used. As the polished samples utilized for the electron microscopy were not etched, observation of these structures by SEM was not possible during this analysis. Hence, there was no chance to identify the composition of these patterns. Hence the composition is uncertain - a comprehensive diagnosis would require transmission electron microscopy and Raman spectroscopy, (XRD is unsuitable as it is inherently for crystalline structures), but these methods were beyond the present scope. It is not impossible that an Al_2O_3 composition may be involved. One possible origin could be from the broken surface oxide layer entering into the weld. It may be relevant to note that these structures were considerably larger than those observed in the literature [40, 41].

That concludes the results of the optical microscopy. Next more precise evidence was provided for grain refinement details using electron microscopy and EBSD.

11.3.2 Electron microscopy

Dynamic recrystallization

Figure 11.7 demonstrates the comparative EBSD maps of the BM and SZ regions showing different grain size and morphology. The drawn patterns based on the crystallographic measurement of the microstructure confirm that the directional large grains of the BM. have converted to the fine grains structure of the SZ with a spherical morphology. The average grain size of the SZ region is less than 10μm, while the BM grains are in the range of 100μm. Similar to the optical micrographs, these features confirm the dynamic recrystallization condition along with successful grain refinement during the thermo-mechanical regime experienced in the BFSW process. The dark features present in the material are attributed to the position of sites which could not be crystallographically detected by EBSD mapping. These features may representative of porosity formed in primary rolling processing of AA6082-T6 plates. However, the SZ microstructure shows that after BFSW processing the number and size of these features are reduced (at the same magnification). This implies an increase of the structure's density across the deformed grains, as the BFSW thermomechanical process –comprising forging and extrusion- can fragment the grains, squeeze the plasticized mass within the fixed gap between shoulders, and provide a condensed texture with decrease in grain size.

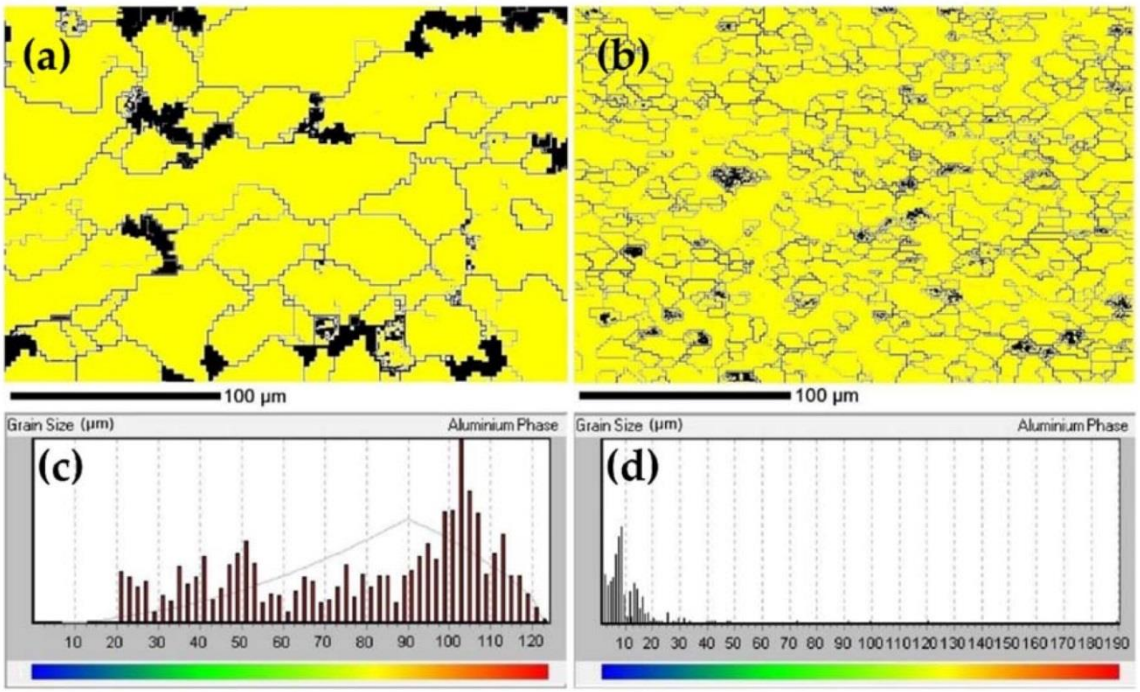

Figure 11.7. EBSD patterns of the phase map for: (a) BM, and (b) SZ and (c,d) the relevant grain distribution histograms.

We tentatively attribute the dark features to porosity, but there are other possible interpretations. It can exclude a pitting effect of the etchants because the surface was a micropolished specimen without any etching. However EBSD is sensitive to micro-cracks and micro-voids as these defects can interrupt the diffraction of backscattered arrays from the surface, hence can leave dark features. So the features may be cracks or voids of origin other than casting porosity. The fact that they become reduced in extent after welding implies they are micro-voids or porosity.

Precipitation

Another subject which requires explanation is precipitation (nucleation, spatial distribution and morphology) in the BFSW weld structure. Using optical microscopy some fine dotted patterns were observed within the grains (Figures 11.3-11.5). However there was no conclusive evidence to determine whether they were precipitates or pitting stains. Pitting stain emerges by over-etching. Figure 11.8 reveals the results of secondary electrons (SE) imaging and their corresponding phase colour contrasting maps for different regions of weld (BM, TMAZ and SZ). The phase map distinguishes the Al matrix phase as the yellow background, from dark spots representative of the secondary precipitate phase. Secondary electrons (SE) imaging is a beneficial analysis for the inspection of the topography of the sample surface. As shown in Figures 11.8a-c, micrographs delineate a wrinkled structure which is representative of the work-hardening and recovery mechanisms during the thermomechanical process. Similarly, the phase maps show that the density of precipitates is enhanced from the BM towards the centre of the weld (SZ), as the thermomechanical effects of the process (shear stress, strain and temperature) become intensified. Figure 11.8c and d shows that round features apparent in SEI (Figure 11.8c) are not evident in the phase map (Figure 11.8d). It concludes that the round features evident in the optical microscopy (see Figure 11.4) are pits rather than precipitates.

In general, artificial ageing and T6 precipitation in the stabilised microstructure of AA6082-T6 needs higher temperature and longer time in the furnace, compared to the BFSW process. It appears that here the precipitation mechanism has been activated by the thermomechanical work. On the other hand, as the grain size is reducing from BM towards the SZ (see Figure **11.**8), the precipitation density increases. Precipitates have a pinning effect which restricts the grain boundaries. Hence, it is inferred that the reduction in grain size is primarily a result in the increased density of precipitates. This is consistent with the literature [170].

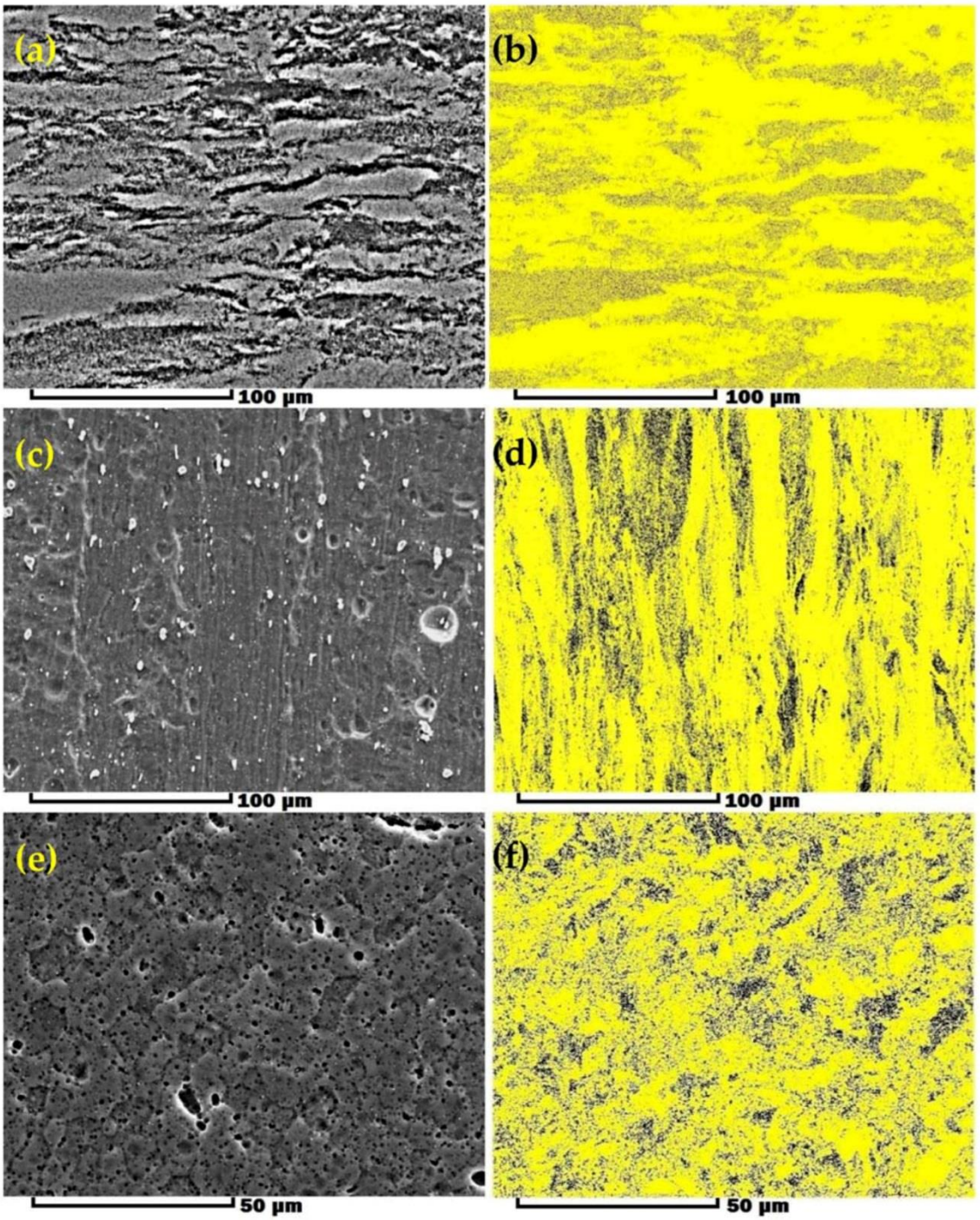

Figure 11.8. Secondary electron imaging (SEI) of different region of the weld and the relevant phase mappings; (a,b) BM; (c,d) TMAZ; (e,f) SZ.

The thermomechanical behavior of the material has conflicting effects on precipitation. First, the shear induced by the severe plastic deformation and the consequent grain fragmentation activate the precipitate nucleation, probably by providing more preferred crystallographic sites for nuclei. Second, the thermal effect causes dissolution of the primary precipitates in the original substrate material, but also forms new secondary precipitates during the recrystallization. These secondary

precipitates are stabilized by the stored strain at cooling. The overall outcome of all these mechanisms facilitates precipitation to occur during the thermomechanical process.

The phase colour contrasting map shows the distribution of the precipitates through different regions of the weld during the BFSW process. Different phases of precipitates may be analyzed by the EDS elemental map. In general, the Al-Mg-Si alloy system has two main precipitate phases: Mg-Si and Al-Mg-Si. The sequence of precipitation is generally recognized to follow this route:

> Super-Saturated Solid Solution (SSSS) → Mg/Si Clusters → GP-Zone (GPZ) → β″–Mg_5Si_6 → β'–Mg_9Si_5 → β–Mg_2Si [195].

The Guinier Preston Zone (GPZ) is a fine-scale metallurgically transitional phenomenon, comprising early stage precipitation where the first metastable phases of precipitates can be characterized. For the Al-Mg-Si systems, U1-Al_2MgSi_2, U2-$Al_4Mg_4Si_4$ and B'-$Al_3Mg_9Si_7$ are the most common metastable GPZ precipitates constrained in an Al matrix. Later however, these metastable phases are resolved to result in β″and β'as the stoichiometry compositions of the terminal β-phase.

To reveal how the precipitates were spatially and morphologically distributed in the BM and SZ of weld region, elemental map observations of the cross-sectional microstructure of the AA6082-T6 joints were carried out. Figures 11.9 and 11.10 show the Back Scattered Electron (BSE) image and corresponding in-situ elemental distributions from EDS mapping of the constituents/phases for the cross section of AA6082-T6 weld sample before and after BFSW processing. The colorful area in each image represents the respective elemental distribution. For both figures, the back-scattered electrons (BSE) imaging for the analyzed regions is also present. BSE imaging can provide a more detailed observation of the surface so the spatial distribution of the spherical-like precipitates phase can be seen distinctively different in morphology from the underlying matrix. The results show that the alloying elements are uniformly composed and distributed in the structures, as there is no large contrast in element maps. Also, in both BM and SZ regions there is no sign of the presence of oxygen in EDS maps. This proves the alloy elements have not reacted with air during the process. Comparison of the EDS maps also reveals that during the T6 ageing cycle only a few precipitations are visible, while in the processed SZ region the number of the precipitates grains is increased. It shows that thermomechanical BFSW process is effective in activation of the phase transformation and precipitation of the secondary phase.

The chemical composition of AA6082-T6 contains alloy elements additional to Al-Mg-Si (e.g. Mn, Ti and Fe), hence it can form different precipitates in addition or instead of the major β phase. As can be seen in Figure 11.9a, in the Al matrix of the BM a limited number of fine particles is distributed over long distances from each other with the average size being under 5μm (white particles). The EDS map of BM (Figure 11.9 b-i) shows a contrast in composition for Mn and Ti containing maps

which indicates that precipitate particles are rich in elements Mn and Ti. According to the Al-Ti-Mn ternary phase diagram it can be expect that the γ-based $TiAl_2Mn$ composition was formed as precipitate particles. The fine $TiAl_2Mn$ crystals were formed in the condition of supersaturated crystallization in Al-based solid solution under T6 tempering. The artificially aged condition of the T6 cycle supplies the driving force for $TiAl_2Mn$ nucleation to form within the crystal. Therefore, in the BM microstructure the supersaturated lattice contains a number of fine precipitates.

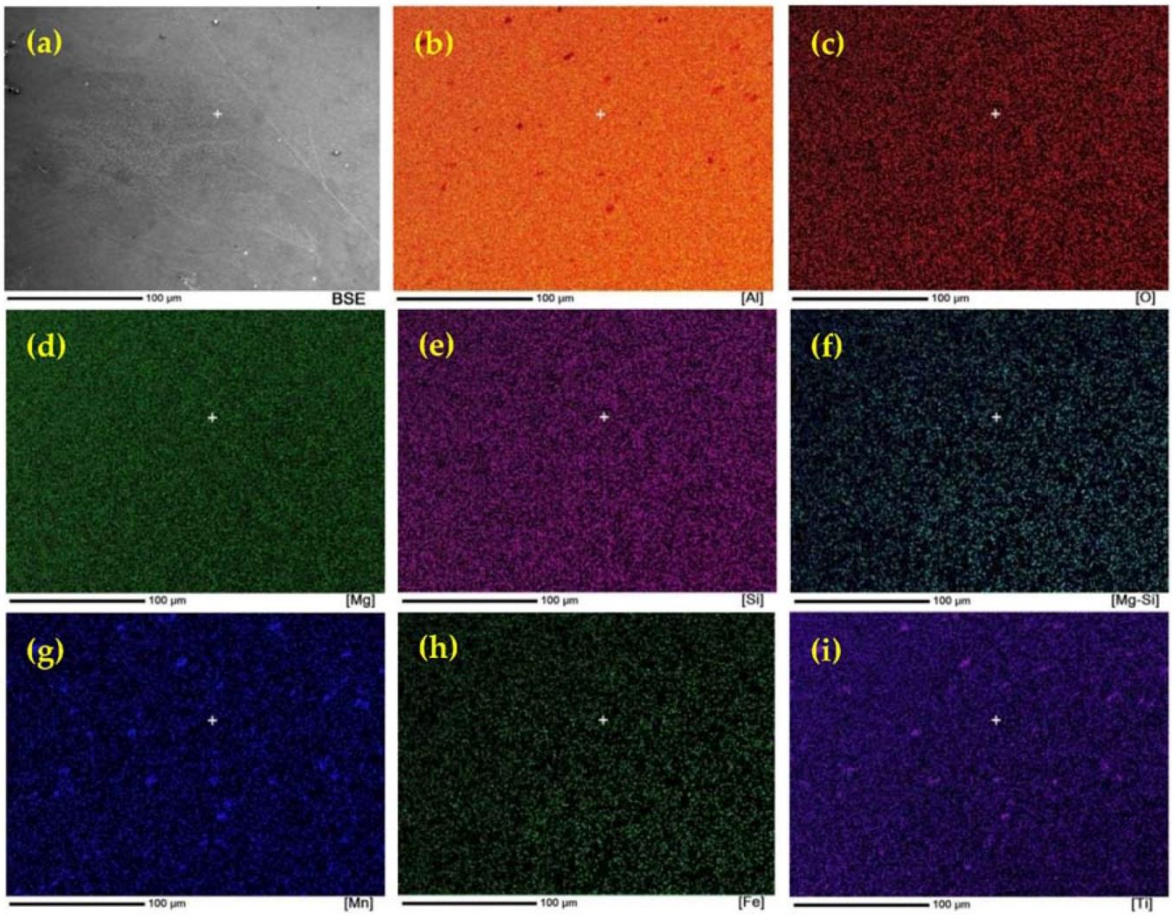

Figure 11.9. Elemental EDS map of the AA6082-T6 microstructure at BM. (a) BSE image and corresponding distribution of (b) Al; (c) O; (d) Mg; (e) Si; (f) Mg-Si; (g) Mn; (h) Fe; and (i) Ti elements.

Compared to the BM, the SZ showed a higher density of white particles of 10µm average size (Figure 11.10a). Similarly, the EDS element mapping measurement reveal a contrast in distribution of particles in the Al-based background as shown in Figures 11.10 b-i. Compared with the BM, the elemental maps of the SZ reveal that in addition to the presence of Mn and Ti, the precipitates contain Mg, Si and Fe. It attributes this change in elements to the heat input generated during the FSW process causing dissolving and recrystallization of precipitates in the SZ. At the

higher temperatures during stirring, the γ–based precipitates dissolved gradually and resulted in an Al-phase supersaturated solid solution. Due to the thermodynamic stability of the microstructure, secondary precipitate crystallization occurs during the cooling. Non-equilibrium heat generation and cooling, and the stored strain in the structure during stirring, are proposed as the driving forces of nucleation. This also activates new crystal orientations, thereby other elements (Fe, Si and Mg) can take part in the composition of the precipitates crystal lattice to form a variety of β and γ phase families. Furthermore, heat preservation during stirring can result in coarsening of the recrystallized precipitates where it formed larger sized particles of 10μm average size. These uniformly distributed larger precipitates play a key role in disruption of the migration of the grain boundary which leads to the strengthening mechanism during the welding process.

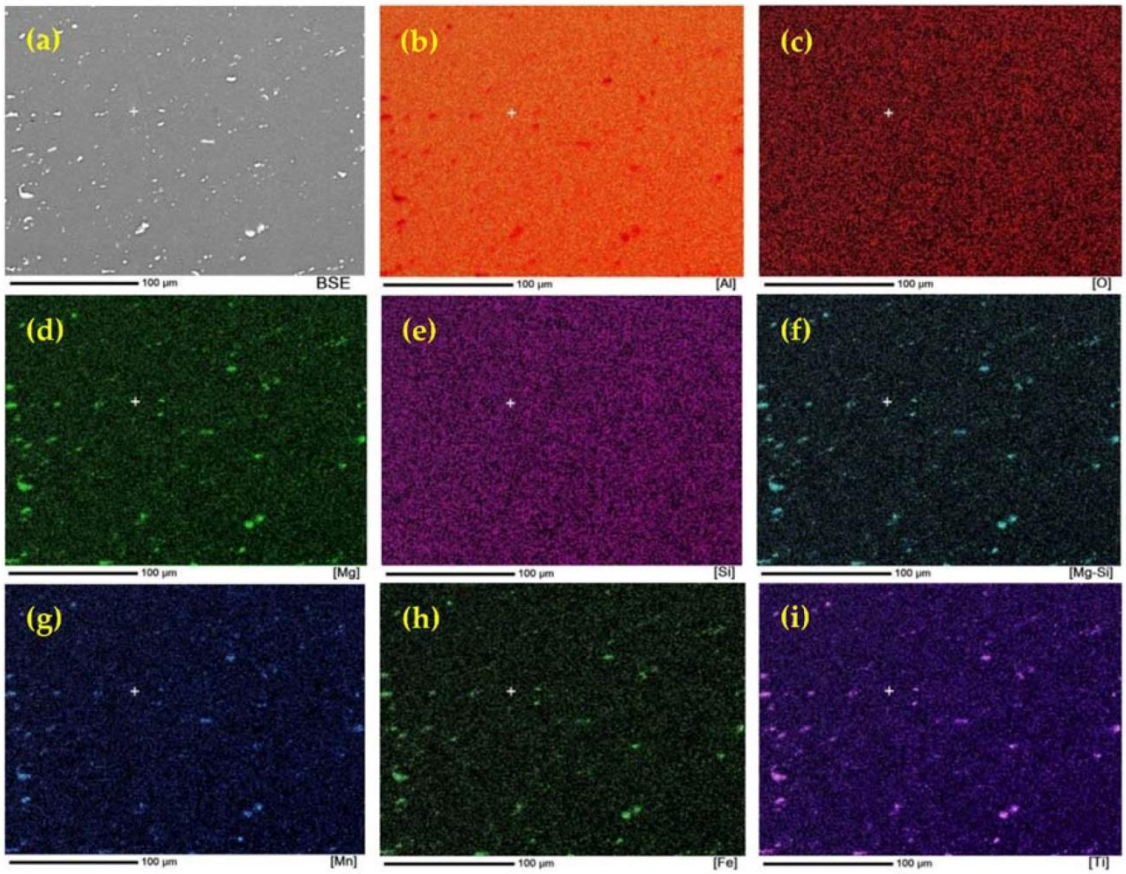

Figure 11.10. Elemental EDS map of the AA6082-T6 BFSW weld at the SZ. (a) BSE image and corresponding distribution of (b) Al; (c) O; (d) Mg; (e) Si; (f) Mg-Si; (g) Mn; (h) Fe; and (i) Ti elements.

11.4. Chapter Discussion

Model for strengthening mechanism

The grain refining occurred in a solid state thermomechanical processing with the same content of element composition of the alloy, without any external refiner. The performance comparison of this thermomechanical grain refinement was made in marine-grade AA6082-T6 aluminum where the T6 microstructure is changed during the BFSW process. The grain microstructure comparison of the aluminium phase confirms the conversion of coarse columnar grains to fine equiaxed grains through the BFSW process. This leads to an increase of the G.B density which consequently can act as blocking features in front of dislocations and improve the strength of the structure. Also, EBSD studies reveal precipitation nucleation which is uniformly distributed in the Al matrix over the whole processed area. This can have a double positive effect on the grain refinement result by activation of the strengthening mechanism using hardening particles with a pinning effect on dislocation movement.

A number of mechanisms have been identified for grain refinement, as illustrated through optical and electron microscopy. It identifies several pathways whereby the thermomechanical process of BFSW contribute to the strengthening of the weld material, and ultimately to improved mechanical properties of the weld. These provide self-healing effects, which counter the mechanisms that cause failure (such as micro-cracks). These beneficial mechanisms are precipitation, grain fragmentation, and strain relief mechanisms.

We propose that the improved mechanical properties are selective, in that not all of strength, hardness, toughness, etc., can be simultaneously optimized. The balance between different features of the microstructure determine these macroscopic properties in ways that are not fully quantified. It summarises the effects and their interactions in Figure 11.11. The details of these processes are described above.

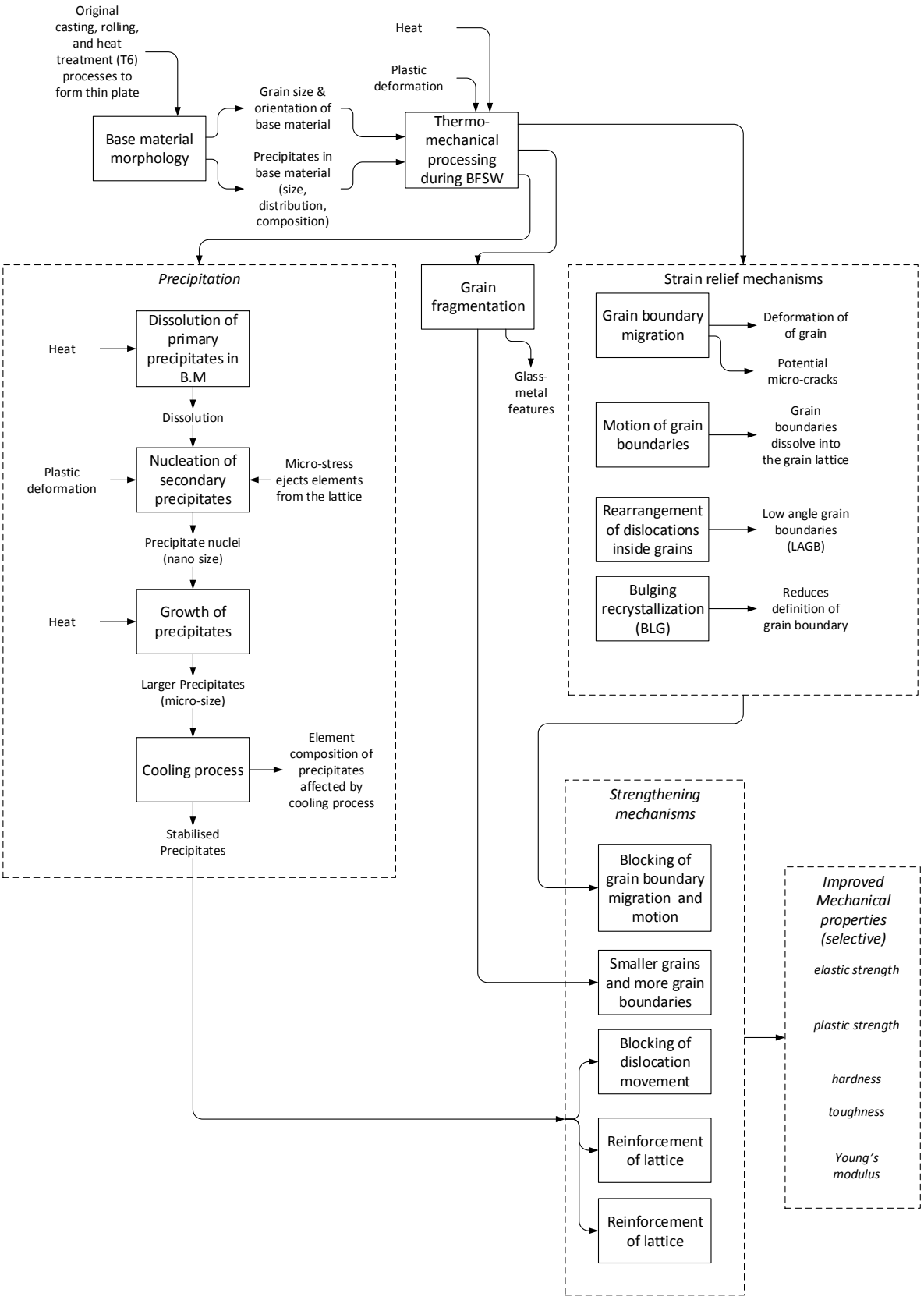

Figure 11.11. Model of the causal mechanisms whereby thermomechanical processing causes grain refinement and hence improved mechanical properties.

Original contributions

Key findings are the identification of specific changes in grain size and precipitation. It identified physical evidence for motion of grain boundaries, bulging recrystallization, grain boundary migration, and low-angle grain boundaries (sub-grain boundaries). These effects are attributed to the thermomechanical nature of this welding process. Glass-metal features were identified in the stirring zone, and these are evidence of localized melting and rapid cooling.

Implications for practitioners

For those using AA6082-T6, e.g. in maritime construction, the implications are that processes should be directed to production of the precipitates and changing of the microstructure during the welding process. BFSW offers the potential for in-situ grain refinement and recovery of mechanical properties. However this material can be difficult to weld, in that a number of flow-based defects can occur, such as tunnel defects [64, 183] and hence the tool design and the process settings can be critical.

Limitations and implications for future research

This chapter was limited to the quantitative description of the grain refinement features induced by the thermomechanical behavior of the BFSW process. Possible further advancements might be achieved by measurement of the heat generation and the stored strain induced by the plastic deformation. A possible line of future investigation may be directed to extracting the weld texture measurement via the Kernel Average Misorientation (KAM) or the Grain Orientation Spread (GOS) analysis to see how thermomechanical features of the BFSW can affect the grain refinement phenomenon.

The accurate composition and percentage of each phase was not determined here, and would require X-ray diffraction (XRD) or quantitative mass spectrometry measurements which could be a subject of further research. However what can be said is that the EBSD method shows the distribution of the secondary phase/precipitates, using the phase colour mapping for the BM and SZ regions. The XRD phase analysis and the EDS mass analysis for the element composition of precipitate particles can reveal the accurate composition and quantity fraction of different nucleated phases before and after precipitation. This can provide a more accurate clarification for the efficiency of the refining process.

11.5. Chapter Conclusions

The microstructural evolution of AA6082-T6 BFSW weld plate was analyzed using optical microscopy and EBSD tests. It was possible to measure grain size, recrystallization and grain-boundary, precipitates spatial distribution character. Both optical and EBSD micrographs show a significant grain refinement with a change in grain morphology from directional columnar in BM to ultrafine equiaxed

morphology in SZ. The qualitative aspects of the thermomechanical processing (BLG, GBM and SGBs/ LAGBs features) were also studied in the TMAZ region. Also the microscopic studies of the SZ introduced a spherical microstructure that resembles the metallic-glass phase. EBSD results consisting of phase mapping and EDS elemental maps provided strong evidence for the existence of precipitate phases which are nucleated and remained with a uniform distribution in the deformed structure of the BFSW weld.

Chapter 12: Texture Evolution in AA6082-T6 BFSW Welds: Optical Microscopy and EBSD Characterisation

Chapter Summary: One of the micro-scale difficulties with bobbin friction stir welding (BFSW) has been the visualisation of microstructure, particularly grain boundaries, and this is especially problematic for materials with fine grain structure, such as AA6082-T6 aluminium as here. Welds of this material were examined using optical microscopy (OM) and electron backscatter diffraction (EBSD). Results show that the grain structures that form depend on a complex set of factors. The motion of the pin and shoulder features transports material around the weld, which induces shear. The shear deformation around the pin is non-uniform with a thermal and strain gradient across the weld, and hence the dynamic recrystallisation (DRX) processes are also variable, giving a range of observed polycrystalline and grain boundary structures. Partial DRX was observed at both hourglass boundaries, and full DRX at mid-stirring zone. The grain boundary mapping showed the formation of low-angle grain boundaries (LAGBs) at regions of high shear as a consequence of thermomechanical nature of the process.

This chapter is a derivative of the following publication:

Tamadon, A.; Pons, D.J.; Clucas, D.; Sued, K. Texture Evolution in AA6082-T6 BFSW Welds: Optical Microscopy and EBSD Characterisation. Materials 2019, 12, 3215.

DOI: https://doi.org/10.3390/ma12193215.

12.1. Introduction

12.1.1. Context

Friction stir welding (FSW) [1, 2] is a solid-phase joining technique whereby a bond is formed between two plates by a severe plastic deformation induced by mechanical friction and the heat generated by a rotating tool. Due to the deformation nature of the process, ductile materials such as aluminium [5] are suitable candidates to be processed by the FSW. One of the difficulties with FSW has been the visualisation of microstructure, particularly grain boundaries [138, 140]. This is especially a problem for those materials that intrinsically have a fine grain structure. A case in point is aluminium AA6082-T6 [139, 141]. This is a marine-grade aluminium alloy [81], with high-strength mechanical properties (Elastic Young's Modulus of 71 GPa, Fatigue

Strength of 95 MPa, Shear Modulus of 26 GPa, Shear Strength of 220 MPa and Ultimate Tensile Strength of 330 MPa) [196], compared to other Al-series. Furthermore, the T6 tempering cycle achieves an artificially aged super-saturated solid solution to meet a high-strength structure compared to other 6xxx-series alloys [6, 197]. The standard chemical composition for AA6082-T6 is shown in Table 12.1. Although this corrosion-resistance Al alloy is a suitable choice for machining, it suffers from poor weldability [81]. It has historically been difficult to demonstrate the microscopic features for this material, which has hindered the diagnosis of the causes of its poor weldability [64].

Recent novel developments have yielded an etchant that is capable of showing microstructures using optical microscopy (OM) [140]. Applications of the etchants have elucidated the grain size and morphology in different regions of the weld texture [141], however, the grain boundary network and thermomechanical features (e.g., dynamic recrystallisation evolution and grain refinement mechanisms) need more advanced and precision measurement such as electron microscopy [65, 198]. There is also a need to compare and contrast the different features evident in the optical and electron methods, and to validate the etchant method. Furthermore, there is a need to better understand the linear features, or flow lines, evident in the cross section.

Table 12.1. Element composition of the AA6082-T6 aluminium alloy (wt %) *[199]*.

Chemical Element	Present (wt %)
Silicon (Si)	(0.70–1.30)
Magnesium (Mg)	(0.60–1.20)
Manganese (Mn)	(0.40–1.00)
Iron (Fe)	(0.0–0.50)
Chromium (Cr)	(0.0–0.25)
Zinc (Zn)	(0.0–0.20)
Titanium (Ti)	(0.0–0.10)
Copper (Cu)	(0.0–0.10)
Other (Each)	(0.0–0.05)
Other (Total)	(0.0–0.15)
Aluminium (Al)	Balance

12.1.2. Background Literature

Due to the severe shear deformation during friction stir welding, it is not straightforward to evaluate the microstructure evolution of the FSW weld [24]. The grain map of the crystallographic texture can provide an accurate analysis to investigate the relationship between the microstructure and the thermomechanical

characteristics of the FSW process [23, 25, 26]. However, the rotating nature of the tool during the FSW process makes it different to conventional deformation processes, such as rolling, extrusion, or compression. While the shear-bands in these processes are aligned with the deformation direction, the deformation orientation induced within the texture varies across the weld region, as a function of the position of the rotating tool during the FSW process [26, 27].

Most of the published research is focused on the characterisation of the grain structure within the FSW weld structure [200]. Another important research strand has been to better understand the material flow [11, 26, 27] and this requires visualisation of the texture variations in the aluminium FSW welds [23, 25, 26].

Furthermore, due to differences in heat generation [38] and flow mechanism [37] between FSW and BFSW, the texture evaluation is expected to be different. This has been observed in the microstructural evolution of the AA6082-T6 BFSW weld structure [138, 140]. The flow arms at the hourglass-borders of the BFSW weld [36] are different to the onion ring patterns in the basin-shaped FSW weld structure. Therefore, these two welding processes show different features, and there is a need to better understand the dynamic recrystallised grain structure and flow-based characteristics of the weld region.

12.1.3. Approach

The present chapter compares the optical microscopy results (using etchant), against electron backscatter diffraction (EBSD) results to analyse the bobbin friction stir welding (BFSW) weld texture of aluminium alloy AA6082-T6 with a focus on the thermomechanical details of the microstructure.

EBSD analysis was used to determine the DRX details. This also allows the flow features to be identified at greater resolution compared to OM. Additionally, the grain boundary network and the content of the grain orientation within the weld texture can be investigated with EBSD.

It should be noted that although the transmission electron microscope (TEM) is capable of resolving the fine feature of the microstructure of FSW welds, this chapter focused on EBSD analysis because of the accessibility and ease of sample preparation.

12.2. Materials and Methods

The AA6082-T6 aluminium plate of 4 mm thickness was used as the workpiece material for the welding trial.

A fixed-gap bobbin-tool, manufactured from H13 tool steel was used for the BFSW welding (Figure 12.1). The tool was fully-featured (threaded tri-flat pin, and 360-degree spiral scrolled shoulders) to create a better stirring flow. The weld was arranged in the butt-joint position no gap between the plates, also no preheating. A

3-axis CNC machine (2000 Richmond VMC Model, 600 Group brand, Sydney, Australia) was used for the welding trial, while the plates were rigidly fixed by strap clamps at the outer faces during the process.

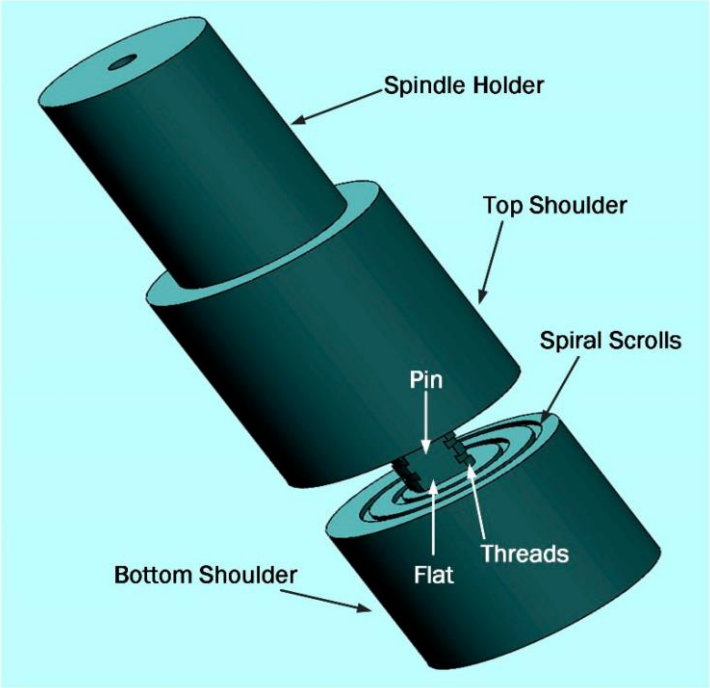

Figure 12.1. Schematic of the fully-featured Bobbin-Tool (tri-flat threaded pin and spiral scrolled shoulders).

Since the aim of the this chapter was to evaluate the weld texture in a defect-free structure, a variety of welding speeds (rotational speed; ω and advancing speed; V) were used to validate the welding process. After running some tests in ω (350–650 rpm) and V (300–400 mm/min) [64, 140, 141, 201], the optimum welding trial, to obtain a defect-free weldment, was performed in clockwise rotational speed (ω) of 600 rpm with an advancing speed (V) of 400 mm/min in the traveling direction. This set of speeds (ω, V) achieved a weld with no crack or void defect on surface, neither any material loss through the weld-seam. Lower speeds were unable to create a bonded weld between the aluminium plates, and higher speeds deteriorated the quality of the weld by material loss. The details of the welding test are listed in Table 12.2.

Table 12.2. The specification of the operation parameters for the AA6082-T6 BFSW weld sample.

Workpiece	Tool Material	Work Temp °C	$D_{Shoulder}$ (mm)	D_{Pin} (mm)	Plate Thickness (mm)	Feed ω (rpm)	Speed V (mm/min)	Thread Pitch (mm)	Number of Threads in the gap
AA6082-T6	H13 Tool	18	21	7	6	600	400	1.5	4

After conducting a 150 mm single-pass weld line, the sample was cut along the transverse direction of the plates for metallographic analysis.

The AA6082-T6 weld samples were prepared first for etching, and then repolished for EBSD. On both cases the polish method was per: standard mechanical polishing with different grades of SiC sand papers (600-grit, 800-grit and 1200-grit). To achieve a mirror surface, the micro-polishing step was conducted on a micro-cloth pad with a 3 μm diamond paste, and finally a 0.05 μm colloidal silica solution [140].

The samples then were etched in a reagent etchant solution with the composition of (0.5 g $(NH_4)_2MoO_4$ + 3.0 g NH_4Cl + 1 mL HF + 18 mL HNO_3 + 80 mL H_2O). The immersion etching was done in an ultrasonic bath for 90 s, at 70 °C. The microstructure of the etched cross-sections was examined by optical microscopy (OM).

Samples were repolished back to 600-grit between optical and EBSD examination. Based on sizes of polishing particles, this might correspond to about 100 μm surface removal. The experience in repolishing for optical work shows that flow features are reasonably consistent after repolishing. Samples were positioned by geometric measurements from the edges of the weld, in such a way to view the same region of the weldment. Repositioning accuracy is estimated to be with 20 μm. For both these reasons the repolished surface features evident in the results may not correspond exactly to each other in the pairs of images.

For EBSD the following process applied: the mounted specimens were examined with a scanning electron microscope (SEM) (JEOL 6100, JEOL Inc., Peabody, MA, USA) with an HKL Nordlys III EBSD detector (Oxford Instruments plc, Abingdon, UK). The EBSD plots for different regions of the weld region were reconstructed with HKL Tango software (HKL Channel 5 Tango software version 5.12.60.0, Oxford Instruments plc, Abingdon, UK) [202].

For the mid-Stirring Zone (SZ) region with the ultrafine grain structure, a magnification step size of 0.75 μm with an overall acquisition area of (~400 × 300 μm) was used for EBSD mapping. Alternatively, for other regions of the weld with larger grains, a step size of 3 μm with an overall acquisition area of 2 mm^2 was used, while all other control parameters such as binning, probe current, accelerating voltage, and exposure time were held constant [141, 202]. The average indexing rate of all collected samples was 97.5%, where the unindexed pixels were filled in with the software [203].

Using the average Taylor factor, the EBSD data was further analysed for the distribution of the grain boundaries within the microstructure [204, 205]. The low-angle grain boundaries (LAGBs) with misorientation degree of 2°–10° were highlighted in blue and the high-angle grain boundaries (HAGBs) with misorientation degree larger than 10° were shown by red [141, 206]. It should be

noted that the twinning boundaries were not analysed but instead included in the LAGBs distribution map.

12.3. Results

12.3.1. Characterisation of the Sample Regions with OM

The samples were from various areas of the weld cross-section as described below and in Figure 12.2. The cross-section is perpendicular to the welding direction as the Advancing Side (AS) of the weld region is situated in the left and the Retreating Side (RS) is on the right at the cross-section.

1. Base metal (BM). This is the parent metal of the workpiece and situated outside of the weld region far away from the active region of the stirring, and thermally and mechanically unaffected by the welding process. In the AA6082-T6 workpiece it is expected that BM would conserve the columnar-shaped directional grain morphology of the rolled structure with the primary average grain size unchanged during the BFSW welding process, and this is what was observed.

2. AS/RS Hourglass Borders. The interfaces between the plastic deformation region or Stirring Zone (SZ) and the transition region adjacent to the weld region are distinguished as hourglass shaped borders at both the AS and RS of the weld. The bent shape of the border at the middle of the cross-section can be attributed to the interaction of the pin and shoulders with the substrate. The pin induces more shear compared to shoulders, therefore the borders are stretched towards the pin position. The grains size and morphology in the texture of hourglass border is observed to be different than both BM and SZ. This is due to the different thermal and mechanical characteristics through the cross-section.

3. Flow-arms. These are characteristic microscopic feature of the BFSW weld structure, evident as elongated bands in direction of the stirring flow lines from the centre of the weld drawn towards the top and bottom shoulders. The formation of the flow-arms is generally attributed to a direct outcome of the shear banding in a continuous plastic deformation, where the layered mass flow is deposited by the advancing of the rotating tool.

4. Sub-shoulder region. A severe plastic deformation is experienced underneath the shoulders. The scrolled features of the shoulders may increase the frictional heat generated in this region of the weld. Study of the sub-shoulder texture in microscopic scale can potentially reveal thermomechanical details of the BFSW process as the thermal and mechanical stress/strain fields are in a maximum rate in this region.

5. Mid-SZ. This is the main region of the weld represented by the ultrafine equiaxed grain texture in comparison with the BM. As will be shown below, the Mid-SZ region experiences full dynamic recrystallisation (DRX) transformation including grain refinement and precipitation, more than any other region in the weldment.

However, because of the specific ultrafine characteristics of the microstructure of the SZ, a precise micro-analysis of the Mid-SZ texture requires electron microscopy rather than the OM metallographic measurements.

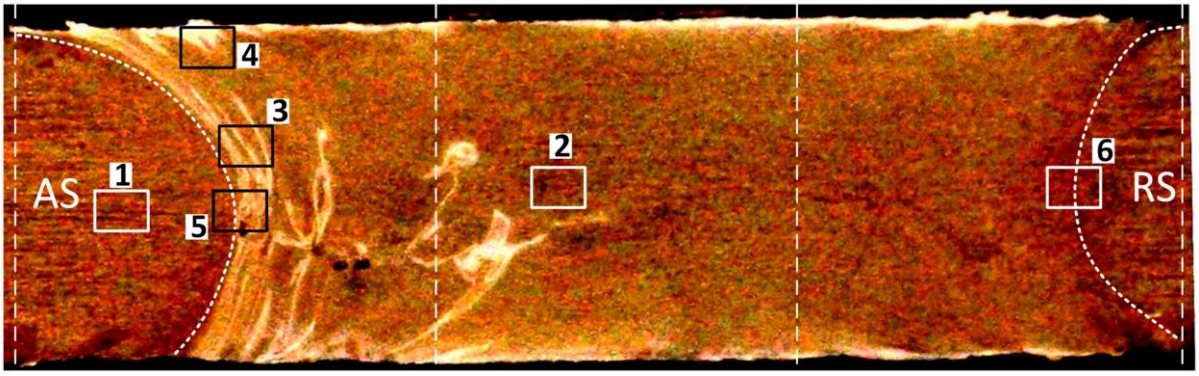

Figure 12.2. Weld cross-section of the AA6082-T6 plates, (1) Base Metal; (2) Middle Stirring Zone; (3) Flow-arms; (4) Sub-shoulder region; (5) Advancing Side (AS) Hourglass border and (6) Retreating Side (RS) Hourglass border. The two dashed-lines in the middle are representative of the position of the pin, the dashed-line in the corners of the cross-section are representative of the width of the shoulders.

12.3.2. Texture Evaluation with EBSD

The crystal orientation texture results from the EBSD mapping should be referenced compared to the RD-TD-ND perpendicular directions as a reference frame. In BFSW welded plates, the proprietary EBSD parameters need to be redefined in TD-ND-WD direction frame, as:

- Transverse direction (TD); perpendicular to the welding direction, parallel to the cross section of the weld, where the AS is in (−) and the RS is situated in the (+) of the TD axis.
- Normal direction (ND); perpendicular to the plate surface, representative of the distance between the top and bottom surface.
- Welding direction (WD); the direction of the advancement of the tool, parallel to the weld-line.

For the texture observation of the AA6082-T6 BFSW weld, the grain maps were indicated in the TD-ND plane for different regions of the weld cross-section. This plane is identical to the cross-section etched for the optical microscopy. The directions of the orientation used for the texture analysis of the EBSD plots are shown in Figure 12.3a.

The maps from the EBSD analysis present the following microscopic information: grain orientation map and grains boundary map. In the first phase, the colour mapping based on the crystallography directions of the grains indicates the crystal orientation map distribution for the analysed region. For the EBSD the standard inverse pole figures (IPF) map was used per Figure 12.3b. This shows the three main

crystallographic directions within the grains distinguished by different colours; red for (001), green for (101) and blue for (111).

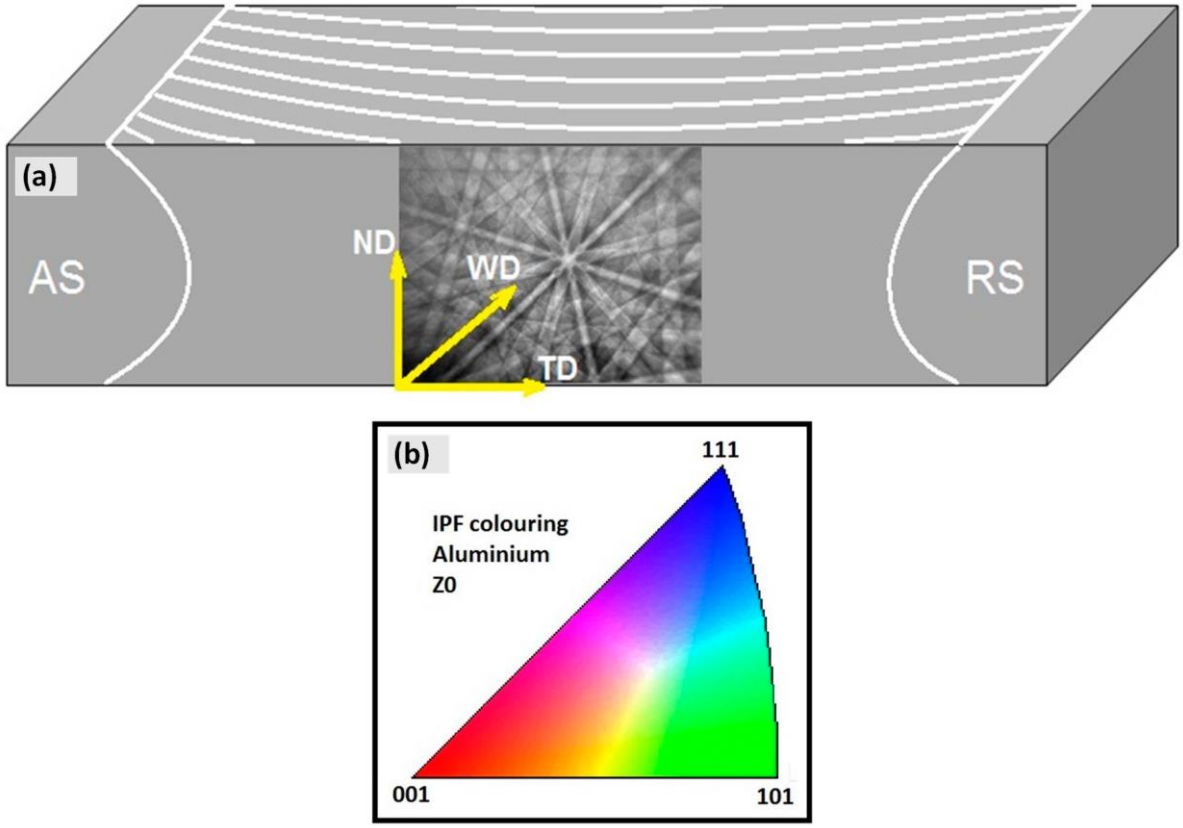

Figure 12.3. Crystallography directions in Aluminium alloys, (**a**) Schematic of ED, ND and TD reference directions, applied for EBSD analysis; (**b**) IPF colour triangle. (Source for (**b**) Ex EBSD machine).

The colours in Figure 12.3b show the corresponding orientation of grains and crystals with respect to (001), (101) and (111) orientations. While the main crystallographic orientations are demonstrated by these three colours of red, green and blue, the other crystallographic directions between these three main crystallographic orientations are shown with the mixed colours. To obtain the grain boundary misorientations it would be necessary to specifically measure the individual misorientation.

In the second phase of the EBSD analysis, the grain boundary maps were derived in the post processing data procedure to measure the density of the high-angle grain boundaries (HAGBs) and low-angle grain boundaries (LAGBs) within the texture. Similar to the grain misorientation mapping, the HAGBs were defined by a misorientation angle greater than 10° and LAGBs were defined as the misorientation angles between 2° and 10°.

In some analyses 15° is used as the LAGBs/HAGBs transition demarcation rather than 10°. This is because at such higher angles the misorientation is more definitive to show the grain boundaries. Nonetheless the misorientation angle between 10° and 15° also can be counted as the HAGBs.

The following sections compare the results from the optical and EBSD approaches.

12.3.3. Base Metal

The optical and EBSD microscopy results (IPF map) are shown in Figure 12.4. This shows that the overall structure is represented similarly between the two methods: columnar grains of rolled base material are evident. The crystal direction (grain orientation) is similar. The colours in the EBSD results show that a variety of orientation occurs, and the rolling effect is observable by a columnar directional alignment in the orientation distribution, similar to the OM micrograph. The grain boundaries are evident in the optical results but not in the EBSD. The magnification scale was kept similar to the OM micrograph, and post-processing/zooming of the EBSD map shows the GBs.

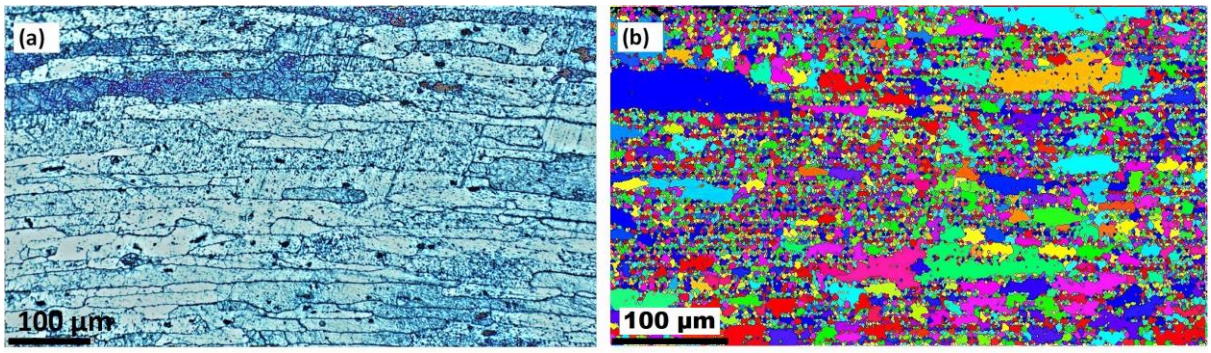

Figure 12.4. Base Metal microstructure, (**a**) Optical microscopy and (**b**) EBSD colour map.

To apply a post-processing clean-up of the EBSD maps, the Euler map is presented below, with a common orientation in each grain to better view the grain details. However, the same EBSD IPF mapping was followed for the weld region, to compare the similarities of the weld texture with OM micrographs.

12.3.4. Stirring Zone

The stirring zone microstructure for optical microscopy and EBSD is shown in Figure 12.5. EBSD verifies (which was not possible with OM) that the grain size average is below 10 microns. The randomly distributed grain with equiaxed morphology is evident by the EBSD map. The EBSD IPF colour map (Figure 12.5b) also demonstrates the microscopic distribution of the misorientation through the SZ

texture, in which is not observable via the OM micrograph. The grain boundaries pattern is still bulged which may be related to the ultrafine grain size within the SZ.

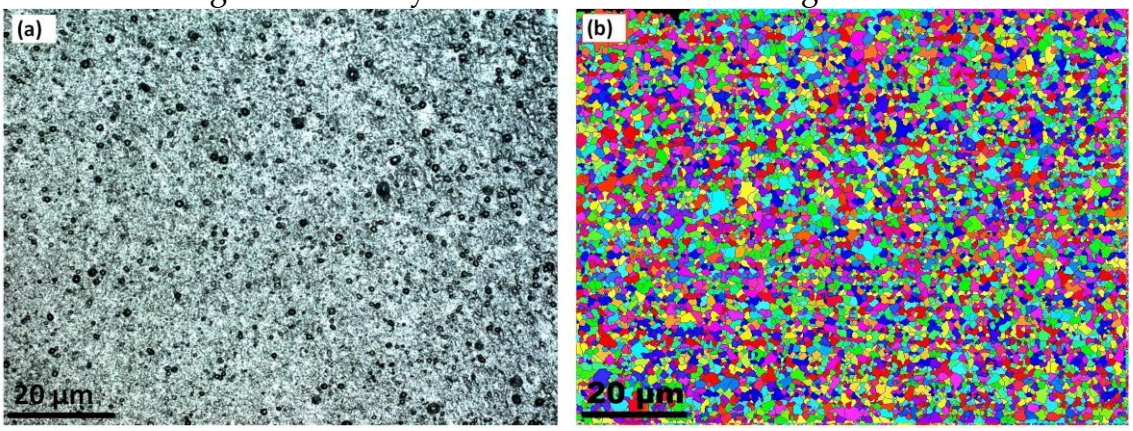

Figure 12.5. The microstructure of the Mid-Stirring Zone (SZ) region, (**a**) Optical microscopy and (**b**) EBSD colour map.

12.3.5. Flow Layers

The elongated micropattern of the flow-arms region was compared by optical microscopy and EBSD method (see Figure 12.6). The continuous flow direction in Figure 12.6b in red colour is situated at the position of each flow-arm, confirming that each flow-arm possess a specific crystallographic direction compared to the neighbouring region. These macro-bands and macro-regions were readily detected by the EBSD detector and is also present in the etched sample. There is some distance between each branch of flow-arms which has been filled by other crystals with different orientations (distinguished by corresponding colours). In this regard, the interpretation is that the macro-regions of shear bands are aligned along the (001) orientation, in a background of grains with a variation in crystallographic orientation.

This is attributed to the discrete transport mechanism whereby packets of stirred material are deposited at the trailing edge of the tool. In turn this is attributed to the interaction between thread-flat features of the pin tool with the substrate material.

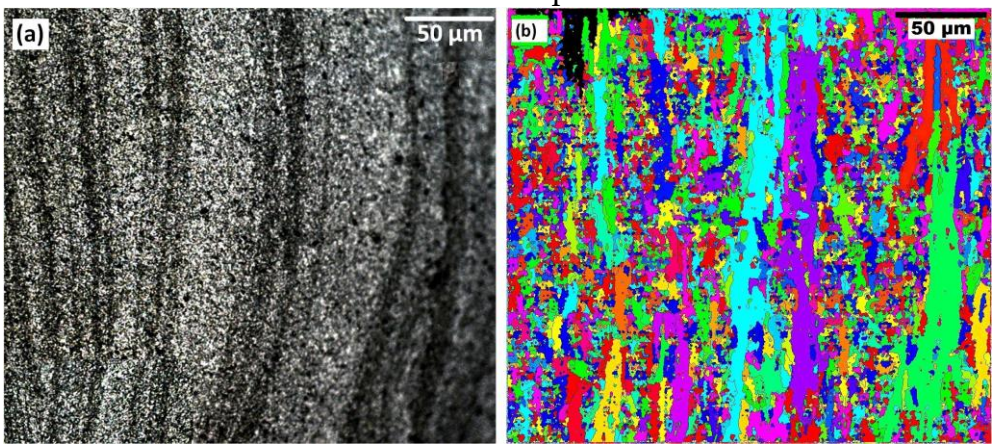

Figure 12.6. The microstructure of Flow layer patterns, (**a**) Optical microscopy and (**b**) EBSD colour map.

12.3.6. Heat Flow (Sub-Shoulder Region)

The microstructural analysis of the sub-shoulder region is shown in Figure 12.7, for OM and the related EBSD mapping. The optical microscopy result of the sub-shoulder weld region (Figure 12.7a) demonstrates the shoulder induced flow. These flow layers represent a transverse transportation of the mass, caused by the frictional behaviour of the shoulder action. Although the microstructure shows a severe plastic deformation underneath the shoulder, it does not contain any specific surface defect. This is attributed to the high compaction effect induced by the direct contact between the shoulder and the top surface of the weld region. The flow patterns are not observed in the deeper areas. This may be representative of the decrease of the compaction effect of the shoulder, and the decreasing effect of the surface shear strain. The flow of the mass at the deeper regions of the stirring zone is more affected by the pin action.

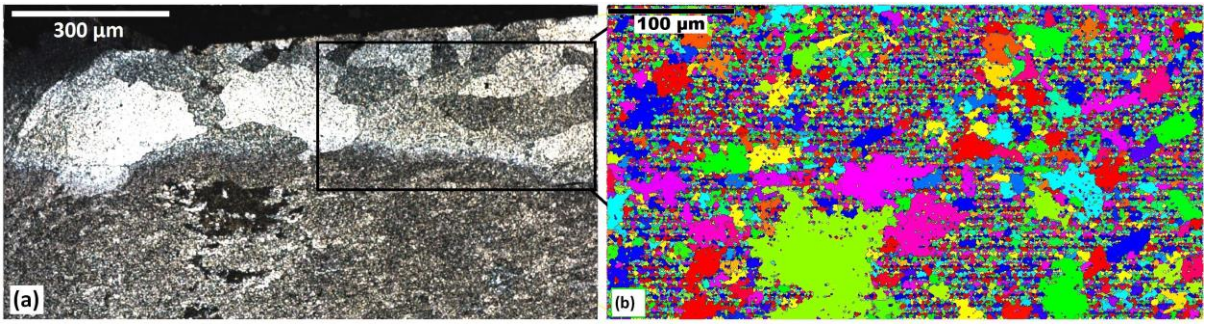

Figure 12.7. The microstructure of the Sub-shoulder region, (**a**) Optical microscopy and (**b**) EBSD colour map.

The selected area from the sub-shoulder region shown in Figure 12.7a has been mapped by the EBSD analysis in Figure 12.7b. The crystallographic texture at the sub-shoulder region is complex. This is attributed to the complex combination of thermal and strain effects. The approximate position of the flow patterns, delineated in Figure 12.7a, can be seen in a colour map in Figure 12.7b. The random dispersion of the grain orientation can be related to the complexity of the strain history in the location, as flow patterns are not evident. However, it should be noted that based on the EBSD standard IPF contouring (colour triangle, Figure 12.3b), the (001) crystallographic direction (red colour) is more pronounced compared to other orientations. This is the preferred crystallographic direction for the shear planes in the lattice of the Al atoms. Therefore, this is interpreted as the shoulder-induced stirring action activating a network of the shear planes in the (001) direction.

12.3.7. Hourglass-Border (AS)

The highly deformed region at the hourglass-border of the weld as the triple junction is characterised in Figures 12.7 and 12.8 for the AS and RS of the weld region, respectively. As shown in Figure 12.8, the tapered-shape triple junction at the middle

of the AS hourglass-border is characterised by a highly deformed elongated grain structure of the base material, stretched towards two opposite directions parting in the middle upwards and downwards. This deformed structure is identified with an upward-downward flow pattern (Figure 12.8a).

The EBSD analysis of the tip of the tapered-shaped triple junction reveals more details regarding the deformed crystalline structure at the outer part of the hourglass border. The grain orientation of the texture shows the grain structure to be elongated towards the top and bottom shoulders. This micro-pattern is interpreted as DRX features of the FSW process whereby the stored strain induced by plastic deformation affects the grain structure of the TMAZ by grain misorientation. This can be detected as the microscopic change in etching response in the optical microscopy (Figure 12.8a), and the grain misorientation alteration in the EBSD colour mapping.

The EBSD pattern (Figure 12.8b) identifies a preferred crystallographic orientation for the deformation-induced grains structure by the red colour representative of the (001) direction from the EBSD standard triangle (Figure 12.3). Similar to the sub-shoulder region (Figure 12.7), the red colour is identified as the preferred crystallographic orientation of the Al-based texture for the formation of the shear bands undergone the plastic deformation.

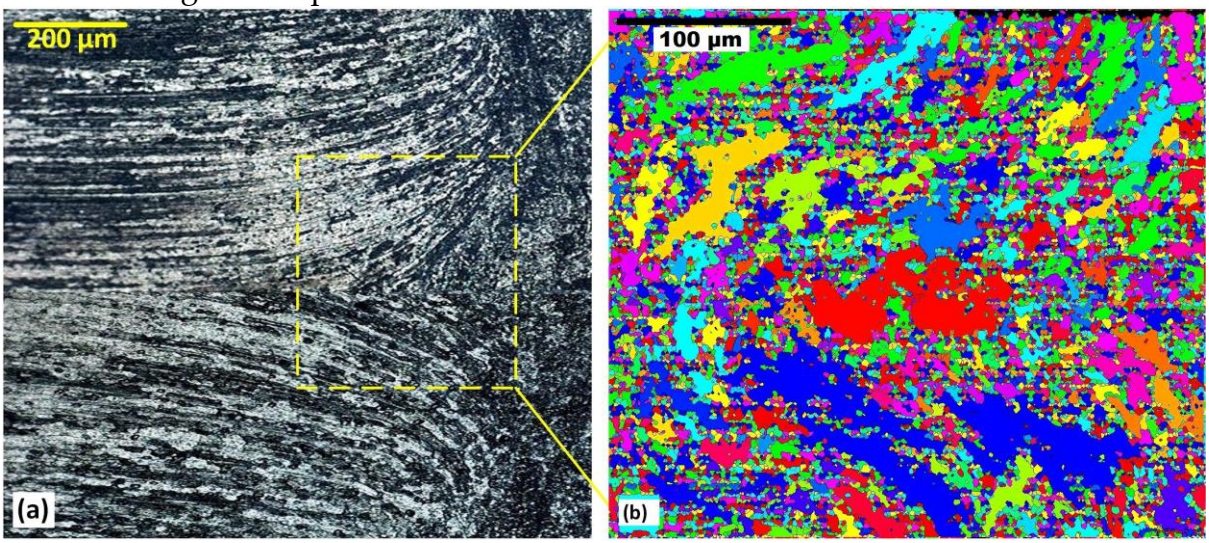

Figure 12.8. The microstructure of the AS Hourglass border, (**a**) Optical microscopy and (**b**) EBSD colour map.

12.3.8. Hourglass-Border (RS)

Similar to the AS hourglass-border in Figure 12.8, the RS of the weld also has a particular transition appearance at the hourglass-border, where an abrupt alteration in microstructure is visible at the TMAZ.

The delineated micropattern in Figure 12.8a reveals an ellipse-shape feature as a separating boundary between the TMAZ and the hourglass-border. This structure shows elongated grains at the edge of the TMAZ. This is not stirred material. The

effect presumably results from the strain induced by the rotational movement of the tool and the frictional heating.

The micrograph showing in Figure 12.9b exhibits the EBSD colour map for the ellipse-shape region at the RS, corresponding to the OM microstructure in Figure 12.9a. It is noted that the EBSD colour map, which shows grain orientation, does not show the same grain morphology apparent in the OM microstructure. Evidently orientation and morphology are decoupled in this region, presumably because of partial recrystallisation. Partly as a result of this somewhat unexpected outcome, it explored the grain angle boundaries in further detail (see the next section).

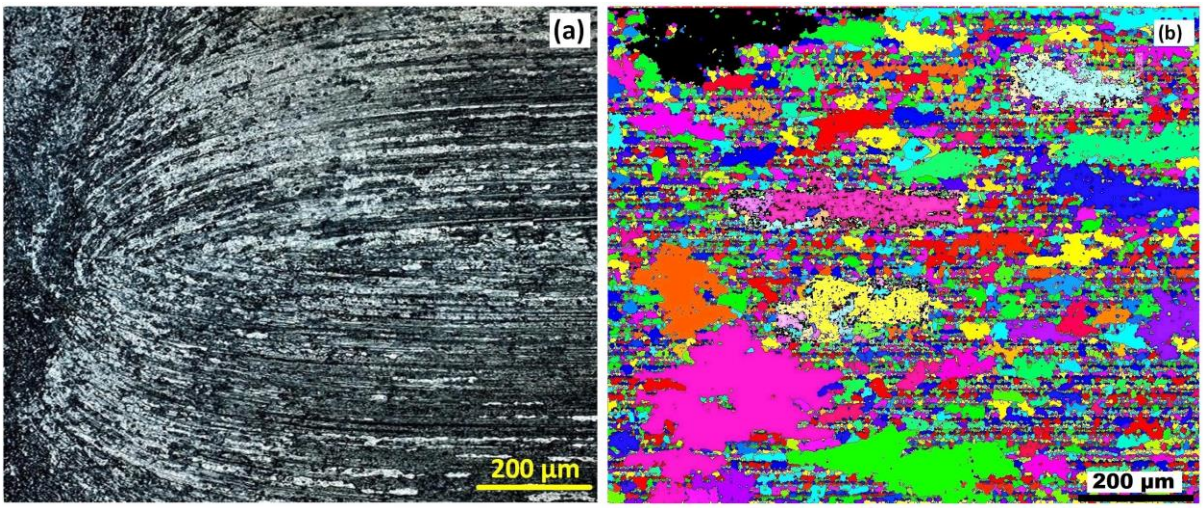

Figure 12.9. The microstructure of the RS Hourglass border, (**a**) Optical microscopy and (**b**) EBSD colour map.

12.3.9. LAGBs and HAGBs (in the Weld Region)

The grain boundary mapping for different regions of the weld are shown in Figure 12.10. The microscopic observations in Figure 12.10 were processed based on the colour identification for the LAGBs and HAGBs, identified as blue colours (Figure 12.10) and red colour (Figure 12.11), respectively.

In the stir zone of Figure 12.10e the density of the blue colour maps is high, indicating the dominance of LAGBs. The interpretation is that the LAGBs are representative of the position of the sub-grain boundaries or precipitates, which are a direct result of the DRX.

The comparison between the grain orientation maps and grain boundary maps indicates that the position of the LAGBs is aligned with the position of the crystallographic misorientation inside the grains. This is more evident in the AS of the weld or the mid-SZ region where the texture experiences severe plastic deformation compared to the rest of the weld region.

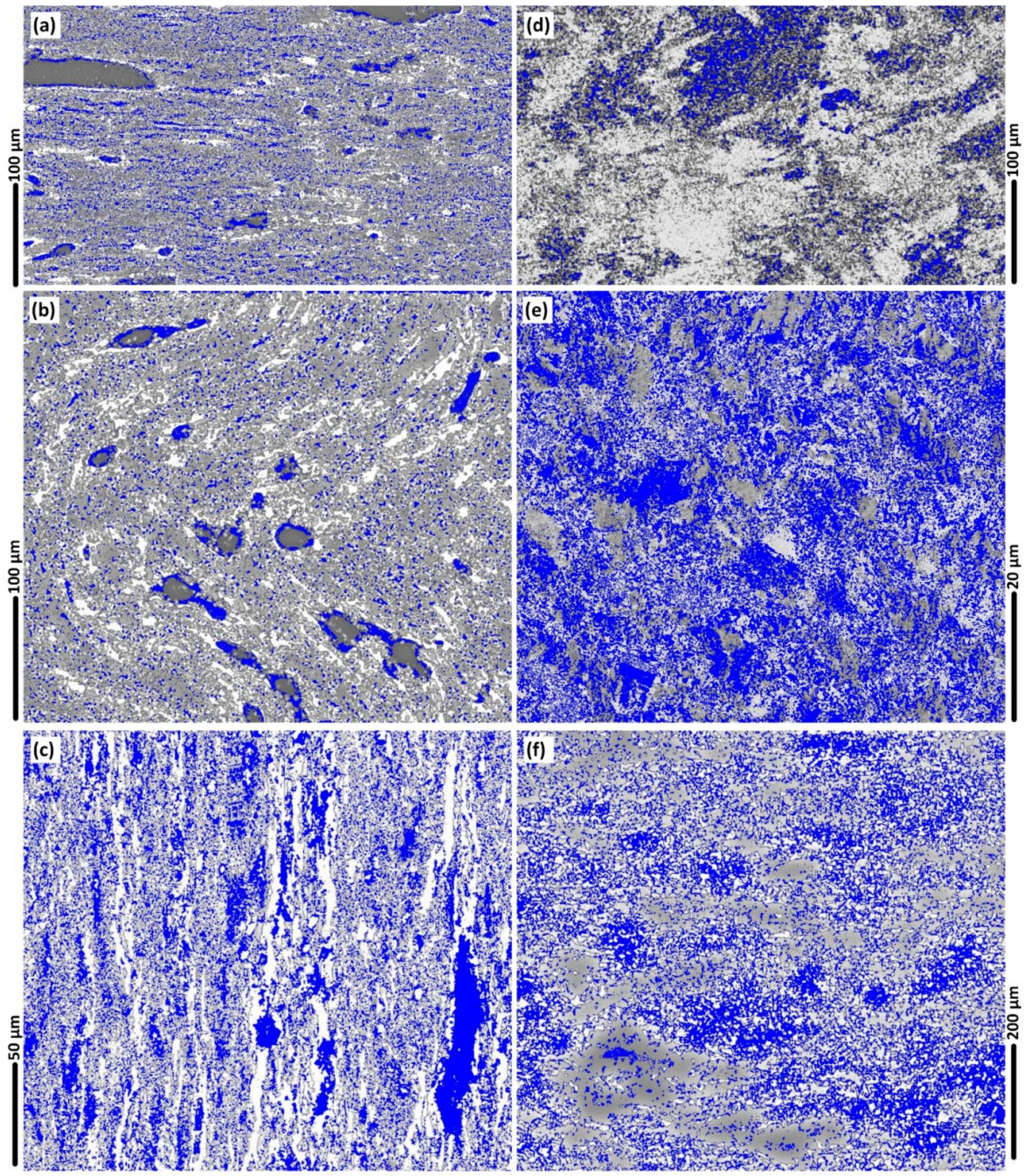

Figure 12.10. The micropatterns of the presence of low-angle grain boundaries (LAGBs, for 2°–10°) (**a**–**f**) in blue colour, for different regions of the weld; Base Metal (BM) (**a**); AS Hourglass border (**b**); Flow-arms (**c**); Sub-shoulder region (**d**); Mid-SZ (**e**); RS Hourglass border (**f**).

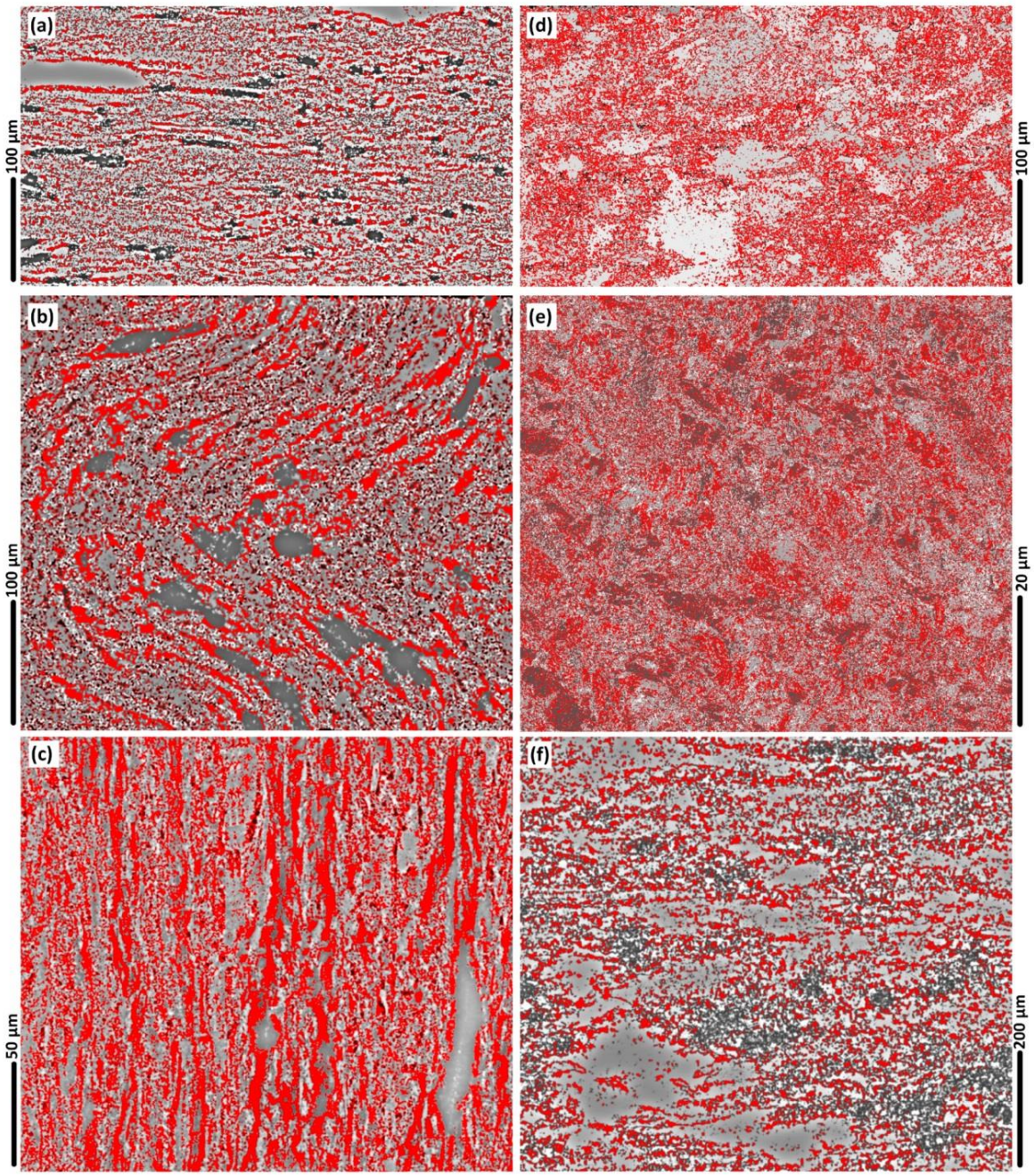

Figure 12.11. The micropatterns of the presence of high-angle grain boundaries (HAGBs, more than 10°) (**a**–**f**) in red colour, for different regions of the weld; BM (**a**); AS Hourglass border (**b**); Flow-arms (**c**); Sub-shoulder region (**d**); Mid-SZ (**e**); RS Hourglass border (**f**).

For a better understanding of the BFSW weld texture, the EBSD Euler contrast maps were constructed by post-processing of the EBSD data to denote the overlaid grain boundaries with a transition misorientation angle of 15°.

Assuming a 15° threshold for grain boundary elucidation, gives the results shown in Figure 12.12. Results emphasise the display of the HAGBs in the Euler orientation

map. Precipitates are more prominent in these views compared to the previous IPF maps. Otherwise the morphology and shear bands show the same outcomes as before, indicating that the results are insensitive to choice of threshold angle. Moreover, compared to IPF maps, the Euler maps are more limited in ability to detect small orientation changes of the LAGBs, hence these are not distinctly observable.

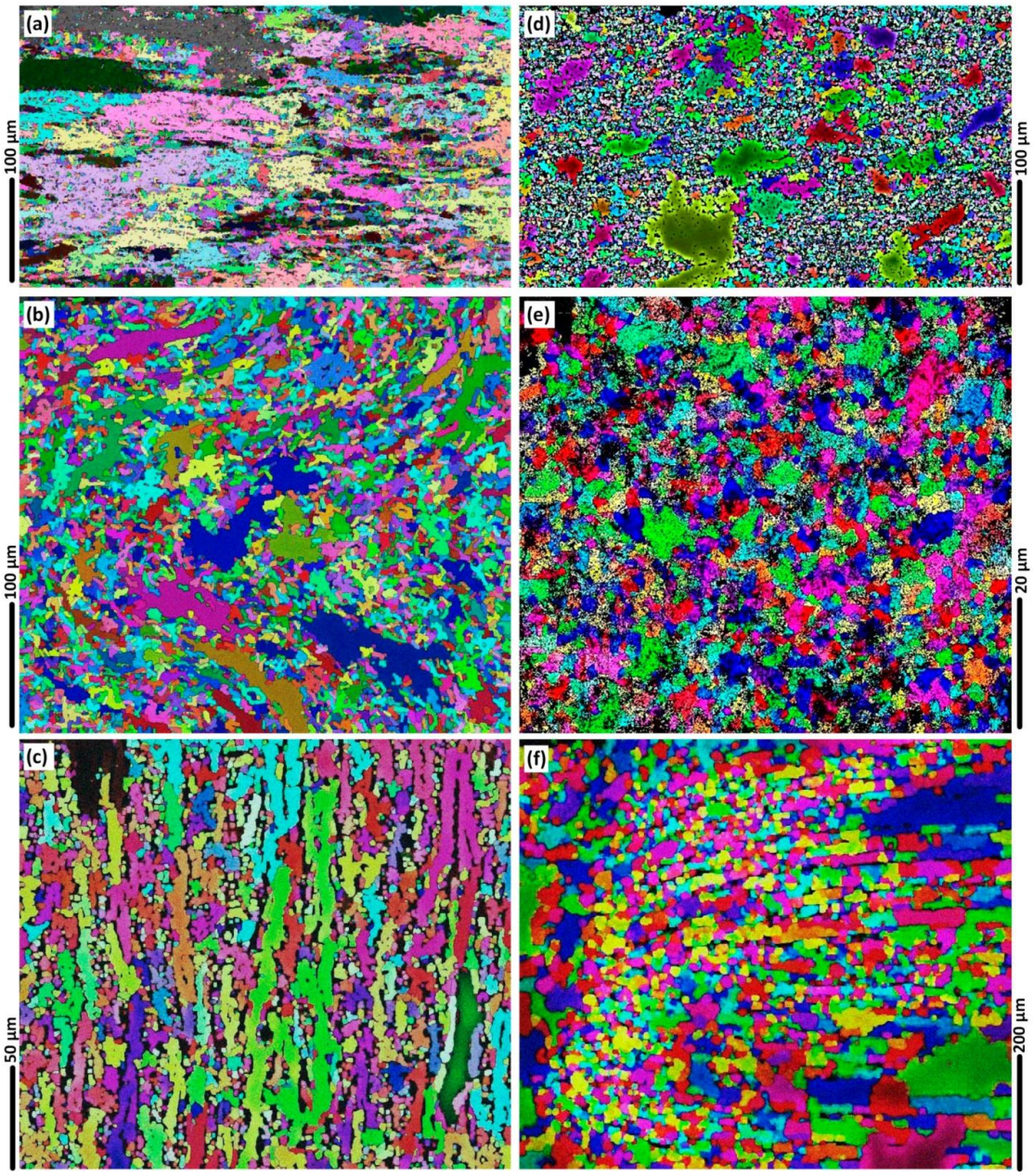

Figure 12.12. The Euler map micropatterns of the presence of HAGBs with post processing using a 15° angle, for different regions of the weld; BM (**a**); AS Hourglass border (**b**); Flow-arms (**c**); Sub-shoulder region (**d**); Mid-SZ (**e**); RS Hourglass border (**f**).

12.4. Chapter Discussion

12.4.1. Comparison between Methods

When applied to the BFSW welding case, the main benefit of optical microscopy (with etchant) is that it shows the size of the grains, i.e., the morphology. It does so at relatively low cost. It should be noted that the optical microscopy micrographs delineate the grains by the same colour without any information regarding the distribution of the crystallographic orientation or lattice structure. Moreover, the AA6082-T6 is difficult to obtain sufficient contrast in OM, and depends on suitable reagents and etching procedures.

A better understanding of weld texture arises from application of EBSD, which shows the grain orientation. This is useful because it shows that adjacent grains often have very different orientations. This is attributed to the stirring action. The EBSD map can show the grain orientation distribution of the sample, illustrating the morphology and size of grains with a precise accuracy constructed with the spatial digital pixel derivation. Based on the EBSD mapping analysis, the neighbouring pixels with similar crystallographic orientations are representative of a grain region, identifying by the same colour.

The study verifies that the method of optical microscopy with etchant gives results that are consistent with EBSD, though naturally the type of information available is different. There are advantages and disadvantages to the two methods (see Table 12.3).

Table12.3. Comparative details of the metallographic measurements performed for the bobbin friction stir welding (BFSW) A6082-T6 weld structure by optical microscopy (OM) and EBSD.

Metallographic Measurement	Pros	Cons
Optical microscopy (with etchant)	Grain boundaries visible (but orientation not)	Precipitation not evident
EBSD	Crystal orientation visible. Misorientation between grains is evident	Precipitation not evident at this level of magnification
Combination of both methods	Characterised microscopic features of the BFSW weld by OM, was validated by EBSD. Further details of the shear texture in different regions of the weld were evaluated by EBSD	Due to repolishing, the measurements are time-consuming and it is not possible to repeat the exact position of the microscopic features

Another powerful instrument for characterisation of the DRX detail and grain growth structures within the weld region is the transmission electron microscope (TEM) [9]. Specifically, TEM also enables detection of precipitation phenomena, often intermixed with the dislocation network and the grain boundaries structure [207, 208]. This might elucidate the solid-state plastic flow mechanism in the BFSW

processed structure of the AA6082-T6 in correlation with the microstructural effect of the T6 temper. This is left for future research, as a TEM study is beyond the scope of this chapter.

12.4.2. Microstructure of Welded AA6086-T6

This chapter presents a metallographic measurement (by OM and EBSD methods) to elucidate some microstructural performance of the AA6086-T6 weld texture, dominant by the thermomechanical nature of the BFSW process.

Shear Bands

From the EBSD colour orientation mapping, it can be concluded that the (100) red and [111] <101> turquoise are the dominant orientations at the hourglass borders, indicated by a layered/fibrous texture.

After the severe shearing, the polycrystalline lattice transforms to the zero-distortion planes by the displacement. The most plausible shear plane with the minimum stacking fault energy in FCC lattice is (100)//WD. Moreover, during the DRX, the slip system of [110] <111>//TD activates the rearrangement of orientation which is revealed as turquoise colour. This is a diffusive transformation to stabilise the interface energy between the shear texture of (100) plane with the shear strained region at its immediate proximity to obtain a coherent interface.

The grain orientation maps of the BFSW sample confirmed that the shear texture at the AS interface of the weld region indicates a more abrupt transition compared to the RS. The occurrence of the discontinuity defects (e.g., tunnel void) occurs at the AS, rather than the RS. Based on this observation, The interpretation is that the texture characteristics in BSW weld correlate with a location-dependency microscopic evolution, where the shear-induced locations (due to the rotation and advancement of the tool) can increase the potential of failure within the weld structure.

The relative motion between the directions of the rotation and advancement of the tool are the same at the AS, which results in an elevated rate of flow (directed forward) and hence plastic deformation. On the other hand, because of the opposite directions of the rotation and advancement of the tool at the RS, the stirred mass is compacted at the trailing edge of the tool, leading to the mixing of the layers (leading to lower level of distinction between the layers in metallographic observations), and refilling of the possible discontinuities (no void formation observed in the RS).

The elongated-shape texture at the hourglass border was studied in TD-ND plane of the EBSD plots. However, because of the dependency of this texture to the (100) shear plane, it needs to be further studied in ND-WD plane through the crystal direction aligned to both ND and RD. These directions may better identify the shear at the circumferential of the tool for the deposited layers along the AS.

The crystallographic nature of these shear band textures may be worth further study. The thermomechanical behaviour of the BFSW and semi-solid plastic deformation are possible explanations for the orientation evolution of the shear texture at the hourglass border interface.

The (100) shear direction in the FCC lattice can be activated when the uniaxial hot deformation compression happens to the texture. The microscopic observations suggest that the high mobility of the grain-boundaries during the deformation results in formation of elongated grains within the (100) shear texture.

In the growth competition between different crystallographic directions, the (100) planes provide a preferential axis for the faster grain-boundary migration. Hence the red (001) material is frequently surrounded by turquoise material [111] <110>. Turquoise is also sheared material, but in the orthogonal orientation. This indicates that there is an element of secondary alignment of grains alongside the main (red) shear bands. Some possible interpretations are that the turquoise material represents material that is compressed between the shear bands. There are also pink and yellow regions, but blue and green are sparse.

During the recovery and DRX after the process, it is assumed that the stored strain and the temperature can provide the driving force to activate other crystallographic systems to change the texture. However, because the elongated grains from the (100) system were formed already during the mechanical stirring process, the similar structures in their proximity has more preference. In the case of FCC metals, the crystallographic system of [111] <110> is a stable orientation for the recovery of the plane-strain compression deformed texture during the recrystallisation. This is the turquoise colour regions in EBSD plots, which is situated between the (111) and (101). In OM these shear bands are evident as dark lines. These lines comprise layers that are sheared and stacked in directions aligned with the shear flow changes.

Shear causes the grains to be compacted (as evidenced in the red (001) orientation). By definition this means fewer stacking faults, and fewer dislocations. The EBSD shows that the shear effect is layered—there is no uniform shear across the section, though there is similarity of orientation between adjacent sheared areas. This has potentially significant implications for the modelling of internal flows via computational fluid dynamics (CFD) modelling, where it is assumed that the flow is locally consistent. In the BFSW samples under examination, the shear occurs in discrete layers. This may have something to do with the transport of material around the pin, in a type of packet flow.

Internal Flow

The homogeneity of the grain structure and the random distributed grain refinement took placed in the SZ (as the middle of the weld region) represent a simultaneous grain fragmentation and severe plastic deformation during the FSW process and the subsequent DRX taking place by the re-cooling, respectively.

The microscopic comparison between the sharp tapered-shape boundary at the AS and the ellipse-shape boundary at the RS may represent a difference in rate of the torsion for the two zones. This can be also related to the different directions of the tool motion and the mass transportation, by which causing different strain rates and the subsequent shearing patterns. Furthermore, different temperature gradient in the AS and RS can directly influence the DRX mechanism subjected to the frictional heating.

The elongated grains as the flow-arm region was characterised as a periodic deformed structure caused by both deformation and thermal load induced by the pin-driven stirring action. Additionally, underneath the shoulder, a continuous plastic flow appears which forms the sub-shoulder region. The microstructure in the sub-shoulder region is slightly coarsened compared to the internal parts of the SZ. This may be related to the cooling conditions experienced by the surface of the workpiece in free contact with the air as the coolant.

The triple flow junction at the middle of the hourglass-border is attributed to the two different characteristics of the flow there. The middle part of the weld region experiences severe thermo-plastic flow regime driven by the stirring action of the pin, which appears to provide two flow path ways towards the upper and lower parts of the cross-section.

12.4.3. Implications: Towards an Interpretation of the Interaction between Physical Metallurgy and Flow

Based on the theory of FSW, the alteration of the texture in different region of the weld (SZ, HAZ, TMAZ) was expected. However, the present chapter elaborates on the structures and DRX mechanisms for the BFSW case. Shear bands features were identified in different microscopic details through the hourglass-borders and the sub-shoulder region. These can be explained by the induced strain and thermal history.

In general, the microscopic observations confirmed that the deformation induced by the rotating BFSW tool is typically in the form of shear. However, due to the physical rotation of the tool, the shear texture shows different local orientation throughout the weld texture. Moreover, it should be noted that the shear flow layers within the weld are affected by the depth of the material as the position of the pin and shoulders can induce different local shearing modes. The shear layers are not necessarily aligned with the weld direction. This can be due to the rotating nature of the tool. For example, even in the middle of the SZ, the equiaxed grain texture shows the minimum of anisotropy within the sample, representative of the uniform distribution of the shear. For the processing of the aluminium alloys, the EBSD texture observations should be compared to the possible shear planes reported in the literature for the face-cantered cubic (FCC) crystallographic unit: red for (001).

The absence of the precipitate phase in the microstructure observations for both of OM and EBSD results implies that the BFSW welding happened without precipitation. However, this is not usual for a dynamic recrystallised texture that experienced a severe plastic deformation accompanied with the frictional heat generation. Possibly this may be related to the scanning mode of the microscope, and hence this may need to be checked in future studies.

The formation of the shear bands is related to the details of the mechanical stirring action. The explanation is as follows. By the contact between the rotating tool and the workpiece, the primary grains located at the advancing edge of the tool undergo fragmentation and subsequent plasticising by the frictional heat and deformation. The simultaneous rotation and advancement of the tool squeeze the softened grains to the trailing edge of the tool. This causes a bending and elongation yielding through the morphology of the grains which are deposited at the AS and RS sides of the tool, where the shear is maximum. However, at the RS because of the opposite directions of the rotation and translation, the flow layers are mixing together, and the elongated grain structure is less clear. Therefore, the hourglass interface between the TMAZ and the SZ on the AS is more observable rather than the RS. In other words, the plastic flow on the AS swept in a smooth narrow shear band at the proximity of the pin, while the irregular transformation of the flow at the hourglass-interface on the RS cause a kind of mixing of the shear-bands. At the AS-RS region behind the tool, the stirring action breaks up the transformed grains into the ultrafine equiaxed grains.

The coarsened and elongated grain textures at the AS and RS compared to the mid-SZ equiaxed grains can be attributed to the multi-directional strain-induced flow fields, caused by the top and bottom shoulders. While in mid-SZ region, pin-induced shear appears to dominate the plastic flow, and the subsequent stored-strain becomes the driving force of the DRX. Therefore, the fully DRX in mid-SZ produce an ultrafine grain structure compared to the AS and RS interface regions, because of a higher rate of stored-strain driven by the direct action of the stirring pin. Moreover, at the sub-shoulder region, the ultrafine DRX grains are intensified by the severe frictional effect of the shoulder and the subsequent thermal dissipation due to the cooling by the free air surrounding the weld surface. Therefore, the sub-shoulder region shows a different flow pattern compared to the mid-SZ region and the hourglass-borders.

Based on the ultrafine equiaxed grain structure, it is proposed that the mid-SZ grains have undergone a severe DRX. In contrast the elongated grains in the transition region at the hourglass interface of the weld region indicate a different morphology implying a local deformation and recovery with partial DRX.

The literature explains that the stirring action is directly responsible of the formation of the shear texture. In the case of BFSW the shear deformation around the pin is non-uniform with a thermal and strain gradient across the weld. Hence in BFSW

welds there is an inherent flow mechanism (induced from the pin and shoulder features), which transports the stirred mass around the weld in discrete packets. This induced shear, which was followed by a DRX process (partial or full depending on the shear), which led to the observed polycrystalline structures (and grain boundaries).

Regarding the texture evolution it should be noted that beside the shearing deformation, the frictional heat input (generated by the interaction between the tool-workpiece) has a key role in microstructural alteration during DRX. Similar to the induced strain, the variation in thermal flux from the position of the pin (mid-SZ) to the top and bottom shoulders, causes local heating on the deformed material. Beside the stored strain, this heat input contributes to accomplish a fully-DRX through the mid-SZ. Other regions of the FSW weld, such as hourglass-borders, TMAZ and HAZ, also are affected by heat, but to a lesser extent. Hence the thermal contribution to the DRX varies according to the location in the weld. Temperature also has a direct effect in formation of LAGBs/HAGBs and precipitation during DRX in different regions of the weld.

Welding process settings (workpiece thickness, tool geometry, welding speeds) are expected to affect the microscopic details of the weld texture. Increase in the thickness of the workpiece may reduce the generated heat and shrink the thermal flux, hence decreasing the DRX process. However, this might possibly be compensated by more complexity in tool geometry to induce more flow through the stirring action. Similarly, increase in welding speeds (ω, V) is expected to increase the frictional heat at the position of the tool-material, resulting in a more severe plastic deformation. Therefore, the DRX mechanism can potentially be intensified by suitable optimisation of the welding parameters. This might be worth investigating via microscopic observation to identify the optimum settings.

12.4.4. Future Work

The 6-series aluminium alloys (Al-Mg-Si) such as AA6082-T6 as here, are generally problematic in FSW processing. It is already known that precipitation occurs during the process [141]. The present study identified that the texture includes shear bands with fibrous morphology in the grain orientation. One of the possible reasons can be work hardening. This is a plausible mechanism based on the progressed observation of the precipitation in Euler maps. However, the characterisation ideally needs to be developed by TEM and in higher magnification to identify the origins of the phenomenon and elucidate the origins of the precipitation mechanism. Hence, it suggests that future work could consider investigating work hardening and anisotropic behaviour of the texture during stirring and DRX.

12.5. Chapter Conclusions

The study verifies that the method of optical microscopy of AA6082-T6 BFSW weld with etchant per [140] gives results that are consistent with EBSD, though naturally

the type of information available is different. The EBSD results, including grain orientation mapping and grain boundary mapping, reveal more details of the weld texture. The EBSD colour mapping demonstrated the grain misorientation in different regions of the weld, caused by the shear during stirring action and the subsequent dynamic recrystallisation (DRX). The grain boundary mapping, based on the Taylor factor, distinguished low-angle grain boundaries (LAGBs) and high-angle grain boundaries (HAGBs) through the weld texture.

It was evident that different grain orientations were formed by the shear strain induced by the tool performance in AS and RS of the weld. The hourglass-border as a direct outcome of the shearing was formed as the aligned bands at the AS, while the complex action of the tool caused the mixing of shear bands at the RS.

The grain structures that occur in AA6082-T6 BFSW welds are due to a complex set of factors. The motion of the pin and shoulder features transports material around the weld, which induces shear. The shear deformation around the pin is non-uniform with a thermal and strain gradient across the weld, and hence the DRX processes are also variable, giving a range of polycrystalline and grain boundary structures.

This micro-pattern is interpreted as DRX features of the FSW process whereby the stored strain induced by plastic deformation affects the grain structure of the TMAZ by grain misorientation. This can be detected as the microscopic change in etching response in the optical microscopy (Figure 12.8a), and the grain misorientation alteration in the EBSD colour mapping.

This chapter makes the original contribution of identifying the content of the flow lines that are evident in the macro-structure. These lines are evident in optical microscopy, but the images in the literature are typically diffuse due to the difficult of etching this material. As shown here, with suitable etchants OM shows the grain boundary features more clearly. More accuracy is evident with EBSD, which also avoids risks of introducing artefacts due to over-etching. The results show the OM and EBSD results are consistent. The overall interpretation is that the welded region contains fine discrete layers of material, of approximately 10 μm thickness. In these the shear has caused dynamic recrystallisation, which has resulted in a string of grains with similar orientation. When etched and observed with OM, these appear as dark and light lines.

Furthermore, these shear bands are found to have different characteristics across the weld section. In turn this is attributed to the different flow and thermal regimes in these locations. A homogeneous continuous fluid would be expected to have a smooth shear field. The actual observer shear occurs in discrete bands. This, plus the abrupt changes in the lines, suggests that the internal flow regime is more complex than might be expected.

Chapter 13: Thermomechanical Characterization of Dynamic Recrystallization for the AA6082-T6 Aluminium Alloy under Bobbin Friction Stir Welding

Chapter Summary: Bobbin friction stir welding (BFSW) is a thermomechanical process which produces novel microstructural details requiring evaluation for optimization of the weld structure. AA6082-T6 aluminium alloy is a challenging material for BFSW processing because of poor response to the conventional metallographic methods which makes it difficult to study the grain size and morphology of the weld region. Electron backscatter diffraction (EBSD) was used to determine microstructural evolution in AA6082-T6 BFSW welds. This revealed details of grain-boundaries in different regions of the weld microstructure. Different polycrystalline transformations were observed through the weld texture. The Stirring Zone (SZ) underwent severe grain fragmentation and a uniform Dynamic Recrystallization (DRX). The transition region experienced stored strain which changed the grain size and morphology via sub-grain-boundary transformations. Other observations were of micro-cracks, the presence of oxidization, and the presence of strain hardening associated with precipitates. Flow arms in welds are caused by DRX processes including shear, and low and high angle grain boundaries. Welding variables affect internal flow which affects microstructural integrity.

13.1. Introduction

Bobbin Friction Stir Welding (BFSW) [1, 2] is a thermomechanical process [141] whereby the stirring action of the tool fragments the grains into an ultrafine microstructure [5, 66]. The frictional heat, generated between the bobbin tool and the workpiece softens the material to a plasticized flow [37, 38] which is mixed by the stirring action between the advancing side (AS) and the retreating side (RS) of the rotating tool [16]. The stir-related plastic flow around the pin can also be vertically squeezed at the sub-shoulder regions of the tool, restricted by the top and bottom shoulders [41, 138, 139]. By advancement of the tool through the weld-line, the combination of these flow regimes deposits the stirring zone (SZ) region at the trailing edge of the tool [83]. The cross-section of the BFSW weld shows the SZ at the middle, corresponding to the position of the tool action, distinguished from the Base Metal (BM) by the hourglass-shaped borders at the AS and RS of the tool position [64, 140]. In addition to the heat generation, the mechanical stirring also induces strain within the SZ and the neighbouring regions of the BM, leading into the formation of a transition region between the BM and the SZ [45, 84]. The immediate

vicinity of the SZ is known as the Thermomechanically Affected Zone (TMAZ), which is followed by the Heat Affected Zone (HAZ) towards the BM [52, 209]. Both of these two regions together are considered the transition region of the BSFW weld structure, where the grain distortion forms a transitional morphology distinct from the BM and SZ microstructures [32, 46].

Thermomechanical behaviour of the BFSW is different from Conventional FSW. In particular, in the former the symmetrical shape of the stirring zone and the formation of the flow-arms at the borders of the weld region indicates a different flow behavior [56, 63]. This is because of the specific geometry of the bobbin-tool, whereby the interaction between the tool and substrate generates the flow-arms at the edge of the hourglass-shaped borders instead of the onion rings in a basin-shaped stirring zone of the conventional FSW [36-38]. Moreover, removal of the backing anvil and its replacement by a rotating bottom-shoulder increases the heat generation and hence affects the weld microstructure [4, 15, 66, 83].

During the cooling of the weldment, dynamic recrystallization can cause many grain-scale and sub-grain-scale changes within the weld texture [25, 32]. It is expected that these microscopic features have a considerable influence on the final properties of the BFSW weld in service. Understanding the thermomechanical mechanisms, as well as finding the origin of the occurrence by microscopic characterization, has the potential to better control the weld properties [139]. In this regard, Grain-Boundary Engineering (GBE) may be used for the study of the thermomechanical nature of the weld texture [23, 24, 26, 210]. The grain-boundary network can alter and improve the physical and mechanical properties of the microstructure [32].

However, for the AA6082-T6 welds, it is difficult to delineate the grain-boundaries in microstructural observations as the poor contrast makes it hard to distinguish the grains. More recently new etchants have been identified for improvement optical microscopy of the AA6082-T6 BFSW welds [140]. The results were successfully able to delineate the grain-scale feature of the weld, where the alteration of grains size and morphology were readily illustrated across the polycrystalline micrographs [140]. However, the optical metallography is not able to provide a suitable resolution in sub-grain-scale magnifications.

While the general microstructure of the BFSW weld has been relatively well-characterised in the literature, the thermomechanical behaviour of the weld texture still requires more elucidation in sub-grain-scale details. The frictional heat generation followed by the dynamic recrystallization induces post-welding variants in the microstructural properties of the weld texture. The heat input and the flow-based mechanical stirring (with its relationship to process parameters) can create a relatively complex strain distribution [45, 55]. This can be stored through the processed material, leading to a variety of microscopic transformations through the polycrystalline lattice of the weld texture [23-25, 27, 211]. These thermomechanical

alterations need to be accurately studied at the sub-grain-scale to characterize the origin of microscopic transformations (e.g. grain refinement, DRX, and precipitation).

This study presents a grain-boundary engineering approach to investigate the details of the thermomechanical mechanisms occurring in EBSD micro-constituents of the BFSW weld texture for AA6082-T6 aluminium alloy. EBSD patterns can also measure the grain misorientation distribution during DRX caused by thermal and mechanical strain in the texture.

13.2. Materials and Methods

For the weld trials, rolled plates of AA6082-T6 (Al–Si–Mg–Mn family) were used as the starting workpiece. BFSW tests were conducted using a geometrically full-featured (including threads, flats and scrolls) bobbin tool manufactured from H13 tool steel with hardness of 560 HV. The schematic of the bobbin tool is shown in Figure 13.1.

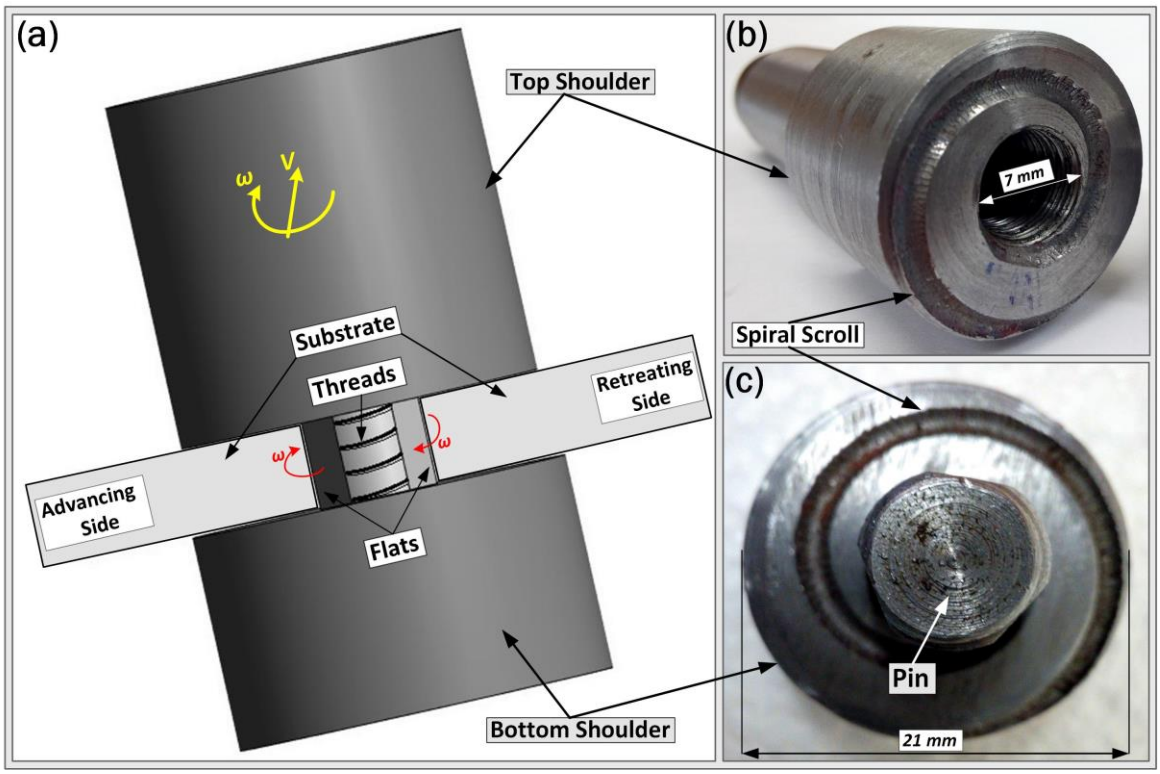

Figure 13.1. Fully-featured Bobbin-Tool (tri-flat threaded pin and spiral scrolled shoulders); (a) Schematic of the bobbin-tool in interaction with the cross-section view of the substrate between the shoulders-gap, (b) disassembled top shoulder with the drilled position of the cantered-pin, (c) disassembled bottom shoulder and the tri-flat pin in the middle.

The butt-joint weldments comprised two pieces of similar plates with dimensions of 250 mm (length) × 75 mm (width) × 6 mm (thickness). The compression ratio of 3.75% (difference between the actual thickness of the plate and the gap between the shoulders of the tool) was considered between the tool and workpiece to compensate the spindle forging force existing in conventional-FSW [81]. The compression ratio conserves the engagement between the plastic flow and the tool at the position of the stirring and avoiding the mass ejection. The welding trials involved a set of operation speeds; spindle rotational speed (ω) and weld travel rate (V). In the experiments, the chosen speeds were (ω=400 rpm) and (V=350 mm/min). The BFSW experiments were performed on a 3-axis CNC machining centre (2000 Richmond VMC Model, 600 Group brand, Sydney, Australia) with a Fanuc control unit and 14-horsepower spindle motor capacity. There were no preheating or post-weld processes before or after the welding process. The direction of tool rotation was clockwise relative to the advance direction of the welding (Figure 13.1). After welding the quality of joints were first checked by visual examination, and then cross sectioned by an electro-discharge wire cutting machine through the middle of the weld seam (perpendicular to the welding direction).

The resulting surfaces were subjected to metallographic inspections. For metallographic analysis, firstly the specimens were prepared using standard mechanical polishing with different grades of SiC sand papers (600-grit, 800-grit and 1200-grit). To achieve a mirror surface, the micro-polishing step was conducted on a micro-cloth pad with a 3μm diamond paste, and finally a 0.05μm colloidal silica solution.

Better understanding of the thermomechanical nature of the BFSW weld can be furthered by the study of the grain-boundary patterns through the texture. A Scanning Electron Microscope (SEM) with an EBSD detector can provide the crystallographic orientation mapping required for the study of the microscopic details of texture and history of recrystallization. EBSD patterns can also reveal the grain-boundary and sub-grain-boundary features with high contrast at a sufficient level of magnification.

Samples were examined with a scanning electron microscope (SEM) (JEOL 6100, JEOL Inc., Peabody, MA, USA) with an HKL Nordlys III EBSD detector (Oxford Instruments plc, Abingdon, UK). The EBSD maps for different regions of the weld cross section were processed using traditional clean-up procedures with HKL Tango software (HKL Channel 5 Tango software version 5.12.60.0, Oxford Instruments plc, Abingdon, UK). As the stirring was conducted over the weld locus, the grain size of the sample varied greatly from BM through to the center of the weld. Thus, to maintain a constant number of pixels for EBSD mapping and estimation of grain size, for small grain-sized regions, a magnification step size of 0.75μm with an overall acquisition area of ~1/16 mm^2 was used. Alternatively, for large grains of BM region, a step size of 3μm with an overall acquisition area of 2 mm^2 was used. All

other control parameters such as binning, probe current, accelerating voltage, and exposure time were held constant. EBSD maps with obscured clarity of the Kikuchi diffraction patterns were rejected. By altering the step size, the average indexing rate of all collected samples was 97.5%, where the unindexed pixels were filled in with the software.

The crystallographic orientation is defined by a crystalline reference local frame in three orthogonal directions; rolling direction (RD), natural direction (ND) and transverse direction (TD). In a polycrystalline texture, the relative difference in crystallographic orientation between two neighbouring grains is called 'Misorientation', a local transformation in the crystallographic frame. In coordinate systems, misorientation is described as the rotating of two grains with regards to their respective crystallographic directions.

Misorientation distribution is a comparative crystallographic function for the local characterization of the grains within the texture. The EBSD analysis provides plots for graphical representation of the grain misorientation distribution in the Euler angles system, describing the misorientation probability for the three-dimensional rotation of grains. The EBSD plotting constructs a section of the crystalline texture by irregular restrictive boundaries between the grains. By using the pole figures and their corresponding RGB colour scheme, the crystallographic planes and orientation direction for each individual grain can be locally specified compared to the rest of texture. The colour scheme is based on a colour key triangle named the Orientation Triangle in which each of its corners has a different colour (red, blue, green) assigned to a determined crystallographic orientation. The inverse Pole Figure (IPF) generates a colour scheme mapping for the microstructure in which the alteration of colours accurately corresponds to the orientation changes.

The polycrystalline texture is formed by a colony of grains aggregated in various crystallographic orientations. While the orientation inside of each grain exhibits a minimal variation, this can easily differ for the surrounding grains. By defining a critical angle of misorientation for the volume of grains, grain-boundaries are drawn as the geometrical interface between the grains, where the area has an over-critical misorientation angle. By pixel mapping in graphical observation, the grain-boundaries can be readily identified as the spatial distribution of a randomly contoured network between the separated grains. In the inverse pole figure, the major crystallographic directions of [111], [001] and [110] are to be considered the standard for the arbitrary distribution of (hkl) poles, based on the miller indices of crystal. The crystallographic directions determine the texture by the graphical distribution in colouring scale for the orientation maps. According to the Miller indices and based on the stereographic parameters of the crystal lattice, the coloured map overlays the [111] direct as blue, [001] as red and [110] as green, as it is standardised in the colour orientation triangle. Other orientations also are coloured in different mixtures of RGB colours, dependent on different directions intercepted

between [111], [001] and [110]. Thereby, by the stereographic projection of crystal planes, misorientation is revealed for multiple points, distinguishable by different colours, compared with the default colours of the unit IPF triangle as the crystal directions of the normal sample. This colour mapping can clearly illustrate the crystallographic directions of the crystal lattice for grains and grain-boundaries, displaying the grain misorientation in a spatial and angular distribution through the polycrystalline texture.

Based on the principles of the mechanical metallurgy, the strength of the texture is directly dependent on the characteristics of the grain-boundary network (morphology, density, and distribution). Furthermore, the grain size distribution and precipitation of secondary phase are also important microstructural features for controlling the mechanical properties during dynamic recrystallization.

The grain orientation represents the crystallographic behaviour of the deformed grains during recrystallization mechanism. The IPF mapping denotes the grain misorientation information for: (1) whole grains in the texture contrasting by grain-boundaries as the High-angle grain boundaries (HAGBs) threshold, and: (2) the orientation alteration within the grains, indicated by the sub-grain-boundaries as the Low-angle grain boundaries (LAGBs) threshold. The thermo-mechanically induced strain during the stirring action and the post-welding re-cooling can lead to accumulation of the dislocation within the grains restricted by the grain boundaries as the High-angle grain boundaries. To reduce the internal stresses in the sub-grain scale, the dislocations adopt a self-arrangement order which leads to the formation of Low-angle grain boundaries (LAGBs) inside the grain. This can result in strain-free grains where the formation of sub-grain boundary represents a misorientation in sub-grain scale.

In IPF maps, the crystallographic orientation for each individual point is shown by the colour pixels attributed to the (hkl) planes, whereby red is representative of (001), green (110), and blue (111). As the deformation and the subsequently induced strain could change the crystallographic orientation of the grains, the colour of pixels is changing through the deformed areas and demonstrates a deformation pattern for the grains. For the deformation sample, the grains misorientation can be displayed in three orthogonal directions perpendicular to the sample surface; normal direction (ND), transverse direction (TD), and rolling direction (RD). Here in BFSW sample, the RD plane is the cross-section of the weld, ND plane is the surface of the weld, and TD plane is situated at the middle of SZ across the weld centerline. Therefore, grain recrystallization can be studied in three different directions. This is a more accurate way of revealing the microstructural details when different transformations occur simultaneously.

Based on the colouring method, the HKL TANGO software can modify the EBSD mapping results to a three-colour map to display the DRX details through the texture: blue for recrystallized portion (completed DRX area), yellow for

substructured region (partial recrystallized), and red representative of the remaining deformed grains (named as the recovered portion where DRX did not occur). This analysis can highlight the DRX history of thermomechanically deformed material.

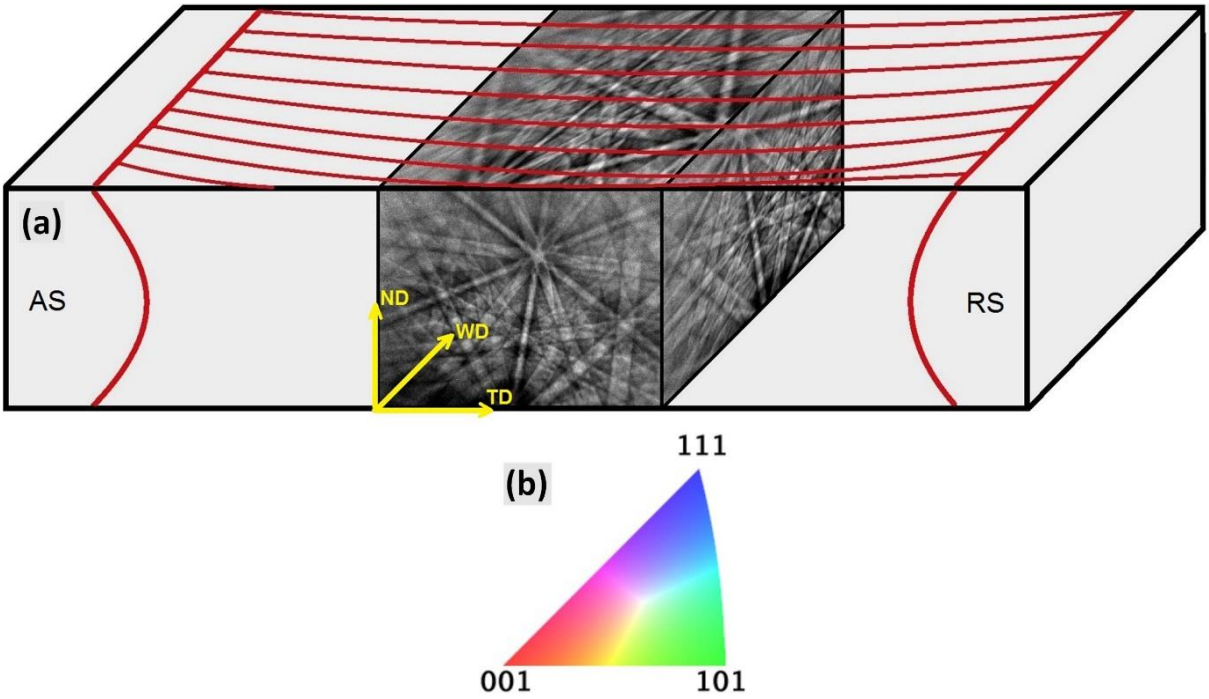

Figure 13.2. The method of EBSD analysis; (a) schematic of ED, ND and TD planes for a 3D EBSD pattern, (b) IPF triangle.

To construct a 3D EBSD map, a serial sectioning procedure was conducted for the different regions of the weld in three different perpendicular planes; TD-ND, ND-WD, TD-WD. The sequential section were mechanically polished and measured by the EBSD IPF mapping. Finally, the 2D EBSD maps for each section (TD-ND, ND-WD, TD-WD) were reconstructed to a 3D microstructural EBSD model. To minimise the possibility of the misinterpretation of the 3D EBSD mode due to misalignment of the measured regions, a further microscopic measurement of different modes of mapping were developed for the TD-ND plane for each region of the weld. By comparing of the microstructure in different maps, the inaccuracy in the misorientation details were minimised for neighbouring grain pixels in each region.

The grain orientation spread (GOS) analysis of the RBSD results used the Schmid factor for different regions of the weld texture. The Schmid factor makes a relationship between the slip systems in crystal and the induced shear stress. Using the EBSD data it is possible to measure the stress in a crystallographic coordinate system which changes the orientation of the crystal. By post-processing of the EBSD data using the HKL software package, the alteration in the Schmid factor (SF) for

neighbouring grains can be determined, which is representative of the misorientation angle.

For transmission electron microscopy (TEM), the cross-sectioned specimen was sliced at the location of the border of the weld region, between the stirring zone and the transition region. These selected sections were mechanically ground to 0.2 mm thickness by a Gatan Model 691 dimple grinder. To achieve a thin section with enough transparency for TEM analysis, a Fischione twin jet electro-polishing unit was used to process the sample in a 20% methanol-diluted HNO_3 solution at 18 °C. TEM imaging was performed by a Philips CM120 cryo-electron microscope instrument, facilitated with the LaB6 emitter, working in accelerating voltage of 120 kV.

13.3. Results

13.3.1. Regions under examination

The cross-section of the AA6082-T6 BFSW weld with the stirring zone at the middle of the weld is shown in Figure 13.3. Different regions of the weld are shown and numbered for further analysis, including the base metal (BM), heat-affected zone (HAZ), thermomechanically-affected zone (TMAZ), and stirring zone. Other features of the BFSW, such as the hourglass-boundary region and micro-cracks, also are selected for analysis.

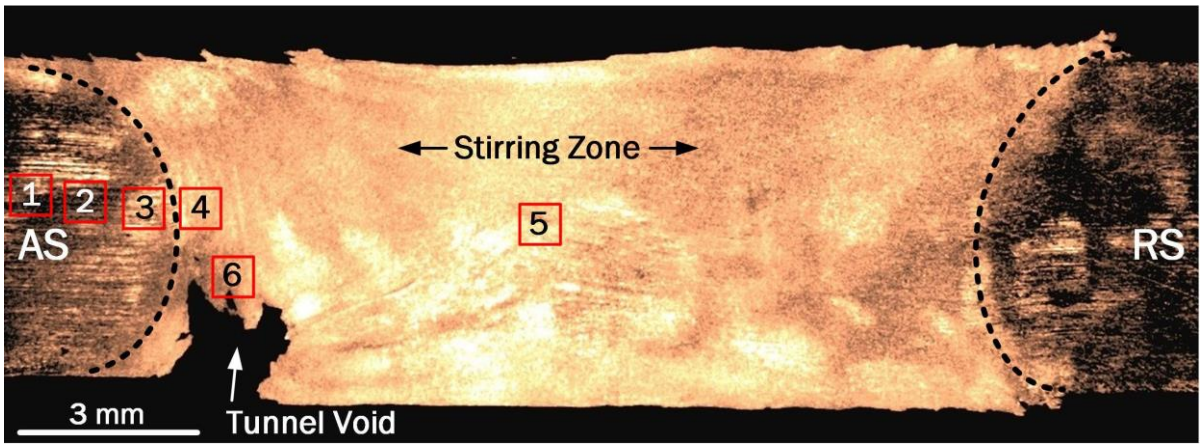

Figure 13.3. Cross-section of the AA6082-T6 BFSW weld with different region of the weld marked for t further analysis; (1) base metal, (2) heat-affected zone, (3) thermomechanically-affected zone, (4) hourglass-boundary region, (5) mid stirring zone, and (6) micro-crack region.

13.3.2. EBSD general texture evaluation

The selected frames (regions 1-6) were subject to EBSD texture evaluation and serial sectioning as described above. Results are shown in Figure 13.4, in the left column. This compares the different regions of the weld.

To achieve more details, the microscopic details in the TD-ND plane were further processed using other maps of EBSD (IPF X, Y, Z, Euler map, and band contrast) by the post-processing of the indexed Kikuchi patterns. This reveals the sub-grain details of the microstructure in a higher resolution. The IPF-coloured mapping of the AA6082-T6 sample in three directions (TD-ND, ND-WD, TD-WD), across the recrystallized grains, is shown in Figure 13.4 (right column). The alteration of colours between adjacent pixels through the map represents the grain misorientation gradient in the texture, varied by the locally stored strain. The change in colour at the intergranular-scale reveals the position of the low-angle grain boundaries (LAGBs) or sub-grain-boundaries depending on the localized crystallographic misorientation.

The text within the image summarises the main characteristics of the grain structure at the various locations across the weld.

The Euler map displays the spatial orientation information in a basic presentation compared to the IPF maps. The IPF maps are measure the orientation based on a RGB colour key, to visualise the specific texture distribution in more detail. However, Euler maps are limited in ability to show small orientation changes. Therefore, the Euler map has less accuracy for spatial distribution of the orientation in the sub-grain-scale. The other qualitative measurement of EBSD is band contrast (BC) which indicates the lattice defects based on the intensification of the Kikuchi bands. The advantage of the BC is to show the high-angle grain boundaries. Map 8 was used to present a better contrast between High-angle and Low-angle grain boundaries.

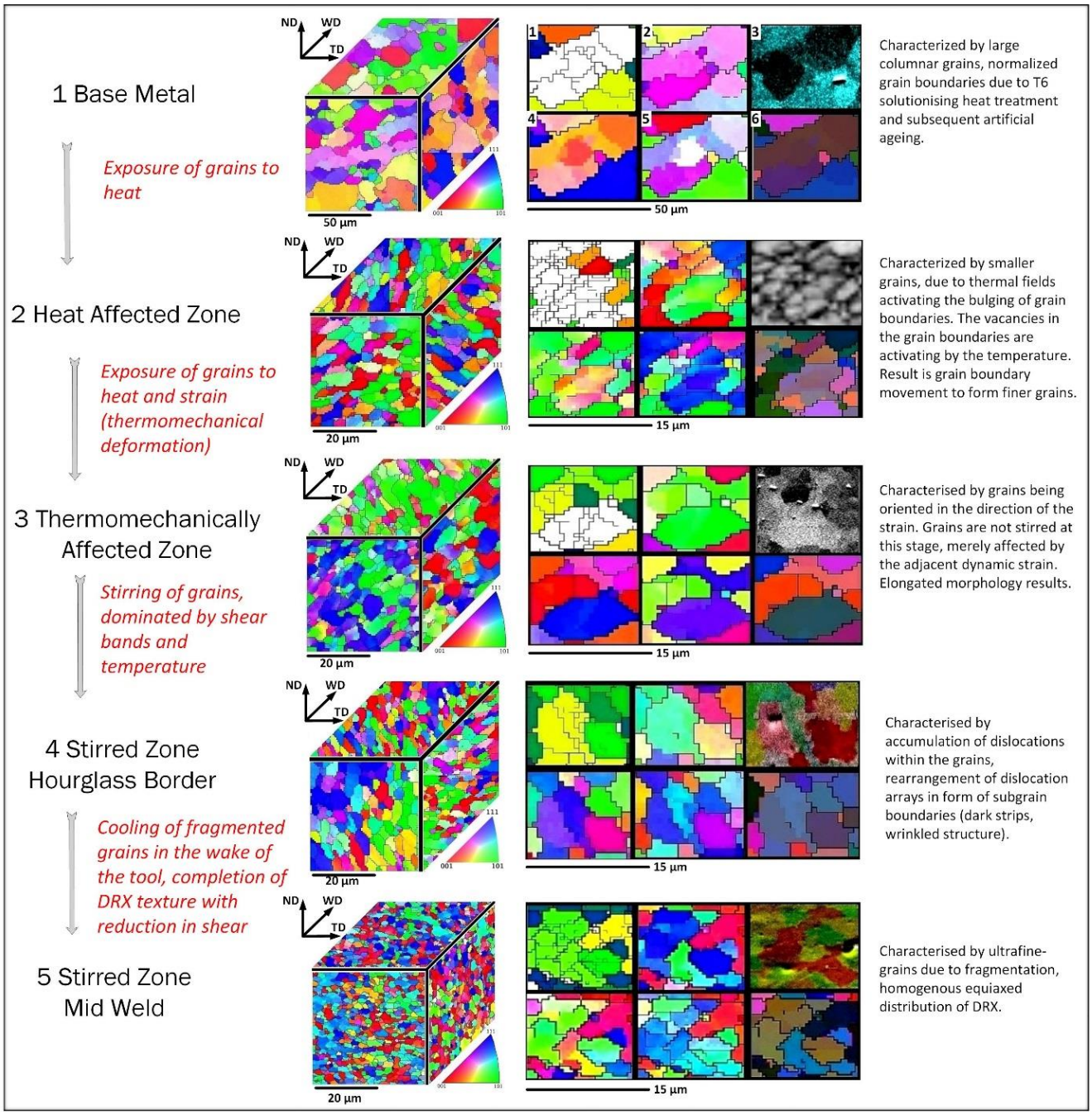

Figure 13.4. 3D-constructed EBSD patterns for different regions of the weld. 3D reconstructed EBSD model and the TD-ND microscopic details (Left to right, top to bottom: 1; map 8, 2; IPF X, 3; band contrast, 4; IPF Y, 5; IPF Z, 6; Euler boundaries).

13.3.3. Dynamic Recrystallization (DRX)

While the IPF maps could specify the misorientation evolution through the weld texture, the DRX details need to be elucidated by further evaluation of the EBSD collected data. As the average grain size in the SZ reduced to the ultrafine scale, the regions of the EBSD maps need to be measured in higher magnification. Furthermore, post-processing was applied to images using HKL Channel 5 software.

The microscopic maps in Figure 13.5 distinguish the progression of the recrystallization through the deformed grain populations by a comparative observation in different regions of the weld texture (BM, HAZ, TMAZ, and SZ).

The post-processed maps by using the Tango software (right column in Figure 13.5) represent the recrystallization detail of the grains texture after DRX. The red, yellow and blue colours represent the deformed, substructured (recovered) and recrystallized fractions of grains, respectively.

From the TANGO post-processed results, presented in Figure 13.5 (right column), it is apparent that after a general deformation the texture was predominantly in the recovery grain state (yellow fraction). Later, in DRX process, the recrystallized grains (blue fraction) are formed, which concurs with the results discussed in Figure13. 4.

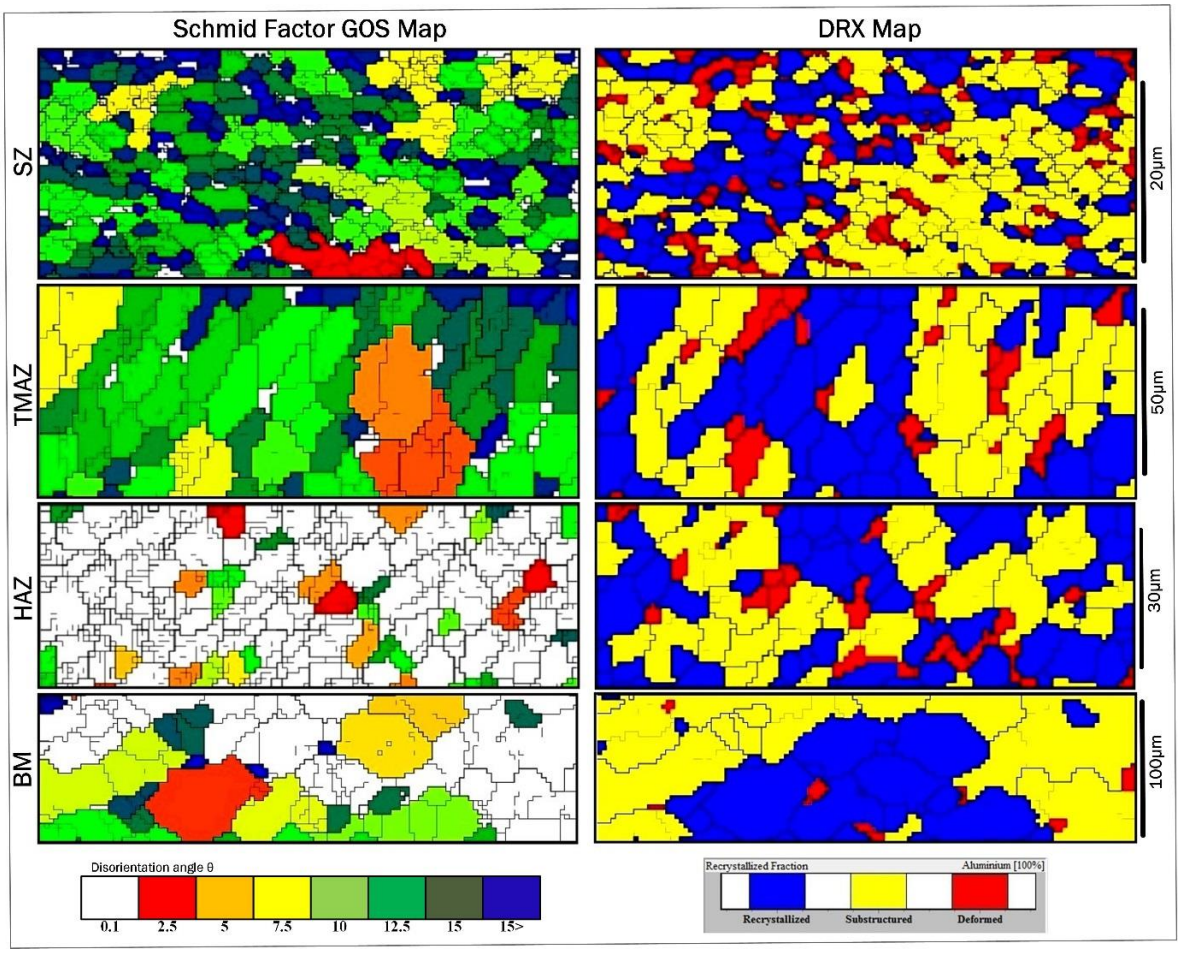

Figure 13.5. Recrystallization textures for different regions of the weld; microstructure comparison for different region of the weld, provided by Euler, IPF and recrystallization maps.

The TANGO DRX maps elucidate the history of the orientation texture spread in different regions of the weld. First, the stirring action deforms the grains. Thereafter

the recovery of the grains occurs in form of a partial recrystallization to change the orientation from the primary deformed state (red). During the recovery phase, stress-relieving occurs and stabilises the grain texture (yellow). With appropriate thermomechanical conditions (temperature and induced strain), full recrystallisation occurs (blue grains). These grains possess a specific new orientation different from the primary deformed grains (red) and partially-DRX in the substructure grains (yellow). The comparison between different regions of the weld shows that in the SZ the recrystallized microstructure is activated to a greater extent (partial DRX in yellow, and fully-DRX in blue), with a significant reduction in grain size compared to the other region of the weld.

Grain Orientation Spread (GOS) maps by Schmid Factor

Local misorientation in deformation-induced recrystallization can be explained by the Schmid Factor (SF) corresponding to the local deformation mode and the direction of force. By comparing the DRX map processed by HKL Channel 5 software, the grain orientation spread (GOS) is presented in Figure 13.5 (left column). The local misorientation between the grains with range 0-15 degrees, are considered as representing the deformation history.

The EBSD DRX maps in Figure 13.5 reveal the preferred SF misorientation for emergence of sub-grain-boundaries (SGBs). The highest population of the accumulated dislocations is between 0-15 degrees. One of the most significant characteristics of the DRX transformation is the rearrangement of the grain boundaries from columnar to equiaxed. The thermal gradient and the shearing strain presumably cause this morphological variation in the grain population. The stored strain from thermal and mechanical stresses would be first released by rearrangement of the crystalline lattice via sub-grain boundaries (or LAGBs). However, in severe plastic deformation with higher levels of SF, these thermomechanical transformations can result in grain boundary movements evident in HAB misorientation. As the texture experiences greater strain, the consequences are higher progression of DRX. To extrapolate these thermomechanical features within the GOS map, the emergence of misorientation can be denoted by the colour changes of pixels corresponding to the angle of orientation content in the neighbourhood area.

The initial strain content activates the stacking fault energy as the driving force of the dislocation movement at the position of the main grain boundaries (HAGBs). This can first create a dislocation migration in low-energy array directions leading to the formation of LAGBs, and after that by additional plastic strain and movement of HAGBs.

The GOS map of the mid-SZ indicates a highly oriented morphology with the dominating disorientation angle of >10-15 degrees, representative of the local misorientation. The continued DRX also induces newly strain content into the grain population which causes this disorientation.

The GOS maps in Figure 13.5 outline higher density of SGBs at the SZ location, identifying the preferential orientation for the accumulation of dislocations at the flow-arms. By comparing the IPF maps between the BM and SZ, a columnar-to-equiaxed transition (CET) was identified regarding the grain morphology alterations during the DRX.

Stirring zone

The selected frame of the mid-SZ (regions 5, Figure 13.3) was subject to EBSD texture evaluation; IPF colour map and corresponding grain boundary map. Results are shown in Figure 13.6. Equiaxed ultrafine grains in mid-SZ are observed with a random grain orientation. The grain size at the mid-SZ is about 5μm or below. The formation of ultrafine equiaxed grains in mid-SZ can be attributed to the mechanical stirring of the pin causing grain fragmentation. The fragmentation rate is presumably related to the speed ratio (ω/V).

Compared to the other weld regions, the SZ is observed to have a greater density of LAGBs. The interpretation is that this arises from the higher shear and greater heat conservation in this region.

The equiaxed grains are attributed to grain breakup during the stirring action, via the formation of micro-shear bands across the large grains. During the dynamic recrystallization process, the internal shear combined with the temperature causes the formation of distinct smaller grains via production of internal HAGBs, as opposed to grain coalescence to form elongated grains. There are still LAGBs evident within the fine grains, presumably due to the large amounts of strain in the system compared to other regions of the weld.

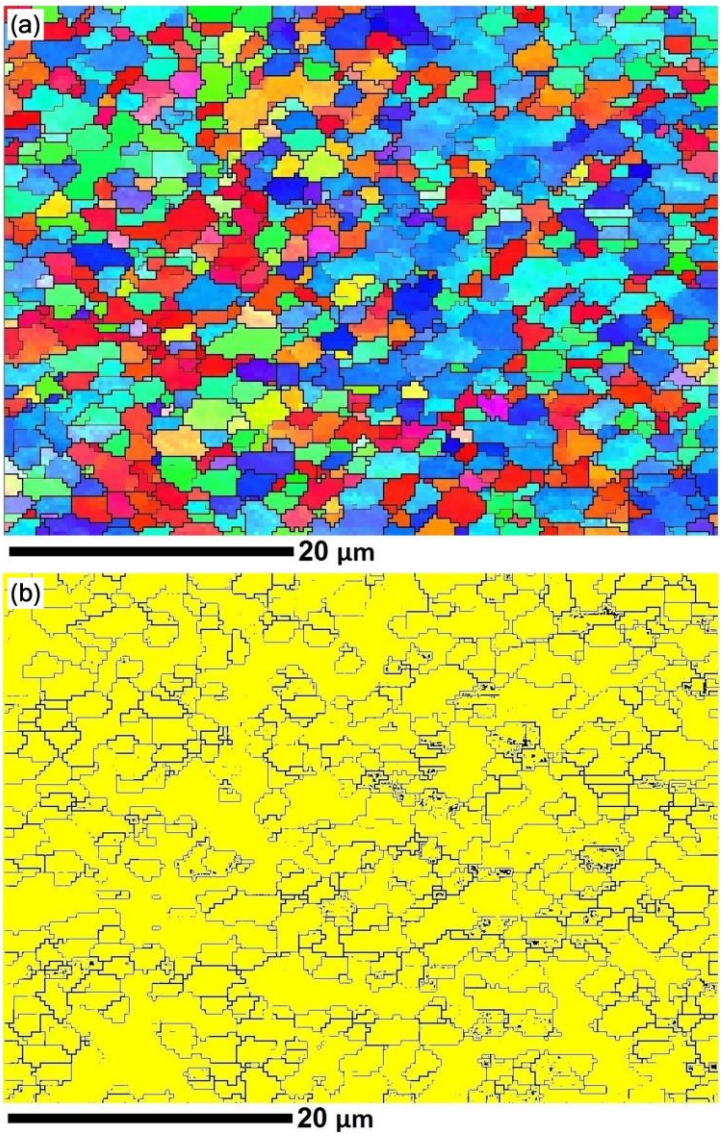

Figure 13.6. EBSD analysis of the mid-SZ region; (a) IPF colour map, (b) grain boundary map of the corresponding IPF map in (a).

13.3.4. Flow-arms and elongated-to-equiaxed transitions of grain-morphology

The IPF maps for the orientation distribution are shown in Figure 13.7 corresponding to the transition region near the hourglass border towards the SZ. It should be noted that Figure 13.7 demonstrates the EBSD mapping of the Region 4 in Figure 13.3 for the hourglass flow-arm region at the AS border. The image shows the finer details inside the flow-arm.

The micrographs show the elongated grain morphology, representative of the flow-based stress-strain fields. The flow-arms along the hourglass-border are attributed to the relative motion between layers of material within the weld (cyclic deformation). The microscale post-processing of the IPF colour map (Figure 13.7a) reveals the morphology of the elongated grain structures within the flow-arms due to this strain. The grain boundary distribution characterized in the Euler map (Figure 13.7b)

displays polycrystalline anisotropy in grain boundary contrast for elongated grain morphology, different to the equiaxed microstructure of the SZ.

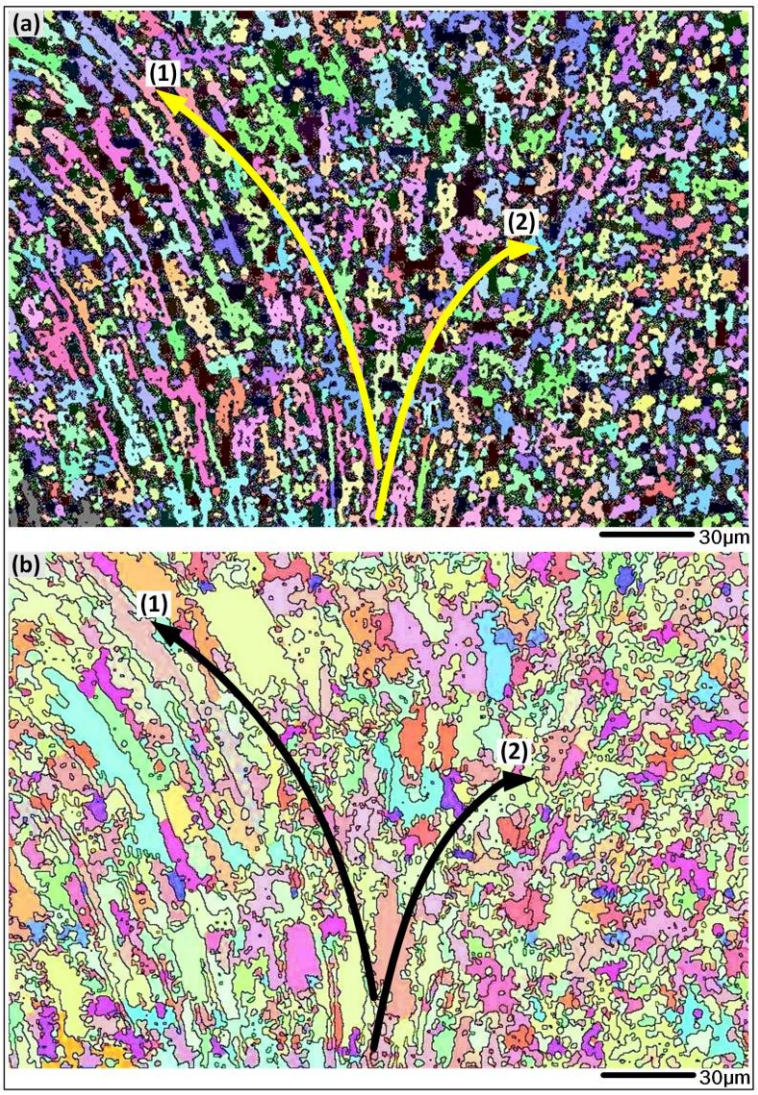

Figure 13.7. The flow-arms morphology at the AS border of the SZ; (a) IPF-map, and (b) Euler Angle. (1) elongated grain morphology in hour-glass boarder region, (2) equiaxed grain morphology in stirring zone.

Our interpretation is that this morphological variation arises from the cyclic deformation in the SZ, driven by the induced strain and the generated heat. The heat also facilitates GBs movement and activation of the sub-grain boundaries. Consequently, during the re-cooling, the DRX causes abnormal grain growth: the stored strain tries to rearrange the crystalline lattice of the grains by an increase in the accumulation of dislocations and the population of sub-grain boundaries and LAGBs. This results in higher density of the SGBs, hence the observed formation of elongated grains as the flow-arms. By more absorption of thermal and mechanical strains, the LAGBs tend to change to HAGBs where the morphological alteration forms the grain misorientation.

The microstructural evolution denotes that a large portion of the grains through the cross-section experience similar effects within their physical neighbourhood. The interpretation is that the initial strain content has dominant influence on the activation of LAGBs, while the additional plastic strain results in the advancement of grain boundary migration as the HAGBs (and the grain fragmentation).

The EBSD maps in the GOS analysis represent the local misorientation across the weld texture, where a highly oriented microstructure dominates at the borders of the SZ. This elongated grain morphology with shear direction is attributed to the higher rates of localized strain concentration at the corners of the SZ close to the hourglass borders, where the shearing bands can form the flow-arms within the grain texture during the DRX. The EBSD results suggest that the flow-arm grain morphology is also elongated parallel to the hourglass borders, oriented in (001) direction where the shear strain is in highest rate.

The microscopic observations confirm that the flow-arm recrystallized zones are dissimilar in morphology at the AS and RS of the weld. This can be attributed to the non-symmetrical thermal flux. The more wrinkled grains texture of the AS flow-arms represents more severe shearing and higher strain imposed into the texture, compared to the morphology of the more coarse grains at the RS neighbouring with more thermal influence rather than deformation.

At the proximity of the flow-arms, there is a grain population with different morphology which is significantly smaller than the transition region and the elongated morphology. This microscopic evolution originated from the localized heat-inducing during the DRX where the stored strain and the accumulation of the dislocations release local heating during the re-cooling. By absorption of this local heating via the neighbouring regions, grain boundary movement is possible which leads to the formation of the ultrafine equiaxed morphology near the shearing bands in a direction parallel to the elongated grains of the flow-arms. The extent of this region might not be symmetrical at the AS and RS borders of the weld, as during the stirring the heat flux and the stored strain content might not be equal.

13.3.5. Micro-crack formation

EBSD analysis was conducted on the crack edge in the stirring zone, see Figure 13.8. Elemental mapping was also performed. As the scale shows, the crack is a small feature, a hairline micro-crack. It is a narrow multi-branched feature that commences at the edge of the tunnel void defect. It is one of many such structures. The interpretation is that it is a crack, rather than a lack of flow bonding in the stirring process, for reasons given below.

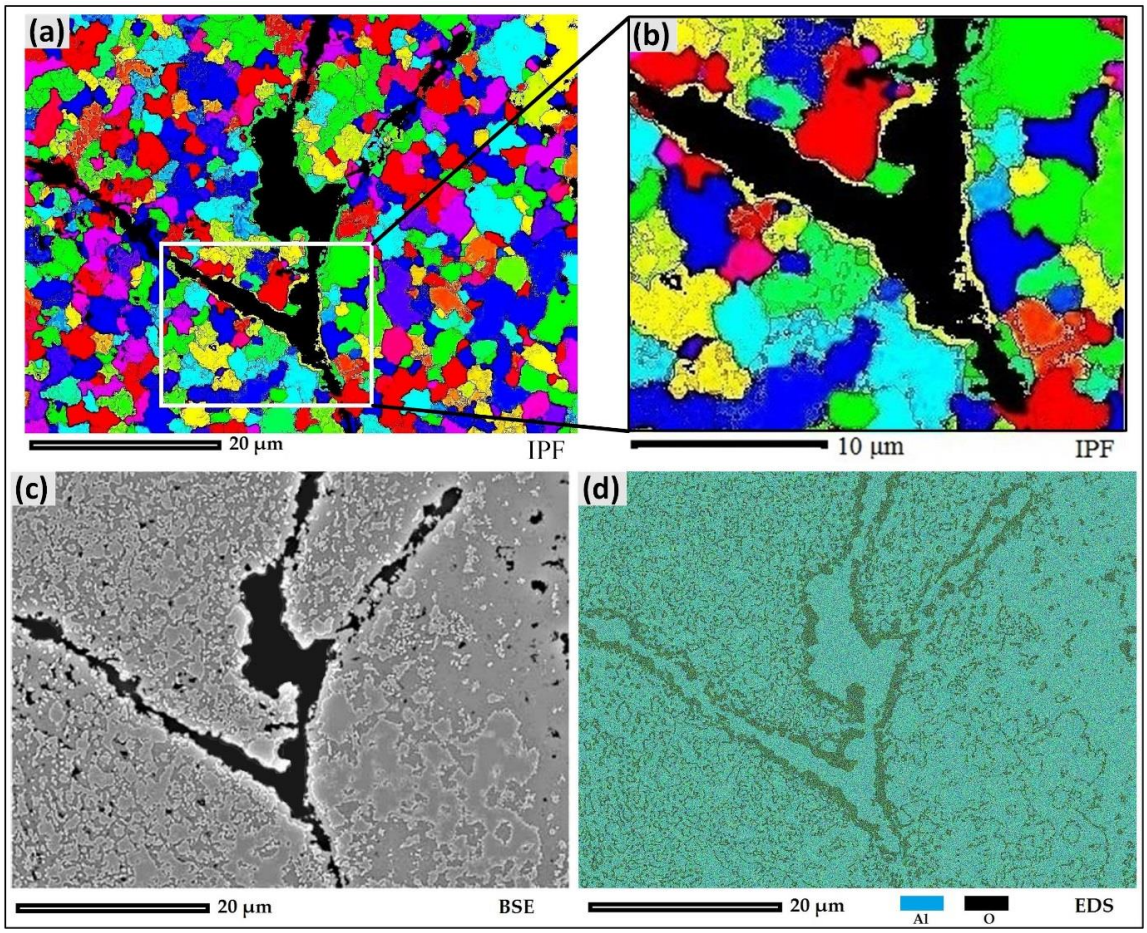

Figure 13.8. Microscopic features of the micro-crack (selected from Region6, Figure 13.3); (a) EBSD map, (b) higher magnification of region 1 in (a), (c) BSE SEM image of the EBSD map, and (d) elemental map for the micro-crack, representative of the distribution of Al and O in micro-crack.

Chemical composition

Key findings are that there is a layer of yellow texture, with orientation (001) <101>. This is the preferred direction for aluminium oxide. The EDS confirms that this is indeed an oxide. This is a potentially novel finding. It has significant implications for the welding process, because the alumina presumably results in inclusions, restricts the reattachment of cracked surfaces and discrete packets of material in the SZ, and reduces mechanical properties.

Crack formation mechanisms

The grain structure at the crack edge has an elongated morphology compared to the smaller grains at the proximity region far away from the crack. The proposed explanation follows. During the crack propagation, the localized high strain deformation induces heat at the crack tip. This also induces a localized plastic deformation which causes a quick accumulation of dislocations near the crack edge. Consequently, the dislocation interaction rearranges the DRX grain evolution to heat-induced recrystallization containing a large quantity of LAGBs. Furthermore,

while most of the grain boundary misorientations at the crack-proximity are HAGBs, the most of the misorientation of GBs at the crack edge are LAGBs, which is representative of the typical recrystallized grains induced by deformation.

13.3.6. Strain hardening

The presence of the precipitates particles within the grain structure of the region of elongated grains was observed, see Figure 13.9. The precipitates presence are shown in the TEM images in Figures 13.9 b,c.

The TEM results show the deposition of the precipitates particles at the position of the GBs between the grain and within the grain at the SGBs. A distortion field around the precipitates at the SGBs position is observable, which can be representative of the strain hardening caused by the precipitates as the blocking barriers of dislocation movement.

Dislocations will accumulate first at the grain boundaries, where the precipitates are observed to be larger, and then inside the grain. The dislocations at the grain boundary contribute to the formation of HAGBs. A low-angle grain boundary is visible in Figure 13.9c, and is associated with a precipitate particle. Plausibly this association is due to the blocking of dislocations by the precipitate particle, and the arrangement of dislocations into the LAGBs. Blocking of dislocations at both high and low-angle boundary positions contribute to strain hardening effects.

The higher rates of the strain hardening can cause a wrinkled texture formed from the severely elongated grains. This condition can consequently lead to the crack propagation parallel to the elongated direction.

For this structural evolution, the high strain rate deformation can locally induce a quick accumulation of dislocations near the GBs. Subsequently, the heat-induced recrystallization can rearrange the dislocation arrays to sub-grain boundaries. This dislocation interaction can reduce the capacity of plasticization at the weld borders, hence strain hardening. Shear tends to nucleate precipitates at grain boundaries, and further limit dislocation mobility, hence also contributing to strain hardening.

Our interpretation is that the DRX grain refinement and the dislocation interaction can prevent the crack emergence by absorption of the strain hardening and stress concentration via releasing of the stored strain in the form of the LAGBs.

It is possible that the observed micro cracks are caused by the effect of strain hardening. In which case there may be benefits to post weld stress relieving by thermal conditioning.

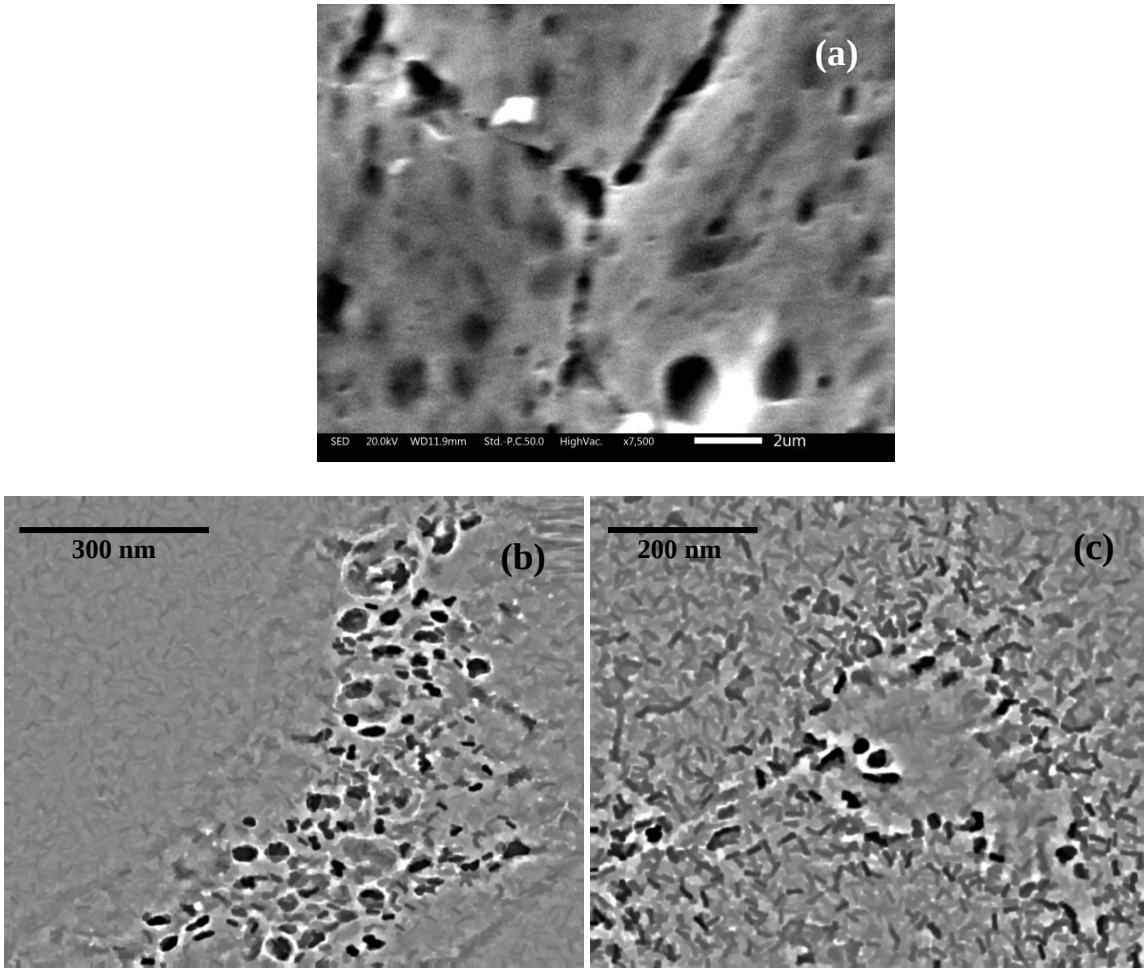

Figure 13.9. presence of the precipitates within the structure, GBs and SGBs. (a) SEM image of the elongated grains, (b) TEM image of the precipitates at the position of the GBs, (c) TEM image of the precipitates inside of the grain, at the position of the SGBs, with a distortion field around the precipitate particle.

13.4. Chapter Discussion

13.4.1. Findings

The work makes the following original contributions to improve the understanding of the grain boundary behaviours in the BFSW welding process of AA6082-T6.

EBSD general texture evaluation; The grain boundary networks at the sub-grain scale (HAGBs and LAGBs) have been identified for multiple regions of the weld cross section, and show different morphology and spatial orientation.

Dynamic Recrystallization (DRX); Extensive grain refinement, reduced to the ultrafine scale, was observed in the SZ, compared to the BM texture. The microscopic evidence is of a DRX process. The alteration in grain size and morphology was observed to relate to the distance from the actual position of the severe plastic deformation (situated at the mid-SZ).

Flow-arms and elongated-to-equiaxed transitions of grain-morphology; Different to the equiaxed microstructure of the SZ, the transition region near the hourglass border shows elongated grain morphology (flow-arms). Evidence from the EBSD micrographs shows this is caused by relative motion between layers of material within the weld (cyclic deformation), and incomplete DRX. In contrast, the grain boundary distribution in the SZ possesses polycrystalline anisotropy in equiaxed grain morphology, which is attributed to the higher temperatures contributing to a more complete DRX.

Micro-crack formation; Hairline micro-cracks are visible at the stirring zone near the tunnel void defect. They are distributed as narrow multi-branched features within the weld texture. The mechanism of the micro-crack formation is attributed to the lack of flow bonding during the stirring process. The formation of an oxidation layer at the edge of the crack may restrict the reattachment of cracked surfaces.

Strain hardening; The presence of precipitate particles at the position of the LAGBs and HAGBs was observed in the elongated grain structure of transition region. It is expected that these precipitates will restrict the movement of dislocations during the plastic deformation phase, hence contributing to the strain hardening effects. The further restriction of the dislocations movement can consequently lead to crack propagation parallel to the elongated direction.

13.4.2. A proposed holistic interpretation of grain boundary effects in BFSW

Based on the EBSD information, it proposes that the rotational dynamic recrystallization is the dominant thermomechanical mechanism within the polycrystalline weld texture. This can be observed in the flow-arm shaped grain zone at the hourglass borders where the shear bands exist as a response to the strongly induced plastic strain.

The rotational dynamic recrystallization can be explained as a continuous DRX mechanism, occurring by the evolution of low-angle grain boundaries to high-angle grain boundaries. By an increase in the degree of misorientation within the polycrystalline grain structure, the sub-grain boundaries experienced a critical mismatch in their crystal lattices. As this mismatch reached a threshold level of misorientation, the sub-grain boundaries evolve to the high-angle grain boundaries or become actual grain boundaries.

This transformation can happen when the migration of dislocations in rearranged low-angle grain boundaries is followed by shearing at the position of the main grain boundaries. Furthermore, the presence of the precipitates can pin the sub-grain boundaries in their position. Consequently, in regions exposed to higher rates of shearing, the sub-grain boundaries extend in elongated shaped grains parallel to the shearing direction. Hence a type of necklace or beading effect becomes visible, with independent grains along a shear flow line.

In this situation, precipitates can consolidate the sub-grain boundaries in their place, which then absorb more dislocations, which eventually transform them into high-angle grain boundaries. This mechanism creates new morphology of the elongated grains, by rotation of low-angle grain boundaries, instead of grain growth. Elevated temperature and induced shearing strain activates dislocation movements and lets them rearrange themselves at the position of the sub-grain boundaries in the form of the rotational/continuous DRX of the elongated grains.

The evolution of the rotational DRX mechanism can be summarized as follows: (i) the stirring action during BFSW process can induce the strain into deformed grains and activate the dislocation interactions in low-angle grain boundaries; (ii) the generated frictional heat can develop the misorientation inside the elongated cells and increase the rearrangement of the dislocation arrays; (iii) the subdivision of the low-angle grain boundaries can geometrically transform them into high-angle grain boundaries by a local crystal misorientation within the lamellar sub-grain boundaries. This can be regarded as the relaxation of the elongated sub-grains during continuous DRX and formation of the elongated grains.

In contrary, the discontinuous DRX comprises the nucleation of new grains and growth at the high-angle grain boundaries as an abnormal grain growth compared to the adjacent grains.

The shear bands are regarded as the region of the localized plastic deformation. During the DRX process, the nonhomogeneous deformation field (induced by the pin) causes an extensive grain deformation which leads to the large elongated grain transformation that make up the flow-arm morphology. The micro-cracks arise between or near the shear bands, due to the effect of grain transformation and LAGBs to HAGBs changes at re-cooling.

The elongated grains at the flow-arms region inherently contain a high density of LAGBs as the sub-grain boundaries. At the end of the re-cooling procedure, some of these sub-grain boundaries which are situated close to the grain boundary interface (HAGBs) can be transmitted across the grain and gradually reinforce the neighbouring LAGBs in other grain. This mechanism can progressively increase the misorientation angle of the sub-grain boundaries and change them to HAGBs. Therefore, the continuous DRX can form larger elongated grains from the primary deformed grains with different orientations.

13.4.3. Implications for practitioners

The microscopic evolution of the severe plastic deformation stirring during the BFSW process was observed with different types of defects namely tunnel void, micro-cracks and oxidation formation. Also the strain-hardening problems can arise from the uncontrolled precipitations through the LABs and HABs of the weld texture. In brief, the formation of these defects can be closely attributed to the flow mechanism and inconsistency in heat input and re-cooling during DRX mechanisms.

From a production quality perspective, the tunnel void is strongly associated with poor metallurgical outcomes as evident in micro-cracks and oxidation formation. Hence it can state that if a tunnel defect exists, there is a high probability of internal defects. The corollary also appears to be trues: that if the tunnel void is absent, then the metallurgical defects are also absent or at least minimized. It is also noted that the original of the tunnel defect is primarily a consequence of the flow failure within the weld, which in turn is related (by ways not entirely clear) to the tool geometry and weld speed parameters (ω, V). Hence there is a coupling between these three: welding variables affect internal flow which affects microstructural integrity. Thus a priority from a practitioner perspective is eliminating of the tunnel void.

13.4.4. Future work

The micro-cracks formed during stirring can adversely affect the strength of the final weld. The failure behaviour of the joint and the microscopic observation of the fracture surface can give a better understanding of the defect formation mechanism, during severe plastic deformation.

In terms of strength, micro-cracks have more influence over the weld strength and could be examined more. It may be interesting to measure the density of these micro-cracks. Furthermore, there are oxide boundaries at the edge of micro-cracks, and it could be valuable to identify whether this is oxide being drawn in from the material surface or air entering between the stirred mass layers.

There is a possibility that the tunnel void acts as a heat sink, since it is contact with air, and hence affects the DRX mechanism. It was observed some defects in this region that are consistent with such an interpretation.

13.5. Chapter Conclusions

The microstructural evolution of AA6082-T6 weld region, processed by Bobbin Friction Stir Welding, was analyzed using EBSD. The microstructural evolution measured the grain size and morphology of the weld texture, with a focus on grain-boundaries characteristics, DRX texture, grain refinement and the relevant misorientation. The structural evolution regarding the deformation, dynamic recrystallization, and post-process recovery were also studied. The thermomechanical outcomes such as flow-arms and micro-cracks were discussed regarding the nature and formation mechanism. The results show the thermomechanical behaviour of the weld structure during the stirring and the subsequent DRX, representing by different grain size and morphology. The severe plastic deformation and fully DRX at the mid-SZ was demonstrated by an ultrafine and equiaxed grain structure, distinct from the elongated grains at the hourglass-borders of the weld region.

CHAPTER 14: AFM Characterization of Stir-Induced Micro-Flow Features within the AA6082-T6 BFSW Welds

Chapter Summary: Bobbin Friction Stir Welding (BFSW) is a thermomechanical process containing severe plastic deformation by mechanical stirring and Dynamic Recrystallization (DRX) during recooling. This chapter reports the three-dimensional characteristics of the micro-flow patterns within the aluminium weld structure. The Surface topography observations by Atomic Force Microscopy (AFM) show the stirred-induced microstructural evolution where the rearrangement of dislocations at the sub-grain scale, and the subsequent High- and Low-Angle Grain Boundaries (HAGBs, LAGBs) exhibit specific alterations in grain size and morphology of the weld texture. The dislocations interaction in different regions of the weld structure also was observed in correlation to the thermomechanical behaviour of the BFSW process. These micro-flow observations within the weld breadth give a new insight into the thermomechanical characteristics of the FSW process during the stirring action where the plastic flow has a key role in the formation of the weld region distinct from the base metal.

This chapter is a derivative of the following publication:

Tamadon, A.; Pons, D.J.; Clucas, D. AFM Characterization of Stir-Induced Micro-Flow Features within the AA6082-T6 BFSW Welds. Technologies 2019, 7, 80.

DOI: https://doi.org/10.3390/technologies7040080.

14.1. Introduction

Bobbin Friction Stir Welding (BFSW) is a modified variant of Friction Stir Welding (FSW) [212] where the conventional tool is replaced by a bobbin-shaped double-sided configuration [64, 66]. The rotating double-shoulder bobbin tool penetrates from the edge through the interface of the side-by-side plates, and mixes the materials into a butt-shaped joint [38, 139, 140]. The heat input [38] generated by the friction between the rotating tool and the workpiece plasticises the material from both sides of the interface, Advancing Side (AS) and Retreating Side (RS), and stirs them together to form a bonded structure [140]. The stirring action causes severe plastic deformation [37] at temperatures well below the usual melting point [38]. Hence, the process is suitable for the joining of low temperature deformable alloys [213]. Aluminium is an ideal material for successful processing under BFSW [66, 113]. AA6082-T6 aluminium is an industrial marine grade alloy with good

machinability which has recently become attractive for FSW processing [116, 117, 214-216].

To achieve a defect-free weld in FSW processes, the material flow regimes have a higher priority than the metallurgical details [217]. Therefore, it is necessary for the continued improvement of the BFSW process to determine the plastic flow patterns in the weld region, which has received minimal attention in the literature compared with metallurgical aspects.

The severe plastic deformation during friction stir welding is the main cause of alteration in grain size and morphology [13, 17, 35]. The sub-grain scale analysis of microstructure can elucidate the relationship between the microstructure and the thermomechanical nature of the FSW process, especially shearing and heat generation [65]. The deformation-induced texture varies across the weld, as the shear is the function of the distance of the stirred flow mass from the position of the rotating tool [13, 23]. Hence, a better understanding of the grain structure has the potential to contribute to knowledge of the evolution of the thermomechanical mechanism.

This chapter presents an innovative study of the three-dimensional topology of the material flow features of BFSW weld texture. By utilising the Atomic Force Microscopy (AFM), the surface topography in the microscopic scale reveals the flow-based characteristics of the weld arising from the stirring action as a severe plastic deformation. This has the potential to give a better understanding of the effect of the microscopic flow regimes on the thermomechanical properties of the BFSW weld texture.

In this chapter, a high-magnification microscopic measurement was used to observe how the micro-scale plastic deformation affects the microstructure. In this regard, microstructural changes with a focus on dislocation and flow-induced imperfections were analysed in diverse regions of the AA6082-T6 BFSW weld structure.

AFM analysis was used to identify the microscopic details of the weld texture. This provides a greater resolution –to the atomic level– compared to other microstructure measurements. More specifically, the dislocation network and the precipitation evolution within the weld texture can be observed with AFM.

14.2. Materials and Methods

The BFSW welding test was conducted with the AA6082-T6 aluminium alloy (Standard; EN AW-6082, ISO: Al Si1MgMn) rolled plates (Aalco Metals Ltd, UK) as the workpiece. The analysed chemical composition of the AA6082-T6 plate with the elemental details is listed in Table 14.1.

Table 14.1. Chemical composition of the AA6082-T6 aluminium alloy, in elemental detail (wt.%).

AA6082-T6 Aluminium Alloy	
Chemical Element	% Present
Silicon (Si)	(0.70–1.30)
Magnesium (Mg)	(0.60–1.20)
Manganese (Mn)	(0.40–1.00)
Iron (Fe)	(0.0–0.50)
Chromium (Cr)	(0.0–0.25)
Zinc (Zn)	(0.0–0.20)
Titanium (Ti)	(0.0–0.10)
Copper (Cu)	(0.0–0.10)
Other (Each)	(0.0–0.05)
Other (total)	(0.0–0.15)
Aluminium (Al)	Balance

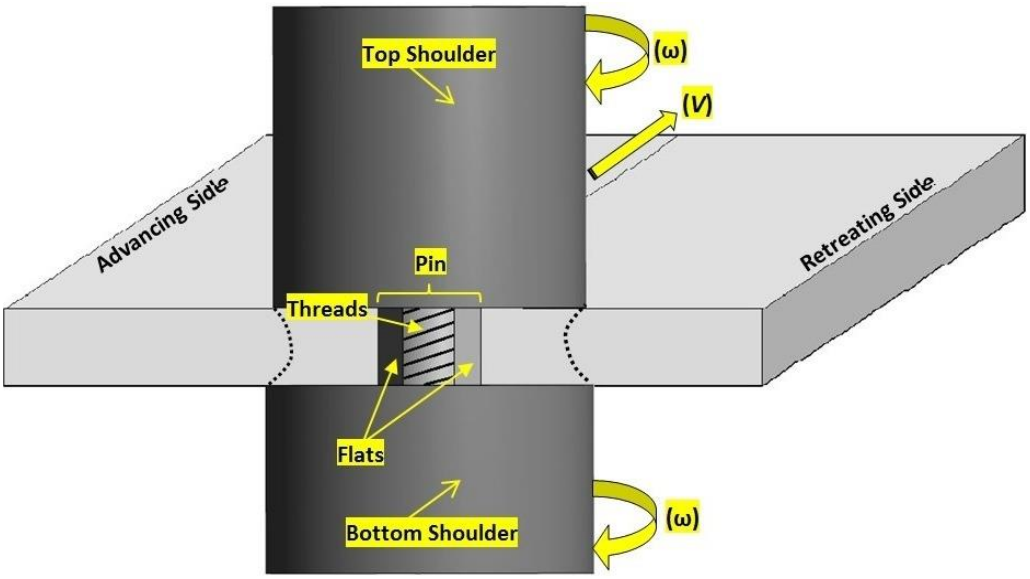

Figure 14.1. Schematic of the Bobbin Friction Stir Welding process; Bobbin-Tool in interaction with the workpiece as the substrate.

The weld samples were in a butt joint configuration comprising two similar plates (250 mm × 75 mm × 6 mm). The geometrically full-featured bobbin tool (included threads, flats and scrolls) was made of H13 tool steel with a hardness of 560 HV [139-141]. The schematic of the BFSW process is shown in Figure 14.1. The BFSW experiments were performed on a 3-axis CNC machining centre (2000 Richmond VMC Model, 600 Group brand, Sydney, Australia) with a Fanuc control unit and 14-horsepower spindle motor capacity. The simultaneous operation speeds consisted of

spindle rotational speed (ω = 650 rpm), and weld travel rate (V = 400 mm/min). The direction of tool rotation was clockwise viewed from above.

The welded plates were cross-sectioned perpendicular to the weld-seam and were micro-polished to a mirror level, according to the standard metallographic preparation [169]. The samples then were etched by using of two modified reagents; (Reagent A: 2 mL HF + 2 mL HBF_4 + 10 mL HNO_3 + 20 mL CH_3COOH + 33 mL H_2O + 33 mL ethanol), and (Reagent B: 0.5 g $(NH_4)_2MoO_4$ + 3.0 g NH_4Cl + 1 mL HF + 18 mL HNO_3 + 80 mL H_2O) per [140, 141]. Previous research has shown these etchants successfully delineate grain-boundary microstructure (Reagent A) and micro-flow patterns (Reagent B) [140, 141]. Both reagents were used for similar etching time and temperature (90 s, 70 °C). For a better cleaning of the samples, the specimens were cleaned in the acetone bath (60 s, 18 °C), under an ultrasonic field of 40 KHz frequency. There is no known corrosive effect of acetone on this material.

To observe the macro-flow patterns within the BFSW weld structure, the etched samples were studied with a stereoscopic microscope (Olympus Metallurgical Microscope, Tokyo, Japan). Microscopic observations of the morphological features were conducted with an atomic force microscope (Veeco Digital Instruments Dimension 3100, from Bruker). The in-situ observations were done in contact mode, equipped with TAP300-G (PDMS imprint and replica) tips (BudgetSensors, USA), in dry conditions at ambient conditions (in air, at room temperature). Visualisation of the recorded mapping data and the three-dimensional topography analysis were processed by Gwyddion software (VERSION 2.45).

14.3. Results

The macro-etched cross-section of the AA6082-T6 BFSW sample (etched by Reagent A) and micrographs of the relevant regions of the weld are shown in Figure 14.2. The microscopic images distinguish different morphological microstructure within the weld region from the Base Metal (BM), through to the transition region; Heat-Affected Zone (HAZ) and Thermomechanically Affected Zone (TMAZ), onwards to the Stirring Zone (SZ); flow arm patterns and middle of SZ. Compared to the base metal, the grain size in other regions of the weld shows an extensive grain refinement (reduction of grain size), and grain morphology.

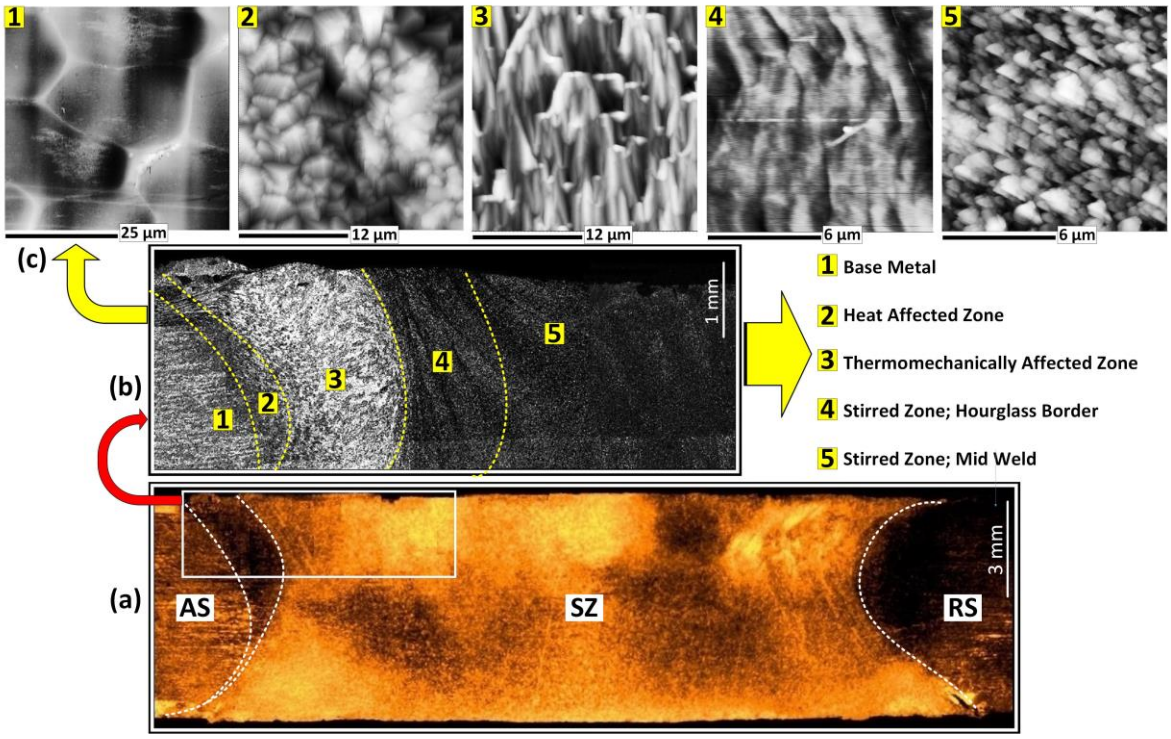

Figure 14.2. Macroscopic and microscopic features of the BFSW weld for the etched cross-section of the AA6082-T6 plate (reagent A); (**a**) Macro-etched cross-section of the AA6082-T6 sample, representative of the hourglass shaped weld structure, (**b**) the selected region from AS region at Figure 14.2a, in higher magnification, distinguishing five different regions for the weld breadth, (**c**) SEM images of 5 different regions of the weld texture, demonstrated in Figure 14.2b. (AS; Advancing Side, RS; Retreating Side, BM; Base Metal, SZ; Stirring Zone).

The thermomechanical nature of the FSW process and the subsequent mechanical and thermal behaviours of the weld texture are believed to be the major activators for this microstructural evolution [141, 144].

The AFM images of the weld region for the AA6082-T6 BFSW sample (etched by Reagent B) are demonstrated in Figure 14.3. After FSW treatment, there are microscopic changes that have taken place in different regions of the weld. The topographic features denote that the BM region (Zone 1) is smoother than the SZ (Zone 5), as well as the transition region at the AS/RS borders of the weld (Zones 3 and 4) where bulging lamellar microbands are evident.

The topographic features are interpreted as micro-flow patterns caused by plastic deformation during stirring. The peak-and-valley-like micropattern is apparent throughout the weld section. Figure 14.3 also shows roughness and texture measures derived from the AFM process. Also given in Figure 14.3 are descriptions of the grain morphology, and the evolution between these states.

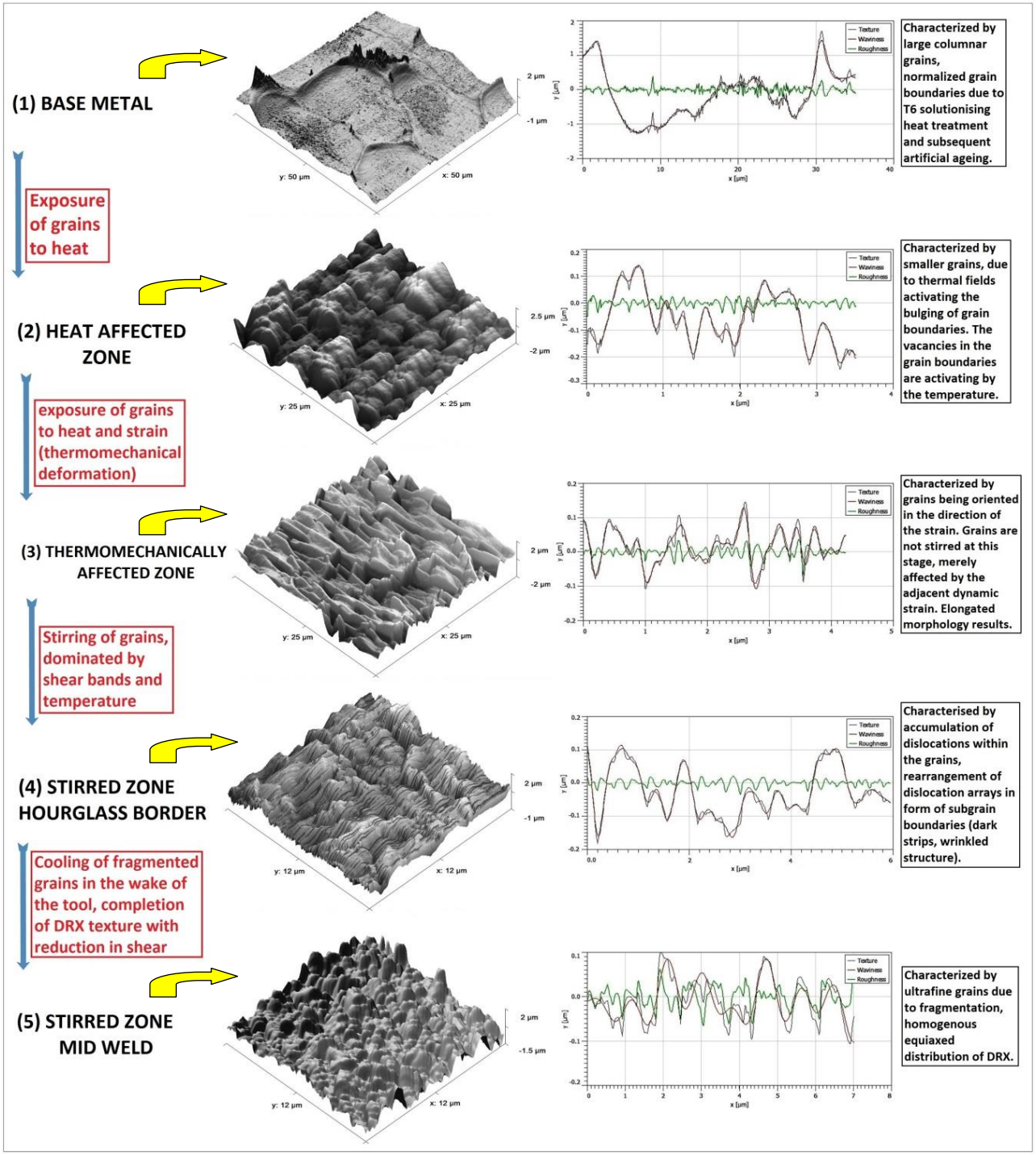

Figure 14.3. 3D topographic AFM images of different regions of the BFSW weld texture measured by the relevant height profiles of the surface roughness and the in detail explanation of the morphological evolution of the microstructure.

Figure 14.3 is left for inspection, but there are several broad comments to be made. Inspection of Zones 3 and 4 (SZ) (Figure 14.3) shows the dominance of wrinkled and linear features, unlike the other regions. Shear is only active in Zones 3 and 4: it does not exist in Zone 1 due to the T6 heat treatment, nor in Zone 2 since this is only

affected by heat flux. The shear is less apparent in mid-SZ (Zone 5), which is consistent with a stress relieving process. The Dynamic Recrystallization (DRX) mechanism uses stored strain and heat to nucleate and recrystallize the microstructure into ultrafine grains, thereby erasing the shear bands that might otherwise be expected at this location [144].

We attribute the wrinkled features in Zones 3 and 4 to activation of dislocations due to shear. Zone 3 shows activation at main grain boundaries (High-Angle Grain Boundaries, HAGBs). There is possible evidence for accumulation of dislocations at grain boundaries. In contrast in Zone 4 the dislocations are arrays within the grains (Low-Angle Grain Boundaries, LAGBs) forming sub-grain boundaries. This rearrangement of dislocations is a typical thermomechanical characteristic of DRX.

The 3D topography maps and roughness profiles are not all the same scale, so care must be taken in interpretation of microscopic features. Overall it is apparent that there is a large change in microstructure from the bases metal to the other zones. The base metal is characterised, as expected, by large grains, absence of sub-grain boundaries, an evidence of precipitation inside the grains (because of the artificial ageing T6 cycle [141]). The AFM method is not ideally suited to the larger scale of 50μm where there may be voids and other surface defects that may introduce noise, hence caution is required in the interpretation of some the features at the larger scale. In the transition regions (Zones 2–4) there is evidence of similar roughness and size of features as quantified by the surface profile, but the 3D images show that the morphology is very different across these zones. In the stirred region (Zone 5) the roughness increases again. This represents the density of grain boundaries, which is confirmed by the 3D image which shows more homogeneity and fineness in morphology.

The question might be asked whether the observations might be explained by corrosion (from the etching process) rather than shear. This suggests that the effects are not due to corrosion, for the following reasons. First, the same etchants have previously been shown not to result in corrosion artefacts [140, 141]. Second, there is no evidence of pitting or a local depletion of the matrix phase around the precipitate particles, as might be expected from an aggressive etching. Neither do the local line scan profiles show any evidence of pitting or protrusions.

We propose the following interpretation of the process. The mechanical stirring induces a shearing distortion to the lattice of the plasticised mass. To mitigate this during DRX, the microshrinkage positions evolve to be at the location of the accumulated shear bands. The etching procedure leads to more clarity of these shearing microbands in 3D surface tomography scanned by the AFM (Zones 3 and 4 in Figure 14.3c, apparent at nanoscale). It is evident that the etchant has a very different effect on the material in Zone 3, compared to the other zones. The grain boundaries are pronounced, creating a three-dimensional interconnected set of ridges. The inside of the grain is locally dissolved to a greater extent. It proposed

that this arises from the selective etching features of the reagent solution, attributing to the sensitivity of the shear bands to this etchant. Specific sample preparation was used to avoid over-etching and production of corrosion artefacts.

The grain boundaries and morphologies were revealed because of different reactions of each region of the weld texture to the applied reagent. In this regards, the surface roughness measurements indicate the morphology alteration in different regions after etching [136, 140]. All samples were treated with the same polishing and etching procedure.

The surface morphology in the flow arm region (Zone 4) is in agreement with the theory of the stirring action in the FSW process. It suggests that the periodicity of the flow arms (visible in Figure 14.2b) is caused by the rotary motion of the pin and its flats create. This causes the deposition, in the wake of the tool at the advancing side, of the parallel arm shapes [136-138]. The microstructure of Zone 4 (in Figure 14.3) was selected from one of these arms, and shows that the sub-grain boundaries (dark lines in Figure 14.3) are arranged parallel to the flow arm.

The actual roughness in the mid-SZ (Zone 5) was reduced, as the grain size has decreased compared to other regions of the weld. The micrograph shows larger variations, which is because of the higher magnification (smaller scale). The graph of surface roughness confirms that the distance of peaks and valleys as a measure of the surface roughness, is minimized for Zone 5.

14.3.1 Observation of precipitate in mid-SZ

The most plausible area for location of the precipitate particles is mid-SZ, which experiences a full DRX compared to other regions of the weld. However, from an imaging perspective there is a risk that the etching might eject the fine precipitates from their position within the microstructure. To minimise this risk, an unetched micropolished sample was used for the precipitation analysis. Furthermore, a variety of channelling modes were used for the AFM analysis.

In addition to the usual height channel mapping, frequency channel was used to provide a better resolution for the free edges of the precipitate in contrast with the matrix. Also to indicate the localized torsional stress field at the interface the precipitate-matrix phase, dissipation channel was used. These different channeling modes provide a more comprehensive observation.

The micrographs (Figures 14.4a–d) and corresponding line profiles (Figure 14.4e) show an ultrafine particle of size less than 100 nm, a platelet morphology, and an embedment in the matrix. The height channel (Figure 14.4a) identifies a platelet shape particle without surface etching. The frequency channel (Figure 14.4b) provides better sharpness of contrast, and shows a localized cleaved pattern at the boundary of the precipitate-matrix. The dissipation channel (Figure 14.4c) also highlights the dissipated energy from the tapping tip of the AFM probe onto the sample surface. The red contrast, constructed at the interface of the precipitate-

matrix phase, shows higher density of dissipated surface energy, attributed to the mechanical torsion at the border of the particle [218]. Frequency channel and dissipation channel both show that the border of the particle and the matrix possesses a distortion which is due to the embedment of the precipitate into the matrix [219, 220]. Therefore, it is not an external particle or sediment at the surface.

In general, precipitation requires diffusion of alloying elements, and is function of time and temperature. DRX occurs within seconds during FSW, not enough time for diffusion to occur to produce precipitates and therefore the precipitating phase particles are expected to be ultrafine size [141, 219], which indeed is demonstrated here (<100nm). The mechanism of precipitation here in FSW process is attributed to the severe shearing in the SZ and the heat. In the T6 artificially ageing process the cycle time is longer, the temperature is higher, and the process is closely controlled, resulting in control over the precipitates [141, 219-221].

The observed platelet morphology has a maximum surface-to-volume, compared to other precipitate morphologies such as spherical or needle shaped. The platelet precipitation can occur in a relatively fast cooling rate at lower reaction temperatures [33, 222]. Hence the observation of such a precipitate is consistent with the FSW condition. The density of precipitates was relatively low in the observed samples, less than might be expected from say fusion welding. This and the shape observed, suggest that the low temperature conditions in FSW result in a reduced precipitation.

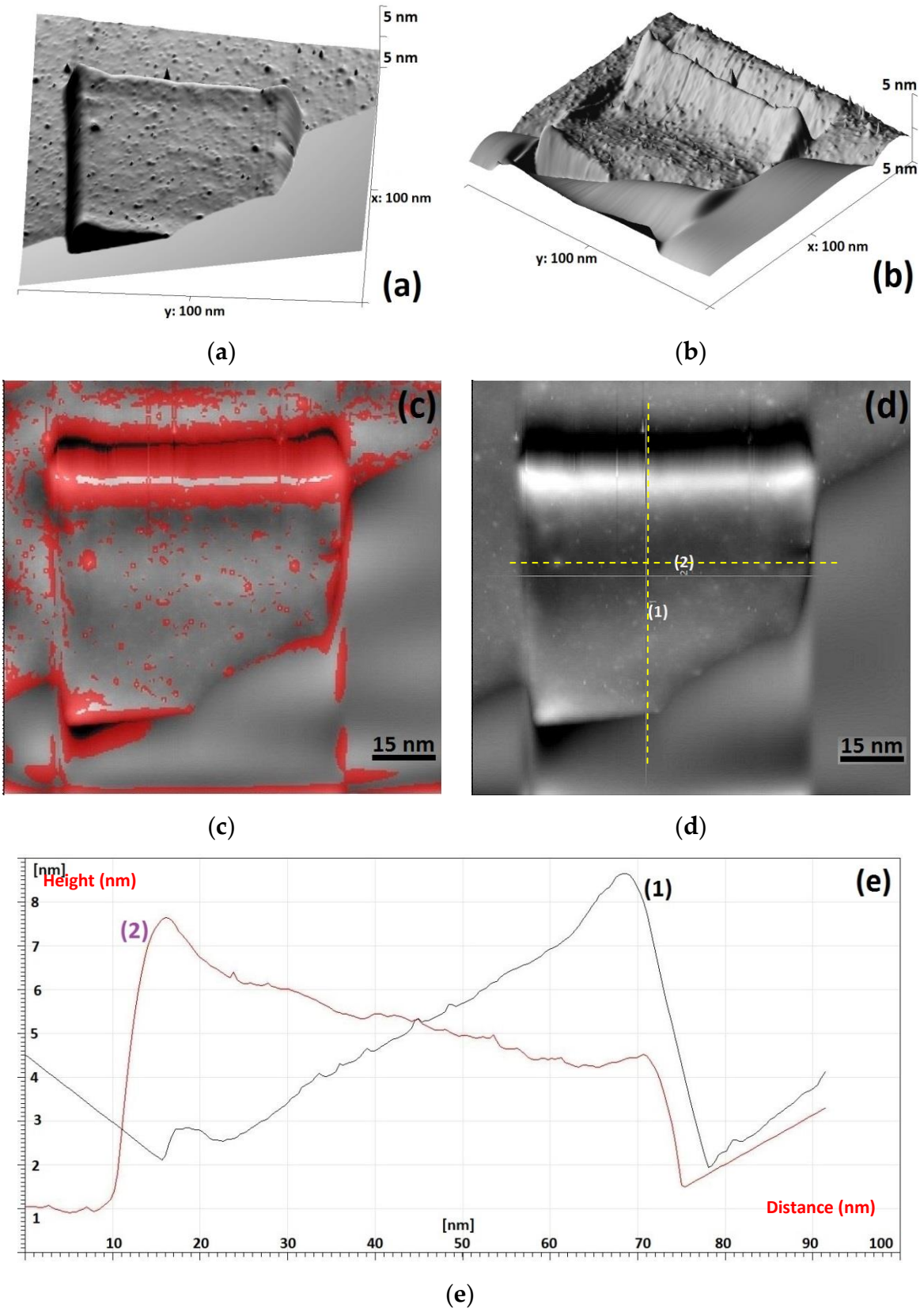

Figure 14.4. Selected surface area demonstrating the platelet shape precipitate, scanned by AFM using different channel modes; (**a**) height channel exposure, (**b**) frequency channel, (**c**) dissipation channel, (**d**) phase contrast micrograph, (**e**) line profiles corresponding to the surface roughness of the particle.

14.3.2 Dislocations

Dislocations are the out-of-position of atoms in the crystal structure of grains. The dislocation patterns within different region of the weld are shown in Figure 14.5. At this high magnification the misarrangement of the crystal layers becomes apparent. The edge dislocations are evident as the crystalline defect in the structure of the aluminium. In general, in polycrystalline structures under shearing (with an intrinsic misorientational angle >0.99) it is expected to observe dislocations as a structural defect through the lattice [65, 144].

During plastic deformation and the subsequent DRX, dislocations are formed in specific preferential orientations within the crystal lattice. Furthermore, during the recooling, interaction and annihilation of dislocation results in rearrangement of dislocation arrays with different density in different regions. This can be related to the amount of the stored strain releasing during the recovery process, also the absorbed heat which is different for each region based on the distance from the frictional stirring action. The dislocations originate from the applied stress during stirring causing shear between the crystal layers. After stirring the DRX process involves movement of the dislocations. They may aggregate to form Low Angle Grain Boundaries (LAGBs) within the grains, or transfer to the grain boundaries and contribute to formation of new High Angle Grain Boundaries (HAGBs) and motion of grain boundaries [141, 144].

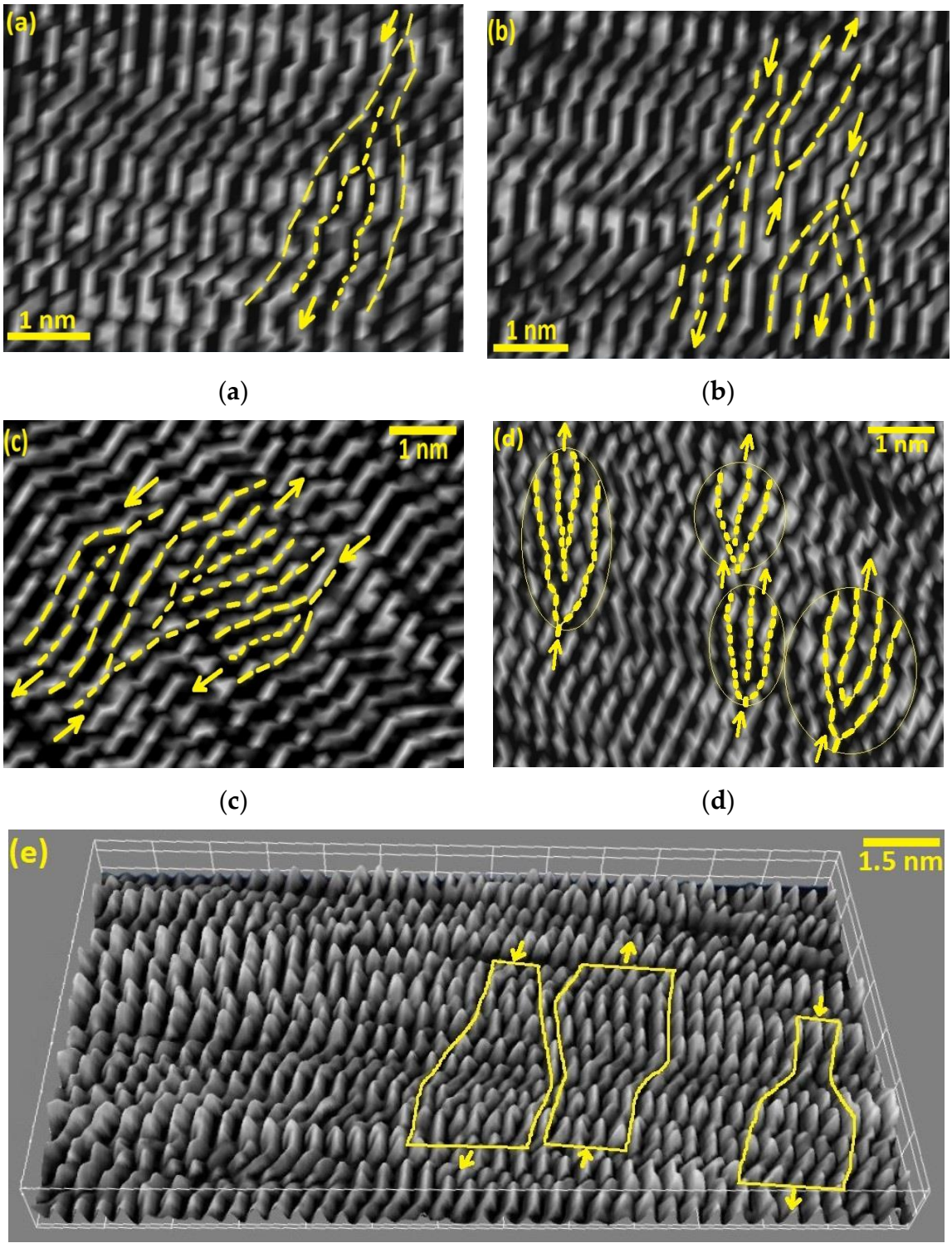

Figure 14.5. Stripped patterns of the crystalline lattice of AA6082-T6 BFSW weld; (**a**–**e**) The landmarks indicates some of edge dislocations between the lattice planes (crystal layers), in different regions of the weld; (**a**) BM, (**b**) HAZ, (**c**) TMAZ, (**d**) Hourglass-border of SZ. (**e**) AFM map with very high resolution crystal structure with corresponding edge Dislocations (mid-SZ).

14.4. Chapter Discussion

This chapter describes joining of an aluminium alloy by bobbin FSW, and investigation of weld microstructural features using the Scanning Electron Microscopy (SEM) and AFM.

A key finding is the identification of three-dimensional micro-flow features with specific changes in grain size and morphology attributed to the stirring action. This has not previously been shown for friction stir welding, and the literature is silent on this aspect.

The AFM technique provides a visualization of features within grains, and by inference provides a record of the flow patterns occurring in a solid-state mechanical stirring by the bobbin-tool FSW [136, 141, 144]. The surface topographic features for different regions of the weld can also be measured quantitatively to compare the surface roughness corresponding to the shearing regime. A tentative flow-induced thermomechanical mechanism has been suggested for the SZ and the transition region, where the stirring-induced shearing stress affects the weld structure through the thermomechanical behaviour of the BFSW process.

A metallurgical transformation during the DRX process is identified by its effects on changing of grain size to ultrafine. This is evident as grain refinement by increasing density of grain boundaries (see Zone 5, Figure 14.3). Precipitation is also expected from DRX, but was not readily observed in etched surfaces. Dislocation interaction in the sub-grain scale was visible in the transition regions (Zones 3 and 4, Figure 14.3), as were HAGBs (Zone 3, Figure 14.3) and LAGBs (Zone 4, Figure 14.3). Hence the transformations preceding and caused by DRX have been observed.

14.4.1. Welding Parameters

The formation of the weld texture is because of the mechanical stirring action at the proximity of the rotating tool [13]. The welding process causes fragmentation, severe plasticizing, shearing deformation and frictional heating. Therefore, the welding process parameters (tool geometry and welding speeds) can have a major effect on the final microscopic characteristics of the weld texture [25, 26]. The complexity of the tool geometry increases the frictional heating generated at the position of the tool-material, inducing more plastic flow through the softened mass [20].

Similarly, the welding speeds (ω, V) also can induce more fragmentation and subsequent plasticising, resulting in more strain and hence DRX during the stirring action [27].

All these can intensify the shearing flow during the mass transportation, and potentially elevate the generated heat useable for the DRX mechanism. Therefore, this might be worthwhile to investigate the role of optimised welding parameters in the microscopic evolution of the weld texture characteristics.

14.4.2. Limitations of this Work and Implications for Future Research

Our 3D visualization analysis of the microscopic features was limited to the ultrafine microstructural details at the scale of the grain structure of the weld. However, there are some macro-size defects such as tunnel void or cracks which may also have shearing-flow effects. In this regard, because of the limitation of the AFM analysis to ultrafine magnification, the macroscopic defects are better analysed by other microscopic measurements, such as optical microscopy or electron microscopy. Furthermore, fractography analysis could evaluate the crack propagation and failure mechanisms. The formation of these macro-size tunnel void and the micro-cracks adversely affects the strength of the final weld, therefore is unacceptable to industry users.

Another possible future research opportunity could be to use AFM to quantify the grain characteristics for the different weld regions. It may be possible to characterise the surface features, and quantify sub-grain boundaries, and mathematical link these metrics to the weld process. Complementary methods such as electron microscopy (e.g., Electron Backscatter Diffraction (EBSD) and Transmission Electron Microscopy (TEM)) might be considered.

14.5. Chapter Conclusions

This chapter determined a physical measurement for describing micro-flow features within the BFSW weld breadth using a three-dimensional surface topography by AFM. It was revealed that the mechanical stirring was associated with complex flow regimes through the stirring zone, also induced shear features at the microscale. These add stored strain to the texture which appears to lead to physical alteration in recrystallization of the weld texture during the post-welding cooling. Therefore, different regions of the BSFW (SZ, TMAZ, HAZ) are identified in different microscopic patterns corresponding to thermomechanical behaviour of the weld.

A key outcome is the use of AFM to better understand the grain structure of the AA6082-T6 material under solid-state friction-stir welding. This is an important industrial material but its thermomechanical behaviour has been poor in this type of welding. The results of this chapter elucidate the grain boundaries and precipitates, and thereby show the results of the thermomechanical processes. AFM has been shown to be a useful tool to better understand the gain boundary engineering, dislocation behaviour, and precipitation of this material.

CHAPTER 15: Discussion – Development of a model of internal material flow

Chapter Summary: Bobbin friction stir welding with a double-sided tool configuration produces a symmetrical solid-state joint. However, control of the process parameters is difficult for achieving defect-free welds. The internal flow features of the AA6082-T6 butt-joints in bobbin friction stir welding were evaluated using a set of developed reagents and optical microscopy. The key findings are that the dark curved patterns (conventionally called 'flow-arms'), are actually oxidation layers at the advancing side, and at the retreating side are elongated grains with a high-density of accumulation of sub-grain boundaries due to dynamic recrystallization. A model of discontinuous flow within the weld is proposed, based on the microscopic observations. It is inferred that the internal flow is characterized by packets of material ('flow patches') being transported around the pin. At the retreating side they experience high localized shearing at their mutual boundaries, as evidenced in high density of sub-grain boundaries. Flow patches at the advancing side are stacked on each other and exposed to oxidization.

This chapter is a derivative of the following publication:

Tamadon, A.; Pons, D.J.; Clucas, D.; Sued, K. Internal Material Flow Layers in AA6082-T6 Butt-Joints during Bobbin Friction Stir Welding. Metals 2019, 9, 1059.

DOI: https://doi.org/10.3390/met9101059.

15.1. Introduction

Bobbin friction stir welding (BFSW) is an innovative variant of the friction stir welding (FSW) process [99], whereby a double-sided rotating tool physically ploughs along the interface of two butted plates [4] without needing the backing anvil and the axial force during the process [66]. The dynamic interaction between the workpiece and the non-consuming tool creates a severe friction condition at the contact interface [67]. Consequently, significant heat is generated due friction which can locally soften the workpiece material sufficient for plastic yielding and stirring at the bonding track [2]. The stirring action arises from the rotation speed (ω) and advance speed (V). While the tool advances along the weld line (Figure 15.1), the mutual interaction of the speeds (ω, V) transports the softened mass from leading edge of the rotating tool to be deposited at the rear or trailing edge of the tool [68].

The side of the weld-seam where the direction of tool rotation is the same as the tool progress is called the advancing side (AS) and the opposite side of the weld-seam is the retreating side (RS) [69]. The region located between the AS and RS borders, named the stirring zone (SZ) [70], experiences a thermomechanical plasticizing and then deposition and consolidation in the weld locus [71]. The adjacent region outside the SZ is the Thermo-Mechanical Affected Zone (TMAZ). The microstructure of this region is formed by the stress-strain fields and heating flux which are induced by the friction and heat generation effects of the stirring action [72]. The next region between the TMAZ and the Base Metal (BM) is the Heat Affected Zone (HAZ). This region is exposed to thermal fields of the stirring process which alter the microstructure [73].

Comparing with the Conventional-FSW (CFSW), in the BFSW the fully-penetrated pin requires more control during the process, as an inconsistency between the process variables can cause more severe failures. The double opposing shoulders system provide a greater contact surface for the frictional heat generation from both sides of the workpiece [71]. The process also replaces the CFSW backing or anvil support plate with the BFSW rotating shoulder at the lower side of the workpiece [74, 75]. The CFSW case requires a downward axial load [76] on the tooling, whereas the BFSW requires a compression ratio [77] (the variance between the inner edge-to-inner edge biting gap of the shoulders and the actual thickness of the plate). These differences cause differences in the flow regimes of the two processes [64, 78].

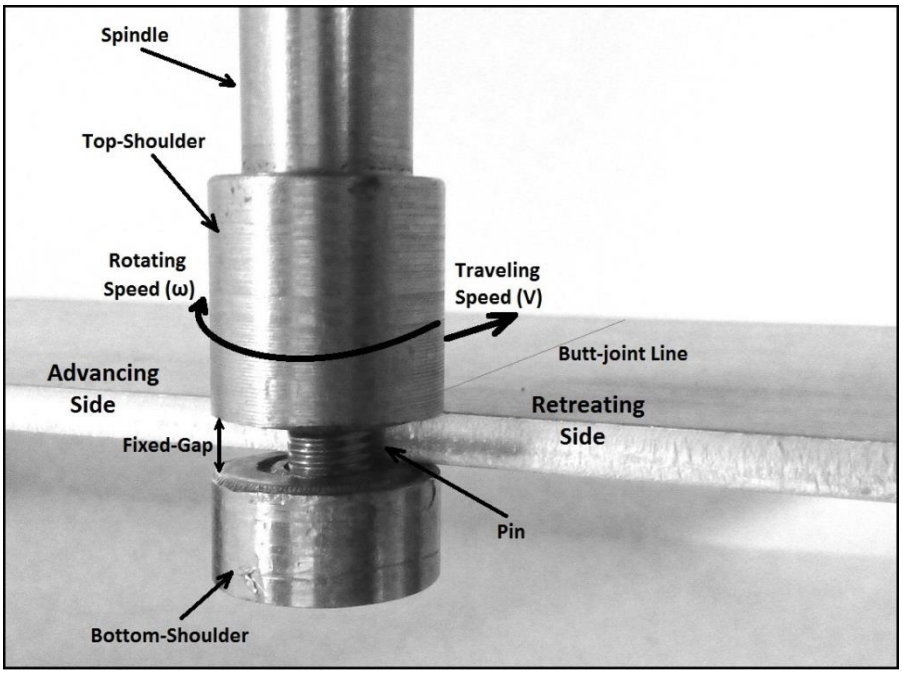

Figure 15.1. Schematic of the BFSW process for a butt-joint position.

As the temperature in FSW processes is lower than fusion welding, it is categorized as a metal forming process [46]. The internal flow regimes related to the plasticized mass play the main role in the welding mechanism rather than metallurgical transformations of melt-and-solidification. In general, the FSW technique is proposed for materials with a high capability of the dynamic plastic deformation. Aluminium that responds well to large plastic deformation is a good candidate material for FSW. In particular, marine grade AA6082-T6 aluminium alloy with good machinability properties would be attractive to be processed by the BFSW, but shows poor weldability in the conventional fusion welding. One of the obstacles to a better understanding of the actual flow regimes is the need to visualise the details of the flow features for the cross section of the weld [70, 79]. This is challenging for AA6082-T6 alloy as the weld region responds poorly to conventional etchant reagents [80]. This problem arises because of the low contrast between grains and grain boundaries for the AA6082-T6 microstructure where the precipitate particles are uniformly dispersed within a supersaturated solid solution treated by artificially ageing per the T6 cycle. Also, severe plastic deformation and grain fragmentation during the BFSW process reduce grain size to ultrafine.

While there is an extensive attention into the microstructural characteristics of the FSW welds [200], the flow mechanism also needs to be identified within the weld structure [11, 26, 27]. In this regards, there are some attempts to elucidate the heat flow [38] and material flow [37] mechanisms in BFSW, as it is expected to be different than conventional-FSW [36].

The aim of this chapter is to identify the causality between flow regimes and physical defects. The approach is to visualise plastic deformation features of AA6082-T6 BFSW welds with new etchants [80], using optical metallography. These reagents show the details and complexity of the plastic flow patterns within the stirring zone, even when there is an element of grain refinement due to the thermomechanical plastic deformation. A benefit of this approach is achieving a detailed microstructural analysis with conventional etching methods and optical metallography, rather than the more costly processes of electropolishing, or electron metallography (e.g. SEM, EBSD, and TEM).

15.2. Materials and Methods

For the weld trials, rolled plates of AA6082-T6 (Al–Si–Mg–Mn family) were used as the workpiece. The chemical composition of the AA6082-T6 aluminium alloy as the base metal is reported in Table 15.1.

Table 15.1. Element composition of the AA6082-T6 aluminium alloy (wt %) [199].

AA6082-T6 Aluminium Alloy	
Chemical Element	% Present
Silicon (Si)	(0.70–1.30)
Magnesium (Mg)	(0.60–1.20)
Manganese (Mn)	(0.40–1.00)
Iron (Fe)	(0.0–0.50)
Chromium (Cr)	(0.0–0.25)
Zinc (Zn)	(0.0–0.20)
Titanium (Ti)	(0.0–0.10)
Copper (Cu)	(0.0–0.10)
Other (Each)	(0.0–0.05)
Other (total)	(0.0–0.15)
Aluminium (Al)	Balance

BFSW tests were conducted using a geometrically full-featured (including threads, flats and scrolls) bobbin tool manufactured from H13 tool steel with hardness of 560 HV. The butt-joint weldments comprised two pieces of similar plates with dimensions of 250 mm (length) × 75 mm (width) × 6 mm (thickness). The welding trials involved two sets of operation speeds; spindle rotational speed (ω) and weld travel rate (V).

Since the aim of the research was to identify the flow features of the BFSW weld in a defect-free structure compared with the presence of defects, a variety of welding speeds (ω, V) were used to produce different weldments. By running some trials in ω (350–650 rpm) and V (300–400 mm/min), two set of welding speeds (ω, V) were identified to obtain defect-free and defect-included welds. In the first set of experiments, the chosen speeds were (ω=400 rpm) and (V=350 mm/min). As the design features of the tool were the same, (ω=650 rpm) and (V=400 mm/min) were used for the second set of experiments, and other welding parameters were kept constant. The first set of speeds (ω=400 rpm, V=350 mm/min) was able to create a bonded weld; however the sample contained some macro-size defects, e.g. tunnel void. The second set of speeds (ω=650 rpm, V=400 mm/min) achieved a defect-free weld with no crack or void on surface or between the aluminium plates, neither any material loss through the weld-seam.

The BFSW experiments were performed on a 3-axis CNC machining centre (2000 Richmond VMC Model, 600 Group brand, Sydney, Australia) with a Fanuc control unit and 14-horsepower spindle motor capacity. There were no preheating or post-weld processes before or after the welding process. The direction of tool rotation was clockwise relative to the advancing direction of the welding (Figure 15.1). Table 15.2

gives more details of the bobbin-tool and the welding operation. After welding the quality of joints were first checked by visual examination, and then cross sectioned by an electro-discharge machine wire cut through the middle of the weld seam (perpendicular to the welding direction). The resulting surfaces were subjected to metallographic measurements.

Table 15.2. Parameters of the BFSW process for the AA6082-T6 weld trials.

Work Temp (°C)	$D_{Shoulder}$ (mm)	D_{Pin} (mm)	$D_{Shoulder}/D_{Pin}$	Plate Thickness (mm)	Compression Ratio	Feed ω (rpm)	Speed V (mm/min)	Thread Pitch (mm)	Number of Threads
18 °C	21	7	3	6	3.75%	400 650	350 400	1.2	5

For metallographic analysis, firstly the specimens were prepared using standard mechanical polishing with different grades of SiC sand papers (600-grit, 800-grit and 1200-grit). To achieve a mirror surface, the micro-polishing step was conducted on a micro-cloth pad with a 3μm diamond paste, and finally a 0.05μm colloidal silica solution. The etching process was designed to remove the oxide film, and then delineate the flow lines. The polished specimens were first pre-etched for 3 min in a solution of (5 g NaOH + 1 g NaCl + 80 mL H_2O) at 70 °C. The developer mixtures are shown in Table 15.3, which describes the composition and other conditions of the chemical solutions (time and temperature). After completion of the etching process, the samples were rinsed in ethanol, and then dried with warm air. The flow patterns of the BFSW weld region were studied using stereoscopic and light optical microscopes. In some cases, where the microscopic features needed to be clarified in more detail, the cross-section sample was re-polished and re-etched with other reagents. For some metallurgical validating, the etched samples were also subjected to elemental mapping using the scanning electron microscope (SEM) (JEOL 6100, JEOL Inc., Peabody, MA, USA) equipped with energy-dispersive X-ray spectrometer (EDS) detector (Oxford Instruments plc, Abingdon, UK).

Table 15.3. Different reagent compositions with separate sequences of processing.

Name of Etchant	Etchant Composition
A	2.5 mL HF + 2.5 mL HCl + 95 mL H_2O (30 s, 50 °C), then: 15 mL H_3PO_4 + 85 mL H_2O (30 s, 70 °C)
B	0.5 g $(NH_4)_2MoO_4$ + 3.0 g NH_4Cl + 1 mL HF + 18 mL HNO_3 + 80 mL H_2O (90 s, 70 °C)
C	10 g CrO_3 + 2 g Na_2SO_4 + 10 mL HNO_3 + 10 mL CH_3COOH + 1 mL HF + 80 mL H_2O (60 s, 70 °C)

15.3. Results

15.3.1. Macrostructure of the cross-section

Figure 15.2 a,b reveal the macrostructural examinations of the AA6082-T6 BFSW joints (etched by Reagent A) for two different sets of welding speeds (longitudinal or rotating), refer to table 15.1. Both joints exhibit a distinctive zone in the middle, processed by thermo-mechanical plastic deformation induced by the bobbin-shaped tool. This hourglass-shaped region –different to the basin-shaped SZ in CFSW [75]– is discernible in the middle of the weld from the base metal (BM) by the symmetrically curved borders at the both advancing side (AS) and retreating side (RS).

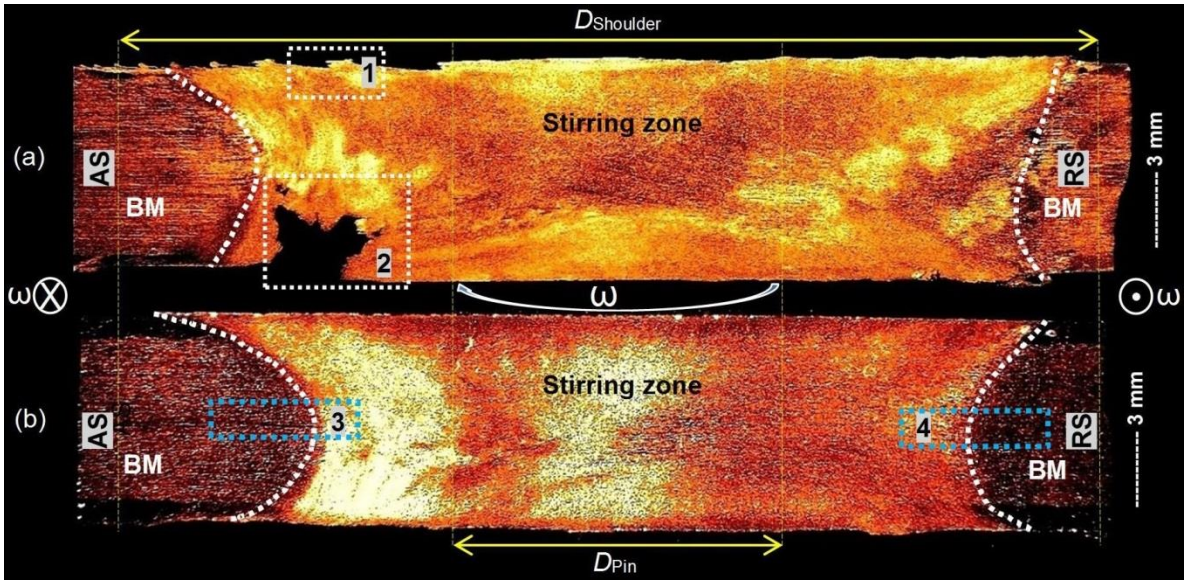

Figure 15.2. Macrostructure of the cross-section of the BFSW joint for two different welding speeds (etched by reagent A), (a) (w=400 rpm, 350 mm/min), and (b) (w=650 rpm, 400 mm/min). Arrows show proposed internal flows. Dashed white lines show the SZ borders. (1) weld crown, (2) tunnel void, (3) AS border, and (3) RS border.

It is observed that the SZ, at the middle of the weld, is larger than the diameter of the pin. This is attributed to (a) the pin recruiting a wider volume of matter through frictional contact with the substrate, and (b) recruitment of the substrate material via frictional heating from the shoulders. Both the pin and shoulders create frictional heat.

Basically, in BFSW the fully contained pin has eliminated the incomplete root penetration of CFSW, but in Figure 15.2a, a macro-size tunnel void has emerged at the bottom surface towards the AS, while Figure 15.2b shows a defect-free weld with an integrated structure. The origins of tunnel void emergence are not fully understood in the literature; however, it is clear that the formation of this macro-size

defect in a solid state process does not seem to be more definite to have a metallurgical explanation. Existing theory attributes the tunnel voids to incomplete backfilling [70, 183], that arises from incompatible welding speed parameters (ω, V), or dynamic interaction between the tool and workpiece [143, 183]. It appears that there is insufficient material. As the metallography samples were cross sectioned from the middle of the weldment, the amount of the material loss can be considered similar to the size of the sprayed tail defect at the entry zone. The continuous tunnel void shows that the plates were not fully butted.

From observation of the macrostructure, it infers the existence of the internal flow directions. This can affect the weld quality, when the failure of the flow regimes leads to the emerging of the defects (e.g. tunnel voids or hair-line micro-cracks). To provide a better explanation for the origins of the defects based on a flow-based observation, the metallographic measurements needed to be conducted in more depth with a focus on microstructural and flow feature integrity.

15.3.2. Microstructure evolution

The transverse section of a BFSW weld-seam should reveal three typical zones; HAZ, TMAZ and SZ, distinguished from the BM towards the centre of the weld. However, macro-sections of the BFSW welds (Figure 15.2) only indicated a primary macrostructural region for the stir zone (SZ) at the centre of the weld. The other transitional zones could not be identified using macro etching. To make the TMAZ and HAZ regions visible, after re-polishing, the etchant B was used and higher magnification for the micrographs was applied.

Figure 15.3 shows the photomontage of the micrographs taken from the transverse cross-section of the BFSW weld (selected from the sample of Figure 15.1b) close to AS and the RS hourglass boundaries, etched by Reagent B. This reveals the deformation-induced grain refinement at the transition region (HAZ/TMAZ) on either side of the SZ.

The latter region exhibits a grain orientation transformation. The transformation is represented in grain size and morphology. The transition region has rotated-elongated grains morphology detectable with a distortion in grains compared with the parent material. Compared to the large columnar grain structure of the BM, the microstructure of the SZ reveals a homogenous distribution of the fine equiaxed grains. This abrupt change in structure separates the TMAZ/HAZ region from the plastically deformed finer-grained SZ, and the large directional grains observed in the BM structure. This is attributed to dynamic recrystallization (DRX), which in turn arises from the thermomechanical (heating & strain) mechanisms during stirring.

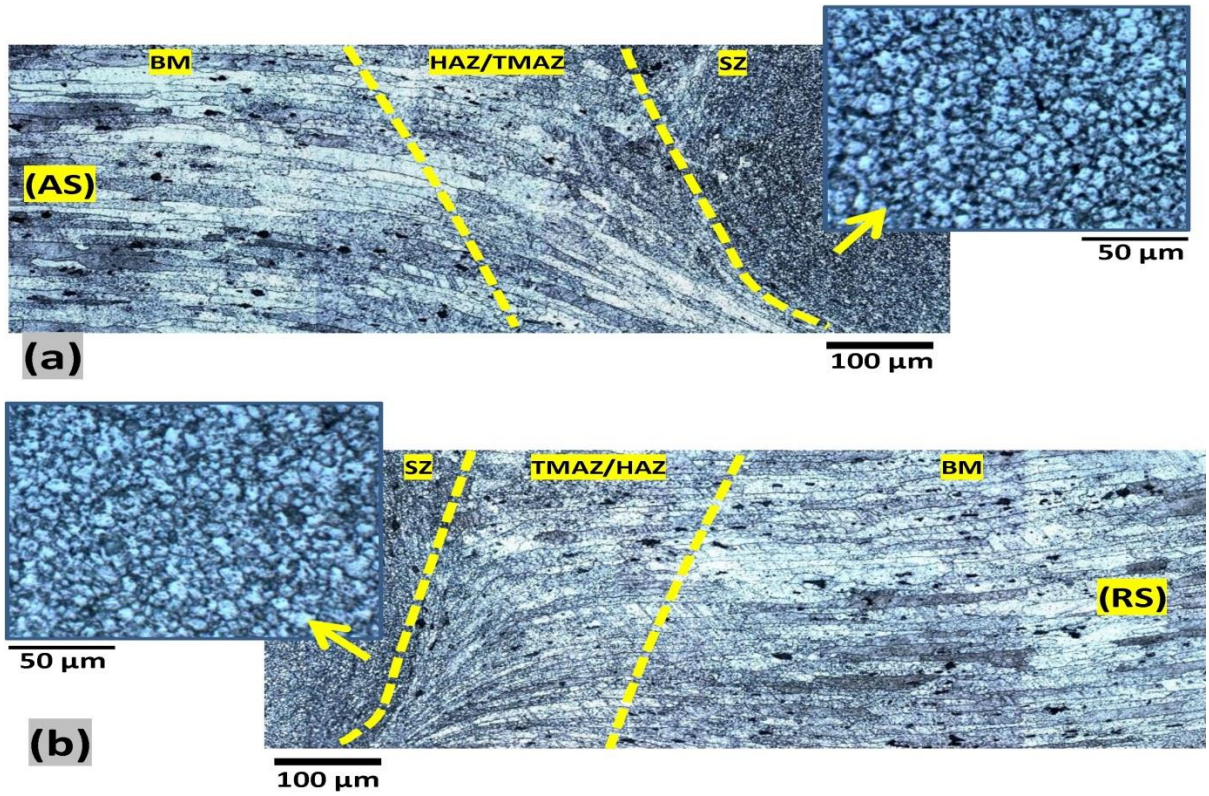

Figure 15.3. Photomontage of the microscopic features for the BFSW weld structure, near the AS and RS borders (etched by Reagent B). (a) transition region in AS border (regions 3 in Figure 15.2b), (b) transition region in RS border (regions 4 in Figure 15.2b).

15.3.3. Material flow features in the weld cross-section

The magnified micrographs in Figure 15.3 from the interface of the SZ and the external region illustrate a metallurgical bonding between the processed weld region and the parent metal. To distinguish the flow patterns from the grains structure, etchant reagent C was used, giving the results in Figure 15.4. For this micro-flow evaluation, the sample of Figure 15.2a was chosen to reveal more details because of the existence of defects (e.g. tunnel void). As is shown in Figures 15.5 a,b, the presence of the flow arms (banded patterns) is evident in the SZ at the hourglass borders for both sides of the weld. The flow arms of the AS are more compacted to each other.

The flow arms become dispersed when reaching the tunnel void (Figure 15.4a). In this case, the flow arms near the bottom surface of the weld follow a finger pattern, stretched from the hourglass boundary (at the circumferential edge of the tunnel void) towards the centre of the weld. It is more evident that the compaction effect from the top shoulder was higher than the bottom shoulder, while their diameters and contact surface conditions are the same. The branching pattern can also be observed when the plastic flow behaviour -between the bottom and top surfaces- is affected by the geometrical features of the tool (threads, flats, scrolls) during the

stirring action. This attributes to an unsteady internal flow, in turn caused by the inability of the flow to completely fill the void left by the tool moving forward. Behind the tool, the material moves from the RS towards the AS, and is deposited at the AS. If there are any insufficiencies in the flow, due perhaps to previous loss of material at entry, or early cooling of the material, then the forward movement of the tool creates a gap that is difficult for the flow to fill. This attributes the striation layers themselves to batches of material cut by the flats out of the base material.

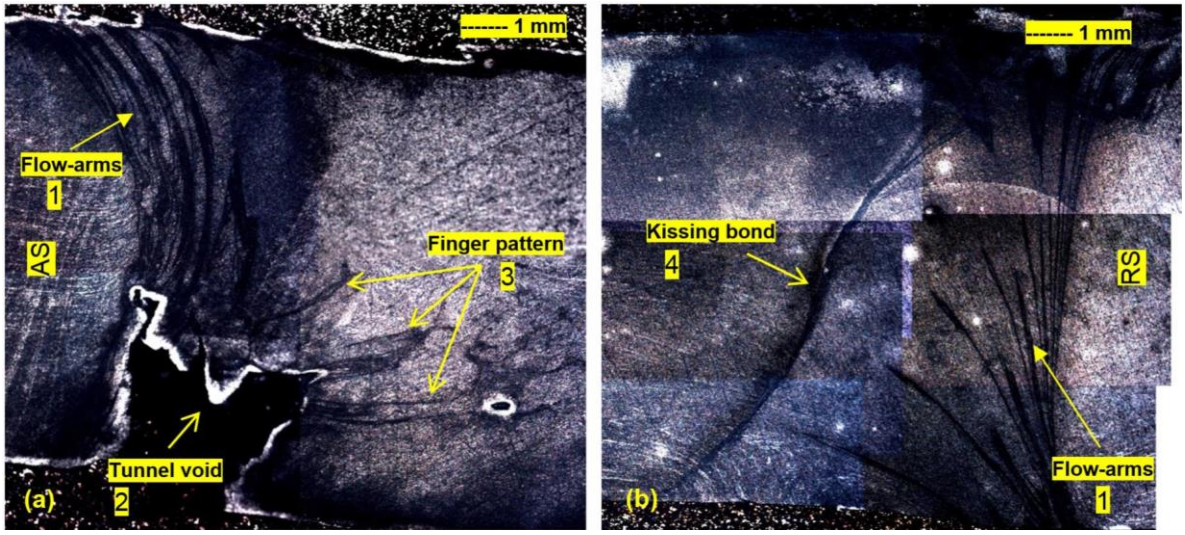

Figure 15.4. Photomontage microfeatures of the BFSW weld at the transverse cross-section (revealed by Reagent C). (a) AS border, (b) RS border. (1) flow-arms, (2) tunnel void, (3) finger patterns, and (4) kissing bond.

The macro-section of the bobbin weld in Figure 15.4b reveals another distinct flow-based problem. The appearance of this linear discontinuity is similar to the kissing bond defect in CFSW; solid-state bonding with poor or no metallurgical adhesion. One of the major causes of kissing bond defects in friction stir welds is insufficient engagement of the tool pin into the plasticized material. It interprets the current findings as due to a recoil/backlash between the pin and the material during the stirring, (such as might be caused by vibration - which was prevalent), causing incomplete joining. It should be noted the kissing bond defect is more prominent in samples produced at lower rotational speeds which can be attributed to the inconsistency in strain distribution due to occurred flow-based condition. Furthermore, the position of the kissing bond defect is located exactly at the position of change in the flow direction from leading edge to the trailing edge of the pin.

It is very difficult to detect or accurately characterize the nature of this defect by the typical analysis methods, e.g. metallography or Nondestructive testing (NDT). However, in Figure 15.4, it was tried to delineate the exact location of the discontinuity line in the microstructure by Reagent C. As it is observable in Figure

15.4b, a continuous and uniform discontinuity flow was vertically delineated between the top surface and bottom surface through the SZ. Furthermore, this microscopic view confirms that the nature of the defect line is not a grain structure.

We propose that it is a kind of oxidation formed during the dynamic recrystallization of the deformed grains. The proposed explanation of is as follows: As the pin possesses a symmetrical thread-flats feature acting through the stirring zone, the rotating angle between the flat surface and the thread surface creates an empty space to allow air to enter into the weld region. During the stirring, which is at considerable temperature, this air causes a surface oxidation between the layers of stirred mass from the AS. Possibly the adiabatic compression of air pockets adds further heating. The surface oxidization enters into the stirring zone with each revolution of the tool.

The darker colour of the flow arms -visible in hourglass borders and around the tunnel void- is also attributed to this oxidation behaviour. In addition, it should be noted that this oxidized layer was formed in the sample containing the tunnel void defect, but not in defect-free samples (no tunnel void). Therefore, another flow-based relation can be assumed between the emergence of the tunnel void in the AS position, and formation of this oxidation bond at the RS proximity of the stirring zone.

While the pin-driven pressure force in the tunnel void region is insufficient to refill the position by a compensating flow, in the RS the pressure is high, which consequently squeezes the flow to the trailing edge of the tool. By revolution of the tool these oxidation bonding layers can be stretched/transferred also towards the RS. However there is less compaction between the flow-arms at the RS and the refilling action and deposition of the stirred mass at the RS does not lead to a discontinuity at the RS.

We suggest the defects and oxidation layers have flow-based origins. Due to the clockwise rotation of the tool, the plastic flow behaviour differs in AS and RS of the SZ. As in the AS the rotation of the tool was in the direction of welding advance, the plastic deformation of the BM moves forward (and approaches the leading edge). Simultaneously in the opposite direction of the tool (RS), the extrusion nature of the process causes the plasticized flow to become squeezed through the region between the tool and base metal. This forms a channelized flow, which is transferred backwards on the trailing edge of the pin.

Similar to a kissing bond, this oxidation bonding likely causes a negative effect on mechanical properties of FSW joints. Typically this brittle-nature defect can affect the fatigue/tensile strength of the weld as it is a stress raiser and eventually a place for initiating the fracture. It is suggested that in the presence of this oxidation layer, the crack initiation location and the crack growth would be mainly along the boundaries of this defect. This can cause a possibility for a failure mode, different to typical fracture in fusion welds.

One of the outcomes of the instability of the internal flow regimes is the emergence of tunnel void. Figure 15.5 shows the micrographs of the AS region to evaluate the flow behaviour around the tunnel void defect.

The corresponding flow arms around the tunnel void and in proximity of AS border are shown in Figure 15.6 which reveals an intersecting layout from the top surface stretching downwards. The striation diagonal lines around the bay-shaped tunnel geometry (Figure 15.5) show the simultaneous effects of the pin (thread marks) and shoulders on the plastic deformation. The reason for the tunnel defect being at the bottom surface can be attributed to the action of the right-handed threads on the pin, which pump material upwards. There is also a mass deficit caused by loss of material at edge-entry. This mass deficit persists as a continuous void on the bottom surface.

Direction of the scrolls compared with the tool rotation provides a circulation towards the centre - this is deliberate and is intended to provide a dynamic sealing of the weld. In an ideal condition, threads and flats on the pin and scrolls on shoulders improve the uniformity of stirring by driving the lateral motion and pumping of material inwards, this reduces spilling [81]. To provide a uniform stirring condition in the sub-shoulder area, the spiral scrolled features started from the edge of the shoulders and ended at the proximity of the pin location. Upward pumping of material (driven by the thread effect) also increases the curvature of hourglass border close to the top shoulder. This shows the compaction of the plasticized flow in this region is more than by the bottom shoulder region.

This upwards flow potentially creates an additional frictional contact between the upper shoulder and the workpiece. If so, it would be expected that the temperature on the top shoulder to be higher than that of the bottom shoulder. Consideration of grain sizes suggests that this indeed the case [80]. This may further contribute to cooling and stiffening of the flow at the bottom surface.

The aim of Figure 15.7 is to clarify the role of the pin features (threads/flats) and the welding parameters (ω/V ratio; rev/mm) in occurrence of the tunnel void. As is shown in Figures 15.5 and 15.6a collection of striation lines accumulated at the AS border. These can be attributed to the simultaneous interaction of the pin threads/flats and the speed ratio (ω/V) to form the flow lines pattern. As a rough measure, the speed ratio by rev/mm is a unit of magnitude of the distance between the flow lines which can form the size of each nib in a saw-tooth like pattern (Figure 15.5) with the same distance between the flow arms. However, the flow complexities cause an interlaced condition for the flow arms which makes it unreliable as an accurate measurement. The pin threads/flats can cause the localization of deformation through the narrow shear zone to form this saw-tooth like pattern at the internal/inward bay of tunnel defect (Figures 15.5 and 15.7d).

It is clear that the tunnel void geometry emerged due to a large lack of bonding, presumably due to the influence of insufficient pushing of material flow during the

stirring. Hence, the tunnel void formation is attributed to insufficiency in compaction of the material flow at the position of the defect. This indicates that for a good weld the material must have good flow forced by the tool geometry and process variables.

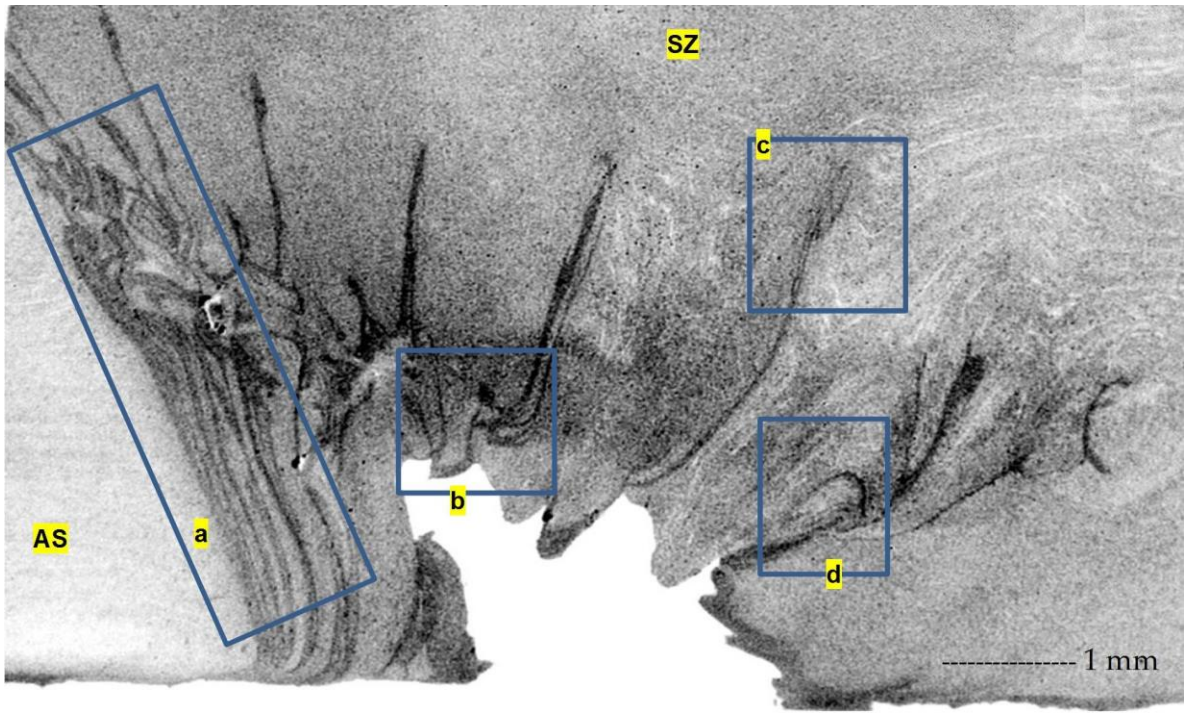

Figure 15.5. Micrograph of the tunnel void and the microflow features around the defect at the circumferential side of the tunnel void (revealed by Reagent C). (a) cascade flow bands, (b) hook lines, (c) finger pattern, (d) swirling lines.

The typical periodic striation lines with the finite width at the border of the AS show the typical forging zone around the pin. These flow lines form a projected area at the circumferential side of the tunnel void where the bonding patterns interlaced abruptly. The interpretation is that, as the bonding lines are separating, the flow velocity gradually decreases which eventually comes to a sharp decrease at the interface of the tunnel defect. This can also change the orientation of the material flow lines, as the interval of the flow lines is maximally separated (compared to the compacted banding pattern in the proximity of the AS border in Figure 15.6).

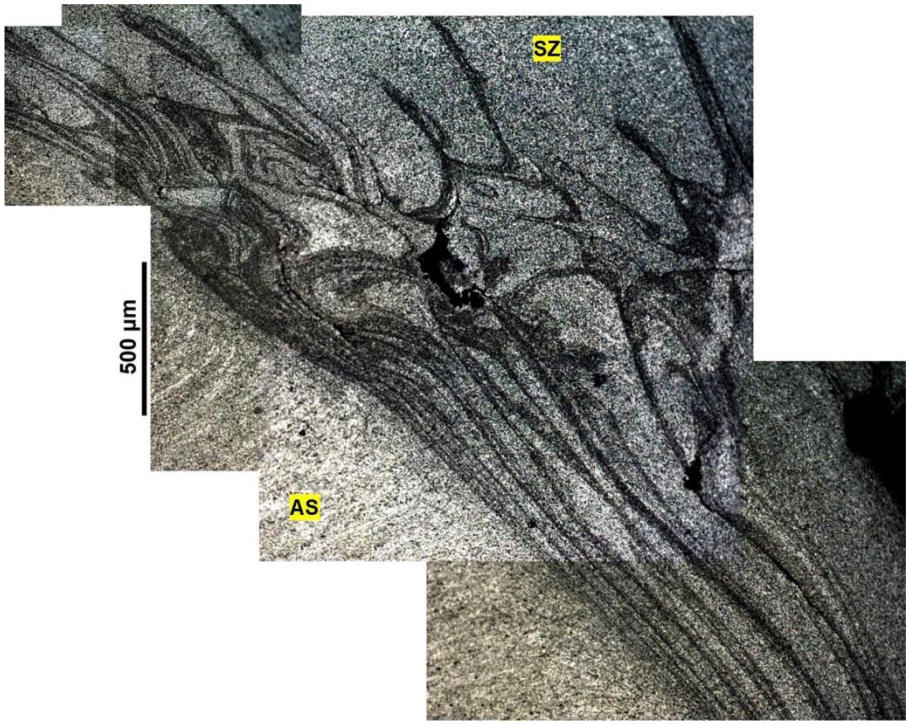

Figure 15.6. Interlaced flow patterns at the AS border of SZ as the following of the cascade microflow (Reagent C).

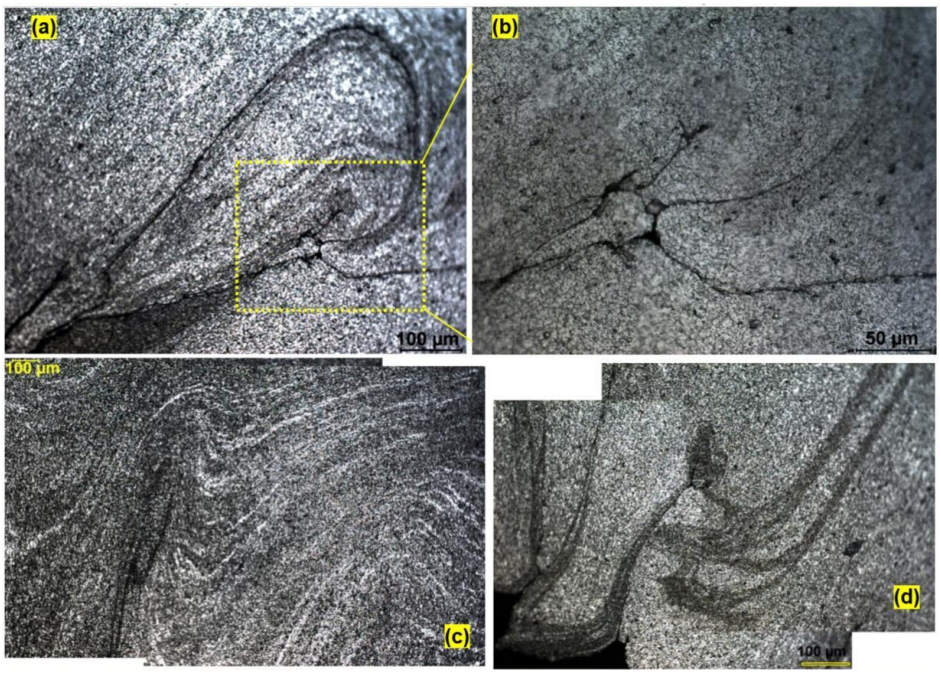

Figure 15.7. Microflows, tangled in different region of the cascade flow region of the SZ (Reagent C). (a) swirling line (region d in Figure 15.5), (b) higher magnification of (a); hair-line micro-crack, (c) magnified finger pattern and the wavy flow lines (region c in Figure 15.5), and (d) hook line flow at the jagged edge of the tunnel void (region b in Figure 15.5).

By comparing the lack of bonding defect with the characteristics of a proper joint geometry, the main reason for formation of the tunnel void appears to be insufficient frictional heat and integrity of material flow, due to the internal force and rotating speed during the process. Poor material flow is attributed to an insufficient heat input, which leads to more bonding defects. Also, the compression ratio is not enough to create a consistent forging/pressure force to extrude the plastic mass and fully/decently compensate/refill the defect position.

The curved striation lines in Figure 15.7a (region d in Figure 15.6) elucidate these flow-based problems where the connection of the flow lines with the main regime has been disrupted. This leads to formation of a tangled flow around the saw-tooth like pattern at the circumferential side of the tunnel void. As shown in Figure 15.7b, this tangled flow is a suitable place for stress concentration within the layers of the mass flow, in which may cause microcracking. The propagation of microcracks could eventually lead to the failure of the weld by coalescence of the macrosize voids. The interlaced flow-lines in Figure 15.7c show a stretched finger pattern (region c in Figure 15.6) which was evident before in Figure 15.5a. This flow defect, similar to the curved flow pattern shown in Figure 15.7a (semi-circular swirling band), can affect the flow integrity as a suitable position for imitation of the micro-crack.

Another flow feature, the enlarged micro-flow shown in Figure 15.7d, reveals the hook line flow patterns positioned at the internal edge of the tunnel void. This feature is interpreted as a lack of material consolidation during stirring, similar to the root flaw in CFSW.

From a metallurgical viewpoint, there is some debate about the nature of the flow-arms as the elongated flow bands with a different colour compared to the matrix. They are not metallographic stains or over-etching. Nor are they some type of intrinsic defects of the base metal formed during the rolling procedure. Rather they are specifically associated with the tunnel defect and visible across multiple different welds. The literature generally terms them flow lines, i.e. attributes them to internal flow of the material. To further understand the nature of the flow-arms, the elemental mapping was applied via EDS to determine the composition of the texture. To observe the exact position of the flow-pattern, the samples after etching were observed by Backscattering Electron (BSE) imaging via SEM microscopy, also supported by the elemental mapping via the energy-dispersive X-ray spectrometer (EDS) detector. The scanning analysis was done for the flow-arms region, also the selected location of the hair-line micro-crack, both shown in Figure 15.8.

In general, the BSE imaging can be used to show the different elements present in the sample. The microscopic analysis of the flow-arms region in Figure 15.8 a,b confirms that the elongated flow-arms are rich in oxygen. This region is delineated as the darker area at the OM etched samples. Additionally, the EDS analysis of the

location of the hair-line micro-crack shows that the edge of the crack is rich in oxygen (Figures 15.8 c,d).

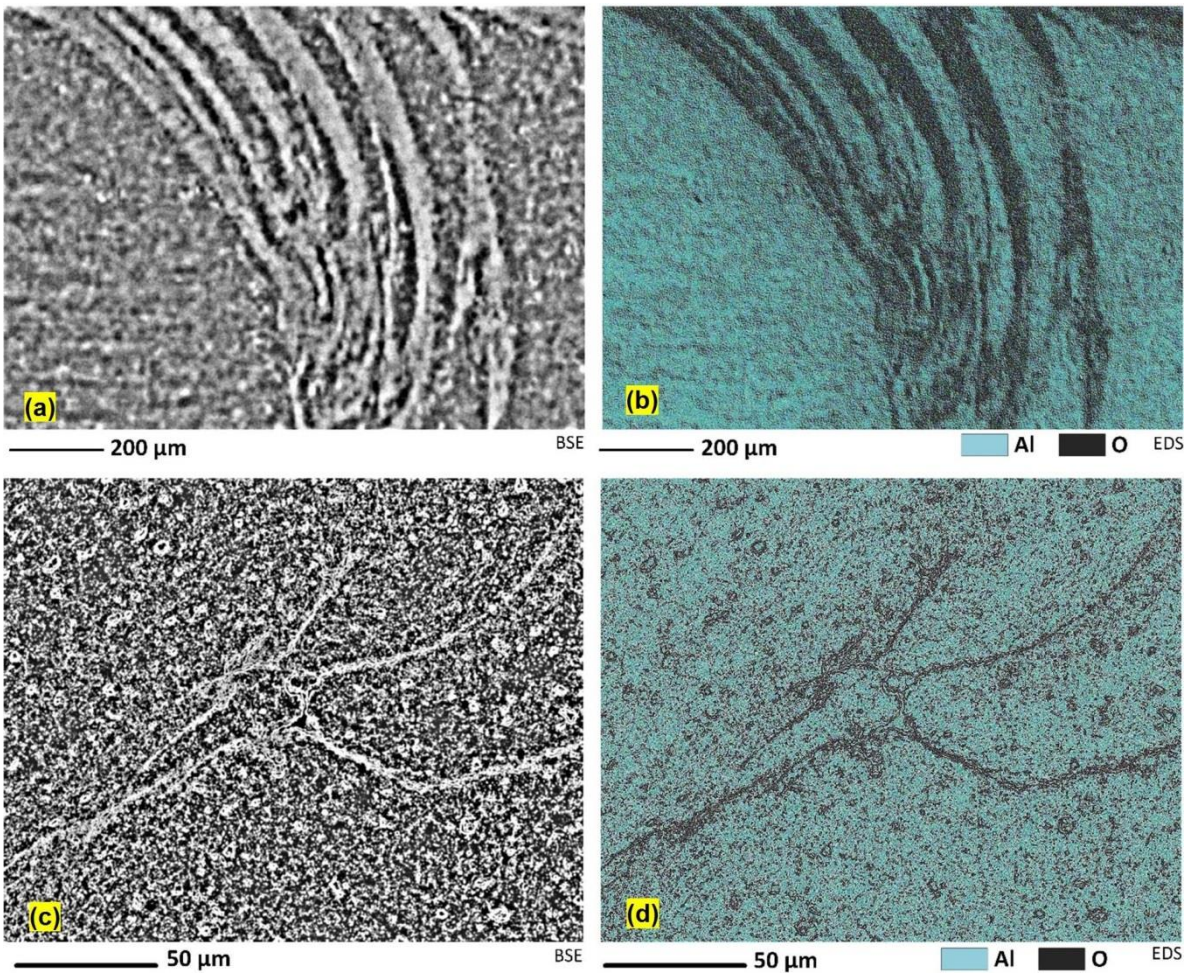

Figure 15.8. Analysis of the flow-arms region (region 1, Figure 15.4a) using (a) BSE, and (b) EDS elemental map, and similarly for (c, d) hair-line micro-crack position (demonstrated in Figure 15.7b). The oxygen-rich areas of the EDS elemental map have been delineated in dark (b, d).

A further SEM study for the Flow-arms pattern in Figure 15.4b were demonstrated in Figure 15.9. The scanned area in Figure 15.9a belongs to the tip of the one of flow-arm branched at the RS of the weld region. The bunch of elongated grains in Figure 15.9a all belong to one flow line pattern in Figure 15.4b. The scanned area reveals that the elongated grains are distinctly separated from each other by main grain boundaries; however there are some sub-grain details inside of the grains. The higher magnification of the inside of the grain (Figure 15.9b) shows that there is a high density of the sub-grain boundaries within the elongated grain. This is a main thermomechanical characteristic of dynamic recrystallization, suggesting that the shearing within the texture can activate the sub-grain boundaries during the re-

cooling process after stirring. It should be noticed that the nature of the sub-grain boundaries can be analysed further by EBSD and TEM techniques, which is beyond the scope of this chapter. From this result it is concluded that the presence of the shearing during the stirring induced a stored strain within the compacted deposited layers of the plasticized mass at the back of the tool. This activated the formation of the microscopic features at the hourglass border, which in RS is revealed as the sub-grain boundaries, appearing as the elongated flow patterns similar to the oxidation layers at the AS. The high density of the sub-grain boundaries can cause a darker band during the etching, delineating a flow-arm shaped pattern similar to the oxidation patterns at the AS of the hourglass border.

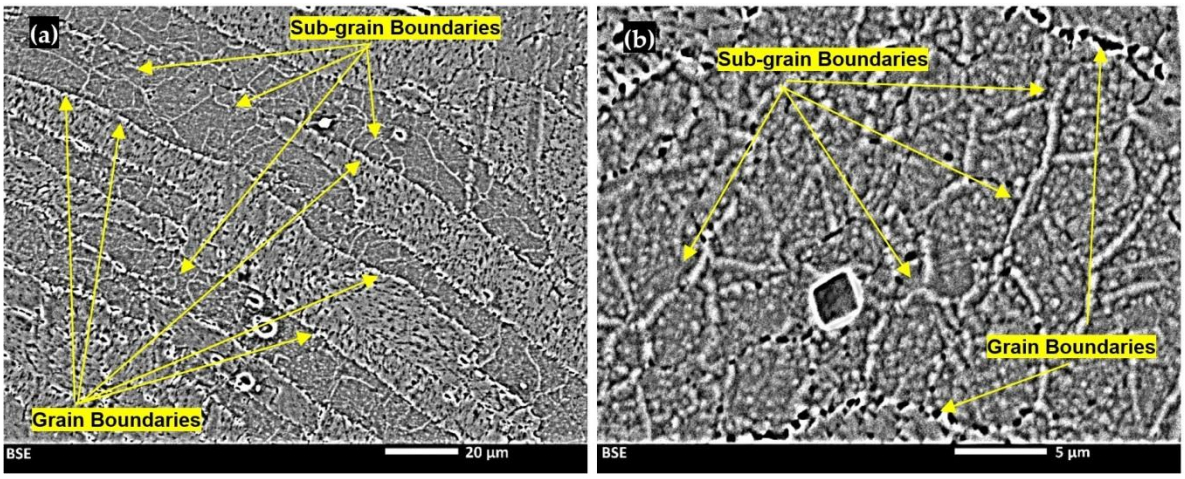

Figure 15.9. SEM analysis of the flow arm shaped branches at the RS. (a) a bunch of elongated grains at the position of the flow pattern, (b) higher magnification of the inside of the grain, representative of the high density of the sub-grain boundaries as a response to the stored strained during the DRX.

15.3.4. Sub-Surface features of the weld

Similar to the transition region HAZ/TMAZ, the surface region of the weld also experiences plastic deformation. The saw-tooth feature at the weld crown (region 1, Figure 15.2a) corresponds to the plastic deformation and the dynamic slip-stick engagement between the material and the shoulder. Figure 15.10 illustrates a gradient of the size of grains laterally (A-B-C).

Cross-section under the weld shoulder

The wavy pattern visible in Figure 15.9a represents the large deformation in the weld crown. The microstructure exhibits a morphological variation from a coarse grain structure at the top (region A), altered to an elongated pattern (region B) which eventually leads to a large number of globular equiaxed grains observable at the inside region (region C). This microstructural subdivision with a gradual trend from

the edge of the sub-shoulder region towards the inner parts of the SZ can be attributed to the grain shape adjustment during the continuous recrystallization induced by the large plastic deformation.

The curving area near the top surface exhibits a random distribution of the coarse grains (Region A). This can be caused by the thermal dissipation gradient near the surface, similar to the chill zone in casting.

At region B a lamellar morphology is initiated at the crown region where the slope increases at the edge and a large shear strain is imposed through the sub-shoulder area which simultaneously experiences the maximum compression rate. In this situation the dynamic recrystallization takes place very fast which pins the grain boundaries and rearrange the grains to an elongated morphology.

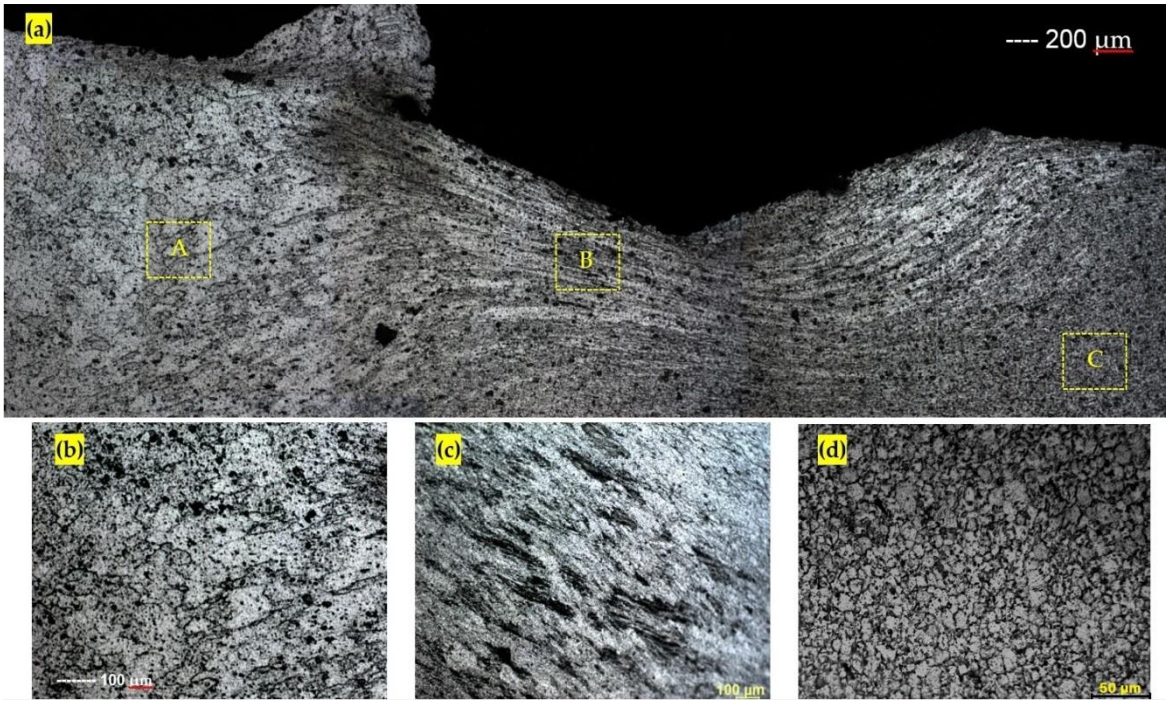

Figure 15.10. Grain and flow details of the sub-shoulder region of the weld crown (Reagent B). Different microscopic features are enlarged as Regions A, B, C.

Stirring is inherently classified as a large strain warm deformation. During the stirring action at the inner layers of mass located far away from the top surface, the pin-driven plastic deformation prevails over the shoulders. This can also be considered a severe grain deformation due to the mechanical stirring action. Consequently, the elongated grains undergo a fragmentation and the subsequent formation of an ultrafine grained microstructure (Region C). On the other hand, because this location is far from the surface, rapid cooling is unlikely. Therefore the grains distribution is homogeneously equiaxed. This is also the region where other

abnormal microscopic features have been observed, such as metallic-glass amorphous structure and localized shrinkage [141].

Plan view under the shoulder (longitudinal axis)

To explore the relationship between the pin and sub-shoulder flow, the flow features of the weld were investigated in the plan view under the shoulder in the longitudinal axis of the weld-line. The results of the sub-shoulder flow observation are illustrated in Figures 15.11 and 15.12.

Figure 15.11 shows the plan view of the sub-shoulder flow for the weld-seam at the centre of the weld-line, where the tool was half way through the weld trial. Figure 15.11a shows a plan view of the actual weld-line, including periodic weld pitches at the weld crown, representative of the deposited stirred mass layers at the trailing edge of the tool. Figures 15.11 a,b show the macro-etched flow patterns of the weld-seam for the same position of the weld in Figure 15.11a. The samples were polished to approximately 0.5 mm in depth, and were macro-etched to show the surface flow pattern both in the AS (Figure 15.11b) and RS (Figure 15.11c).

As shown in Figures 15.11 b,c, the flow patches at the plan view of the weld-line exist at both sides; AS and RS. This is consistent with the explained interpretation that the sub-shoulder flow lines arise from the deposition of the stirred layers of mass at the trailing edge of the tool. The periodic deposition of the mass flow creates a pitch pattern for the surface flow which extends to some depth, driven by the action of the shoulder during the stirring. These features are not created by the pin, but rather the shoulder.

The features in Figures 15.11 a,b are smeared material that extends to some depth below the surface, reveal that the flow lines at the edge of the weld-line, and different features are evident at the AS and RS.

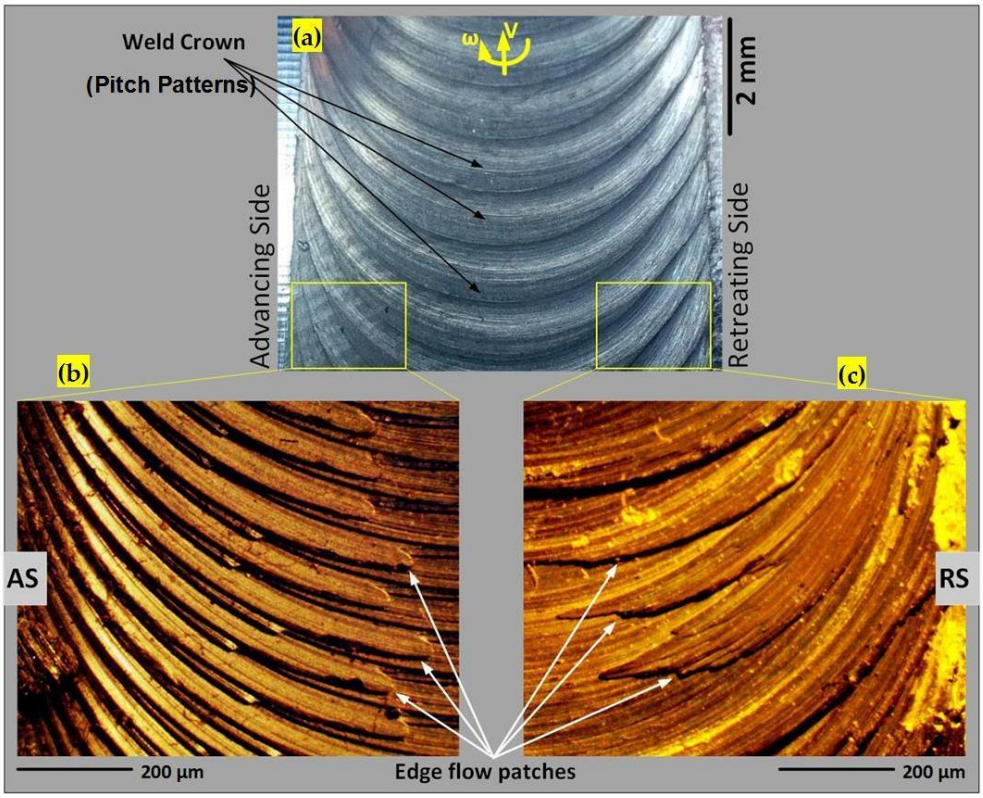

Figure 15.11. Surface flow patterns at the centre of the weld-line. (a) Plan view of the weld surface, (b) Macro-etched sub-shoulder (0.5mm deep) flow patterns at the AS, and (c) Macro-etched sub-shoulder (0.5mm deep) flow patterns at the RS.

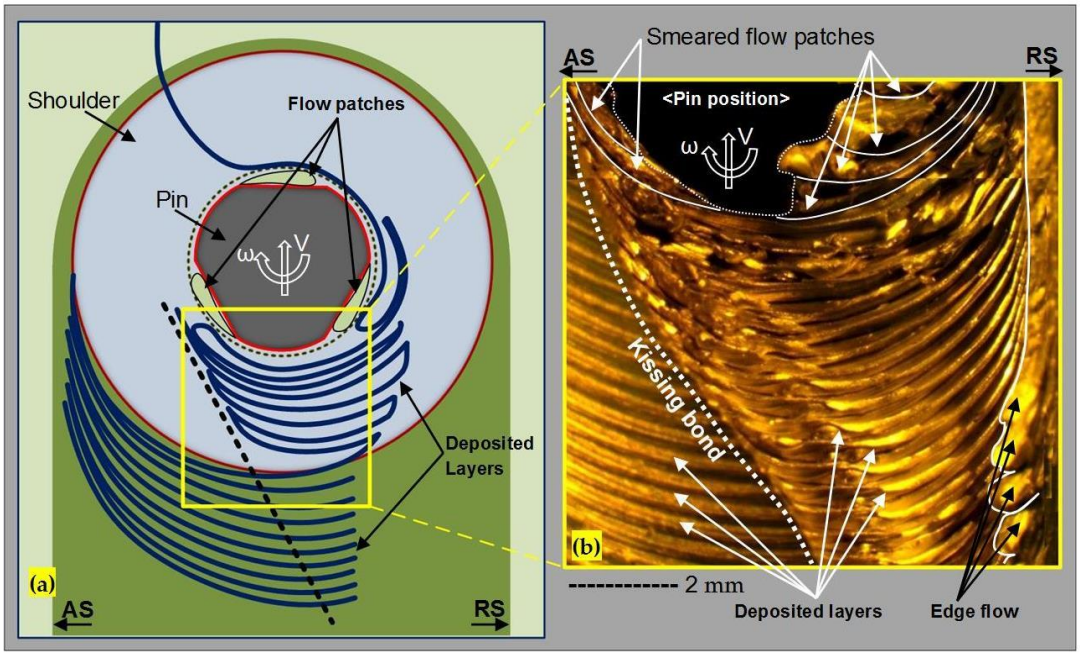

Figure 15.12. The top view of the sub-shoulder region with a proposed model for the flow-lines 0.5mm underneath the shoulder during the stirring action. (a) the flow model of the sub-shoulder area, (b) the macro-etched sub-shoulder region including the actual flow patterns, at the position of the exit zone.

Exit zone

The region where the tool exits the weld provides a unique opportunity to examine the location of flow features without the complication of the packing and deposition that occurs elsewhere in the weld. The surface and subsurface (approximate depth of 0.5 mm) results for this region is shown in Figure 15.12.

The tentative explanation is that this region shows the combined effect of smeared flow patches from the shoulder (to the left of Figure 15.12 b), and the flow patches from the pin (centre-right of Figure 15.12 b). In between the two there appears to be a region of disturbed flow.

15.3.5. Building a model of internal flow and defect formation

We propose a number of new mechanisms that affect flow, and the formation of defects.

Proposed composition of flow layers

The metallurgical analysis in Figures 15.8 and 15.9 shows that the flow line patterns evident in optical microscopy are in fact oxidation effects in the AS, and the accumulation of the shearing and formation of high-density sub-grain boundaries during the DRX procedure in the RS. Thus it proposes that what are conventionally called flow arms are better understood as 'flow layers'.

We believe the more accurate interpretation, for the AS, is that they represent the oxidised fronts between packets of material that have been transported through the weld by tool motion and rotation. Where they occur, they are evident in all cross sections along the weld. An oxidization explanation is feasible considering the high temperature of the stirring process, though an explanation is needed for how the air enters the weld - more on this below. It interprets the layers as being a packing (or stacking) mechanism in the AS, i.e. the flow motion is orthogonal to the flow layer in this region. It is interesting to note that the metallographic macro/micrographs showed that the defect-free samples (see Figure 15.2) do not reveal flow-arms to the same extent.

For the RS the flow layers represent shearing between different layers, i.e. the flow motion may be in/out of the page. This is inferred from by the microstructure in Figure 15.9, which shows elongated grains with internal accumulation of sub-grain boundaries that have been subject to self-rearrangement during dynamic recrystallization. More specifically, the proposed DRX mechanism is that the stirred flow packets experience severe shearing, and hence stored strain is induced. By using the heat generated during re-cooling, the elongated grains cause a self-rearrangement to relieve the stored strain, leading to a high-density accumulation of sub-grain boundaries inside the grain. As the elongated grains have similar crystallographic orientation, so too the newly formed sub-grain boundaries have

similar crystallographic direction. Consequently both the grain boundaries and sub-grain boundaries etch similarly, and more so than the matrix. The dark colour of these layers under optical microscopy arises from the etching of these sub-grain boundaries with the characteristic darker contrast compared to the matrix.

Proposed principles of motion of flow layers

In this regard, and based on the metallurgical improvements, the suggested model in Figure 15.13 provides an explanation for the entering of the air into the weld region and beginning of the oxidation in flow layers. It introduces the concept of a *flow patch*. This is a chip of material that is excised from the base material, transported around the weld as a lump, and deposited in the wake of the weld as a flattened layer.

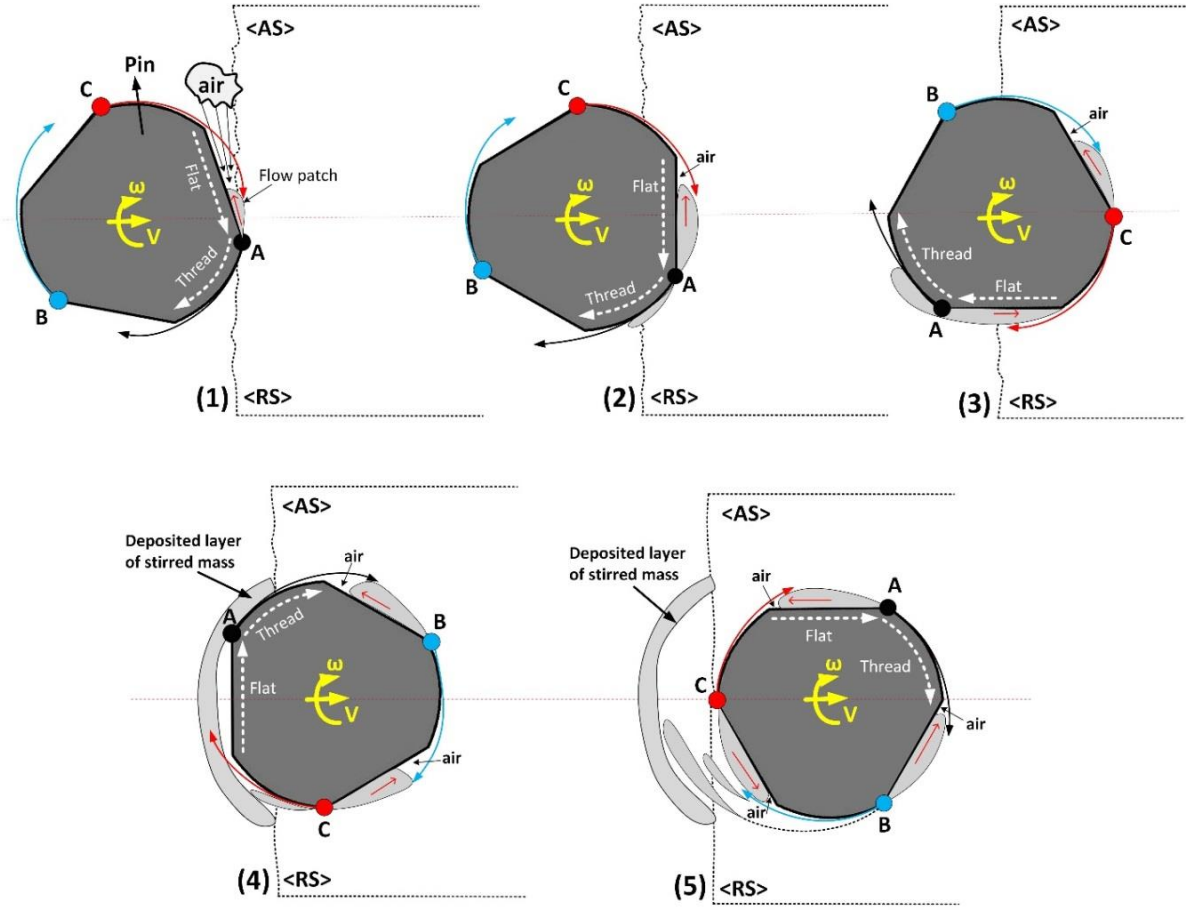

Figure 15.13. Schematic of the entering of the tool into the workpiece, with a proposed model for the entering of the air into the weld region and formation of the oxidation layer between the deposited mass layers at the trailing edge of the tool.

As shown in step 1 in Figure 15.13, the entering of the tool into workpiece initiates the excision of the flow patches on the tool, as chip formation on the flat area of the tool. These flow patches are softened by the heat generated from the friction and in

contact with the air form an oxide surface layer. By the further embedding of the tool into the workpiece, the flow patch is also pushed into the stirring zone between the AS and the RS (step 2). Simultaneously, a volume of the air also enters into the material which is mostly because of the angled geometry of the flat-thread configuration (steps 2 and 3). Air is readily available in the weld due to the shaking and vibration of the tool-substrate. This trapped air forms as an air-pocket at the corners of the flat-thread geometry and intensifies the oxidation layers of the plasticized mass during the stirring (steps 3 and 4). Eventually, the stirred mass is transported to the trailing edge of the tool, where they plough into the RS and are deposited as the flow layers of the weld (step 5). The oxidized surfaces of these flow patches are the flow layers that are observed in the cross section. They are deposited as periodic layers, corresponding to multiple flow patches.

- EXTRACTION AND FRAGMENTATION OF SUBSTRATE

The first step of the stirring action is the fragmentation of the solid grains, from the body of the workpiece. The frictional heat from this grain fragmentation can soften the mass and form the plasticized mass which enters into the stirring zone. Hot material is broken into large fragments by the tool features (threads and flats). These fragments may be partially attached to the weld mass, or they may be completely severed but retained within the confines of the weld. These fragments are evident in the lacerations on the internal weld surfaces at the entry of the weld, and as loose granules that fall out of the weld. The fragments are cut from the workpiece in an arc from the leading edge of the tool, from the advancing to retreating sides. It proposes that the fragments are delineated by the flow layers, i.e. the region between any two flow arms represents a fragment of material that once had exposed surfaces in the region of the flow arms.

- TRANSPORT AND FORCED DEPOSITION

The weld mass, including attached and detached fragments, is moved by the rotation of the tool into the trailing edge space behind the tool. The motion is from the RS towards the AS and results in deposition of the material. This deposition process involved squeezing of the weld bulk and the fragments. This involves shear and forging-like processes, whereby the fragments are squashed back together in a plastic process. The shear adds a heating effect which softens the material and facilitates their solid state bonding.

As the plasticised mass moves closer towards the AS, so the fragments are flattened and quashed up against the AS hourglass border. This proposes the reason for the increasingly fine spacing between the flow arms closer to the AS compared to the centre of the weld. The final result is thin streaks of flow arms, hence the observed interlaced flow.

Proposed principles of formation of surface features

This next explanation addresses the correspondence between internal and surface features.

Figure 15.14 presents a flow model to explain this transport deposition. By revolution of the tool the transportation and deposition of the mass layers happens by the speed ratio (ω/V). The final flow patterns are observable as the flow-arms at the cross-section of the weld, and the related weld pitch patterns at the surface of the weld-line.

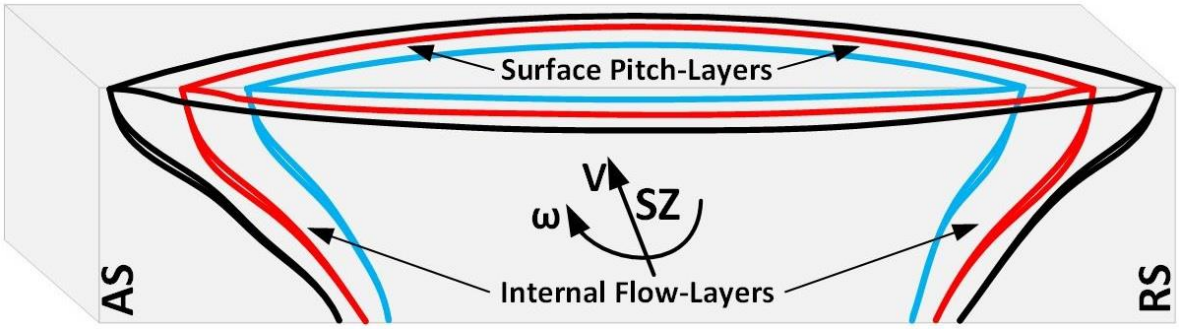

Figure 15.14. The proposed flow patterns for the flow-arms and the weld pitch patterns at the cross-section and surface of the weld region, respectively. The model aims to reveal the flow lines during the revolution of the tool and deposition of the layered mass at the trailing edge of the tool.

In general, the weld pitch patterns at the surface of the weld are directly dependent on the speed ratio between the rotation and advancing actions of the tool, simply as the number of revolution per forward movement, in which can directly influence the formation of the deposited layers at the stirring zone. It should be noted that the pressure imposed underneath the shoulder can affect the shape and size of these bonded layers and compact them together. Also, adding of the new deposited layers into the previous layers leads to increase in compaction condition at the back of the tool.

Integrated weld transport model

In Figure 15.15, the simultaneous formation of the surface flow patches (pitch layers) and the internal flow layers has been demonstrated as a discontinuous flow model for the plasticized batches of the mass which are formed by the revolution of the tool. As the shoulder action is directly responsible for the formation of the surface flow patches at the sub-shoulder region, the rotation and the advancement of the pin at the mid-SZ area generates the plasticized flow batches at the proximity of the tool, at the breadth of AS-RS. The deposited flow layers at the trailing edge of the tool

form the bended flow layers at the borders of the AS and RS, which are revealed as the hourglass-boundaries within the cross-section of the weld.

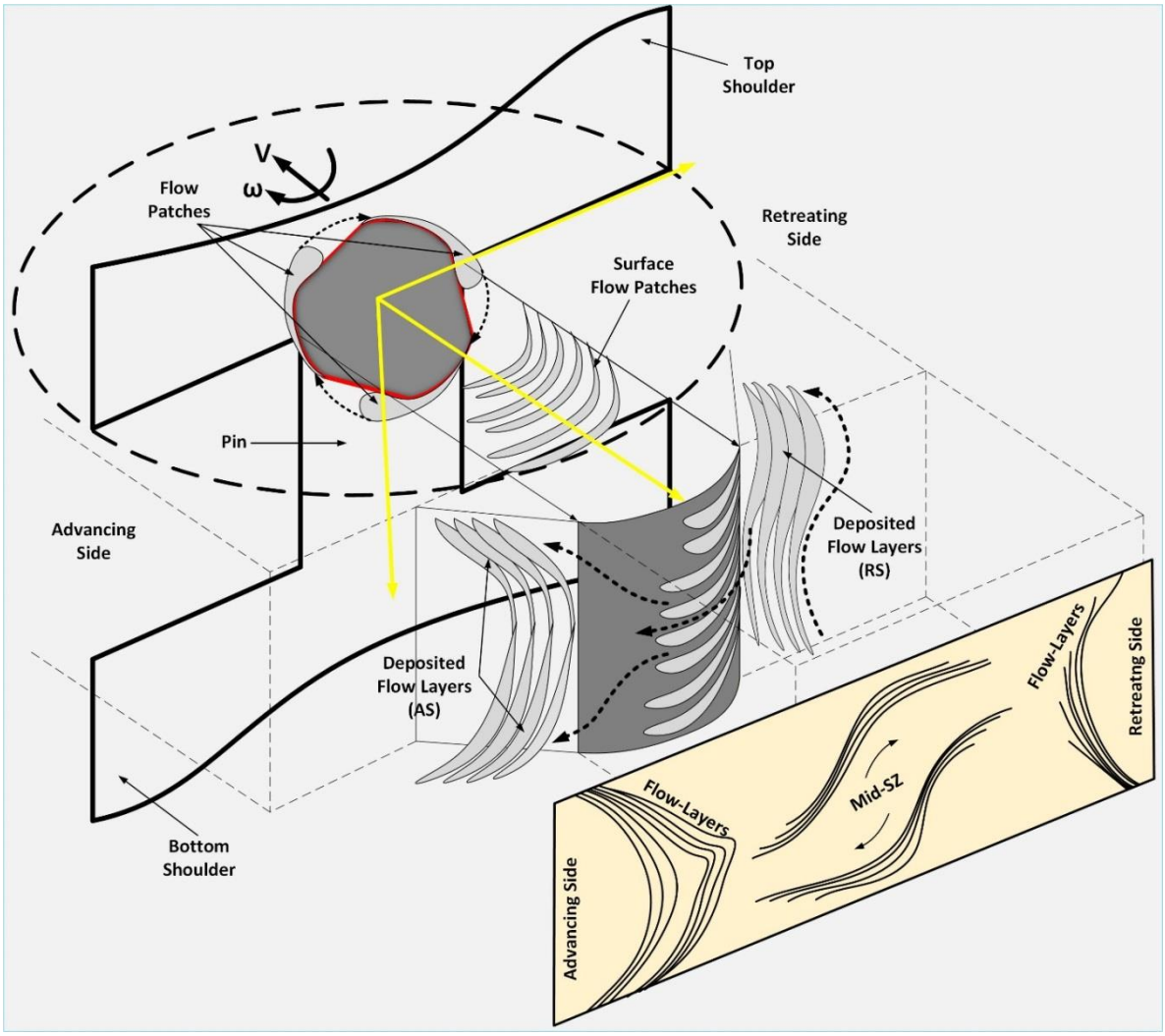

Figure 15.15. Schematic of the cross-section of the weld with a proposed model for the formation mechanism of the flow-arms at the breadth of the stirring zone, between the AS and RS.

15.4. Chapter Discussion

15.4.1. Originality

The work makes the following original contributions to the understanding of the welding of AA6082-T6.

Characterization of the flow layers at the hourglass-borders

The combination of the metallographic delineation in optical microscopy and the metallurgical analysis by the SEM and EDS, confirms that the dark curved patterns in the AS and RS hourglass borders of flow-arms, being oxidation layers (AS) and

elongated grains with a high-density of accumulation of the sub-grain boundaries as the result of the shearing and DRX (RS).

Visualization of flow layers

In this chapter, based on the microscopic observations, it was elucidated the internal flow features of the plastic deformation in different regions of the stirring zone during the bobbin friction stir processing. Key concepts that emerge are:

- Packets of material ('flow patches') are transported around the pin.
- Flow patches are transported round the RS to the back of the tool, where they experience high localized shearing at their mutual boundaries, as evidenced in high density of sub-grain boundaries.
- Flow patches are transported all the way round the tool to the AS, where they are stacked on each other and flattened in the process. Air enters at or before this stage and causes oxidization of the boundaries, as evidenced in EDS elemental mapping.

Proposing a model of the internal flow processes

Many other studies have been based on the assumption of continuous flow within the stirring zone. However, such approaches have not had much success in predicting the actual flow. It has been particularly difficult to model the tunnel void as a flow-based defect using continuous flow assumptions. The present chapter puts this into context, by finding that the flow is highly discontinuous, based on observation of the microstructure. In turn this has been facilitated by discovery of a suitable reagent and metallographic measurement. Consequently the present results imply that methods based on continuous flow computational fluid dynamics (CFD) are unlikely to be successful in explaining flow defects.

The discontinuous flow regime is a consequence of the thread-flat pin geometry. In the literature of FSW, the onion rings in the conventional-FSW weld structure are assumed as a geometric effect of the tool, and the discontinuous flow during stirring zone has been correlated to the tool-material interaction during the friction and stirring mechanism [44]. However, here for the bobbin-tool, it proposes that the flow batches of the stirred mass are formed by the revolution of the thread-flat features of the tool with a discontinuous nature. Similar to the conventional-FSW process [44], the thickness of these flow layers are related to the speed ration (ω/V) in one revolution of the tool. However, the flow layers deposited at the trailing edge of the tool are packed to each other. Hence, they are not observed exactly at the same expected thickness (ω/V ratio; rev/mm) via microscopic observations.

15.4.2. Implications for practitioners

Industry users of AA6082-T6 should note that tunnel defects are associated with internal oxidization of the weld cross section. This has the potential to cause reduced mechanical properties, corrosion resistance and the fatigue strength as the tunnel

void as a macro-size discontinuity can deteriorate the integrity-related properties of the weld.

15.4.3. Limitations of this work and implications for future research

Our analyses of the flow layers were limited in the number of such layers investigated. It cannot exclude the possibility that flow layers may have features of both oxidization and DRX sub-grain boundary formation. A potential future research project could examine multiple flow layers, at different positions along their length, and evaluate both microstructure (e.g. using SEM or TEM) and elemental composition.

3D visualization of the flow layers was not possible during optical and electron microscopy. A possible research question could be to progressively re-polish the surface in a controlled manner to build up a 3D representation of the flow layers.

In this research the aim was to propose a physical model for the internal material flow based on the metallography analysis. Hence, the measurement of the mechanical properties of the weld in correlation to the flow features is beyond the scope of this chapter and is left for future research. Nevertheless, it is concluded that the formation of the macro-size tunnel void and the micro-cracks during stirring action can extensively affect the strength of the final weldment. It suggests a comprehensive study of the mechanical properties of the weld (e.g. via tensile or bending test) to measure the effect of these structural defects on plausible failure under loading. Regarding the oxide layers, the fractography of the fatigue or creep tests also can elucidate the failure mechanism of the weldment in presence of the defect as the initial position of the crack propagation.

15.5. Chapter Conclusions

The internal flow features of the AA6082-T6 BFSW were evaluated using a set of developed reagents and optical microscopy. The key findings are that the dark curved patterns (conventionally called 'flow-arms'), are actually oxidation layers at the advancing side, and at the retreating side are elongated grains with a high-density of accumulation of sub-grain boundaries due to DRX. A model of discontinuous flow within the weld is proposed, based on the microscopic observations. It is inferred that the internal flow is characterized by packets of material ('flow patches') being transported around the pin. At the RS they experience high localized shearing at their mutual boundaries, as evidenced in high density of sub-grain boundaries. Flow patches at the AS are stacked on each other and exposed to oxidization.

Chapter 16: Conclusions

16.1. Original contributions

The initial objectives of the work were to present a flow-based model for the internal plastic interaction during the BFSW process to develop the understanding of the formation mechanism of the tunnel void. The eliminating of the flow-based origins of the defect can improve the stability of the stirring flow process. Hence by preventing the defects to occur, can improve the quality of the produced BFSW weldment.

In the first step of the research, the analogue model of the weld was constructed by the plasticine samples, with a focus on the flow visualization at the stirring zone (chapters 4-7). The plasticine analogue results indicate a suitable level of accuracy to be representative of the metal joint, regarding revealing the plastic flow details. By comparing between the plasticine analogue and the aluminium welding trials, it was concluded that the flow instability during the stirring action has the main role in emerging of the discontinuity defects, e.g. tunnel void.

To characterize the physical features of the weld, the research was progressed by developing a variety of the experiments based on the metallographic measurement of the weld structure (chapters 8-10). The microstructural evolution of the BFSW weld proceeded for different grades of the aluminium (1xxx, 3xxx, 6xxx), also dissimilar Al-Cu hybrid joint was studied to identify the effective welding variables with an impact on the defect emergence.

The microscopic observations reveal a need of the understanding of the thermomechanical nature of the BFSW process, inducing some metallurgical phenomena (e.g. DRX, precipitation, grain boundaries, grain refinement, dislocations), affecting the final properties of the weld. These microstructural alterations were studied by a focus to identify the role of the thermomechanical behaviour of the process, contributing to the formation of the weld defects (chapters 11-14).

By the study of relevant physical interactions between the tool and the material, also considering the metallurgical behaviour of the internal mass flow during and after the process, a physical model was present to elucidate the formation mechanism of the tunnel void defect within the body of the weld (chapter 15).

16.2. Original contributions

This work makes the following novel contributions to the understanding of the evolution of the friction stir welded joint.

Anatomy of the BFSW weld structure

By the analogue modelling, validates by the aluminium welds, the anatomy of the weld structure with identifying the details of different regions of the weld were elucidated. By varying the process parameters (welding speeds; rotational and advancing velocity, also the tool geometry), material flow studies introduced two formation mechanisms, size and the shape of the emerged defects within the weld structure.

Development of the aluminium etchants

A new suite of etchants have been developed for macro- and micro-etching of A6082-T6 bobbin welds. This grad of aluminium shows a poor reaction to the common etchant regains of the aluminium alloys. The progressed etching procedure provided the microstructures observable to high magnification using optical microscopy. The microstructure of the grain boundaries was revealed for the different regions within the weld structure. Results showed the grain size variation with distinct morphological patterns, making it possible to conduct optical microscopy, where previously only more expensive methods (e.g. electron microscopy) were suitable. Etchants were able to elucidate microflow patterns and crystalline coherency of the interface at a high level of accuracy for high optical magnification. This is an advancement on the level of detail apparent in the published literature.

Thermomechanical nature of the BFSW process

The microstructural evolution of BFSW aluminium welds measured a set of thermomechanical phenomena happening during the stirring process and the subsequent re-cooling. A comprehensive set of electron microscopy analysis (SEM, TEM, EDS, EBSD, AFM) were performed to measure the possible thermomechanical features within the weld texture. The polycrystalline grain structure of the aluminium alloys demonstrated a significant grain refinement, including huge reduction in grain size and ultrafine equiaxed grain morphology within the weld region. Other metallurgic transformations, including dynamic recrystallization, grain-boundary engineering (LAGBs and HAGBs rearrangement), precipitation hardening, and dislocations interaction, were characterized and compared within different regions of the weld. The grain misorientation and quantifying of the stored stain within the weld texture were also measured as the main thermomechanical characteristic of the deformed structure of the BFSW aluminium weld.

Physical model of the material flow mechanism

Using a comprehensive metallographic observation, the internal flow features of the BFSW aluminium weld were studied. A model of discontinuous flow within the stirring region of the weld was proposed, to elucidate the internal plastic flow is characterized by packets of material ('flow patches') being transported around the

pin. The intermixing interaction of the flow layers Flow patches at the advancing side, and at the retreating side of the weld, proposes a high localized shearing flow around the rotating pin. The model proposed that the flow failure, arising by the inconsistency between the welding parameters, is responsible for the emergence of the discontinuity defects (e.g. tunnel void) within the deposited layers of the stirred mass, as the tool leaves the weld seam.

16.3. Implications for future research and development of the field

The microscopic evolution of the severe plastic deformation stirring during the BFSW process was observed with different types of defects namely tunnel void, micro-cracks and oxidation formation. In brief, the formation of these defects can be closely attributed to the flow mechanism and inconsistency in heat input and re-cooling during DRX mechanisms.

From a production quality perspective, the tunnel void is strongly associated with poor metallurgical outcomes as evident in micro-cracks and oxidation formation. Hence, it can state that if a tunnel defect exists, there is a high probability of internal defects. The corollary also appears to be true: that if the tunnel void is absent, then the metallurgical defects are also absent or at least minimized. It is also noted that the original of the tunnel defect is primarily a consequence of the flow failure within the weld, which in turn is related (by ways not entirely clear) to the tool geometry and weld speed parameters (rotational and advancing). Hence there is a coupling between these three: welding variables affect internal flow which affects microstructural integrity. Thus, a priority from a practitioner perspective is eliminating of the tunnel void.

In this research the main aim was to study the material flow mechanism and propose a physical model for the internal material flow based on the metallographic observations. Hence, the measurement of the mechanical properties of the weld in correlation to the flow features was beyond the scope of this research. Nevertheless, it is concluded that the formation of the macro-size tunnel void and the micro-cracks during stirring action can extensively affect the strength of the final weldment. In this regard, a comprehensive study of the mechanical properties of the weld (e.g. via tensile or bending test) is required to measure the effect of these structural defects on plausible failure under loading. Regarding the tunnel void and the plausible localized oxidation, the fractography of the fatigue or creep tests also can elucidate the failure mechanism of the weldment in presence of the defect as the initial position of the crack propagation.

In terms of strength, micro-cracks have more influence over the weld strength and could be examined more. It may be interesting to measure the density of these micro-cracks. Furthermore, there are oxide boundaries at the edge of micro-cracks, and it could be valuable to identify whether this is oxide being drawn in from the material surface or air entering between the stirred mass layers.

The micro-cracks formed during stirring can adversely affect the strength of the final weld. The failure behaviour of the joint and the microscopic observation of the fracture surface can give a better understanding of the defect formation mechanism, during severe plastic deformation.

There is a possibility that the tunnel void acts as a heat sink, since it is contact with air, and hence affects the DRX mechanism. Some defects in this region were observed that are consistent with such an interpretation.

3D visualization of the flow layers was not possible during optical and electron microscopy. A possible research question could be to progressively re-polish the surface in a controlled manner to build up a 3D representation of the flow layers.

References

1. Thomas, W., Nicholas, E., Needham, J., Murch, M., Temple-Smith, P., and Dawes, C., *Friction stir butt welding, International Patent Application no.* PCT/GB92 Patent application, 1991(9125978.8).

2. Thomas, W. and Nicholas, E., *Friction stir welding for the transportation industries.* Materials & design, 1997. 18(4-6): p. 269-273.

3. Colligan, K., *Material flow behavior during friction welding of aluminum.* Weld J, 1999. 75(7): p. 229s-237s.

4. Thomas, W., Wiesner, C., Marks, D., and Staines, D., *Conventional and bobbin friction stir welding of 12% chromium alloy steel using composite refractory tool materials.* Science and Technology of welding and Joining, 2009. 14(3): p. 247-253.

5. Threadgill, P., Leonard, A., Shercliff, H., and Withers, P., *Friction stir welding of aluminium alloys.* International Materials Reviews, 2009. 54(2): p. 49-93.

6. Aginagalde, A., Gomez, X., Galdos, L., and García, C., *Heat treatment selection and forming strategies for 6082 aluminum alloy.* Journal of Engineering Materials and Technology, 2009. 131(4): p. 044501.

7. Argesi, F.B., Shamsipur, A., and Mirsalehi, S.E., *Dissimilar Joining of Pure Copper to Aluminum Alloy via Friction Stir Welding.* Acta Metallurgica Sinica (English Letters), 2018. 31(11): p. 1183-1196.

8. Barcellona, A., Buffa, G., Fratini, L., and Palmeri, D., *On microstructural phenomena occurring in friction stir welding of aluminium alloys.* Journal of Materials Processing Technology, 2006. 177(1-3): p. 340-343.

9. Cabibbo, M., Meccia, E., and Evangelista, E., *TEM analysis of a friction stir-welded butt joint of Al–Si–Mg alloys.* Materials Chemistry and Physics, 2003. 81(2-3): p. 289-292.

10. Caseiro, J.F., Valente, R.A.F., Andrade-Campos, A., and Yoon, J.W., *On the elasto-plastic buckling of Integrally Stiffened Panels (ISP) joined by Friction Stir Welding (FSW): Numerical simulation and optimization algorithms.* International Journal of Mechanical Sciences, 2013. 76: p. 49-59 DOI: http://dx.doi.org/10.1016/j.ijmecsci.2013.09.002.

11. Coelho, RS., Kostka, A., Dos Santos, J., and Pyzalla, A.R., *EBSD Technique Visualization of Material Flow in Aluminum to Steel Friction-stir Dissimilar Welding.* Advanced Engineering Materials, 2008. 10(12): p. 1127-1133.

12. Cui, L., Yang, X., Zhou, G., Xu, X., and Shen, Z., *Characteristics of defects and tensile behaviors on friction stir welded AA6061-T4 T-joints.* Materials Science and Engineering: A, 2012. 543: p. 58-68.

13. Dialami, N., Cervera, M., and Chiumenti, M., *Effect of the tool tilt angle on the heat generation and the material flow in friction stir welding.* Metals, 2019. 9(1): p. 28.

14. Dialami, N., Chiumenti, M., Cervera, M., Agelet de Saracibar, C., and Ponthot, J.P., *Material flow visualization in friction stir welding via particle tracing.* International Journal of Material Forming, 2015. 8(2): p. 167-181 DOI: 10.1007/s12289-013-1157-4.

15. Dong, P., Dou, Z., and Zhang, P., *3D numerical simulation of temperature and stress evolution in friction stir welding of aluminum alloy.* Hanjie Xuebao/Transactions of the China Welding Institution, 2015. 36(4): p. 71-74.

16. Durga, B.S., *Research Scholar Optimization of Friction Stir Welding Parameters (Tool Material, Tool Geometry And Tool Speed) On Aluminium Alloys 6061 Using Taguchi Method" Advanced Research Journals of Science and Technology (ARJST) 5.2 (2018): 385-407.* INTRODUCTION Friction stir welding (FSW): Friction Stir Welding (FSW), a solid state welding invented by The Welding Institute (TWI) in, 1991.

17. Egea, AS., Rodriguez, A., Celentano, D., Calleja, A., and de Lacalle, L.L., *Joining metrics enhancement when combining FSW and ball-burnishing in a 2050 aluminium alloy.* Surface and Coatings Technology, 2019. 367: p. 327-335.

18. Elrefaey, A., Gouda, M., Takahashi, M., and Ikeuchi, K., *Characterization of aluminum/steel lap joint by friction stir welding.* Journal of materials engineering and performance, 2005. 14(1): p. 10-17.

19. Fonda, R. and Bingert, J., *Microstructural evolution in the heat-affected zone of a friction stir weld.* Metallurgical and materials transactions A, 2004. 35(5): p. 1487-1499.

20. Fuse, K. and Badheka, V., *Bobbin tool friction stir welding: a review.* Science and Technology of Welding and Joining, 2019. 24(4): p. 277-304.

21. Kassim, M., Sued, M., and Pons, D., *MECHANICAL PROPERTIES OF THICK AND THIN AA1100 WELDED USING BOBBIN FRICTION STIR WELDING.* Journal of Advanced Manufacturing Technology (JAMT), 2019. 13(2 (1)).

22. Fonda, R. and Bingert, J., *Precipitation and grain refinement in a 2195 Al friction stir weld.* Metallurgical and materials Transactions A, 2006. 37(12): p. 3593-3604.

23. Fonda, R. and Bingert, J., *Texture variations in an aluminum friction stir weld.* Scripta Materialia, 2007. 57(11): p. 1052-1055.

24. Fonda, R., Bingert, J., and Colligan, K., *Development of grain structure during friction stir welding.* Scripta materialia, 2004. 51(3): p. 243-248.

25. Fonda, R. and Knipling, K., *Texture development in friction stir welds.* Science and Technology of welding and joining, 2011. 16(4): p. 288-294.

26. Fonda, R., Knipling, K., and Bingert, J., *Microstructural evolution ahead of the tool in aluminum friction stir welds.* Scripta Materialia, 2008. 58(5): p. 343-348.

27. Fonda, R., Reynolds, A., Feng, C., Knipling, K., and Rowenhorst, D., *Material flow in friction stir welds.* Metallurgical and Materials Transactions A, 2013. 44(1): p. 337-344.

28. Gadakh, V.S. and Adepu, K., *Heat generation model for taper cylindrical pin profile in FSW.* Journal of Materials Research and Technology, 2013. 2(4): p. 370-375 DOI: http://dx.doi.org/10.1016/j.jmrt.2013.10.003.

29. Gadakh, V.S., Kumar, A., and Vikhe Patil, G.J., *Analytical modeling of the friction stir welding process using different pin profiles.* Welding Journal, 2015. 94(4): p. 115s-124s.

30. Garg, A., Raturi, M., and Bhattacharya, A., *Influence of additional heating in friction stir welding of dissimilar aluminum alloys with different tool pin profiles.* The International Journal of Advanced Manufacturing Technology: p. 1-21.

31. Gharavi, F., Ebrahimzadeh, I., Amini, K., Sadeghi, B., and Dariya, P., *Effect of Welding Heat Input on the Microstructure and Mechanical Properties of Dissimilar Friction Stir-Welded Copper/Brass Lap Joint.* Materials Research, 2019. 22(4).

32. Grujicic, M., Ramaswami, S., Snipes, J.S., Avuthu, V., Galgalikar, R., and Zhang, Z., *Prediction of the Grain-Microstructure Evolution Within a Friction Stir Welding (FSW) Joint via the Use of the Monte Carlo Simulation Method.* Journal of Materials Engineering and Performance, 2015 DOI: 10.1007/s11665-015-1635-6.

33. Gubicza, J., Krállics, G., Schiller, I., and Malgyn, D. *Evolution of the microstructure of Al 6082 alloy during equal-channel angular pressing*. in *Materials Science Forum*. 2005. Trans Tech Publ.

34. Hasan, A.F., Bennett, C.J., and Shipway, P.H., *A numerical comparison of the flow behaviour in Friction Stir Welding (FSW) using unworn and worn tool geometries.* Materials & Design, DOI: http://dx.doi.org/10.1016/j.matdes.2015.08.016.

35. He, X., Gu, F., and Ball, A., *A review of numerical analysis of friction stir welding.* Progress in Materials Science, 2014. 65: p. 1-66.

36. Hilgert, J., Dos Santos, J., and Huber, N., *Shear layer modelling for bobbin tool friction stir welding.* Science and Technology of Welding and Joining, 2012. 17(6): p. 454-459.

37. Hilgert, J., Hütsch, L.L., dos Santos, J., and Huber, N. *Material flow around a bobbin tool for friction stir welding*. in *Excerpt from the Proceedings of the COMSOL Conference*. 2010.

38. Hilgert, J., Schmidt, H., Dos Santos, J., and Huber, N., *Thermal models for bobbin tool friction stir welding.* Journal of Materials Processing Technology, 2011. 211(2): p. 197-204.

39. Ji, S., Meng, X., Zeng, Y., Ma, L., and Gao, S., *New technique for eliminating keyhole by active-passive filling friction stir repairing.* Materials & Design, 2016. 97: p. 175-182.

40. Kestens, L. and Pirgazi, H., *Texture formation in metal alloys with cubic crystal structures*. 2016, Taylor & Francis.

41. Khan, N.Z., Siddiquee, A.N., Khan, Z.A., and Shihab, S.K., *Investigations on tunneling and kissing bond defects in FSW joints for dissimilar aluminum alloys.* Journal of Alloys and Compounds, 2015. 648: p. 360-367 DOI: http://dx.doi.org/10.1016/j.jallcom.2015.06.246.

42. Kimapong, K. and Watanabe, T., *Friction stir welding of aluminum alloy to steel.* Welding journal, 2004. 83(10): p. 277.

43. Knipling, K. and Fonda, R., *Texture development in the stir zone of near-α titanium friction stir welds.* Scripta materialia, 2009. 60(12): p. 1097-1100.

44. Krishnan, K., *On the formation of onion rings in friction stir welds.* Materials science and engineering: A, 2002. 327(2): p. 246-251.

45. Kumar, S.S., Ravisankar, B., and Raviram, R.D. *Evaluation of mechanical properties of friction stir welded commercially pure aluminium*. in *MATEC Web of Conferences*. 2018. EDP Sciences.

46. Liechty, B. and Webb, B., *Modeling the frictional boundary condition in friction stir welding.* International Journal of Machine Tools and Manufacture, 2008. 48(12-13): p. 1474-1485.

47. Lu, S., Yang, D.L., Xiao, S.Y., and Chen, S.J., *Three-dimensional investigation on temperature distribution and mechanical properties of AZ31 Mg alloy joint welded by FSW*, in *Proceedings of the 1st International Joint Symposium on Joining and Welding*, Fujii, H., Editor. 2013, Woodhead Publishing. p. 67-72 ISBN: 978-1-78242-163-4 DOI: http://dx.doi.org/10.1533/978-1-78242-164-1.67.

48. Malik, V., Sanjeev, N.K., Hebbar, H.S., and Kailas, S.V., *Time Efficient Simulations of Plunge and Dwell Phase of FSW and its Significance in FSSW.* Procedia Materials Science, 2014. 5: p. 630-639 DOI: http://dx.doi.org/10.1016/j.mspro.2014.07.309.

49. Mehta, K.P. and Badheka, V.J., *A review on dissimilar friction stir welding of copper to aluminum: process, properties, and variants.* Materials and Manufacturing Processes, 2016. 31(3): p. 233-254.

50. Miyasaka, F., Yoshikawa, G., and Matsuzawa, S., *Development of mathematical modeling for FSW with particle method*, in *Proceedings of the 1st International Joint Symposium on Joining and Welding*, Fujii, H., Editor. 2013, Woodhead Publishing. p. 287-290 ISBN: 978-1-78242-163-4 DOI: http://dx.doi.org/10.1533/978-1-78242-164-1.287.

51. Moradi, M.M., Aval, H.J., and Jamaati, R., *Effect of tool pin geometry and weld pass number on microstructural, natural aging and mechanical behaviour of SiC-incorporated dissimilar friction-stir-welded aluminium alloys.* Sādhanā, 2019. 44(1): p. 9.

52. Murr, L., Flores, R., Flores, O., McClure, J., Liu, G., and Brown, D., *Friction-stir welding: microstructural characterization.* Material Research Innovations, 1998. 1(4): p. 211-223.

53. Muthu, M.F.X. and Jayabalan, V., *Tool travel speed effects on the microstructure of friction stir welded aluminum–copper joints.* Journal of Materials Processing Technology, 2015. 217: p. 105-113.

54. Nasir, S.N.N.M., Sued, M.K., and Abidin, M.Z.Z., *The Effects of Rotational Tool Speed on Mechanical Properties of Bobbin Friction Stir Welded AA1100*, in *Advances in Material Sciences and Engineering*. 2020, Springer. p. 337-342.

55. Pal, S. and Phaniraj, M.P., *Determination of heat partition between tool and workpiece during FSW of SS304 using 3D CFD modeling.* Journal of Materials

Processing Technology, 2015. 222: p. 280-286 DOI: http://dx.doi.org/10.1016/j.jmatprotec.2015.03.015.

56. Ramulu, P.J., Narayanan, R.G., Kailas, S.V., and Reddy, J., *Internal defect and process parameter analysis during friction stir welding of Al 6061 sheets.* The International Journal of Advanced Manufacturing Technology, 2013. 65(9-12): p. 1515-1528.

57. Reilly, A., Shercliff, H., Chen, Y., and Prangnell, P., *Modelling and visualisation of material flow in friction stir spot welding.* Journal of Materials Processing Technology, 2015. 225: p. 473-484 DOI: http://dx.doi.org/10.1016/j.jmatprotec.2015.06.021.

58. Richter-Trummer, V., Suzano, E., Beltrão, M., Roos, A., dos Santos, J.F., and de Castro, P.M.S.T., *Influence of the FSW clamping force on the final distortion and residual stress field.* Materials Science and Engineering: A, 2012. 538: p. 81-88 DOI: http://dx.doi.org/10.1016/j.msea.2012.01.016.

59. Saeid, T., Abdollah-Zadeh, A., and Sazgari, B., *Weldability and mechanical properties of dissimilar aluminum–copper lap joints made by friction stir welding.* Journal of Alloys and Compounds, 2010. 490(1-2): p. 652-655.

60. Sarvghad-Moghaddam, M., Parvizi, R., Davoodi, A., Haddad-Sabzevar, M., and Imani, A., *Establishing a correlation between interfacial microstructures and corrosion initiation sites in Al/Cu joints by SEM–EDS and AFM–SKPFM.* Corrosion science, 2014. 79: p. 148-158.

61. Shah, L., Othman, N., and Gerlich, A., *Review of research progress on aluminium–magnesium dissimilar friction stir welding.* Science and Technology of Welding and Joining, 2018. 23(3): p. 256-270.

62. Sharma, N. and SIDDIQUEE, A.N., *Friction stir welding of aluminum to copper—an overview.* Transactions of Nonferrous Metals Society of China, 2017. 27(10): p. 2113-2136.

63. Shrivastava, A., Pfefferkorn, F.E., Duffie, N.A., Ferrier, N.J., Smith, C.B., Malukhin, K., and Zinn, M., *Physics-based process model approach for detecting discontinuity during friction stir welding.* International Journal of Advanced Manufacturing Technology, 2015. 79(1-4): p. 605-614 DOI: 10.1007/s00170-015-6868-x.

64. Sued, M., Pons, D., Lavroff, J., and Wong, E.-H., *Design features for bobbin friction stir welding tools: Development of a conceptual model linking the underlying physics to the production process.* Materials & Design (1980-2015), 2014. 54: p. 632-643.

65. Tayon, W.A., Domack, M.S., Hoffman, E.K., and Hales, S.J., *Texture evolution within the thermomechanically affected zone of an Al-Li alloy 2195 friction stir weld.* Metallurgical and Materials Transactions A, 2013. 44(11): p. 4906-4913.

66. Threadgill, P.L., Ahmed, M., Martin, J.P., Perrett, J.G., and Wynne, B.P. *The use of bobbin tools for friction stir welding of aluminium alloys*. in *Materials Science Forum*. 2010. Trans Tech Publ.

67. Thomas, W. and Wiesner, C. *Recent developments of FSW technologies: evaluation of root defects, composite refractory tools for steel joining and one-pass welding of thick sections using self-reacting bobbin tools*. in *Trends in Welding Research: Proceedings of the 8th International Conference, June 1-6, 2008, Callaway Gardens Resort, Pine Mountain, Georgia, USA*. 2009. ASM International.

68. Svensson, L.-E., Karlsson, L., Larsson, H., Karlsson, B., Fazzini, M., and Karlsson, J., *Microstructure and mechanical properties of friction stir welded aluminium alloys with special reference to AA 5083 and AA 6082.* Science and Technology of Welding and Joining, 2000. 5(5): p. 285-296.

69. Russell, M. and Shercliff, H., *Analytical modelling of microstructure development in friction stir welding.* 1999.

70. Sued, M., Tamadon, A., and Pons, D., *Material flow visualization in bobbin friction stir welding by analogue model.* Proceedings of Mechanical Engineering Research Day 2017, 2017. 2017: p. 368-369.

71. Waldron, D.J., Roberts, R.W., Dawes, C.J., and Tubby, P.J., *Friction Stir Welding-A Revolutionary New Joining Method*. 1998, SAE International.

72. XU, H., TANG, H., LIU, Z., XIE, M., and JIAO, J., *Microstructure and Mechanical Properties of 6082 Aluminum Alloy Joints Welded by MIG [J].* Hot Working Technology, 2010. 1: p. 042.

73. Zhang, H., Wang, M., Zhang, X., and Yang, G., *Microstructural characteristics and mechanical properties of bobbin tool friction stir welded 2A14-T6 aluminum alloy.* Materials & Design (1980-2015), 2015. 65: p. 559-566.

74. Martin, J. and Wei, S., *Friction Stir Welding Technology for Marine Applications*, in *Friction Stir Welding and Processing VIII*. 2015, Springer. p. 219-226.

75. Esmaily, M., Mortazavi, N., Osikowicz, W., Hindsefelt, H., Svensson, J., Halvarsson, M., Martin, J., and Johansson, L., *Bobbin and conventional friction stir welding of thick extruded AA6005-T6 profiles.* Materials & Design, 2016. 108: p. 114-125.

76. Chen, C. and Kovacevic, R., *Thermomechanical modelling and force analysis of friction stir welding by the finite element method.* Proceedings of the Institution of Mechanical Engineers, Part C: Journal of Mechanical Engineering Science, 2004. 218(5): p. 509-519.

77. Chen, Z., Pasang, T., and Qi, Y., *Shear flow and formation of Nugget zone during friction stir welding of aluminium alloy 5083-O.* Materials Science and Engineering: A, 2008. 474(1): p. 312-316.

78. Gopi, S. and Manonmani, K., *Microstructure and mechanical properties of friction stir welded 6082-T6 aluminium alloy.* Australian Journal of Mechanical Engineering, 2013. 11(2): p. 131-138.

79. Tamadon, A., Pons, D., Sued, M., Clucas, D., and Wong, E., *ANALOGUE MODELLING OF BOBBIN TOOL FRICTION STIR WELDING.*

80. Tamadon, A., Pons, D.J., Sued, K., and Clucas, D., *Development of Metallographic Etchants for the Microstructure Evolution of A6082-T6 BFSW Welds.* Metals, 2017. 7(10): p. 423.

81. Sued, M.K., *Fixed bobbin friction stir welding of marine grade aluminium.* 2015.

82. Ting, P.L., Tsai, C.Y., Chiu, L.H., and Cheng, C.P. *Tensile strength and metallurgical analysis in anodized Al/Cu joint using friction stir welding*. in *Key Engineering Materials*. 2015. Trans Tech Publ.

83. Trueba, L., Torres, M.A., Johannes, L.B., and Rybicki, D., *Process optimization in the self-reacting friction stir welding of aluminum 6061-T6.* International Journal of Material Forming, 2018. 11(4): p. 559-570.

84. Uthayakumar, M., Balasubramanian, V., Rani, A.M.A., and Hadzima, B. *Effects Of Welding On The Fatigue Behaviour Of Commercial Aluminum AA-1100 Joints*. in *IOP Conference Series: Materials Science and Engineering*. 2018. IOP Publishing.

85. Wahid, M.A., Siddiquee, A.N., Khan, Z.A., and Asjad, M., *Friction stir welds of Al alloy-Cu: an investigation on effect of plunge depth.* Archive of Mechanical Engineering, 2016. 63(4): p. 619-634.

86. Wang, G.-Q., Zhao, Y.-H., and Tang, Y.-Y., *Research Progress of Bobbin Tool Friction Stir Welding of Aluminum Alloys: A Review.* Acta Metallurgica Sinica (English Letters): p. 1-17.

87. Zahari, S.N., Sani, M.S.M., and Ishak, M. *Finite element modelling and updating of friction stir welding (FSW) joint for vibration analysis*. in *MATEC Web of Conferences*. 2017. EDP Sciences.

88. He, X.C. *Computational investigation of mechanical behaviour of FSW joints*. in *Applied Mechanics and Materials*. 2013. Trans Tech Publ.

89. Colegrove, P. and Shercliff, H., *Two-dimensional CFD modelling of flow round profiled FSW tooling.* Science and technology of welding and joining, 2004. 9(6): p. 483-492.

90. Kim, S.-D., Yoon, J.-Y., and Na, S.-J., *A study on the characteristics of FSW tool shapes based on CFD analysis.* Welding in the World, 2017. 61(5): p. 915-926.

91. Raguraman, D., Muruganandam, D., Senthilkumar, N., and Kumaraswamidhas, L., *Tensile Strength Prediction on Different FSW Tools Using ANN And Regression Equations.* International Journal of Applied Engineering Research, 2015. 10(49): p. 2015.

92. Krishnan, M.M., Maniraj, J., Deepak, R., and Anganan, K., *Prediction of optimum welding parameters for FSW of aluminium alloys AA6063 and A319 using RSM and ANN.* Materials Today: Proceedings, 2018. 5(1): p. 716-723.

93. Meyghani, B., Awang, M.B., Emamian, S.S., Mohd Nor, M.K.B., and Pedapati, S.R., *A comparison of different finite element methods in the thermal analysis of friction stir welding (FSW).* Metals, 2017. 7(10): p. 450.

94. Xu, S.-w., Deng, X., Reynolds, A.P., and Seidel, T., *Finite element simulation of material flow in friction stir welding.* Science and Technology of Welding and Joining, 2001. 6(3): p. 191-193.

95. Chen, C. and Kovacevic, R., *Finite element modeling of friction stir welding—thermal and thermomechanical analysis.* International Journal of machine tools and manufacture, 2003. 43(13): p. 1319-1326.

96. Zhang, Z. and Zhang, H., *A fully coupled thermo-mechanical model of friction stir welding.* The International Journal of Advanced Manufacturing Technology, 2008. 37(3-4): p. 279-293.

97. Al-Badour, F., Merah, N., Shuaib, A., and Bazoune, A., *Coupled Eulerian Lagrangian finite element modeling of friction stir welding processes.* Journal of Materials Processing Technology, 2013. 213(8): p. 1433-1439.

98. Zhao, H., *Friction stir welding (FSW) simulation using an Arbitrary Lagrangian-Eulerian (ALE) moving mesh approach*. 2005: West Virginia University ISBN: 0542468786.

99. Thomas, W., *Friction stir welding.* International Patent Appl. N° PCT/GB92/02203, 1991.

100. Arbegast, W.J., *A flow-partitioned deformation zone model for defect formation during friction stir welding.* Scripta materialia, 2008. 58(5): p. 372-376.

101. Morisada, Y., Imaizumi, T., and Fujii, H., *Clarification of material flow and defect formation during friction stir welding.* Science and Technology of Welding and Joining, 2015. 20(2): p. 130-137.

102. Waldron, D., Roberts, R., Dawes, C., and Tubby, P., *Friction Stir Welding-A Revolutionary New Joining Method*. 1998, SAE Technical Paper.

103. Zhang, Z. and Zhang, H., *Effect of welding parameters on mixing of materials in nugget zone of friction stir welds.* ACTA METALLURGICA SINICA-CHINESE EDITION-, 2007. 43(3): p. 321.

104. Leonard, A. and Lockyer, S. *Flaws in friction stir welds*. in *4th international symposium on friction stir welding*. 2003. Park City, Utah, USA.

105. Leal, R.M. and Loureiro, A. *Defects formation in friction stir welding of aluminium alloys*. in *Materials Science Forum*. 2004. Trans Tech Publ.

106. Le Jolu, T., Morgeneyer, T.F., Denquin, A., and Gourgues-Lorenzon, A.-F. *Effect of welding defects on plastic behaviour and fatigue lifetime of friction stir welded Al-Cu-Li alloy*. in *13th international conference on fracture*. 2013.

107. Dickerson, T. and Przydatek, J., *Fatigue of friction stir welds in aluminium alloys that contain root flaws.* International Journal of Fatigue, 2003. 25(12): p. 1399-1409.

108. Neumann, T., Zettler, R., Vilaca, P., Dos Santos, J., and Quintino, L., *Analysis of self-reacting friction stir welds in a 2024-T351 alloy.* Friction Stir Welding and Processing IV, 2007: p. 55-72.

109. Sued, M.K. and Pons, D.J., *Dynamic interaction between machine, tool, and substrate in bobbin friction stir welding.* International Journal of Manufacturing Engineering, 2016. 2016.

110. Chen, J., Fujii, H., Sun, Y., Morisada, Y., and Ueji, R., *Fine grained Mg–3Al–1Zn alloy with randomized texture in the double-sided friction stir welded joints.* Materials Science and Engineering: A, 2013. 580: p. 83-91.

111. Hejazi, I. and Mirsalehi, S.E., *Effect of pin penetration depth on double-sided friction stir welded joints of AA6061-T913 alloy.* Transactions of Nonferrous Metals Society of China, 2016. 26(3): p. 676-683.

112. Dolby, R., Sanderson, A., and Threadgill, P. *Recent developments and applications in electron beam and friction technologies*. in *7th International Aachen Welding Conference*. 2001.

113. Shen, J., Wang, F., Suhuddin, U.F., Hu, S., Li, W., and Dos Santos, J.F., *Crystallographic texture in bobbin tool friction-stir-welded aluminum.* Metallurgical and Materials Transactions A, 2015. 46(7): p. 2809-2813.

114. Li, W., Fu, T., Hütsch, L., Hilgert, J., Wang, F., Dos Santos, J., and Huber, N., *Effects of tool rotational and welding speed on microstructure and mechanical properties of bobbin-tool friction-stir welded Mg AZ31.* Materials & Design, 2014. 64: p. 714-720.

115. Liu, H., Hou, J., and Guo, H., *Effect of welding speed on microstructure and mechanical properties of self-reacting friction stir welded 6061-T6 aluminum alloy.* Materials & Design, 2013. 50: p. 872-878.

116. Wan, L., Huang, Y., Lv, Z., Lv, S., and Feng, J., *Effect of self-support friction stir welding on microstructure and microhardness of 6082-T6 aluminum alloy joint.* Materials & Design, 2014. 55: p. 197-203.

117. Wan, L., Huang, Y., Guo, W., Lv, S., and Feng, J., *Mechanical properties and microstructure of 6082-T6 aluminum alloy joints by self-support friction stir welding.* Journal of Materials Science & Technology, 2014. 30(12): p. 1243-1250.

118. Simões, F. and Rodrigues, D., *Material flow and thermo-mechanical conditions during friction stir welding of polymers: literature review, experimental results and empirical analysis.* Materials & Design, 2014. 59: p. 344-351.

119. Buffa, G., Donati, L., Fratini, L., and Tomesani, L., *Solid state bonding in extrusion and FSW: process mechanics and analogies.* Journal of Materials Processing Technology, 2006. 177(1): p. 344-347.

120. Genevois, C., Girard, M., Huneau, B., Sauvage, X., and Racineux, G., *Interfacial reaction during friction stir welding of Al and Cu.* Metallurgical and Materials Transactions A, 2011. 42(8): p. 2290.

121. Hilgert, J., dos Santos, J.F., and Huber, N., *Investigation of the Material Shear Layer in Bobbin Tool Friction Stir Welding.* Friction Stir Welding and Processing VI, 2011: p. 187-193.

122. Lin, S.-B., Zhao, Y.-H., He, Z.-Q., and Wu, L., *Modeling of friction stir welding process for tools design.* Frontiers of Materials Science, 2011. 5(2): p. 236-245.

123. Sued, M., Pons, D., and Lavroff, J. *Compression ratio effects in bobbin friction stir welding*. in *10th International Friction Stir Welding Symposium*. 2014.

124. Chouhan, D., Pal, S.K., and Garg, S., *Experimental study on the effect of welding parameters and tool pin profiles on mechanical properties of the FSW joints.* Dimensions, 2013. 806: p. 28.

125. Ragupathy, V., Bhat, M., and Prasad, M., *An Experimental Study of Discontinuities in Friction Stir Welded Joints through Nondestructive Testing.* Materials Evaluation, 2017. 75(3): p. 406-412.

126. Conti, P. and De Paulis, A., *A simple model to simulate the interlaminar stresses generated near the free edge of a composite laminate*, in *Delamination and debonding of materials*. 1985, ASTM International.

127. Seidel, T. and Reynolds, A.P., *Visualization of the material flow in AA2195 friction-stir welds using a marker insert technique.* Metallurgical and materials transactions A, 2001. 32(11): p. 2879-2884.

128. Reynolds, A.P., *Flow visualization and simulation in FSW.* Scripta materialia, 2008. 58(5): p. 338-342.

129. Liu, Z., Xin, R., Liu, D., Shu, X., and Liu, Q., *Textural variation in triple junction region of friction stir welded Mg alloys and its influence on twinning and fracture.* Materials Science and Engineering: A, 2016. 658: p. 185-191.

130. Liu, D., Xin, R., Sun, L., Zhou, Z., and Liu, Q., *Influence of sampling design on tensile properties and fracture behavior of friction stir welded magnesium alloys.* Materials Science and Engineering: A, 2013. 576: p. 207-216.

131. Liechty, B. and Webb, B., *Modeling the frictional boundary condition in friction stir welding.* International Journal of Machine Tools and Manufacture, 2008. 48(12): p. 1474-1485.

132. Liechty, B. and Webb, B., *Flow field characterization of friction stir processing using a particle-grid method.* journal of materials processing technology, 2008. 208(1): p. 431-443.

133. Liechty, B. and Webb, B., *The use of plasticine as an analog to explore material flow in friction stir welding.* Journal of Materials Processing Technology, 2007. 184(1): p. 240-250.

134. Zhu, Z., Wang, M., Zhang, H., Zhang, X., Yu, T., and Wu, Z., *A Finite Element Model to Simulate Defect Formation during Friction Stir Welding.* Metals, 2017. 7(7): p. 256.

135. Gratecap, F., Girard, M., Marya, S., and Racineux, G., *Exploring material flow in friction stir welding: Tool eccentricity and formation of banded structures.* International journal of material forming, 2012. 5(2): p. 99-107.

136. Tamadon, A., Pons, D.J., Clucas, D., and Sued, K., *Internal Material Flow Layers in AA6082-T6 Butt-Joints during Bobbin Friction Stir Welding.* Metals, 2019. 9(10): p. 1059.

137. Tamadon, A., Donthi Sudarshan, K.C., Pons, D., Sued, M.K., Clucas, D., and Wong, E.-H., *ANALOGUE MODELLING OF BOBBIN TOOL FRICTION STIR WELDING*, in *International Conference on Innovative Design and Manufacturing (ICIDM)*. 2016: Auckland.

138. Sued, M., Tamadon, A., and Pons, D., *Material flow visualization in bobbin friction stir welding by analogue model.* Proceedings of Mechanical Engineering Research Day, 2017. 2017: p. 1-2.

139. Tamadon, A., Pons, D., Sued, K., and Clucas, D., *Formation mechanisms for entry and exit defects in bobbin friction stir welding.* Metals, 2018. 8(1): p. 33.

140. Tamadon, A., Pons, D., Sued, K., and Clucas, D., *Development of metallographic etchants for the microstructure evolution of A6082-T6 BFSW welds.* Metals, 2017. 7(10): p. 423.

141. Tamadon, A., Pons, D., Sued, K., and Clucas, D., *Thermomechanical grain refinement in AA6082-T6 thin plates under Bobbin friction stir welding.* Metals, 2018. 8(6): p. 375.

142. Tamadon, A., Pons, D.J., and Clucas, D., *AFM Characterization of Stir-Induced Micro-Flow Features within the AA6082-T6 BFSW Welds.* Technologies, 2019. 7(4): p. 80.

143. Donthi Sudarshan, K.C., Tamadon, A., Pons, D., Sued, M.K., Clucas, D., and Wong, E.-H., *PREPARATION OF PLASTICINE MATERIAL FOR ANALOGUE MODELLING*, in *International Conference on Innovative Design and Manufacturing (ICIDM)*. 2016: Auckland.

144. Tamadon, A., Pons, D.J., Clucas, D., and Sued, K., *Texture Evolution in AA6082-T6 BFSW Welds: Optical Microscopy and EBSD Characterisation.* Materials, 2019. 12(19): p. 3215.

145. Xue, P., Ni, D., Wang, D., Xiao, B., and Ma, Z., *Effect of friction stir welding parameters on the microstructure and mechanical properties of the dissimilar Al–Cu joints.* Materials science and engineering: A, 2011. 528(13-14): p. 4683-4689.

146. Wiedenhoft, A.G., Amorim, H.J.d., Rosendo, T.d.S., Tier, M.A.D., and Reguly, A., *Effect of Heat Input on the Mechanical Behaviour of Al-Cu FSW Lap Joints.* Materials Research, 2018. 21(4).

147. Schneider, J., Cobb, J., Carpenter, J.S., and Mara, N.A., *Maintaining nano-lamellar microstructure in friction stir welding (FSW) of accumulative roll bonded (ARB) Cu-Nb nano-lamellar composites (NLC).* Journal of Materials Science & Technology, 2018. 34(1): p. 92-101.

148. Thomas, W. and Nicholas, E., *Friction stir welding for the transportation industries.* Materials & Design, 1997. 18(4): p. 269-273.

149. Adamowski, J. and Szkodo, M., *Friction Stir Welds (FSW) of aluminium alloy AW6082-T6.* Journal of Achievements in Materials and Manufacturing Engineering, 2007. 20(1-2): p. 403-406.

150. Scialpi, A., De Filippis, L., and Cavaliere, P., *Influence of shoulder geometry on microstructure and mechanical properties of friction stir welded 6082 aluminium alloy.* Materials & design, 2007. 28(4): p. 1124-1129.

151. De Giorgi, M., Scialpi, A., Panella, F., and De Filippis, L., *Effect of shoulder geometry on residual stress and fatigue properties of AA6082 FSW joints.* Journal of Mechanical Science and Technology, 2009. 23(1): p. 26-35.

152. Moreira, P., De Jesus, A., Ribeiro, A., and De Castro, P., *Fatigue crack growth in friction stir welds of 6082-T6 and 6061-T6 aluminium alloys: a comparison.* Theoretical and Applied Fracture Mechanics, 2008. 50(2): p. 81-91.

153. Moreira, P., Santos, T., Tavares, S., Richter-Trummer, V., Vilaça, P., and De Castro, P., *Mechanical and metallurgical characterization of friction stir welding joints of AA6061-T6 with AA6082-T6.* Materials & design, 2009. 30(1): p. 180-187.

154. Nandan, R., Roy, G., Lienert, T., and Debroy, T., *Three-dimensional heat and material flow during friction stir welding of mild steel.* Acta Materialia, 2007. 55(3): p. 883-895.

155. Sued, M.K. and Pons, D.J., *Dynamic Interaction between Machine, Tool, and Substrate in Bobbin Friction Stir Welding.* International Journal of Manufacturing Engineering, 2016. 2016: p. 14 DOI: 10.1155/2016/8697453.

156. Sharma, M., Singh, A., Singh, P., Pathak, K., and Agnihotri, G., *Experimental Investigation of the effect of die angle on extrusion process using plasticine.* Experimental Techniques, 2011. 35(6): p. 38-44.

157. Dai, Q., Wang, X., Hou, Z., Wu, J., and Shi, Q., *Microcavities accompanying a zigzag line in friction stir welded A6082-T6 alloy joint.* Science and Technology of Welding and Joining, 2015. 20(1): p. 68-74.

158. Davis, J.R., *Aluminum and aluminum alloys, JR Davis & Associates, ASM International.* Handbook Committee. 711.

159. Sasabe, S. and Matsumoto, T., *Mechanical properties of A6082 welded joints with Nd–YAG laser.* Welding International, 2012. 26(5): p. 351-359.

160. Mohamed, A. and Samuel, F., *A review on the heat treatment of Al-Si-Cu/Mg casting alloys*, in *Heat Treatment-Conventional and Novel Applications*. 2012, InTech.

161. Heurtier, P., Jones, M., Desrayaud, C., Driver, J.H., Montheillet, F., and Allehaux, D., *Mechanical and thermal modelling of friction stir welding.* Journal of Materials Processing Technology, 2006. 171(3): p. 348-357.

162. Mrówka-Nowotnik, G. and Sieniawski, J., *Influence of heat treatment on the microstructure and mechanical properties of 6005 and 6082 aluminium alloys.* Journal of Materials Processing Technology, 2005. 162: p. 367-372.

163. Panagopoulos, C., Georgiou, E., and Gavras, A., *Corrosion and wear of 6082 aluminum alloy.* Tribology International, 2009. 42(6): p. 886-889.

164. Birol, Y. and Seracettin, A., *Cooling slope casting to produce EN AW 6082 forging stock for manufacture of suspension components.* Transactions of Nonferrous Metals Society of China, 2014. 24(6): p. 1674-1682.

165. Frigaard, Ø., Grong, Ø., and Midling, O., *A process model for friction stir welding of age hardening aluminum alloys.* Metallurgical and materials transactions A, 2001. 32(5): p. 1189-1200.

166. Vander Voort, G. and Manilova, E.P., *Metallographic Etching of Aluminum and Its Alloys.* Buehler Ltd, EUA, 2009.

167. Myhr, O., Klokkehaug, S., Grong, O., Fjær, H., and Kluken, A., *Modeling of microstructure evolution, residual stresses and distortions in 6082-T6 aluminum weldments.* WELDING JOURNAL-NEW YORK-, 1998. 77: p. 286-s.

168. Airod, A., *Fundamental Analysis of the Deformation Behaviour of 5083 and 6082 Aluminium Alloys*. 2006, Ghent University.

169. Vander Voort, G.F., Lampman, S.R., Sanders, B.R., Anton, G.J., Polakowski, C., Kinson, J., Muldoon, K., Henry, S.D., and Scott Jr, W.W., *ASM handbook.* Metallography and microstructures, 2004. 9: p. 44073-0002.

170. Zipperian, D.C., *Metallographic handbook.* Chief Technical Officier PACE Technologies, Tucson (AR), 2011.

171. Schneider, J., Chen, P., and Nunes Jr, A.C., *Formation of Oxides in the Interior of Friction Stir Welds.* 2016.

172. Schneider, J. and Nunes Jr, A.C., *Origins of Line Defects in Self-Reacting Friction Stir Welds and Their Impact on Weld Quality.* 2016.

173. Kah, P., Rajan, R., Martikainen, J., and Suoranta, R., *Investigation of weld defects in friction-stir welding and fusion welding of aluminium alloys.* International Journal of Mechanical and Materials Engineering, 2015. 10(1): p. 26.

174. McNelley, T., Swaminathan, S., and Su, J., *Recrystallization mechanisms during friction stir welding/processing of aluminum alloys.* Scripta Materialia, 2008. 58(5): p. 349-354.

175. Nandan, R., DebRoy, T., and Bhadeshia, H., *Recent advances in friction-stir welding–process, weldment structure and properties.* Progress in Materials Science, 2008. 53(6): p. 980-1023.

176. Schmidt, H. and Hattel, J., *A local model for the thermomechanical conditions in friction stir welding.* Modelling and simulation in materials science and engineering, 2004. 13(1): p. 77.

177. Nandan, R., Roy, G., and Debroy, T., *Numerical simulation of three-dimensional heat transfer and plastic flow during friction stir welding.* Metallurgical and materials transactions A, 2006. 37(4): p. 1247-1259.

178. Song, M. and Kovacevic, R., *Thermal modeling of friction stir welding in a moving coordinate system and its validation.* International Journal of Machine Tools and Manufacture, 2003. 43(6): p. 605-615.

179. Sofuoglu, H. and Rasty, J., *Flow behavior of Plasticine used in physical modeling of metal forming processes.* Tribology International, 2000. 33(8): p. 523-529.

180. Kumar, K. and Kailas, S.V., *The role of friction stir welding tool on material flow and weld formation.* Materials Science and Engineering: A, 2008. 485(1-2): p. 367-374.

181. Babu, G.R., Murti, K., and Janardhana, G.R., *An experimental study on the effect of welding parameters on mechanical and microstructural properties of AA 6082-T6*

friction stir welded butt joints. ARPN Journal of engineering and applied sciences, 2008. 3(5): p. 68-74.

182. Seidel, T. and Reynolds, A.P., *Two-dimensional friction stir welding process model based on fluid mechanics.* Science and technology of welding and joining, 2003. 8(3): p. 175-183.

183. Tamadon, A., Pons, D.J., Sued, K., and Clucas, D., *Formation Mechanisms for Entry and Exit Defects in Bobbin Friction Stir Welding.* Metals, 2018. 8(1): p. 33.

184. Jata, K. and Semiatin, S., *Continuous dynamic recrystallization during friction stir welding of high strength aluminum alloys*. 2000, AIR FORCE RESEARCH LAB WRIGHT-PATTERSON AFB OH MATERIALS AND MANUFACTURING DIRECTORATE.

185. Tamadon, A., DS, K.C., Pons, D., Sued, M., Clucas, D., and Wong, E., *ANALOGUE MODELLING OF BOBBIN TOOL FRICTION STIR WELDING.*

186. Czubayko, U., Sursaeva, V., Gottstein, G., and Shvindlerman, L., *Influence of triple junctions on grain boundary motion.* Acta materialia, 1998. 46(16): p. 5863-5871.

187. Wang, D., Xiao, B., Ma, Z., and Zhang, H., *Friction stir welding of Zr55Cu30Al10Ni5 bulk metallic glass to Al–Zn–Mg–Cu alloy.* Scripta Materialia, 2009. 60(2): p. 112-115.

188. Fujii, H., Sun, Y., Inada, K., Ji, Y., Yokoyama, Y., Kimura, H., and Inoue, A., *Fabrication of Fe-based metallic glass particle reinforced Al-based composite materials by friction stir processing.* Materials Transactions, 2011. 52(8): p. 1634-1640.

189. Sun, Y., Ji, Y., Fujii, H., Nakata, K., and Nogi, K., *Microstructure and mechanical properties of friction stir welded joint of Zr55Cu30Al10Ni5 bulk metallic glass with pure copper.* Materials Science and Engineering: A, 2010. 527(15): p. 3427-3432.

190. Li, F., Zhang, D., Luo, Z., Tan, C., and Lin, J., *Microstructure and mechanical properties of friction stir welded joint of Zr46Cu46Al8 bulk metallic glass with pure aluminum.* Materials Science and Engineering: A, 2013. 588: p. 196-200.

191. Sato, Y.S., Yamashita, F., Sugiura, Y., Park, S.H.C., and Kokawa, H., *FIB-assisted TEM study of an oxide array in the root of a friction stir welded aluminium alloy.* Scripta materialia, 2004. 50(3): p. 365-369.

192. Sato, Y.S., Takauchi, H., Park, S.H.C., and Kokawa, H., *Characteristics of the kissing-bond in friction stir welded Al alloy 1050.* Materials Science and Engineering: A, 2005. 405(1-2): p. 333-338.

193. Kobata, J., Takigawa, Y., Chung, S., Tsuda, H., Kimura, H., and Higashi, K., *Nanoscale amorphous "band-like" structure induced by friction stir processing in Zr55Cu30Al10Ni5 bulk metallic glass.* Materials Letters, 2007. 61(17): p. 3771-3773.

194. Ogura, T., Saito, Y., Nishida, T., Nishida, H., Yoshida, T., Omichi, N., Fujimoto, M., and Hirose, A., *Partitioning evaluation of mechanical properties and the interfacial microstructure in a friction stir welded aluminum alloy/stainless steel lap joint.* Scripta Materialia, 2012. 66(8): p. 531-534.

195. Frøseth, A.G., Høier, R., Derlet, P.M., Andersen, S.J., and Marioara, C.D., *Bonding in MgSi and Al-Mg-Si compounds relevant to Al-Mg-Si alloys.* Physical Review B, 2003. 67(22): p. 224106.

196. Avallone, E.A. and Baumeister III, T., *Marks' standard handbook for mechanical engineers.* 1986.

197. Mohamed, A. and Samuel, F., *A review on the heat treatment of Al-Si-Cu/Mg casting alloys.* Heat Treatment-Conventional and Novel Applications, 2012: p. 55-72.

198. Davies, P., Wynne, B., Rainforth, W., Thomas, M., and Threadgill, P., *Development of microstructure and crystallographic texture during stationary shoulder friction stir welding of Ti-6Al-4V.* Metallurgical and Materials Transactions A, 2011. 42(8): p. 2278-2289.

199. Davis, J.R., *Aluminum and aluminum alloys*. 1993: ASM international ISBN: 087170496X.

200. Prangnell, P. and Heason, C., *Grain structure formation during friction stir welding observed by the 'stop action technique'.* Acta Materialia, 2005. 53(11): p. 3179-3192.

201. Tamadon, A., Pons, D., Sued, M., Clucas, D., and Wong, E., *PREPARATION OF PLASTICINE MATERIAL FOR ANALOGUE MODELLING.*

202. Beardsley, A., Bishop, C., and Kral, M., *EBSD Characterization of Pilgered Alloy 800H After Heat Treatment.* Materials Performance and Characterization, 2016. 5(5): p. 717-739.

203. Jackson, M.A., Groeber, M.A., Uchic, M.D., Rowenhorst, D.J., and De Graef, M., *h5ebsd: an archival data format for electron back-scatter diffraction data sets.* Integrating Materials and Manufacturing Innovation, 2014. 3(1): p. 4.

204. Paul, H., Driver, J., Tarasek, A., Wajda, W., and Miszczyk, M., *Mechanism of macroscopic shear band formation in plane strain compressed fine-grained aluminium.* Materials Science and Engineering: A, 2015. 642: p. 167-180.

205. Li, R., Xie, Q., Wang, Y.-D., Liu, W., Wang, M., Wu, G., Li, X., Zhang, M., Lu, Z., and Geng, C., *Unraveling submicron-scale mechanical heterogeneity by three-dimensional X-ray microdiffraction.* Proceedings of the National Academy of Sciences, 2018. 115(3): p. 483-488.

206. Jeong, H.T., Park, S.D., and Ha, T.K., *Evolution of shear texture according to shear strain ratio in rolled FCC metal sheets.* Metals and Materials International, 2006. 12(1): p. 21-26.

207. Murr, L., Liu, G., and McClure, J., *A TEM study of precipitation and related microstructures in friction-stir-welded 6061 aluminium.* Journal of Materials Science, 1998. 33(5): p. 1243-1251.

208. Lityńska, L., Braun, R., Staniek, G., Dalle Donne, C., and Dutkiewicz, J., *TEM study of the microstructure evolution in a friction stir-welded AlCuMgAg alloy.* Materials Chemistry and Physics, 2003. 81(2-3): p. 293-295.

209. Murr, L., Liu, G., and McClure, J., *Dynamic recrystallization in friction-stir welding of aluminium alloy 1100.* Journal of materials science letters, 1997. 16(22): p. 1801-1803.

210. Fonda, R. and Knipling, K., *Texture development in near-α Ti friction stir welds.* Acta Materialia, 2010. 58(19): p. 6452-6463.

211. Fonda, R., Knipling, K., and Rowenhorst, D., *EBSD analysis of friction stir weld textures.* Jom, 2014. 66(1): p. 149-155.

212. Thomas, W., Nicholas, E., Needham, J., Murch, M., Temple-Smith, P., and Dawes, C., *Friction stir butt welding, Int. Patent No*. 1991, PCT/GB92/02203.

213. Wang, F., Li, W., Shen, J., Wen, Q., and dos Santos, J., *Improving weld formability by a novel dual-rotation bobbin tool friction stir welding.* Journal of Materials Science & Technology, 2018. 34(1): p. 135-139.

214. Huang, Y., Wan, L., Lv, S., and Feng, J., *Novel design of tool for joining hollow extrusion by friction stir welding.* Science and Technology of Welding and Joining, 2013. 18(3): p. 239-246.

215. Węglowska, A., *The Use of a Bobbin Tool in the Friction Stir Welding of Plates Made of Aluminium Alloy EN AW 6082–T6.* Biuletyn Instytutu Spawalnictwa w Gliwicach, 2018. 62.

216. Chen, S., Lu, A., Yang, D., Lu, S., Dong, J., and Dong, C. *Analysis on flow pattern of bobbin tool friction stir welding for 6082 aluminum*. in *Proceedings of the 1st International joint symposium on joining and welding*. 2013. Elsevier.

217. Hilgert, J., Dos Santos, J.F., and Huber, N., *Shear layer modelling for bobbin tool friction stir welding.* Science and Technology of Welding and Joining, 2012. 17(6): p. 454-459.

218. Barényi, I., Eckert, M., Majerík, J., and Bezecný, J., *AFM and nanoindentation study of selected aluminium alloys.* Zeszyty Naukowe Politechniki Rzeszowskiej. Mechanika, 2018: p. 143-152.

219. Chrominski, W. and Lewandowska, M., *Precipitation phenomena in ultrafine grained Al–Mg–Si alloy with heterogeneous microstructure.* Acta Materialia, 2016. 103: p. 547-557.

220. Marioara, C., Andersen, S., Jansen, J., and Zandbergen, H., *Atomic model for GP-zones in a 6082 Al–Mg–Si system.* Acta Materialia, 2001. 49(2): p. 321-328.

221. Dadbakhsh, S. and Karimi Taheri, A., *Study on static strain aging of 6082 aluminium alloy.* Materials Science and Technology, 2010. 26(2): p. 169-175.

222. Marioara, C., Andersen, S., Jansen, J., and Zandbergen, H., *The influence of temperature and storage time at RT on nucleation of the β ″phase in a 6082 Al–Mg–Si alloy.* Acta Materialia, 2003. 51(3): p. 789-796.

Appendix A: Publications

Deputy Vice-Chancellor's Office
Postgraduate Research Office

UNIVERSITY OF CANTERBURY
Te Whare Wānanga o Waitaha
CHRISTCHURCH NEW ZEALAND

Co-Authorship Form

This form is to accompany the submission of any thesis that contains research reported in co-authored work that has been published, accepted for publication, or submitted for publication. A copy of this form should be included for each co-authored work that is included in the thesis. Completed forms should be included at the front (after the thesis abstract) of each copy of the thesis submitted for examination and library deposit.

Please indicate the chapter/section/pages of this thesis that are extracted from co-authored work and provide details of the publication or submission from the extract comes:

CHAPTER 4

Please detail the nature and extent (%) of contribution by the candidate:

80%

Author Contributions: Conceptualization, A.T. and D.J.P.; Methodology, A.T.; Validation, A.T.; Formal analysis, A.T. and D.J.P.;Writing—original draft preparation, A.T.;Writing—review and editing, A.T. and D.J.P.; Supervision, D.J.P., K.S. and D.C.

Tamadon, A.; Pons, D.J.; Sued, K.; Clucas, D. Formation Mechanisms for Entry and Exit Defects in Bobbin Friction Stir Welding. Metals 2018, 8, 33.

DOI: https://doi.org/10.3390/met8010033

Certification by Co-authors:

If there is more than one co-author then a single co-author can sign on behalf of all

The undersigned certifies that:

- The above statement correctly reflects the nature and extent of the Doctoral candidate's contribution to this co-authored work
- In cases where the candidate was the lead author of the co-authored work he or she wrote the text

Name: *Dirk Pons* Signature: *DP* Date: *28 Nov 2019*

Deputy Vice-Chancellor's Office
Postgraduate Research Office

UNIVERSITY OF CANTERBURY
Te Whare Wānanga o Waitaha
CHRISTCHURCH NEW ZEALAND

Co-Authorship Form

This form is to accompany the submission of any thesis that contains research reported in co-authored work that has been published, accepted for publication, or submitted for publication. A copy of this form should be included for each co-authored work that is included in the thesis. Completed forms should be included at the front (after the thesis abstract) of each copy of the thesis submitted for examination and library deposit.

Please indicate the chapter/section/pages of this thesis that are extracted from co-authored work and provide details of the publication or submission from the extract comes:

CHAPTER 5

Please detail the nature and extent (%) of contribution by the candidate:

80%

Author Contributions: Conceptualization, A.T. and D.J.P.; methodology, A.T; validation, A.T.; formal analysis, A.T. and D.J.P; writing—original draft preparation, A.T.; writing—review and editing, A.T., D.J.P., and D.C.; supervision, D.J.P. and D.C. All authors have read and agreed to the published version of the manuscript.

Tamadon, A.; Pons, D.J.; Clucas, D. Flow-Based Anatomy of Bobbin Friction-Stirred Weld; AA6082-T6 Aluminium Plate and Analogue Plasticine Model. Appl. Mech. 2020, 1, 3-19.

DOI: https://doi.org/10.3390/applmech1010002

Certification by Co-authors:

If there is more than one co-author then a single co-author can sign on behalf of all

The undersigned certifies that:

- The above statement correctly reflects the nature and extent of the Doctoral candidate's contribution to this co-authored work
- In cases where the candidate was the lead author of the co-authored work he or she wrote the text

Name: *Dirk Pons* Signature: *DP* Date: *18 Feb 2020*

Deputy Vice-Chancellor's Office
Postgraduate Research Office

UNIVERSITY OF CANTERBURY
Te Whare Wānanga o Waitaha
CHRISTCHURCH NEW ZEALAND

Co-Authorship Form

This form is to accompany the submission of any thesis that contains research reported in co-authored work that has been published, accepted for publication, or submitted for publication. A copy of this form should be included for each co-authored work that is included in the thesis. Completed forms should be included at the front (after the thesis abstract) of each copy of the thesis submitted for examination and library deposit.

Please indicate the chapter/section/pages of this thesis that are extracted from co-authored work and provide details of the publication or submission from the extract comes:

CHAPTER 5

Please detail the nature and extent (%) of contribution by the candidate:

80%

Author Contributions: Conceptualization, A.T. and D.J.P.; Methodology, A.T.; Validation, A.T., KC. DC.; Formal analysis, A.T. and D.J.P.;Writing—original draft preparation, A.T.;Writing—review and editing, A.T. and D.J.P.; Supervision, D.J.P., K.S., E.W. and D.C.

Tamadon, A.; DS, K.C.; Pons, D.; Sued, M.; Clucas, D.; Wong, E. Analogue modelling of bobbin tool friction stir welding. In Proceedings of the International Conference on Innovative Design and Manufacturing, Auckland, New Zealand, 14–16 September 2016.

Certification by Co-authors:

If there is more than one co-author then a single co-author can sign on behalf of all

The undersigned certifies that:

- The above statement correctly reflects the nature and extent of the Doctoral candidate's contribution to this co-authored work
- In cases where the candidate was the lead author of the co-authored work he or she wrote the text

Name: *Dirk Pons* Signature: *DP* Date: *28 Nov 2019*

Deputy Vice-Chancellor's Office
Postgraduate Research Office

UNIVERSITY OF CANTERBURY
Te Whare Wānanga o Waitaha
CHRISTCHURCH NEW ZEALAND

Co-Authorship Form

This form is to accompany the submission of any thesis that contains research reported in co-authored work that has been published, accepted for publication, or submitted for publication. A copy of this form should be included for each co-authored work that is included in the thesis. Completed forms should be included at the front (after the thesis abstract) of each copy of the thesis submitted for examination and library deposit.

Please indicate the chapter/section/pages of this thesis that are extracted from co-authored work and provide details of the publication or submission from the extract comes:

CHAPTER 6

Please detail the nature and extent (%) of contribution by the candidate:

80%

Author Contributions: Conceptualization, A.T. and D.J.P.; methodology, A.T.; validation, A.T.; formal analysis, A.T. and D.J.P.; writing—original draft preparation, A.T.; writing—review and editing, A.T., D.J.P., and D.C.; supervision, D.J.P. and D.C. All authors have read and agreed to the published version of the manuscript.

Tamadon, A.; Pons, D.J.; Clucas, D. Structural Anatomy of Tunnel Void Defect in Bobbin Friction Stir Welding, Elucidated by the Analogue Modelling. Appl. Syst. Innov. 2020, 3, 2.

DOI: https://doi.org/10.3390/asi3010002

Certification by Co-authors:

If there is more than one co-author then a single co-author can sign on behalf of all

The undersigned certifies that:

- The above statement correctly reflects the nature and extent of the Doctoral candidate's contribution to this co-authored work
- In cases where the candidate was the lead author of the co-authored work he or she wrote the text

Name: *Dirk Pons* Signature: *DP* Date: *18 Feb 2020*

Deputy Vice-Chancellor's Office
Postgraduate Research Office

UNIVERSITY OF CANTERBURY
Te Whare Wānanga o Waitaha
CHRISTCHURCH NEW ZEALAND

Co-Authorship Form

This form is to accompany the submission of any thesis that contains research reported in co-authored work that has been published, accepted for publication, or submitted for publication. A copy of this form should be included for each co-authored work that is included in the thesis. Completed forms should be included at the front (after the thesis abstract) of each copy of the thesis submitted for examination and library deposit.

Please indicate the chapter/section/pages of this thesis that are extracted from co-authored work and provide details of the publication or submission from the extract comes:

CHAPTER 6

Please detail the nature and extent (%) of contribution by the candidate:

80%

Author Contributions: Conceptualization, A.T. and D.J.P.; Methodology, A.T.; Validation, A.T.; Formal analysis, A.T. and D.J.P.;Writing—original draft preparation, A.T.;Writing—review and editing, A.T., K.S. and D.J.P.; Supervision, D.J.P., and K.S.

Sued, M.; Tamadon, A.; Pons, D. Material flow visualization in bobbin friction stir welding by analogue model. In Proceedings of the Mechanical Engineering Research Day 2017, Melaka, Malaysia, 30 March 2017; Volume 2017, pp. 1–2.

Certification by Co-authors:

If there is more than one co-author then a single co-author can sign on behalf of all

The undersigned certifies that:

- The above statement correctly reflects the nature and extent of the Doctoral candidate's contribution to this co-authored work
- In cases where the candidate was the lead author of the co-authored work he or she wrote the text

Name: *Dirk Pons* Signature: *DP* Date: *28 Nov 2019*

Deputy Vice-Chancellor's Office
Postgraduate Research Office

UNIVERSITY OF CANTERBURY
Te Whare Wānanga o Waitaha
CHRISTCHURCH NEW ZEALAND

Co-Authorship Form

This form is to accompany the submission of any thesis that contains research reported in co-authored work that has been published, accepted for publication, or submitted for publication. A copy of this form should be included for each co-authored work that is included in the thesis. Completed forms should be included at the front (after the thesis abstract) of each copy of the thesis submitted for examination and library deposit.

Please indicate the chapter/section/pages of this thesis that are extracted from co-authored work and provide details of the publication or submission from the extract comes:

CHAPTER 7

Please detail the nature and extent (%) of contribution by the candidate:

65%

Author Contributions: Conceptualization, A.T., KC. DC., and D.J.P.; Methodology, A.T., KC.DC.; Validation, A.T.; Formal analysis, A.T. KC.DC., and D.J.P.;Writing—original draft preparation, KC.DC. and A.T.;Writing—review and editing, A.T. and D.J.P.; Supervision, D.J.P., K.S., E.W. and D.C.

Donthi Sudarshan, K.C.; Tamadon, A.; Pons, D.; Sued, M.; Clucas, D.; Wong, E. Preparation of Plasticine Material for Analogue Modelling. In Proceedings of the International Conference on Innovative Design and Manufacturing (ICIDM 2016), Auckland, New Zealand, 24–26 January 2016.

Certification by Co-authors:

If there is more than one co-author then a single co-author can sign on behalf of all

The undersigned certifies that:

- The above statement correctly reflects the nature and extent of the Doctoral candidate's contribution to this co-authored work
- In cases where the candidate was the lead author of the co-authored work he or she wrote the text

Name: *Dirk Pons* Signature: *DP* Date: *28 Nov 2019*

Deputy Vice-Chancellor's Office
Postgraduate Research Office

UNIVERSITY OF CANTERBURY
Te Whare Wānanga o Waitaha
CHRISTCHURCH NEW ZEALAND

Co-Authorship Form

This form is to accompany the submission of any thesis that contains research reported in co-authored work that has been published, accepted for publication, or submitted for publication. A copy of this form should be included for each co-authored work that is included in the thesis. Completed forms should be included at the front (after the thesis abstract) of each copy of the thesis submitted for examination and library deposit.

Please indicate the chapter/section/pages of this thesis that are extracted from co-authored work and provide details of the publication or submission from the extract comes:

CHAPTER 9

Please detail the nature and extent (%) of contribution by the candidate:

80%

Author Contributions: Conceptualization, A.T. and D.J.P.; Methodology, A.T.; Validation, A.T.; Formal analysis, A.T. and D.J.P.;Writing—original draft preparation, A.T.;Writing—review and editing, A.T. and D.J.P.; Supervision, D.J.P., K.S. and D.C.

Tamadon, A.; Pons, D.J.; Sued, K.; Clucas, D. Development of Metallographic Etchants for the Microstructure Evolution of A6082-T6 BFSW Welds. Metals 2017, 7, 423.

DOI: https://doi.org/10.3390/met7100423

Certification by Co-authors:

If there is more than one co-author then a single co-author can sign on behalf of all

The undersigned certifies that:

- The above statement correctly reflects the nature and extent of the Doctoral candidate's contribution to this co-authored work
- In cases where the candidate was the lead author of the co-authored work he or she wrote the text

Name: *Dirk Pons* Signature: *DP* Date: *28 Nov 2019*

Deputy Vice-Chancellor's Office
Postgraduate Research Office

UNIVERSITY OF CANTERBURY
Te Whare Wānanga o Waitaha
CHRISTCHURCH NEW ZEALAND

Co-Authorship Form

This form is to accompany the submission of any thesis that contains research reported in co-authored work that has been published, accepted for publication, or submitted for publication. A copy of this form should be included for each co-authored work that is included in the thesis. Completed forms should be included at the front (after the thesis abstract) of each copy of the thesis submitted for examination and library deposit.

Please indicate the chapter/section/pages of this thesis that are extracted from co-authored work and provide details of the publication or submission from the extract comes:

CHAPTER 11

Please detail the nature and extent (%) of contribution by the candidate:

80%

Author Contributions: Conceptualization, A.T. and D.J.P.; Methodology, A.T.; Validation, A.T.; Formal analysis, A.T. and D.J.P.;Writing—original draft preparation, A.T.;Writing—review and editing, A.T. and D.J.P.; Supervision, D.J.P., K.S. and D.C.

Tamadon, A.; Pons, D.J.; Sued, K.; Clucas, D. Thermomechanical Grain Refinement in AA6082-T6 Thin Plates under Bobbin Friction Stir Welding. Metals 2018, 8, 375.

DOI: https://doi.org/10.3390/met8060375

Certification by Co-authors:

If there is more than one co-author then a single co-author can sign on behalf of all

The undersigned certifies that:

- The above statement correctly reflects the nature and extent of the Doctoral candidate's contribution to this co-authored work
- In cases where the candidate was the lead author of the co-authored work he or she wrote the text

Name: *Dirk Pons* Signature: *DP* Date: *28 Nov 2019*

Deputy Vice-Chancellor's Office
Postgraduate Research Office

UNIVERSITY OF CANTERBURY
Te Whare Wānanga o Waitaha
CHRISTCHURCH NEW ZEALAND

Co-Authorship Form

This form is to accompany the submission of any thesis that contains research reported in co-authored work that has been published, accepted for publication, or submitted for publication. A copy of this form should be included for each co-authored work that is included in the thesis. Completed forms should be included at the front (after the thesis abstract) of each copy of the thesis submitted for examination and library deposit.

Please indicate the chapter/section/pages of this thesis that are extracted from co-authored work and provide details of the publication or submission from the extract comes:

CHAPTER 12

Please detail the nature and extent (%) of contribution by the candidate:

80%

Author Contributions: Conceptualization, A.T. and D.J.P.; Methodology, A.T.; Validation, A.T.; Formal analysis, A.T. and D.J.P.;Writing—original draft preparation, A.T.;Writing—review and editing, A.T. and D.J.P.; Supervision, D.J.P., K.S. and D.C.

Tamadon, A.; Pons, D.J.; Clucas, D.; Sued, K. Texture Evolution in AA6082-T6 BFSW Welds: Optical Microscopy and EBSD Characterisation. Materials 2019, 12, 3215.

DOI: https://doi.org/10.3390/ma12193215

Certification by Co-authors:

If there is more than one co-author then a single co-author can sign on behalf of all

The undersigned certifies that:

- The above statement correctly reflects the nature and extent of the Doctoral candidate's contribution to this co-authored work
- In cases where the candidate was the lead author of the co-authored work he or she wrote the text

Name: *Dirk Pons* Signature: *DP* Date: *28 Nov 2019*

Deputy Vice-Chancellor's Office
Postgraduate Research Office

UNIVERSITY OF CANTERBURY
Te Whare Wānanga o Waitaha
CHRISTCHURCH NEW ZEALAND

Co-Authorship Form

This form is to accompany the submission of any thesis that contains research reported in co-authored work that has been published, accepted for publication, or submitted for publication. A copy of this form should be included for each co-authored work that is included in the thesis. Completed forms should be included at the front (after the thesis abstract) of each copy of the thesis submitted for examination and library deposit.

Please indicate the chapter/section/pages of this thesis that are extracted from co-authored work and provide details of the publication or submission from the extract comes:

CHAPTER 14

Please detail the nature and extent (%) of contribution by the candidate:

80%

Author Contributions: Conceptualization, A.T. and D.J.P.; Methodology, A.T.; Validation, A.T.; Formal analysis, A.T. and D.J.P.;Writing—original draft preparation, A.T.;Writing—review and editing, A.T. and D.J.P.; Supervision, D.J.P. and D.C.

Tamadon, A.; Pons, D.J.; Clucas, D. AFM Characterization of Stir-Induced Micro-Flow Features within the AA6082-T6 BFSW Welds. Technologies 2019, 7, 80.

DOI: https://doi.org/10.3390/technologies7040080

Certification by Co-authors:

If there is more than one co-author then a single co-author can sign on behalf of all

The undersigned certifies that:

- The above statement correctly reflects the nature and extent of the Doctoral candidate's contribution to this co-authored work
- In cases where the candidate was the lead author of the co-authored work he or she wrote the text

Name: *Dirk Pons* Signature: *DP* Date: *28 Nov 2019*

Deputy Vice-Chancellor's Office
Postgraduate Research Office

UNIVERSITY OF CANTERBURY
Te Whare Wānanga o Waitaha
CHRISTCHURCH NEW ZEALAND

Co-Authorship Form

This form is to accompany the submission of any thesis that contains research reported in co-authored work that has been published, accepted for publication, or submitted for publication. A copy of this form should be included for each co-authored work that is included in the thesis. Completed forms should be included at the front (after the thesis abstract) of each copy of the thesis submitted for examination and library deposit.

Please indicate the chapter/section/pages of this thesis that are extracted from co-authored work and provide details of the publication or submission from the extract comes:

CHAPTER 15

Please detail the nature and extent (%) of contribution by the candidate:

80%

Author Contributions: Conceptualization, A.T. and D.J.P.; Methodology, A.T.; Validation, A.T.; Formal analysis, A.T. and D.J.P.;Writing—original draft preparation, A.T.;Writing—review and editing, A.T. and D.J.P.; Supervision, D.J.P., K.S. and D.C.

Tamadon, A.; Pons, D.J.; Clucas, D.; Sued, K. Internal Material Flow Layers in AA6082-T6 Butt-Joints during Bobbin Friction Stir Welding. Metals 2019, 9, 1059.

DOI: https://doi.org/10.3390/met9101059

Certification by Co-authors:

If there is more than one co-author then a single co-author can sign on behalf of all

The undersigned certifies that:

- The above statement correctly reflects the nature and extent of the Doctoral candidate's contribution to this co-authored work
- In cases where the candidate was the lead author of the co-authored work he or she wrote the text

Name: *Dirk Pons* Signature: *DP* Date: *28 Nov 2019*